Time-resolved step-scan FTIR spectroscopy on photosystem II

im Fachbereich Physik der
Freien Universität Berlin
eingereichte Dissertation
zur Erlangung des Grades
eines Dr. rer. nat.

von Matthias Benjamin Schönborn

2017

Date of defense: 2017-11-08
First supervisor: Prof. Dr. Holger Dau
Second supervisor: Prof. Dr. Joachim Heberle

1. Abstract

Photosystem II is the water-splitting protein active in oxygenic photosynthesis. Its function is to split water into electrons and protons, creating molecular oxygen as a by-product. Ongoing research aims at unravelling the details of this water-splitting process. One major motivation to understand this process is to gain insight into key mechanisms, so as to use this knowledge to create artificial catalysts for water splitting and hydrogen production. These catalysts will play a key role in the future's hydrogen economy: the efficient creation of hydrogen from water is a conceivable way to store excess energy obtained from renewable, but volatile energy sources such as wind and solar power.

Photosystem II has been investigated using FTIR spectroscopy for 25 years. So far almost exclusively steady-state spectra have been obtained, which only show the final changes between certain semi-stable steps in the catalytic cycle. Time-resolved FTIR measurements on the other hand make it possible to follow the catalytic transition and to identify intermediate steps.

Our work group started working on FTIR spectroscopy on PSII more than 10 years ago. First time-resolved step-scan data was obtained between 2010 and 2012 but abandoned for the lacking signal-to-noise ratio. During my work I improved the existing setup in crucial ways, the key improvements being a working cooling system and a laser alignment system to align the actinic beam with the infrared beam. In total I obtained about 1100 time-resolved interferograms; the measurement time for one step-scan dataset amounted to several months of non-stop measurements, only interrupted by setting up the fully automated measurement runs twice per week. During my work I processed roughly 100 kg of spinach to obtain enough purified photosystem II protein.

I successfully obtained time-resolved step-scan measurements in H_2O and D_2O with a time resolution of about 10 µs and sufficient signal-to-noise ratio, so that the S-state transitions can be tracked in realtime. The data reveals, inter alia, the FTIR spectrum of the oxygen evolution step: for the first time the vibrational modes involved in the oxygen evolution reaction are directly visible. Vibrational modes mirroring the electron transfer process via Y_Z have been identified. Finally, the influence of ammonia on photosystem II has been recorded for all S-state transitions.

Contents

2. Abbreviations

DAS	decay associated spectrum/spectra
DCBQ	2,6-dichloro-benzoquinone
DMSO	dimethyl sulfoxide
EPR	electron paramagnetic resonance
ET	electron transfer
FFT	fast Fourier transform
FTIR	Fourier-transform infrared
HDD	hard-disc drive
HTTP	hyper text transfer protocol
KIE	kinetic isotope effect
LLS	linear least squares
MCT	mercury cadmium telluride
OEC	oxygen-evolving complex
PBD	photothermal beam deflection
PCET	proton-coupled electron transfer
PPBQ	phenyl-p benzoquinone
PSII	photosystem II
PT	proton transfer
SNR	signal-to-noise ratio
SSD	solid-state disc
TRRS	time-resolved rapid-scan
XAS	x-ray absorption spectroscopy
ν_{as}	asymmetrical stretching mode
ν_{s}	symmetrical stretching mode

3. Introduction

This chapter is divided into three main parts: in section 3.1 the structure and dynamics of photosystem II are introduced. The subsequent section introduces FTIR spectroscopy. Finally, section 3.3 summarizes previous work done on FTIR spectroscopy on PSII. The two sections 3.1 ("Structure and dynamics of photosystem II") and 3.3 ("FTIR spectroscopy on photosystem II") serve as foundation for the discussion in chapter 6.

3.1. Structure and dynamics of photosystem II

Perhaps the most comprehensive book about photosystem II has been published by Wydrzynski, Freeman, and Satoh (2006) and covers a variety of topics, including FTIR spectroscopy on photosystem II (pp. 367-387).

A major breakthrough was the successfull acquisition of a high resolution (1.9 Å) PSII crystal structure (Umena et al. 2011). Although the manganese ions were severely reduced due to the high X-ray radiation, many new insights were gained. The study was followed by a radiation damage-free structure four years later. (Suga et al. 2015).

In their recent review, Krewald, Retegan, and Pantazis (2016) focus on the oxygen evolving complex and the biological water oxidation mechanism from the viewpoint of EPR/ENDOR measurements. Important points addressed are the oxidation states of the Mn ions and the O-O bond formation mechanism. Another review focuses on the same topic from a slightly different perspective (Pérez-Navarro et al. 2016).

3.1.1. Acceptor side

The acceptor side accepts the electron which is generated through charge separation at P_{680}. It consist of two identical plastoquinone molecules termed Q_A and Q_B between which a single non-heme iron is located (de Wijn and van Gorkom 2001; Chernev et al. 2010; Chernev et al. 2011). Upon charge separation after light excitation Q_A accepts the electron within 200 ps and passes it on to Q_B (McEvoy and Brudvig 2006). The fastest phase of Q_A^- reoxidation is ~500-900 µs (Klauss, Haumann, and Dau 2015). During the electron transfer from Q_A to Q_B the non-heme iron is not oxidized (Chernev et al. 2010; Chernev et al. 2011),

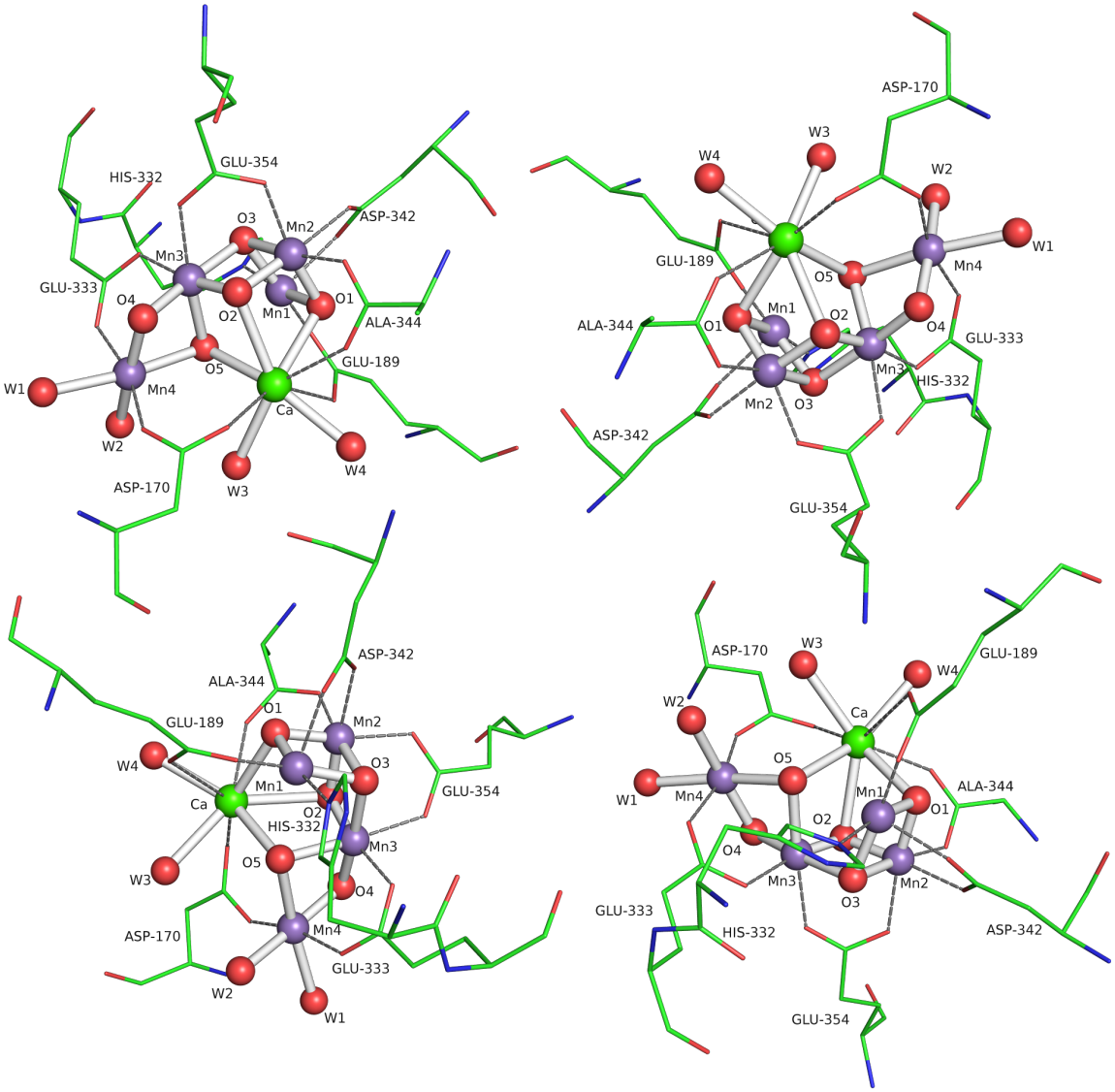

Figure 3.1.: The oxygen evolving complex (OEC), crystal structure 4UB6 from the Protein Database (Suga et al. 2015) with bonds chosen to represent an "open cubane" structure. Dashed lines represent possible interactions between amino acid residues and the complex.

and the salt concentration in the buffer can have a strong influence on Q_A^- reoxidation (Klauss, Haumann, and Dau 2015). While Q_A is rigidly fixed within the protein, Q_B can leave the binding site after accepting two electrons and two protons from the stroma in the form of Q_BH_2. Thus, in dark adapted PSII the Q_B site may be initially empty in some species.

Because there are only so many Q_B molecules in any sample, "artificial" electron acceptors are added to the sample, for example ferricyanide, PPBQ, or DCBQ (Zimmermann and Rutherford 1986). Ferricyanide oxidises the non-heme iron and becomes ferrocyanide

within seconds; this implies restrictions in the flash spacing (see e.g. Hienerwadel and Berthomieu 1995; Service, Hillier, and Debus 2014). For a discussion of the FTIR signals from the different electron acceptors see section 3.3.3 on page 20.

In this study, PPBQ (phenyl-p benzoquinone) has been used as exogenous electron acceptor. Earlier work in our group (Menzel 2009) showed that using PPBQ leads to a significantly lower miss-factor compared to ferricyanide (for a discussion of the miss-factor, see section 4.17 on page 65). A side-effect is the oxidation of the non-heme iron by PPBQ: Zimmermann and Rutherford (1986) investigated this effect using EPR spectroscopy and showed that the non-heme iron is oxidized on odd-numbered flashes and reduced on even-numbered flashes in a flash sequence. On the first flash, the generated electron reduces PPBQ to $PPBQ^{-}$; in this semiquinone form, $PPBQ^{-}$ is unstable and extracts another electron from the non-heme iron to eventually form $PPBQH_2$. On the second flash, the provided electron recudes the Fe^{3+} to Fe^{2+}. On each subsequent flash these events will be repeated in an alternating way, leading to a period-of-two pattern regarding the iron signals. For a discussion of the associated FTIR signals, see section 3.3.3 on page 20.

How exactly PPBQ oxidizes Q_A and the non-heme iron is not clear. The oxidation could either take place through Q_B; another possibility is PPBQ directly occupying the Q_B pocket (Zimmermann and Rutherford 1986). Previous results of our work group suggest the former option (results not shown).

3.1.2. Sequence of events on every flash

Once a photon has been absorbed by the protein's light harvesting systems, the energy is transferred to the special chlorophyl pair P_{680} where charge separation takes place and an electron hole pair is generated. The electron is transferred to the primary electron acceptor Q_A via pheophytin within less than a nanosecond (Buchta, Grabolle, and Dau 2007). ${P_{680}}^{+}$ is reduced within nanoseconds by an electron from Y_Z, which can be measured as flash-induced absorption change at 827 nm (Ahlbrink et al. 1998). The charge separated state ${Y_Z}^{+\bullet}{Q_A}^{-}$ causes a compensating volume contraction and is formed within 1 µs; therefore, given the time resolution of ~10 µs, this "initial" state is formed instantly in the step-scan data set.

Two points were discussed in older literature: Y_Z was suggested to abstract protons from bound substrate water, and Y_Z's phenolic proton was suggested to leave into the bulk upon oxidation of Y_Z. These are both not the case. Upon oxidation of Y_Z, the positive charge causes Y_Z's phenolic proton to shift to the neighbouring D1-His190 and the positive charge stays at this moiety (Ahlbrink et al. 1998; Nakamura et al. 2014; Klauss, Haumann, and Dau 2015). Y_Z does not abstract hydrogen from substracte water (Ahlbrink et al. 1998).

The creation of the charge separated state leads to a negative charge at Q_A^- and a positive charge at $Y_Z^{+\bullet}$ which attract each other. This leads to a contraction of the whole molecule which is reverted by charge-compensating proton removal from the OEC (Klauss, Haumann, and Dau 2015). These contractions and expansions should be visible through changes in the amide I region in the FTIR step-scan data. Additionally, the positive charge at $Y_Z^{+\bullet}$ may lead to changes in the water bonding network around Ca and $Y_Z^{+\bullet}$ (Nakamura et al. 2014). Even the creation of a hydrogen release path with the water bonding network change and/or the proton shift between Y_Z and D1-His190 acting a rate-determining steps may be possible (Nakamura et al. 2014).

After the creation of the charge separated state $Y_Z^{+\bullet}$ oxidises the OEC within micro- to milliseconds depending on the S-state transition (Klauss, Haumann, and Dau 2015).

3.1.3. S-state cycling

$S_1 \rightarrow S_2$ transition ($S_1^n \rightarrow S_2^+$)

The $S_1 \longrightarrow S_2$ transition is the only S-state transition during which no proton is removed from the OEC (Fowler 1977; Saphon and Crofts 1977; Klauss, Haumann, and Dau 2015) The electron is removed within 120 µs (at 10 ℃) with a low KIE of 1.3 (Klauss, Haumann, and Dau 2012; Klauss, Haumann, and Dau 2015; Zaharieva, Dau, and Haumann 2016). The time constant of the electron transfer is almost pH independent (Klauss, Haumann, and Dau 2015). A time constant of 100 µs (KIE=1.15, 23 ℃) was observed by Gerencsér and Dau (2010).

$S_2 \rightarrow S_3$ transition ($S_2^+ \rightarrow S_2^n \rightarrow S_3^+$)

In the $S_2 \longrightarrow S_3$ transition proton removal precedes electron removal. The S_2^n state was first observed by Klauss, Haumann, and Dau (2012). Because the manganese complex has been oxidized in the preceding transition without charge compensation, a second oxidation of the OEC by Y_Z^{ox} is prohibited by the high redox potential. First, $Y_Z^{ox(+)}$ causes a proton to leave the complex so that subsequently oxidation of the Mn complex can proceed (Klauss, Haumann, and Dau 2012; Service, Hillier, and Debus 2014).

The proton leaving the cluster ($S_2^+ \longrightarrow S_2^n$) is supposed to leave from a cluster of water molecules near Y_Z^{ox} and His190 (Klauss, Haumann, and Dau 2012). This creates a vacancy which is highly delocalized in the water cluster, but resides near $Y_Z^{ox(+)}$. This proton transfer showed a time constant of about 60 µs at 10 ℃ and has a high KIE of 5.6 (Klauss, Haumann, and Dau 2012, fig. 3). XAS measurements showed a time constant of ~25 µs in H_2O and ~115 µs in D_2O at room temperature (Zaharieva, Dau, and Haumann 2016). Delayed fluores-

cence measurements revealed time constants of 18 µs and 100 µs at 10 ℃ in H_2O (Zaharieva, Grabolle, et al. 2013).

In the subsequent electron transfer to $Y_Z^{ox(+)}$ ($S_2{}^n \longrightarrow S_3{}^+$), a proton leaves the Mn cluster to fill the vacancy in the water cluster (Klauss, Haumann, and Dau 2012). The existence of this PCET is also strongly suggested by its KIE (Klauss, Haumann, and Dau 2015), its high activation energy, and its pronounced pH dependence and may therefore be the only true PCET during the S-state cycle (Zaharieva, Dau, and Haumann 2016). A time constant of 280 µs (KIE=1.7, 23 ℃) was observed by Gerencsér and Dau (2010). Because CP43-Arg357 is located relatively far away from Mn1 and Y_Z, its deprotonation is unlikely (Klauss, Haumann, and Dau 2012). The deprotonation of the water cluster supports findings highlighting the importance of the pK value of water molecules connected to the Ca ion (Klauss, Haumann, and Dau 2012). The path to the lumen is supposed to be a different one than the one used in the $S_3 \longrightarrow S_0$ transition (Klauss, Haumann, and Dau 2012). The electron transfer time constant at room temperature was reported to equal~320 µs in H_2O and ~570 µs in D_2O (Zaharieva, Dau, and Haumann 2016). Delayed fluorescence measurement revealed a time constant of 330 µs (Zaharieva, Grabolle, et al. 2013) at 10 ℃ in H_2O.

$S_3 \rightarrow S_0$ transition ($S_3{}^+ \rightarrow S_3{}^n \rightarrow S_4{}^+ \rightarrow S_0{}^+ \rightarrow S_0{}^n$)

The $S_3 \longrightarrow S_0$ transition is a multiphasic process; the sequence of events has only been disentangled in the recent years (Klauss, Haumann, and Dau 2015).

The $S_3{}^+ \longrightarrow S_3{}^n$ transition is a multiphasic process in itself involving three or more sequential steps as shown by delayed fluorescence measurements (Buchta, Grabolle, and Dau 2007). The determined time constants of this study (Buchta, Grabolle, and Dau 2007) are 14 µs, 65 µs, and 203 µs. This study was followed by another delayed fluorescence study (Zaharieva, Grabolle, et al. 2013) which reported time constants of 20 µs, 100 µs, and 400 µs.

The initial formation of $Y_Z{}^{+\bullet}Q_A{}^-$ radical pair leads to a volume contraction which acts as relaxation process and precedes the PT phase on the tens to hundreds of microseconds timescale (Klauss, Haumann, and Dau 2015). It was suggested that the positive charge on $Y_Z{}^{+\bullet}$ causes a proton to be removed from CP43-Arg357 or a cluster of water molecules (as in the $S_2 \longrightarrow S_3$ transition) (Service, Hillier, and Debus 2014). The proton removal was first identified in time-resolved XAS measurements as a ~200 µs lag-phase (Haumann, Liebisch, et al. 2005); a ~170 µs lag-phase with a KIE of 2.4 was found in absorption spectroscopy experiments at 360 nm and 23 ℃ (Gerencsér and Dau 2010; Gerencsér and Dau 2013). In these UV-vis experiments, the lag phase was extended in D_2O and at low pH, supporting a proton transfer process as underlying mechanism. A small and rapid ~25 µs rising phase followed by a ~250 µs rising phase in PBD experiments were assigned to this PT step (Klauss,

Haumann, and Dau 2015); these two phases slowed down in a D_2O buffer with more acidic pH at lower temperatures. Time-resolved XAS measurements showed time constants of ~150 µs in H_2O and ~380 µs in D_2O at room temperature (Zaharieva, Dau, and Haumann 2016). The rate of proton removal is not significantly affected by the salt concentration in the buffer (Karge, Bondar, and Dau 2014).

After the first proton transfer an electron is removed within milliseconds ($S_3{}^n \longrightarrow S_4{}^+$). A prominent ~1.6 ms, pH independent rising phase in PBD experiments was attributed to this ET step (Klauss, Haumann, and Dau 2012), as well as a mostly pH and KIE independent 1.6 ms exponential decrease at 23 ℃ in 360 nm absorption spectroscopy experiments (Gerencsér and Dau 2010; Gerencsér and Dau 2013). At 10 ℃ the transition takes 2.8 ms (Klauss, Haumann, and Dau 2012, fig. 3). In time-resolved XAS measurements at room temperature the electron removal takes ~1.6 ms in H_2O and ~2.2 ms in D_2O (Zaharieva, Dau, and Haumann 2016). Delayed fluorescence measurements revealed a value of ~2.2 ms at 10 ℃ and and activation energy of 231 meV (Buchta, Grabolle, and Dau 2007); a refined evaluation revealed a time constant of 2.4 ms at 10 ℃ in H_2O.

The positive charge on $Y_Z{}^{+\bullet}$ might shift the equilibrium from bound water to peroxide to prepare the formation of oxygen (Ahlbrink et al. 1998). In passing in S_4 the oxidation states are $Mn(IV)_3$—$Mn(V)_1$ (Iuzzolino et al. 1998).

After O-O bond formation and oxygen release two substrate waters bind to the OEC ($S_4{}^+ \longrightarrow S_0{}^+$). Finally, another proton leaves the OEC ($S_0{}^+ \longrightarrow S_0{}^n$).

$S_0 \rightarrow S_1$ transition ($S_0{}^n \rightarrow S_1{}^+ \rightarrow S_1{}^n$)

In the $S_0 \longrightarrow S_1$ transition, first an electron is removed ($S_0{}^n \longrightarrow S_1{}^+$) before a proton is removed ($S_1{}^+ \longrightarrow S_1{}^n$) from the OEC. For the electron transfer rate different time constants have been reported, ranging from 40 µs to 300 µs. For the electron transfer step time constants of ~50 µs in H_2O, ~65 µs in D_2O have been reported. These time constants have been obtained by observing lag phases in $S_0{}^n \longrightarrow S_1{}^+$ XAS transients (Zaharieva, Dau, and Haumann 2016).

A proton is removed from the OEC after the formation of the $S_1{}^+$ state since Mn oxidation sufficiently lowers the pK of a Mn ligand (Klauss, Haumann, and Dau 2012). The proton removal results in the formation of the $S_1{}^n$ state. The $S_1{}^+ \longrightarrow S_1{}^n$ transition showed a time constant of 160 µs at 10 ℃ with a KIE of 3.0 (Klauss, Haumann, and Dau 2012, fig. 3)

Summary of reported time constants

Table 3.1 summarizes the time constants that have been introduced in the previous sections. The time constants have been calculated for 10 ℃ using the activation energies reported by

Klauss, Haumann, and Dau (2012) using the relation

$$\tau_2 = \tau_1 \exp\left[-\frac{E_a}{k_B}\left(\frac{T_2 - T_1}{T_1 T_2}\right)\right]. \tag{3.1}$$

3.2. Fourier transform infrared (FTIR) spectroscopy

FTIR spectroscopy is a valuable tool in photosystem II research (Mäntele 1996; Debus 2015). While crystal structures have provided static information about the ground state of the protein (Umena et al. 2011; Suga et al. 2015), crystal structures have not provided dynamic information so far. There are efforts to measure crystal structures in other S-states than the S_1-state (Alonso-Mori et al. 2016), but this will still give no direct information about the actual S-state transitions. FTIR spectroscopy is the ideal counterpart here because it does not provide direct structural information, but readily provides dynamic information about changes in certain chemical moieties in the protein during the actual S-state transition. A thorough theoretic introduction to vibrational spectroscopy can be found in *Infrared and raman spectra of inorganic and coordination compounds* (Nakamoto 1986).

FTIR spectroscopy has been used to determine general protein structure manifesting in amide I bands (Jackson and Mantsch 1995). Because of the high absorption of these protein bands and water combined with nonlinearity problems of IR detectors, the optical density of any sample needs to be kept below 1 at any wavenumber. Thus, the thickness of a typical sample is around 10 µm or less (Jackson and Mantsch 1995). Jackson and Mantsch (1995) are sceptical about dried samples because of the nonphysiological state of the sample. Moreover, they have criticized a rehydration approach using a water vapor stream passing over a dried film of protein as the "decreased hydration may have important structural and spectroscopic consequences" (Jackson and Mantsch 1995). They demonstrate band reduction and band shifting in the FTIR spectrum of concavalin A upon drying and rehydration. Furthermore, the authors advise against the usage of organic solvents as, for example, membrane mimetics. They state that the dielectric constants are very different, that "significant structural effects are possible even in aqueous mixtures containing very low concentrations of halogenated alcohols" (Jackson and Mantsch 1995), and a reduction of the denaturation temperature of up to 20℃ suggesting a destabilization of the protein. Likewise, low concentrations of DMSO lead to thermal destabilization. The authors suggest that the best way to study membrane-associated proteins and peptides is to use an aqueous protein-lipid dispersion in order to avoid structural artifacts which can occur when using membrane mimetic solvents.

S-state transition		τ	T_1	ref.	KIE	τ_H, 10 ℃	τ_D, 10 ℃
$S_1 \longrightarrow S_2$	${S_1}^n \longrightarrow {S_2}^+$	120 µs	10 ℃	α	1.3	120 µs	156 µs
		100 µs	23 ℃	β	1.2	133 µs	160 µs
$S_2 \longrightarrow S_3$	${S_2}^+ \longrightarrow {S_2}^n$	60 µs	10 ℃	α	5.6	60 µs	336 µs
		25 µs	RT	γ	4.6	66 µs	303 µs
		18 µs 100 µs	10 ℃	η	N/A	18 µs 100 µs	
	${S_2}^n \longrightarrow {S_3}^+$	280 µs	23 ℃	β	1.7	535 µs	910 µs
		320 µs	RT	γ	1.8	673 µs	1.2 ms
		330 µs	10 ℃	η	N/A	330 µs	
$S_3 \longrightarrow S_0$	${S_3}^+ \longrightarrow {S_3}^n$	200 µs	RT	δ	N/A	290 µs	
		14 µs 65 µs 200 µs	20 ℃	ε	N/A	18 µs 84 µs 257 µs	
		170 µs	23 ℃	β	2.4	235 µs	564 µs
		25 µs 250 µs	20 ℃	ζ	> 2	32 µs 322 µs	>64 µs >643 µs
		150 µs	RT	γ	2.5	217 µs	543 µs
		20 µs 100 µs 400 µs	10 ℃	η	N/A	20 µs 100 µs 400 µs	
	${S_3}^n \longrightarrow {S_0}^n$	1.7 ms	23 ℃	β	1.2	2.6 ms	3.1 ms
		2.8 ms	10 ℃	α	1.3	2.8 ms	3.6 ms
		1.6 ms	RT	γ	1.4	2.6 ms	3.6 ms
		2.2 ms	10 ℃	ε	N/A	2.2 ms	
		2.4 ms	10 ℃	η	N/A	2.4 ms	
$S_0 \longrightarrow S_1$	${S_0}^n \longrightarrow {S_1}^+$	50 µs	RT	γ	1.3	55 µs	72 µs
	${S_1}^+ \longrightarrow {S_1}^n$	160 µs	10 ℃	α	3.0	160 µs	480 µs

α	Klauss, Haumann, and Dau (2012)
β	Gerencsér and Dau (2010)
γ	Zaharieva, Dau, and Haumann (2016)
δ	Haumann, Liebisch, et al. (2005)
ε	Buchta, Grabolle, and Dau (2007)
ζ	Klauss, Haumann, and Dau (2015)
η	Zaharieva, Grabolle, et al. (2013)

Table 3.1.: Time constants for S-state transitions (top) as reported in the literature (bottom). The time constants for 10 ℃ have been calculated using the activation energies reported in Klauss, Haumann, and Dau (2012).

3.2.1. Development of FTIR spectroscopy

It was already shown in 1950 that FTIR spectroscopy can provide information on secondary structure of proteins (Jackson and Mantsch 1995). A major breakthrough in FTIR spectroscopy was the invention of the fast Fourier transform (FFT) algorithm in 1965 (Griffiths and Haseth 1986). Previously, the calculation of the discrete Fourier transform of one spectrum would take 15 minutes on average, providing no advantage over grating spectrometers. In the early 1980s it was possible to calculate the Fourier transform of a 8192 point interferogram in (on average) 2 minutes, down to under 5 seconds using special equipment (Griffiths and Haseth 1986). It may very well be for this reason that Jackson and Mantsch (1995) report an "explosive growth" in applications and laboratories using this technique in the late Eighties.

The calculation time was improved further through the advance of faster computers. On my personal computer (purchased in 2012) a complex FFT of 8192 points takes 1.2 ms (measured using the `python timeit` module, 10.000 iterations). Thus, many discussions from early FTIR spectroscopy seeking to reduce the number of points in the interferogram especially by measuring single-sided interferograms are obsolete in this regard; nevertheless, the theoretic findings still prove useful in other ways.

Nowadays, the calculation time of the Fourier transform does not pose as much as a hindrance as the size of the generated data. In this work the generated data amounts to about 3 TB: therefore, the read and write speed and capacity of the HDD or SSD used limit the data processing speed. Compared to the necessary read and write operations the Fourier transform is calculated in an instant.

3.2.2. Phase correction: Forman method

The goal of any phase correction is to remove the sinusodial component in the interferogram. While there is always the option to calculate the power spectrum (the absolute value of the Fourier transform, see Connes 1963), the power spectrum exhibits nonlinearities regarding noise (Griffiths and Haseth 1986). In this work, the phase correction proposed by Forman, Steel, and Vanasse (1966) is used. The pictorial essay (figure 3.2) is inspired by Griffiths and Haseth (1986).

After Fourier-transforming an uncorrected interferogram, the spectrum $I(\nu)$ contains a real and an imaginary part (panel B in figure 3.2):

$$I(\nu) = I_{\mathrm{Re}}(\nu) + iI_{\mathrm{Im}}(\nu). \tag{3.2}$$

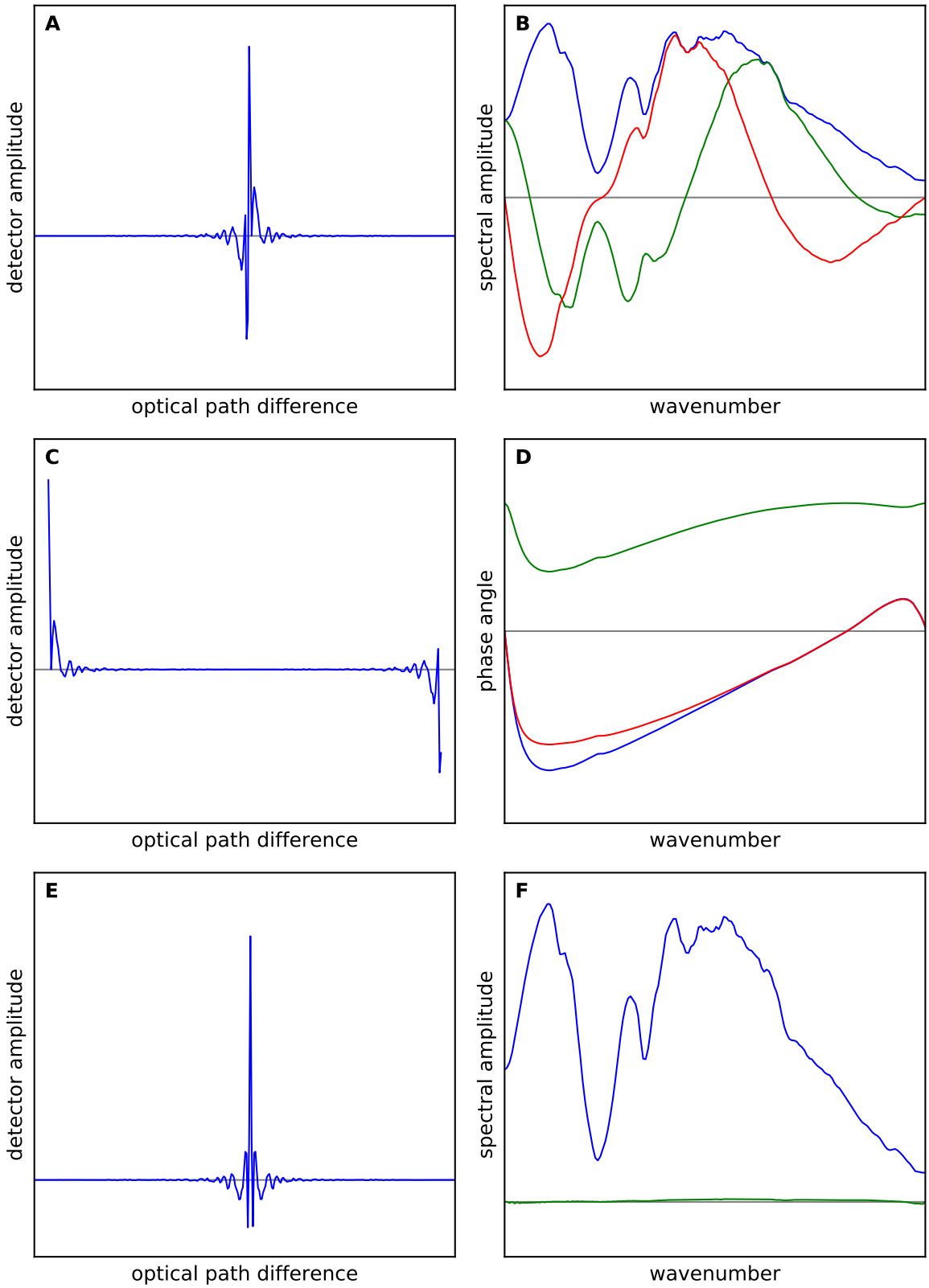

Figure 3.2.: A: measured interferogram. B: absolute (blue), real (green) and imaginary (red) part of the Fourier transform of the interferogram shown in A. C: shortened and rolled interferogram. D: phase angle θ (blue), $\cos\theta$ (green), $\sin\theta$ (red). E: phase corrected interferogram. F: real (blue) and imaginary (green) part of the Fourier transform of E.

The power spectrum is calculated as

$$|I(\nu)| = \sqrt{|I_{\mathrm{Re}}(\nu)|^2 + |I_{\mathrm{Im}}(\nu)|^2} \tag{3.3}$$

and is related to the complex spectrum $I(\nu)$ via the phase angle θ:

$$I(\nu) = e^{i\theta}|I(\nu)|. \tag{3.4}$$

The phase angle itself (panel D in figure 3.2) can be calculated from the real and imaginary parts of the spectrum:

$$\theta(\nu) = \arctan \frac{I_{\mathrm{Im}}(\nu)}{I_{\mathrm{Re}}(\nu)}. \tag{3.5}$$

Assuming that the phase angle varies only slowly with the wavenumber ν, the interferogram used to obtain the complex spectrum to calculate ν is usually a shortened interferogram (panel C in figure 3.2). With the same argument equation 3.4 can be rewritten to give the phase corrected spectrum $I'(\nu)$:

$$I'(\nu) = I(\nu)e^{-i\theta} = I_{\mathrm{Re}}(\nu)\cos\theta + I_{\mathrm{Im}}(\nu)\sin\theta. \tag{3.6}$$

Note that I' and $|I|$ represent the same spectrum, but I' does not show the noise nonlinearities of $|I|$.

Equation 3.6 can be read in the following way: to obtain the purely real spectrum $I'(\nu)$, one needs to multiply the Fourier transforms $I(\nu)$ and $\theta(\nu)$. This operation can also be processed in the interferogram domain, since a multiplication in the spectral domain corresponds to a convolution in the interferogram domain: the phase corrected interferogram (panel E in figure 3.2) is obtained by convolving the measured interferogram with the interferogram ζ representing the phase angle. Since the phase angle θ is the Fourier transform of its phase angle interferogram ζ, ζ can be obtained through the inverse Fourier transform:

$$\zeta(\delta) = \int_{-\infty}^{\infty} e^{-i\theta} e^{i2\pi\nu\delta} d\nu, \tag{3.7}$$

which enables us to obtain the phase corrected interferogram $J'(\delta)$ through a convolution:

$$J'(\delta) = J(\delta) * \zeta, \tag{3.8}$$

where $*$ denotes convolution.

The phase corrected interferogram now is symmetric and therefore, a cosine Fourier

transform can be used to calculate the spectrum (panel F in figure 3.2). In practice one can either calculate the complex Fourier transform and just retain the real part or call specialiced real Fourier transform routines for additional performance.

It is possible to apply this correction methods multiple times to further improve the phase correction.

3.2.3. Fourier-transforming difference interferograms

The goal of this section is to show how difference spectra can be obtained from Fourier-transforming difference interferograms. We first start with the Beer-Lambert law, motivate the general calculation of difference spectra and then investigate the possibility of calculating difference spectra from difference interferograms.

Given an optically attenuating material, incident light with an intenisty I_0 is attenuated to an intensity I after passing a distance x in the material according to

$$I = I_0 \exp(-\lambda x), \tag{3.9}$$

with λ acting as extinction coefficient. We define the absorbance of the sample as λx and recast the equation to obtain the formula for A:

$$A = -\ln\left(\frac{I}{I_0}\right). \tag{3.10}$$

Now in difference spectroscopy it is desired to observe the change of absorbance upon a certain event, e.g. comparing the absorbance before and after a flash of light has modified the sample. The difference absorbance is

$$\Delta A = A_2 - A_1 = \left(-\ln\left(\frac{I_2}{I_0}\right)\right) - \left(-\ln\left(\frac{I_1}{I_0}\right)\right) \tag{3.11}$$

$$= \ln\left(\frac{I_1}{I_0}\right) - \ln\left(\frac{I_2}{I_0}\right) = \ln\left(\frac{I_1/I_0}{I_2/I_0}\right) \tag{3.12}$$

$$= \ln\left(\frac{I_1}{I_2}\right) = \ln(I_1) - \ln(I_2). \tag{3.13}$$

The latter part of the above equation holds only if the background I_0 does not change during the measurement, as for the given example with the flash of light.

To obtain a spectrum in FTIR spectroscopy, an interferogram J_i has to be Fourier transformed to obtain the spectrum $I_i = \mathrm{FFT}(J_i)$. The spectra can then be ratioed or subtracted as shown above to obtain the difference spectrum.

With this equation it is not possible to Fourier-transform a difference interferogram to

get the difference spectrum, because there is no way to rewrite

$$\ln(I_1/I_2) = \ln(\mathrm{FFT}(J_1)/\mathrm{FFT}(J_2)) \quad \text{or} \quad \ln(\mathrm{FFT}(J_1)) - \ln(\mathrm{FFT}(J_2)) \tag{3.14}$$

in a way that the desired result can be obtained by taking the logarithm of a single Fourier-transform with J_1 and J_2 as arguments. The problem with the form at the left side is that $\mathrm{FFT}(J_1)/\mathrm{FFT}(J_2) \neq \mathrm{FFT}(J_1/J_2)$ and the problem with the form at the right side is that the Fourier transform is the inner argument of the logarithm.

This problem is solved by calculating the Taylor series of $\ln(I)$ around the point 1. Because the changes in the difference spectra ΔA are smaller than 0.001, we can safely assume that $I_1/I_2 \approx 1$ and

$$\Delta A = \ln\left(\frac{I_1}{I_2}\right)\Bigg|_1 \approx \ln(1) + \frac{I_1}{I_2} - 1 = \frac{I_1 - I_2}{I_2}, \tag{3.15}$$

by calculating the Taylor expansion taking into acount the first derivative term and recalling that $\ln(1) = 0$. Now the difference spectrum $I_1 - I_2$ can be calculated from the difference interferogram $J_1 - J_2$, since the Fourier transform is a linear operation:

$$I_1 - I_2 = \mathrm{FFT}(J_1) - \mathrm{FFT}(J_2) = \mathrm{FFT}(J_1 - J_2). \tag{3.16}$$

It remains to exchange the natural logarithm for the decadic logarithm. By virtue of $\ln(I) = \log(I)\ln(10)$ and the fact that the derivative of $\log(x)$ is $1/(x\ln(10))$, we arrive at

$$\Delta A = \frac{1}{\ln(10)} \frac{\mathrm{FFT}(J_1 - J_2)}{I_2}. \tag{3.17}$$

3.3. FTIR spectroscopy on photosystem II

The first FTIR spectra on PSII have been obtained 25 years ago (Berthomieu, Boussac, et al. 1992; Noguchi, Ono, and Inoue 1992) . Mäntele (1996) doubts that "we shall ever be able to fully exploit the wealth of information contained in an IR difference spectrum". While this is certainly true especially for time-resolved spectra, a wealth of information has been gained about PSII through the use of FTIR spectroscopy.

This section aims to give an overview of the FTIR spectroscopy work done on Photosystem II regarding the mid-frequency region of 1800-1050 cm^{-1}. The mid-frequency region has been investigated because of the direct access to e.g. the amino acid residues' signals (Mäntele 1996), but also other wavenumber regions are of interest: at lower wavenumbers, Mn-O and Mn-Mn bonds can be investigated, and at higher wavenumbers, water molecules

and strong hydrogen bonds appear in the spectra (Noguchi 2013). Because of the wavenumber range of 1800–1050 cm^{-1} of this work's step-scan, the following discussion focuses on the mid-frequency range. For discussions concerning other frequency ranges, the reader is kindly referred to the reviews mentioned below.

A number of reviews about FTIR on photosystem II have been published (Mäntele 1996; Noguchi 2013; Debus 2015; Mezzetti and Leibl 2016).

Noguchi and Sugiura (2003) give a comprehensive overview of the FTIR spectroscopy studies conducted between 1993 and 2003. Mäntele (1996) gives a table summarizing infrared-active amino acid side chain vibrations relevant to photosynthetic pigment-protein complexes.

Noguchi and Sugiura (2003) analyzed and assigned flash-induced difference spectra of PSII by universally labelling the sample with ^{15}N or ^{13}C. According to this study, features above 1700 cm^{-1} reflect C=O stretching vibrations of protonated carboxylic groups, while features between 1600 and 1700 cm^{-1} correspond to amide I vibrations. The only edge case is a feature at 1704 cm^{-1} which could correspond to either group.

Between 1500 and 1600 cm^{-1} amide II and $\nu_{as}(COO^-)$ vibrations are overlapping: Noguchi and Sugiura (2003) assigned features at 1588, 1564, ~1536, 1525, and 1511 cm^{-1} to $\nu_{as}(COO^-)$ vibrations, while all other features (at 1577, 1553, 1544, and 1511 cm^{-1}) were assigned to amide II modes. One exception is the feature at 1570 cm^{-1}: at this wavenumber, contributions from both amide II and $\nu_{as}(COO^-)$ modes seem to be present. Features between 1450 and 1300 cm^{-1} were uniquely assigned to $\nu_s(COO^-)$ vibrations. One last feature, around 1255 cm^{-1}, was tentatively assigned to COH deformation vibrations and may correspond to Tyr modes.

This study (Noguchi and Sugiura 2003) also established that features observed during the first and second flashes ($S_1 \longrightarrow S_2$ and $S_2 \longrightarrow S_3$) are reversed during the third and fourth flashes ($S_3 \longrightarrow S_0$ and $S_0 \longrightarrow S_1$) applied.

Based on measured IR absorptions of amino acid side chains (Venyaminov and Kalnin 1990; Rahmelow, Hübner, and Ackermann 1998; Barth 2000), Noguchi and Sugiura (2003) argue that in the amide I region features stemming from Gln, Asn and Arg should be visible. While this study would not be able to differentiate between Gln and Asn on the one hand and amide II modes on the other hand, Arg modes should be distinguishable because the asymmetric and symmetric stretching vibrations of a guanidinium group at ~1675 cm^{-1} and ~1635 cm^{-1} respectively should show a relatively large downshift upon ^{15}N labeling. Because these changes were not observed, the authors concluded that there would be only a minor contribution, if any, of Arg in this region.

Noguchi and Sugiura (2003) concluded that the different S-state intermediates differ only partially in their protonation states (if at all) due do only weak signals in the protonated

carboxylate region.

The first $S_1 \longrightarrow S_2$ FTIR difference spectrum was reported by Noguchi, Ono, and Inoue (1992) (see also Murata 1992, pp. 309–312). The authors concluded since no proton is released in the $S_1 \longrightarrow S_2$ transition (Fowler 1977; Saphon and Crofts 1977) and one Mn atom is oxidized (Cole et al. 1987), there should be no breakage or formation of chemical bonds. Therefore, the difference spectrum of this transition should reflect the changes in force constants of the ligands' vibrational modes. The authors interpreted their signals in the following way: in the amide I region, two differential bands at 1683/1675 cm^{-1} and 1651/1640 cm^{-1} respectively were assigned to either the CO stretch of the -$CONH_2$ group of Gln or Asn ligated to Mn, or the CO stretch of backbone amides. The former differential feature would in the latter case correspond to changes in β-turn structures while the latter feature would correspond to changes in β-sheet structure or unordered structure.

As for the lower wavenumber region, based on the notion that antisymmetric and symmetric modes of ionized carboxyls (COO^-) are absorbing around 1550 cm^{-1} and around 1400 cm^{-1} respectively, Noguchi, Ono, and Inoue (1992) assigned positive bands at 1590, 1552, and 1501 cm^{-1} and negative bands at 1561, 1544, and 1523 cm^{-1} to antisymmetric COO^- vibrations. Positive bands at 1436 and 1364 cm^{-1} and negative bands at 1419 and 1404 cm^{-1} were assigned to symmetric COO^- vibrations. It was concluded that Glu or Asp residues may ligate the OEC. The amino acid residues ligating the OEC can be seen in figure 3.1 on page 4. Additionally, the amide II modes of the protein backbone are visible around 1550 cm^{-1} and should thus overlap with the antisymmetric carboxylate modes.

Jackson and Mantsch (1995) summarized general FTIR absorption frequencies of protein structures (see also table 3.2). The maximum absorption for predominantly helical proteins can be found between 1648–1658 cm^{-1}. Of this absorption peak, 10 to 15% of the total intensity may arise from side chains, in particular from aspartate, glutamate, arginine, tyrosine, lysine, and glutamine. In aqueous solution, primarily α-helical structured proteins exhibit amide I and II absorptions at 1652–1657 cm^{-1} and 1545–1551 cm^{-1} respectively. While the amide I mode primarily consists of contributions from the C=O stretching vibration of the amide group with a minor contribution from the C-N stretching vibration, the amide II feature consists of about 60% N-H bending and 40% C-N stretching modes.

Non-hydrogen-bonded amide C=O groups in a low-dielectric constant surrounding may absorb above 1670 cm^{-1} but usually, protein amide C=O groups without hydrogen bonds show features around 1666 cm^{-1} or lower. A tyrosine ring shows absorption around 1515–1516 cm^{-1}, and the $\nu_{as}(COO^-)$ vibration of aspartate shows a feature at 1585 cm^{-1}. Finally, Jackson and Mantsch (1995) propose that if there are no sharp absorptions to be seen between 1700–1800 cm^{-1} the spectrum can be judged to be water vapor-free.

Structure	Amide I frequency (cm^{-1})
antiparallel β-sheet/aggregated strands	1675–1695
3_{10}-Helix	1660–1670
α-Helix	1648–1660
Unordered	1640–1648
β-Sheet	1625–1640
Aggregated strands	1610–1628

Table 3.2.: Correlations between common protein structures and amide I frequency (Jackson and Mantsch 1995).

3.3.1. Y_Z and Y_D

Y_D^{ox}/Y_D difference spectra were reported by Hienerwadel, Boussac, et al. (1997); the authors assigned a feature at 1504 cm^{-1} to the ν(CO) mode of the Y_D^{ox} radical.

Y_Z^{ox}/Y_Z and Y_D^{ox}/Y_D difference spectra were reported by Berthomieu, Hienerwadel, et al. (1998). In the same year a different research group published spectra addressing these spectra as well, but the spectra were largely affected by acceptor side signal (S. Kim and Barry 1998; Berthomieu, Hienerwadel, et al. 1998). The spectra published by Berthomieu, Hienerwadel, et al. (1998) were reproduced by Nakamura et al. (2014), with the exception of a band at 1279 cm^{-1}.

The reported spectrum of Y_Z^{ox} (Berthomieu, Hienerwadel, et al. 1998) shows positive features at 1701 cm^{-1}, 1676 cm^{-1}, 1641 cm^{-1}, 1549 cm^{-1}, and 1512 cm^{-1} (strong), and negative features at 1706 cm^{-1}, 1662 cm^{-1}, 1626 cm^{-1}, 1542 cm^{-1} (weak), 1454 cm^{-1} (weak), 1252 cm^{-1}, and 1107 cm^{-1}. ^{13}C labelling Y_Z strongly affects the features at 1512 cm^{-1} and 1255 cm^{-1}; the authors assigned these features to the ν(CO) and δ(COH) modes.

A feature at 1279 cm^{-1} was assigned to the $\nu_{7'a}$(CO) mode of Y_Z (Berthomieu, Hienerwadel, et al. 1998), but this was not observed by Nakamura et al. (2014). Instead, the latter group assigned a relatively broad band at 1256 cm^{-1} to overlapping δ(COH) and ν(CO) vibrations.

Nakamura et al. (2014) showed that in D_2O the Y_Z^{ox} mode at 1256 cm^{-1} shifts to 1262 cm^{-1}. They also argued oxidation of Y_Z leads to an electrochromic shift of the keto CO band of P_{680}, which causes a differential band at 1705/1697 cm^{-1}. This band was also observed by Zhang et al. (1997) and Berthomieu, Hienerwadel, et al. (1998). The changes in the amide I region (1560, 1553, 1544 cm^{-1}) were confirmed to be due to backbone amides' response of the polypeptide main chains surrounding Y_Z by ^{15}N substitution (Nakamura et al. 2014). The ^{15}N substitution also showed a shift from 1101 cm^{-1} to 1095 cm^{-1}, which should be caused by a histidine side chain.

Upon investigation of the pH effect it was found while the feature at 1514 cm^{-1} does not shift with pH, the feature at 1256 cm^{-1} does shift from 1256 cm^{-1} to 1259 cm^{-1} when lowering the pH from 7.5 to 5.5 (Nakamura et al. 2014). This supports the assignment summarized above.

3.3.2. The special chlorophyll pair P_{680} and accessory chlorophyll Chl_Z

Noguchi, Inoue, and Satoh (1993) measured a FTIR difference spectrum of the triplet state of P_{680} at 80 K. Features in the spectrum were visible at 1723 cm^{-1}(−), 1716 cm^{-1}(+), 1707 cm^{-1} (−), 1669 cm^{-1}(−), 1659 cm^{-1}(+), 1627 cm^{-1}(+), 1556 cm^{-1}(−), 1539 cm^{-1}(−), 1510 cm^{-1}(+), 1345 cm^{-1} (−), 1322 cm^{-1}(+), 1284 cm^{-1}(−), 1178 cm^{-1}(−), 1134 cm^{-1}(+), 1124 cm^{-1}(−), 1101 cm^{-1}(+), and 1044 cm^{-1}(−). The negative peaks at 1669 cm^{-1} and 1707 cm^{-1} as well as the positive peaks at 1627 cm^{-1} and 1659 cm^{-1} were assigned to the keto C=O stretching mode of P_{680}. Additionally, a light-induced difference spectrum of purified chlorophyll *a* was obtained, which showed peaks at 1697 cm^{-1}(−), 1666 cm^{-1}(+), 1597 cm^{-1}(−) (weak), 1552 cm^{-1}(−), 1500 cm^{-1} (+), 1365 cm^{-1}(+), 1348 cm^{-1}(−), 1323 cm^{-1}(+), 1290 cm^{-1}(−), and 1178 cm^{-1}(−).

The spectrum of photooxidized $P_{680}{}^{+}$ was obtained by Allakhverdiev et al. (1994). Features in the spectrum were visible at 1735 cm^{-1}(−), 1714 cm^{-1}(+), 1694 cm^{-1}(−), 1676 cm^{-1}(+), 1626 cm^{-1}(−), 1577 cm^{-1}(+), 1566 cm^{-1}(−), 1542 cm^{-1}(+), 1512 cm^{-1}(−), 1477 cm^{-1}(+), 1460 cm^{-1} (−), 1436 cm^{-1}(+), 1427 cm^{-1}(−), and 1404 cm^{-1}(+). Additionally, very small shoulder features were identified at 1656 cm^{-1}, 1652 cm^{-1}, 1607 cm^{-1}, and 1393 cm^{-1}. The authors concluded that two negative peaks at 1694 cm^{-1} and 1652 cm^{-1} or 1626 cm^{-1} can be assigned to the 9-keto groups of the P680 Chl, and that these modes are shifted to 1714 cm^{-1} and 1676 cm^{-1} respectively upon formation of $P_{680}{}^{+}$. The assignment of a 1626 cm^{-1}(−) mode to a 9-keto group by Allakhverdiev et al. (1994) is in contradiction of the assignment of a 1627 cm^{-1}(+) mode to the keto C=O stretching mode of P_{680} by Noguchi, Inoue, and Satoh (1993); therefore, the 9-keto group may have a negative feature at 1652 cm^{-1} and not 1626 cm^{-1}.

The light induced difference spectrum of the accessory chlorophyll (Chl_Z^{+}/Chl_Z) was measured by Noguchi and Inoue (1995b) using Mn-depleted PSII membranes. The spectrum showed features at 1747 cm^{-1}(+), 1736 cm^{-1}(−), 1714 cm^{-1}(+), 1684 cm^{-1}(−), 1660 cm^{-1}(−), 1614 cm^{-1}(−), 1551 cm^{-1}(−), 1537 cm^{-1}(−), 1491 cm^{-1}(−), 1346 cm^{-1}(−), 1317 cm^{-1}(+), 1286 cm^{-1} (−), and 1182 cm^{-1}(−).

The goal of Berthomieu, Hienerwadel, et al. (1998) was to obtain difference spectra of Y_Z and Y_D. To prove that the spectra are free of other contributions, the authors also recorded a $P_{680}Chl^{+}/P_{680}Chl$ difference spectrum using Mn-depleted samples of a mutant lacking Y_D.

Features are visible at 1725 cm^{-1}(+), 1710 cm^{-1}(+), 1700 cm^{-1}(−), 1680 cm^{-1}(−), 1658 cm^{-1}(−), 1629 cm^{-1}(−), 1571 cm^{-1}(+), 1550 cm^{-1}(−), 1504 cm^{-1}(+), 1343 cm^{-1}(−), 1310 cm^{-1}(+), 1285 cm^{-1} (−), and a differential feature at 1180 (−)/1168 cm^{-1}(+).

Another P_{680}^{+}/P_{680} spectrum was measured by Okubo et al. (2007) for different types of samples. For PSII membranes of spinach, the spectrum showed features at 1743 cm^{-1} (+) (weak), 1735 cm^{-1}(−) (weak), 1723 cm^{-1}(+), 1711 cm^{-1}(+), 1701 cm^{-1}(−), 1682 cm^{-1}(−) (weak), 1658 cm^{-1}(−) (weak), 1650 cm^{-1}(+), 1630 cm^{-1}(−), 1615 cm^{-1}(−) (weak), 1557 cm^{-1} (−), 1549 cm^{-1}(−), 1531 cm^{-1}(+), 1521 cm^{-1}(−), 1510 cm^{-1}(+), 1492 cm^{-1}(−), 1477 cm^{-1}(+) (weak), 1345 cm^{-1}(−), 1310 cm^{-1}(+), 1286 cm^{-1}(−), 1218 cm^{-1}(+), 1202 cm^{-1}(−) (weak), 1181 cm^{-1}(−) (strong), and 1170 cm^{-1}(+).

3.3.3. Acceptor-side signals

The advantage of using ferricyanide/ferrocyanide as electron acceptors are isolated strong signals at 2116/2039 cm^{-1} which are excellent indicators for the electron abstraction process (Hienerwadel and Berthomieu 1995; Noguchi 2013). It may be necessary though to trypsinize the PSII sample if it has been obtained from spinach Murata 1992, pp. 309–312 . Furthermore, the pH needs to be chosen carefully so as not to oxidize the non-heme iron (Noguchi, Ono, and Inoue 1995). The first reported $S_1 \longrightarrow S_2$-spectra (Murata 1992, pp. 309–312; Noguchi, Ono, and Inoue 1992) exhibited small signals stemming from the non-heme iron. In later reports the same group managed to prevent the oxidation of the non-heme iron by lowering the pH to 5.5 (Noguchi, Ono, and Inoue 1995).

Hienerwadel and Berthomieu (1995) used Tris-washed PSII membranes which were pre-oxidized using ferricyanide to measure the Fe^{2+}/Fe^{3+} FTIR difference spectrum. Since bicarbonate is a ligand of the non-heme iron (see also Chernev et al. 2011), its CO stretching modes are influenced by the iron's charge. To differentiate between the effect of the non-heme iron on the bicarbonate and on other parts of the protein, the authors studied the effect of ^{13}C isotope labeling of bicarbonate measured in H_2O, D_2O, and with ^{15}N-labeled PSII membranes. Hienerwadel and Berthomieu (1995) assigned the ν_{as}(CO) and ν_s(CO) modes of bicarbonate in the Fe^{2+} state at 1530±10 cm^{-1} and 1338 cm^{-1} respectively. These modes shift to 1658±20 cm^{-1} and 1228 cm^{-1} respectively upon iron oxidation. At the lower wavenumber region, modes at 1111/1102 cm^{-1} and 1094 cm^{-1} are assigned to histidine ligands of the iron. The negative signal at 1094 cm^{-1} is supposed to be caused by a histidine ligand of the iron whose side chain deprotonates in the Fe^{3+} state. Further signals assigned to histidine side-chain modes are positive ones at 1476 cm^{-1} and 1150 cm^{-1}, and a negative one at 1465 cm^{-1}. The authors furthermore argued that bicarbonate is a bidentate ligand to the iron in its Fe^{2+} state, and a monodentate ligand in its Fe^{3+} state. Finally,

the general appearance of the Fe^{2+}/Fe^{3+} spectrum was tentatively assigned to peptide NH groups, a tyrosine (1257, 1517 cm^{-1}) and an aspartate or glutamate side chains which are supposed to participate in a hydrogen-bond network around the bicarbonate (Hienerwadel and Berthomieu 1995). A strong positive feature at 1478 cm^{-1} and a small positive feature at 1643 cm^{-1} were assigned to the $\nu(C = O)$ vibration of the semiquinone anion. Further signals were visible at 1673, 1660, 1552, 1539, and 1064 cm^{-1}.

3.3.4. Ala344

In a recent comment Debus (2016) stated that to date "only a single carboxylate group has been clearly identified", referencing a study (Chu, Hillier, and Debus 2004) assigning a peak at ~1356 cm^{-1} in the S_1 state and a peak at either ~1339 cm^{-1} or ~1320 cm^{-1} in the S_2 state. The original goal of the study was to prove that Ala344 ligates the OEC, which was later confirmed by crystallographic results (see figure 3.1 on page 4). These measurements were done on wild-type and mutant cells of the cyanobacterium *Synechocystis* sp. PCC 6803. The argument of the assignment is this: when treating the cells with labelled L-[1-^{13}C]alanine not only the C-terminal α-COO^- group of the D1 polypeptide at D1-Ala344 will be altered, but also all alanine-derived peptide carbonyl groups. If now the point mutations D1-A344G and D1-A344S are introduced, the peptide carbonyl groups will still be altered, but the C-terminus will not be altered by the previous alanine labelling. In this way, the difference spectrum for specifically D1-Ala344 can be obtained by comparing the alanine labelled wild type and mutants.

An additional point which was made in that report (based on the magnitude of the corresponding wavenumber shifts) is that D1-Ala344 should be a unidentate ligand of the Mn-ion which is oxidized in the $S_1 \longrightarrow S_2$ transition. Combined with crystallographic information (Suga et al. 2015) this means that Mn-2 should be oxidized in the $S_1 \longrightarrow S_2$ transition. This conflicts with reports stating that Mn-2 is not oxidized at all during the S-state cycle (Krewald, Retegan, Cox, et al. 2015).

3.3.5. CP43-Glu354

In an effort to identify the vibrational modes of CP43-Glu354, two research groups have created site-directed mutants of this residue (Shimada et al. 2009; Service, Yano, et al. 2011). The assignmend was not so clear though, since Shimada et al. (2009) assigned certain bands to the residue itself, while Service, Yano, et al. (2011) assigned the bands to unspecific amide II modes (Noguchi 2013).

3.3.6. Ammonia

Chu, Feng, et al. (2004) were the first to investigate the influence of ammonia on PSII FTIR difference spectra, specifically, the $S_1 \longrightarrow S_2$ transition. They showed a pronounced decrease of the amplitude of a feature at 1365 cm^{-1} and the appearance of a new positive feature at 1379 cm^{-1} under the influence of 100 mM NH_4Cl in the buffer before centrifugation. Chu, Feng, et al. (2004) argued that this is a real wavenumber upshift since there was no wavenumber shift of the new feature observable when treating the PSII with $^{15}NH_4Cl$ instead of the normal $^{14}NH_4Cl$. If the new feature at 1365 cm^{-1} were caused by a NH_3 derived species, the feature would shift due to the different isotope used. In a later study it was found that these results, which were obtained at 250 K, are not obtainable when the sample has a higher temperature of 4 ℃ (Huang, Wang, and Chu 2008).

Based on results by Noguchi, Ono, and Inoue (1995) and Kimura and Ono (2001), Chu, Feng, et al. (2004) expected an effect on the vibrational modes at 1402 cm^{-1} since the corresponding symmetric carboxylate stretching mode to 1365 cm^{-1} should be found at that wavenumber, but the absence of an effect on this mode was reported. These two wavenumbers have been assigned to a Mn-ligating carboxylate which changes from bridging or chelating to unidentate ligation coordination during the $S_1 \longrightarrow S_2$ transition (Noguchi, Ono, and Inoue 1995; Kimura and Ono 2001; Chu, Feng, et al. 2004). This was also the author's main argument that ammonia binds directly to the OEC. No wavenumber upshift was reported for treatment with ND_4Cl in D_2O buffer.

Additional changes at 1699 cm^{-1}, 1628 cm^{-1}, 1567 cm^{-1}, 1403 cm^{-1}, and 1353 cm^{-1} were reported (Chu, Feng, et al. 2004). The authors hypothesized that these differences are either due to structural perturbations caused by the bound ammonia, or due to differences in ionic effects of NH_4Cl compared to NaCl on PSII.

Tsuno et al. (2011) investigated the influence of ammonium on photosystem II using FTIR and EPR setups. They reported a decrease in oxygen evolution activity by about 40% upon addition of 100 mM NH_4Cl independent of the pH (5 – 8). In their report the authors raised the point that the PsbQ and PsbP extrinsic proteins may be removed by 50 mM NH_4Cl treatment under room light and therefore removed the PsbQ and PsbP polypeptides in advance by 2 M NaCl treatment. When measuring at 283 K, the FTIR difference spectra of the $S_1 \longrightarrow S_2$ transition showed the following differences: features at (-)1392 cm^{-1}, (-)1354 cm^{-1}, (+)1329 cm^{-1}, and (-)1564 cm^{-1} increased in intensity; a negative band at 1668 cm^{-1} decreased in intensity; and new bands appeared at (+)1521 cm^{-1} and (+)1698 cm^{-1}. However, the wavenumber upshift reported previously by Chu, Feng, et al. (2004) was not observed. This was explained by the difference in measurement temperature, also referring to the study by Huang, Wang, and Chu (2008). When Tsuno et al. (2011) conducted a similar experiment at

250 K, the upshift was visible. Thus, Tsuno et al. (2011) concluded that the results at the two different temperatures have different origins(possibly different ammonia binding sites).

The binding of ammonium to PSII was reported to have a K_i value of ~160 mM (Tsuno et al. 2011) at 283 K. Tsuno et al. (2011) reported that preliminary data suggested that the $S_3 \longrightarrow S_0$ transition is mainly inhibited in the presence of NH_4Cl, but to my knowledge, no further article was published.

Noguchi (2013) summarizes the current understanding of ammonia/ammonium influence on PSII in the following way: While NH_4^+ interacts with carboxylate as a hydrogen bond donor or counter ion, NH_3–being a close analog of water–is supposed to replace a water ligand to a Mn ion and thereby affect the interaction of a carboxylate ligand.

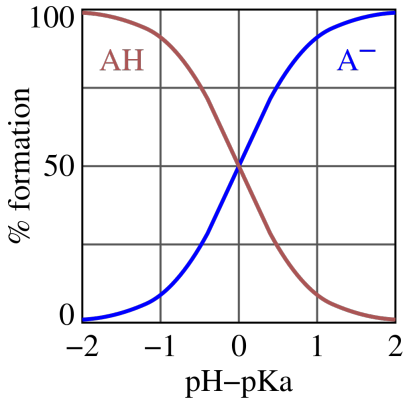

Figure 3.3.: The relative formation of an acid AH and its conjugate base A^- depends on the difference between pH and pK_a. The pK_a of NH_3 is 9.25.

3.3.7. Time-resolved FTIR

The first time-resolved FTIR spectra of PSII were recorded by Zhang et al. (1997). The time resolution of these rapid-scan measurements was 50 ms. Starting from a $Y_Z^{ox}Q_A^-/Y_ZQ_A$ difference spectrum of Tris-washed PSII samples obtained from spinach, the authors were able to differentiate between Y_Z^{ox}/Y_Z and Q_A^-/Q_A contributions by judging individual features' kinetic response to the addition of DCMU (additionally, ferri/ferrocyanide was present). This is feasible because Q_A is influenced by DCMU while Y_Z is not (Zhang et al. 1997). One of the interesting findings of this article is that a differential band at 1706/1699 cm^{-1} was assigned to Y_Z oxidation, also based on the comparison of the decay of this band with EPR and fluorescence measurements of the decays of Y_Z^{ox} and Q_A^- respectively. Although Zhang et al. (1997) stated that time-resolved rapid-scan FTIR spectroscopy is a powerful tool to investigate photosystem II, no FTIR study with a time-resolution better than 1 s has

been published so far (for a review on time-resolved FTIR spectroscopy see Mezzetti and Leibl 2016).

4. Materials and methods

The goal of this chapter is to describe the experimental protocols as detailed as possible. The intended reader kept in mind for these instructions is the untrained (in the field of molecular biology) physicist working at the Freie Universität Berlin who has never before held a pipette in his life.

4.1. Buffers

It is good practice to prepare buffers with ultrapure water, since purified water (typically deionized water) does not contain any salt but it most likely still contains biological material like funghi and bacteria. Ultrapure water does not contain these and thus is less likely to develop mold while stored in the fridge. In addition, the absence of biological material benefits the storage of the PS II membrane particles.

Buffers are mixed in the following way. The ingredients are weighed for the desired volume and put in a large enough beaker. Before weighing the molecular weight of the available ingredient should be compared with the molecular weight used for the calculation of the absolute weight. The beaker is filled with roughly three quarters of the desired volume with ultrapure water and mixed with the help of a magnetic stirrer. The stirrer can be taken out later with a magnetic rod being led at the outside of the beaker, pulling the stirrer along the wall of the beaker.

The pH is then adjusted. Especially when doing pH series measurements, the pH meter should be calibrated before use. In any event the accuracy of the pH value given should be checked using the correct calibration solution. When calibrating the pH meter the right calibration solutions should be used. After use, the pH electrode should be stored in saturated KCl solution. The pH is adjusted typically using 1 M to 3 M NaOH or HCl, since the elements of these bases and acids are already present in the solution. Refer to the pH meter manual for additional instructions.

When the pH has been adjusted the solution is transferred to a measuring cylinder and filled up to the desired volume with the rest of the ultrapure water. To make sure that the solution is properly mixed it should be poured back into the beaker and then transferred to

the storage containers.

Buffers are frozen when not used and thawed the day before usage. It is advisable to freeze the buffer in aliquots if small volumes are needed in the foreseeable future. In this way the multiple thawing and freezing of the same buffer volume, which would encourage mold growth, is avoided and the thawing time is reduced.

Every container has to be labelled with the name of the owner, the mixing date, the content, and any applicable safety alert symbol.

The ingredients are given in table A.1 on page 237. The molecular weights underlying the table are: sodium ascorbate, 198.11; BSA, ~60000; $CaCl_2$, 110.99; EDTA, 292.2; betaine, 117.15; HEPES, 238.3; MES, 195.24; $MgCl_2{\cdot}6H_2O$, 203.3; NaCl, 58.44; saccharose, 342.3. The absolute weight in gram is given by $V \cdot M_{\text{bottle}} \cdot M_{\text{target}}$, with V the desired volume in liter, M_{bottle} the molecular weight in $^{\text{g}}/_{\text{mol}}$, and M_{target} the desired concentration in $^{\text{mol}}/_{\text{l}}$.

50 ml Triton stock solution is prepared by mixing 12.5 ml Triton X-100 with 37.5 ml buffer C which has been prepared without betaine.

Note that buffers C and D are almost the same, differing only in 5 mM of $MgCl_2{\cdot}6H_2O$. Replacing buffer C or D with the other might help to simplify the protocol and the associated lab routine.

4.2. Obtaining photosystem II from spinach

Photosystem II can be obtained from both cyanobacteria and higher life plants. The advantage of obtaining PSII from higher life plants like spinach is that these are virtually unlimited as long as they are comercially available. Additionally, the yield of each preparation is much higher. An important disadvantage is that mutations are much more difficult to introduce and maintain in higher life plants.

4.2.1. Development of the preparation protocol

A photosystem II preparation from higher life plants was first proposed by Berthold, Babcock, and Yocum (1981) and the samples produced by this protocols have been termed “BBY particles”. The authors reported that this was the first oxygen-evolving extraction of photosystem II particles from higher life plants, whereas the extraction of oxygen-evolving photosystem II from cyanobacteria had already been achieved. The key step they introduced was to use intact thylakoid preparations and separate photosystem II from photosystem I by treating the sample with Triton X-100, a mild detergent. The incubation time was 30 min at an Triton X-100 concentration of 25 $^{\text{mg}}/_{\text{mg Chl}}$ (w/w). The salt concentrations they chose in their buffers was reported to prevent the inhibition of oxygen evolution by denaturation

caused by Triton X-100. This treatment reportedly features complete separation of photosystem I from photosystem II, an advantage over preparations from cyanobacteria from the time which were not able to achieve this. The separation of the two different photosystem types is achieved by differentiation of the thylakoids in grana (PS II-rich stacked regions) and stroma (non-stacked regions which mainly contain PS I) (Schiller and Dau 2000).

Dau, Andrews, et al. (1995) gave a more detailed description of the protocol, noting that the procedure should be done in the dark and at 4 ℃ and describing additional centrifugation steps as well as a procedure to create oriented PS II membrane samples on mylar tape.

A major improvement on the activity of the obtained preparations was to add glycinebetaine (Schiller, Dittmer, et al. 1998; Schiller and Dau 2000). Glycinebetaine is supposed to stabilize the protein complex by preventing the dissociation of small extrinsic proteins. The removal of starch can be achieved by additional centrifugation steps and by creating layered pellets with a white layer at the bottom of the centrifugation tube consisting of the starch, and a dark-green layer on top of the white layer (Schiller, Dittmer, et al. 1998; Schiller and Dau 2000). The layering can be improved by first centrifugating at a low speed to prepare the starch layer and then ramping up the speed to add the green layer on top of it. In these studies the detergent concentration was kept at 25 $^{mg}/_{mg\ Chl}$ with a Chlorophyl concentration of 2 $^{mg}/_{ml}$, and the incubation time was 20 min while stirring as slowly as possible. In another study (Iuzzolino et al. 1998) the incubation time was decreased to as short as 1 min, and this is the incubation time used in this study.

In the following the preparation of photosystem II from spinach as it has been done for this study shall be discussed in detail.

4.2.2. Preparations done the day before

Ideally the day before the preparation everything is put in order. The buffers (1 l buffer A, 1 l buffer D, 250 ml buffer B, 250 ml buffer C, 100 ml tritone stock solution, see section 4.1) are either freshly prepared (with ultrapure water) or thawed and set aside in the fridge. There should be enough acetone and purified water for the Chlorophyl determination.

The availability of the following items should be checked for: automatic pipettes (100 µl to 5 ml), brushes for resuspending the pellets, a labelled (preparation number) box with Eppendorf-like containers (“eppis”), the blender and its top part, gauze, Miracloth, a magnetic stirrer including fish and rod, two small and two large tubs, three buckets, a funnel, a two liter flask, six large centrifuge containers, two pairs of centrifuge tubes for the table centrifuge, a scale, cuvettes and ten 10 ml flasks for the Chlorophyl measurement, four measurement cylinders (100 ml), three beakers (200 ml), and at least 38 small centrifuge tubes.

Brushes are used for resuspending the pellets. Brushes with natural hair contain many little gaps providing space for dirt, bacteria and funghi. This reason the comparably smooth synthetic hair brushes are better suited.

4.2.3. Before the preparation start

Purchase up to 5 kg of spinach. Since many supermarkets will not have that much spinach in a good quality, it is often beneficial to call the supermarket a few days before and order the spinach. It is also possible to have it delivered, which often comes with the advantage of the spinach being in relative darkness longer. The spinach should be kept in the dark as long as possible before the preparation, because the grana stacks are built in the dark; the grana stacks are separated from the stroma thylakoid when adding the detergent. However, the start of the preparation should not be delayed in favor of a longer dark adaptation time.

The dark adaptation is a good time to prepare the Chlorophyl measurements by preparing 100 ml acetone 80/20 and filling it in the 10 ml flasks. The centrifuge should be turned on to cool down to 4 ℃. Buffer A is completed by adding 1 g albumin (BSA) and 1 g sodium ascorbate. Subsequently the pH is adjusted to 7.5 with KOH. The flask, funnel, tubs, gauze, and Miracloth are set in place.

4.2.4. Obtaining thylakoid membranes

The following steps until the end of the preparation should be done as fast as possible. The spinach is washed in batches once with normal water and then with purified water. The stalks and large veins are removed, the leaves are stored in a bucket on ice. Only fresh, crisp, undamaged leaves should be used, damaged leaves should be discarded. As the leaves are ripped apart the process of degradation starts, so the steps until the first centrifugation should be done as fast as possible.

After all leaves have been processed the spinach is homogenized using a blender with buffer A. The liquid is squeezed trough double-layered gauze, and then through Miracloth. While force should be exercised when squeezing the spinach through the gauze, the pre-filtered liquid should flow through the Miracloth without leaving behind a lot of residue. The liquid is then centrifuged for 10 minutes at 17000 g. During this time it is a good opportunity to keep 16 small centrifuge tubes and buffer B ready as well as cleaning the tools and the laboratory where needed.

The supernatant is discarded and the chloroplast-containing pellets resuspended with large brushes and buffer B. When resuspeding the pellet with a brush, it is important to start with a very small buffer volume to create a cream, therefore the added buffer volume

should not be larger than the volume of the pellet. Once the pellet has been resuspended into a cream, more buffer can be added to dilute the cream into a liquid. If one starts resuspending the pellet with a large buffer volume, the pellet will be released in clumps, leading to a mediocre buffer exchange and a bad state concerning the next centrifugation as well as effects of new chemicals on the pellet.

Clumps in the solution can be found by filtering the solution through Miracloth: the chunks will be caught in the Miracloth and can be resuspended using a brush and some additional buffer. This is indicated before doing low-speed centrifugations in order to remove cell debris and starch.

Buffer B is a high-salt buffer meant to destroy the chloroplasts by osmosis. The following centrifugation step is therefore meant to separate cell debris and starch from the intact thylakoid membrane: the solution is centrifuged for 2 minutes at 1100 g and subsequently the pellet is discarded. If the pellet is dark-green after the centrifugation though it seems likely that not only cell debris (which should not contain chlorophyl), but also thylakoid membranes have been pelletted. This happens especially when the pellet is not homogenized properly with the brush, i.e. when the pellet is removed in chunks from the bottom of the centrifuge tube. The size and color of the pellet should be judged on a case-by-case basis. The supernatant is collected and centrifuged for 12 minutes at 50000 g to collect the intact thylakoid as pellet.

Historically, 50000 g was the fastest speed the rotor SS34 of our centrifuge Sorvall RC26 could handle. Nowadays our new cooling centrifuge can reach up do 80000 g. Further optimizations may be possible by adjusting the 50000 g centrifugation speeds and times.

4.2.5. Separating grana and stroma through detergent treatment

The pellet is resuspended with not more than 100 ml buffer C. Determine the volume and chlorophyl concentration of the suspension (section 4.4). The amount of buffer C needed is $V_C = V_0(2C/5 - 1)$ in ml with C being the chlorophyl concentration. The amount of tritone stock solution needed is $V_T = CV_0/10$ in ml (see section 4.2.1). Add the buffer C volume to the sample. Then start stirring the solution gently and slowly add the tritone solution. Incubate the sample for one minute starting from the initial tritone addition.

The next centrifugation step again should separate cell debris and starch from the PS II membranes: centrifuge the solution for 2 minutes at 1100 g and keep the supernatant. Again, observe the pellet for pelletting of thylakoid membranes. Collect the supernatant and centrifuge it for 15 minutes: start the centrifugation with a low speed (e.g. 1100 g) and after a few minutes ramp the speed up to 50000 g. With the new cooling centrifuge it is also possible to choose a slower acceleration. For example, when starting the centrifugation and

selecting as ramp up speed setting number 5, the ramp up will take about four minutes and increase the speed exponentially. This should help the layering of the starch and cell debris below the PS II membrane particles.

The result from the previous centrifugation will be a white layer at the bottom of the tube, possibly with a differently colored spot from cell debris. The upper green layer is resuspended with a soft brush in buffer D. The previous centrifugation ("washing step") is repeated until no starch is left in the sample.

Caution should be exercised when repeating the washing step. Too many centrifugations will make the pellet very hard, which is a sign for low sample quality. In later steps typically a shorter centrifugation time may be used in this case, e.g. 12 or even 8 minutes. To increase the centrifugation efficiency, as many tubes as possible (8) should be used. Large volumes in the tubes are preferred.

When the sample is ready, all pellets are resuspended in a total volume of 50 ml buffer D. The chlorophyl concentration should be at least 2 mg/ml. Distribute the suspension in appropriate aliquots to the eppies, label the box (if it is not labelled already), record the benchmark data in the −80 ℃ book and store the sample in the −80 ℃ freezer. The freezer should only be opened under dim green light. Finally all tools and the lab are thoroughly cleaned.

4.3. Centrifugation

The centrifuge should be turned on well in advance of sample centrifugation to allow for the device to cool down. The tubes inserted in the centrifuge rotor should be balanced pairwise as good as possible: this does not only prevent the centrifuge from being damaged, but also benefits the quality of the centrifugation step because the better the rotor is balanced, the less it vibrates and shakes the sample. When balancing the tubes the lids should be taken into account as well. The tubes have to be dry at the outside before balancing.

The rotor should be inspected before centrifugation. Most caps are not leak-proof, and occasionally sample residue of the previous user can be found at the bottom of the rotor cavities. Of course, in this case the rotor is not completely balanced and it has to be cleaned before use.

The centrifugation tubes should be filled to 80 % of their volume for better stability. Centrifuging the sample in a larger volume also gives better results. During the PS II preparation one should use as many centrifugation tubes as possible. However, if only a few tubes or even only a single tube is used, the steps can be sped up considerably. Before centrifuging acids or bases check whether the material of the tubes can handle the solution.

The rotor or even the whole centrifuge might otherwise be seriously damaged or destroyed. The tubes should not be written on because solvents contained in the ink of many markers may make the tube brittle.

During the centrifugation the sample is well enough protected from outside light, so the light in the lab can be turned on as long as the centrifuge is closed.

After turning off the centrifuge the lid should be let open so that any condensed water vapor can evaporate again. Most likely ice will have formed inside the centrifuge; this should be removed with a paper towel after it has thawed.

4.4. Chlorophyl determination

The correct determination of the chlorophyl concentration by visible light spectroscopy is an important task for a variety of tasks in the lab. It is not only a qualitative, but quantitative measurement and therefore has to be done very carefully.

If a frozen sample shall be measured, it should be thawed for at least one hour on ice and washed by centrifugation in buffer D. The supernatant is removed and the resulting pellet has to be resuspended very carefully (see section 4.2.4) in buffer D so as to avoid releasing the pellet in clots.

A fraction of the sample will be dissolved in acetone, which should be handled under the fume hood while wearing safety equipment. A solution of 80/20 acetone/water is freshly prepared and distributed to 10 ml volumetric flasks. Two of these flasks are needed for sample dilution and one is needed for the background determination. The flasks should always be closed with lids to prevent evaporation of the acetone. A 20% water content in the solvent may prevent the complete extraction of chlorophyl a and β-carotene (Lichtenthaler 1987); however, as long as the pigments stay in the solution the concentration determination will be exact enough for our purposes.

40 µl of the sample are pipetted into one 10 ml flask. Two flasks are prepared in this way. Each time a new pipet tip has to be used, otherwise the sample will be contaminated with acetone. Upon visual inspection no green particles should be visible. When the sample has been completely dissolved the volumes are transferred to two glas centrifuge tubes for the table centrifuge; these centrifuge tubes are not to be confused with TXRF sample tubes, since the latter ones will break in the centrifuge. In this case, remove the liquid from the centrifuge bucket, then remove the respective centrifuge bucket by tilting it upside down and clean it thoroughly.

The sample is centrifuged for 4 minutes at 3000 rpm to precipitate any particles which have not been dissolved, especially starch. If the pellet is green, then parts of the sample

have not been resuspended correctly and the procedure should be started again. The aim of the centrifugation is to remove any light-scattering particles from the solution which would distort the measurement in the spectrometer. The whole procedure should be done under dim light. Although Photosystem II is destroyed anyway, the pigments themselves can be easily photobleached since they are extremely light sensitive (Lichtenthaler 1987).

A part of the solution of each centrifuge tube is then transferred to a cuvette respectively; the cuvettes should be sealed with special tape if it is anticipated that the measurement will take longer than a few minutes to avoid evaporation of the acetone. An aliquot of the unused, pure acetone/water mixture is transferred to another cuvette to be used for the background measurement in the spectrometer.

The spectra are collected using the "simple reads" mode using the "multiple collect" option with the following functions (values obtained by Lichtenthaler (1987) modified by Wellburn (1994)):

```
(12.21 * Read(663) - 2.81 * Read(646)) * 0.25;
(20.12 * Read(646) - 5.03 * Read(663)) * 0.25
```

The additional factor 0.25 stems from the ratios of sample volume versus solvent volume. Without any additional effort it would be possible to measure the carotenoid content with the following line (Lichtenthaler 1987): `(250 * Read(470) - 1.82 * Ca - 85.02 * Cb) / 198`, where `Ca` and `Cb` are the respective chlorophyl concentrations. However, this was not investigated nor needed in this thesis.

First the background is measured ("zero"), then the two cuvettes with the sample are measured and averaged. The first column gives the chlorophyl a concentration, the second column gives the chlorophyl b concentration. Together one can obtain the total concentration in g/l.

After the measurement, left over acetone solution (this includes the measured sample) must not be disposed of in the sink. Instead, it should be collected in a beaker and put in the fume hood to evaporate. The beaker can be cleaned once the solution has evaporated completely.

4.5. Oxygen evolution activity measurement

The activity of the sample is given in terms of the quantity of oxygen released per chlorophyl per second and measured using a clark-type electrode (Gorkom and Gast 1996). Just like the chlorophyl concentration measurement this quantitative measurement has to be done

very careful in order to obtain reliable results.

The cathode and anode of the electrode are separated from the sample by a teflon membrane which is not permeable to water or ions but to oxygen (Gorkom and Gast 1996). Upon light illumination, the PSII in the sample generates oxygen from water; the sample is carefully stirred, and the oxygen diffuses to the electrode. At the electrode it is detected by the current which is flowing through oxygen reduction: upon application of a low cathode potential of about -0.7 V relative to the anode, the platinum cathode reduces oxygen to hydroxyl. At the anode, first AgCl and later AgOH is created (Gorkom and Gast 1996). The experimentally measured value is then the voltage over a resistor through which the current flows.

The measurement is done in a special buffer containing 1 M betaine, 25 mM MES, 15 mM NaCl, and 5 mM $CaCl_2$. The sample should therefore be centrifuged and resuspended in this buffer before the chlorophyl concentration and the oxygen evolution activity of the very same sample are subsequently measured.

Before the start of the measurement, the membrane needs to be checked. If the sample compartment has dried out, the old membrane should be discarded. The electrode is cleaned to remove AgCl and AgOH. 3 M KCl is applied to the electrode before it is covered with a new membrane. The temperature of the circulating water and the buffer is set to 28 ℃ well before the measurement.

The total volume of the sample is 2 ml, and the measurable chlorophyl concentration is 5 µg/ml. Therefore, 10 µg are added to this volume. The reason to use such a small amount of chlorophyl is to make sure that the light intensity used is saturating. For this measurement it is especially critical that the pellet obtained by centrifugation is resuspended very carefully (see above). If the particles are too large or start to shield each other from the incoming light because the concentration in the buffer is too high, the measured oxygen activity will be lower than the real value. However, it should be worthwhile to measure a saturation curve and see whether higher amounts of chlorophyl can be used in the future to increase the signal-to-noise ratio.

For the calibration, sodium dithionite is used. It removes all molecular oxygen from a solution via the following reaction:

$$Na_2S_2O_4 + O_2 + H_2O \longrightarrow NaHSO_4 + NaHSO_3 \tag{4.1}$$

Therefore, adding sodium dithionite to the buffer will lead to a negative signal. Since the saturation concentration of oxygen in the buffer as well as the added buffer volume of 2 ml is known and small amounts of sodium dithionite suffice to capture all the molecular oxygen, the resulting measured amplitude provides an absolute scale for the signal

which is measured later. After this calibration, the sample compartment needs to be purged very thoroughly using the measurement buffer a few times to remove all traces of sodium dithionite.

For the measurement of the sample, first 2 ml of buffer are added. Then, 40 µl FeCy solution (50 mM of FeCy(III) in H_2O) are added. The sample is added as the volume coresponding to 10 µg of chlorophyl. Finally, 10 µl DCBQ solution (50 mM DCBQ in DMSO) are added. The data aquisition is started and a few seconds later the light is turned on. The recorded timecourse will be flat in the beginning and turn into the slope when the light is turned on. The slope gives the oxygen evolution in mmol/mg·h. Several measurements are averaged. The individual measurements should not take too long and the slope will taper off after a relatively short time.

After the measurement the sample compartment should be filled with buffer, otherwise the membrane will degrade.

4.6. The setup and its improvements

The FTIR setup used was first set up by Dr. Björn Süss (Süss 2011). It consists of a commercial spectrometer (Bruker, Vertex 70, see also section 4.11) combined with a custom built sample chamber featuring two linear stages for sample exchange. The two most important features of the setup are that it is able to measure almost 2000 sample spots and that it is able to measure fully automated. These two features are necessary to achieve a sufficient SNR in the step-scan mode. A scheme is displayed in figure 4.1.

The heart of every FTIR spectrometer is the Michelson interferometer. The interferometer of the Vertex 70 is a rocking cube construction, in which both mirrors are moving corner reflectors. The beamsplitter is made of KBr.

The path of the IR beam has been modified using mirrors to focus it. Typically during a measurement the largest diameter for the aperture near the globar is chosen (8 mm). This results in a focussed beam with a 2σ diameter of 1.6 mm.

Two linear stages move a sample stage which is able to accomodate up to 45 CaF_2 sandwiches with 25 mm diameter. Each CaF_2 disc has a thickness of 2 mm; the discs were purchased from Crystal GmbH (Berlin, Germany). Choosing a typical sample spot diameter of 2.5 mm (see below) results in 1980 measurement spots in total. The current implementation of the custom control software (see below) fully automates the data sampling.

The detector is a liquid nitrogen cooled MCT detector used in DC mode. The IR amplitude measured at an empty pair of CaF_2 plates is typically 24000 (unitless value shown by Opus).

The spectrometer communicates with the connected computer through the local area net-

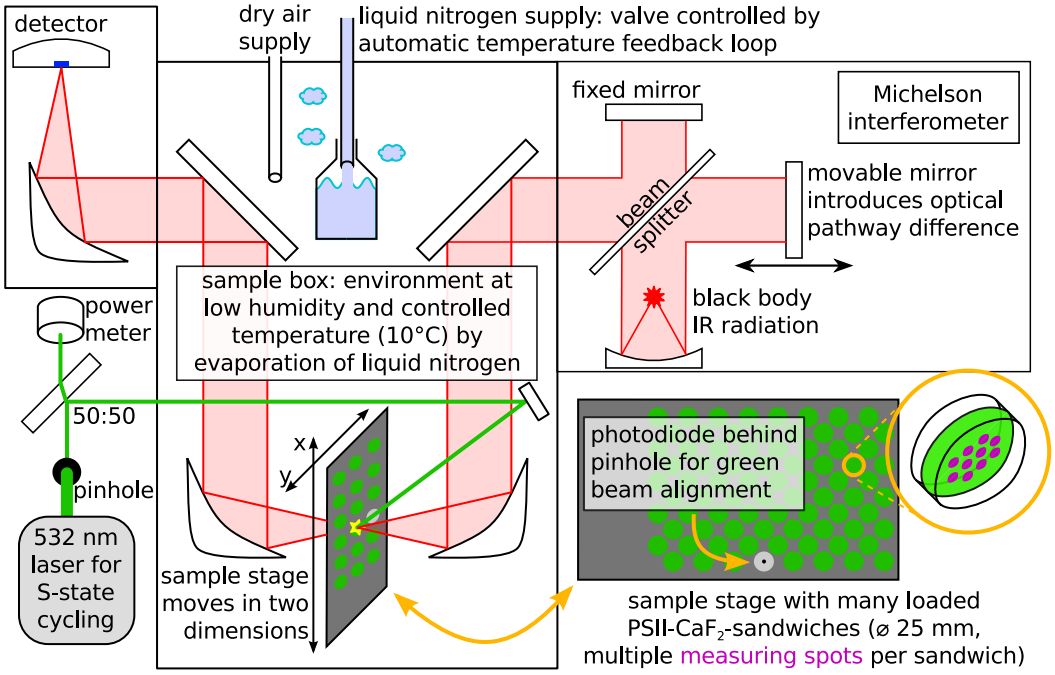

Figure 4.1.: Scheme of the FTIR setup.

work and HTTP commands. Measurement files can be obtained by issuing GET requests to the Vertex. Most users will use the commercial software "Opus" sold by the manufacturer Bruker to communicate with the Vertex. While there is some possibility for customization of the measurements through macros and programming interfaces, eventually in our setup we took control of the Vertex on our own using a custom made software (which also controlls all the other hardware and is maintained by Dr. Petko Chernev) through HTTP commands. This was necessary to handle repeated freezing of the Vertex's server (see section 4.11). Unfortunately the HTTP interface is poorly documented and so Dr. Petko Chernev had to resort to reverse engineering to make the HTTP commands sufficiently reliable.

During my work I have improved the setup significantly in several regards. First of all, the temperature control system as originally designed did not work. Four water-cooled Peltier elements were attached to the sample stage at one side, supposedly cooling the CaF_2 sandwiches through the good thermal conductivity of the metal sample plate. Temperature measurements conducted at each CaF_2-sandwich position using a Pt1000 element embedded in an aluminium plate while setting the target temperature as low as possible resulted in the temperature gradient shown in figure 4.2.

When the temperature was set as low as possible at the Peltier controller, a large temperature gradient could be observed across the sample plate. If the temperature was set to 10 ℃ at the controller, the temperature at the column next to the Peltier elements was

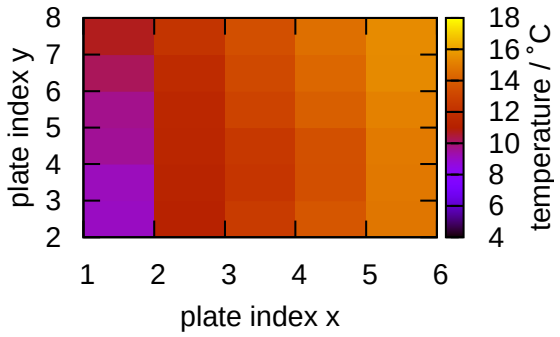

Figure 4.2.: Temperature at different CaF_2 positions using the former Peltier element approach. The temperature at the controller was set as low as possible. In this view, the Peltier elements would be mounted left to the sample plate.

around 18 ℃ (data not shown). This was unacceptable and much time was spent designing and implementing a new cooling system.

After several failed attempts using Peltier elements at the outside of the sample box, I decided to augment the liquid nitrogen system which is attached to the setup because of the MCT detector. The first attempt was to cool the air in the sample chamber using the evaporated nitrogen from the dewar, but without success. The final approach was to inject liquid nitrogen into a reservoir in the dewar which then promptly evaporates and cools down the atmosphere in the sample chamber. The sample chamber can be cooled down very quickly in this way, but this approach has the disadvantage that the measurement has to be stopped every time liquid nitrogen is injected. In a future experiment, the sample chamber should be designed to be insulated from the start and cooled from the outside using air cooled Peltier elements (water cooled Peltier elements introduce too much noise through the circulating water; see Süss 2011).

The second improvement is the complete redesign of the laser beam path. Formerly, it was neither possible to measure the shape of the beam at the sample spot nor to measure its position. The laser source was changed from a Quantel Omega to a Minilite II. To measure the shape and position of the laser spot, I manufactured a holder featuring a pinhole for a compact large-surface photodiode and connected it to appropriate electronics (reverse bias 20 V). The photodiode behind the pinhole can be moved across the laser spot right at the sample position, accurately measuring the position as well as the beam shape. The pinholes have approximate diameters of 0.6 ± 0.1 mm; smaller pinholes (300 µm or 100 µm) may be implemented in the future. The laser beam spot now features a radially symmetric boxcar profile of adjustable diameter. It is important to be able to measure the beam's position

after setting up the experiment, because the experiment rests on an air-cushion table. Once one closes the sample box the table will generally move. Most of the times, but not always, it will move back into its original position. Since the laser rests on a different table, the alignment will change in this case. Therefore it is necessary to check the position after the experiment has been set up. It is instructive to watch the intensity at the photodiode while moving the table and during its slow recovery.

I have measured the intensities at both arms of the laser pathway and found that the intensity is twice as large in the detector arm than in the sample arm. Therefore, the measured intensity (at the power meter) has to be divided by a factor of two to calculate the intensity arriving at the sample spot.

The custom sample plate is comparatively large; the movement of the translation stages has to be adjusted carefully to reflect the movement of the IR beam over the sample. Using two pinholes located at opposite corners of the sample stage the IR beam position can be accurately determined. This information is used to calibrate the movement of the sample plate greatly improving the accuracy of the translation stages. A calibration of the sample stage generally results in a corrected misalignment of approximately 1 mm.

4.7. FTIR sample preparation

The sample is stored at −80 ℃ and thawed on ice for at least one hour before the measurement. It is handled in the dark or dim green light and on ice or in the cooling chamber at all times. After thawing I resuspended the sample in a centrifuge tube and filled the tube with the measurement buffer. The sample was then centrifuged at 50000 g for 12 minutes in the cooling centrifuge, which was set to 4 ℃ (D_2O: 8 ℃ to prevent freezing). When the measurement buffer was different than the storage buffer D, I repeated the previous washing step, resuspending the pellet in new buffer in between. During the centrifugation I prepared the CaF_2 plates. Usually I prepared about 110 CaF_2 plates by laying them out on paper cloth and applying two dots of vacuum grease at opposite spots near the edge of the plates to half of the plates.

After the centrifugation I collected the pellet on a Petri dish, added the electron acceptor and stirred the mixture with a spatula. Subsequently, I applied aliquots of the sample to each of the ~110 CaF_2 plates. In the cooling chamber this takes long enough to dry the sample to just the right humidity (personal subjective assessment). Then I prepared the sandwiches by putting one CaF_2 plate without two dots of vacuum grease onto one with two dots of vacuum grease and subsequently rotating the plates against each other. This distributed the vacuum grease along the edge of the sandwich creating a ~2mm width ring

of grease, creating an air-tight seal. Grease contamination in the sample is determined by the presence or absence of characteristic absorption bands. At the beginning of my work I just applied grease to the finished sandwich; this proved to be insufficient to stop the sample from drying out. The described approach prevents drying out of the sample very well.

The ~55 sandwiches where then transferred to the FTIR lab to adjust the thickness. A sample preparator was constructed by Björn Süss (Süss 2011) which makes it possible to decrease the thickness of the sample while monitoring the IR absorption in realtime. Each sample was prepared in such a way. During the thickness adjustment one or two pre-flashes were applied to the sample. After the thickness of the sample has been adjusted to not exceed an OD of 1 at any wavenumber, I selected the best 45 sandwiches to go into the sample box.

4.8. Electron acceptor: PPBQ in DMSO

PPBQ has been used as electron acceptor in this study (see section 3.1.1). 516 mg of PPBQ have been dissolved in 4 ml of DMSO, leading to a 700 mM stock solution. The stock solution has been stored in 40 µl aliquots at −80 ℃. After thawing, the solution should be stirred (for example using a spare pipet tip) to make sure no PPBQ crystals are floating in the solution. During experiments, for each mg of chlorophyl in the sample 1 µl of the stock solution has been added to the pellet after centrifugation and collecting the sample on a Petri dish on ice. Assuming a sample density of about 50 $^{mg}/_{ml}$ and taking into account that the added volume (typically 30 µl) dilutes the sample, this corresponds to approximately 30 mM of final PPBQ concentration in the pellet.

The electron acceptor stock solution should only be handled while wearing gloves. Left over solution should be correctly disposed of, i.e. labeled and placed in a contaminated waste container for incineration.

4.9. Selecting the right spots: thickness vs. IR intensity

Typically, before the start of the real measurement, the thickness at each individual measurement spot has been measured. If a spot was too thin or too thick, it was discarded. If a spot is too thin, the measured difference signal will be very small; if it is too thick, too little photons arrive at the detector. The limits chosen as acceptable are 1 ± 0.2 OD at the maximum of the absorption (for both H_2O and D_2O). Typically about 90% of all spots met this criterium.

It is also possible to just measure all spots and throw out later the measurements where

the thickness was not acceptable; measuring the "good" spots before the main measurement saves some measurement time though. For a rapid-scan measurement I recommend to measure all spots when there is more than one kind of sample in the sample stage (for example, NaCl as well as NH_4Cl) so that the measurement files can be separated easily. Going through all spots in a step-scan measurement will result in a period-of-45 oscillation in the interferogram though: When moving to a new spot after each mirror position which lies on a new CaF_2 sandwich, after 45 mirror positions all CaF_2 plates will have been measured once. Because one interferogram has more than 300 mirror positions, this will result in the period-of-45 oscillation. A possible remedy is to implement a kind of random selection of the next spot to be measured.

4.10. Laser warmup, intensity and spacing

The laser used is a Minilite II by Continuum. Its flashlamps were only triggered when lasing was required, i.e. with about 1.4 Hz (700 ms flash spacing during a train of ten flashes). A power-meter recorded the intensity of each individual laser flash. In figure 4.3 (top) the average intensity of the flashes is shown. While there was an occasional pause between each train of ten flashes, the first flash shows the same intensity as the other flashes. This can also be seen in figure 5.11 on page 92 where the signal recorded by the MCT detector is shown. The flashes show an expected standard deviation of 10%.

Since the heat signal caused by the incident laser flash scales linearly with the laser intensity (Görlin 2012), it is necessary to find the minimum laser intensity required. In figure 4.3 the result of a measurement with varying laser intensity is shown. To find the minimal laser energy, single laser flashes with varying intensity were applied to dark-adapted sample spots and the difference spectra ΔA were recorded. Pairs of peaks have been selected to measure the overall amplitude of the transition: (+)1658 cm^{-1} - (-)1645 cm^{-1}; (+)1500 cm^{-1} - (-)1545 cm^{-1}; and the mininum of the difference spectrum ΔA has been subtracted from its maximum. The three resulting sets of data points have been fitted with single-exponential functions. Finally, I decided to use a laser power of 5 mJ/cm^2 so as to ensure complete S-state advancement even when an individual flash has a lower energy than the average, but avoid to increase the heat-induced signal too much. The diameter of the laser flash on the sample was 2 mm.

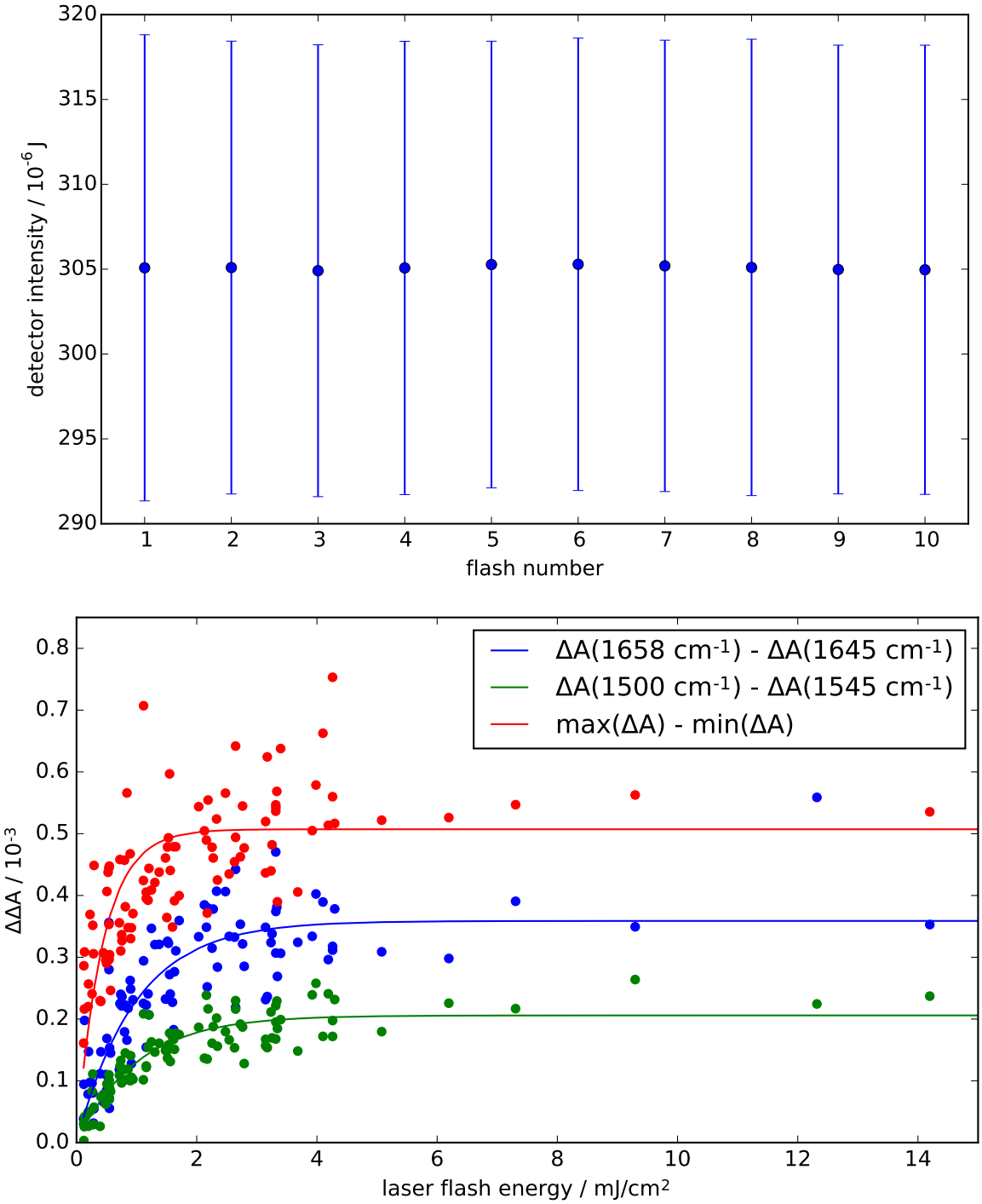

Figure 4.3.: Top: the laser flash intensity as recorded by the power meter. The bars represent the standard deviation. Bottom: saturation curves for the $S_1 \longrightarrow S_2$ transition. Three different double differences have been calculated as indicated in the legend and fitted with single-exponential functions.

4.11. Vertex 70 bugs and workarounds

A number of the spectrometer's bugs significantly complicated the research, especially in the step-scan mode. Unfortunately none of these could be alleviated by the manufacturer (Bruker Corporation). The complications and their workarounds are described here.

- The spectrometer often has to be reset. It seems to get stuck in its routines randomly, which complicates long automatic measurements significantly. The different error messages did not indicate the reason, even to Brukers' employees. Dr. Petko Chernev of our workgroup devised routines to check whether or not the Vertex is stuck, reset it, and adjust the measurement accordingly. Many measurements were unsuccessful before these routines were finally implemented, which was a pitty considering that setting up one experiment takes at least ten hours and the sample is lost. To apply this remedy we had to give up on using Opus and call the Vertex directly with HTTP commands. Unfortunately this is not documented and it was not possible to obtain any kind of documentation from the company.

- The form of the interferogram depends on a variable called "absolute peak position". To me it is not clear how this value is calculated, but it may or may not change when the spectrometer is reset. It is set when one opens the "Justiermodus" in Opus and selects "Peak Position speichern". The shape of the interferogram is different in the rapid-scan and step-scan modes. We only recognized this after half of the H_2O step-scan data was completed; there was no way to recover the shape of the interferogram from the measured data. Therefore I measured a set of interferograms with different "absolute peak positions" and determined through fitting the actual shape of the spectrum (see section 4.14.1 on page 46). In the future, the shape of the step-scan interferogram should be measured for each step-scan position in the step-scan mode.

- In the step-scan mode the lowpass filter is set randomly, whether or not it is selected at the start of the measurement. This is a pitty because it seems to be a Chebycheff type filter which unnecessarily introduces ringing to the timecourse. In any event it is only a digital filter which is applied after digitalization, so nothing is gained, but information is lost. It would be much better to just record the unfiltered data and apply a digital filter later during the data processing as needed. This seems to be a bug in the firmware, but the manufacturer of the spectrometer did not find a remedy.

- Another bug in the firmware is the buffer overflow of a circular buffer. This results in the step-scan timecourses sometimes being recorded in a shifted way, with data points

which belong to the beginning of the timecourse shifted to its end. The corresponding workaround is described in section 4.14.2 on page 47. The first timecourse of the first flash is always off by eight data points.

- Sometimes the first few values of a step-scan timecourse have a huge error. As a safety measure I always discard the first ten points of every timecourse.

- The acquisition of the data points does not correspond to the timing of the TTL pulses, i.e. some delay is introduced somewhere. The pulse generator is set so that the laser flash should be applied 1000 data points (6 ms) after the spectrometer starts recording. However, the maximum of the flash is found at point 1016, which is a delay of about 96 µs. The shifting of the time axis is covered in section 5.7 on page 109.

- The offset of the step-scan timecourses is different for each flash applied and varies randomly. This is not a real issue, but if the offset were always the same one could also use the dark spectrum of the following flash to record data 700 ms after the flash has been applied. Additionally, the difference after a train of flashes compared to the dark state could be calculated, which is not possible with the present measurements.

- It seems that not every part of the system shares the same ground potential, and thus it can happen that an output at zero volts is interpreted as a positive signal by the connected input. In this case it helps to disconnect the trigger cables at the trigger box while a measurement is running and reconnect them again. In our experience restarting the computer and the Vertex does not help.

4.12. Infrared beam and green laser beam profiles

To reliably align the infrared and the laser beams, I measured their profiles using pinholes. For the IR data, the pinhole (about 0.6 mm diameter) was moved across the profile and the absolute amplitude at the MCT detector was recorded. For the laser beam, the photodiode which is located right behind another pinhole (about 0.5 mm diameter) was used to record the intensity of the incident beam. The result is shown in figure 4.4.

The IR beam shows a Gaussian profile with a 4σ value of less than 1.6 mm. Therefore I chose to shape the laser beam profile so as to achieve a 2 mm diameter spot, so that minor alignment inaccuracies would not lower the signal amplitude. Both profiles have been measured using pinholes with diameters that are large enough to lead to convolution effects in the measured data, and these effects have been taken into account. While the unconvoluted IR beam profile does not differ a lot from the original measured data, the laser beam

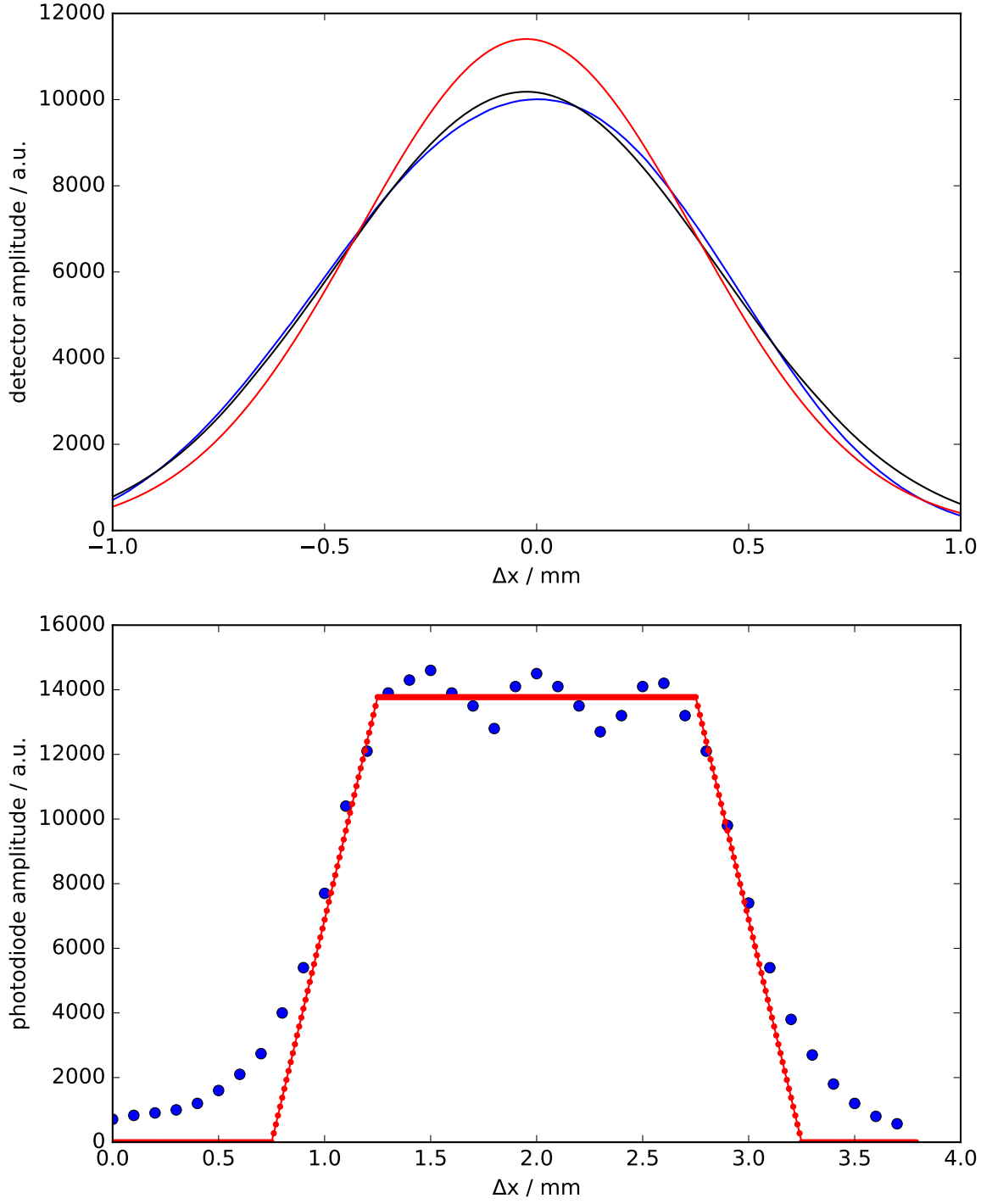

Figure 4.4.: Top: profile of IR beam (8 mm aperture selected). Blue: measured data; black: fit consisting of Gauß-curve convoluted with 0.66 mm boxcar function; red: unconvoluted Gauß-curve with $4\sigma < 1.6$ mm.

Bottom: profile of laser beam. Blue: measured data; red: 2 mm boxcar function (diameter of beam-shaping pinhole) convoluted with 0.5 mm boxcar function (diameter of the pinhole right in front of the photodiode).

profile shows strong convolution effects. Since it corresponds well to the simulated profile (two convoluted boxcar functions), the laser beam profile can be safely assumed to realize a steep boxcar profile with a diameter of 2 mm. The side wings which can be seen in the laser beam profile data most likely resemble diffraction rings which cannot be resolved with the photodiode pinhole.

For the measurement I selected spots which have a diameter of 2.5 mm. This makes sure that the actinic laser flashes never influence neighboring spots. This is always the case, independent of whether or not the IR beam and the laser beam are perfectly aligned. In any event, during all my measurements I did not measure all the spots on a CaF_2 sandwich before moving to the next sandwich; instead, I measured the same spot on all sandwiches before moving to the next spot. This allows for a brief dark-adaptation period between measuring two neighboring spots.

As a side note, I also measured the IR beam profile when the 3 mm aperture is selected (data not shown). The IR beam diameter was almost unchanged; therefore, the 8 mm aperture should always be selected to have as many photons as possible arrive at the MCT detector.

The measurements shown above were also done for the vertical dimension y; qualitatively the same results have been obtained (data not shown).

4.13. Typical measurement day

The day before I started a measuremet I refilled the liquid nitrogen dewar, made sure that there are enough clean CaF_2 plates, and put the measurement buffer in the fridge after thawing it.

The first thing in the morning (I usually started at 9 a.m.) is to get some ice to thaw the sample in. While the sample was thawing and centrifuging, I prepared the CaF_2 plates by laying them out on paper towels and adding the vacuum grease to half of them. I also put the sample creator in the sample chamber and generally prepared the setup. After the centrifugation finished the pellet is transferred to a Petri dish using a spatula and the electron acceptor is added. then the pellet is distributed in parts to all ~110 CaF_2 plates. After the sample was distributed I combined two CaF_2 plates (one with and one without vacuum grease) to form a sandwich. The time this took was just right to have the pellet dry enough but not too much. Afterwards I stored the samples on ice in a black box which I put in the fridge. Because there are so many samples to assemble this already takes a few hours, so at this point I took my lunch break (usually between 1 and 2 p.m.).

In the afternoon I would typically adjusting the thickness of the sample. Because this is

semi-automated, I used to handle two sandwiches at the same time: while one was in the "sample creator" which rotated the two CaF_2 plates against each other while exerting light pressure, I pre-flashed the previous sandwich. Because I widened the laser beam up to the whole sandwich I used one saturating flash for the H_2O samples and two sub-saturating flashes for the D_2O samples (because the D_2O samples absorbed more light in the visible range than the H_2O samples the green pre-flash was not saturating anymore). This usually took three to four hours, so I would finish this between 6 and 7 p.m.. Then I put the samples into the box (which took about 20 minutes), closed the box and started the liquid nitrogen cooling. At this point I would take a small break to wait for the box to be cooled; It is better to do the subsequent tasks without liquid nitrogen being injected into the box.

When the box was closed and I would not have to touch it anymore, I checked the alignment of the IR and laser beams. First I checked the adjustment of the sample plate by finding the focus of the IR beam with two pinholes which were set in two opposite corners of the sample plate. With this information, the exact position of every sample spot can be calculated. Then I moved the sample plate to the position of the photodiode to adjust the laser. By moving the stage by ±1 mm around the laser profile, I could determine its position very accurately and adjust accordingly.

After the adjustment of the two beams I would start to measure the thickness of all spots and go for dinner around 8 p.m., since this measurement takes about 45 minutes. This information was used later to select only spots with a maximum OD of 1 ± 0.2.

After the thickness measurement finished, the laser power was adjusted to the right value and the main measurement set up. Sometimes I would check the $S_1 \longrightarrow S_2$ transition of a few spots to get a rough impression of the overall activity of the sample. Setting up the main measurement also takes some time because there are many different parameters and hardware adjustments (e.g. the setting of the triggering cables) that need to be double-checked. Setting only one parameter wrong could cause the whole measurement to fail. After starting the measurement I always checked some interferogram timecourses to see the incident laser and its effect on the timecourse. If everything went fine, I would be able to leave the lab between 10 and 11 p.m.; but often due to the complexity of the setup all kinds of problems arose which had to be solved first.

Many measurements failed because the Vertex crashed some time after starting the measurement. After Dr. Petko Chernev implemented the workarounds the setup could run fully automatic for three days. Therefore, I started the measurements twice a week, and the setup was measuring almost continuously for several months.

4.14. From the interferogram to the spectrum

This section is divided into several parts to show how an interferogram is transformed into a spectrum. The different parts are modular; for example, the next subsection (4.14.1) only applies to step-scans which record a set of timecourses at a different sample position per mirror position. Most of the subsections only apply to time-resolved step-scan data; the Forman phase correction has been applied to all data shown in this thesis though.

4.14.1. Shifting step-scan timecourses to rapid-scan interferograms

In a typical step-scan measurement a new spot on a different CaF_2 plate is measured for each step-scan mirror position. The differing sample thickness results in a vastly distorted absolute interferogram. This distortion can be resolved by shifting the very beginning of the step-scan timecourses to a dark spectrum measured in the rapid-scan mode, thus applying only the *changes* recorded during the step-scan measurement to a (steady-state) dark spectrum measured in a rapid-scan measurement (Süss 2011).

The overall shape of the interferogram depends on a Vertex 70 variable called "APB", which presumably stands for "absolute peak position". The value is typically around 59200 and presumably describes the index of the HeNe fringe at which the maximum value of the interferogram can be found. This value can be set manually, but also changes upon each reset of the Vertex 70.

It is important to note that when measuring a rapid-scan interferogram and subsequently a step-scan interferogram, the forms of the two interferograms differ vastly (for unknown reasons). Thus it is not possible to simply record a dark-spectrum before starting the step-scan measurement. The approach I chose is to measure all possible dark-spectra with the APB value ranging from 59150 to 59250 and then compare each rapid-scan interferogram with the step-scan interferogram. The best fit is then taken as dark interferogram. In the following I will describe this process in detail.

To get the rapid-scan spectra one can use the sample in the setup after finishing a step-scan run (provided there is still liquid nitrogen in the dewar). Choose a sample spot with an OD which is the one you are aiming for during your measurement. Set the ABP to 59150. Repeat 100 times: Set ABP to ABP+1, then measure 100 scans.

The next step is to group the step-scan data into groups which share the same absolute interferogram shape. This applies to all complete interferograms which have been recorded during one measurement without the Vertex having to be reset. For example, if the Vertex has to be reset once during a measurement (see section 4.11), the measured interferograms are divided into two groups: one group before the reset and the other one after. It is con-

venient to define the groups using the JSON syntax in a separate file and load it in the corresponding evaluation programs.

One can then load the data as described in section A.1.3 (modifying the routine as appropriate). Since it may take some time to find the dark interferogram of each file it is advisable to save the dark values for each file in a dictionary (and `pickle` it). The goal is to average the dark spectra of each group to get an average dark interferogram: this average dark interferogram for a group can then be compared to all the rapid-scan dark spectra. The matching rapid-scan dark interferogram is the one for which $\sum_i |I_i^{\text{step}} - I_i^{\text{rapid}}|$ is smallest, in other words: the matching rapid-scan dark interferogram minimizes the sum of the absolute differences of the amplitudes at each mirror position. To find this dark interferogram, one calculates `np.sum(np.abs(step_ifg - dark_ifg))` for all `dark_ifg` and finds the matching dark interferogram as the one which minimizes the sum. The result can then be saved in a dictionary and used later to shift each step-scan interferogram to the corresponding rapid-scan values, thus adding the changes measured by the step-scan to the steady-state values provided by the rapid-scan.

4.14.2. Correcting circular buffer errors

On average, about every 1000th step-scan timecourse shows the phenomenon of a circular buffer being shifted. The result is that in the timecourse, the very large signal produced by the flash heat excitation appears e.g. at a later time, while the very last points of the timecourse are shifted to the beginning.

A first approach in tackling this problem is simply to calculate the absolute minimum of the timecourse. This generally corresponds to the negative signal caused by the laser flash. For the timecourses at the centerburst however, the noise caused by the mirror vibrations may be larger in amplitude than the laser flash, leading to the errorneous detection of false positives. Moreover, if the noise of the mirror vibrations has a systematic frequency (for example 50 Hz), the detected absolute minimum will correspond to a minimum of this oscillation. By shifting the timecourse so that the minimum is always at a certain position all these oscillations become in phase which each other and thus contribute much more than if they would have been left unchanged.

Additionally, for timecourses recorded without lowpass filter (see also section 4.11) the detection of the minimum may be difficult due to the high noise.

To circumvent these problems it is suitable to filter the timecourses with a bandpass before locating the minimum. A bandpass is created with the command `b, a = scipy.signal.butter(1, [0.05, 0.2], 'bandpass')` which creates a Butterworth bandpass filter of first order with the cutoff frequencies being 0.05 and 0.2 times the Nyquist

frequency. The filter is applied to the timecourse via `timecourse_filtered = signal.filtfilt(b, a, timecourse)`; This module does not introduce a phase shift and is therefore appropriate to find the minimum.

Through the application of the filter the negative peak of the sample heated by the laser is retained, and an additional positive peak about seven points before the minimum is introduced. When having detected the minimum the additional detection of this positive peak helps to prevent false positives.

It seems to be the case that in the shifted timecourses about 10 points are recorded before the flash and correspondingly less points after it, since the total number of recorded points does not change. It is therefore advisable to discard the last points of each timecourse so as not to introduce artifacts. Since at the end of the timecourse about 1000 points are averaged anyway (see section 4.14.6) this does not matter much.

4.14.3. Forman phase correction

In section 4.14.1 it was shown that different groups of step-scan measurements correspond to different types of dark interferograms. Without further treatment it would not be possible to average the data of two different groups; the only possibilty would be to calculate the Fourier transform for each of these groups and then average the Fourier transforms weighted by the number of interferograms recorded for each Fourier transform. A much more elegant way is to phase correct each interferogram, average all of the interferograms and take the cosine Fourier transform of this average. This is possible since the interferograms have the same form after the phase correction.

The Forman phase correction follows the outline given in section 3.2.2. The steps are realized programatically as follows:

1. Level the interferogram:

   ```
   interferogram = interferogram - np.mean(interferogram[10:130])
   ```

   As a side-effect, through the leveling of the interferograms all signals which are indepented of the mirror position, e.g. the wavenumber-independent heat signal, are removed from the dataset.

2. Calculate the center of the interferogram by averaging the positions of the maximum and minimum:

   ```
   center = int(np.mean([np.argmax(interferogram[10:-10]),
                         np.argmin(interferogram[10:-10])])) + 10
   ```

3. Use a shortened copy of the interferogram (e.g. 320 points) to calculate the phase spectra:

   ```
   shortie = interferogram[center-160:center+160+1]
   ```

4. Roll the shortened interferogram so that its maximum is at the beginning of the array:

   ```
   shortie = np.roll(shortie, len(shortie)/2)
   ```

5. Calculate the Fourier transform of the shortened interferogram:

   ```
   shortie_fft = np.fft.fft(shortie)
   ```

6. Calculate the phase angle by using the obtained Fourier transform:

   ```
   theta = np.arctan2(np.imag(shortie_fft), np.real(shortie_fft))
   ```

   The usage of `arctan2` instead of `arctan` has the advantage of casting the angle into the right quadrant by using the signs of the two input variables.

7. Calculate the phase interferogram:

   ```
   phase_ifg = np.fft.irfft(np.exp(-1j * theta[:len(theta)/2]))
   ```

8. Roll the phase interferogram so that the centerburst is in the middle of the array, like the original interferogram:

   ```
   phase_ifg = np.roll(phase_ifg, len(phase_ifg)/2)
   ```

9. Convolve the two interferograms:

   ```
   np.convolve(interferogram, phase_ifg, mode='same')
   ```

   The mode is set to 'same' so that the output also has 334 mirror positions. The output yields the phase corrected interferogram.

In practice, since the dataset is so large and takes a long time to process, one tries to open the data only once. For each file that is processed first the timecourses are inspected for circular buffer errors, then the timecourses are shifted according to the rapid-scan interferograms, and afterwards the forman correction is applied to each interferogram. For the next step, the file is split up: each timecourse is saved in a separate folder which is named after the mirror position and the laser flash number. After all files have been processed split up in this way, each of the folders is visited and all timecourses in a folder are saved to a single `numpy` file. This has to be done since it is virtually impossible to load 500 GB of data into RAM, and selectively loading the right timecourses from larger files would be too impractical.

4.14.4. Selecting and averaging the timecourses

The variance should detect mirror oscillations or otherwise noisy timecourses. This noise is much slower than the sampling frequency, so to properly detect it the timecourses should be filtered with a lowpass filter (`b, a = signal.cheby2(2, 40, 0.25)`) before the variance is calculated (`np.std(timecourse)**2`). A proper limit should be chosen upon the observation of the general trend; different limits should be chosen for the centerburst and for the wings of the interferogram.

In theory it would also be possible to select good timecourses based on the thickness of the sample spot during the measurement. The offset of the timecourse corresponds to the absolute IR intensity incident on the detector, which is linearly correlated to the sample thickness. This information is lost during the Forman correction though, since after the phase correction no distinct interferogram point corresponds to a certain measurement file. The thickness selection is therefore neglected in favor of the ability to relate all interferograms to each other through the Forman correction.

When averaging the remaining timecourses, these should be averaged corresponding to their inverse variances. In this way the average has the least possible variance.

4.14.5. Replacing the timecourses at noisy mirror positions

At this point in the analysis is a good opportunity to replace the values of a number of mirror position timecourses around the center peak. Replacing values in the interferogram at or near the centerburst effects offset-changes or offset-like changes in the shape of extremely broad peaks in the spectrum. On the other hand, the centerburst timecourses are strongly affected by 50 Hz noise: since the first derivative of values around the centerburst is very large, minute changes in the mirror position causes a large effect in the interferogram amplitude at that mirror position. Because the electronic feedback system which controls the position of the sweeping mirrors is affected by 50 Hz noise, this noise can be seen in the timecourses corresponding to mirror positions next to the centerburst, whereas this is negligible at other mirror positions (see also Görlin 2012). Therefore it is advisable to replace the noisiest positions.

Given the standard deviation for every timecourse is saved in an array `stds`, a sorted list of the noisiest mirror position indices can be calculated using `np.argsort`. Then a number of timecourses (typically less than 9) of the noisiest mirror positions can be set to zero in the difference interferograms as discussed below (section 4.14.7).

4.14.6. Logarithmic averaging

Each timecourse is subsequently logarithmically averaged as shown in section A.1.4 on page 233. The number of raw data points averaged is displayed in figure 4.5.

4.14.7. Cosine Fourier transform

The difference cosine Fourier transform (see section 3.2.3) is calculated after the phase corrected interferogram timecourses have been logarithmically averaged (see section 4.14.6). First, the dark interferogram is calculated from the first 19 points:

```
dark_ifg = np.mean(ifgs[0:19], axis=0)
```

Section A.1.5 on page 234 shows how difference spectra are calculated using python.

Having obtained the pure time-resolved step-scan difference spectra the data processing is completed. Before thorough analysis is possible though a dominating signal caused by heating of the sample through the laser flash has to be accoundet for. This process is covered in section 5.6.

4.15. Fitting time-resolved spectral data

After we have obtained the spectra from the interferograms it is time to obtain time constants from the data. This section discusses different aspects of fitting models to the obtained data and establishes the different methods used in this work.

4.15.1. Linear least squares: closed form solution

Given data points y_i, ($i = 1, 2, ..., n$), a "fit" is typically achieved by finding coefficients β_j so that

$$\sum_{j=1}^{n} X_{ij}\beta_j = y_i. \tag{4.2}$$

The "Linear Least Squares" approach aims to minimize

$$\|\mathbf{y} - \mathbf{X}\beta\|^2, \tag{4.3}$$

with the term $||\mathbf{x}||^2 = \sqrt{x_1^2 + ... + x_n^2}$ being the Euclidian norm, or l_2 norm. If $\mathbf{X}$ is unknown, the above equation has to be minimized in an iterative way. If $\mathbf{X}$ is known, this term even

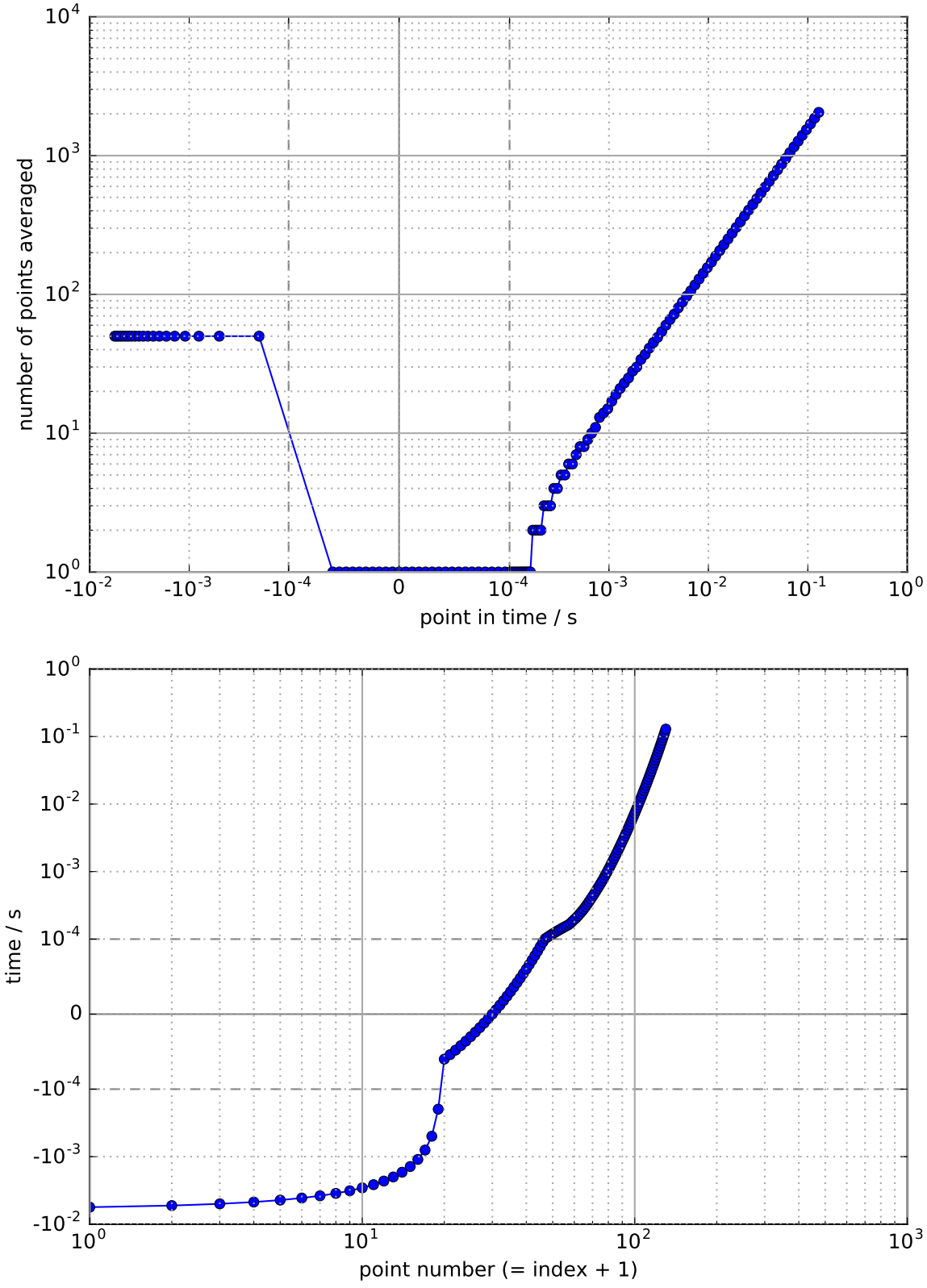

Figure 4.5.: Visualization of the result of the logarithmic averaging.

has an analytical solution. The name "Linear Least Squares" stems from the fact that the set of equations $\mathbf{X}\beta = \mathbf{y}$ is linear in β, and the squared residuals $\|\mathbf{y} - \mathbf{X}\beta\|^2$ are to be minimized.

Let us discuss the application of the closed form solution to find a fit for a time course y_i with N data points corresponding to N time points t_i. The model for our fit consists of a sum of L exponential terms with known τ_l and an offset c:

$$f(t) = \sum_{l=1}^{L} \left(\beta_l \cdot \mathrm{e}^{-t/\tau_l}\right) + c. \tag{4.4}$$

We call $f(t)$ the fit function. Typically, $L < 10$. Note that $f(t)$ is a linear function in all β_l (but not in τ_l). Thus we can write the system as:

$$\begin{pmatrix} \mathrm{e}^{-t_1/\tau_1} & \mathrm{e}^{-t_1/\tau_2} & \dots & \mathrm{e}^{-t_1/\tau_L} & 1 \\ \mathrm{e}^{-t_2/\tau_1} & \mathrm{e}^{-t_2/\tau_2} & \dots & \mathrm{e}^{-t_2/\tau_L} & 1 \\ \vdots & \vdots & \ddots & \vdots & 1 \\ \mathrm{e}^{-t_N/\tau_1} & \mathrm{e}^{-t_N/\tau_2} & \dots & \mathrm{e}^{-t_N/\tau_L} & 1 \end{pmatrix} \begin{pmatrix} \beta_1 \\ \beta_2 \\ \vdots \\ \beta_L \\ c \end{pmatrix} = \begin{pmatrix} y_1 \\ y_2 \\ \vdots \\ y_N \end{pmatrix} \tag{4.5}$$

Since this set of equations has a closed form solution as long as the matrix $\mathbf{X}$ is known, in a computer program one can write the fit function solely dependent on τ_l and compute the corresponding amplitudes accordingly in the definition block of the fit function. In other words: one does not need to fit the amplitudes β_l, fitting the time constants and calculating the amplitudes on the fly is much more elegant. The time constants are covered in the next section; we will continue finding the amplitudes for given time constants.

The closed form solution for β is found by solving the set of equations given by

$$\mathbf{X}\beta = \mathbf{y} \tag{4.6}$$

$$\Leftrightarrow \left(\mathbf{X}^T \cdot \mathbf{X}\right) \cdot \beta = \mathbf{X}^T \cdot \mathbf{y} \tag{4.7}$$

$$\Leftrightarrow \beta = \left(\mathbf{X}^T \cdot \mathbf{X}\right)^{-1} \cdot \mathbf{X}^T \cdot \mathbf{y}, \tag{4.8}$$

although this direct solution of the above normal equations is not generally the best way to find the solutions to β (Press et al. 1997). Nevertheless, one can find all values for β in one step by inversing the matrix $\mathbf{X}^T\mathbf{X}$.

Given that the matrix inversion can be calculated without any problems, this algorithm will always result in the best fit given a fixed set of τ_l and a vector $\mathbf{y}$. It should be used when the model function $f(t)$ can be motivated through other findings, since this method will not (i) create a sparse solution (involving much less phases τ_l than initially given), nor

(ii) find a solution where the set of amplitudes β_l are reasonably small, nor (iii) perform grouping, that is, compare different $\mathbf{y}$ and find all highly correlating τ_l.

It may be the case that the matrix inversion shown above may not be calculated directly because of numerical limitations. In theses cases, the pseudo-inverse may still be calculated through singular value decomposition (SVD): if $A = U\Sigma V^*$ is the SVD decomposition of A, then $A^+ = V\Sigma U^*$ is the pseudo-inverse of A, which for our practical applications serves as the inverse of A. The python library `np.linalg.pinv` conventiently returns the pseudo-inverse B of A through `B = np.linalg.pinv(A)`.

For more convenience, python also provides the library `numpy.linalg.lstsq` which returns the least-squares solution to a linear matrix equation. A parameter can be passed which sets a cut-off ratio for small singular values of the coefficient matrix. Using this library, only the coefficient matrix $\mathbf{X}$ has to be constructed and passed to the library together with the solution vector $\mathbf{y}$. The coefficients β are derived by the program from the form of $\mathbf{X}$.

A function which returns the amplitudes and an offset calculated for an array of known time constants is given in section A.1.6 on page 235. The pseudo-inverse can be provided as optional parameter; this can speed up the progress significantly if the same matrix can be re-used many times. Additionally, the fit is calculated and returned as well.

4.15.2. Fitting time constants

Now that we know how to calculate the amplitudes, we can go on to fit the time constants. This problem is not linear anymore since the time constants are the arguments of the exponential functions, so we have to resort to non-linear least squares fitting. SciPy (Jones, Oliphant, and Peterson 2017) provides a routine called `least_squares`, which should not be confused with the superseded `leastsq` routine or NumPy's `lstsq`. This routine minimizes a residual function according to its input parameters and can optionally take an array which takes lower and upper bounds for each parameter. A sample implementation is given in section A.1.7 on page 235, which relies on the function calculating the amplitudes given in section A.1.6 on page 235.

4.15.3. Global fit

A global fit aims to find the same time constant for timecourses at different wavenumbers. For example, one could select the timecourses at the wavenumbers which correspond to the reduced quinone; these should all share the same time constants. The advantage is that the fit will be more robust and return better results.

Programmatically this is implemented much like in the previous section; the only difference is that the residual function is now a long list with all residuals at the individual wavenumbers concatenated and flattened. In the residual function a loop calculates the fit for every timecourse at each wavenumber individually, i.e. each timecourse uses the same time constants but different amplitudes and offsets. The fit is subtracted from the data and concatenated to the residual. The same applies if one wants to fit timecourses corresponding to different flashes.

In this scenario it is crucial to calculate the matrix and invert it before calculating the amplitudes for each individual timecourse; this will speed up the calculation enormously.

4.15.4. Penalization and elastic net

To improve the performance of the Linear Least Squares algorithm, several penalization techniques have been proposed (Zou and Hastie 2005). For example, minimizing

$$\|\mathbf{y} - \mathbf{X}\beta\|^2 + \|\Gamma\beta\|^2 \tag{4.9}$$

with Γ often chosen $\alpha\mathbf{I}$ incorporates a penalty term on the solution β, such that only small β will be found. Still, generally $\beta_j \neq 0 \; \forall \; j$.

If the number of predictors (β_j) is high, a linear regression model should preferably create a sparse solution, with only as few β_j remaining as possible. Introducing an l_1 penalty by minimizing

$$\|\mathbf{y} - \mathbf{X}\beta\|^2 + \|\Gamma\beta\|_1 \tag{4.10}$$

will both perform absolute shrinkage and automatic variable selection, i.e. reduce the number of β_i if the number of predictors is high. Note that in the above term, $\|\mathbf{x}\|_1 = \sum |x_i|$ (l_1-norm). This is the LASSO (least absolute shrinkage and selection operator) approach.

There is one more desirable property, which is grouping. If there are strong correlations between predictors, these predictors should be chosen preferrably. The lasso typically only catches one variable from the group and rejects the others.

A minimization term which performs shrinkage, automatic variable selection and grouping is

$$\left|\mathbf{y} - \mathbf{X}\beta\right|_2 + \alpha \left|\beta\right|_2 + \gamma \left|\beta\right|_1 . \tag{4.11}$$

Here, $\|\mathbf{x}\|_2 = \sum \mathbf{x}^2$. This approach has been termed the elastic net, since it is "like a stretchable fishing net that retains 'all the big fish'" (Zou and Hastie 2005).

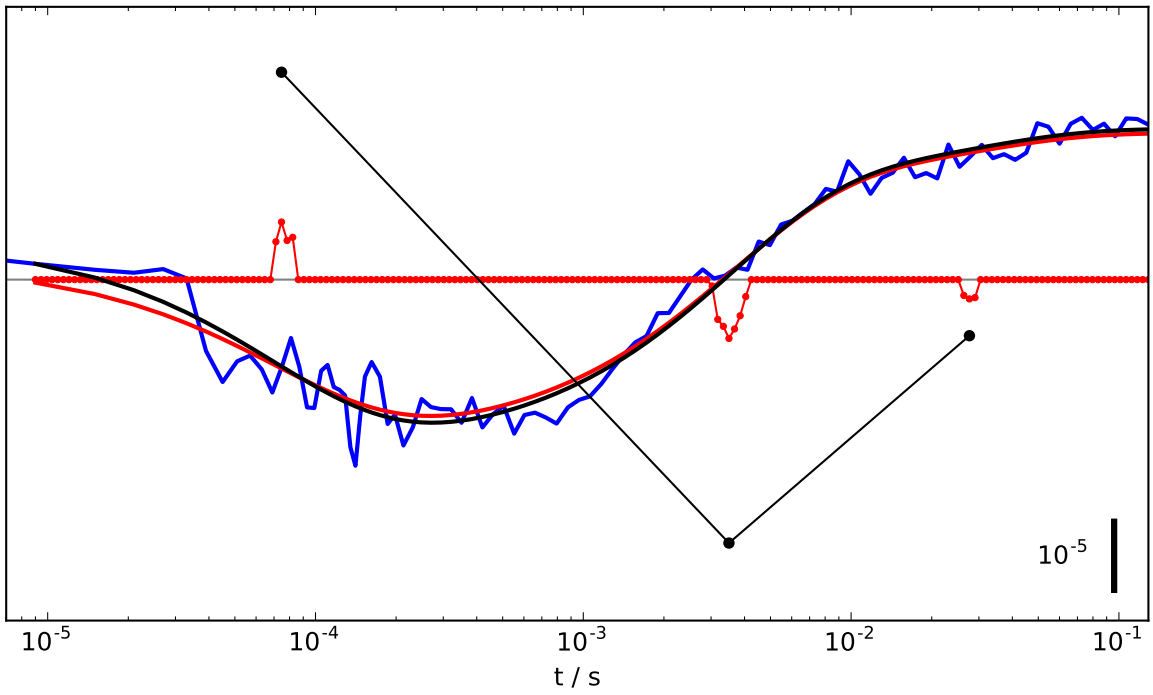

Figure 4.6.: Example for a fit obtained by elastic net fitting. Blue: data points for the third flash at 1400 cm^{-1}. Red points: Each point corresponds to one time constant involved in the elastic net fit. For this wavenumber, the fit set the amplitude of the vast majority of time constants to zero, while retaining three groups of time constants. Red line: Fitted line obtained by plotting a sum of exponential terms $a \cdot e^{-t/\tau}$, with a and τ being the amplitude and time constant of one red dot respectively. Black points: By selecting the local extrema of the red dots array, three time constants have been selected. The corresponding amplitudes have been calculated through matrix inversion (see section 4.15.1). Black line: Fit obtained by plotting a sum of three exponential terms, using the values of the black dots as parameters.

The traits of the elastic net fit allow to implement an alternative global fit routine which automatically determines the number of time constants used. The idea is to provide a large number of available time constants, and have the elastic net choose the "best" time constants (Till Stensitzki, private communication). An example is given in figure 4.6. After performing an elastic net fit on the whole dataset, the fit returned three clusters of time constants for the third flash at 1400 cm^{-1}. Note that the three clusters were chosen by the routine through the grouping, i.e. by comparing the data at 1400 cm^{-1} with the timecourses at all other wavenumbers. The three clusters can be processed into three discrete time constants and the amplitudes can be calculated accordingly. The resulting fit (black line) closely resembles the red line, which represents the fit corresponding to the three clusters of time constants.

In python, the procedure can be implemented in the following way. First, the proce-

dure is imported from the scikit-learn package (Pedregosa et al. 2011): `import sklearn.linear_model as lm`. The base is created (for example) in the following way:

```
taus = np.logspace(np.log10(times[base_start]), np.log10(times[-1]),\
                   number_of_taus)
base = np.exp(-times[base_start:,None]/taus[None, :])
```

The actual calculation is initiated by the following commands:

```
data = collection[flash,base_start:]
alpha = 1e-6
max_iter = 1e9
rho = 0.1
analysis = lm.ElasticNet(alpha=alpha, max_iter=max_iter, l1_ratio=rho,\
                         selection='random', warm_start=True)\
             .fit(base, data)
result = analysis.predict(base)
coefs = analysis.coef_.copy()
```

The results and coefficients are then stored in the variables `result` and `coefs`.

4.15.5. Elastic net fit example

The following example compares the global fit approach with the elastic net approach. In figure 4.7 (top) simulated data is shown. Seven features at six different wavenumbers have been included. The features ($a \cdot \exp(-t/\tau) + c$) have time constants τ of 100 µs or 3 ms, amplitudes a of $\pm 1 \cdot 10^{-4}$, varying offsets, and spectral widths of 10 cm^{-1}.

A global fit with two time constants will yield the used time constants of 100 µs and 3 ms very accurately. The fits are shown in figure 4.8 and the corresponding decay associated spectra to the two phases are shown in figure 4.7. To generate a decay associated spectra, the amplitudes a corresponding to a time constant τ are plotted against wavenumber. Since in a global fit exactly the same time constants are given at any wavenumber a decay associated spectrum can be obtained in a straightforward way (figure 4.7, bottom).

The elastic net fit will determine clusters of time constants corresponding to one timecourse at one wavenumber as shown in the previous section. The fits determined are shown in figure 4.9. The time constants and their amplitudes determined by the elastic net fit are shown as black lines in figure 4.9. The most important difference between the global fit and the elastic net fit is that in the elastic net fit, the number of time constants is not predetermined. Compare, for example, the timecourses at 1420 cm^{-1} and 1450 cm^{-1} in figures 4.8

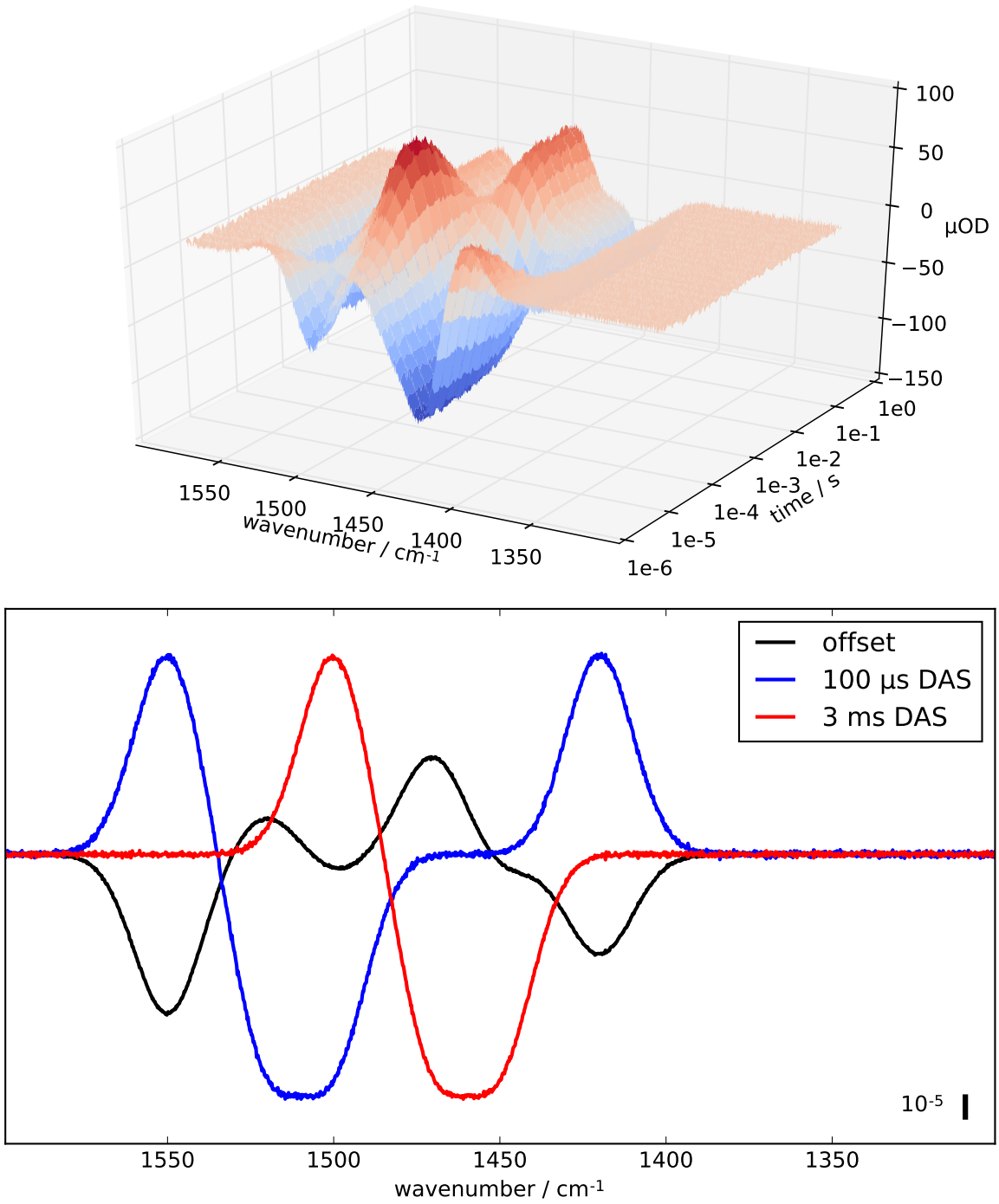

Figure 4.7.: Top: Surface plot of simulated noisy data. The data consists of seven features at six different wavenumbers with time constants of 100 µs and/or 3 ms, amplitudes of $\pm 1 \cdot 10^{-4}$, and different offsets. Bottom: Decay associated spectra found by globally fitting two time constants.

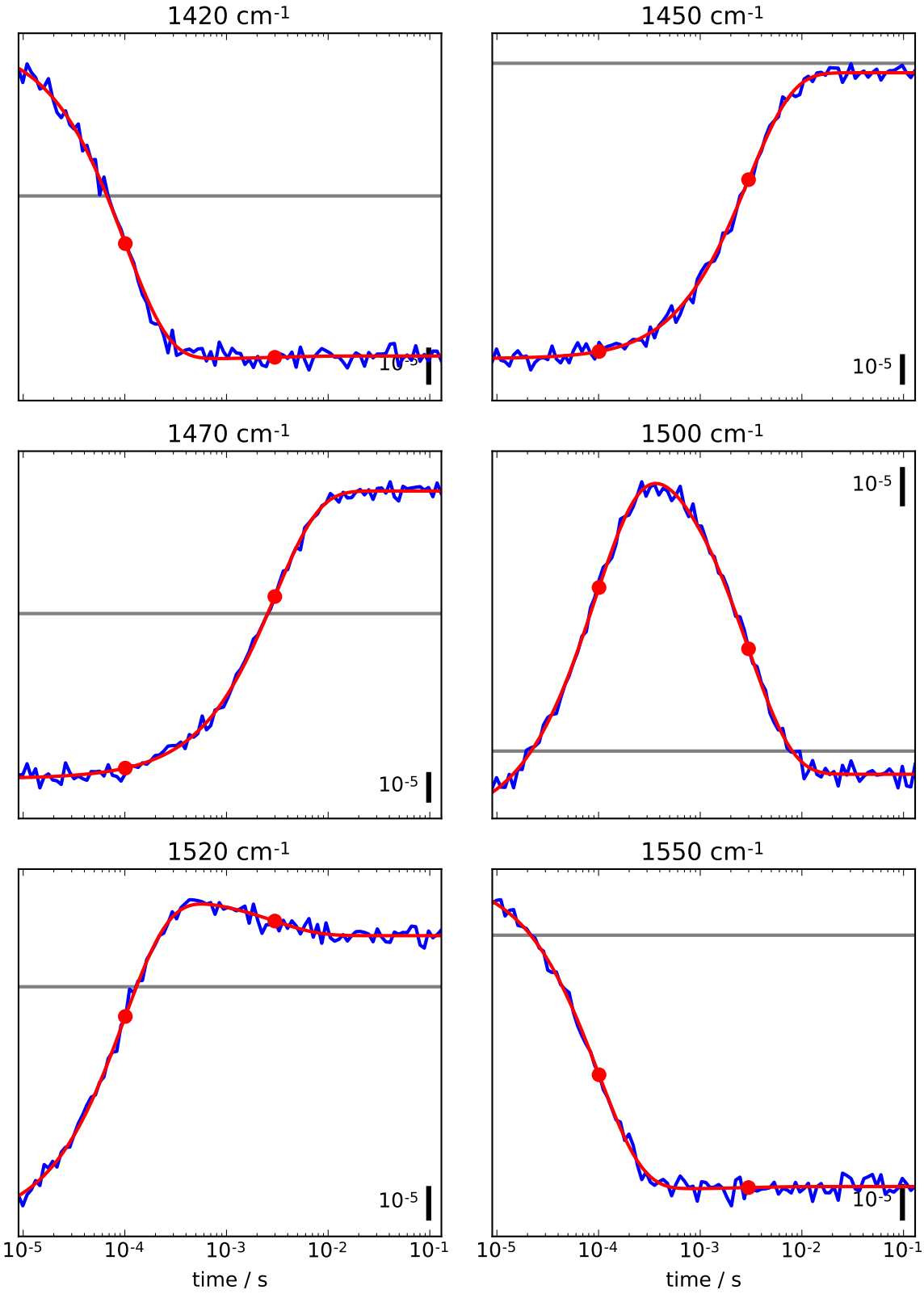

Figure 4.8.: Simulated noisy data (blue) and fits obtained through globally fitting two time constants (red). The red dots mark the time constants 100 µs and 3 ms.

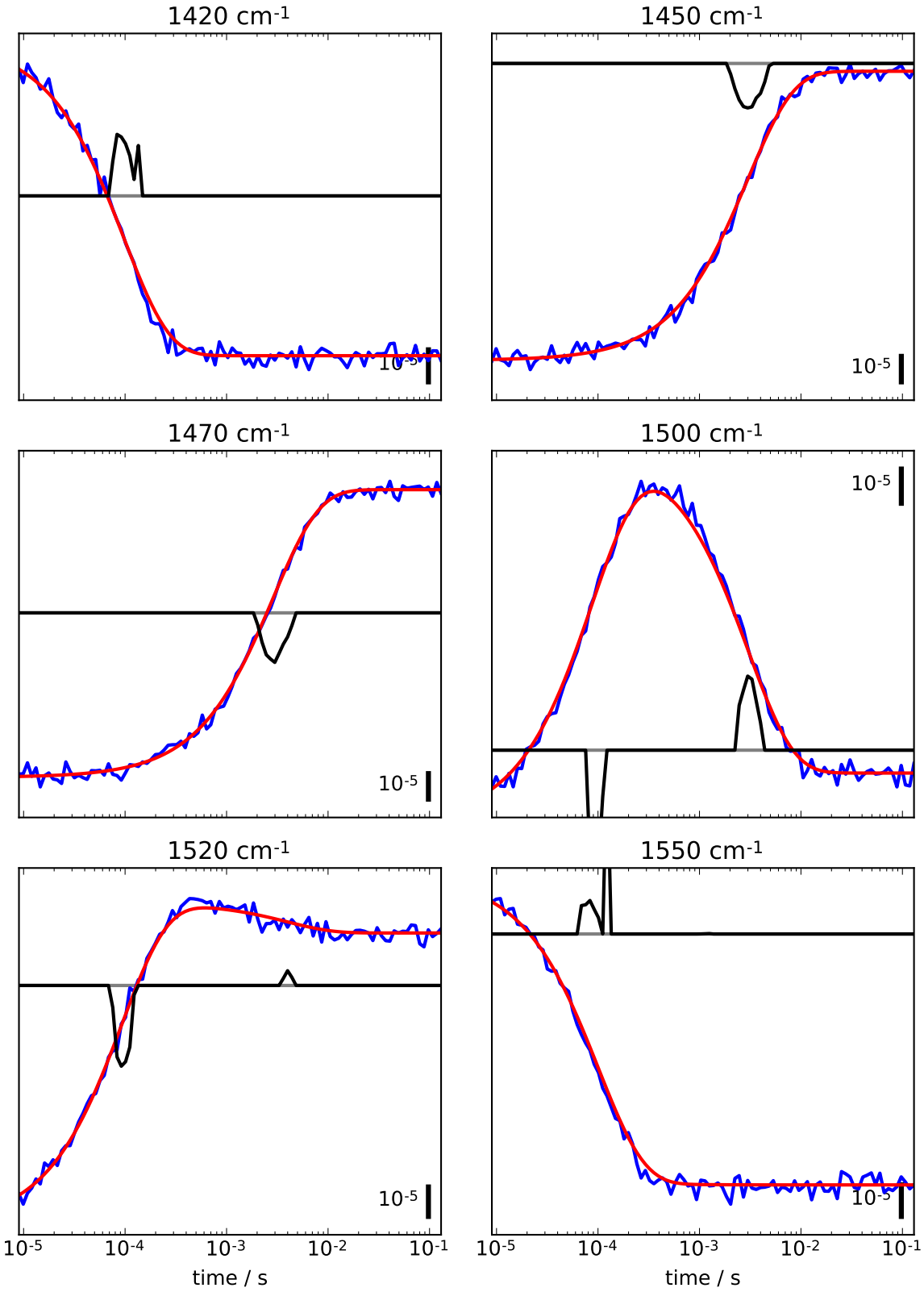

Figure 4.9.: Simulated noisy data (blue) and fits obtained through an elastic net fit (red). The black lines shows the time constants and their amplitudes determinated by the elastic net fit.

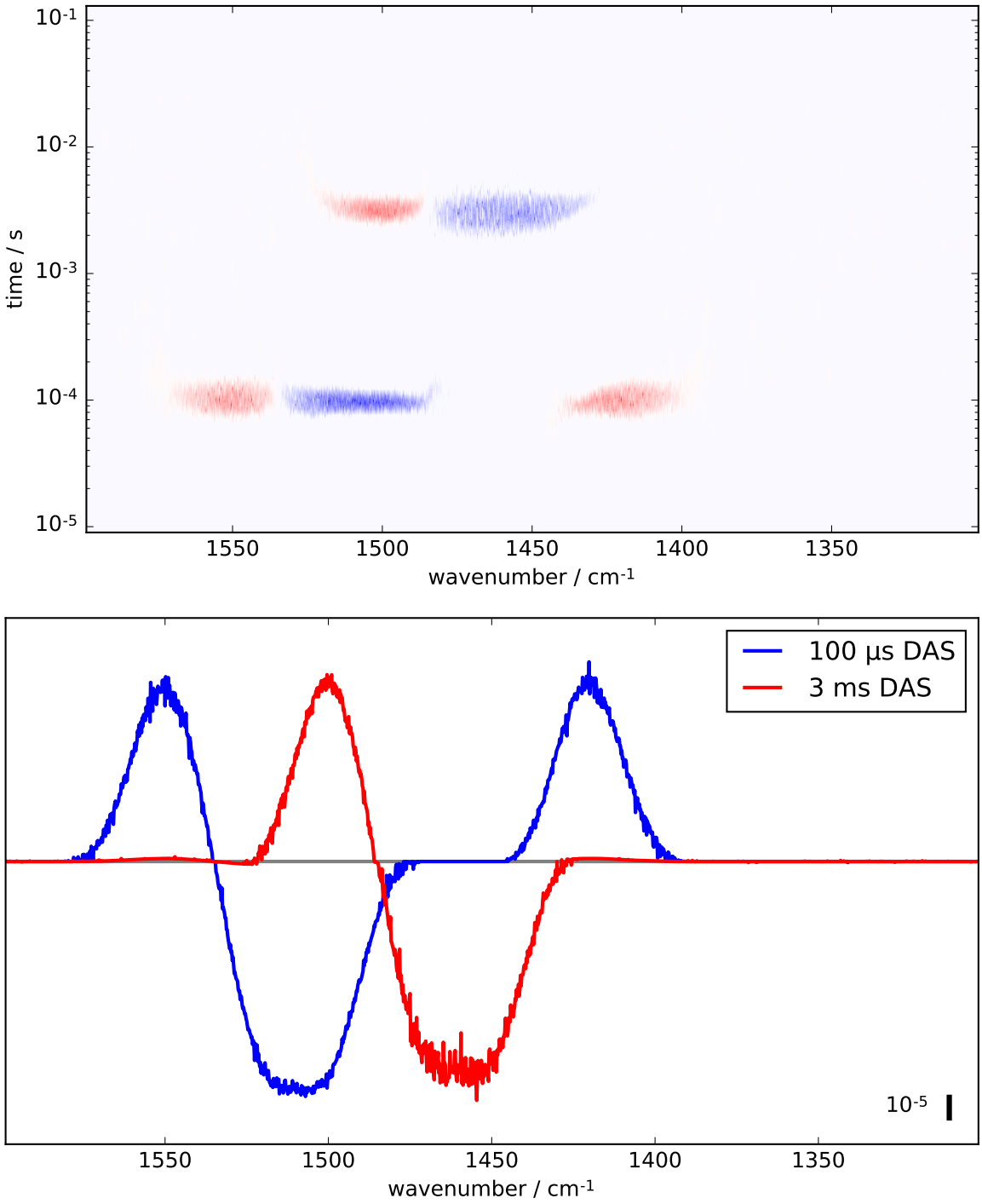

Figure 4.10.: Top: lifetime map obtained through an elastic net fit. Positive amplitudes are shown in red, negative ones blue. Bottom: the associated decay associated spectra have been obtained by summing up the amplitudes of the time constants given for a certain phase (100 µs or 3 ms) and wavenumber.

and 4.9: while there are always the same time constants given in the global fit, there is only one cluster of time constants (corresponding to one discrete time constant, see previous section) determined through the elastic net routine.

The determined time constants and their amplitudes can be plotted versus wavenumber to create a lifetime map (Till Stensitzki, personal communication); the lifetime map for the given example is shown in figure 4.10 (top). Red areas show positive amplitudes and therefore decays, while blue areas show negative amplitudes and therefore rises. The lifetime map shows very clearly that two phases are sufficient to describe the behaviour of the dataset; moreover, a lifetime map visualizes wavenumbers which only exhibit behaviour of the slow, the fast, or both time constants.

Decay associated spectra can also be obtained from elastic net fits, although not as straightforward as in a global fit. It would be possible, although not feasible, to plot one decay associated spectrum for each time constant provided to the elastic net routine. In this example this would lead to 100 decay associated spectra. In figure 4.9 and in the lifetime map it is shown how (in the clusters) the time constants scatter around a central time constant. Decay associated spectra can be obtained then by selecting a phase and applying a Gaussian window in time to the data. For example, the fast phase in the lifetime map can be selected by multiplying the amplitudes with a Gaussian profile centered around 100 µs with σ = 20 µs. Then for each wavenumber the amplitudes are just summed up. The result is a decay associated spectrum for the 100 µs phase.

The decay associated spectra for the elastic net fit are shown in figure 4.10 (bottom). It can be seen that the spectra are noisier than their global fit counterparts, which is a result from the scatter of the time constants in a certain cluster of time constants. In this example, decay associated spectra of different phases (100 µs and 3 ms) are shown; in the results section, decay associated spectra of the same time constant but of different S-state transitions are compared.

4.16. Wavenumber shifts and their analysis

Since quite a lot of features in the step-scan data appear to change their maximum wavenumber position with time, it stands to reason to investigate how the temporal behaviour of these features should be evaluated. This section aims to provide a well-defined time-resolved spectrum to elucidate possible pitfalls in the evaluation process.

It follows from the step-scan's resolution of 10 cm^{-1} that (in terms of wavenumbers) very close neighboring modes in the spectra will not be fully resolved. When the amplitude of one of these vibrational modes decreases with time while the other's incrreases, this

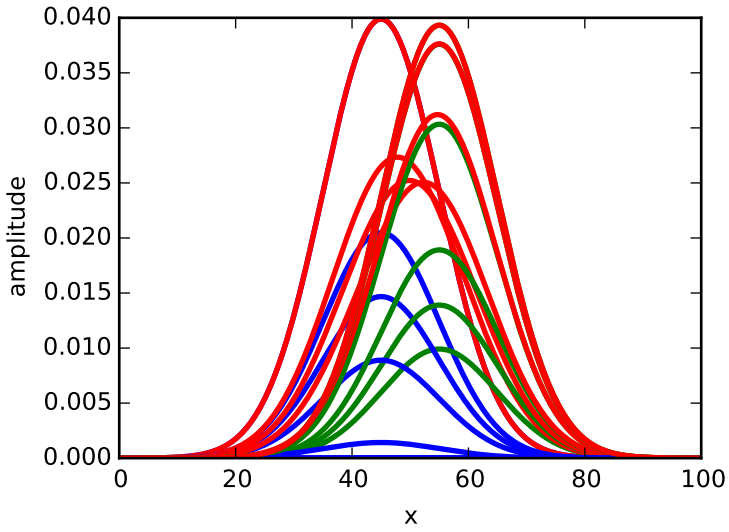

Figure 4.11.: Two separate spectral features disappearing (blue, maximum position = 45) and appearing (green, maximum position = 55) with time, displayed for times 0, 2, 3, 4.5, 10, 20, and 29.8. The two curves are calculated from equation (4.12) with $\mu_1 = 45$ and $\mu_2 = 55$ respectively and $\sigma = 10$. The blue curve decays as described by equation (4.13) with $\tau_1 = 3$; the green curve rises with $\tau_2 = 7$. The red curve is the sum of the blue and green curves and shifts its maximum from $x = 45$ to 55.

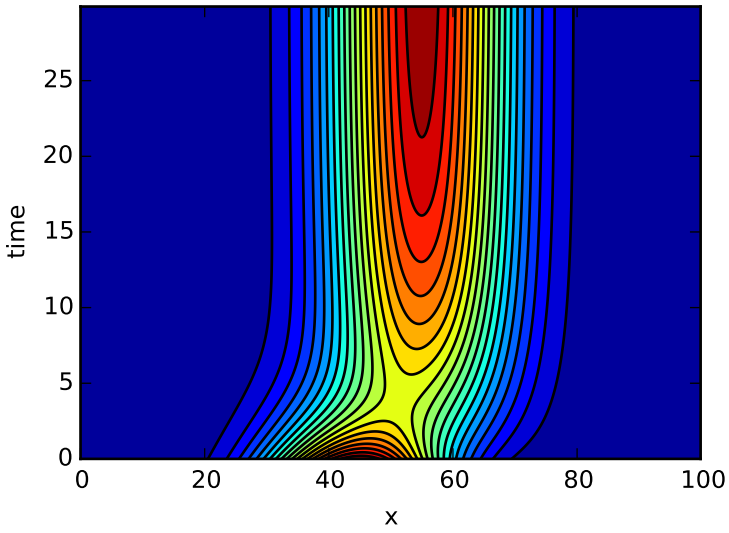

Figure 4.12.: Contour plot of the red curve (compare with figure 4.11). The maximum of the curve decreases, shifts position, and increases.

will be seen in the spectra as one feature which changes its maximum. To investigate the

properties of such a transition we start with two gaussian distributions of the form

$$A(x, \mu, \sigma) = \frac{1}{\sigma\sqrt{2\pi}} \, \mathrm{e}^{-\frac{(x-\mu)^2}{2\sigma^2}}, \tag{4.12}$$

with $\mu = 45$ and $\mu = 55$ respectively and $\sigma = 10$ in both cases. The latter feature shall decay with time and be scaled by

$$c(t, a, \tau, \gamma) = a\mathrm{e}^{-t/\tau} + \gamma, \tag{4.13}$$

with $a = 1$, $\tau = 3$, and $\gamma = 0$. The former feature shall feature a rise of the same form with $a = -1$, $\tau = 7$, and $\gamma = 1$. These spectra as well as their sums are depicted in figure 4.11 for selected times; figure 4.12 shows a contour plot of the sum of the two features which resembles what would be measured in the step-scan.

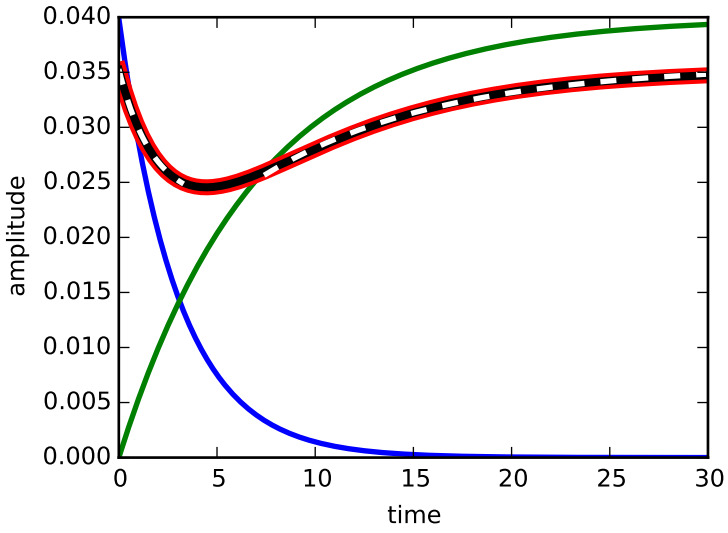

Figure 4.13.: The amplitudes of the red and blue curves as well as their sum (red curve) at $x = 50$ versus time. Blue curve: $A(x, \mu, \sigma)$, equation 4.12, with $\mu = 45$ and $\sigma = 10$; decay time constant $\tau_1 = 3$ (equation (4.13)). Green curve: $A(x, \mu, \sigma)$, equation 4.12, with $\mu = 55$ and $\sigma = 10$; rise time constant $\tau_1 = 7$ (equation (4.13)). Dashed white lines: Separate fits for the fast decay and slow rise of the red line using $c(t, a_1, \tau_1, \gamma_1)$ and $c(t, a_2, \tau_2, \gamma_2)$ respectively yielding wrong values $\tau_1 = 1.7$ and $\tau_2 = 9.1$. Black line: combined fit using $c(t, a_1, \tau_1, \gamma) + c(t, a_2, \tau_2, \gamma)$ yielding the true values $\tau_1 = 3$ and $\tau_2 = 7$.

The question is now how from the "measured" spectra (red curves in figure 4.11; data in figure 4.12) the time constants of its components can be recovered. In figure 4.13, the time courses for the sum and its components at $x = 50$ is shown.

To recover the time constants of the two components, a least-squares fit (see section 4.15.1 on page 51) is the method of choice. However, as shown in figure 4.13, a combined fit is necessary (black curve); if one attempts to only fit the decay or the rise (white dashed lines) of the "measured" signal, wrong time constants $\tau_1 = 1.7$ and $\tau_2 = 9.1$ are obtained.

One additional insight is that it is not necessary to follow the maximum of the "measured" curve (red): as the (arbitrarily) chosen index x of the time courses changes, only the obtained amplitudes a_i of the fit (and not the obtained time constants τ_i) will change. This implies that the fitting of Gaussian curves as done by Görlin (2012) does, from a theoretical point of view, not seem necessary to obtain the data of interest.

4.17. Miss factor determination

The oxygen evolving complex advances step-wise through four semi-stable S-states to oxidize water and release molecular oxygen upon the absorption of four photons. The absorption of one photon provides the energy to advance from S_n to S_{n+1}. This S-state transition is not always successful: the energy provided by the photon can be lost, e.g. by back reactions of radical pair states, excited-state decay by fluorescence emission, recombination after primary charge separation, and additional recombination routes (Grabolle and Dau 2007). Even after the $S_2 \longrightarrow S_3$ transition an electron at Q_A^- can still recombine with the S_3 state to result in the starting state S_2 (Han, Mamedov, and Styring 2012). Several factors influence the miss factor; for example, a very low or very high salt concentration drastically increases the miss factor (Karge, Bondar, and Dau 2014). The lowest miss factor achieved in this study was 9% (Karge, Bondar, and Dau 2014).

The possibility of the OEC to not advance to the next S-state upon the absorption of a photon was already built in into the S-state model and called a "miss" event (Kok, Forbush, and McGloin 1970). Typically, a single probability for a miss-event is taken into account for each S-state transition which leads to satisfying results, although the probability for a miss-event is different for each S-state transition (Grabolle and Dau 2007; Han, Mamedov, and Styring 2012). Using EPR measurements, Han, Mamedov, and Styring (2012) reported that the highest miss-factor corresponds to the $S_2 \longrightarrow S_3$ transition and thereby confirmed that the $S_3 \longrightarrow S_0$ transition is not the "most difficult" one, as proposed earlier (Haumann, Grundmeier, et al. 2008). This finding is compatible with the $S_2^+ \longrightarrow S_2^n$ transition having a high activation energy of 470 meV (Klauss, Haumann, and Dau 2012).

In this section I will describe how the miss-factor can be calculated from FTIR spectra. First, we will find the relative occupation of the different S-states after applying a number of flashes, and then calculate the IR amplitudes of the corresponding S-states. Finally we

will be able to find the actual miss-factor m by using a non-LLS algorithm. In the following several simplifications are assumed:

- If photosystem II is given enough time to dark-adapt, most centers will be in the S_1-state, although some centers will be in the S_0-state. In a different experiment of our group using a similar sample, it was found that there is only a negligible fraction of centers in the S_0 state (Karge, Bondar, and Dau 2014). In this experiment, additionally a single flash was applied to the sample before the dark adaptation time. In the following I will assume that all centers are in the S_1-state.

- Furthermore, neither double hits nor backward reactions are taken into account. Double hits refer to the possibility of one OEC to advance two times upon the application of a single light flash. This is possible when using long flashes from e.g. a Xenon flash lamp, but does not occur for 5 ns laser flashes. Backward reactions describe the complete reversal of a S-state transition; this may take tens of seconds when using PPBQ as electron acceptor (Han, Mamedov, and Styring 2012) and is not considered here as well.

- Some centers may only advance to the S_2 state, but not further. This problem is not treated with in the mathematics below, but can be tackled by omitting the first flash when calculating the miss-factor using the measured data. In my work I have omitted the first flash from all miss-factor calculations.

Let us use P_n to denote the relative populations of the four semi-stable S-states in percent after applying n actinic flashes: $P_n = (p_{n,1}, p_{n,2}, p_{n,3}, p_{n,0})$ and $\sum_i p_{n,i} = 1$. For example, in the dark ($n = 0$) every center is in the S_1 state: $P_0 = (1, 0, 0, 0)$. Given a certain miss-factor m (for example, $m = 0.09 = 9\%$), the populations can be calculated using the matrix M (Menzel 2009):

$$P_{n+1} = M^n P_0 = M P_n = \begin{pmatrix} m & 0 & 0 & 1-m \\ 1-m & m & 0 & 0 \\ 0 & 1-m & m & 0 \\ 0 & 0 & 1-m & m \end{pmatrix} \begin{pmatrix} p_{n,1} \\ p_{n,2} \\ p_{n,3} \\ p_{n,0} \end{pmatrix}. \tag{4.14}$$

The matrix can be modified to represent individual miss-factors for each S-state transition, but here only an average miss-factor is considered. In this way, for any given miss-factor m the relative populations of each S-state can be calculated. In table 4.1 an example is given for $m = 9\%$.

	number of applied flashes										
	0	1	2	3	4	5	6	7	8	9	10
S_1 / %	100	9	1	0	69	31	8	2	47	38	17
S_2 / %	0	91	16	2	0	62	34	11	3	43	39
S_3 / %	0	0	83	22	4	1	57	36	13	3	40
S_0 / %	0	0	0	75	27	6	1	52	37	15	5

Table 4.1.: Population of the different S-states in percent after the application of a different number of flashes. In this example a miss factor of 9% and complete occupation of the S_1 state after dark-adaptation were assumed (see also section 5.8.3 on page 112).

As the S-states get more and more mixed, the FTIR difference spectra do not represent the pure spectra of a single transition anymore. A flash pattern $A = (a_1, ..., a_{10})$ at a certain wavenumber ν will contain contributions of two or more "pure" IR amplitudes α_i:

$$A = \begin{pmatrix} a_1 \\ \vdots \\ a_{10} \end{pmatrix} = \begin{pmatrix} p_{1,1} & p_{1,2} & p_{1,3} & p_{1,0} \\ \vdots & \vdots & \vdots & \vdots \\ p_{10,1} & p_{10,2} & p_{10,3} & p_{10,0} \end{pmatrix} \begin{pmatrix} \alpha_1 \\ \alpha_2 \\ \alpha_3 \\ \alpha_0 \end{pmatrix} = P\alpha \tag{4.15}$$

Here, each row of the population matrix P has been obtained by repeated application of the matrix M to the starting population (see above). Thus, for a certain miss-factor m, the amplitudes α_i which correspond to the pure IR amplitudes of the S_i-state are obtained by a matrix multiplication with P (which can be calculated) to give the measured flash pattern A. This is a linear least squares problem, and the solution is given by:

$$P\alpha = A \tag{4.16}$$

$$\Leftrightarrow \alpha = \left(P^T \cdot P\right)^{-1} \cdot P^T \cdot A. \tag{4.17}$$

In python, this problem can be solved using the integrated LLS solver `numpy.linalg.lstsq` (see also section 4.15.1 on page 51). One has to be careful though, because the (pseudo-)inverse of P can sometimes feature extremly small singular values. To deal with this problem the parameter `rcond` which is passed to `lstsq` has to be chosen appropriately, so that extremely small singular values are ommitted. I found that `rcond = 1e-6` works well for my data. The solver is called in the following way:

```
result = lstsq(lstsq_matrix, pattern[skip:], rcond=1e-6)[0]
```

with `lstsq_matrix` being the population matrix P including an additional column to in-

clude an offset in the fit, just like the last column in the matrix in equation 4.5. The variable `skip` just equals 1 and takes care to omit the first flash from the calculation. The `result` will then contain the unmixed, pure amplitudes α and the offset.

Once the least squares matrix has been computed, any pattern can be used to calculate the pure amplitudes α. This approach can be used to deconvolute timecourses: if flash patterns (and therefore the unmixed amplitudes) are calculated for each point in time, the resulting pure amplitudes can be plotted vs time to represent the deconvoluted timecourses.

Now that we can find the IR amplitudes for a certain miss-factor m, let us try to find the miss-factor m itself. There is no simple analytical solution to get the miss-factor out of the data; instead, an iterative process is used. I decided to use the *nonlinear* least squares solver `least_squares` (not to be confused with `lstsq`) provided by `scipy.optimize`. The solver is invoked using the following line:

```
result = least_squares(global_miss, guess, args=([patterns]))
```

`global_miss` is the residual function which is optimized, `guess` equals `0.10`, and `patterns` contains an array of flash patterns which are going to be used for the fit. The `result` will be the miss-factor.

The function `global_miss` takes a miss-factor m and an array of patterns. From the miss-factor it calculates the population matrix (see above) and from the patterns it can infere the pure amplitudes. From this information, model flash patterns can be constructed. The function then returns the difference between the model and the data, and this residual is minimized by `least_squares` by choosing an appropriate miss-factor m. In this way m is fitted to the data.

The effect of deconvolution is shown for selected timecourses in figures A.40-A.42 on pages 302-304.

4.18. Simulation of the heat signal upon laser excitation

The incident laser light is partially converted to heat, which causes a signal visible in the interferogram time courses (mirror position independent heat signal) and a signal which is visible in the spectra domain (mirror position dependent heat signal). In my master's thesis I simulated the heat decay in a laser crystal using time-resolved 3D finite-difference methods (Douglas Jr. 1955; Schönborn 2012); therefore I set up a simulation with µs resolution to investigate the 3D heat decay. The results are shown in figure 4.14.

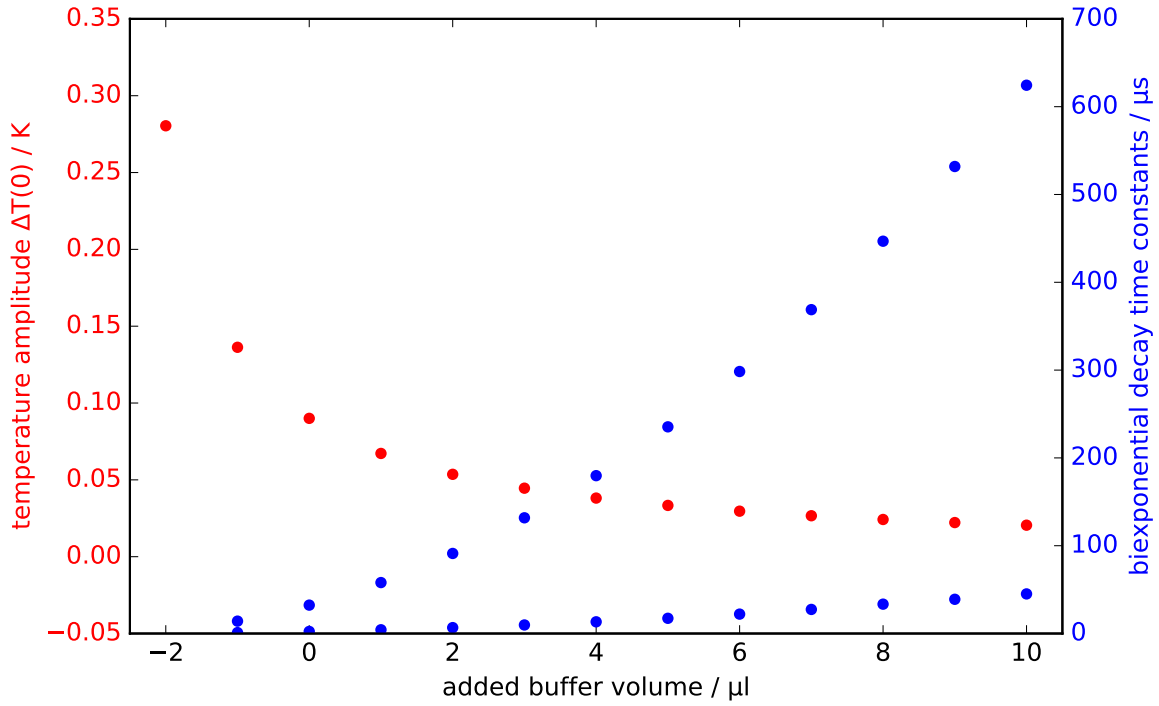

Figure 4.14.: Results from a finite-difference time-resolved heat distribution simulation. The goal of the simulation was to investigate the influence of the humidity of the sample (x-axis). Red: maximum temperature increase caused by the incident laser flash. Blue: time constants of biexponential heat signal decay.

For the investigation of the heat decay I observed the temperature at a single point: the point on the rotational symmetry axis which is hit by the incident laser beam first. This is the point which would have the highest temperature at any time. The temperature decay at this point is clearly biexponential in that a biexponential fit perfectly matches the data (not shown).

To investigate the influence of the humidity of the sample, I virtually added or removed buffer solution, effectively changing the concentration of the sample between the two CaF_2 discs. The result is that for very dry samples the initial temperature increase will be large, but the heat decay will be fast. For humid samples, the initial temperature increase will be small, but the heat decay will be slower, especially the slow component.

As a side note, I also simulated a single CaF_2 sandwich which is cooled at its rim with a copper holder, but exposed to room temperature air at its surfaces. No air convection was included in the simulation. This was done when I first conceived that the Peltier element of the sample stage would not suffice to keep the sample temperature low.

The result was that most of the CaF_2 sandwich showed room temperature, while its outer part lowered in temperature exponentially until the rim took on the temperature of the

copper holder (data not shown). I conclude that a thermostated copper holder is less than ideal to keep a sample between two CaF_2 discs at a certain temperature. Certainly the air surrounding the sandwich needs to be kept at a fixed temperature to guarantee that the sample has the same temperature. This will only be possible in a closed and insulated compartment which is thermostated in its entirety.

4.19. Proposals for future methodology

This section does not cover methodology used in this work, but which may be used in future projects. While working to obtain the FTIR step-scan data and manufacturing the oxygen polarography electrodes I considered the weak points of the setups and possible solutions, which are presented here.

4.19.1. Double-spiral oxygen polarography electrodes

The assembly of the oxygen polarography electrodes as outlined in section A.4 on page 238 is quite complicated and requires many steps. Furthermore, the special geometry of the bare metal electrodes poses a big challenge for the juwellers. Finally, to obtain an acceptable response time the platinum and silver rings need to be as close as possible. These problems can be solved by manufacturing double-spiral electrodes from platinum and silver foils.

The idea of double-spiral electrodes is to use simple metal foils as raw materials. The foils should have a thickness of less than 1 mm so that they can be bent easily (e.g. 5 mm × 0.7 mm × 30 mm). To each foil a ~1 mm diameter silver wire is attached. To obtain a double-spiral, a stack is made of a platinum foil, an insulating foil (e.g. PVC), a silver foil, and another insulating foil. Between the layers two-component adhesive is applied. Then the stack is curled up staring at one of its shorter sides to obtain a cylinder. A sketch is shown in figure 4.15. A drawback of the double spiral design is the challenge to not illuminate the silver electrode when applying the actinic flash. It may be possible to use two platinum foils instead.

This process has the advantage that the raw metal parts should be readily obtainable; besides attaching the silver wires, no manufacturing is needed by the juweller. The response time of the electrode should be very small, since there is always only a very short distance between the silver and the platinum electrodes. The distance between the metal electrodes is governed by the thickness of the insulating layer used. The overall surface is chosen by the thickness of the metal foils.

Further steps in the assembly should include to put the cylinder in a PVC bucket filled with two-component adhesive. After eliminating any air bubbles and hardening of the glue,

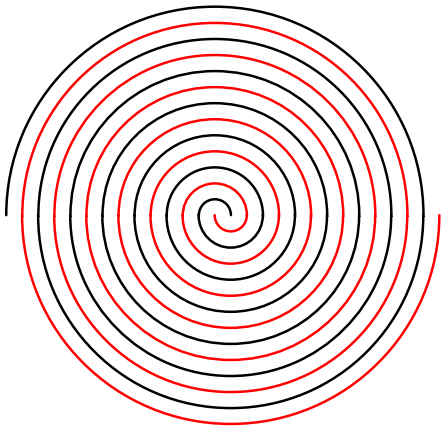

Figure 4.15.: Scheme of a double-spiral oxygen polarography electrode. Red: platinum; black: silver; white: insulating material. The insulating material should be much thinner than the metals to achieve a very small distance between the metals and a high overall metal surface.

the bucket could be cut in a turning machine to free the double-spiral profile.

To get rid of possible air bubbles it should be possible to centrifuge the half-finished electrode upside-down in a swinging bucket rotor: the glue should then be pushed to the top of the electrode, displacing any air bubbles towards the bottom of the upside-down electrode where they are released into the room volume. This step may also be applicable to the old design with modifications. Care must be taken not to damage the silver wires during the centrifugation.

4.19.2. Single-disc FTIR spectroscopy

Because of the many CaF_2 plates it takes a very long time to set up the FTIR experiment (see section 4.13). The sample chamber is also quite large which leads to problems on its own (e.g. a large volume to keep cool, long travelling times). A single, but large CaF_2 disc would be more effective in these regards. The diameter of such a disc to accomodate 2000 spots (like in the existing setup) would be about 12 cm, the size of a CD-ROM. The radius R of such a CaF_2 disc to accomodate N points with radius r is:

$$R = \sqrt{r^2 N \frac{2\sqrt{3}}{\pi}}. \tag{4.18}$$

CaF_2 discs with a diameter of up to 20 cm can be produced (Crystal GmbH, Berlin).

If the creation of such a large sample disc is feasible, this would be a huge improvement to the existing FTIR setup. The sample stage can be easily exchanged for another sample

stage which can accomodate one to three large sample discs. Additional 25 mm diameter holes would be included to accomodate pinholes and the photodiode.

The thickness of the disc could be set up with a separate setup employing an IR LED and a photodiode. Thickness measurements in the visible range would also be possible and should employ dim green light. The amount of sample pellet needed should be readily quantifyable using a precision scale.

The individual measurement points on such a disc would be aligned in a hexagonal packing. To access each point, a linear translation stage moves the disc up and down; the disc itself should be fixed in essence to the center of a cogwheel which is driven by another, much smaller cogwheel.

The whole assembly could be fixed onto a manual translation stage to be used during the alignment of the two beams to move the assembly horizontally. The assembly should then feature three exactly vertically stacked pinholes which can be moved to the center of the IR beam using the two translation stages: the upper and the lower ones would serve to find the center of the IR beam, the center one would feature a photodiode behind the pinhole to align the green laser beam (just like in the available setup).

An insulated and actively cooled sample chamber would serve as sample compartment. Air-cooled Peltier elements are preferred, but may not feature enough cooling power. When using water-cooled Peltier elements vibrations from the water pump should be decoupled using a heavy object through which the water flows. The sample compartment should be connected to the spectrometer using accordion tubing which contains the beam path. The sample box should be designed in a way that it can be set into the spectrometer's chamber in a plug-and-play fashion, so that other uses are not ruled out.

Dry air which is pumped into the sample box needs to be released in a controlled fashion.

The described setup would be very compact. Travelling times would be low. Most importantly, currently a whole day is used to create the sample plates; using a single disc, the measurement would have to be interrupted only for a brief time. Creating a single disc would use much less sample, since currently during the thickness adjustment of each sandwich some sample is lost.

Giving up external IR mirrors to focus the IR beam should lead to a better overall alignment. However, depending on the aperture selected the spot size should be measured; the decrease in SNR upon selection of a smaller aperture would have to be quantified.

To double the measurement speed, two spots could be measured at the same time. Currently, about 130 ms of data acquisition are followed by 570 ms of waiting time because of the acceptor side events. During these 570 ms, the disc could be moved to the next spot within 100 ms and another 130 ms timecourse measured after ~100 ms of equilibration. Afterwards, the setup would move back to the first spot to measure the second flash.

Still, neighboring spots should be measured directly after each other. For example, odd-numbered spots could be measured before even-numbered spots. It is a challenge though to calculate the fastest way to cycle between two points using the outer cogwheel and the y-translation stage, especially in the center of the disc. The equilibration and travelling times would need to be determined experimentally.

Finally, independent of the setup used, another way of measuring the heat-introduced signal could be to measure a very strong laser signal after the ten saturating laser flashes at each sample spot. This would require a pulse generator with a counting function. A microcontroller will most likely not meet the required nanosecond time resolution.

4.19.3. Stroboscope FTIR spectroscopy

The time resolution achievable by classical rapid-scan FTIR spectroscopy can be as high as 5 ms (Mezzetti and Leibl 2016); this is too slow to resolve events at the OEC in PSII. Recently, a rapid-scan FTIR spectrometer with a time resolution of 13 µs has been reported (Süss, Ringleb, and Heberle 2016); it is still in an experimental stage though and not commercially available yet. This section aims to describe a measurement protocol which should enable commercial rapid-scan FTIR spectrometers to achieve a much higher time resolution, although many more individual measurements to achieve the same spectral SNR are needed (Mäntele 1996). A scheme is shown in figure 4.16.

During a rapid-scan, the spectrometer scans the detector amplitude at every mirror position. In a double-sided forward-backward scan, the spectrometer first scans both sides of the interferogram by moving the movable mirror in one direction, and then scans both sides of the interferogram by moving the mirror back again. This is resembled by the red data points in figure 4.16. In this example, the spectrometer needs $T = 10$ ms to record two interferograms with $P = 21$ positions each (the centerburst is located at position 10). This leads to a time resolution of 5 ms, because the forward and backward scans can be regarded as individual measurements.

The scan corresponding to the red data points has been started right after a trigger signal has been given (i.e., the laser flash has been applied to the sample). Additionally, 40 more measurements are shown; these have been delayed by positive or negative integer multiples of T/P.

From the figure it becomes clear that through the delayed measurements, now at every mirror position data is available with a time-spacing of T/P, that is, the time resolution has been reduced by a factor of $1/P$. All there is to do is to combine the data of the different measurements at one time point. With this approach, time resolutions of better than 100 µs seem to be possible.

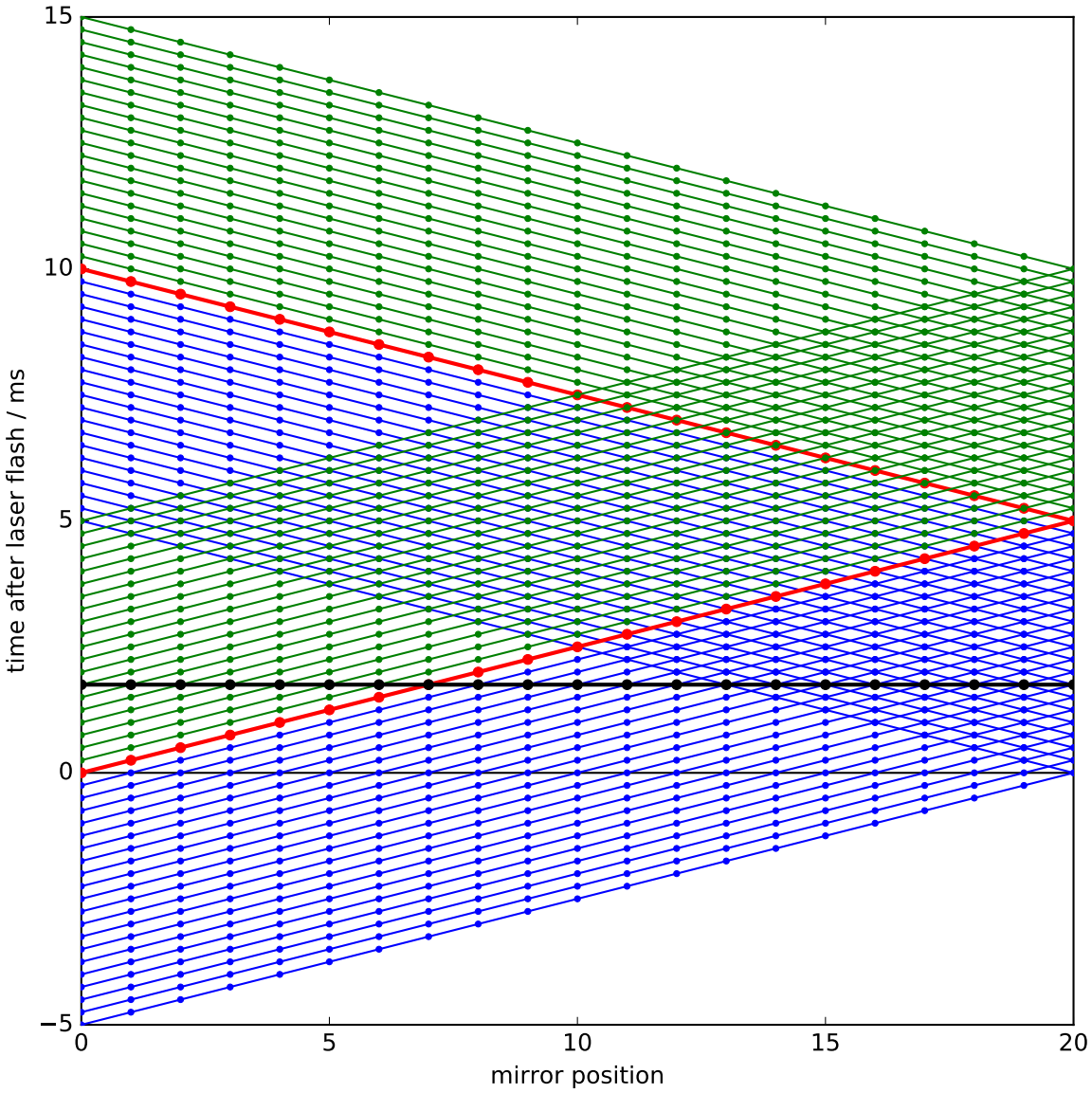

Figure 4.16.: Recording schemes of double-sided forward-backward rapid-scan interferograms (time vs. mirror position). The interferograms have 21 mirror positions with the centerburst located at position 10. Red: a typical double-sided forward-backward rapid-scan started after a laser flash has been applied at $t = 0$ ms. Blue: rapid-scans that have been started earlier; green: rapid-scans that have been started later. Black: a time-resolved rapid-scan with much higher time resolution which has been assembled from many individual measurements.

This approach stands between "slow" rapid-scans and the faster step-scans. It presumably does not lead to a very high time-resolution, but it may not need as many measurements as a step-scan (depending on the integration time at the detector). Therefore I envision such a measurement mode as valuable to observe the oxygen evolving process under varying conditions. Furthermore, with every measurement, valuable information can be obtained: the thickness and humidity of each sample spot can be observed individually. Even the activity of each sample spot can be obtained from the steady-state data. This is an important advantage compared to the step-scan.

Some caveats have to be considered. First, it is unlikely that the moving mirror moves homogeneously in time; the velocity will most likely vary with mirror position. To measure the real time axis the zero crossings in the HeNe signal should be observed (e.g. by amplifying the signal to a fixed value while keeping the sign, and taking the derivative afterwards). Strong variations in mirror velocity might prevent this scheme. The HeNe laser signal might also be needed to accurately delay the laser flash.

5. Results

In this chapter the results of different rapid-scan and step-scan measurements on photosystem II are shown. When not stated otherwise the data shown has been obtained in H_2O. The first section presents the absolute spectrum of PSII and its cryo-buffer. The second section shows how rapid-scan difference spectra do not change despite the long measurement time proving the long-time stability of the sample. The third section presents rapid-scan results about the influence of ammonia on photosystem II. The former two sections show steady-state rapid-scan data; the first time-resolved data, although obtained in the rapid-scan mode, is shown in section 5.4 and reveals acceptor side dynamics. The later sections deal with step-scan data: first, the timecourses in the interferogram domain are shown and discussed in section 5.5. These timecourses are the basis for heat correction approaches which are shown in section 5.6; different correction approaches are introduced and discussed. A short section follows which concerns the time-axis in the step-scan measurements. Finally, section 5.8 presents time-resolved FTIR step-scan data on photosystem II with microsecond time resolution for all four S-state transitions.

5.1. Absolute spectrum of photosystem II and its buffer

Figure 5.1 shows the absolute spectrum of PSII and its cryo-buffer. The betaine in the cryo-buffer, which leads to increased stability of PSII in solution, gives rise to various bands in the infrared spectrum. To avoid the influence of these bands in the time-resolved measurements, the betaine has been removed from the measurement buffer. The following section shows that nevertheless the PSII is very stable in the prepared "CaF_2-sandwich" form.

5.2. Long-time stability of photosystem II in the used setup

The data of the time-resolved rapid-scan has been acquired over the course of several days. To investigate the impact of the long measuring time on PSII, the data has been split up in several batches. The batches are displayed in figure 5.2.

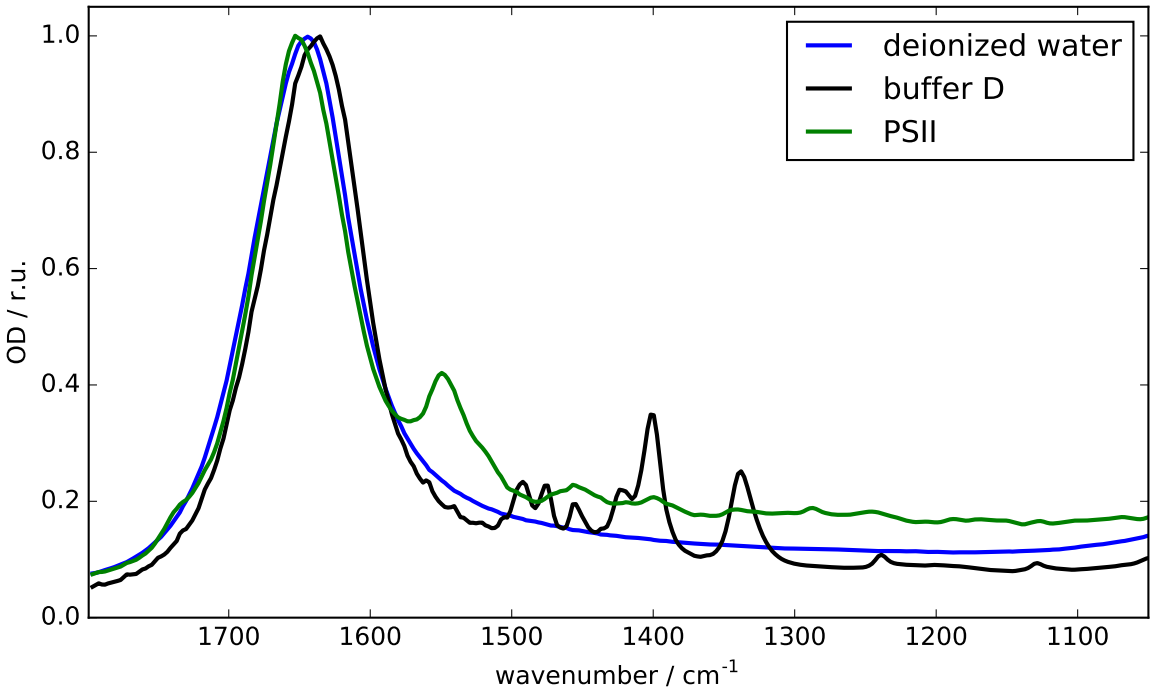

Figure 5.1.: Absolute spectra of deionized water (blue), PSII (green), and buffer D (black) rescaled to an OD of 1 at the maximum of each spectrum.

If the sample holder is completely full there are 1980 sample spots. About 10% of the spots are sorted out before the start of the measurement due to inappropriate sample thickness. To assess the long-time stability, the data has been divided into 500 measurements per batch, leading to 11 batches. Each batch is plotted in figure 5.2. The first batch contains the 500 sample spots which have been measured right at the start of the measurement and is shown in dark blue. The very last batch has been measured about 60 hours after the start of the measurement and is shown in yellow. Note that once the (less than) 1980 spots have been measured once, the measurement continued with the first spot. To measure the whole sample plate once takes about 12 hours, which is plenty of dark adaptation time.

The result is that the sample quality stays constant with time. This may have to do with the sample being kept at 10 ℃ during the measurement, and additionally the sample is being measured as pellet, which could lead to better stability of the protein.

The first batch shows a higher amplitude at 1478 cm^{-1} and lower amplitude at 1676 cm^{-1} than the other batches. This is remarkable since the other batches contain exactly the same sample, except for on other CaF_2 plates. On the other hand it is hard to argue that this difference arises due to different physical properties (like thickness or hydration) of the samples of this batch because only these two wavenumbers are affected. Moreover, it does not appear that the sample was contaminated as later measurements of the very same spots

Figure 5.2.: Long time stability of photosystem II. For a detailed description of the plot please refer to the text.

are missing these anomalies. In any event the difference is minor and is no indication of sample aging.

5.3. Influence of NH_3 on photosystem II

The influence of ammonia on PSII FTIR difference spectra has been discussed in section 3.3.6 on page 22. In this section I present the first FTIR dataset showing the influence of 120 mM ammonia on PSII on all semi-stable S-state transitions (figure 5.4). Changes of particular interest are marked by colored arrows; text labels refert to mutations previously done which show similar changes (Strickler et al. 2008; Service, Yano, et al. 2011; Debus 2014; Pokhrel, Debus, and Brudvig 2015).

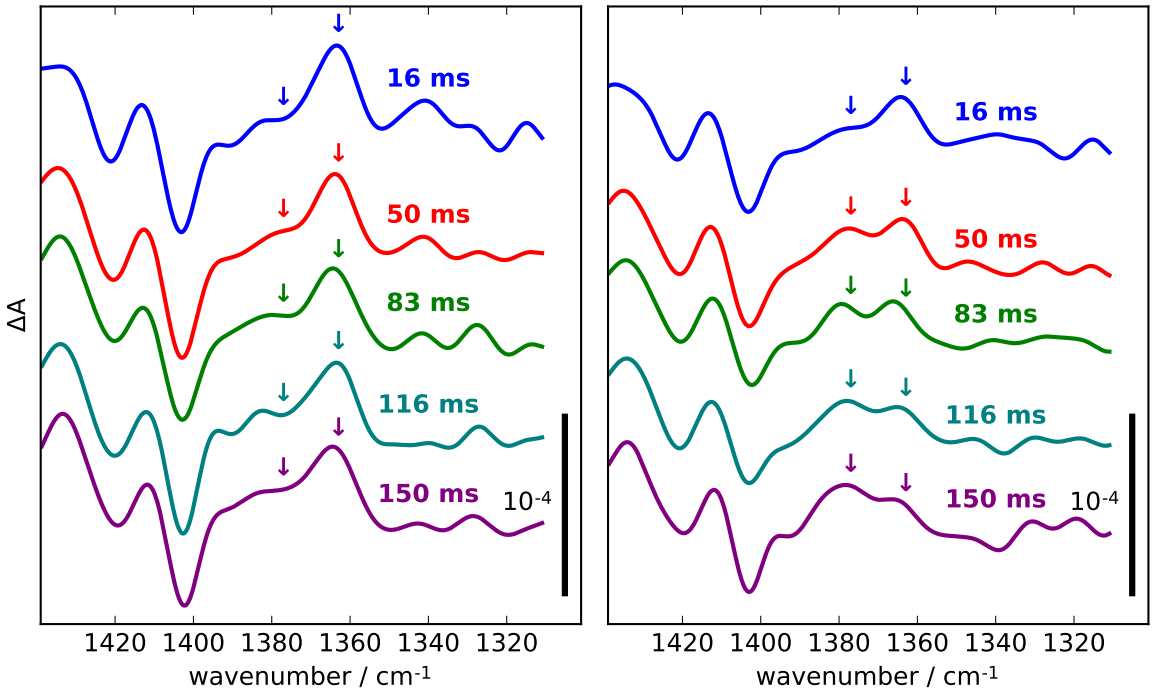

Figure 5.3.: Time-resolved first flash difference spectra under the influence of 120 mM NaCl (left) and 120 mM NH_4Cl (right). The spectra have been obtained using the rapid-scan mode and thus have a time resolution of about 34 ms (see next section). The difference spectra have been shifted by $N \cdot 5 \cdot 10^{-5}$ respectively. The arrows (1363 cm^{-1} and 1377 cm^{-1}) mark features that do not change under the influence of NaCl, but do change with time under the influence of NH_4Cl. Both spectra at 16 ms (NaCl and NH_4Cl) show the same features. After 83 ms, an appearing peak at 1377 cm^{-1} has the same amplitude as a disappearing peak at 1363 cm^{-1}. After 150 ms, the appearing peak is larger than the disappearing peak.

In the $S_1 \longrightarrow S_2$ transition, under the influence of ammonia a positive feature at about 1363 cm^{-1} is diminished and a new positive feature appears at about 1377 cm^{-1} (figure 5.4).

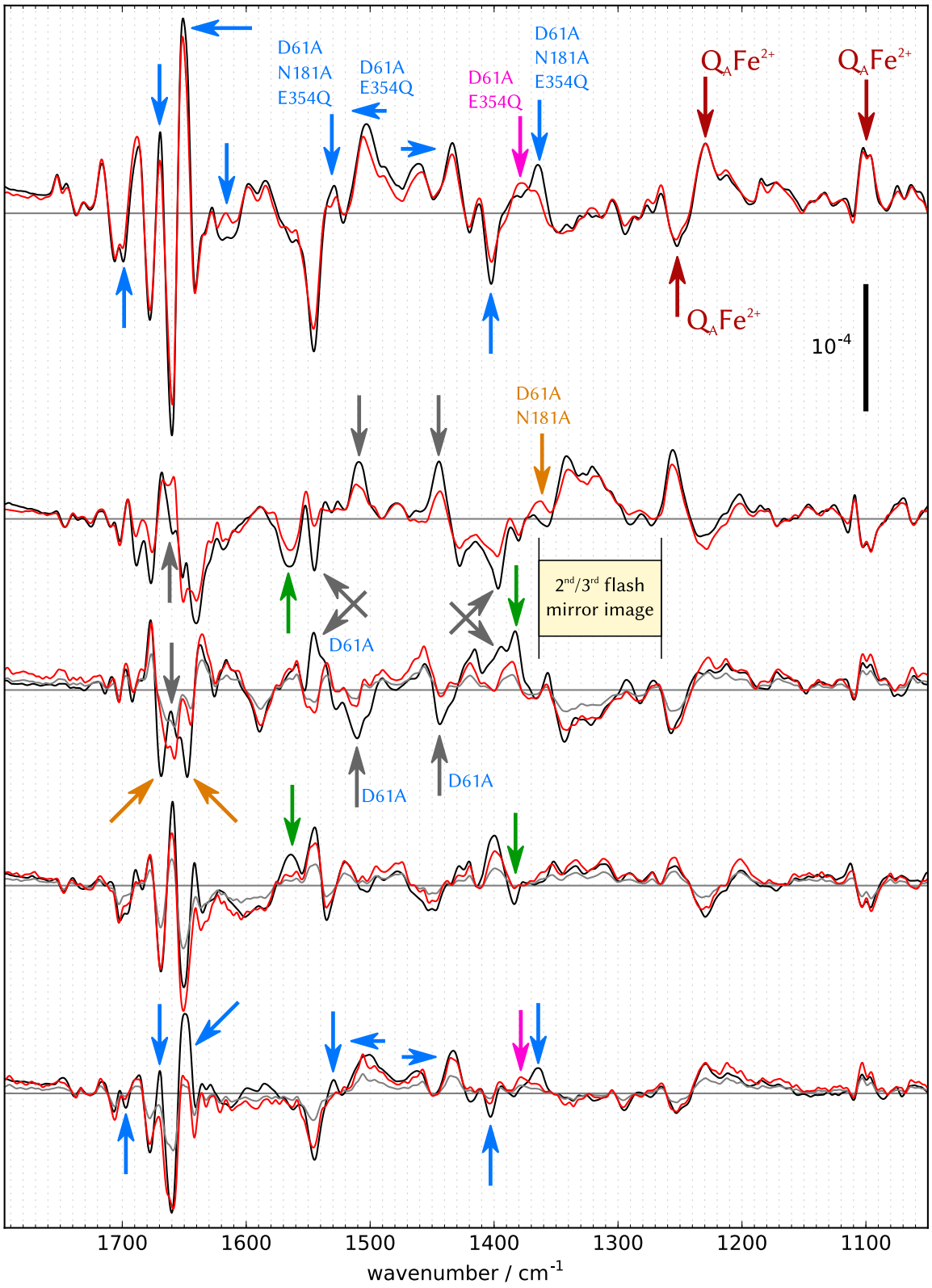

Figure 5.4.: **Black**: S-state difference spectra of PSII, pH=7.5, buffer D + 120 mM NaCl, first cycle. Shown are flashes one to five from top to bottom. Resolution: 4 cm^{-1}, window: Norton-Beer medium. **Red**: Likewise, but using a buffer containing 120 mM NH_4Cl instead of NaCl. On the 3rd, 4th, and 5th flash, the NH_4Cl spectra (gray) were rescaled (red) to match the magnitude of the acceptor side features in the NaCl spectra. Text labels refer to genetic PSII variants by Debus et al., see main text.

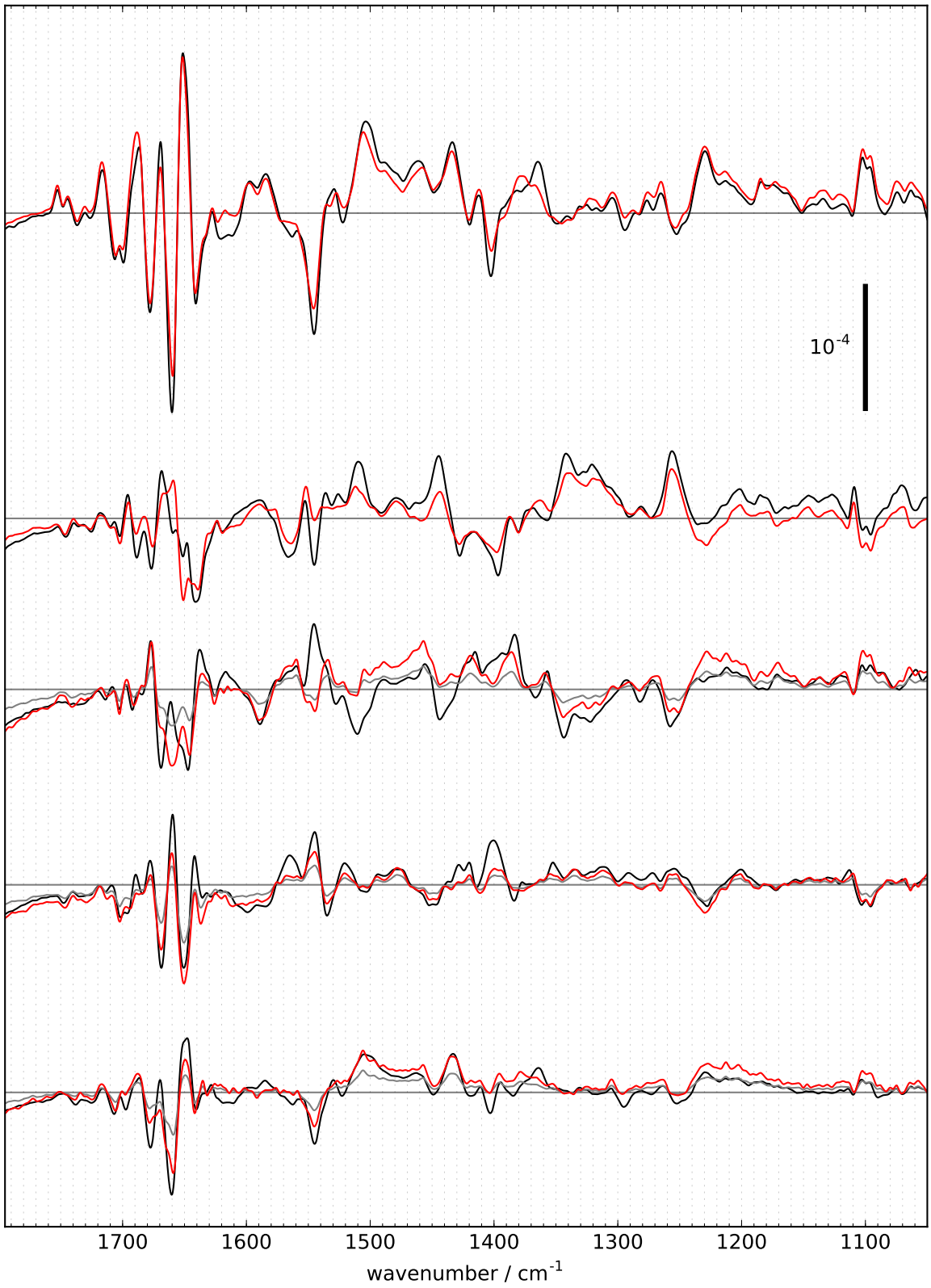

Figure 5.5.: **Black**: S-state difference spectra of PSII, pH=7.5, buffer D + 120 mM NaCl, second cycle. Shown are flashes one to five from top to bottom. Resolution: 4 cm^{-1}, window: Norton-Beer medium. **Red**: Likewise, but using a buffer containing 120 mM NH_4Cl instead of NaCl. On the 3rd, 4th, and 5th flash, the NH_4Cl spectra (gray) were rescaled (red) to match the magnitude of the acceptor side features in the NaCl spectra.

This change completes within 100 ms as evident from figure 5.3. Figure 5.3 shows time-resolved rapid-scans of the $S_1 \longrightarrow S_2$ transition in PSII under the influence of NaCl (left panel) and NH_3 (right panel). 16 ms after the applied laser flash the two spectra are very similar; only after 83 ms does the appearing peak have the same amplitude as the disappearing peak. After 150 ms the change is complete. There may be an associated reversal of this phenomenom in the following S-state transition ($S_2 \longrightarrow S_3$). Additional features changing in this transition can be found at 1402 cm^{-1}, 1461 cm^{-1}, 1529 cm^{-1}, 1615 cm^{-1}, 1651 cm^{-1}, and 1699 cm^{-1}. Features at wavenumbers lower than 1350 cm^{-1} are virtually the same in the two buffers.

In the $S_2 \longrightarrow S_3$ transition more features are severely affected by ammonium treatment, but again only features above 1350 cm^{-1} are affected, while features below 1350 cm^{-1} are unaffected.

The amplitude of the $S_3 \longrightarrow S_0$ transition under the influence of ammonia is significantly reduced compared to NaCl treatment (gray curve in figure 5.4). The gray curve has been scaled according to the amplitudes of the two measurements at 1234 cm^{-1} and 1257 cm^{-1} and is displayed as red curve. The rescaled ammonia difference spectrum shows many differences when compared to the NaCl measurement above 1350 cm^{-1}.

The amplitude of the $S_0 \longrightarrow S_1$ transition is diminished as well under the influence of ammonia. The ammonium spectrum has been rescaled according to the amplitudes at 1228 cm^{-1} and 1254 cm^{-1}. After rescaling, the ammonium spectrum resembles the NaCl spectrum below 1380 cm^{-1} but shows differences above 1380 cm^{-1}.

After completing a full S-state cycle, the second $S_1 \longrightarrow S_2$ transition shows a diminished amplitude as well. When rescaled according to the amplitudes at 1229 cm^{-1} and 1254 cm^{-1}, The ammonium difference spectrum compares very well to the initial $S_1 \longrightarrow S_2$ transition difference spectrum. Minor differences in the amide I region can be explained by an offset error: because the original amplitude is so small (gray curve) and rescaled, the amide I peaks depend critically on a correct offset. All samples have been measured twice; figure 5.4 shows the initial measurement, while figure 5.5 shows a measurement applying a second train of flashes to each sample. In this measurement, the amide I changes under the influence of ammonia of the fifth flash compare well to the amide I changes of the first flash.

5.4. Time-resolved rapid-scan in H_2O and in D_2O

The time resolution of a rapid-scan measurement is determined by the scan speed of the moving mirror, in other words, the time needed to scan the whole optical path difference range to record one interferogram. In this measurement, double-sided forward-backward

interferograms have been recorded. In 700 ms, 10 double-sided forward-backward interferograms have been recorded. The flash spacing was the same as in the step-scan measurements. The interferograms recorded in forward and backward direction were split up two gain 20 double-sided interferograms. Each interferogram has a time resolution of 34 ms, with the first interferogram scanning from 0 ms to 34 ms, the second from 34 ms to 68 ms (with time points 17 ms, 51 ms, ...) and so on. This should be considered when interpreting the 57 ms phase introduced further below.

In figure 5.6 the steady-state S-state difference spectra are shown. The amplitude of the first flash difference is especially large, much larger than the amplitudes of the fifth and ninth flash (see also figure 5.8). Figure 5.6 also shows binary and quaternary oscillations. Regions where the orange and turquoise (first and third flash) as well as the aquamarine and pink (second and fourth flash) spectra overlap, particularly with opposite sign, shows primarily acceptor side behaviour since this is equivalent to having the same feature every other flash. On the other hand, regions where e.g. the orange and aquamarine (first and second flash) as well as turquoise and pink (third and fourth flash) spectra overlap show quaternary oscillations and therefore imply S-state dependent features.

In figure 5.7 the time-resolved flash patterns of the TRRS data are displayed. Each panel contains 20 flash patterns corresponding to one selected wavenumber. The flash patterns are colored according to the colors of the rainbow, with the first flash pattern colored red and the last one blue. The order of the colors in between can best be seen in the panel for 1478 cm^{-1}.

For wavenumbers which are traditionally associated with electron transport at the acceptor side (see introductory chapter) as 1478 cm^{-1}, 1100 cm^{-1}, and 1228 cm^{-1}, the first few flash patterns do not correspond well to the respective later ones. Generally, these flash patterns show period-of-two oscillations. The period-of-two oscillation at 1478 cm^{-1} disappears after ~120 ms. At 1717 cm^{-1}, the flash pattern shows first a period-of-two oscillation, but later it features a period-of-four oscillation. The period-of-two oscillation at 1100 cm^{-1}, 1228 cm^{-1}, and to some extent at 1252 cm^{-1} increases in amplitude with time.

In figure 5.8 timecourses are shown for selected wavenumbers. Each timecourse corresponds to a certain flash, with the first flash colored red and the tenth flash colored blue. The colors in between follow the colors of the rainbow. Period-of-two oscillations correspond to the noise introduced by separating forward-backward scans into two separate double-sided interferograms.

Especially at 1478 cm^{-1} and 1717 cm^{-1}, but also at other wavenumbers (notably 1545 cm^{-1}) slow decays can be seen. Together with the period-of-two pattern at 1717 cm^{-1} seen in figure 5.7 the signals seen at 1717 cm^{-1} can be assigned to processes at the acceptor side.

For each flash-induced time-resolved difference spectrum, two time constants have been

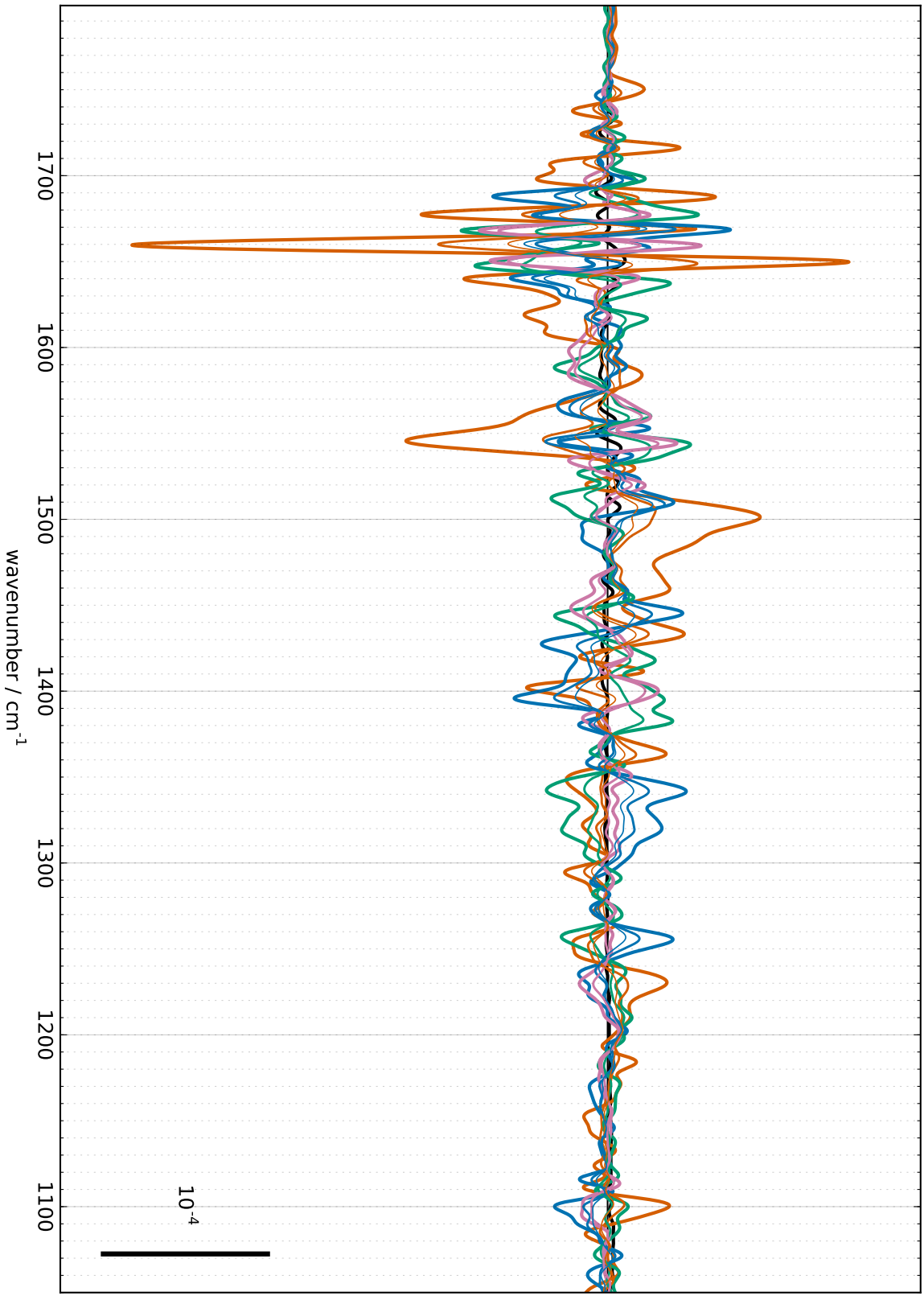

Figure 5.6.: Steady-state FTIR difference spectra (H_2O). Orange: flashes 1, 5, 9, blue: flashes 2, 6, 10, green: flashes 3, 7, pink: flashes 4, 8. Thick lines: flashes 1-4, medium lines: flashes 5-8, thin lines: flashes 9, 10. Black line: dark-dark spectrum.

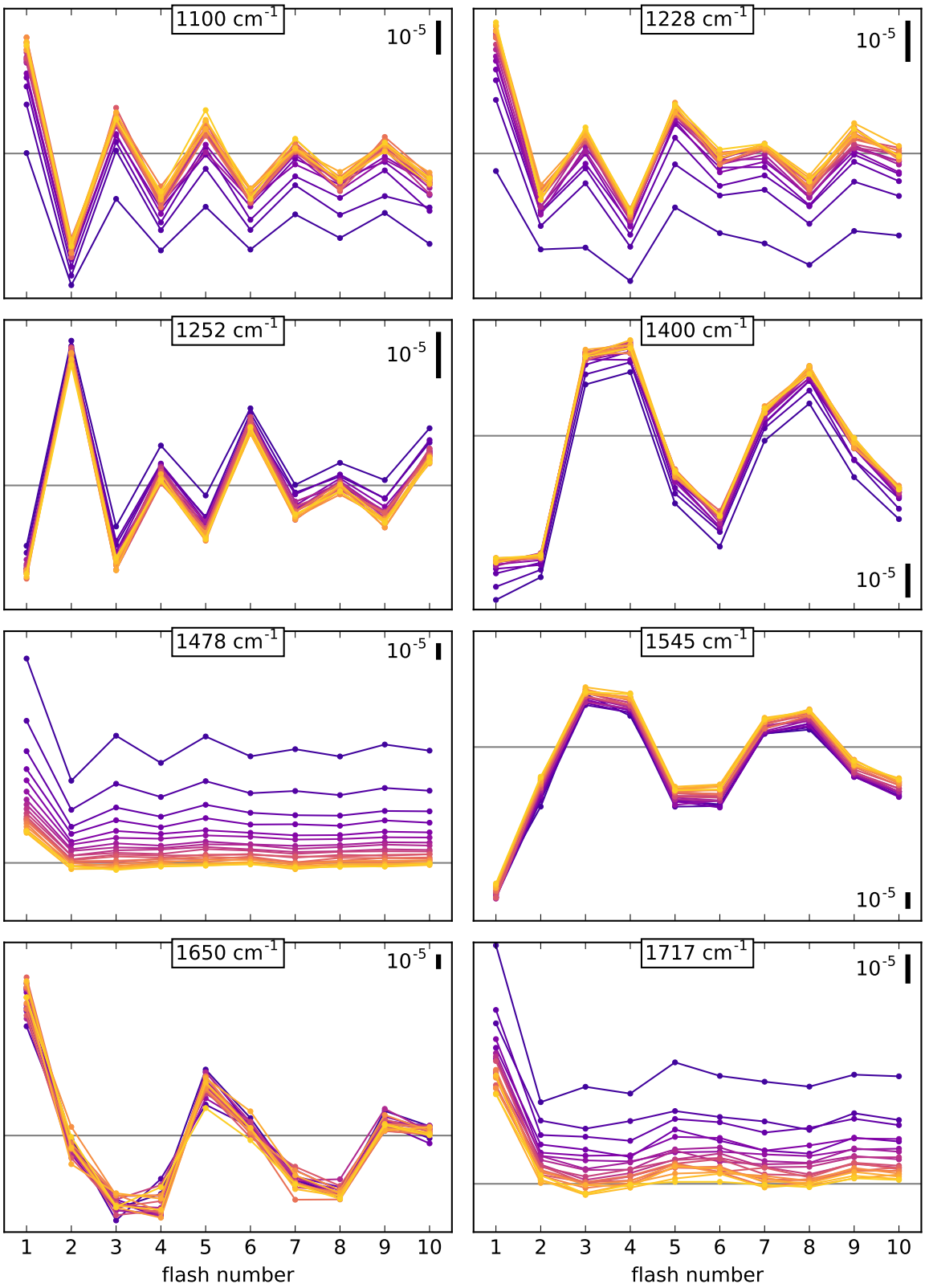

Figure 5.7.: TRRS Flash patterns for selected wavenumbers (H_2O). Dark blue: 17 ms after flash excitation; yellow: 660 ms after flash excitation. The order of the colors in between can be seen well in the panel for 1478 cm^{-1}.

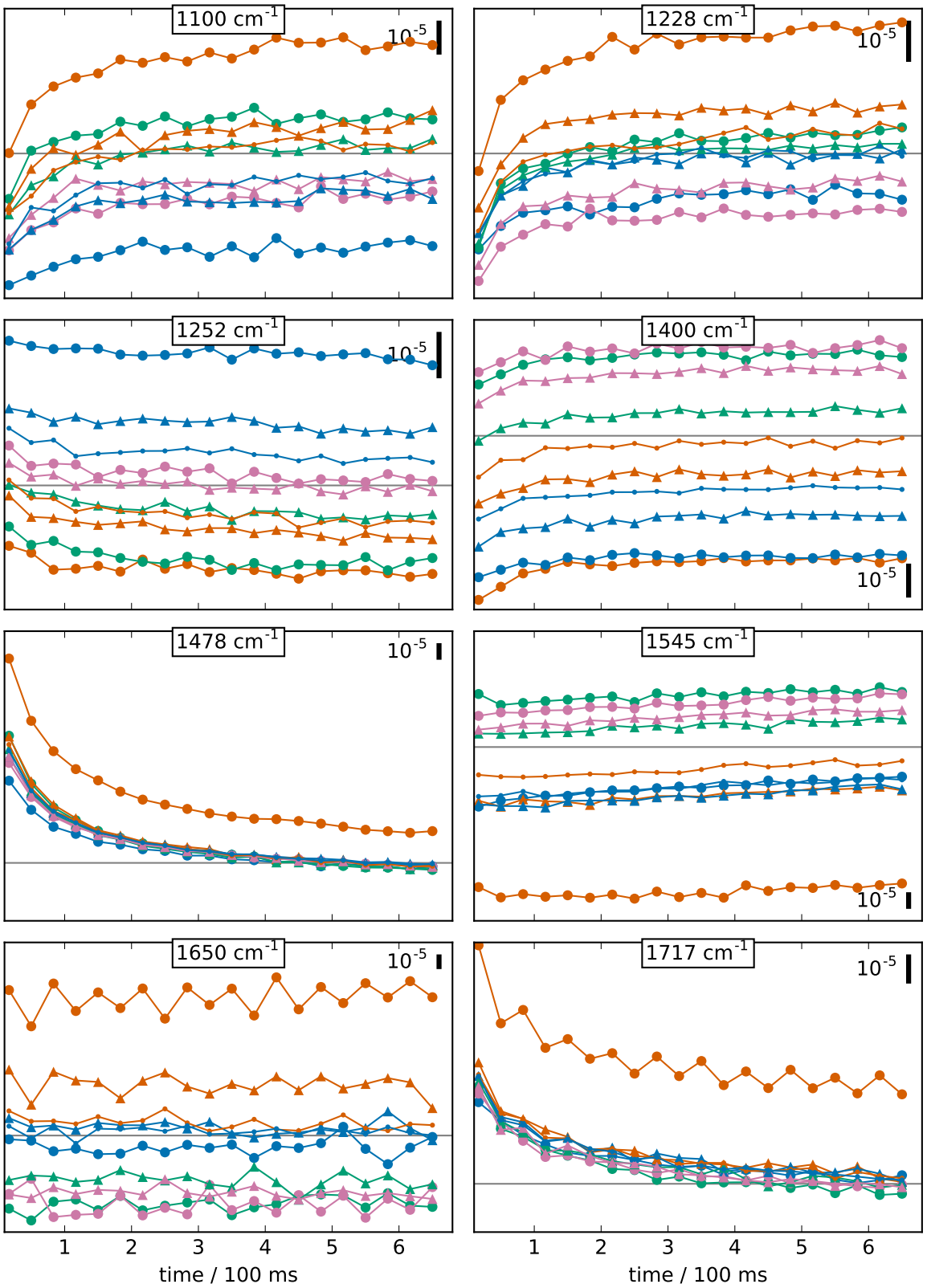

Figure 5.8.: TRRS Timecourses for selected wavenumbers (H_2O). Each timecourse corresponds to one flash. Red: flashes 1, 5, 9. Blue: flashes 2, 6, 10. Green: flashes 3, 7. Magenta: flashes 4, 8. Large dots: flashes 1 to 4. Triangles: flashes 5 to 8. Small dots: flashes 9 and 10. The first points in the timecourses correspond to the spectra in figure 5.9.

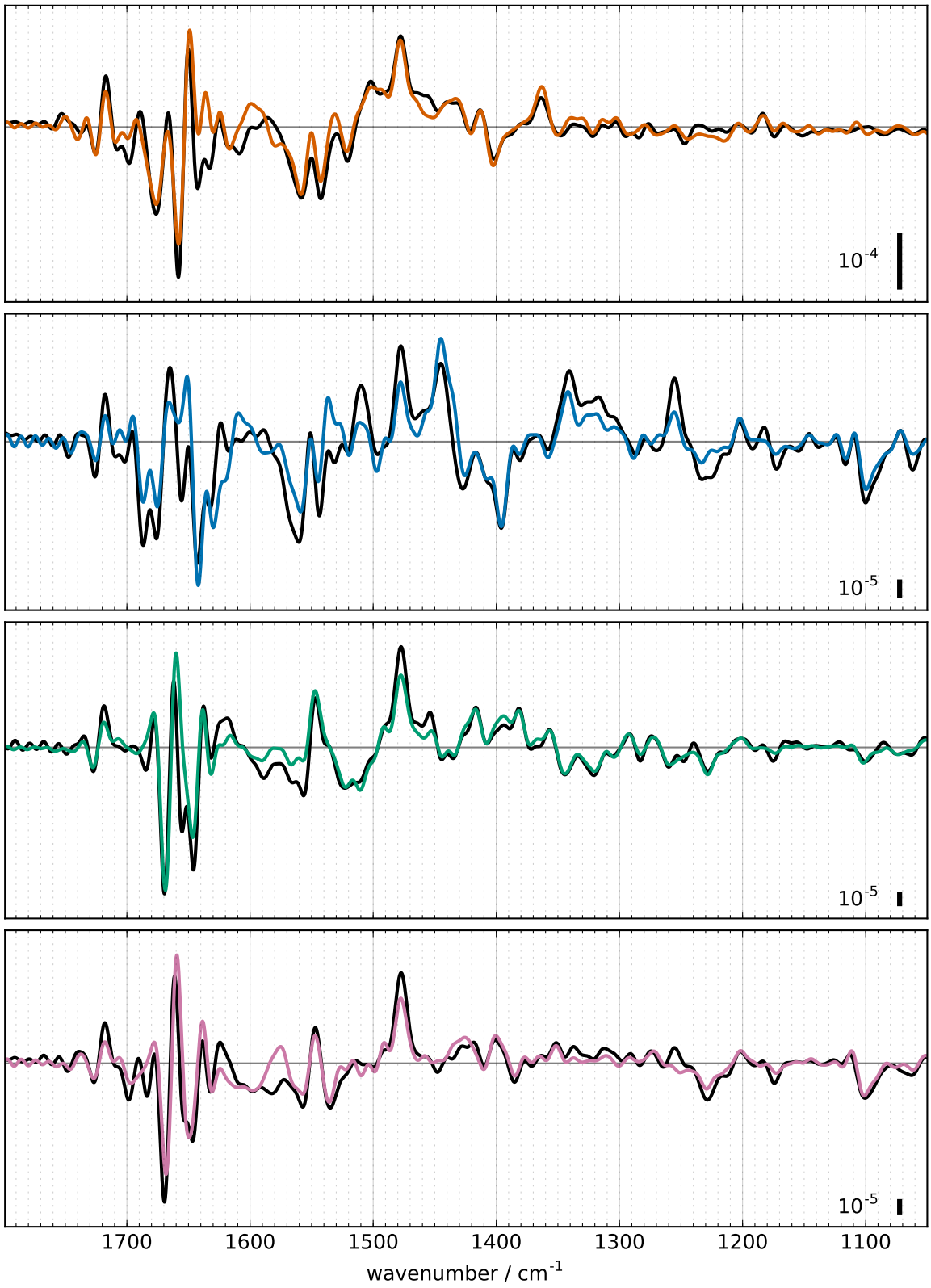

Figure 5.9.: Rapid-scan data of PSII in H_2O (black) and D_2O (colored) 17 ms after laser flash excitation. From top to bottom: flashes one to four. The spectra correspond to the first points in the timecourses in figure 5.8.

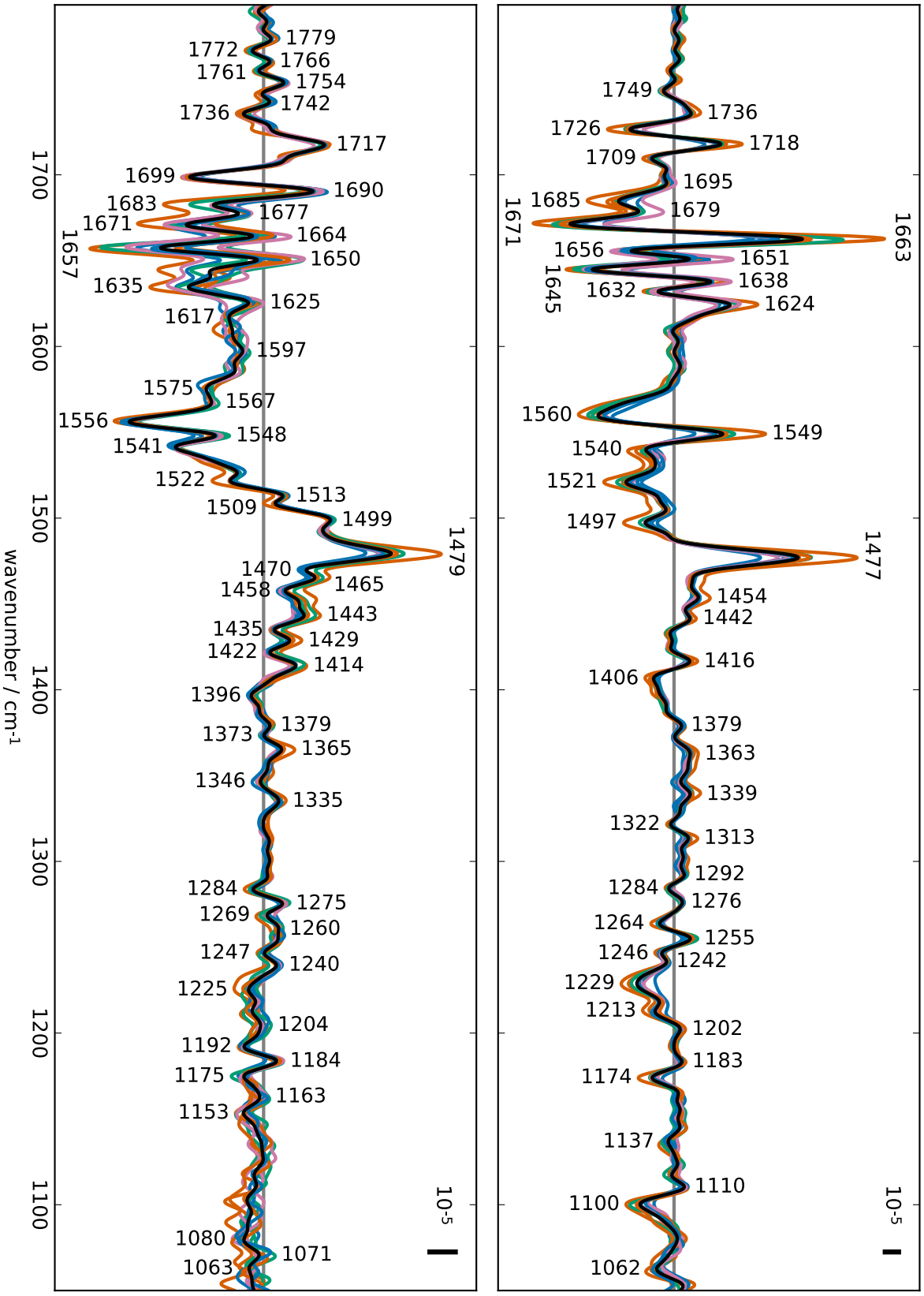

Figure 5.10.: Decay associated spectra (H_2O). Right: Fast phase with τ = 58 ms, left: slow phase with τ = 473 ms. Black: average of all spectra corresponding to one phase. Orange: flashes 1, 5, 9, blue: flashes 2, 6, 10, green: flashes 3, 7, pink: flashes 4, 8. The numbers indicate positions of features of the black curves.

obtained by global fitting. The time constants are given in table 5.1.

flash number	first phase	second phase
1	61 ms	980 ms
2	57 ms	570 ms
3	52 ms	279 ms
4	57 ms	480 ms
5	55 ms	340 ms
6	61 ms	580 ms
7	54 ms	480 ms
8	60 ms	410 ms
9	57 ms	550 ms
10	55 ms	270 ms

Table 5.1.: Time constants for each flash-induced transition as obtained by flash-dependent global fitting two time constants (H_2O).

For the fast phase, a small period-of-two oscillation around 57 µs can be conceived. The time constants of the slow phase vary considerably; there are weak indications for a period-of-two oscillation. The first flash time constants are an exception to these oscillations, because the two phases are especially slow after the first flash.

To show decay-associated spectra two time constants have been found by globally fitting all ten transitions. The result is $\tau_1 = 58\,\text{ms}$, $\tau_2 = 473\,\text{ms}$. The decay associated spectra are shown in figure 5.10. In these spectra no clear binary oscillation can be observed.

5.5. Interferogram domain step-scan timecourses

In FTIR spectroscopy a spectrum is never directly measured; rather, an interferogram is recorded and transformed into a spectrum through a Fourier transform. This section shows the time-resolved form of the recorded data.

To obtain microsecond time resolution it is necessary to measure in step-scan mode. This mode had been called the slow-scan in earlier times, since the spectrometer fixes the moving mirror at one position, records the intensity, and moves to the next mirror position. The interferogram is recorded position by position. Modern spectrometers do not only record a single intensity at a given mirror position, but use the modern detectors' capability to record many time-resolved values. A time resolution in the nanosecond regime is possible. Our time resolution is limited to 6 µs by the AD converter.

The recorded timecourses (see figure 5.11) are dominated by events which are independent of the mirror position. Signals which are independent of the mirror position have no

influence on the resulting spectra: since any such signal adds the same value to the interferogram at every mirror position, it will be whiped out when the offset of the interferogram is subtracted before the Fourier transform is calculated.

In figure 5.11 the timecourses of the H_2O step-scan measurements have been averaged for each flash. In the figure, a semi-logarithmic x-axis is used: the "kink" in the curve corresponds to the transition from linear to logarithmic scale. One hundred mirror positions have been averaged, leading to 50,000 timecourses averaged per flash. The most prominent feature is a sharp peak pointing down, which is caused by the sample being heated up instantly by the incoming laser flash. The minimum of the timecourse is reached within 18 µs (three sampling points): since the heatup of the sample happens—on this timescale—instantaneously, these 18 µs mark the rise time of the setup.

The signal then decays and for a simple thermal signal a strict monotonous relaxation to the zero level would be expected. Surprisingly, the signal crosses the zero line and then very slowly approaches the zero value again. In addition, this is much more pronounced on the first flash: in subsequent flashes this behaviour can also be seen, albeit not as strong.

Taking the difference of the first and the second flash the (seemingly non-thermal) secondary signal is recovered (teal line in figure 5.11). It rises with a time constant of 45 µs and decays with a time constant of about 41 ms. The secondary signal can be subtracted from the thermal signal in the following way: since we can safely assume that the primary heat-induced signal H is the same for each flashes, and each flash is affected by a secondary signal S with a varying amplitude:

$$M_1 = H + \alpha S \quad \text{and} \tag{5.1}$$

$$M_2 = H + \beta S, \tag{5.2}$$

the original heat-induced signal H can be recovered by finding S and β or α. In this way, the blue curve shown in the second plot of figure 5.11 has been calculated. It should correspond to the directly heat-induced signal. A fit with a sum of three exponential terms describes the decay very well. The gray bars in the plot correspond to the three pairs of fit parameters. The time constants of the heat signal are 37 µs, 220 µs, and 1.5 ms.

The fastest time constant of 37 µs indicates that extracting real PSII donor-side kinetics in this time-domain will depend critically on the heat signal compensation.

On a side note, it can be seen from figure 5.11 that the first flash does not differ in intensity from following flashes, since the negative amplitudes of the peaks are virtually identical. This shows that letting the Minilite's flash lamps flash before the measurement to warm them up is not necessary.

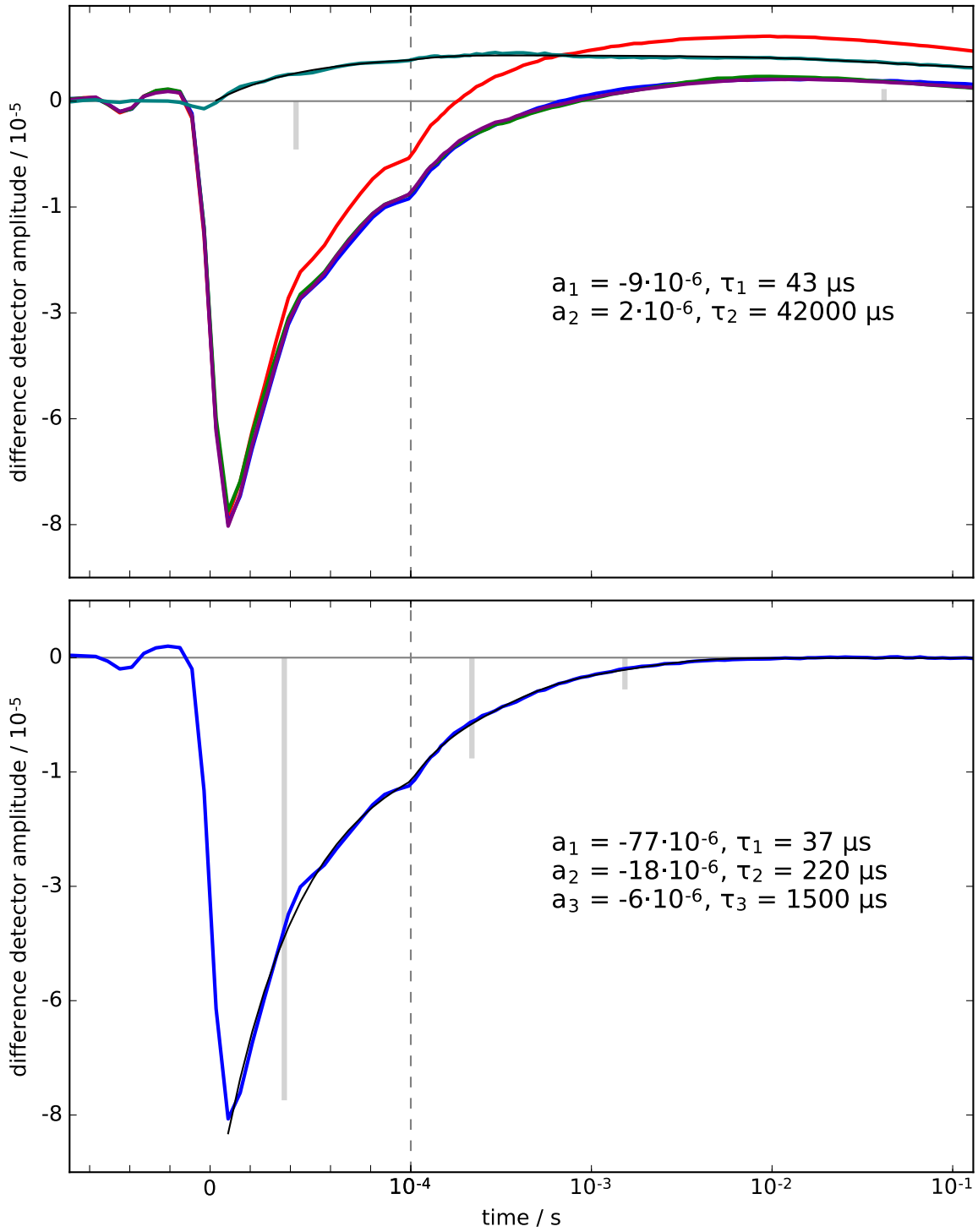

Figure 5.11.: **Top**: Step-scan timecourses for flash 1 (red), 2 (blue), 3 (green), and 4 (purple). The teal-colored curve shows the difference between the first and the second flash; it has been fitted with a sum of two exponential functions (black curve).
Bottom: The second flash timecourse has been corrected for the difference signal (teal curve in the plot above). It has been fitted with a sum of three exponential functions (black curve).
The gray bars indicate fit parameters. The figure uses a semi-logarithmic x-axis: the "kink" in the data corresponds to the transition from linear to logarithmic display.

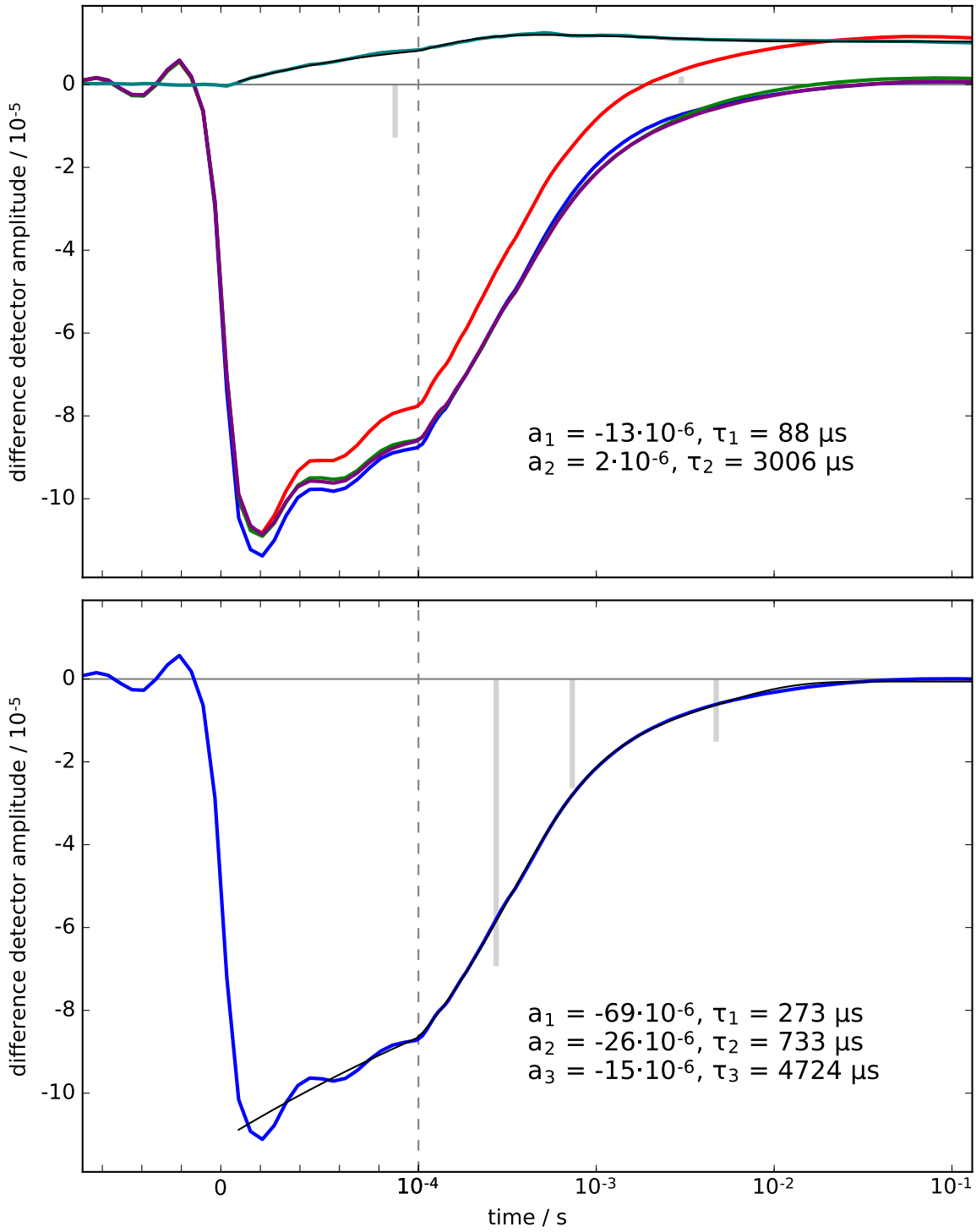

Figure 5.12.: **Top**: D_2O Step-scan timecourses for flash 1 (red), 2 (blue), 3 (green), and 4 (purple). The teal-colored curve shows the difference between the first and the second flash; it has been fitted with a sum of two exponential functions (black curve).
Bottom: The second flash timecourse has been corrected for the difference signal (teal curve in the plot above). It has been fitted with a sum of three exponential functions (black curve).
The gray bars indicate fit parameters. The figure uses a semi-logarithmic x-axis: the "kink" in the data corresponds to the transition from linear to logarithmic display.

5.6. Heat-induced FTIR signals

There are several factors contributing to a time and wavenumber dependent laser flash induced IR signal corresponding to the release of heat in the sample. As indicated by the linear relationship between the laser flash intensity and the heat signal amplitude (Görlin 2012), it can be seen that the laser photons are absorbed by the PSII's chlorophylls and dissipated into heat. Furthermore, the light harvesting yield as well as the fractional energy yield of PSII is about 34% respectively (Dau and Zaharieva 2009); the other 66% are dissipated as heat. Damaged PSII centers will dissipate all of the captured light energy as heat.

All of these processes that lead to heat generation complete, compared to the time resolution of the setup, instantaneously. The dissipation of the heat, on the other hand, shows time constants in the same regime as the S-state transition spectra. Therefore it is very important to separate the heat signal from the real S-state transition kinetics, and to perform a heat compensation is necessary.

In the following I will present different attempts to isolate the heat signal in order to subtract it from the step-scan data. First, I will show the measured step-scan data with the uncompensated heat signal in section 5.6.1. In section 5.6.2 absolute spectra of different samples at varying temperatures are shown. The spectra are surprisingly complex, but may relate to temperature induced geometric changes of the whole sample assembly, whereas in the step-scan measurement the heat is induced only locally. In section 5.6.3 I present results from different step-scan measurements to measure the heat-induced signal directly. An important finding is that the heat signal spectrum shows the same decay characteristics at every wavenumber; yet, the measured spectra do not seem to fully represent the heat signal in the main step-scan measurement. Finally, in section 5.6.6 I present a method to obtain the heat spectrum from the main step-scan measurement by fitting the heat decay timecourse at each wavenumber to the step-scan timecourses. This is the compensation method I decided to use to investigate S-state dependent changes. The different methods are discussed in section 5.6.7.

5.6.1. Amide region double-difference timecourses

The amide region dynamics are influenced to a large extent by the heat signal. The uncorrected amide I region spectra have been plotted in figure 5.13 for every flash at 9 µs, when the amplitude reaches its maximum.

It can be seen that narrow features are overlapping a very broad feature. The narrow features may represent changes in PSII relating to water oxidation chemistry while the very broad feature may solely represent the heat signal. Assuming that the heat spectrum

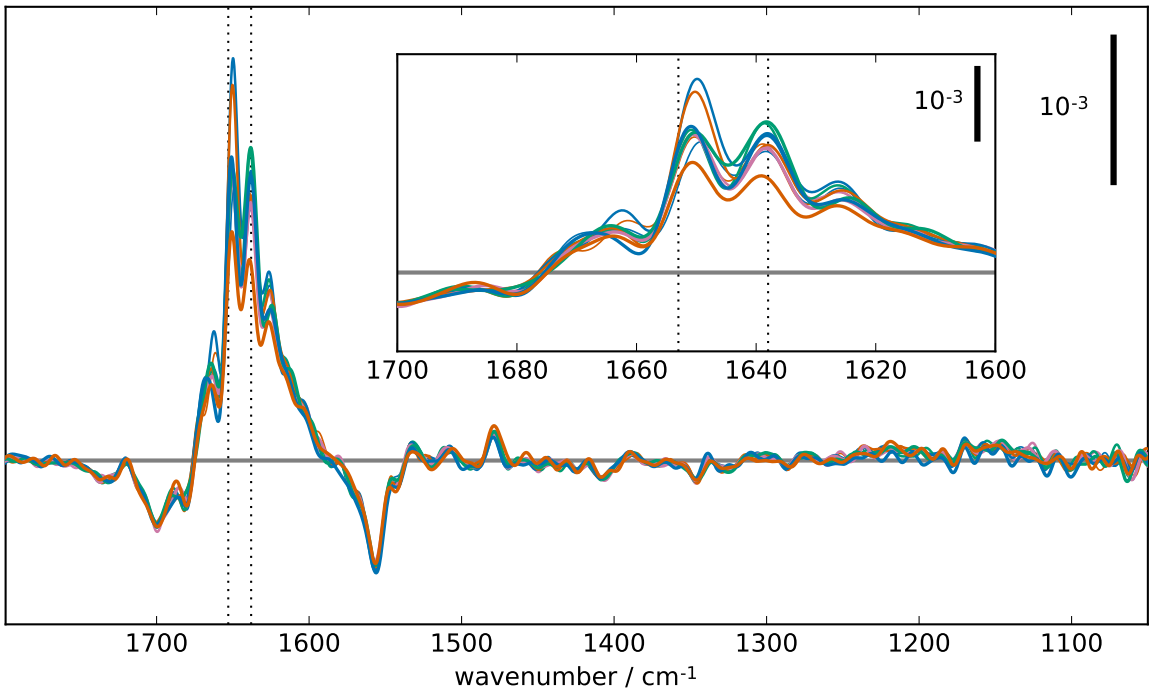

Figure 5.13.: Difference spectra for all ten flashes at 9 µs after laser flash excitation before heat correction. Orange: flashes 1, 5, 9, aquamarine: flashes 2, 6, 10, turquoise: flashes 3, 7, pink: flashes 4, 8. Thick lines: flashes 1-4, medium lines: flashes 5-8, thin lines: flashes 9, 10. The vertical lines mark signals at 1653 cm^{-1} and 1638 cm^{-1}.

is very broad and decays with the same time constants at every wavenumber while the PSII photochemistry features are rather narrow, pure PSII photochemistry timecourses should be obtainable by subtracting two uncorrected timecourses at different wavenumbers.

The timecourses at 1653 cm^{-1} and 1638 cm^{-1} have been subtracted flash by flash and are shown in figure 5.14. Comparing with figure 5.13, it can be seen that 9 µs after flash laser excitation a period-of-four oscillation is visible at 1638 cm^{-1}, while there is no such oscillation at 1653 cm^{-1}. Furthermore, a ~25 µs rise is visible for the 3rd and 7th flash in the double difference timecourses while there is no such phase visible for the other flashes. This rise then corresponds to a decay at 1638 cm^{-1}.

5.6.2. Temperature difference FTIR spectra

In order to investigate and compare the laser flash induced heat spectrum, various temperature difference spectra have been recorded. The investigated samples are 1. a CaF_2 sandwich with air in between the CaF_2 plates, 2. a CaF_2 sandwich with purified water in between the plates, 3. a CaF_2 sandwich with purified water, betaine and vacuum grease, and 4. a PSII sample collected after a measurement completed.

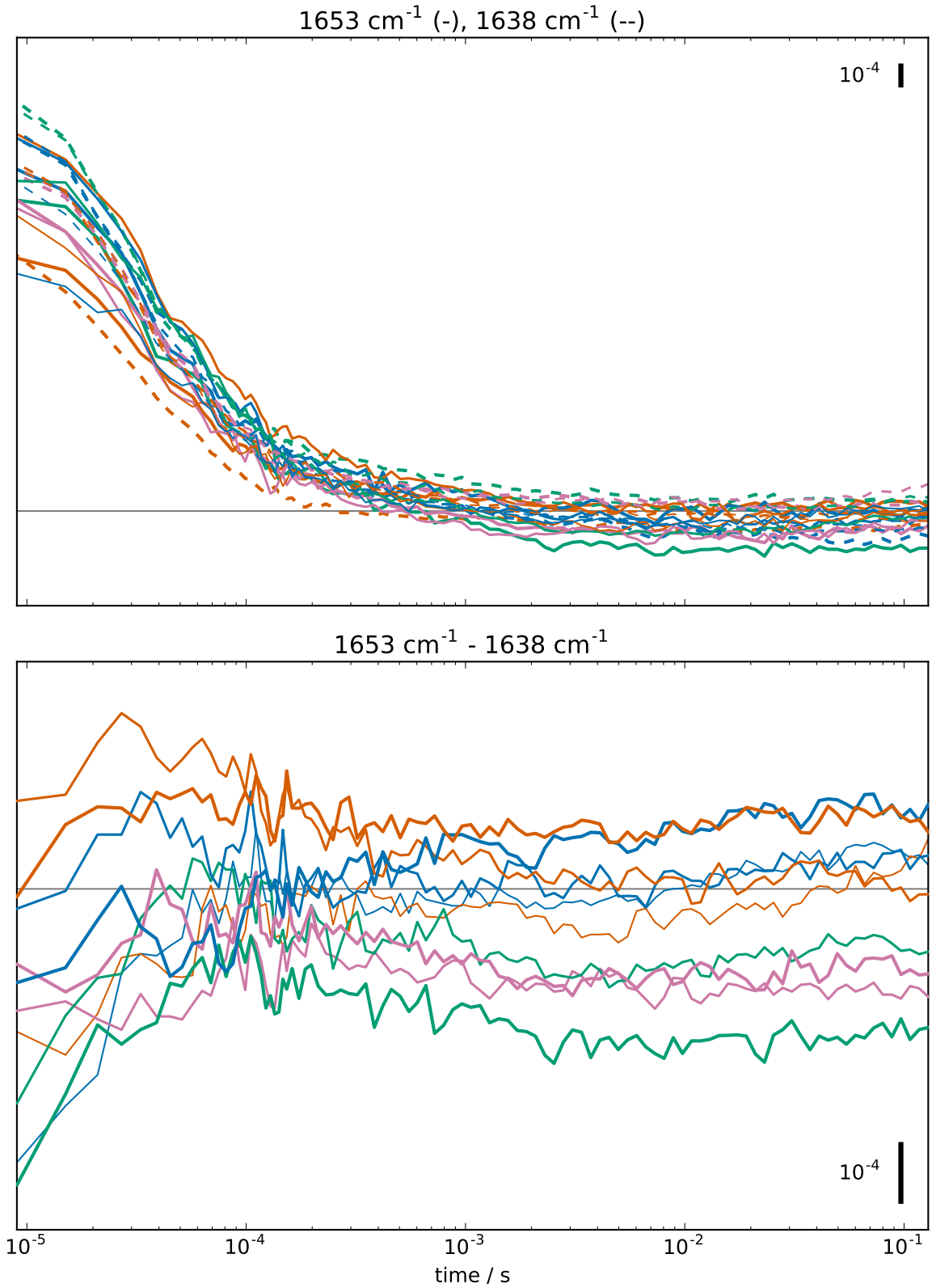

Figure 5.14.: Top: Uncorrected (regarding the heat signal) timecourses at 1653 cm^{-1} (solid lines) and 1638 cm^{-1} (dashed lines). Bottom: For each flash the corresponding double difference timecourse is shown. Orange: flashes 1, 5, 9, blue: flashes 2, 6, 10, green: flashes 3, 7, pink: flashes 4, 8. Thick lines: flashes 1-4, medium lines: flashes 5-8, thin lines: flashes 9, 10.

All the samples have been kept at 4 ℃ and measured at room temperature. When one sample was to be measured, its surfaces where shortly blown on with compressed air to remove any condensed water; then the sample was put into the sample creator and the measurement was started. For a couple of minutes, repeatedly 50 scans were measured and averaged (10 cm^{-1} resolution), until no further significant change could be observed (i.e. the sample reached room temperature). The results are shown in figures 5.15 and 5.16.

It was stipulated that the temperature difference spectrum of PSII corresponds to the derivative of the PSII's absolute IR absorption (Görlin 2012). However, this holds only if the temperature difference spectra are baseline-corrected by subtraction of a polynomial of third degree (Görlin 2012). The uncorrected spectra are shown in figures 5.15 and 5.16.

It is surprising that already two CaF_2-plates with and without water between them (figure 5.15) show very complex behaviour. Although the absolute spectra shown in figure 5.17 are virtually identical in the lower wavenumber region up to 1300 cm^{-1}, the temperature difference spectra show very different behaviours in this wavenumber region. Around 1460 cm^{-1}, in both absolute spectra a positive, broad feature can be found, which leads to a strong positive feature in the temperature difference spectrum of dry CaF_2, whereas it leads to a moderate negative feature in the CaF_2 sample with additional purified water. In the latter sample, a very sharp differential feature around 1580 cm^{-1} can be assigned to the vacuum grease, which has been used to seal the sample, due to its positive feature in the absolute spectrum at this wavenumber. In the case of the dry CaF_2 sample, the warming up is a nonlinear process. Especially between 1500 cm^{-1} and 1600 cm^{-1} one can find features which show an increasing amplitude at first and a decreasing amplitude later.

Betaine has been used to increase the PSII's stability during preparation and measurements (Schiller and Dau 2000). The temperature difference spectra (figure 5.16, top) shows that betaine leads to strong, sharp bands, which would be very difficult to compensate for. These bands are directly attributable to the respective bands in the absolute spectrum. A temperature difference spectrum of a typical PSII sample after a measurement run (figure 5.16, bottom) does not show these bands, since for the step-scan measurements, the betaine has been removed from the sample by centrifugating once in betaine-free buffer.

There are two major differences in this measurement compared to the step-scan experiment. First, the spectra here have been recorded with the whole CaF_2 sandwich warming up, with the heat from the room's air penetrating through the CaF_2 plates to the sample. In the step-scan measurement, the heat is directly generated at the sample and the dissipation to the CaF_2 plates should be negligible. Second, the infrared beam shape during the measurement is different. While in this measurement the beam diameter is very wide, in the step-scan measurement the sample sits in the focus of the IR beam. This will lead to dynamic effects like thermal lensing which has an effect on the kinetics of the heat decay

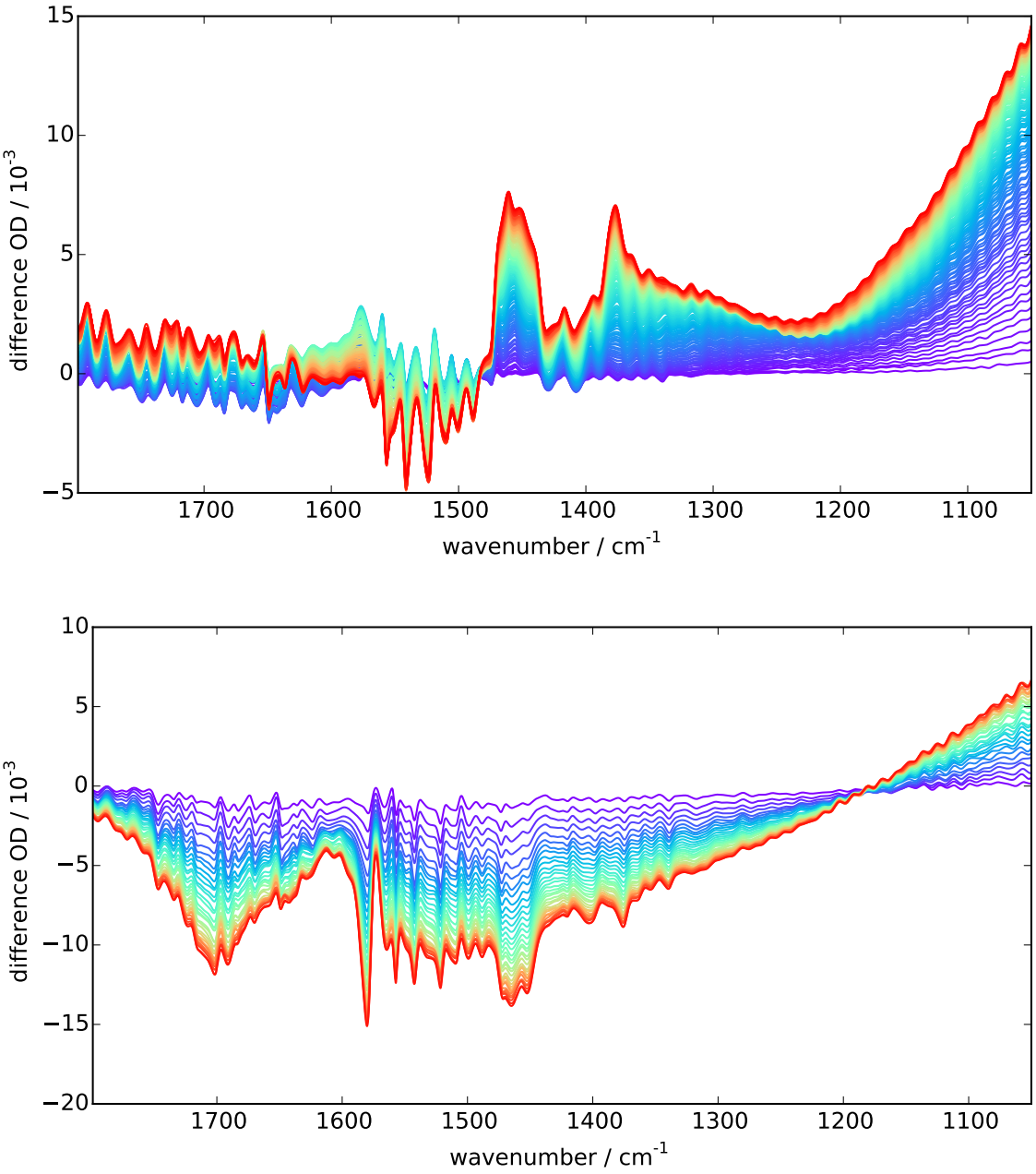

Figure 5.15.: Temperature difference spectra from cold to warm, 50 scans per spectrum, 10 cm^{-1} resolution. The temperature increases from about 4 °C (violet) to room temperature (red).

Top: Two CaF_2 plates sandwiched together with air in between them. **Bottom**: Two CaF_2 plates sandwiched together with purified water in between them.

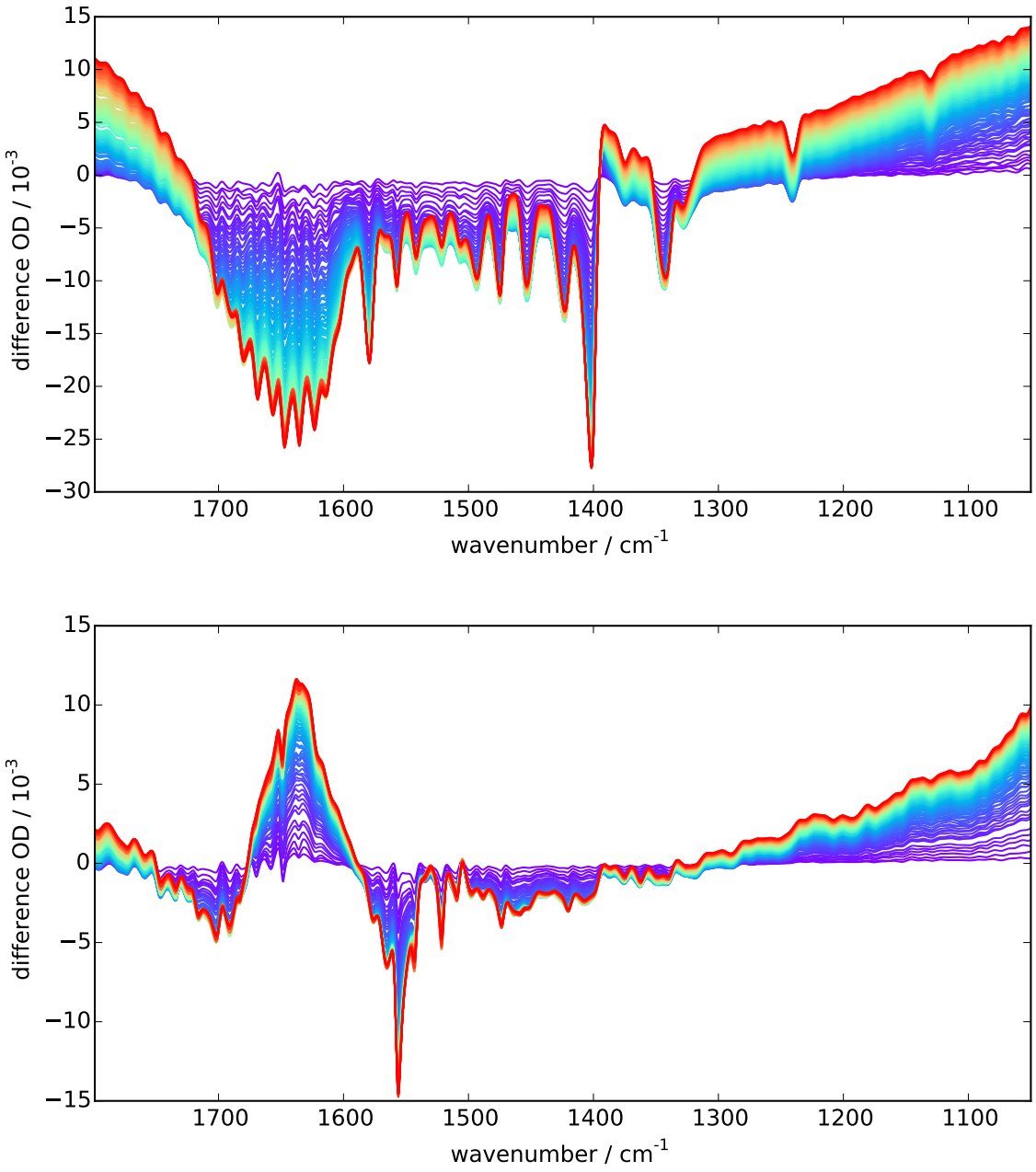

Figure 5.16.: Temperature difference spectra from cold to warm, 50 scans per spectrum, 10 cm^{-1} resolution. The temperature increases from about 4 °C (violet) to room temperature (red).

Top: Two CaF_2 plates sandwiched together with betaine dissolved in water in between them. **Bottom**: Two CaF_2 plates sandwiched together with PSII in between them.

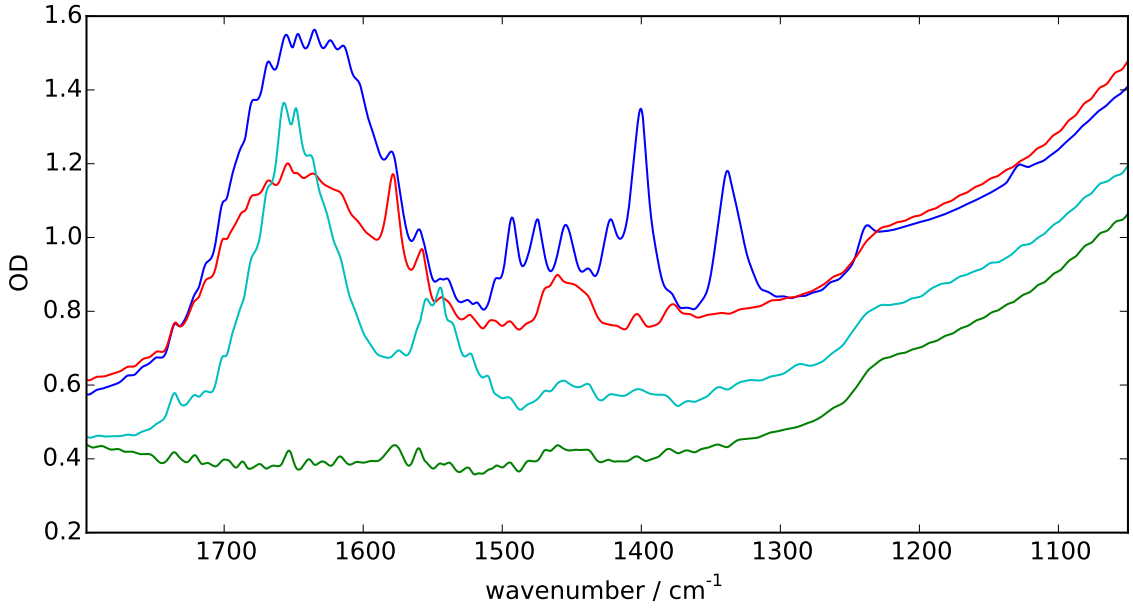

Figure 5.17.: Absolute IR spectra of CaF_2 (green), purified water and vacuum grease sandwiched between CaF_2 (red), purified water with a high concentration of betaine sandwiched between CaF_2 (blue), and PSII sandwiched between CaF_2 (cyan).

and may also influence the shape of the apparent spectrum.

In conclusion, a reliable correction of the laser induced heat signal can only be obtained by measuring the shape of the heat signal using the time-resolved step-scan mode of the setup. An alternative would be to measure the temperature change spectrum in the rapid-scan mode while exciting the sample with a cw laser of the same shape as the pulsed laser. The temperature difference spectra (figures 5.15 and 5.16) can be considered as references to compare the obtained time-resolved spectra with.

5.6.3. Step-scan measurements on PSII lacking natural or artificial electron acceptor

To measure the shape and decay of the laser induced heat signal of the step-scan spectra, several different high power step-scan measurement have been conducted.

High power step-scan experiment and results

The most straightforward way to measure the heat signal is to run a step-scan experiment with increased (factor 2.4) laser power. No electron acceptor was added to the sample, and the laser flash frequency was increased to 15 Hz. In this way, 30 flashes were applied to a

single sample position. The first 6 flashes were discarded from the averaging. The resulting spectrum is shown in figure 5.18.

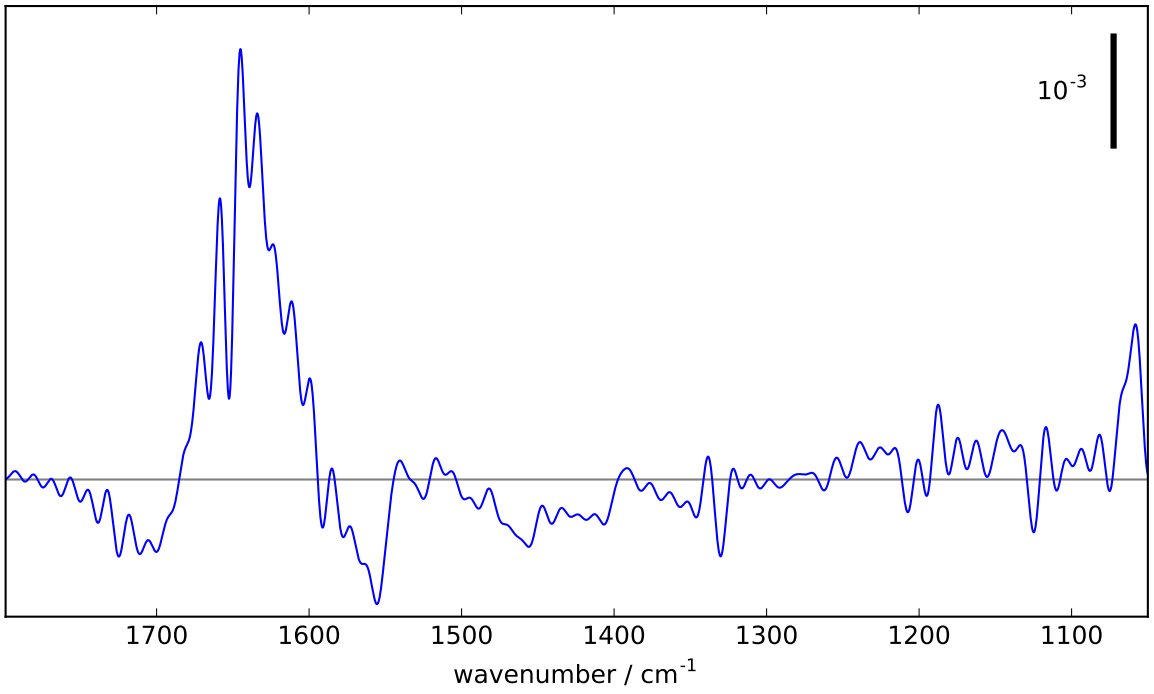

Figure 5.18.: Heat spectrum obtained from high power step-scan measurement.

The spectrum shows several sharp features. Although it has been recorded at a higher laser energy, the SNR is quite poor.

Single point high power step-scan experiment

In these high power step-scan measurements, the sample has been prepared as in the main step-scan measurement, but without electron acceptor. Furthermore, more than 30 pre-flashes have been applied to each sample plate before the start of the measurement so as to reduce all available quinones in the plastoquinone pool. In this way, the first flash of a train of flashes illuminating a sample spot should lead to Q_A^-/P_{680}^+ formation; any later flash should, as always, induce a heat signal, but no other signal. Consequently a complete interferogram has been recorded at one single sample spot. After the completion of one interferogram, the next sample spot was used.

Since there was no need to wait for the S-state transition to complete, the measurement could be sped up a lot by recording multiple flashes per mirror position. The highest laser repetition rate of 15 Hz has been used leading to three laser flashes per mirror position. In this way, each complete interferogram leads to three times more information compared to the main step-scan.

340 mirror positions have been measured instead of 334; the measurements at the very ends of the interferograms have been discarded and served solely as additional preflashes.

Because the sample was not to be changed after each mirror position and there was no waiting time necessary between laser flashes, a complete interferogram could be recorded in a matter of minutes instead of roughly two hours, which is the case for the main step-scan measurement.

These step-scans have been measured using a laser power 2.4 times higher than the main step-scan, leading to a significant increase in the SNR (note also the scale in figure 5.19).

Single point high power step-scan results

In figure 5.19, the resulting spectra (9 µs after laser flash excitation) are shown (blue and red). No rescaling has been applied. The spectra are very similiar, with the exception of distinct large, narrow features. These could correspond to the formation of triplet states, which are quenched by oxygen. A possible explanation for the drastic difference of the amplitudes of these features is that before resuspending the samples, the buffer has been shaken and thus saturated with oxygen before one of the measurements, while it has not been shaken before the other.

The triplet states are populated if the laser flash energy is large enough. Since these distinct features are not visible in the main step-scan dataset (due to the lower laser flash energy), they should be corrected for. Conveniently, the double difference spectrum (purple / brown curve in figure 5.19) can be scaled and subtracted from the average of the two original spectra (orange curve, figure 5.19) to obtain the compensated temperature spectrum (green curve, figure 5.19).

The purple curve (which is the difference of the individually measured spectra, blue and red curves) shows also three very broad features. From the position of these features and their comparison to the temperature difference spectra measured before it can be concluded that they correspond to different sample hydration and thickness in the two measurements. To obtain the pure oxygen triplet spectrum (brown curve) these broad features have been removed by high-pass filtering the double difference (purple curve).

In contrast to the manually recorded temperature difference spectra (see subsection 5.6.2), the decay does not depend on the wavenumber. In figure 5.20 (bottom), the same spectra from figure 5.20 (top) have been normalized to 1637 cm^{-1}. Since all the normalized spectra correspond very well to each other, the decay of the laser induced heat signal is wavenumber independent.

It is the corrected spectra measured 9 µs after laser flash excitation, shown in figure 5.19 (green curve), which will be used as compensating spectrum for the main step-scan data

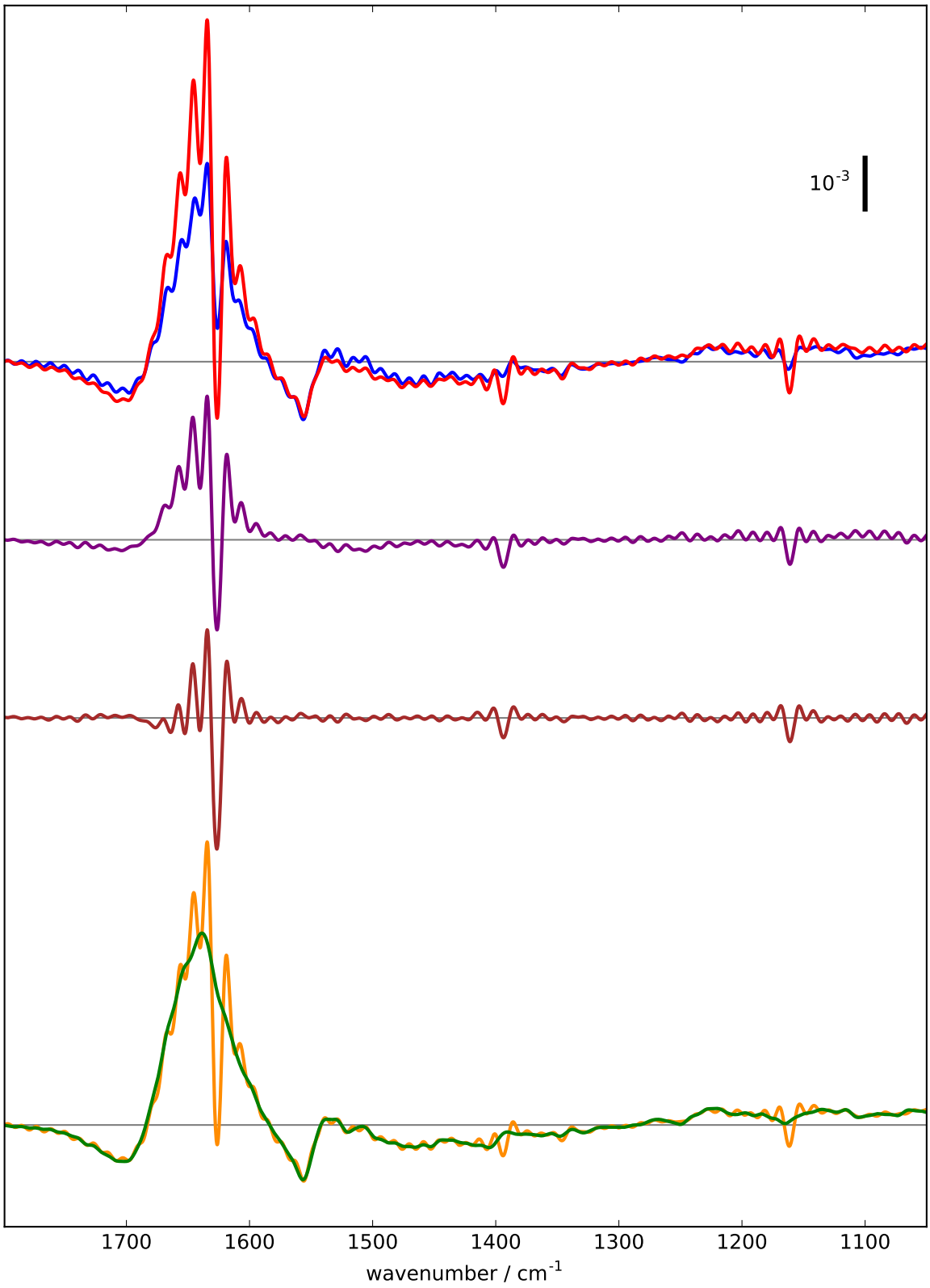

Figure 5.19.: Red and blue: two indepentent single-point step-scan measurements using high laser energy 9 µs after laser flash excitation. Purple: difference of the two measurements. Brown: The purple curve has been high-pass filtered to remove the Gaussian background. Orange: average of the blue and red curve. Green: the orange curve minus the brown curve has been filtered using a lowpass filter. Note the scale at the top right.

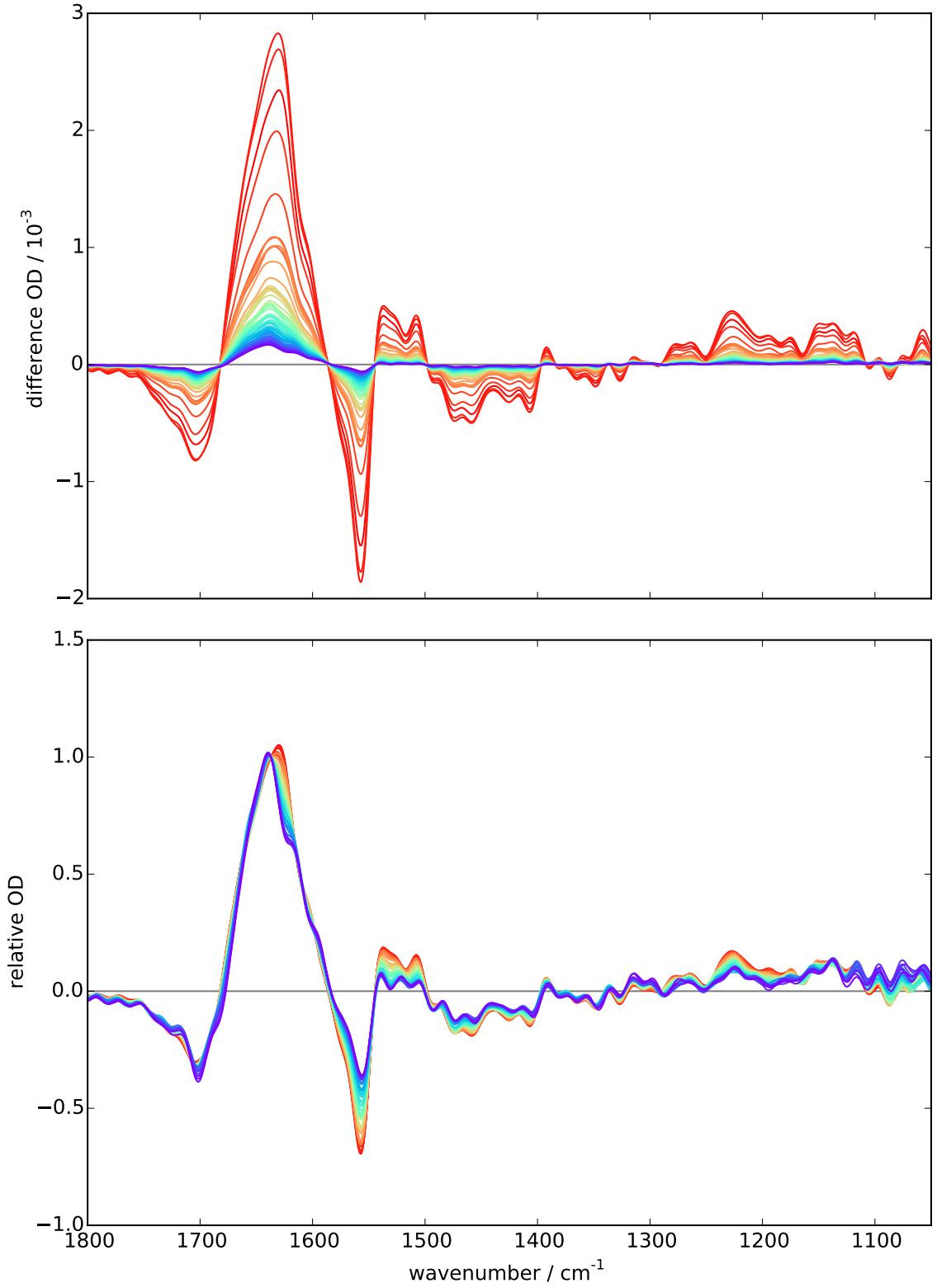

Figure 5.20.: Laser-induced temperature change signal decay, from 9 µs to 1.3 ms after the laser flash. **Top**: The signal as it decreases with the sample cooling down to room temperature after laser flash heat-up. **Bottom**: The spectra from the plot above have been rescaled to unity at 1637 cm^{-1}.

(see subsection 5.6.5).

5.6.4. Decay of the laser induced heat signal

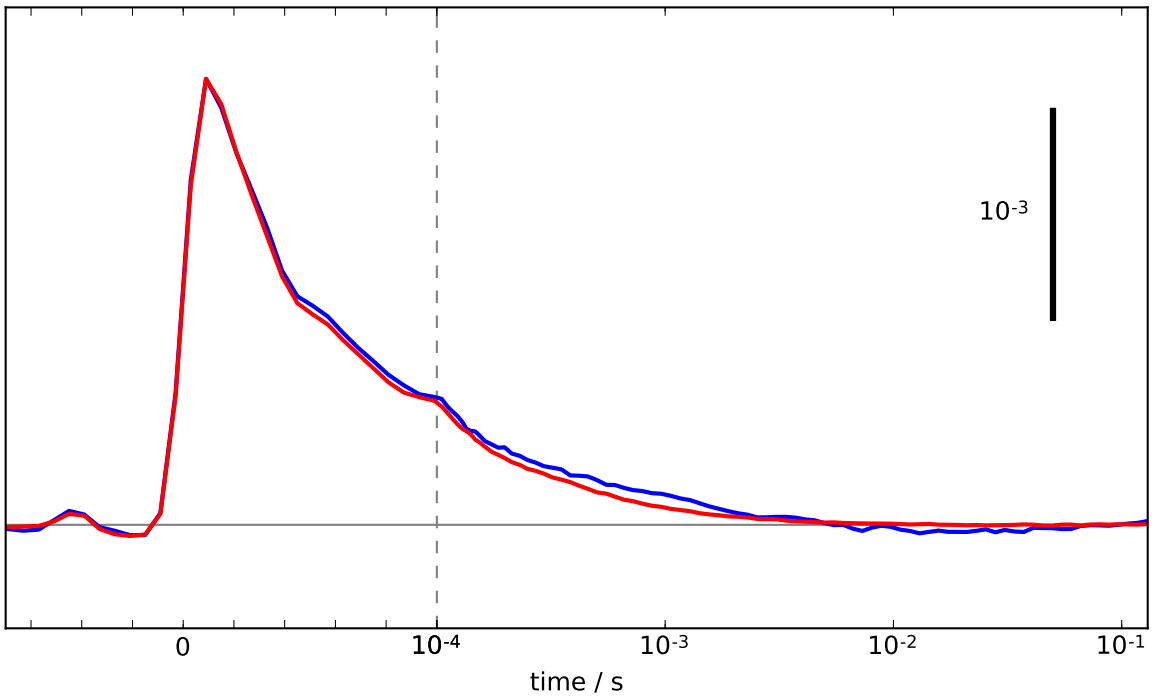

Figure 5.21.: Comparison of the timecourse used for the heat signal compensation (red) with the average of flashes two to ten of the uncorrected step-scan data at 1650 cm^{-1} (blue). Note the scale: The overall amplitude of the step-scan spectra is not expected to exceed $5 \cdot 10^{-4}$. The red curve has been obtained from the interferogram time courses: it is the same curve as shown in figure 5.11 (bottom), scaled to the amplitude of the step-scan spectral timecourse. The data is plotted versus a semi-logarithmic time scale.

As shown in figure 5.20 on page 104, the decay of the laser flash induced heat signal is wavenumber independent. The decay of the spectrum can be found using the decay of the interferogram domain time courses. Since the laser flash induced IR signal features a very large component which is independent of the interferogram mirror position and is lost during the Fourier-transform, we can average all interferogram time courses and obtain a high SNR heat signal decay curve as discussed in section 5.5 and shown in figure 5.21 (red curve).

For several reasons it is be preferable to directly use the main step-scan interferogram time course, since there is virtually no contribution from the S-state cycle (red curve in figure 5.21). A separate measurement would not guarantee that the sample is in the same

condition as in the main measurement; a different hydration and/or thickness would influence the time constants of the heat relaxation decay.

5.6.5. Compensation method A: compensating the laser induced heat signal using the heat spectrum and the interferogram timecourse

The obtained step-scan spectra $S(\nu, t)$ can now be compensated for the heat signal to obtain the corrected spectra $S'(\nu, t)$ via the equation

$$S'(\nu, t) = S(\nu, t) - a \cdot c(t) \cdot T(\nu)$$

where a is a scaling factor, $c(t)$ is the scaling time course (red curve in figure 5.21), and $T(\nu)$ is the temperature induced spectrum (green curve in figure 5.19).

To obtain a, $T(\nu)$ has been scaled to fit the average of flashes 2 to 10 of the main step-scan measurement (see figure 5.22) 9 µs after laser flash excitation. Through a linear least squares calculation it is found that $a = 0.36$, which corresponds to the ratio of the laser energies used for the main and the high power step-scans. Additionally, a polynomial background is subtracted from the spectrum. The factor a is only calculated once and then used for all the data; this also holds for $c(t)$ and $T(\nu)$. One advantage of this approach is that the same heat signal $a \cdot c(t) \cdot T(\nu)$ is subtracted from all flash-dependent time courses, so that the heat compensation will not introduce errors when comparing time courses from different flashes.

Since all factors of the equation above have been derived, the step-scan data can be compensated for the heat signal. In figure 5.22 the correction for selected times is shown.

5.6.6. Compensation method B: fitting the detector timecourse at each wavenumber

This section describes an alternative heat compensation approach which works without any knowledge of the heat spectrum and solely relies on the decay of the heat signal (see section 5.6.4). At any wavenumber, the heat signal should be the same for every flash applied to the sample. Additionally, each flash shows S-state dependent IR signals. The idea is now to fit all ten timecourses at one fixed wavenumber with a single scaling factor a_h which scales the heat signal's decay and M exponential decay terms. The central aspect of this approach is that one single scaling factor is used for the heat signal's decay, while the exponential terms feature flash-dependant amplitudes. Finally, a flash-dependent offset c_i is included. In total,

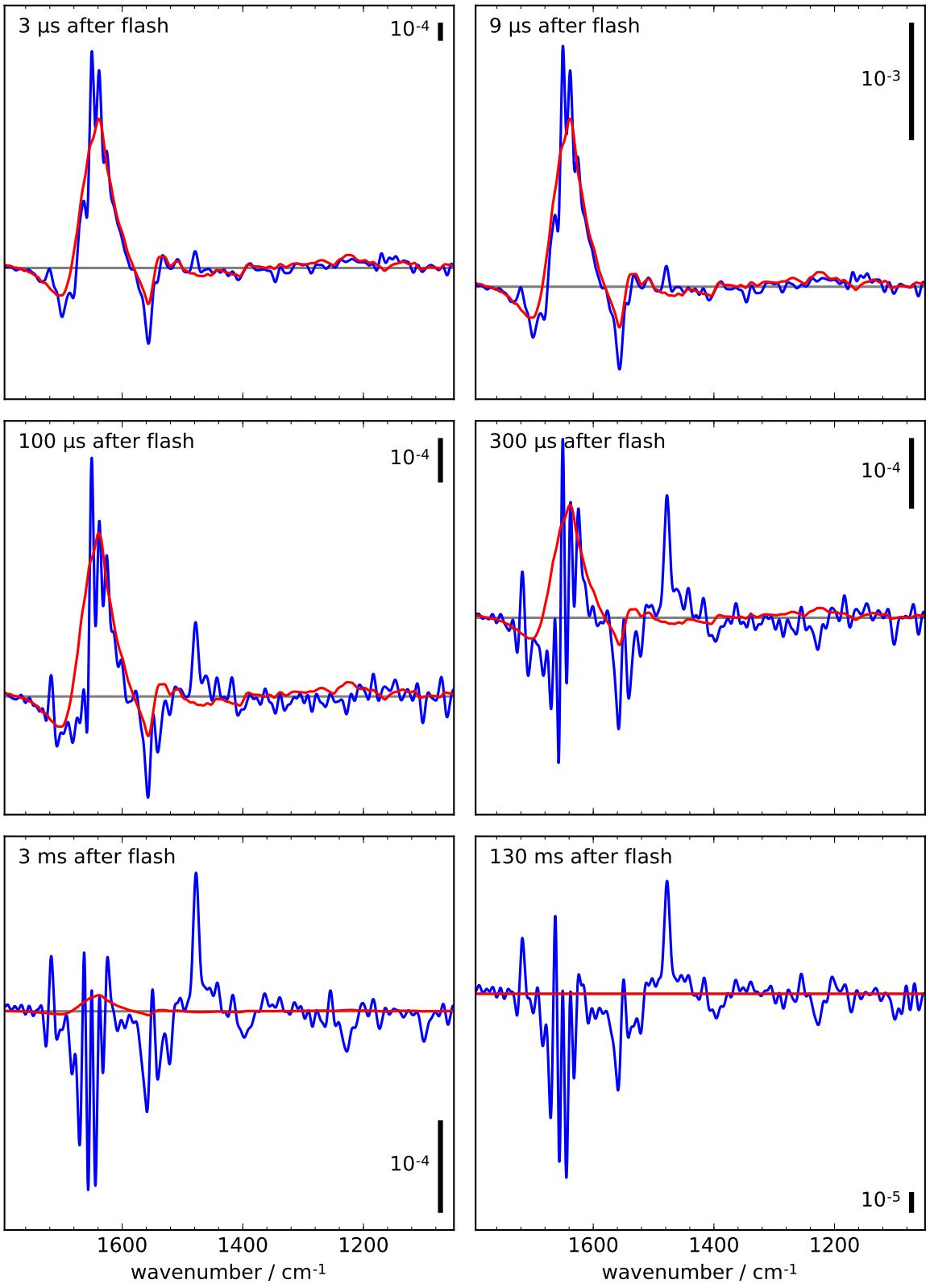

Figure 5.22.: Step-scan spectra after laser flash excitation. Blue: main step-scan measurement, average of flashes 2 to 10. Red: scaled single point high power step-scan.

the LLS formulation includes 1 (heat amplitude a_h) + 10 (offsets c_i) + $M \cdot 10$ (amplitudes $a_{\tau_i,j}$) = 11 + 10M parameters. Equation (5.3) shows the form of this LLS problem.

$$
\begin{array}{c}
\\
1 \\
\vdots \\
N \\
N+1 \\
\vdots \\
\vdots \\
10N
\end{array}
\begin{array}{c}
\begin{array}{ccccccccccc}
1 & 2 & 3 & 4 & \dots & 11 & 12 & 13 & 14 & \dots & 11+10M
\end{array} \\
\begin{pmatrix}
h_1 & 1 & 0 & 0 & \dots & 0 & 1.0 & 0 & 0 & \dots & 0 \\
\vdots & \vdots & \vdots & \vdots & \vdots & \vdots & \vdots & \vdots & \vdots & \vdots & \vdots \\
h_N & 1 & 0 & 0 & \dots & 0 & 0.0 & 0 & 0 & \dots & 0 \\
h_1 & 0 & 1 & 0 & \dots & 0 & 0 & 1.0 & 0 & \dots & 0 \\
\vdots & \vdots & \vdots & \vdots & \vdots & \vdots & \vdots & \vdots & \vdots & \vdots & \vdots \\
\vdots & \vdots & \vdots & \vdots & \vdots & \vdots & \vdots & \vdots & \vdots & \vdots & \vdots \\
h_N & 0 & 0 & 0 & \dots & 1 & 0 & 0 & 0 & \dots & 0.2
\end{pmatrix}
\end{array}
\begin{pmatrix}
a_h \\
c_1 \\
\vdots \\
c_{10} \\
a_{\tau_1,1} \\
\vdots \\
a_{\tau_1,10} \\
a_{\tau_M,1} \\
\vdots \\
a_{\tau_M,10}
\end{pmatrix}
=
\begin{pmatrix}
y_{1,1} \\
\vdots \\
y_{1,N} \\
\vdots \\
y_{10,1} \\
\vdots \\
y_{10,N}
\end{pmatrix}
\tag{5.3}
$$

In the first column, the heat timecourse with data points h_1 to h_N is repeated ten times. The data vector y contains the data of the ten timecourses with N data points each. In the multiplication with the parameter vector, for each flash the same parameter a_h will be multiplied with the heat decay. The columns 2 to 11 correspond to the offset parameters c_1 to c_{10}, thus each column contains N entries with the value 1 (see also section 4.15.1 on page 51 to see how the offset is included in the matrix). The following columns represent exponential decays of the form e^{-t/τ_i} with the corresponding amplitudes $a_{\tau_i,j}$ in the parameter vector (where j denotes the j-th flash). The matrix can be constructed in python as per the following code.

```
matrix = np.zeros([10*N, 11+10*M])
for flash in range(10):
    matrix[flash*N:(flash+1)*N, 0] = heat
    matrix[flash*N:(flash+1)*N, flash+1] = 1.0
    for index, tau in enumerate(taus):
        matrix[flash*N:(flash+1)*N,\
               11+flash*(M)+index] = np.exp(-times/tau)
```

For the correction I chose the time constants *tau* as 300 µs, 2.2 ms, and 30 ms. The fit was restricted to data between 15 µs and 70 ms.

In this section it was assumed that the time constants $\tau_{m,j}$ are fixed. However, it is possible to implement the routine described above in a function which outputs the residual

of the data minus the LLS fit for a certain set of time constants. This function can then be minimized using a nonlinear LLS solver to also fit the time constants.

5.6.7. Comparison of different heat compensation methods

In figure 5.23 the different attempts at correcting the heat induced signal are shown. The average of the main step-scan measurement is shown in blue, while the different approaches are shown in red (multi-spot high power measurement), green (single-spot high power measurement), and magenta (fitting the detector timecourse at each wavenumber) respectively.

First of all it is obvious that the multi-spot high power measurement does not solely represent the heat induced signal; the SNR is very low. The single-spot high power measurement matches the blue curve more closely, but there are still deviations. Moreover, in the derivation it was assumed that the spectrum does not contain very sharp features. Finally, there seems to be an offset problem at the lower wavenumbers. Nevertheless, this approach might be useful to compensate the heat signal in the amide I region.

The results presented in sections 5.8.6 ("Elastic fit, lifetime maps, and time constants") and 5.8.6 to 5.8.6 have been obtained using the last approach, that is by fitting the detector timecourse at each wavenumber. This approach is prone to delete signals which are identical in every S-state transition, but do not belong to the heat signal. This can be seen for example at 1717 cm^{-1} in figure 5.23 (magenta curve), where an acceptor side signal may have been overcompensated. On the other hand, the strong Q_A^- signal at 1478 cm^{-1} has not been removed by the procedure. Nevertheless, this method is almost sure to delete any heat correlated signal. It is the method of choice to investigate timecourses which show period-of-four oscillations, since the subtracted signal is the same for every flash. If the timecourses at a fixed wavenumber show a period-of-four oscillation it will not be influenced by this procedure.

5.7. Time axis zero

Judging from the experimental setup, one would expect to see the flash induced signals at the $t = 0$ point, or at least near to it. Unfortunately this is not the case. The time axis is consistently shifted by an arbitrary value, and as such the time point $t = 0$ has to be chosen manually.

In figure 5.24 the heat-corrected timecourse (using the heat spectrum and the interferogram timecourse) at 1472 cm^{-1} is shown in blue. It shows a sigmoidal shape which stems from the filters applied during the measurement (see section 4.11). For comparison, the step-response of a Butterworth filter is shown in red. The step function used for the calcu-

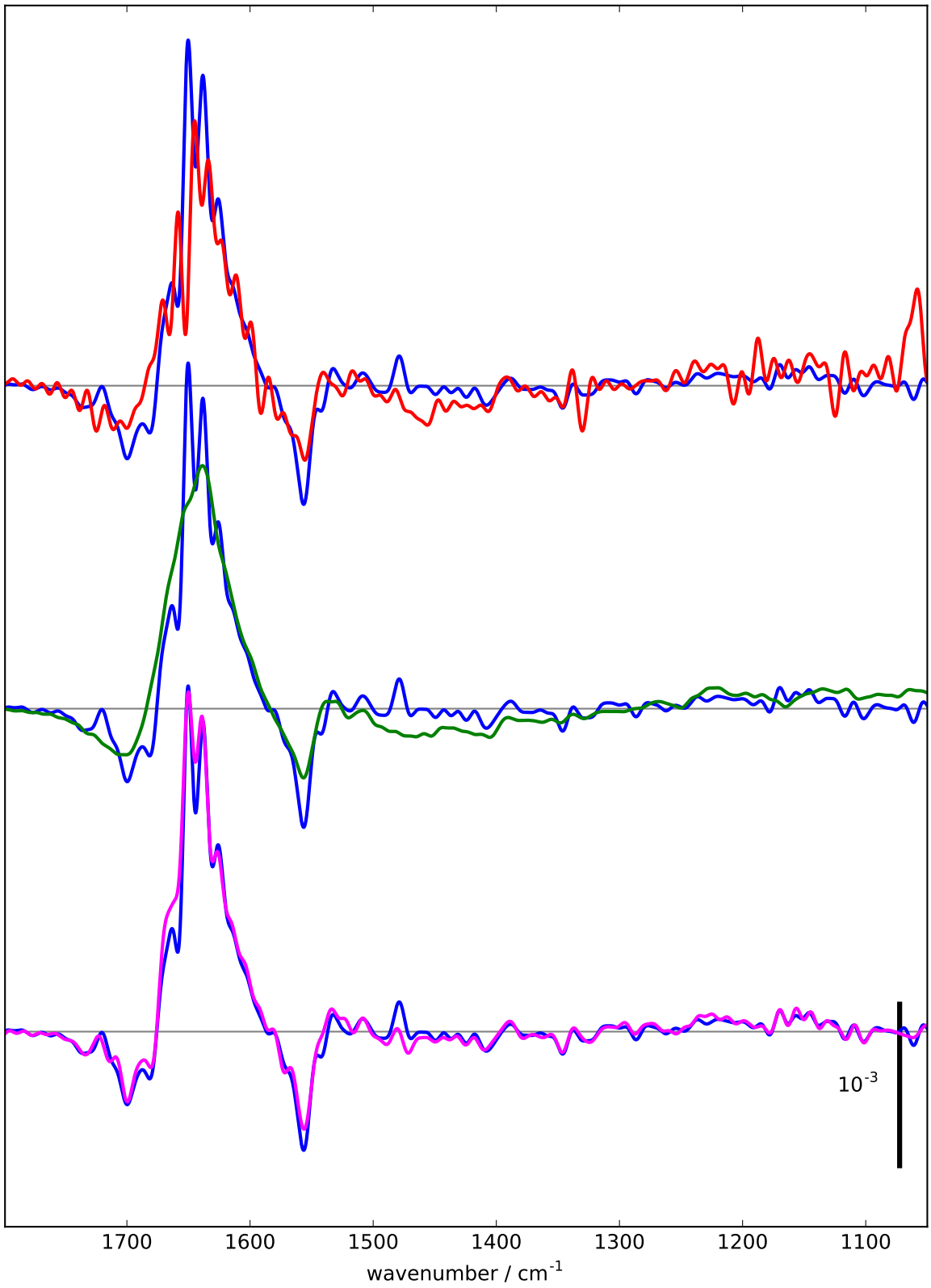

Figure 5.23.: Comparison of heat spectra obtained using different methods. Blue: average step-scan data 9 µs after laser flash excitation. Red: heat spectrum obtained through the multi-spot high power measurement. Green: heat spectrum obtained through the single-spot high power measurement. Magenta: heat spectrum obtained using the fitting approach. No offset correction has been applied.

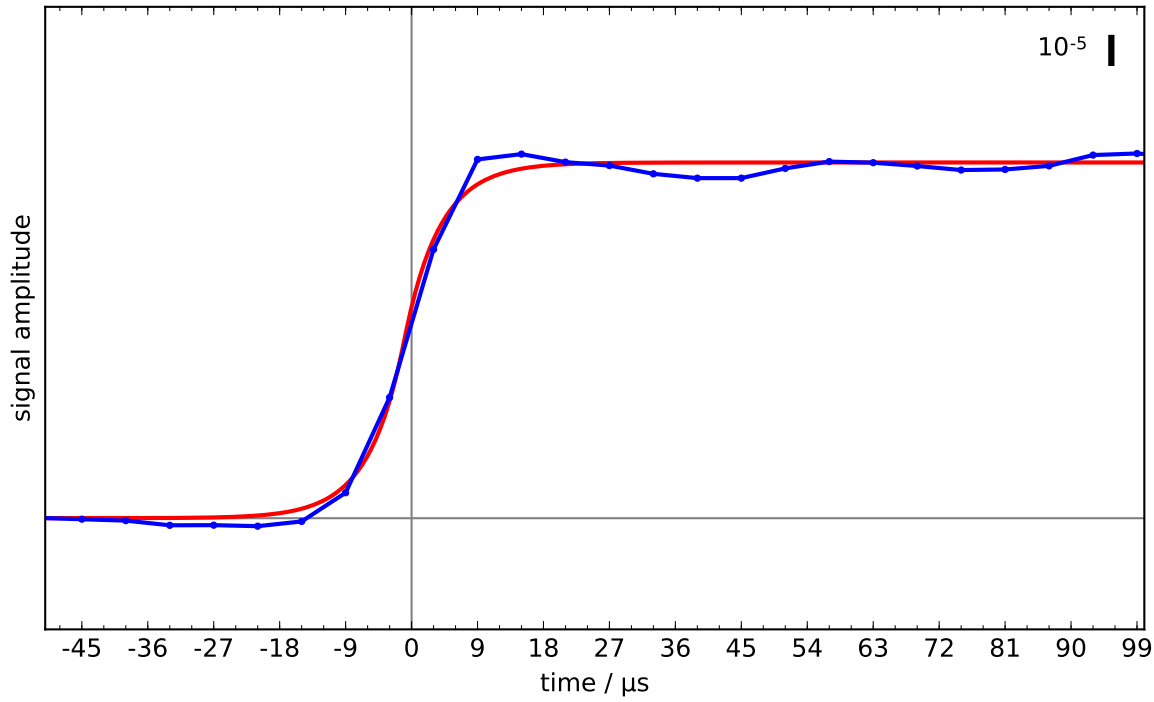

Figure 5.24.: Blue: FTIR step-scan timecourse at 1472 cm^{-1} on a linear scale after heat signal correction. One data point has been sampled every 6 µs. Red: Step-response of a Butterworth filter of first order with a cutoff frequency chosen so as to have the step-response match the data. The step function used for the step-response equals zero for negative and unity for positive times.

lation of the step-response equals zero for negative and unity for positive times. It can be seen that the filter has the effect of the signal smearing out into both positive and negative times. I chose to define $t = 0$ as in the step-function. This means that there is no data point at $t = 0$; there are data points at $t = -3\,\mu s$ and $t = +3\,\mu s$. Furthermore, in the evaluation of the timecourses the first data point used will be the one at $t = 9\,\mu s$.

The physical meaning of the time axis is that at $t = 0$ the nanosecond laser flash hits the sample. Due to the application of the digital filters, the step signal gets smeared out into negative times. Although originally no signal should be seen before the laser hits the sample, due to the filters used this changes.

In figure 5.24 some oscillations can be seen. These oscillations stem from the fact that the Vertex 70 uses a Chebychev-type filter (exact specifications unknown) as low-pass filter; this type of filter is known to introduce ringing when the signal changes abruptly (see section 4.11).

5.8. Step-scan results

In the following I present the heat-compensated step-scan data (for the details of the heat compensation, see section 5.6.6 on page 106). First, the step-scan data is compared to the rapid-scan data in section 5.8.1. Afterwards, I show that both D_2O and H_2O datasets feature a miss factor of 9% in section 5.8.3 on page 112. The miss factor calculations are used to deconvolute the data, which is then shown in the following sections in the form of time-resolved difference spectra and timecourses. The deconvoluted data is carefully analyzed for period-of-four oscillations using a global fit approach and the results are summarized in section 5.8.6 on page 134; the fit approach itself, the elastic net fit, was introduced in section 4.15.4 on page 55. The details of the elastic net fits are given in sections 5.8.6 to 5.8.6.

5.8.1. Comparison with rapid-scan data

In figures 5.25 and 5.26 the TRRS data is compared to the step-scan data. The two datasets agree quite well. Surprisingly the H_2O step-scan dataset shows a larger amplitude in the amide I bands while it shows the same amplitude as the rapid-scan dataset at lower wavenumbers. Note that there are practically no features visible below 1350 cm^{-1} in the first and third flash spectra. Two prominent negative features visible in the second and fourth flash can be found around 1100 cm^{-1} and 1230 cm^{-1}; these peaks therefore show period-of-two oscillations. Two large positive peaks at 1258 cm^{-1} and 1342 cm^{-1} are only visible in the second flash and therefore represent period-of-four oscillation patterns.

5.8.2. Comparison of step-scan data at 9 s and 10 ms after laser flash excitation

In figure 5.27 the step-scan data at 9 µs and 10 ms after laser flash excitation is shown for the first four flashes. In this case, the heat signal has been removed by subtracting the heat spectrum obtained through a separate high-power step-scan experiment.

5.8.3. Miss factor and deconvoluted timecourses

For both datasets (H_2O and D_2O) the miss factor has been determined as described in section 4.17 on page 65. In both cases a miss factor of 9% has been determined; the miss factor has been calculated taking into account six selected wavenumbers (see figures 5.28 and 5.29). Previously it was shown that a miss factor of 9% is expected for the buffers used (Karge, Bondar, and Dau 2014). The miss factor was not increased upon the exchange of

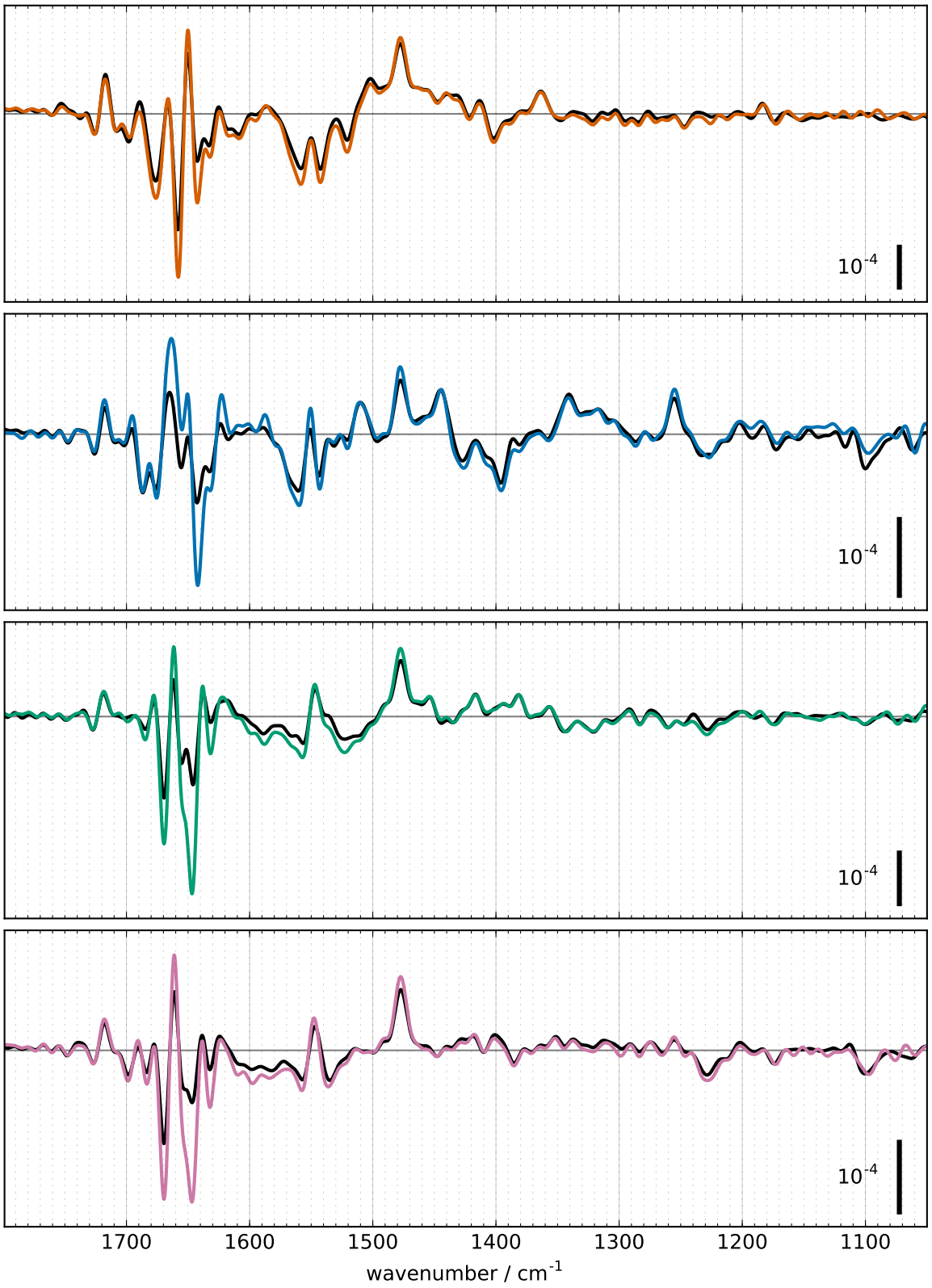

Figure 5.25.: Rapid-scan data (black) and step-scan data (colored) in H_2O 17 ms after laser flash excitation, flashes one to four from top to bottom. The step-scan data has not been corrected for heat signals.

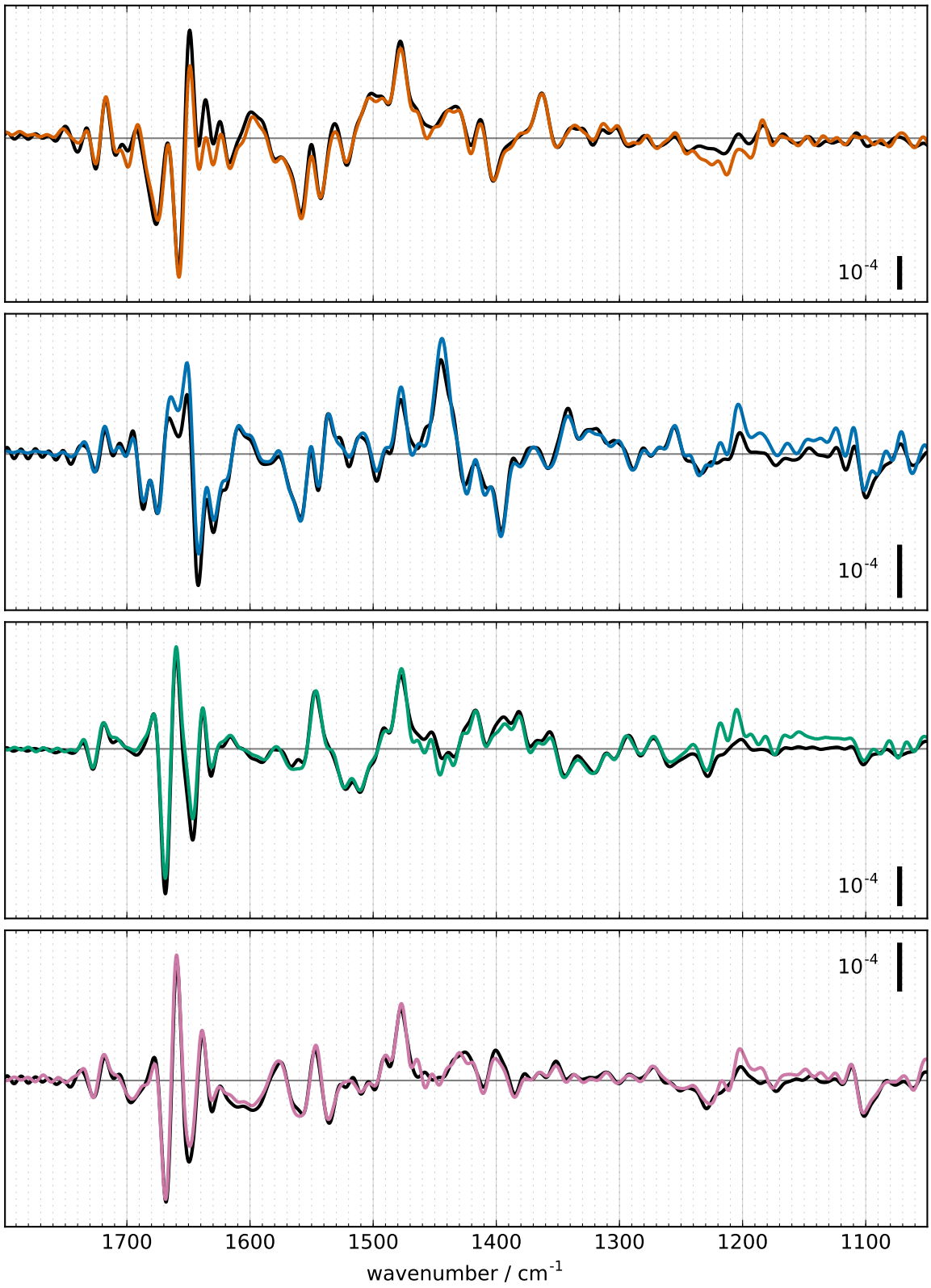

Figure 5.26.: Rapid-scan data (black) and step-scan data (colored) in D_2O 17 ms after laser flash excitation, flashes one to four from top to bottom. The step-scan data has not been corrected for heat signals.

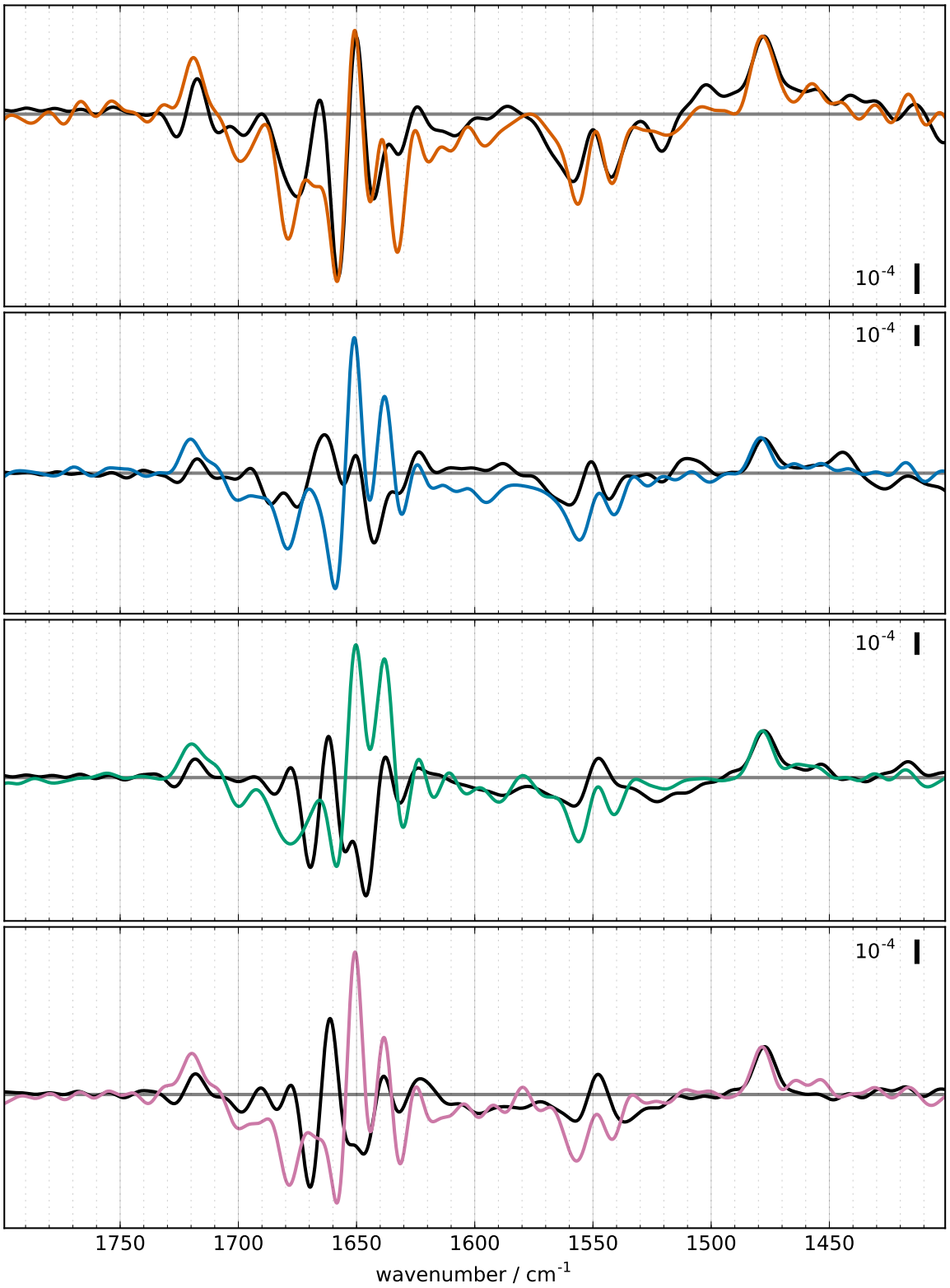

Figure 5.27.: Comparison of the step-scan spectra (orange, aquamarine, turquoise and pink for flashes 1, 2, 3, and 4) 9 µs after laser flash excitation, where the amplitude is maximal, versus the spectra at 10 ms after laser flash excitation (black). The 10 ms spectra have been rescaled so that their amplitude at 1478 cm^{-1} matches the amplitude of the 9 µs spectra; accordingly, the amplitude scales (black bars) show the amplitude 9 µs after laser flash excitation.

H_2O for D_2O, although previous reports reported an increase of the miss factor in this case (Haumann, Bögershausen, et al. 1997; Gerencsér and Dau 2010).

The calculation of the miss factor automatically yields the deconvoluted timecourses. These deconvoluted timecourses—as obtained from the heat corrected data (see section 5.6.6)—will be used in the following sections. The effect of deconvolution is shown for selected timecourses in figures A.40-A.42 on pages 302-304.

5.8.4. Difference spectra

The deconvoluted step-scan data is shown in figures 5.30-5.36 as time-resolved difference spectra for both H_2O and D_2O. In D_2O, there are two major absorption peaks in the absolute spectrum; the strong absorption in these regions lowers the SNR. The regions affected are 1510 cm^{-1}-1390 cm^{-1} and 1240 cm^{-1}-1110 cm^{-1}.

5.8.5. Timecourses

In this section timecourses at selected wavenumbers are shown. The figures show the timecourses of the four S-state transitions in orange, aquamarine, turquoise, and pink. Elastic net fits are given in red, blue, green, and magenta. The amplitudes and time constants found by the elastic net fit are represented by triangles. The subtracted artefact is given in gray.

Figure 5.37 shows timecourses at 1400, 1511, 1443, and 1544 cm^{-1}. They are compared to the corresponding changes in the ammonia investigation (figure 5.4 on page 81) and discussed in section 6.4.

In figure 5.38 on page 127 timecourses are shown which will be discussed in section 6.6 on page 207. Chu, Hillier, and Debus (2004) assigned vibrational modes of D1-Ala344 to ~1356 cm^{-1} in the S_1 state and a peak at either ~1339 cm^{-1} or ~1320 cm^{-1} in the S_2 state (see section 3.3 on page 15). In figure 5.38 the timecourses in H_2O at 1364 cm^{-1}, 1356 cm^{-1}, 1343 cm^{-1} and 1320 cm^{-1} are shown.

Section 6.2.5 on page 189 discusses timecourses which show the decay of instantaneously created amplitudes. The timecourses are shown in figure 5.39 on page 128.

The use of PPBQ as electron acceptor gives rise to several characteristic bands, which are shown in figure 6.8 on page 209 and discussed in section 6.8 on page 208. Characteristic iron band timecourses are shown in figure 5.40 on page 129, while Q_A^- band timecourses are shown in figure 5.41 on page 130.

Figure 5.42 on page 131 shows timecourses which show significant changes with a time constant of about 20 µs at every transition. These changes are discussed in section 6.5 on page 202.

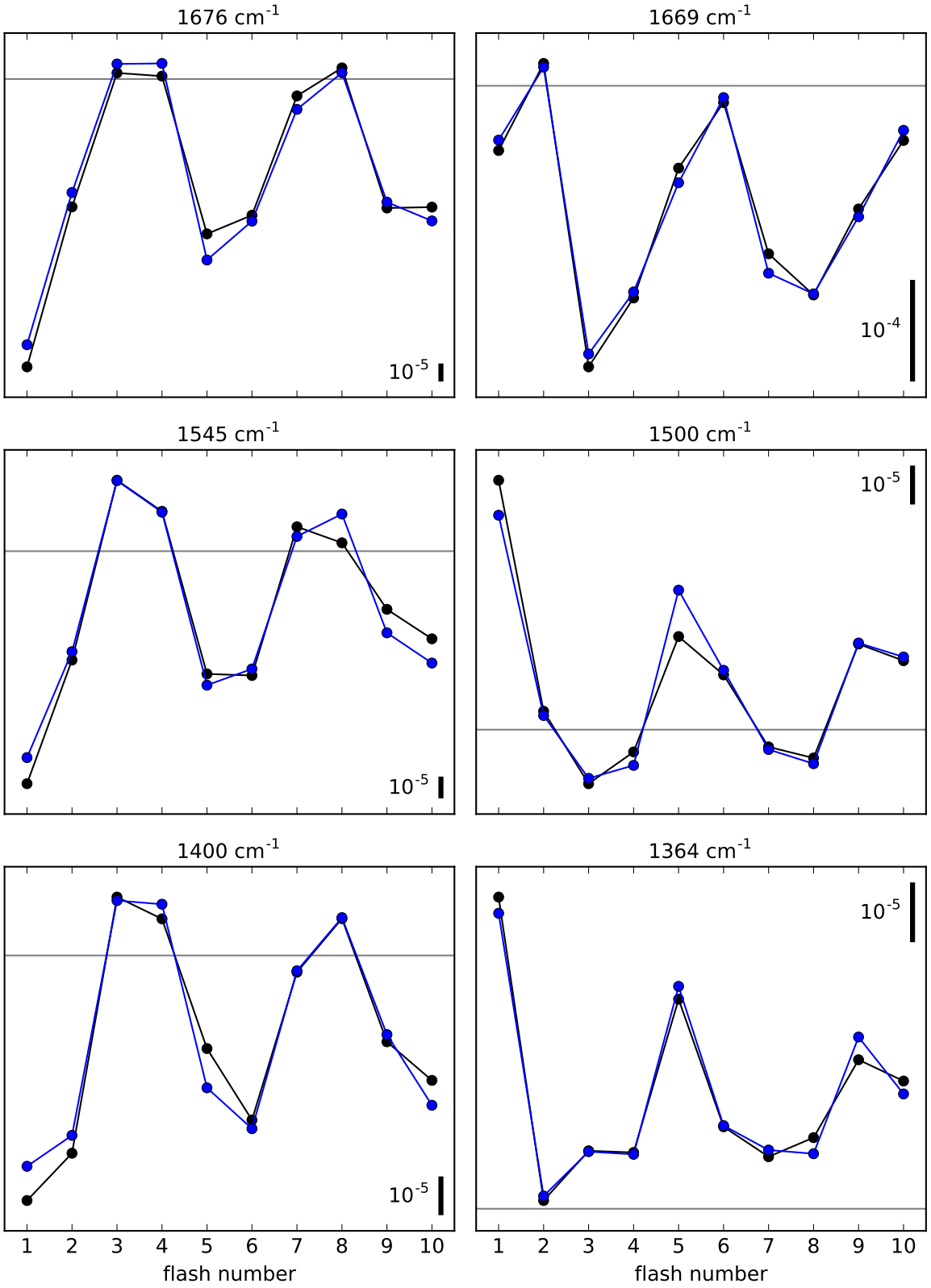

Figure 5.28.: A miss factor of 9% has been determined for the H_2O step-scan data using a joint fit for six wavenumbers. The data considered is the data recorded 5 ms after a laser flash has excited the sample. Black: measured data, blue: joint fit. See also section 4.17 on page 65.

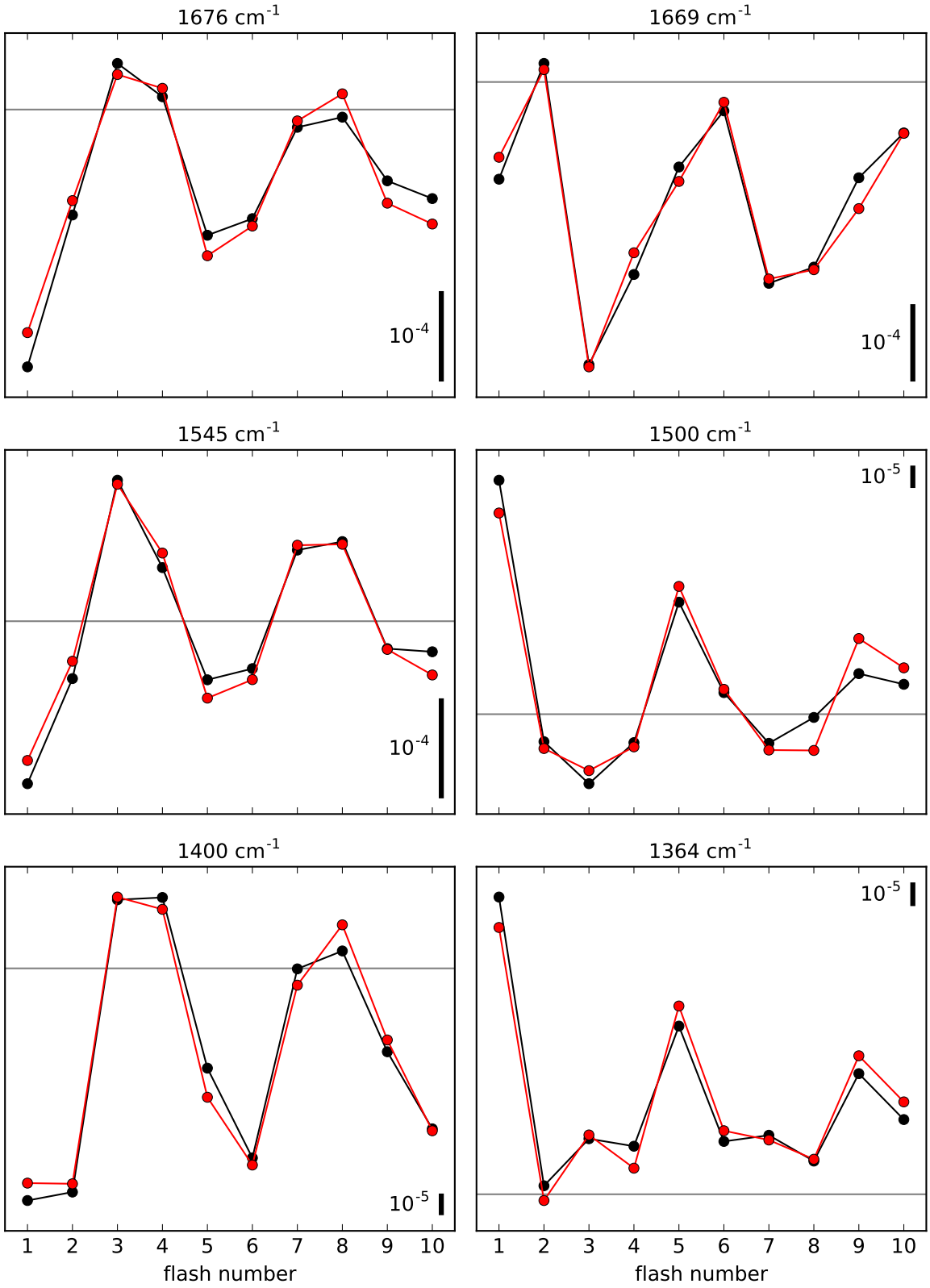

Figure 5.29.: A miss factor of 9% has been determined for the D_2O step-scan data using a joint fit for six wavenumbers. The data considered is the data recorded 5 ms after a laser flash has excited the sample. Black: measured data, red: joint fit. See also section 4.17 on page 65.

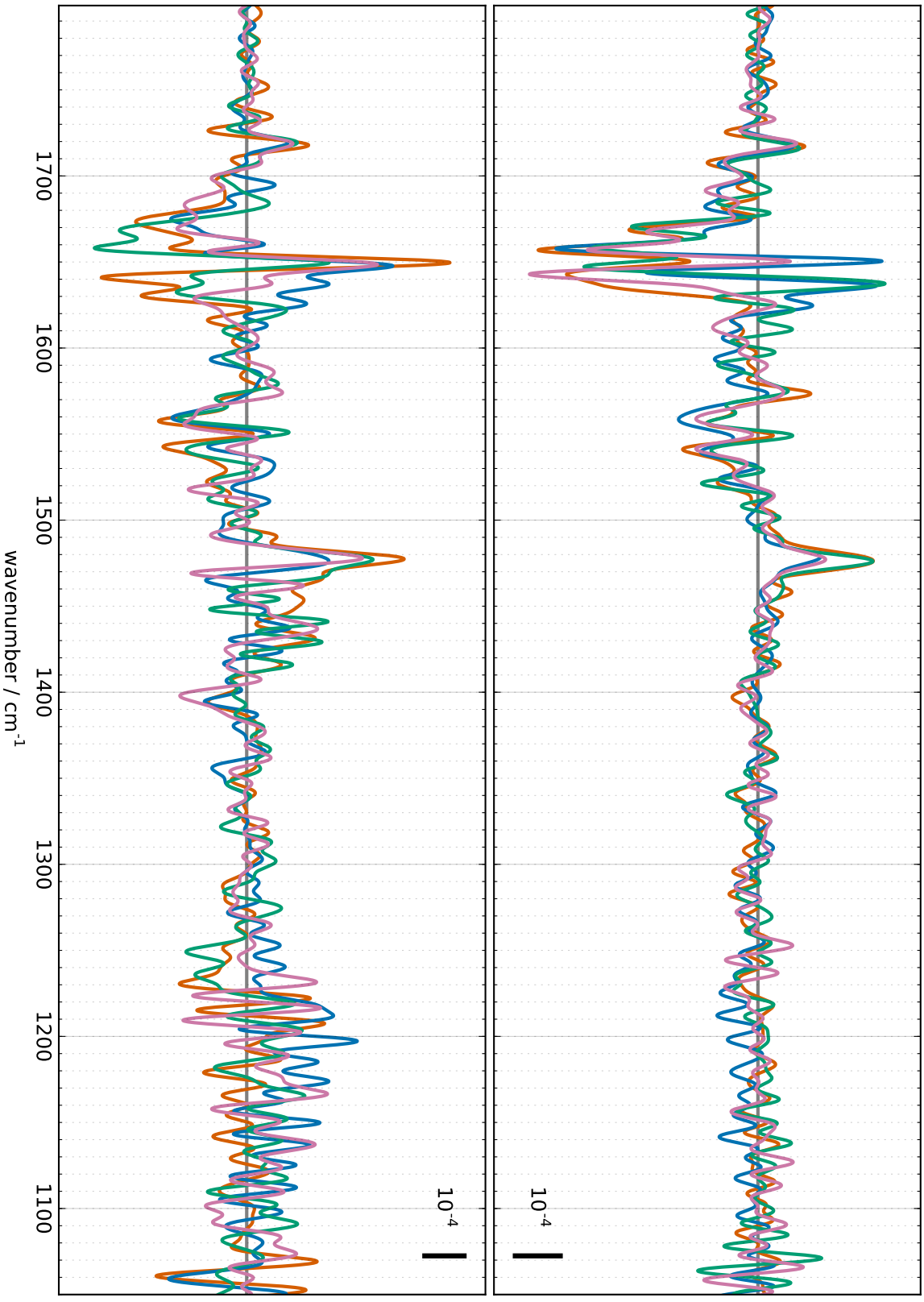

Figure 5.30.: Deconvoluted difference spectra 9 µs after laser flash application. **Left/bottom**: D_2O, **right/top**: H_2O. Orange: $S_1 \longrightarrow S_2$, aquamarine: $S_2 \longrightarrow S_3$, turquoise: $S_3 \longrightarrow S_0$, pink: $S_0 \longrightarrow S_1$.

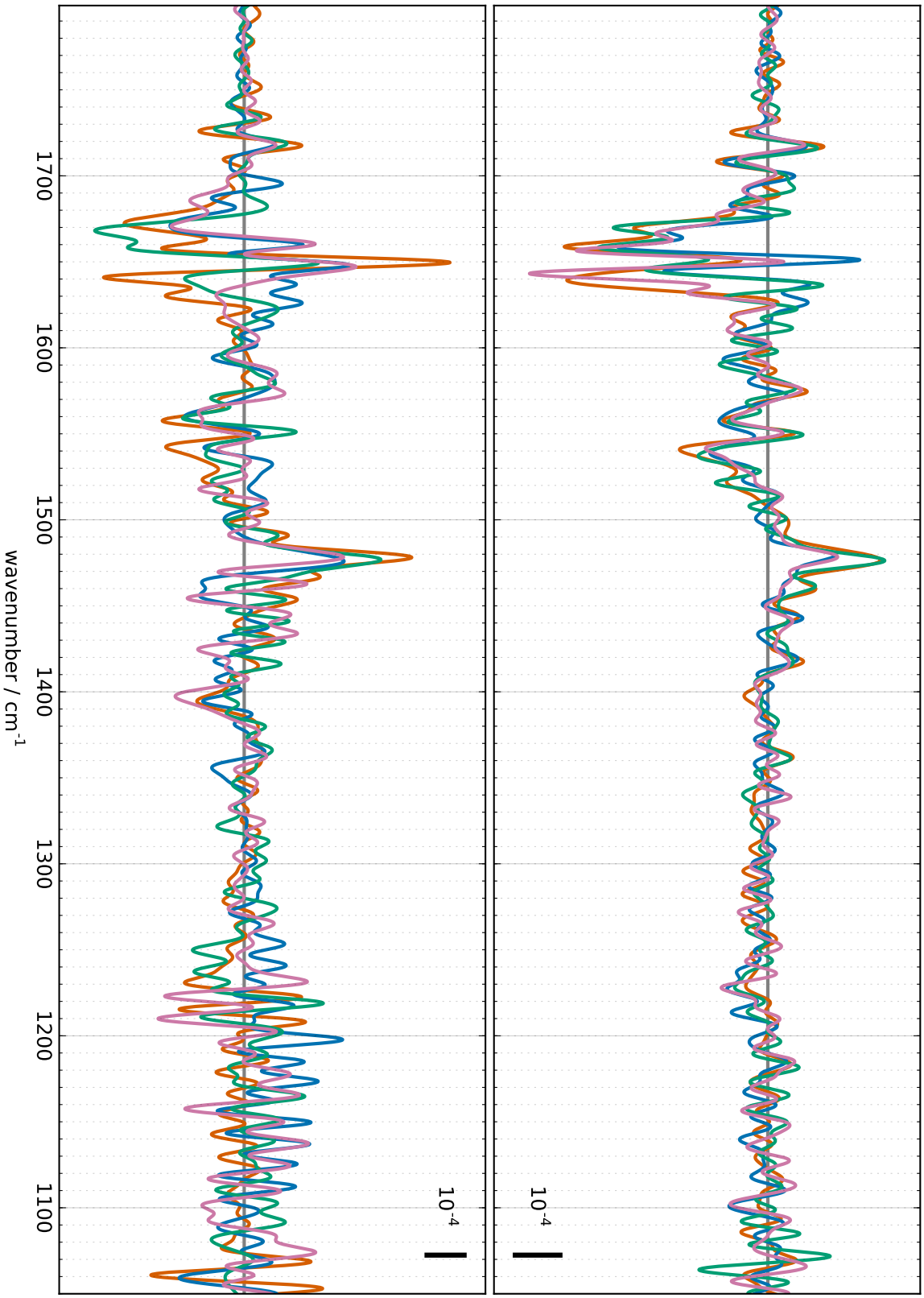

Figure 5.31.: Deconvoluted difference spectra 30 µs after laser flash application. Left/bottom: D_2O, right/top: H_2O. Orange: $S_1 \longrightarrow S_2$, aquamarine: $S_2 \longrightarrow S_3$, turquoise: $S_3 \longrightarrow S_0$, pink: $S_0 \longrightarrow S_1$.

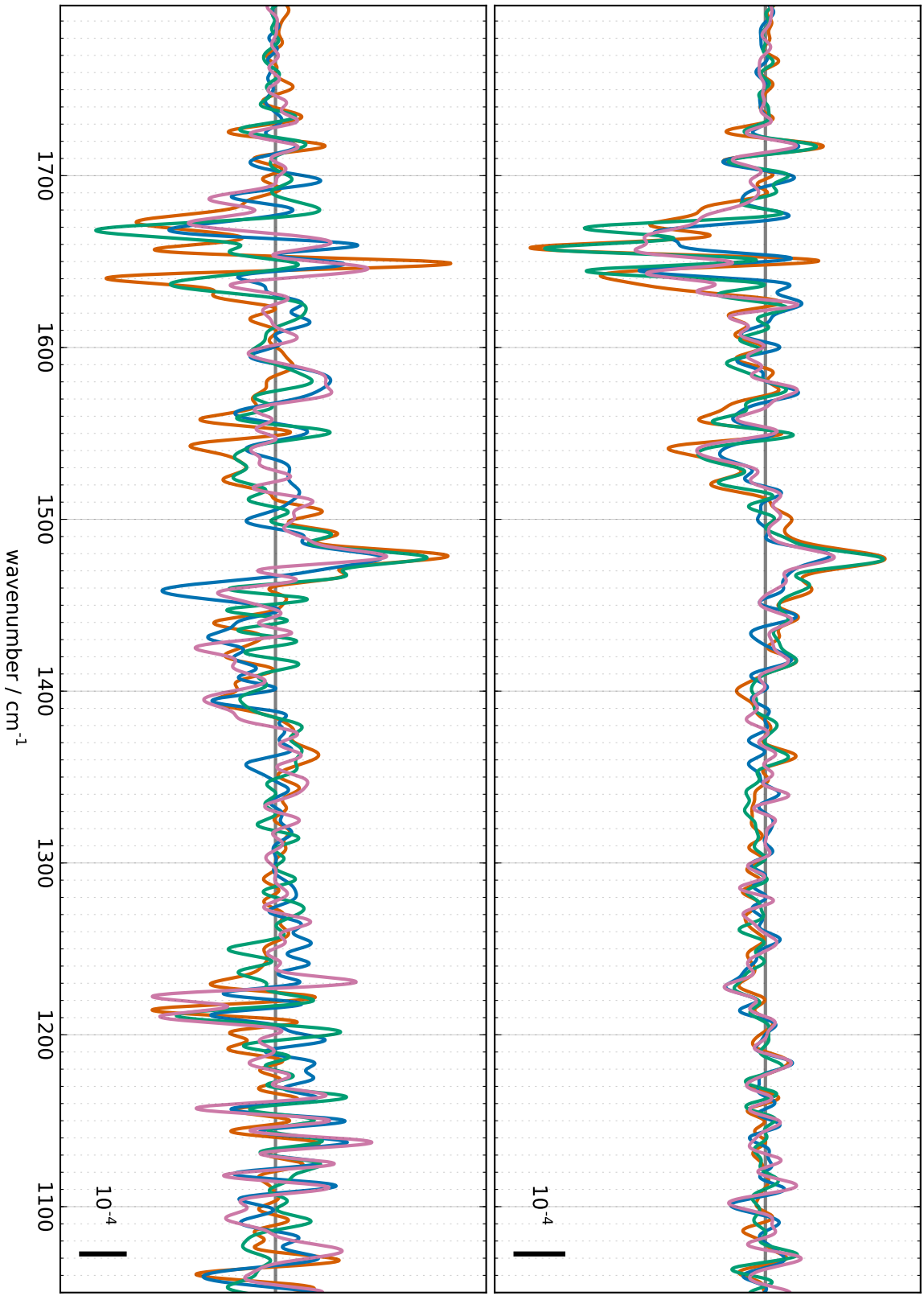

Figure 5.32.: Deconvoluted difference spectra 100 µs after laser flash application. Left/bottom: D_2O, right/top: H_2O. Orange: $S_1 \longrightarrow S_2$, aquamarine: $S_2 \longrightarrow S_3$, turquoise: $S_3 \longrightarrow S_0$, pink: $S_0 \longrightarrow S_1$.

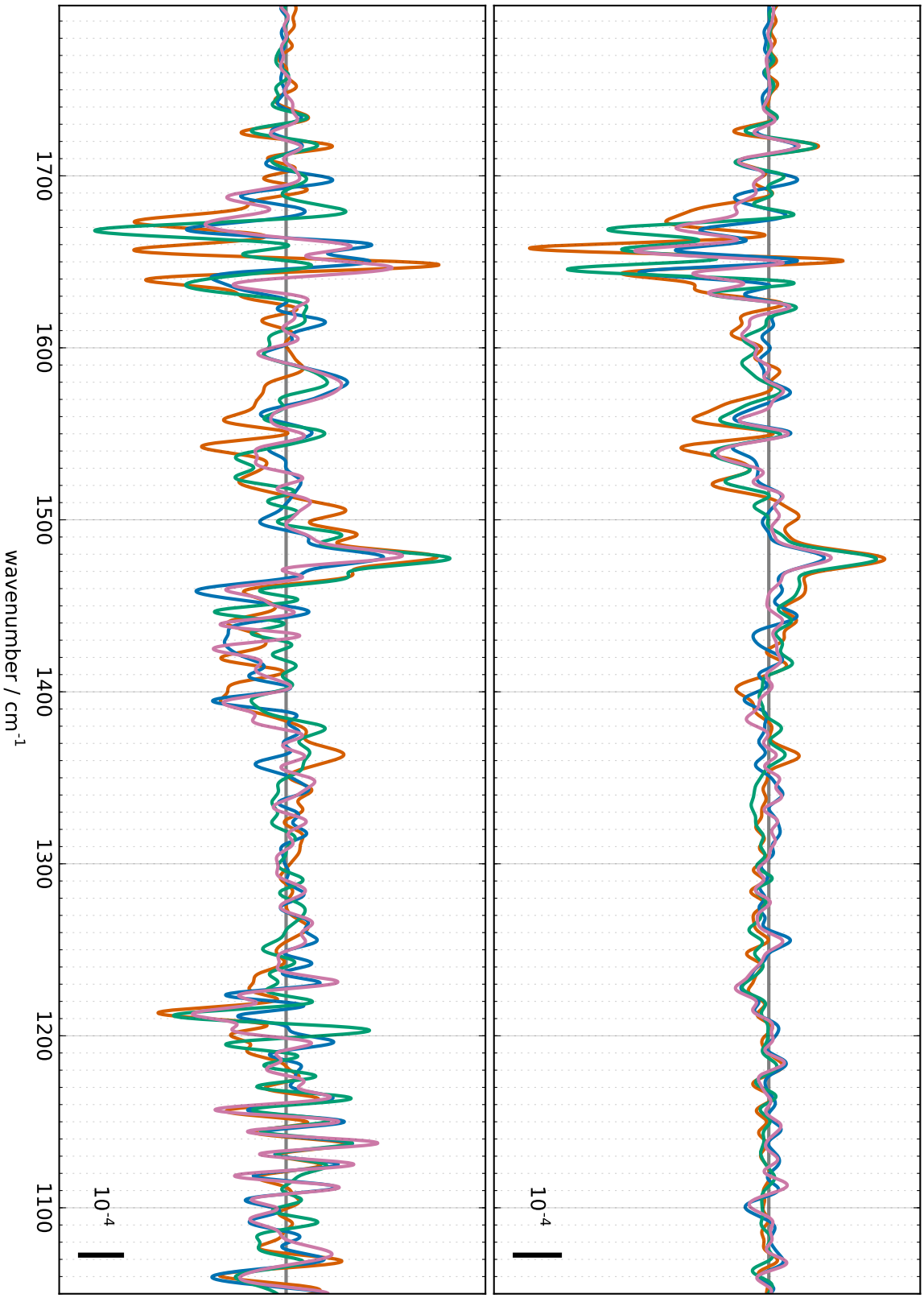

Figure 5.33.: Deconvoluted difference spectra 300 µs after laser flash application. Left/bottom: D_2O, right/top: H_2O. Orange: $S_1 \longrightarrow S_2$, aquamarine: $S_2 \longrightarrow S_3$, turquoise: $S_3 \longrightarrow S_0$, pink: $S_0 \longrightarrow S_1$.

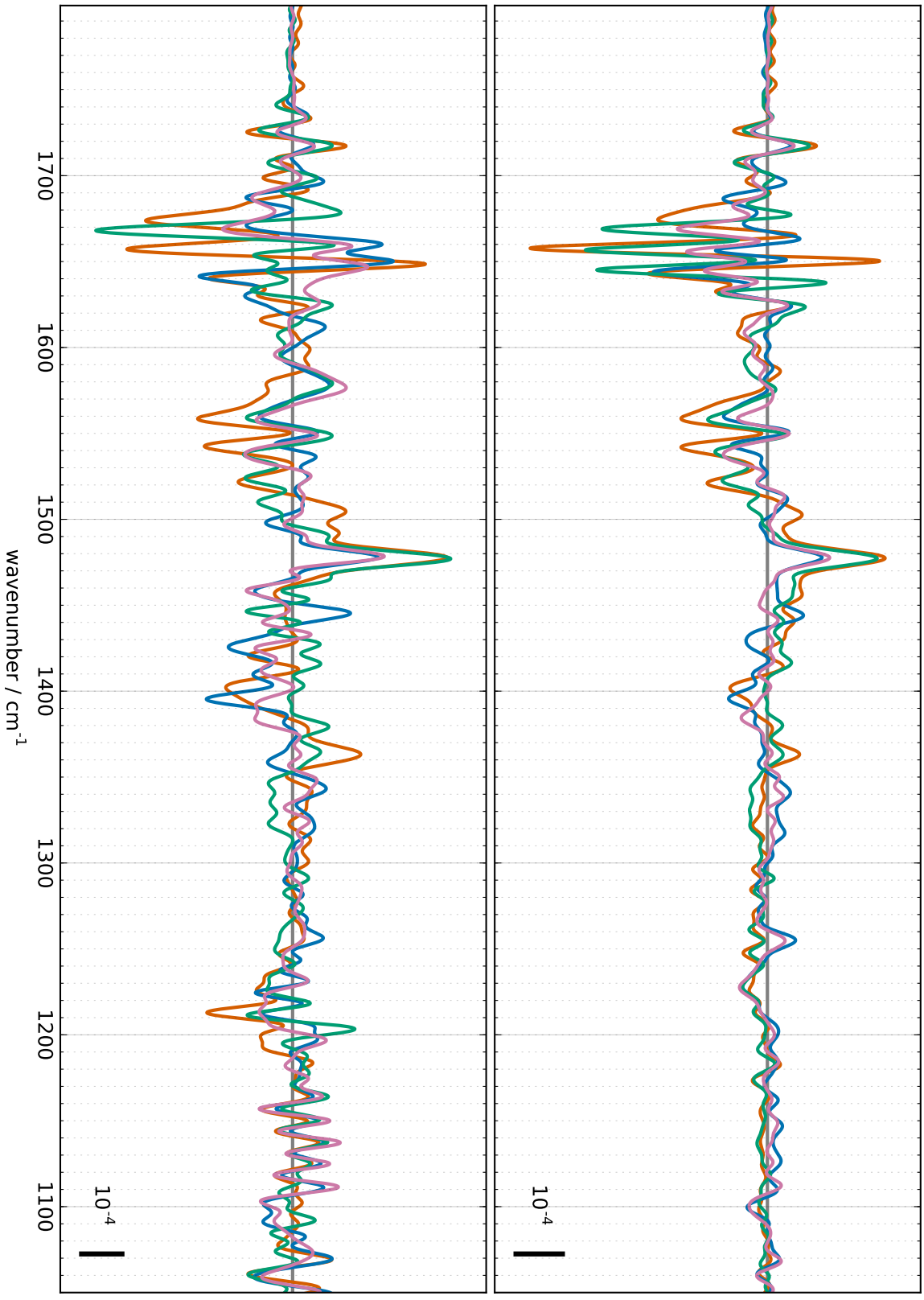

Figure 5.34.: Deconvoluted difference spectra 1 ms after laser flash application. Left/bottom: D_2O, right/top: H_2O. Orange: $S_1 \longrightarrow S_2$, aquamarine: $S_2 \longrightarrow S_3$, turquoise: $S_3 \longrightarrow S_0$, pink: $S_0 \longrightarrow S_1$.

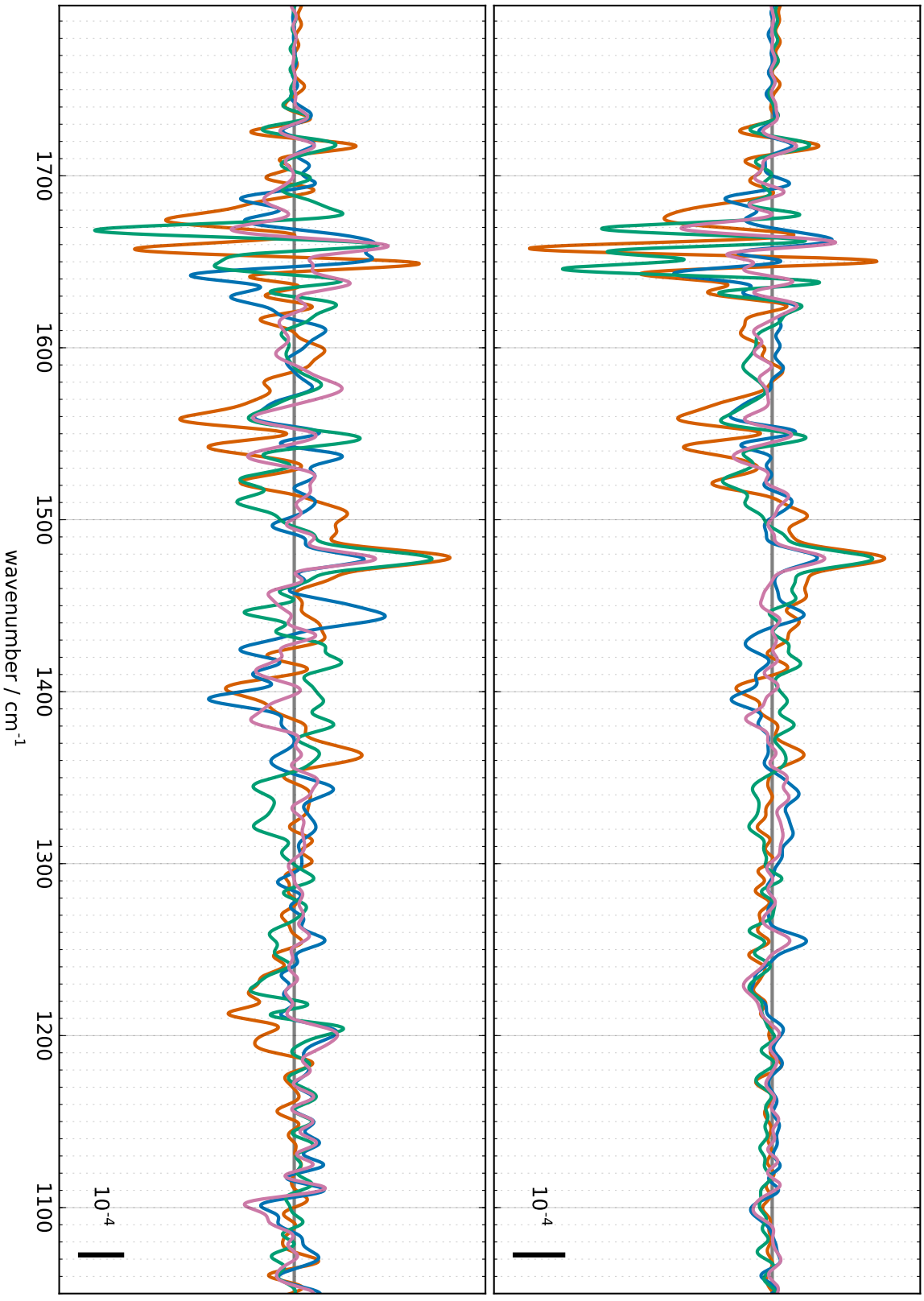

Figure 5.35.: Deconvoluted difference spectra 3 ms after laser flash application. Left/bottom: D_2O, right/top: H_2O. Orange: $S_1 \longrightarrow S_2$, aquamarine: $S_2 \longrightarrow S_3$, turquoise: $S_3 \longrightarrow S_0$, pink: $S_0 \longrightarrow S_1$.

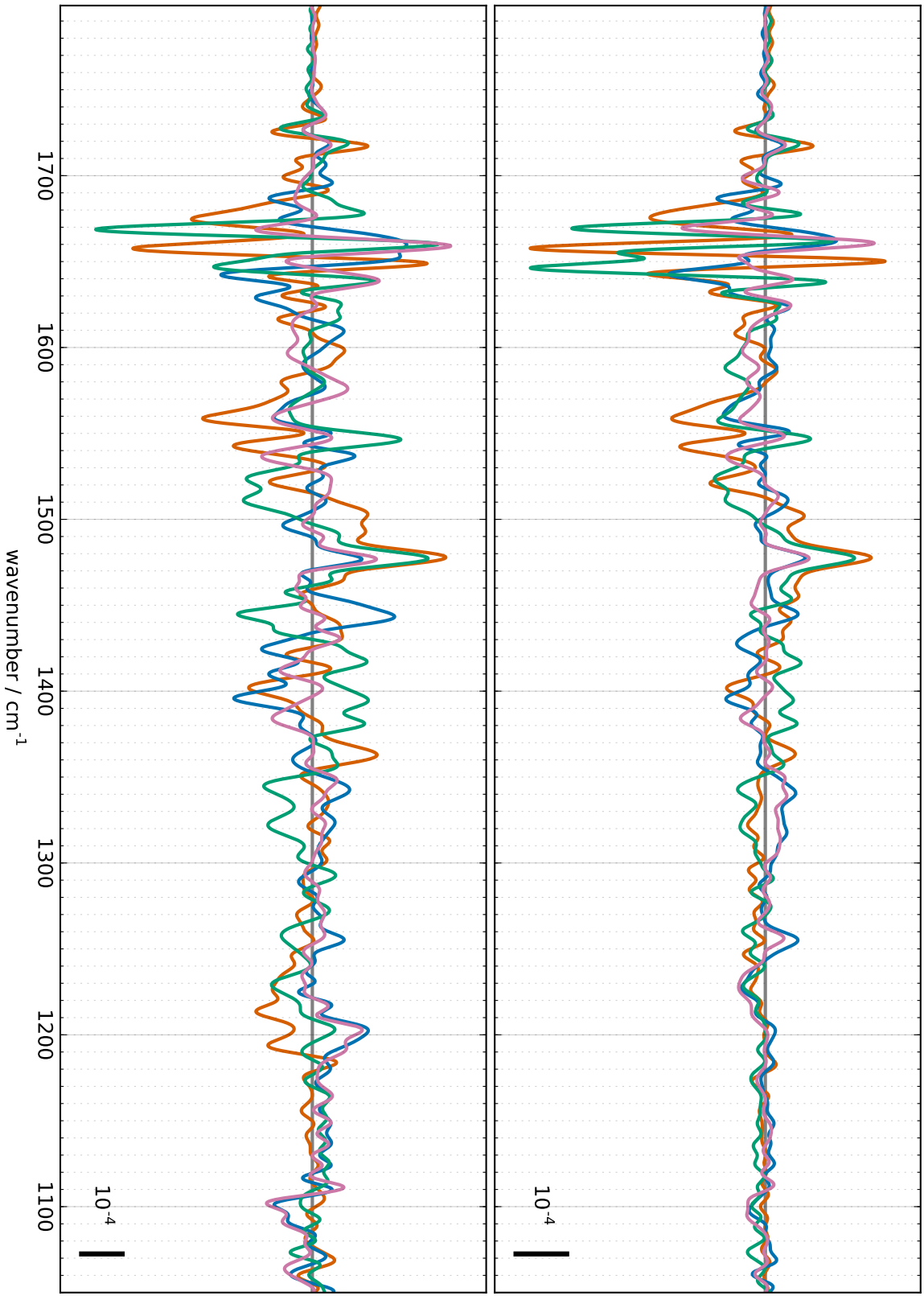

Figure 5.36.: Deconvoluted difference spectra 10 ms after laser flash application. Left/bottom: D_2O, right/top: H_2O. Orange: $S_1 \longrightarrow S_2$, aquamarine: $S_2 \longrightarrow S_3$, turquoise: $S_3 \longrightarrow S_0$, pink: $S_0 \longrightarrow S_1$.

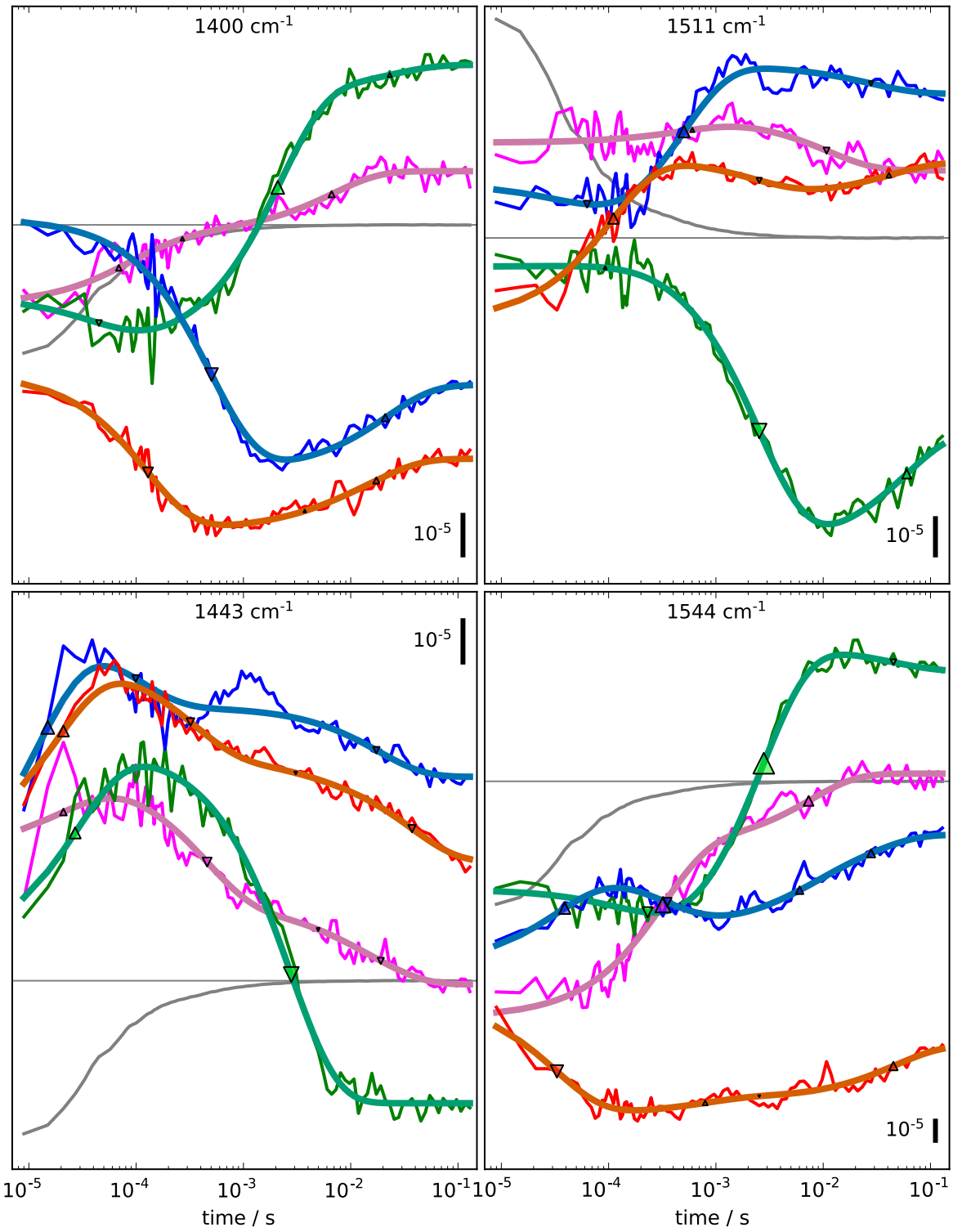

Figure 5.37.: Deconvoluted timecourses in H_2O at selected wavenumbers. Top left: 1400 cm^{-1}, top right: 1511 cm^{-1}, bottom left: 1443 cm^{-1}, bottom right: 1544 cm^{-1} . Red: $S_1 \longrightarrow S_2$, blue: $S_2 \longrightarrow S_3$, green: $S_3 \longrightarrow S_0$, magenta: $S_0 \longrightarrow S_1$. Elastic net fits are colored orange, aquamarine, turquoise, and pink respectively . The triangles resemble the time constants used in the fit. The gray curve is the subtracted heat signal.

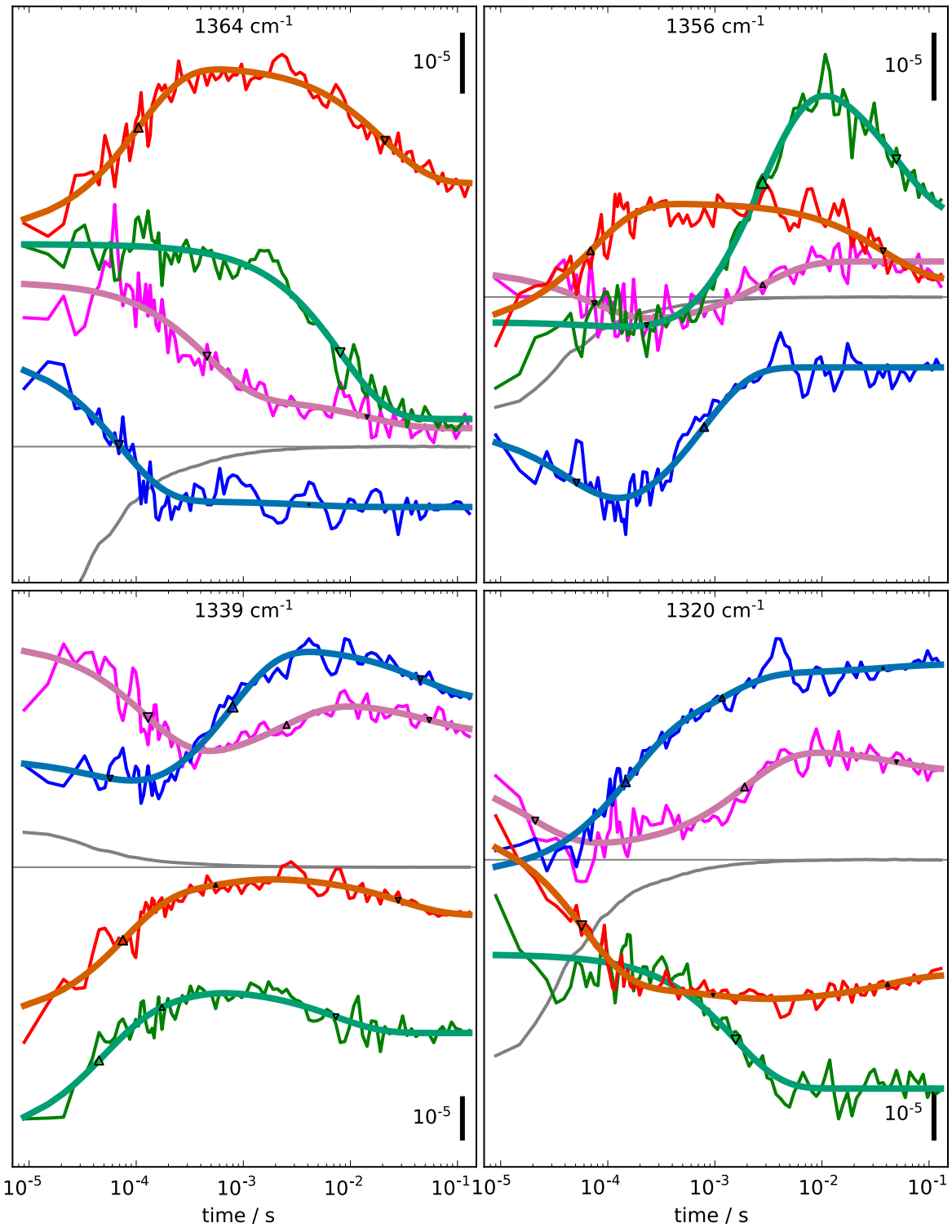

Figure 5.38.: Deconvoluted timecourses in H_2O at selected wavenumbers. Top left: 1364 cm^{-1}, top right: 1356 cm^{-1}, bottom left: 1339 cm^{-1}, bottom right: 1320 cm^{-1} . Red: $S_1 \longrightarrow S_2$, blue: $S_2 \longrightarrow S_3$, green: $S_3 \longrightarrow S_0$, magenta: $S_0 \longrightarrow S_1$. Elastic net fits are colored orange, aquamarine, turquoise, and pink respectively . The triangles resemble the time constants used in the fit. The gray curve is the subtracted heat signal.

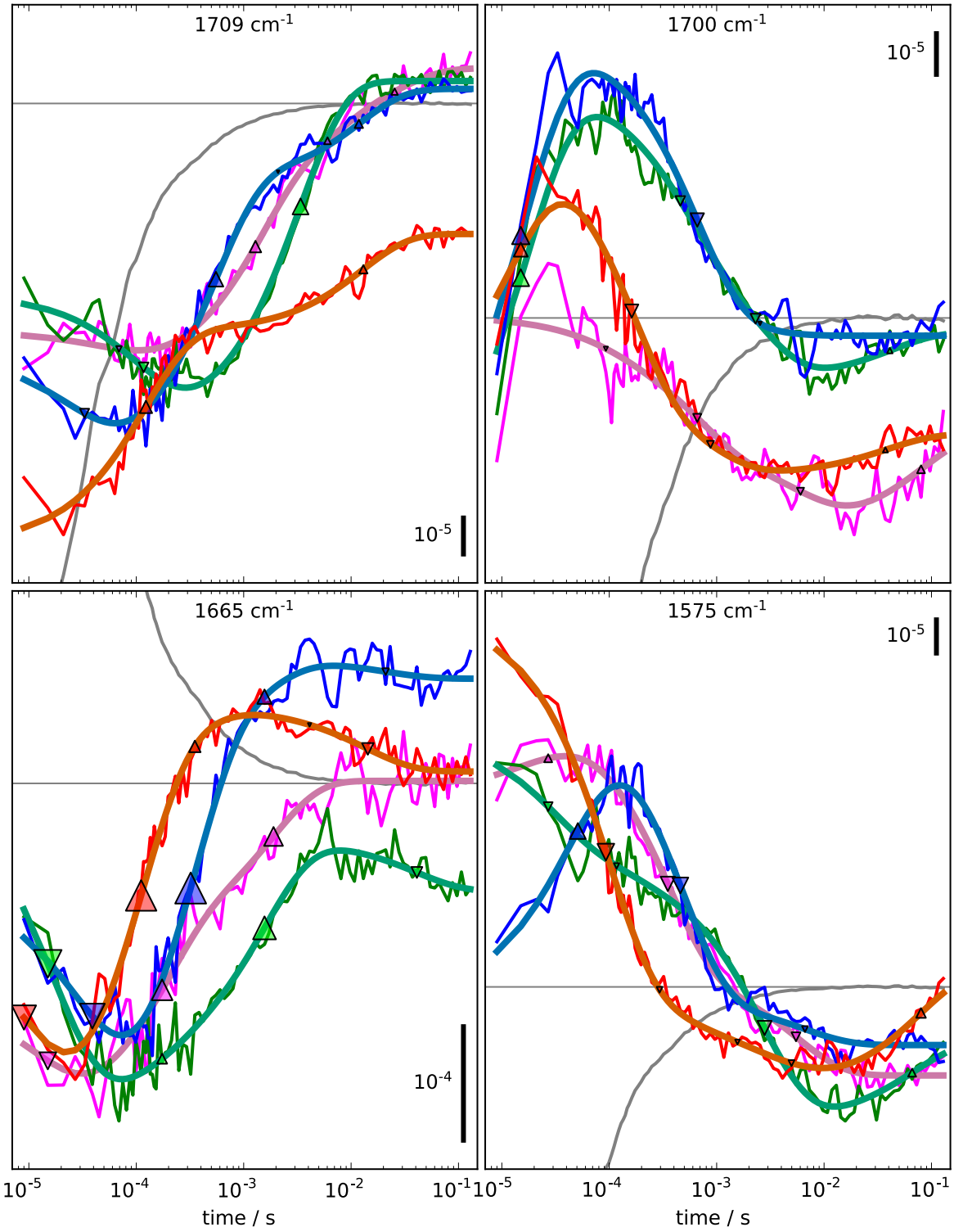

Figure 5.39.: Deconvoluted timecourses in H_2O at selected wavenumbers. Top left: 1709 cm^{-1}, top right: 1700 cm^{-1}, bottom left: 1665 cm^{-1}, bottom right: 1575 cm^{-1} . Red: $S_1 \longrightarrow S_2$, blue: $S_2 \longrightarrow S_3$, green: $S_3 \longrightarrow S_0$, magenta: $S_0 \longrightarrow S_1$. Elastic net fits are colored orange, aquamarine, turquoise, and pink respectively . The triangles resemble the time constants used in the fit. The gray curve is the subtracted heat signal.

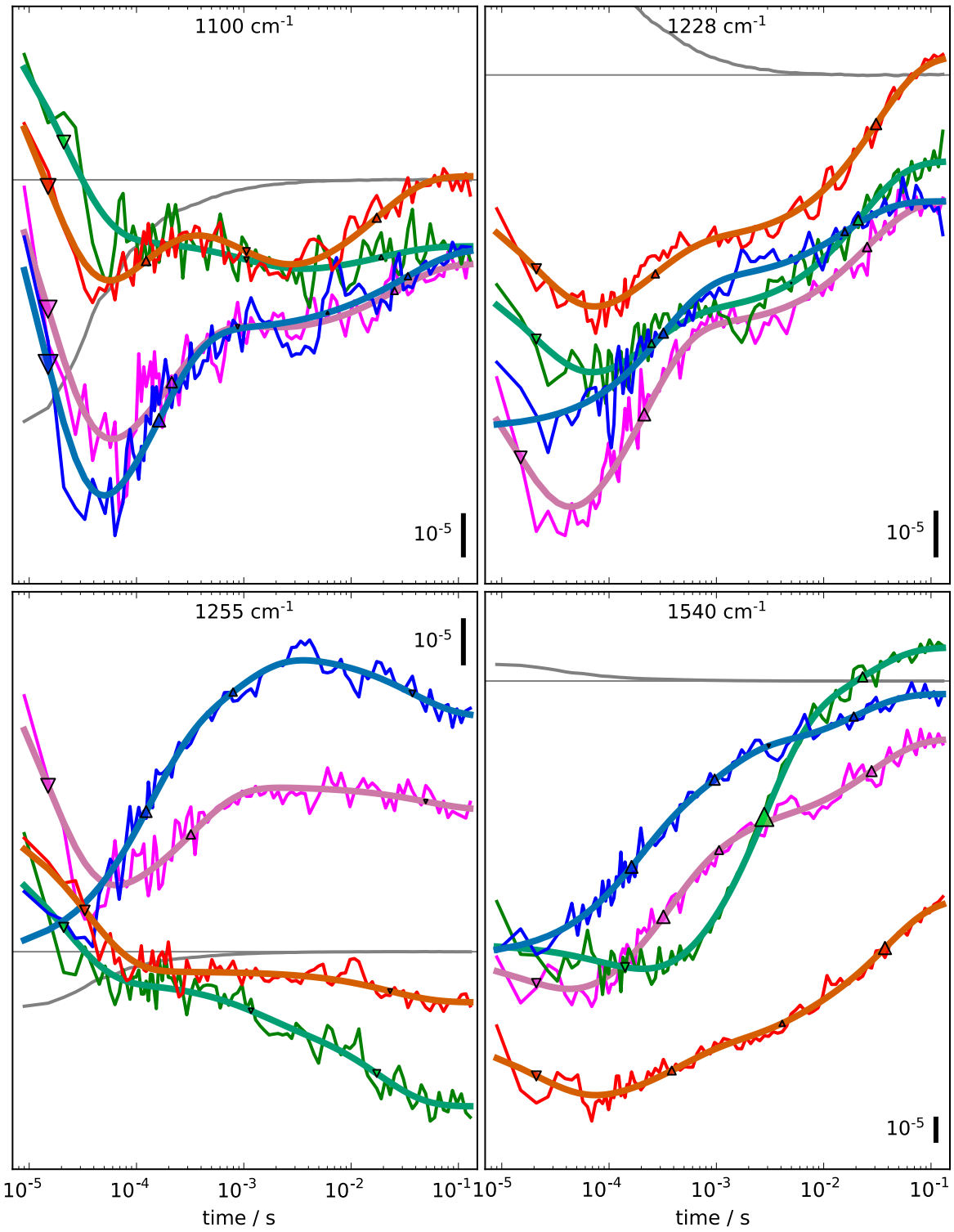

Figure 5.40.: Deconvoluted timecourses in H_2O at selected wavenumbers. Top left: 1100 cm^{-1}, top right: 1228 cm^{-1}, bottom left: 1255 cm^{-1}, bottom right: 1540 cm^{-1} . Red: $S_1 \longrightarrow S_2$, blue: $S_2 \longrightarrow S_3$, green: $S_3 \longrightarrow S_0$, magenta: $S_0 \longrightarrow S_1$. Elastic net fits are colored orange, aquamarine, turquoise, and pink respectively . The triangles resemble the time constants used in the fit. The gray curve is the subtracted heat signal.

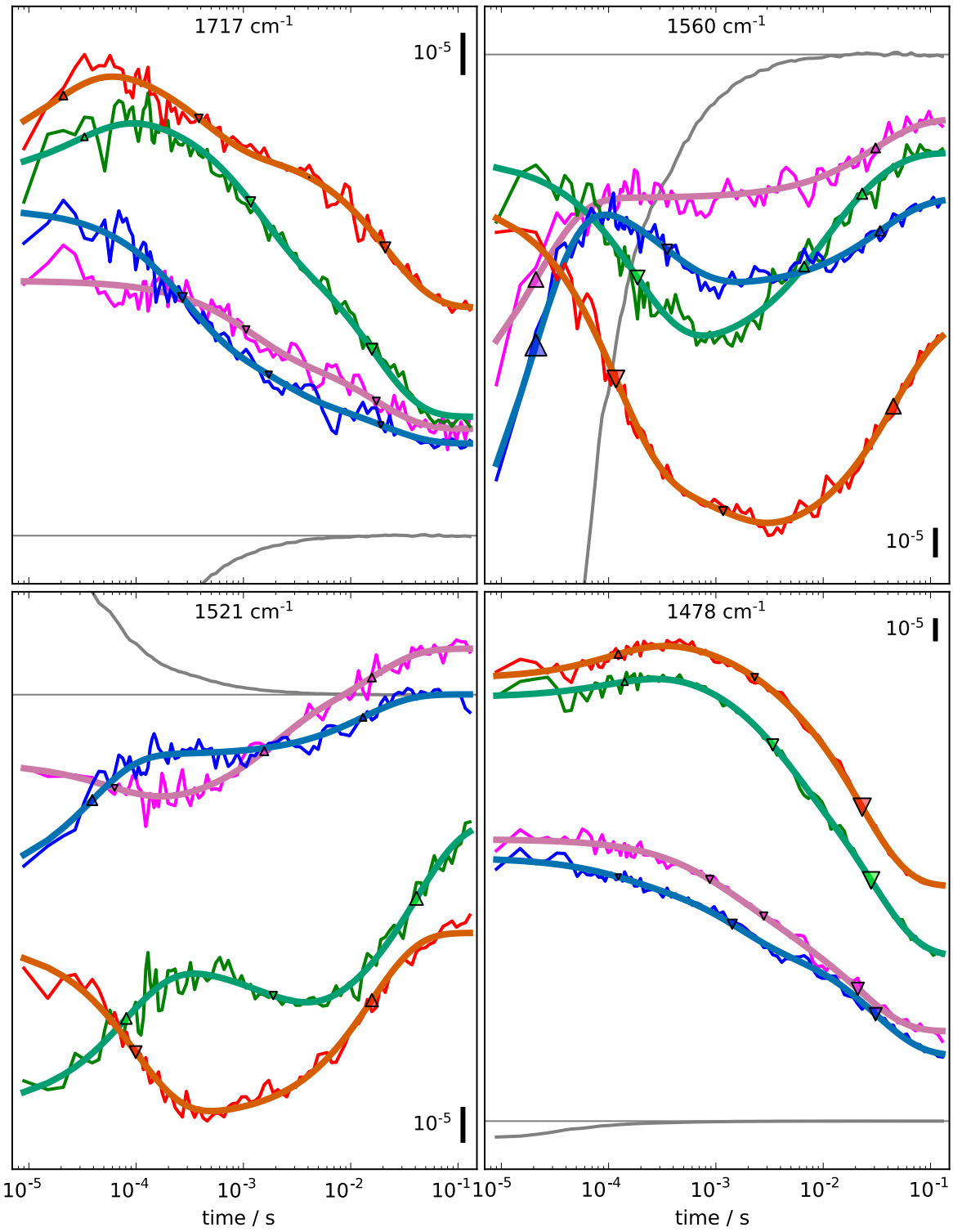

Figure 5.41.: Deconvoluted timecourses in H_2O at selected wavenumbers. Top left: 1717 cm^{-1}, top right: 1560 cm^{-1}, bottom left: 1521 cm^{-1}, bottom right: 1478 cm^{-1} . Red: $S_1 \longrightarrow S_2$, blue: $S_2 \longrightarrow S_3$, green: $S_3 \longrightarrow S_0$, magenta: $S_0 \longrightarrow S_1$. Elastic net fits are colored orange, aquamarine, turquoise, and pink respectively . The triangles resemble the time constants used in the fit. The gray curve is the subtracted heat signal.

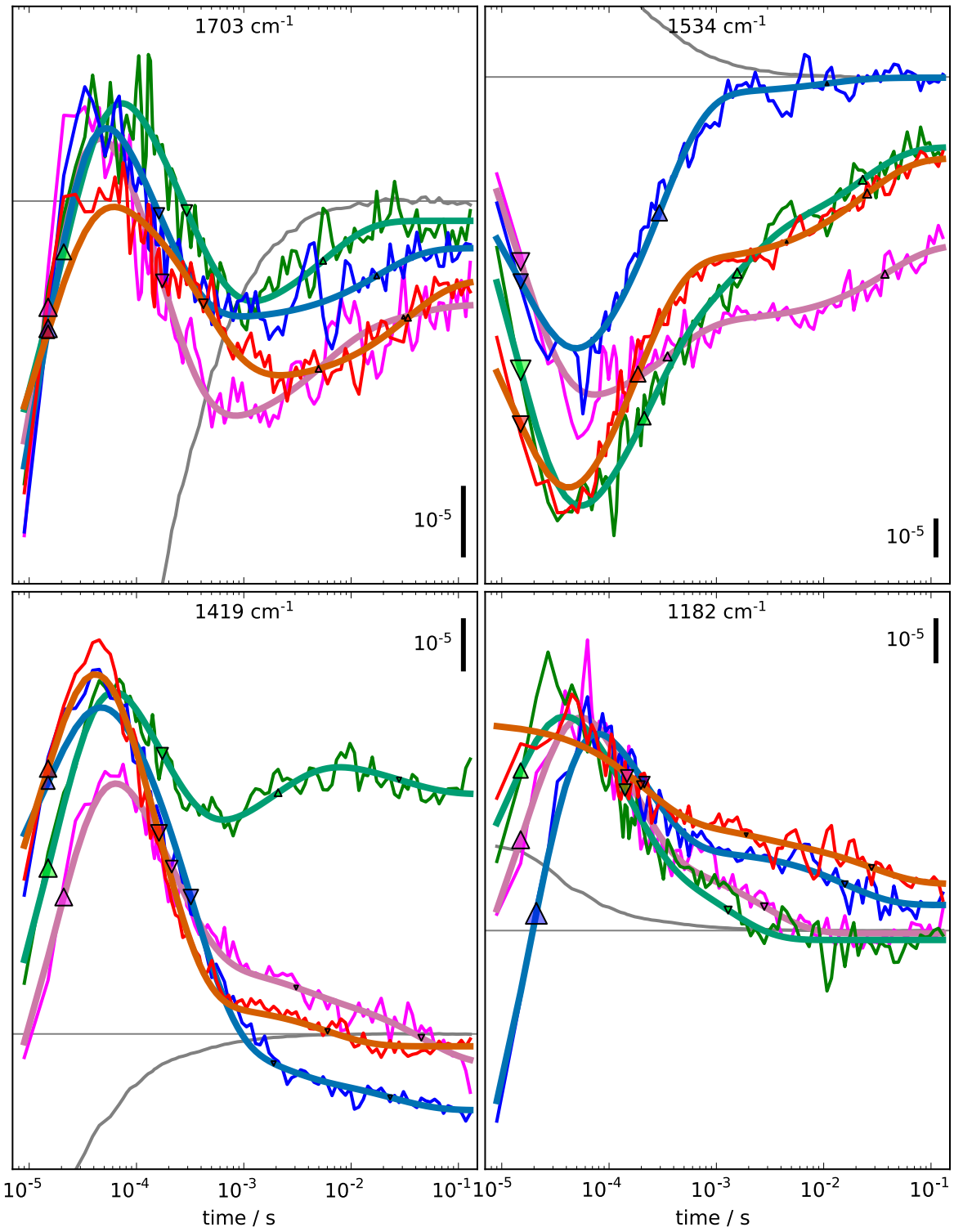

Figure 5.42.: Deconvoluted timecourses in H_2O at selected wavenumbers. Top left: 1703 cm^{-1}, top right: 1534 cm^{-1}, bottom left: 1419 cm^{-1}, bottom right: 1182 cm^{-1} . Red: $S_1 \longrightarrow S_2$, blue: $S_2 \longrightarrow S_3$, green: $S_3 \longrightarrow S_0$, magenta: $S_0 \longrightarrow S_1$. Elastic net fits are colored orange, aquamarine, turquoise, and pink respectively . The triangles resemble the time constants used in the fit. The gray curve is the subtracted heat signal.

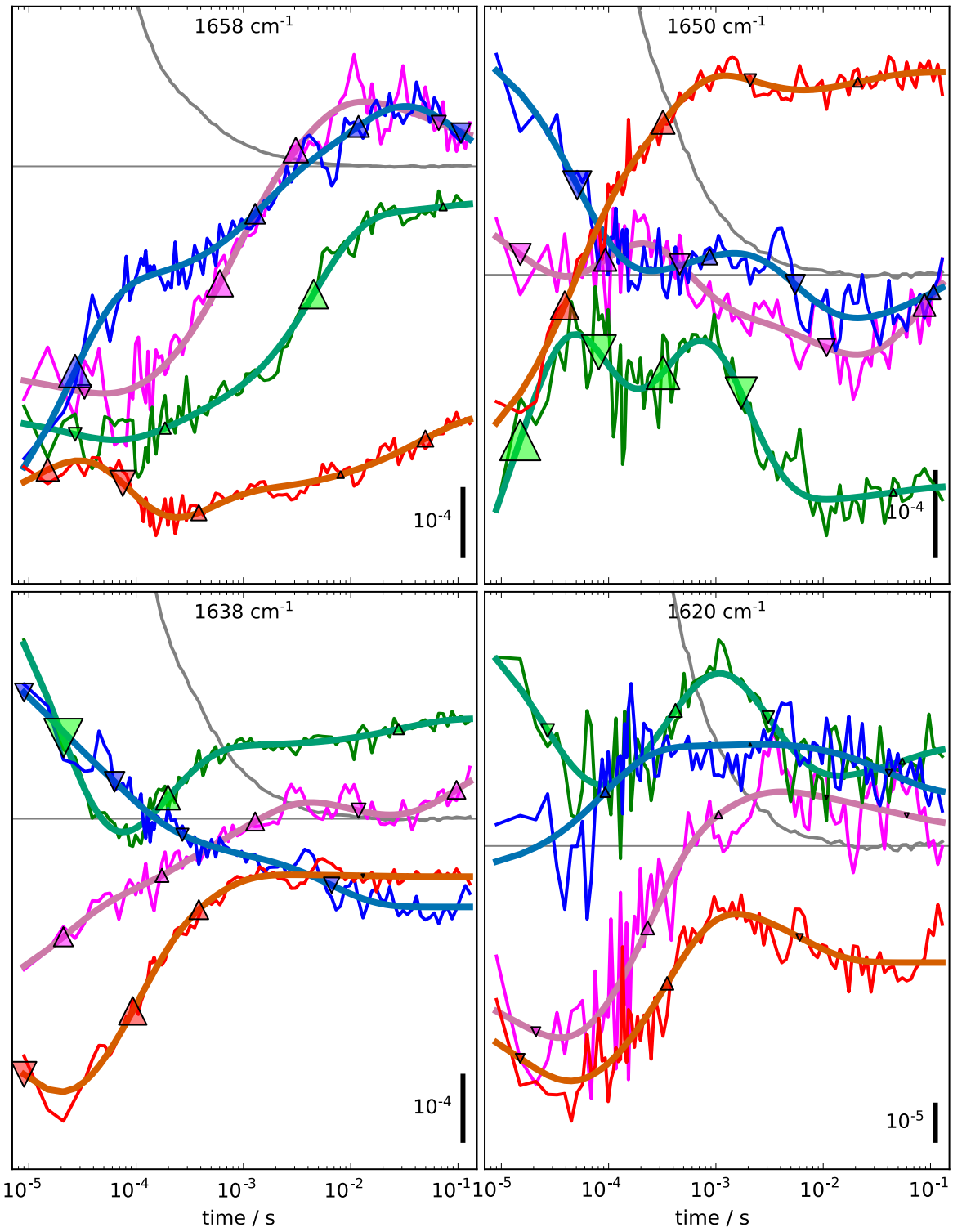

Figure 5.43.: Deconvoluted timecourses in H_2O at selected wavenumbers. Top left: 1658 cm^{-1}, top right: 1650 cm^{-1}, bottom left: 1638 cm^{-1}, bottom right: 1620 cm^{-1} . Red: $S_1 \longrightarrow S_2$, blue: $S_2 \longrightarrow S_3$, green: $S_3 \longrightarrow S_0$, magenta: $S_0 \longrightarrow S_1$. Elastic net fits are colored orange, aquamarine, turquoise, and pink respectively . The triangles resemble the time constants used in the fit. The gray curve is the subtracted heat signal.

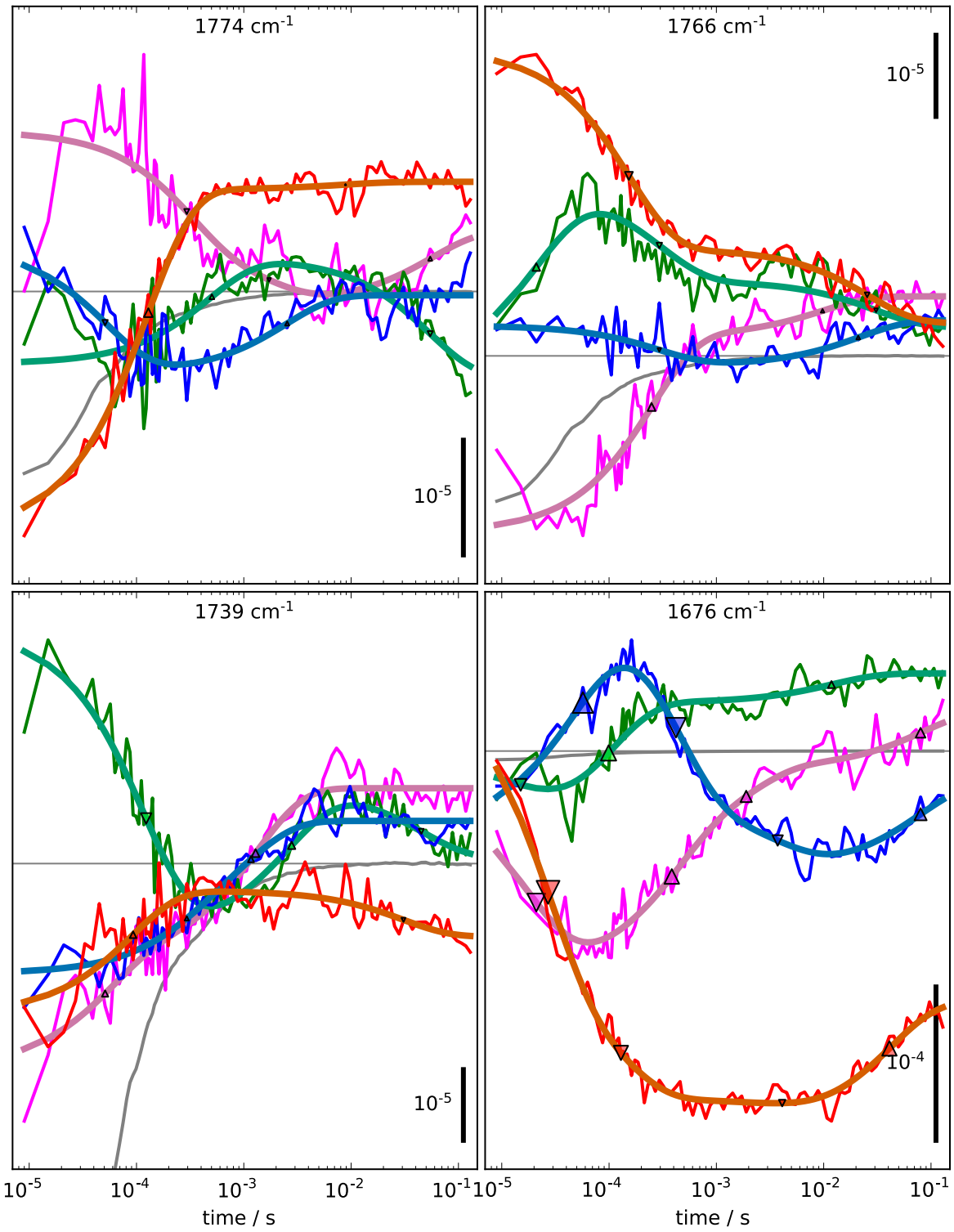

Figure 5.44.: Deconvoluted timecourses in H_2O at selected wavenumbers. Top left: 1774 cm^{-1}, top right: 1766 cm^{-1}, bottom left: 1739 cm^{-1}, bottom right: 1676 cm^{-1} . Red: $S_1 \longrightarrow S_2$, blue: $S_2 \longrightarrow S_3$, green: $S_3 \longrightarrow S_0$, magenta: $S_0 \longrightarrow S_1$. Elastic net fits are colored orange, aquamarine, turquoise, and pink respectively . The triangles resemble the time constants used in the fit. The gray curve is the subtracted heat signal.

Figures 5.43 and 5.44 show amide I and II as well as ν(COOH) timecourses. They will be discussed in section 6.3 on page 193 where decay associated spectra are compared to steady-state spectra.

5.8.6. Elastic fit, lifetime maps, and time constants

The elastic net method has been introduced in section 4.15.4 on page 55. Calculating the elastic net fit over the whole wavenumber range for a single S-state transition returns time constants for every timecourse; the results are shown in the following sections.

The time constants and their amplitudes which are obtained through the elastic net fit are plotted as lifetime maps. In this representation, the time constants of a timecourse are plotted versus the timecourse's wavenumber. Positive amplitudes are colored red, negative ones blue; amplitudes with large magnitude are darker colored than amplitudes with smaller ones. A "phase" is identified as a cluster of dots with different wavenumbers which share a common time constant. Moreover, a phase should be S-state transition specific; this is verified using the decay associated spectra (see below). Clusters of special interest are marked with black circles; these clusters are also marked in the decay associated spectra (see below). The average time constant of the black circles is given as gray line, which corresponds to the values given in the tables (see below). The time constants of the fitted timecourses of the marked wavenumbers are given in tables which follow the decay associated spectra. In the caption to the table the obtained average time constant is indicated. Table 5.2 summarizes the obtained results.

	H_2O	D_2O
$S_1 \longrightarrow S_2$	106 µs (table A.2, page 247)	103 µs (table A.3, page 248)
$S_2 \longrightarrow S_3$	19 µs (table A.4, page 251) 48 µs (table A.5, page 252)	76 µs (table A.7, page 254)
	393 µs (table A.6, page 253)	860 µs (table A.8, page 255)
$S_3 \longrightarrow S_0$	18 µs (table A.9, page 261)	50 µs (table A.12, page 263)
	142 µs (table A.10, page 261)	500 µs (table A.13, page 263)
	2.9 ms (table A.11, page 262)	4.0 ms (table A.14, page 269)
$S_0 \longrightarrow S_1$	22 µs (table A.15, page 270)	30 µs (table A.17, page 272)
	200 µs (table A.16, page 271)	191 µs (table A.18, page 273) 327 µs (table A.19, page 273)

Table 5.2.: Time constants obtained from the elastic net fits.

Selected timecourses of some of the marked wavenumbers are shown following the lifetime maps. The time constants of interest are indicated in the plots.

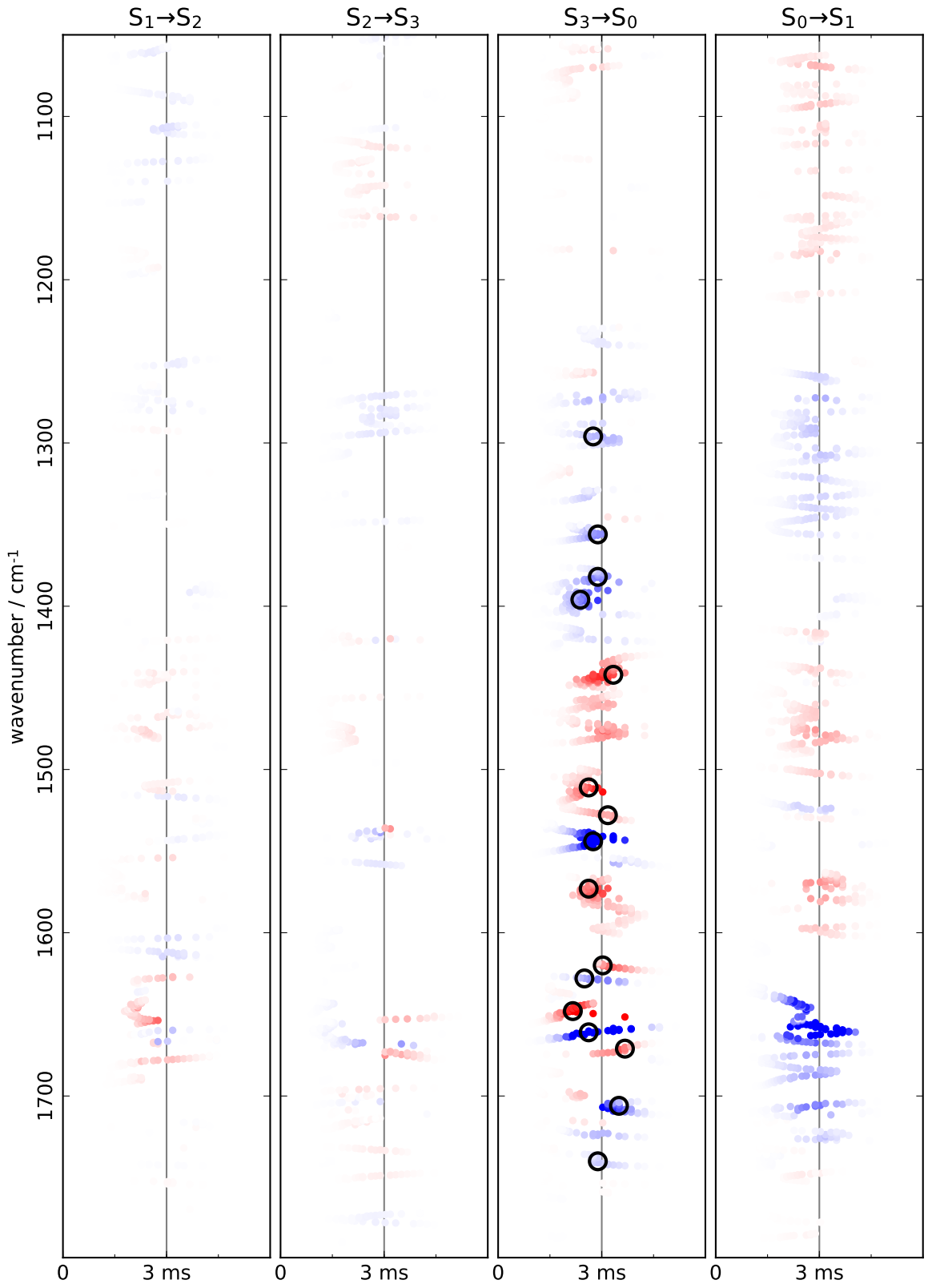

Figure 5.45.: Example for a windowed lifetime map. The lifetime maps for the four transitions have been windowed using the Gaussian function (eq. 5.4) with $\tau = 3\,\text{ms}$ and $\sigma = 600\,\mu\text{s}$.

The lifetime maps do not easily facilitate the comparison of different S-state transitions. To this end, decay associated spectra are shown following the selected timecourses. In the following I will show how a spectrum is obtained using the $S_3 \longrightarrow S_0$ transition as example. First, in the lifetime map (figure 5.62 on page 158) a 3 ms phase is identified as clusters with different wavenumbers which are grouped around 3 ms. To obtain a decay associated spectra which focuses on the 3 ms phase, the data is windowed using the following gaussian function with $\tau = 3\,\text{ms}$ and $\sigma = 600\,\mu\text{s}$:

$$G(t, \tau, \sigma) = \mathrm{e}^{-(t-\tau)^2/2\sigma^2}. \tag{5.4}$$

The result is shown in figure 5.45. In the next step, the goal is to remove the time dimension so that the amplitudes of the time constants can be plotted versus the wave number. This is achieved by simply adding all the amplitudes of the windowed time constants to achieve one amplitude per wavenumber. The result is the black curve in figure 5.46.

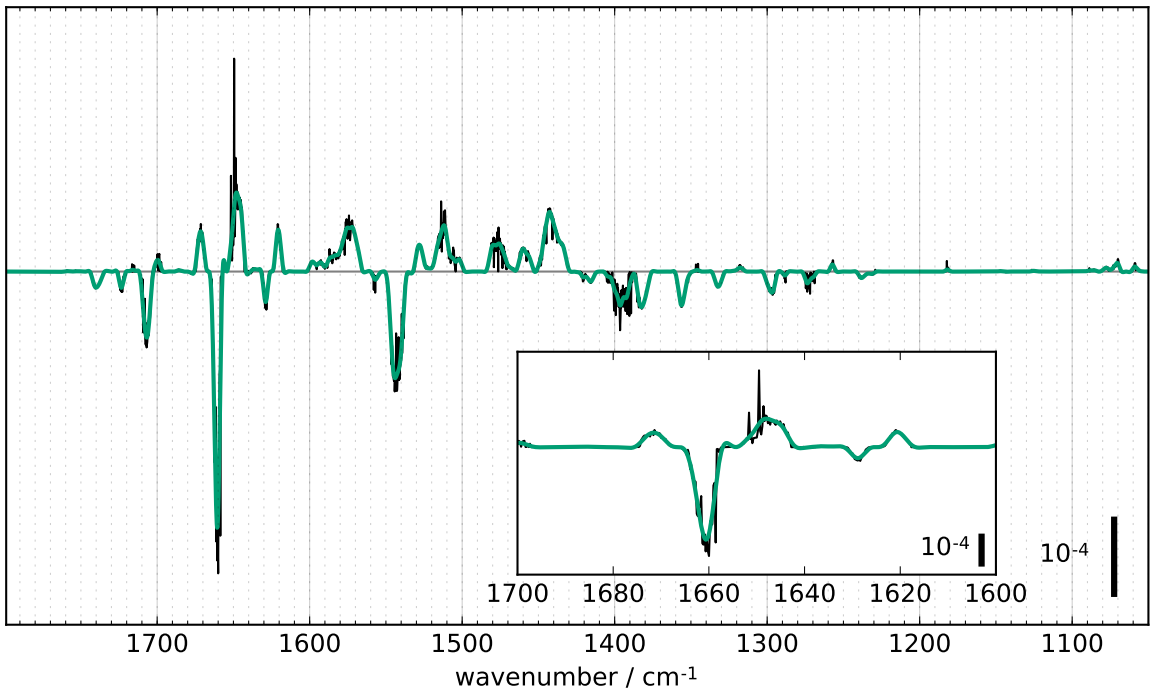

Figure 5.46.: Decay associated spectra representing the amplitudes of the time constants around 3 ms in the $S_3 \longrightarrow S_0$ transition. The black curve was obtained by summing the amplitudes of the windowed time constants (see figure 5.45) as described in the text. The green curve was obtained from the black curve by filtering the data with a lowpass filter.

Finally, the data (black curve in figure 5.46) has been filtered with a Butterworth filter (`b, a = signal.butter(3, 0.1); filtered = signal.filtfilt(b, a, spectrum)`) to

obtain the green curve. The features of the green spectrum now correspond to decays and rises in the $S_3 \longrightarrow S_0$ transition with a time constant of about 3 ms.

The $S_1 \rightarrow S_2$ transition in H_2O and in D_2O

In figures 5.47 and 5.48 the result of the elastic net fits—the "lifetime maps"—are shown. Time constants with positive amplitudes are shown in red, time constants with negative amplitudes are shown in blue. In the D_2O dataset regions which are affected by the heat signal are grayed out. The black circles denote clusters of special interest: they mark time constants which are only visible in the $S_1 \longrightarrow S_2$ transition. The time constants marked by the black circles are given in tables A.2 and A.3. The $S_1 \longrightarrow S_2$ transition shows no kinetic isotope effect: in both H_2O and D_2O the clusters show an average time constant of about 100 µs. The timecourses for selected wavenumbers are given in figures A.5 and A.6.

In figures 5.47 and 5.48, a comparison with the other transitions is not possible. A comparison becomes possible when plotting decay associated spectra. To achieve this, the time constants of a given flash for a dataset have been multiplied with a Gaussian function (eq. 5.4) so as to apply a window function. To obtain the decay associated spectra for this transition, I chose τ = 110 µs and σ = 15 µs. When multiplied with the Gaussian function, only the time constants of interest remain and the time constants for this transition can be shown in one figure (see figures 5.49 and 5.50). Each peak which is marked with its wavenumber corresponds to a black circle in the lifetime maps. Regions which are affected by the heat signal are again grayed out.

106 µs spectrum, H_2O (fig. 5.49)	103 µs spectrum, D_2O (fig. 5.50)
1708 cm^{-1}(–)	1708 cm^{-1}(–) (small, not marked)
1665 cm^{-1}(–)	1667 cm^{-1}(–)
1655 cm^{-1}(+)	1653 cm^{-1}(+) (fig. A.6)
1576 cm^{-1}(+) (fig. A.5, p. 249)	1576 cm^{-1}(+) (fig. A.6, p. 250)
1511 cm^{-1}(–) (fig. A.5, p. 249)	1511 cm^{-1}(–)
1403 cm^{-1}(+) (fig. A.5, p. 249)	1399 cm^{-1}(+)
1281 cm^{-1}(–) (fig. A.5, p. 249)	1280 cm^{-1}(–) (fig. A.6, p. 250)
1102 cm^{-1}(–)	1104 cm^{-1}(–) (small, not marked)

Table 5.3.: Comparison of $S_1 \longrightarrow S_2$ transition H_2O and D_2O decay associated spectra (figures 5.49 and 5.50). The referenced figures show the timecourses at the respective wavenumbers.

Several peaks can be identified in the decay associated spectra. Peaks that appear in both H_2O and D_2O datasets are summarized in table 5.3. The peaks around 1511 cm^{-1} and 1403 cm^{-1} in the H_2O dataset are, concerning the D_2O dataset, in a region which is affected

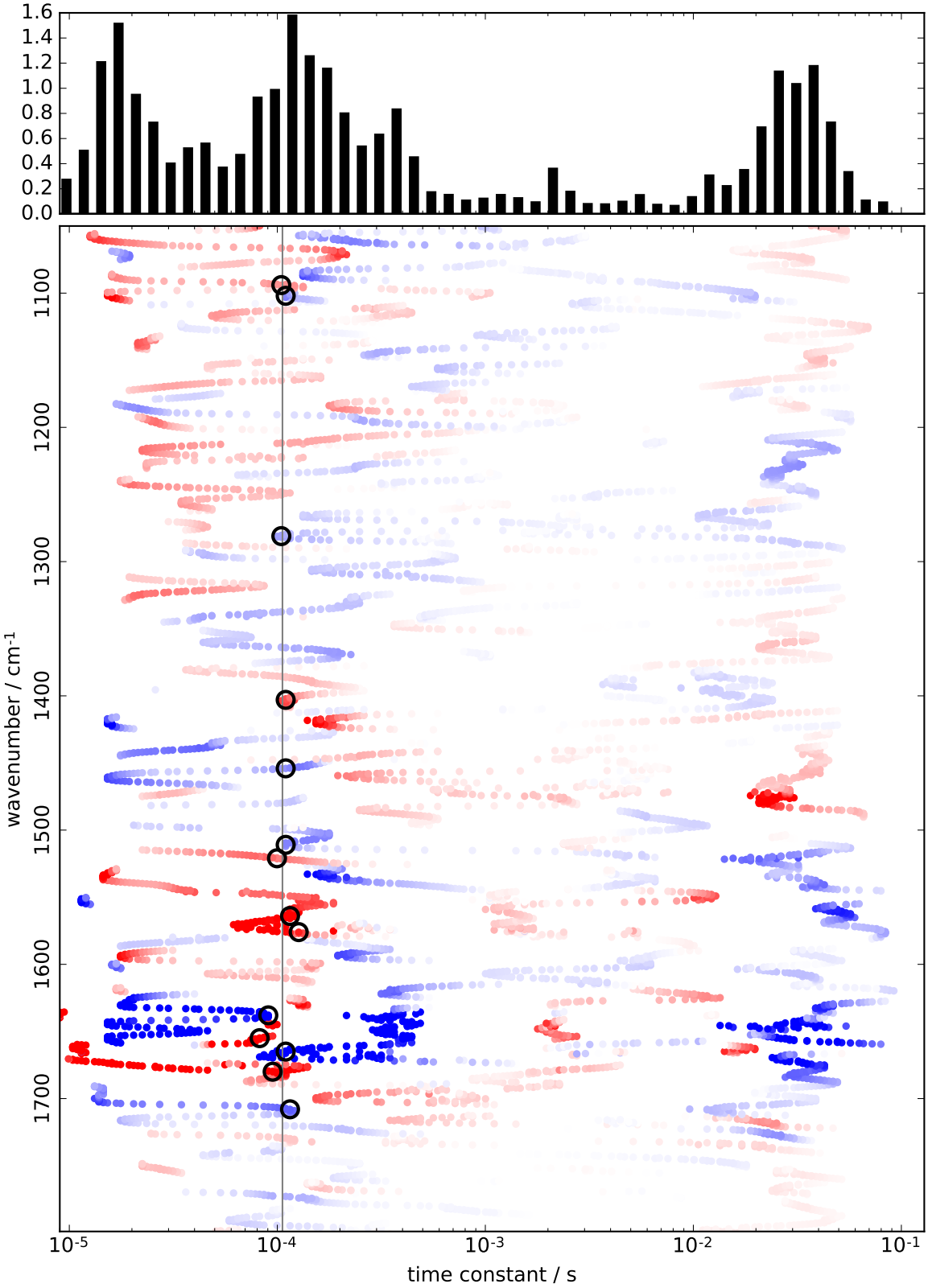

Figure 5.47.: H_2O time constants and their respective amplitudes as obtained through elastic net fitting for the $S_1 \longrightarrow S_2$ transition. Positive amplitudes are colored red, negative ones blue.

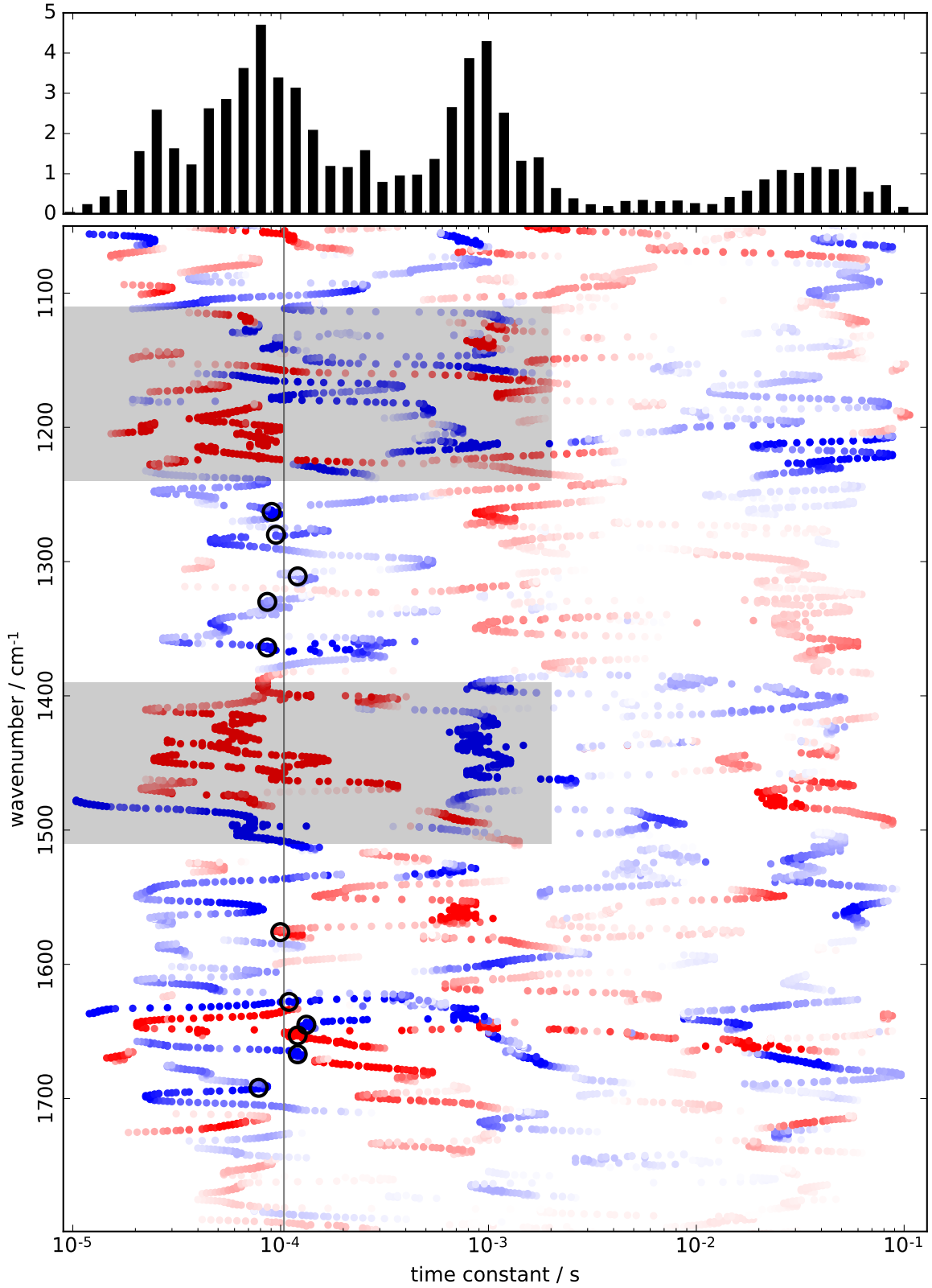

Figure 5.48.: D_2O time constants and their respective amplitudes as obtained through elastic net fitting for the $S_1 \longrightarrow S_2$ transition. Positive amplitudes are colored red, negative ones blue. Regions which are affected by the heat signal are grayed out.

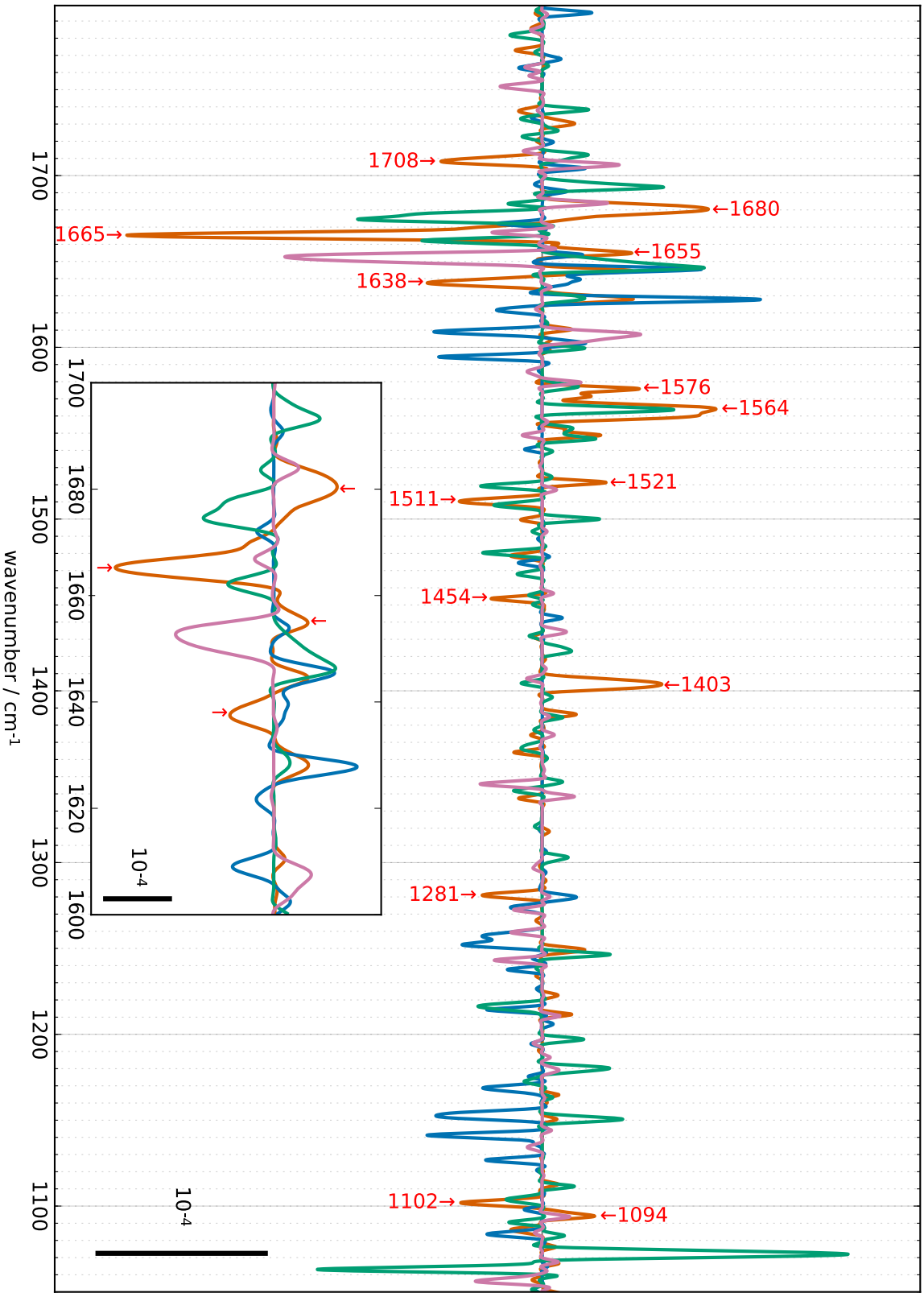

Figure 5.49.: Decay associated spectra (H_2O) obtained by multiplying the time constants obtained through a elastic net fit with a Gaussian function (5.4) where τ = 110 µs and σ = 15 µs. Orange: $S_1 \longrightarrow S_2$, aquamarine: $S_2 \longrightarrow S_3$, turquoise: $S_3 \longrightarrow S_0$, pink: $S_0 \longrightarrow S_1$.

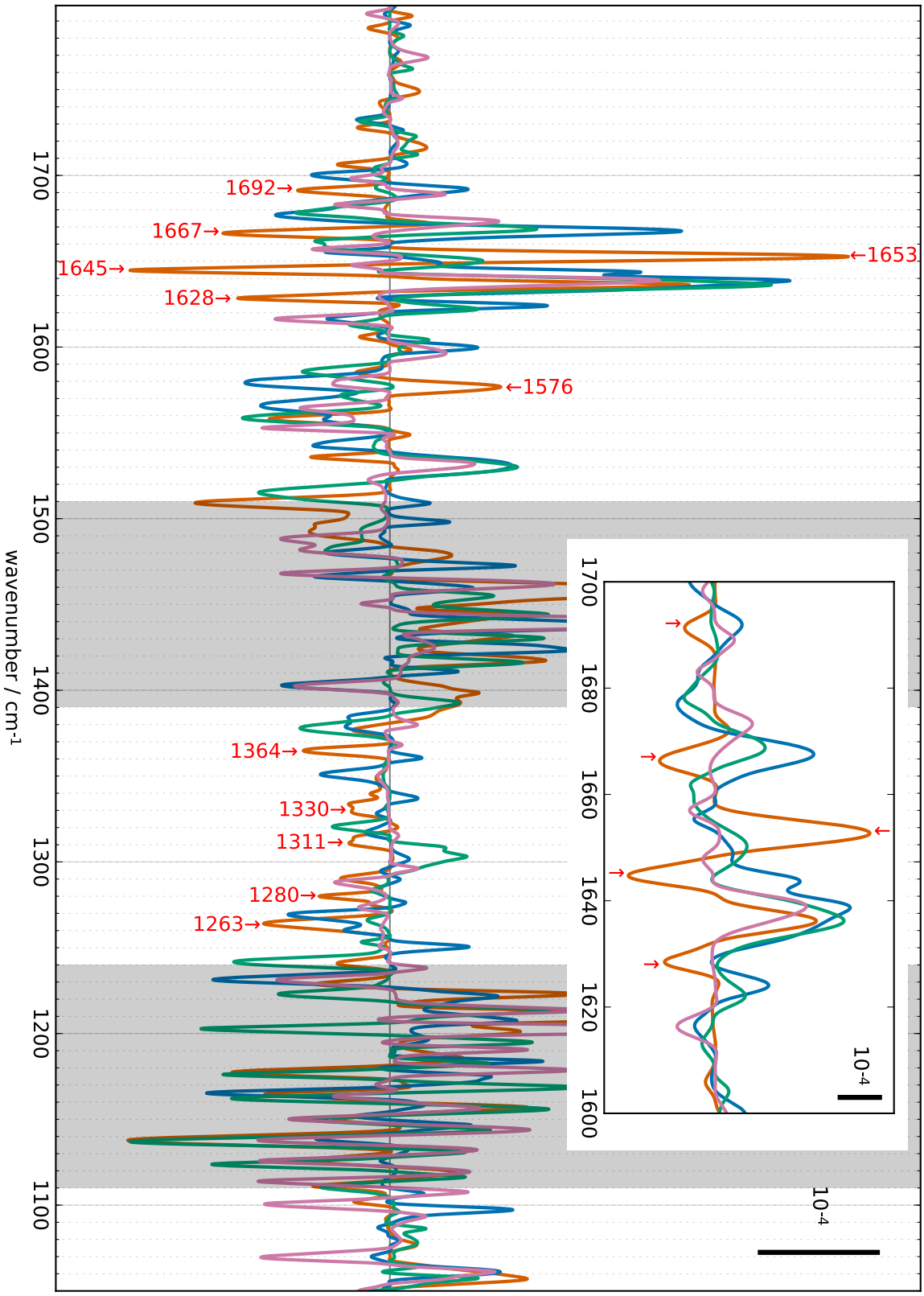

Figure 5.50.: Decay associated spectra (D_2O) obtained by multiplying the time constants obtained through a elastic net fit with a Gaussian function (5.4) where τ = 110 µs and σ = 15 µs. Orange: $S_1 \longrightarrow S_2$, aquamarine: $S_2 \longrightarrow S_3$, turquoise: $S_3 \longrightarrow S_0$, pink: $S_0 \longrightarrow S_1$. Regions which are affected by the heat signal are grayed out.

by the heat signal. Although their counterparts are observable in the D_2O spectrum, they have been omitted in the further analysis of the time constants.

Peaks that can only be identified in the H_2O dataset appear at 1680 cm^{-1}(+), 1638 cm^{-1} (–), 1564 cm^{-1}(+), 1521 cm^{-1}(+), 1454 cm^{-1}, and 1094 cm^{-1}. The peak at 1454 cm^{-1} is very weak and cannot be resolved in the corresponding D_2O spectrum due to the high noise in this region. Peaks only visible in the D_2O spectrum appear at 1692 cm^{-1}(–), 1645 cm^{-1}(–), 1628 cm^{-1}(–), and several negative peaks at 1364 cm^{-1}, 1330 cm^{-1}, 1311 cm^{-1}, and 1263 cm^{-1}. There may be counterparts to 1364 cm^{-1} and 1330 cm^{-1} in the H_2O spectrum, but they are very small.

At 1564 cm^{-1} in H_2O, a peak can also be seen for the third transition; this period-of-two oscillation hints at processes at the acceptor side, although the Fe^{2+}/Fe^{3+} spectrum only has a small negative feature here (Hienerwadel and Berthomieu 1995; Noguchi and Inoue 1995a). Likewise, the Q_A^-/Q_A spectrum features a small negative peak at 1559 cm^{-1}. The Fe^{2+}/Fe^{3+} spectrum does have a larger peak at 1100 cm^{-1}, but the signal in the third transition is rather weak here.

The $S_2 \rightarrow S_3$ transition in H_2O and in D_2O

In the $S_2 \longrightarrow S_3$ transition in H_2O, three phases can be identified: a fast phase (20 µs; selected timecourses in figure A.7) which is followed by a phase (50 µs; selected timecourses in figure A.8) featuring almost exclusively amide I and II changes. Finally, the most prominent phase is visible around 400 µs (selected timecourses in figure A.9). In D_2O, only two phases around 80 µs and 850 µs can be identified.

The 20 µs phase in H_2O (table A.4) features the following negative (–) peaks: 1700 cm^{-1}, 1692 cm^{-1}, 1658 cm^{-1}, 1616 cm^{-1}, 1602 cm^{-1}, 1559 cm^{-1}, 1223 cm^{-1}, 1182 cm^{-1}, 1144 cm^{-1}, 1110 cm^{-1}, and 1094 cm^{-1}. Positive peaks can be found at 1669 cm^{-1}, 1622 cm^{-1}, and 1451 cm^{-1}. Some features (1692 cm^{-1}, 1559 cm^{-1}, 1209 cm^{-1}, 1182 cm^{-1}, 1110 cm^{-1}) show smaller intensities for the $S_0 \longrightarrow S_1$ transition; therefore binary oscillations are visible at those wavenumbers at this time constant. Only very small features can be found between 1450 cm^{-1} and 1230 cm^{-1}.

Three prominent amide I peaks at 1666 cm^{-1}(+), 1650 cm^{-1}(–), and 1639 cm^{-1}(+) can be assigned to the $S_3 \longrightarrow S_0$ transition.

The 50 µs phase in H_2O (table A.5) features mainly amide I and II peaks. They are located at 1679 cm^{-1}(–), 1664 cm^{-1}(+), 1651 cm^{-1}(+), 1576 cm^{-1}(–), 1550 cm^{-1}(–), and 1519 cm^{-1}(–). Additional smaller negative peaks can be found at 1387 cm^{-1}, 1212 cm^{-1}, and 1198 cm^{-1}.

The most prominent phase in H_2O shows a time constant of 390 µs (see table A.6). Prominent peaks in the decay associated spectrum (figure 5.55) can be seen at 1667 cm^{-1}(–) and 1676 cm^{-1}(+) (timecourse in figure A.9) in the amide I region; these two peaks take the

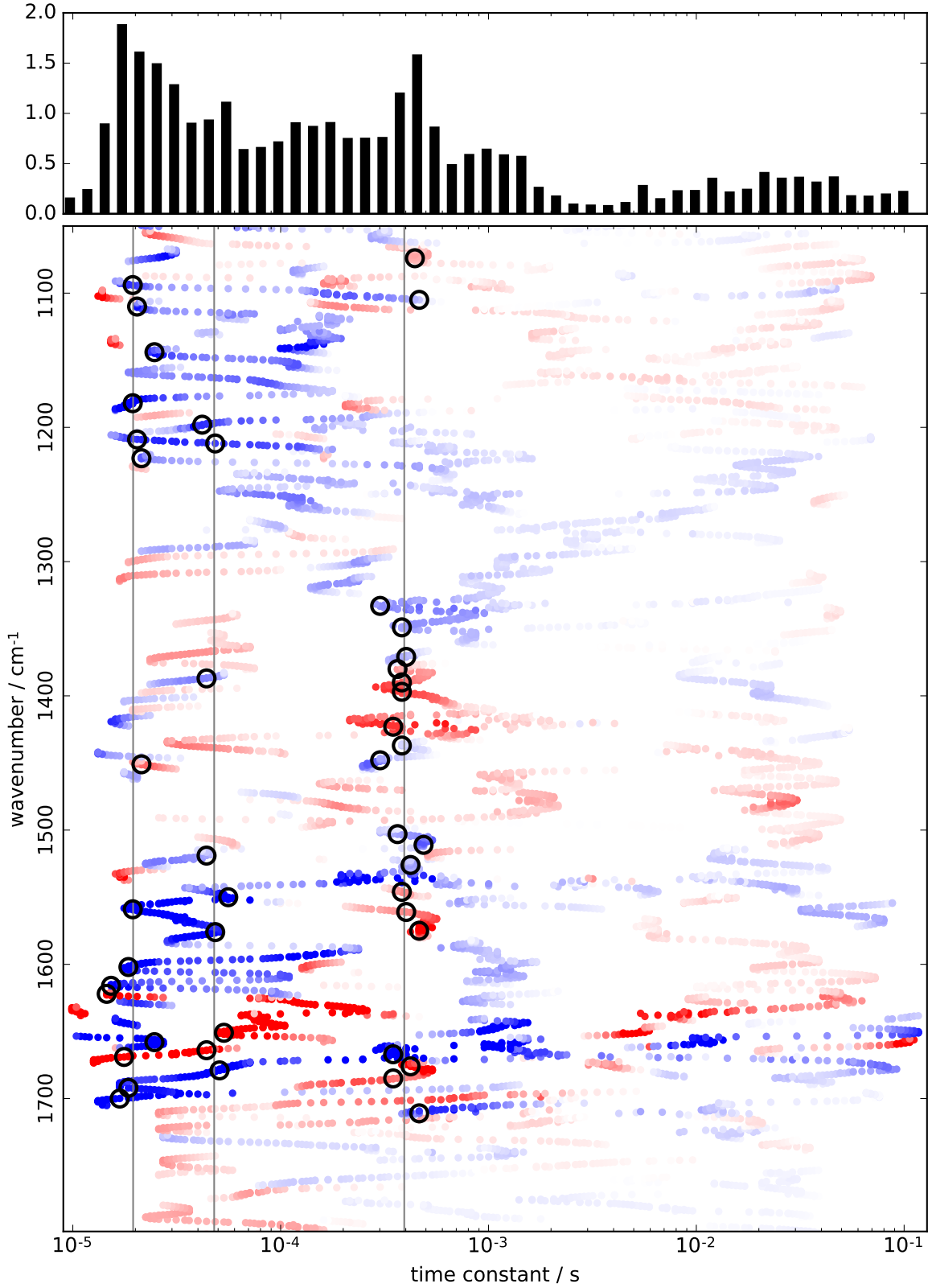

Figure 5.51.: H_2O time constants and their respective amplitudes as obtained through elastic net fitting for the $S_2 \longrightarrow S_3$ transition. Positive amplitudes are colored red, negative ones blue.

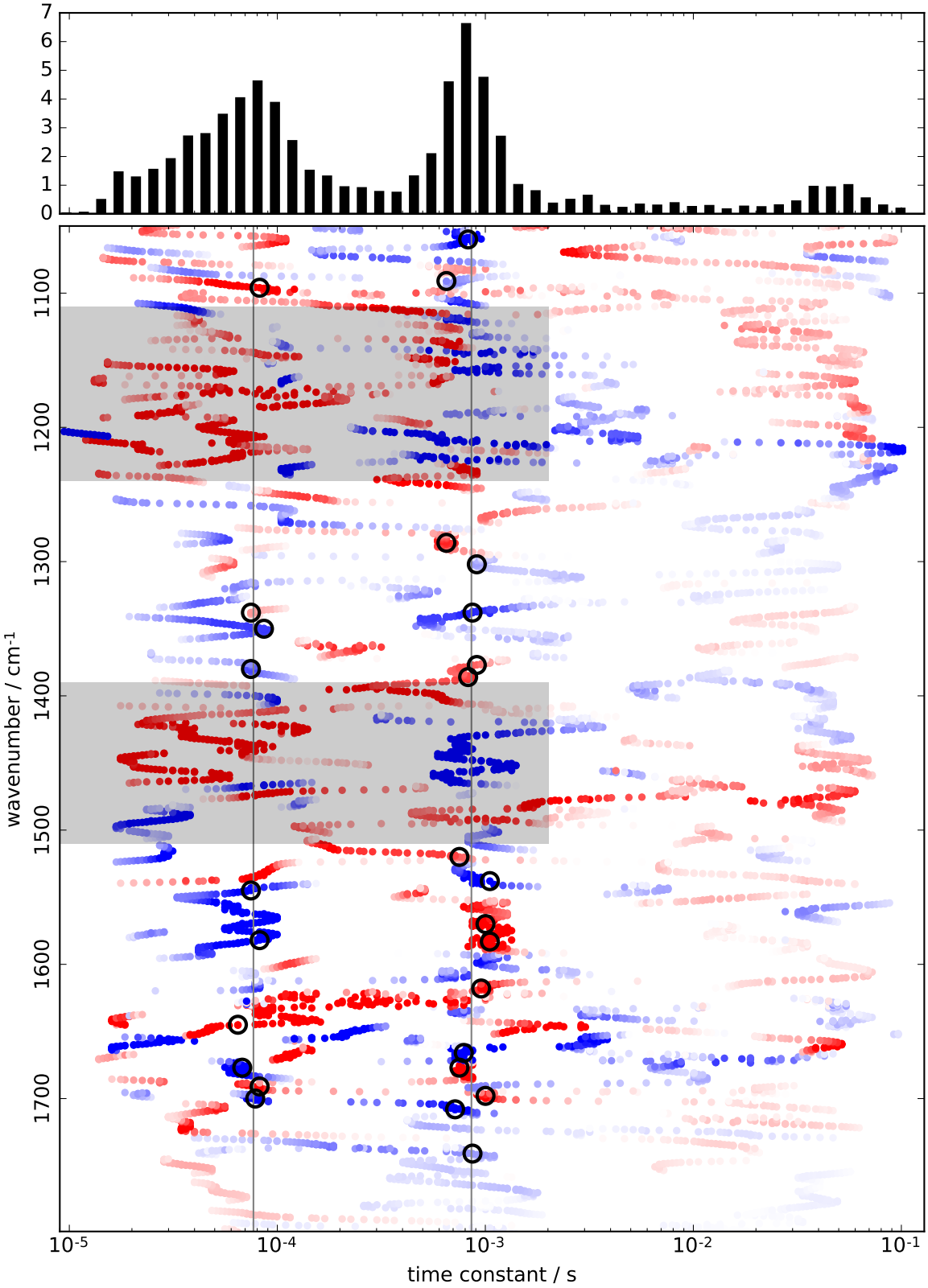

Figure 5.52.: D_2O time constants and their respective amplitudes as obtained through elastic net fitting for the $S_2 \longrightarrow S_3$ transition. Positive amplitudes are colored red, negative ones blue. Regions which are affected by the heat signal are grayed out.

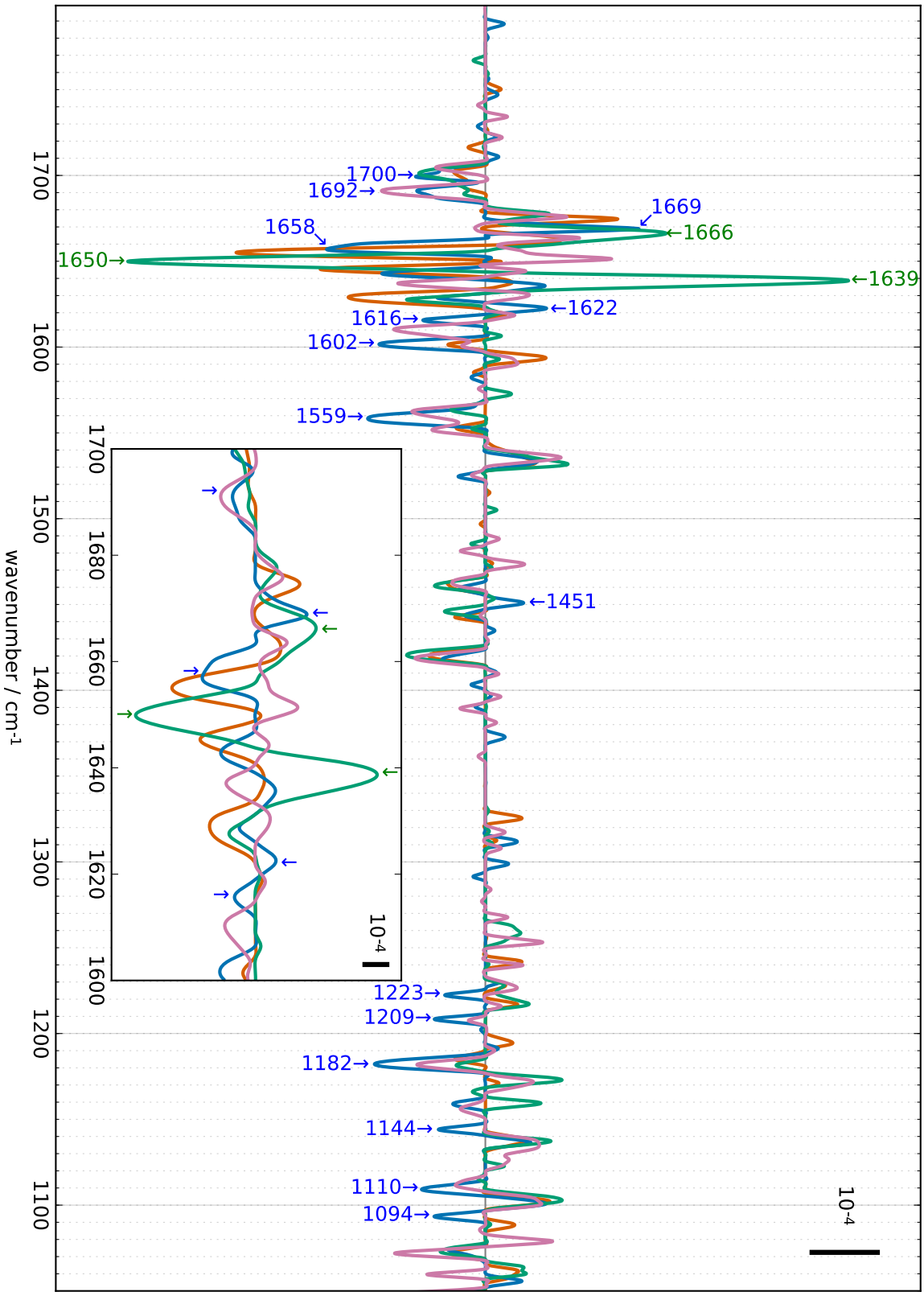

Figure 5.53.: Decay associated spectra (H_2O) obtained by multiplying the time constants obtained through a elastic net fit with a Gaussian function (5.4) where $\tau = 20\,\mu s$ and $\sigma = 6\,\mu s$. Orange: $S_1 \longrightarrow S_2$, aquamarine: $S_2 \longrightarrow S_3$, turquoise: $S_3 \longrightarrow S_0$, pink: $S_0 \longrightarrow S_1$.

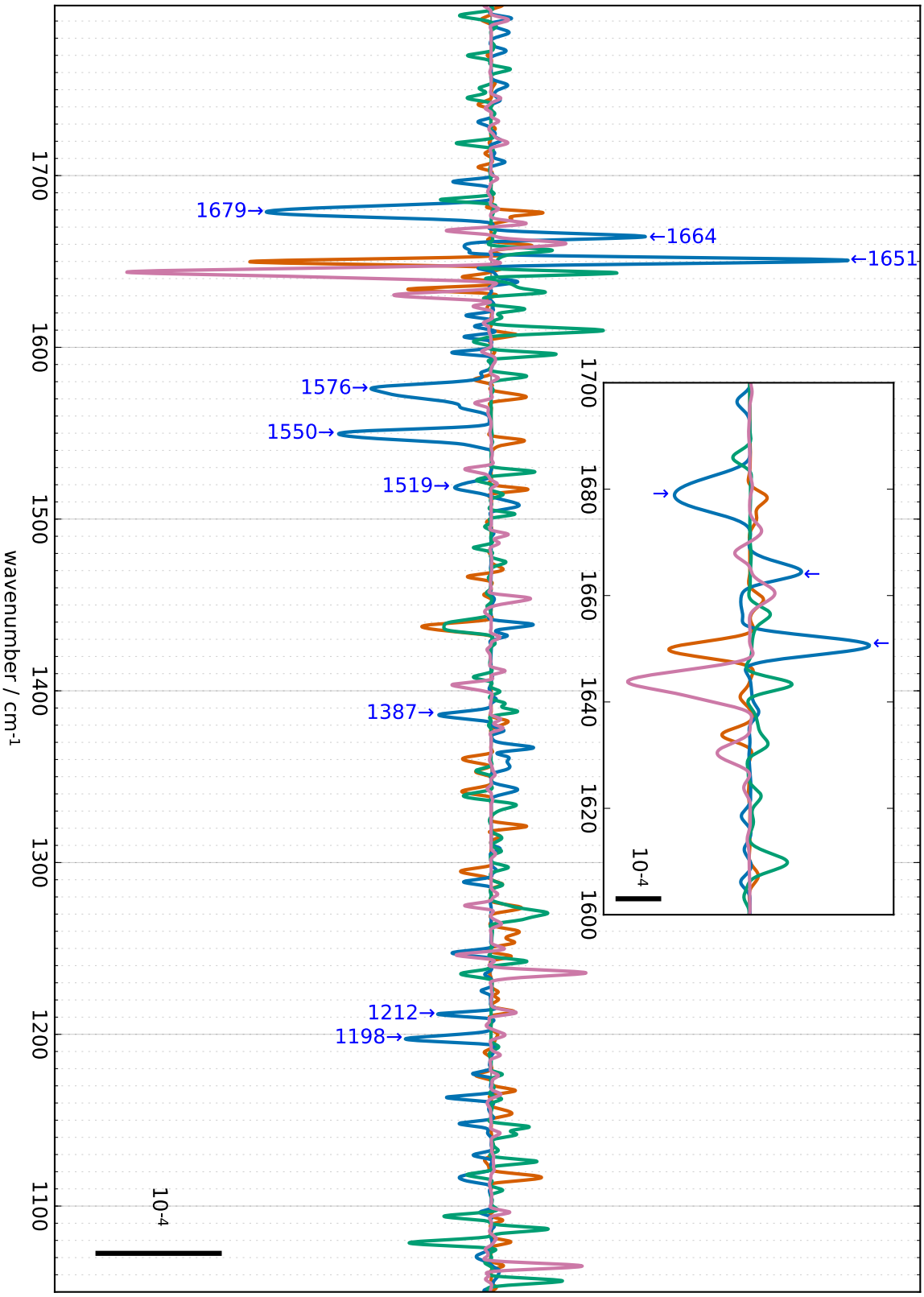

Figure 5.54.: Decay associated spectra (H_2O) obtained by multiplying the time constants obtained through a elastic net fit with a Gaussian function (5.4) where τ = 50 µs and σ = 10 µs. Orange: $S_1 \longrightarrow S_2$, aquamarine: $S_2 \longrightarrow S_3$, turquoise: $S_3 \longrightarrow S_0$, pink: $S_0 \longrightarrow S_1$.

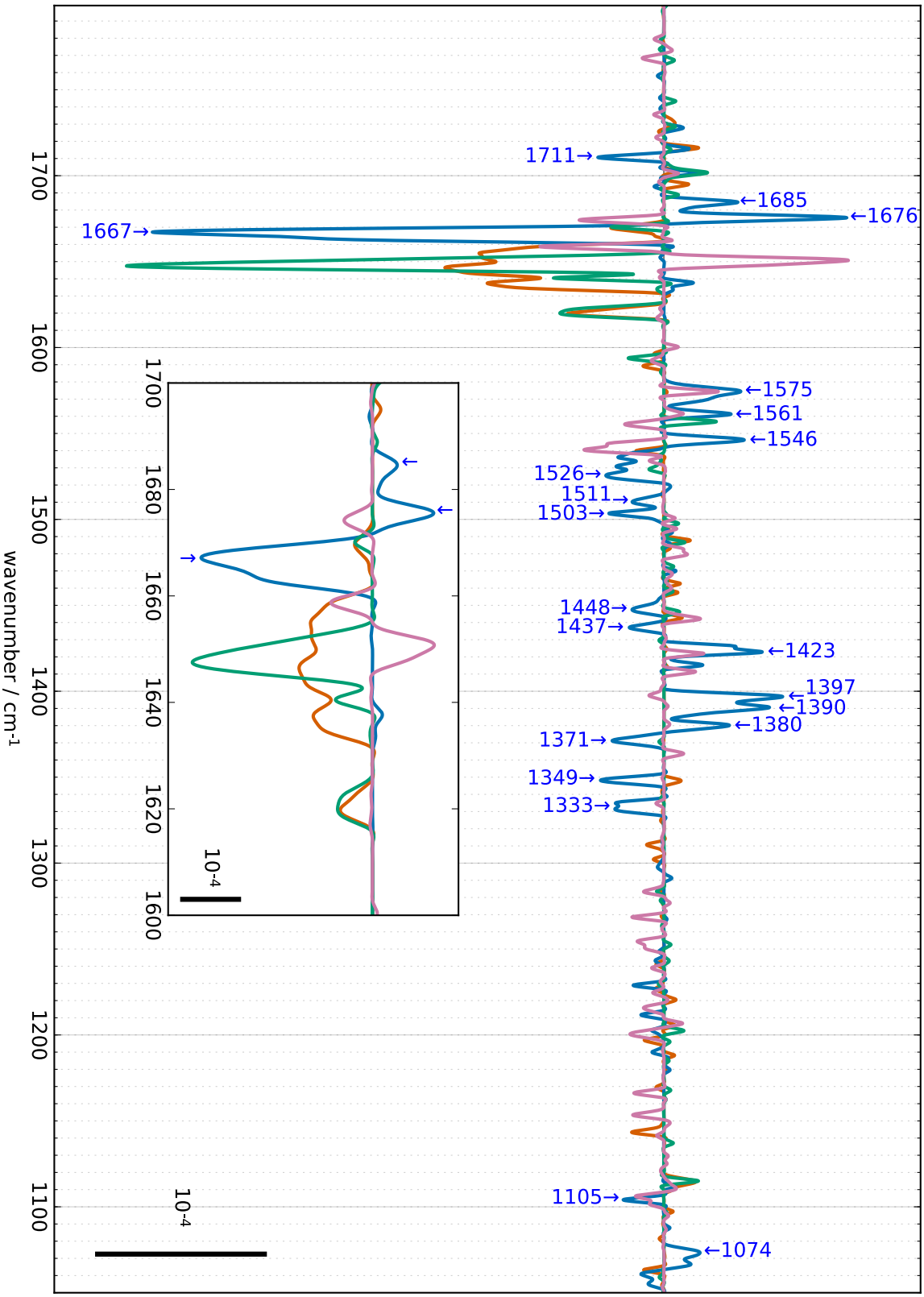

Figure 5.55.: Decay associated spectra (H_2O) obtained by multiplying the time constants obtained through a elastic net fit with a Gaussian function (5.4) where τ = 390 µs and σ = 60 µs. Orange: $S_1 \longrightarrow S_2$, aquamarine: $S_2 \longrightarrow S_3$, turquoise: $S_3 \longrightarrow S_0$, pink: $S_0 \longrightarrow S_1$.

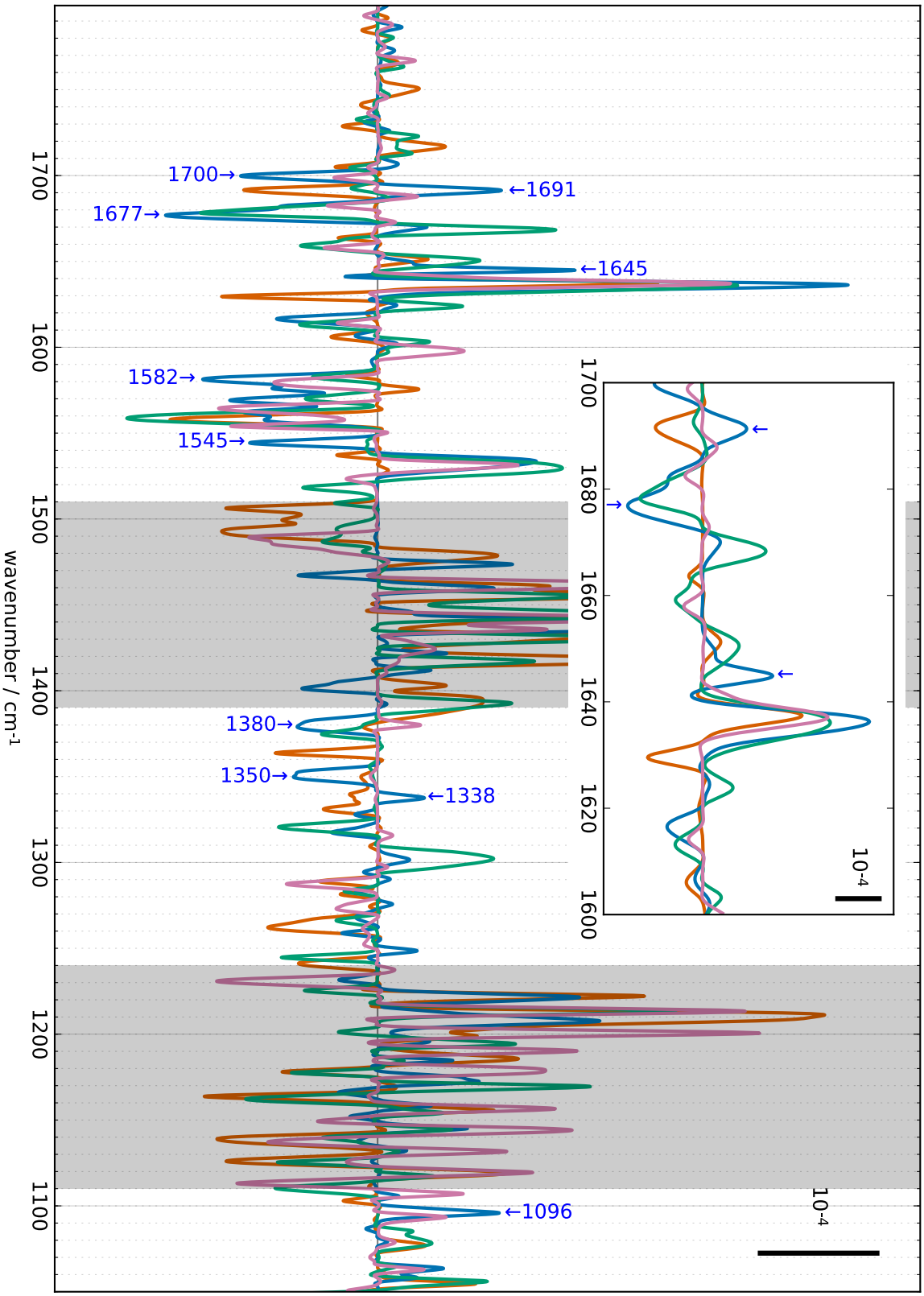

Figure 5.56.: Decay associated spectra (D_2O) obtained by multiplying the time constants obtained through a elastic net fit with a Gaussian function (5.4) where $\tau = 80\,\mu s$ and $\sigma = 15\,\mu s$. Orange: $S_1 \longrightarrow S_2$, aquamarine: $S_2 \longrightarrow S_3$, turquoise: $S_3 \longrightarrow S_0$, pink: $S_0 \longrightarrow S_1$. Regions which are affected by the heat signal are grayed out.

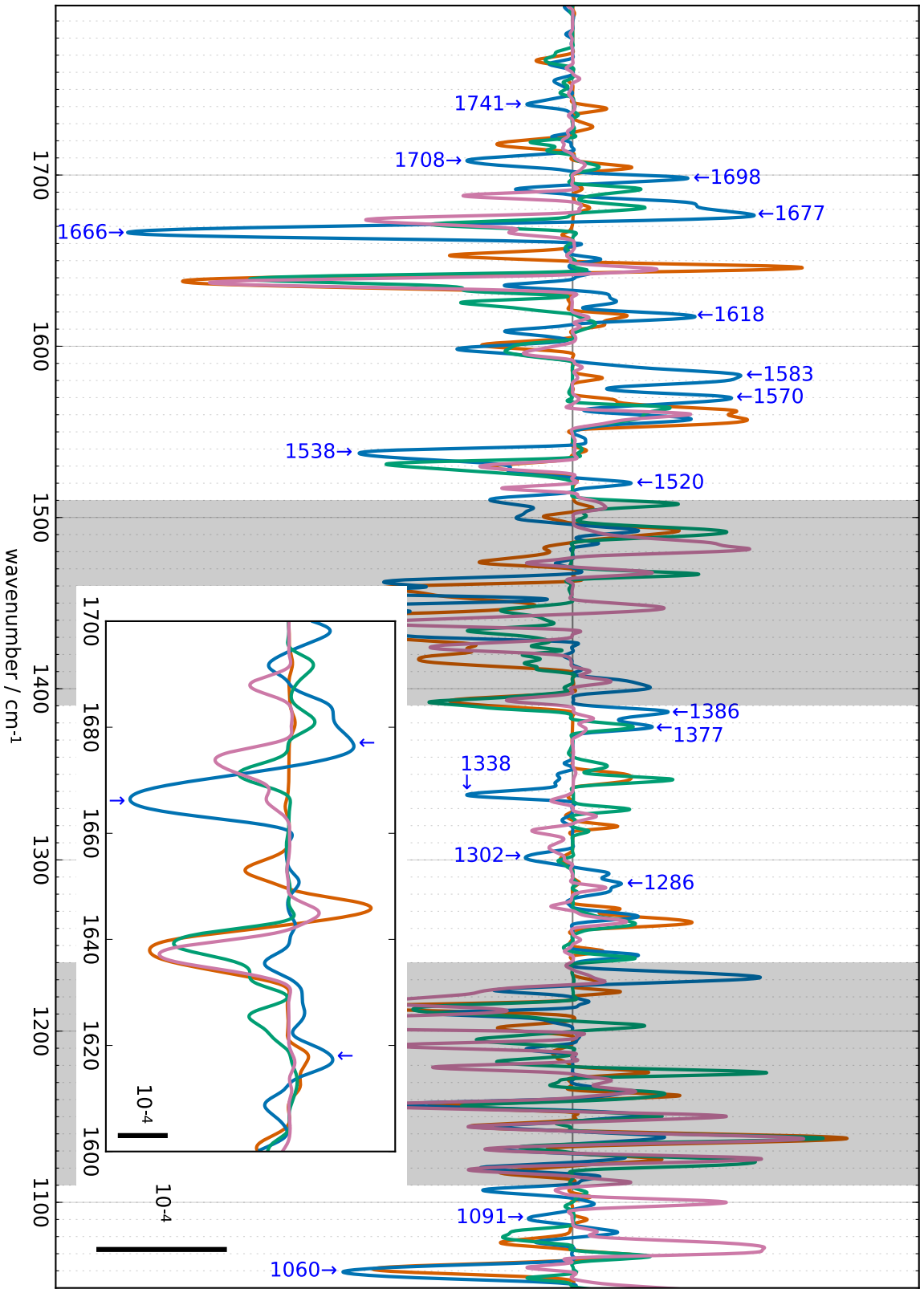

Figure 5.57.: Decay associated spectra (D_2O) obtained by multiplying the time constants obtained through a elastic net fit with a Gaussian function (5.4) where τ = 900 µs and σ = 200 µs. Orange: $S_1 \longrightarrow S_2$, aquamarine: $S_2 \longrightarrow S_3$, turquoise: $S_3 \longrightarrow S_0$, pink: $S_0 \longrightarrow S_1$. Regions which are affected by the heat signal are grayed out.

form of a derivative feature. Additional features can be found at 1711 cm^{-1}(−), 1685 cm^{-1} (+), 1575 cm^{-1}(+) (timecourse in figure A.9), 1561 cm^{-1}(+), 1546 cm^{-1}(+) (timecourse in figure A.9), 1526 cm^{-1}(−), 1511 cm^{-1}(−) (timecourse in figure A.9), 1503 cm^{-1}(−), 1448 cm^{-1}(−), 1437 cm^{-1}(−) (timecourse in figure A.9), 1423 cm^{-1}(+), 1397 cm^{-1}(+), 1390 cm^{-1}(+), 1380 cm^{-1} (+), 1371 cm^{-1}(−) (timecourse in figure A.9), 1349 cm^{-1}(−), 1333 cm^{-1}(−), 1105 cm^{-1}(−), 1074 cm^{-1} (+). There are features which also show intensity in the $S_0 \longrightarrow S_1$ transition for this time constant, that is at 1575 cm^{-1}(+), 1423 cm^{-1}(+), and 1105 cm^{-1}(−).

Some features in the 50 µs decay associated spectrum have counterparts with opposite sign in the 390 µs spectrum; a comparison is given in table 5.4. Only three features in the 50 µs decay associated spectrum do not have counterparts in the 390 µs decay associated spectrum: 1651 cm^{-1}(+), 1212 cm^{-1}(−), and 1198 cm^{-1}(−). Likewise, some features visible in the 20 µs decay associated spectrum are reversed in the 390 µs spectra. The 20 µs and 50 µs phases only share a common positive feature around 1667 cm^{-1} and do not mutually reverse any features.

20 µs spectrum	50 µs spectrum	390 µs spectrum
1692 cm^{-1}(−)		1685 cm^{-1}(+)
	1679 cm^{-1}(−)	1676 cm^{-1}(+)
1669 cm^{-1}(+)	1664 cm^{-1}(+)	1667 cm^{-1}(−)
	1576 cm^{-1}(−)	1575 cm^{-1}(+)
1559 cm^{-1}(−)		1561 cm^{-1}(+)
	1550 cm^{-1}(−)	1546 cm^{-1}(+)
	1519 cm^{-1}(−)	A “positive” feature flanked by negative features at 1511 cm^{-1} and 1526 cm^{-1}
1451 cm^{-1}(+)		1448 cm^{-1}(−)
	1387 cm^{-1}(−)	1390 cm^{-1}(+)

Table 5.4.: Comparison of $S_2 \longrightarrow S_3$ transition (H_2O) features in the 20 µs, 50 µs and 390 µs decay associated spectra (figures 5.53, 5.54 and 5.55).

In the $S_2 \longrightarrow S_3$ transition in D_2O, two phases can be indentified: a 80 µs phase (timecourses in figure A.10, page 259) is followed by a 860 µs phase (timecourses in figure A.11, page 260). The decay associated spectra of these two phases are shown in figures 5.56 (p. 148) and 5.57 (p. 149). All time constants for the wavenumbers which are marked in the decay associated spectra and in the lifetime maps are shown in tables A.7 (p. 254) and A.8 (p. 255).

In the 80 µs phase (fig. 5.56, p. 148), the following features can be identified: 1700 cm^{-1}(−) (timecourse in figure A.10), 1691 cm^{-1}(+) (timecourse in figure A.10), 1677 cm^{-1}(−) (timecourse in figure A.10), 1645 cm^{-1}(+), 1582 cm^{-1}(−) (timecourse in figure A.10), 1545 cm^{-1}

(–) (timecourse in figure A.10), 1380 cm^{-1}(–) (timecourse in figure A.10), 1350 cm^{-1}(–), 1338 cm^{-1}(+), and 1096 cm^{-1}(+).

In the 860 µs phase (fig. 5.57, p. 149), the following features can be identified: 1741 cm^{-1} (–), 1708 cm^{-1}(–), 1698 cm^{-1}(+), 1677 cm^{-1}(+) (timecourse in figure A.11), 1666 cm^{-1}(–), 1618 cm^{-1} (+), 1583 cm^{-1}(+), 1570 cm^{-1}(+) (timecourse in figure A.11), 1538 cm^{-1}(–), 1520 cm^{-1}(+) (timecourse in figure A.11), 1386 cm^{-1}(+), 1377 cm^{-1}(+), 1338 cm^{-1}(–) (timecourse in figure A.11), 1302 cm^{-1}(–) (timecourse in figure A.11), 1286 cm^{-1}(+) (timecourse in figure A.11), 1091 cm^{-1} (–), and 1060 cm^{-1}(–). At 1060 cm^{-1} a strong negative signal also appears for the $S_0 \longrightarrow S_1$ transition.

As shown above for the 50 µs and 390 µs phases in H_2O, there are many matching and reversed features in the 80 µs and 860 µs phases in D_2O. These are summarized in table 5.5. Additionally, in the decay associated spectra, a reversed contribution at 1400 cm^{-1} can be found. Because this wavenumber might be affected by the heat signal it has not been further considered here. Features in the 80 µs phase which are not reversed in the 860 µs phase can be found at 1645 cm^{-1}(+), 1545 cm^{-1}(–), 1350 cm^{-1}(–), and 1096 cm^{-1}(+). The fast change at 1645 cm^{-1} in D_2O which is not reversed in the slow phase may correspond to the fast change at 1651 cm^{-1} in H_2O which is not reversed as well.

80 µs spectrum (fig. 5.56)	860 µs spectrum (fig. 5.57)
1700 cm^{-1}(–) (fig. A.10, p. 259)	1698 cm^{-1}(+)
1691 cm^{-1}(+) (fig. A.10, p. 259)	1692 cm^{-1}(–) (weak, not marked)
1677 cm^{-1}(–) (fig. A.10, p. 259)	1677 cm^{-1}(+) (fig. A.11, p. 260)
1582 cm^{-1}(–) (fig. A.10, p. 259)	1583 cm^{-1}(+)
1380 cm^{-1}(–) (fig. A.10, p. 259)	1377 cm^{-1}(+)
1338 cm^{-1}(+)	1338 cm^{-1}(–)

Table 5.5.: Comparison of $S_2 \longrightarrow S_3$ transition (D_2O) features in the 80 µs and 860 µs decay associated spectra (figures 5.56 and 5.57). The referenced figures show the timecourses at the respective wavenumbers.

The two slowest phases in H_2O and D_2O (390 µs and 860 µs respectively) compare reasonably well. A comparison is given in table 5.6. In both cases there are three positive peaks between 1590 cm^{-1} and 1540 cm^{-1}. The three peaks in the D_2O dataset are 9 cm^{-1} upshifted compared to the H_2O features. Additionally, the 1333 cm^{-1}(–) may be upshifted to 1338 cm^{-1} (–) in D_2O. There are several features which compare quite well between 1510 cm^{-1} and 1395 cm^{-1} (regarding their positions, not their amplitudes); however, in the D_2O dataset this region is affected by the heat signal.

390 µs phase in H_2O	860 µs phase in D_2O
1711 cm^{-1}(−)	1708 cm^{-1}(−)
1702 cm^{-1}(+) (unmarked)	1698 cm^{-1}(+)
1685 cm^{-1}(+)	1684 cm^{-1}(+) (unmarked shoulder)
1676 cm^{-1}(+)	1677 cm^{-1}(+)
1667 cm^{-1}(−)	1666 cm^{-1}(−)
1575 cm^{-1}(+)	1583 cm^{-1}(+) (see text)
1561 cm^{-1}(+)	1570 cm^{-1}(+) (see text)
1546 cm^{-1}(+)	1558 cm^{-1}(+) (see text)
1538 cm^{-1}(−) (unmarked)	1538 cm^{-1}(−)
1526 cm^{-1}(−)	1527 cm^{-1}(−) (unmarked shoulder)
1503 cm^{-1}(−)	1500 cm^{-1}(−) (unmarked, see text)
1448 cm^{-1}(−)	1448 cm^{-1}(−) (unmarked, see text)
1437 cm^{-1}(−)	1437 cm^{-1}(−) (unmarked, see text)
1397 cm^{-1}(+)	1400 cm^{-1}(+) (unmarked, see text)
1390 cm^{-1}(+)	1386 cm^{-1}(+)
1380 cm^{-1}(+)	1377 cm^{-1}(+)
1349 cm^{-1}(−)	1350 cm^{-1}(−) (unmarked shoulder)
1333 cm^{-1}(−)	1338 cm^{-1}(−) (see text)
1060 cm^{-1}(−) (very small)	1060 cm^{-1}(−)

Table 5.6.: Comparison of 390 µs phase in H_2O and 860 µs phase in D_2O in the $S_2 \longrightarrow S_3$ transition.

The $S_3 \rightarrow S_0$ transition in H_2O and in D_2O

In both H_2O and D_2O, in the $S_3 \longrightarrow S_0$ transition three phases can be distinguished (figures 5.58 and 5.59, p. 154f.). The fastest phase (20 µs and 50 µs respectively) consists solely of amide changes: in H_2O, changes can be found at 1666 cm^{-1}(+), 1650 cm^{-1}(−), and 1639 cm^{-1} (+) (see figure 5.53 on page 145). In D_2O, two prominent peaks are found at 1658 cm^{-1}(−) and 1650 cm^{-1}(+). Smaller peaks are found at 1601 cm^{-1}(+) and 1542 cm^{-1}(−) (see figure 5.64 on page 160).

In H_2O, two slower phases show time constants of 140 µs and 2.9 ms respectively. In the 140 µs phase (figure 5.60 on page 156), features can be found at the following wavenumbers: 1740 cm^{-1}(+) (timecourse in figure A.12), 1673 cm^{-1}(−) (timecourse in figure A.12), 1660 cm^{-1}(−), 1637 cm^{-1}(−), 1589 cm^{-1}(−), 1570 cm^{-1}(−) (timecourse in figure A.12), 1562 cm^{-1} (+), 1360 cm^{-1}(+) (timecourse in figure A.12), 1248 cm^{-1}(+), 1181 cm^{-1}(+), 1159 cm^{-1}(−) (timecourse in figure A.12), 1152 cm^{-1}(+), 1070 cm^{-1}(+), and 1062 cm^{-1}(−) (timecourse in figure A.12). The features at 1660 cm^{-1} and 1562 cm^{-1} are overlapping with features of the $S_1 \longrightarrow S_2$ transition and therefore show a period-of-two pattern. There are two more features overlapping with $S_1 \longrightarrow S_2$ features at 1420 cm^{-1}(+) and 1452 cm^{-1}(−) (not marked in the decay associated spectrum 5.60).

The slowest phase of the $S_3 \longrightarrow S_0$ transition in H_2O shows a time constant of 2.9 ms (table A.11) and a very clear decay associated spectrum (figure 5.62 on page 158). Features in this spectrum are found at 1740 cm^{-1}(−), 1706 cm^{-1}(−) (timecourse in figure A.14), 1671 cm^{-1}(+), 1661 cm^{-1}(−), 1648 cm^{-1}(+), 1628 cm^{-1}(−), 1620 cm^{-1}(+) (timecourse in figure A.14), 1573 cm^{-1}(+), 1544 cm^{-1}(−) (timecourse in figure A.14), 1528 cm^{-1}(+), 1511 cm^{-1}(+) (timecourse in figure A.14), 1442 cm^{-1}(+) (timecourse in figure A.14), 1396 cm^{-1}(−) (timecourse in figure A.14), 1382 cm^{-1}(−), 1356 cm^{-1}(−), and 1296 cm^{-1}(−) (weak).

Some features in the 140 µs spectrum are reversed in the 2.9 ms spectrum; these are summarized in table 5.7. None of the 140 µs features below 1300 cm^{-1} have a counterpart in the 2.9 ms spectrum; in fact, there is almost no signal below 1250 cm^{-1} in the 2.9 ms spectrum.

The 500 µs phase of the $S_3 \longrightarrow S_0$ transition in D_2O is shown in figure 5.61. The following features can be found: 1706 cm^{-1}(+) (timecourse in figure A.13), 1674 cm^{-1}(−), 1652 cm^{-1}(−), 1636 cm^{-1}(−) (timecourse in figure A.13), 1615 cm^{-1}(+), 1573 cm^{-1}(−) (timecourse in figure A.13), 1555 cm^{-1}(+) (timecourse in figure A.13), 1540 cm^{-1}(+) (timecourse in figure A.13), 1352 cm^{-1}(+) (timecourse in figure A.13), 1333 cm^{-1}(+), 1105 cm^{-1}(+), and 1054 cm^{-1}(−).

In D_2O, the slowest phase of the $S_3 \longrightarrow S_0$ transition has a time constant of about 4 ms. From the lifetime map (figure 5.59) and the selected timecourses (figure A.15) it is found that there is some scatter in the time constant for different wavenumbers. The decay associated spectrum (figure 5.63) shows a plethora of features: 1740 cm^{-1}(+) (timecourse

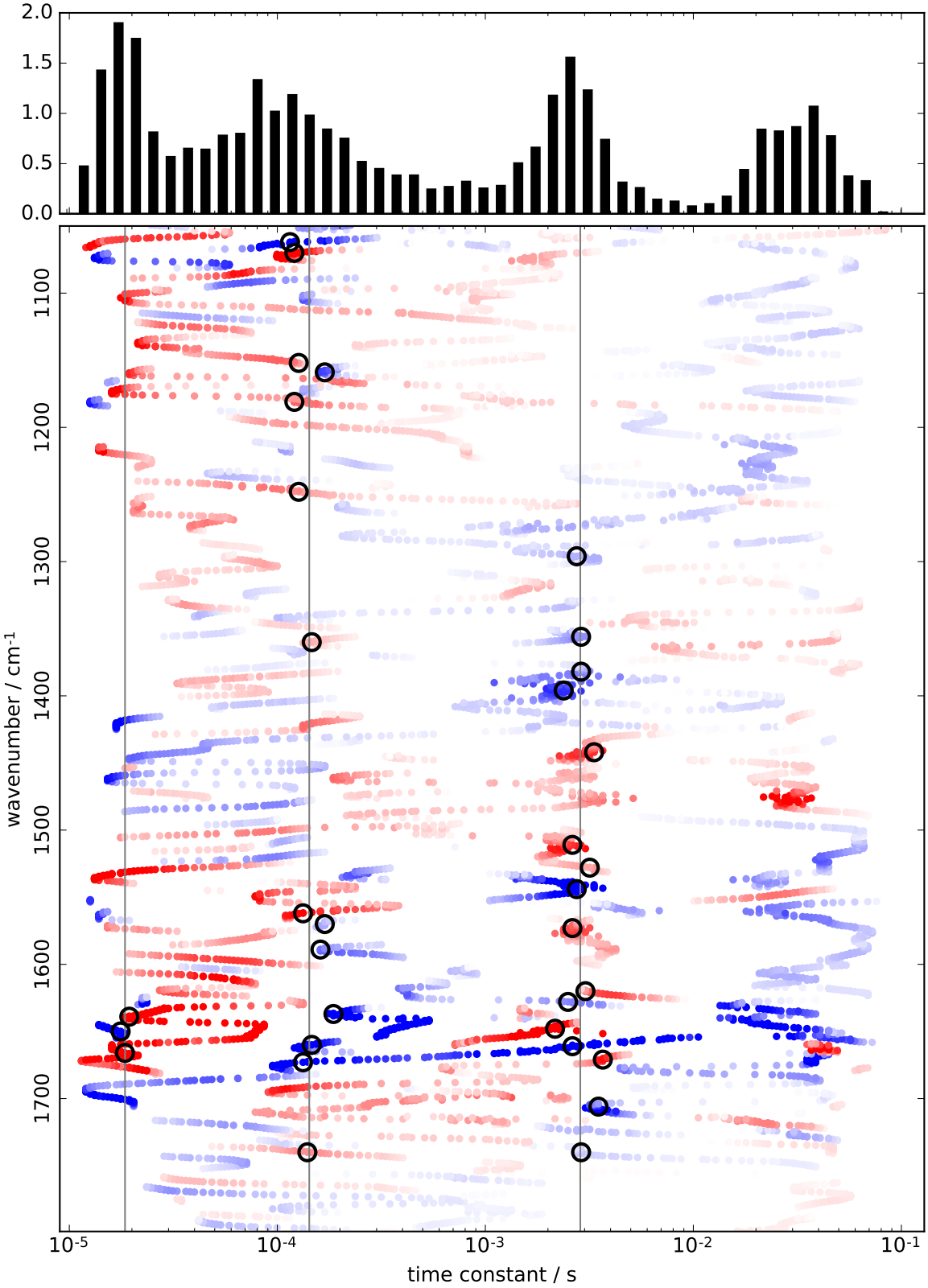

Figure 5.58.: H_2O time constants and their respective amplitudes as obtained through elastic net fitting for the $S_3 \longrightarrow S_0$ transition. Positive amplitudes are colored red, negative ones blue.

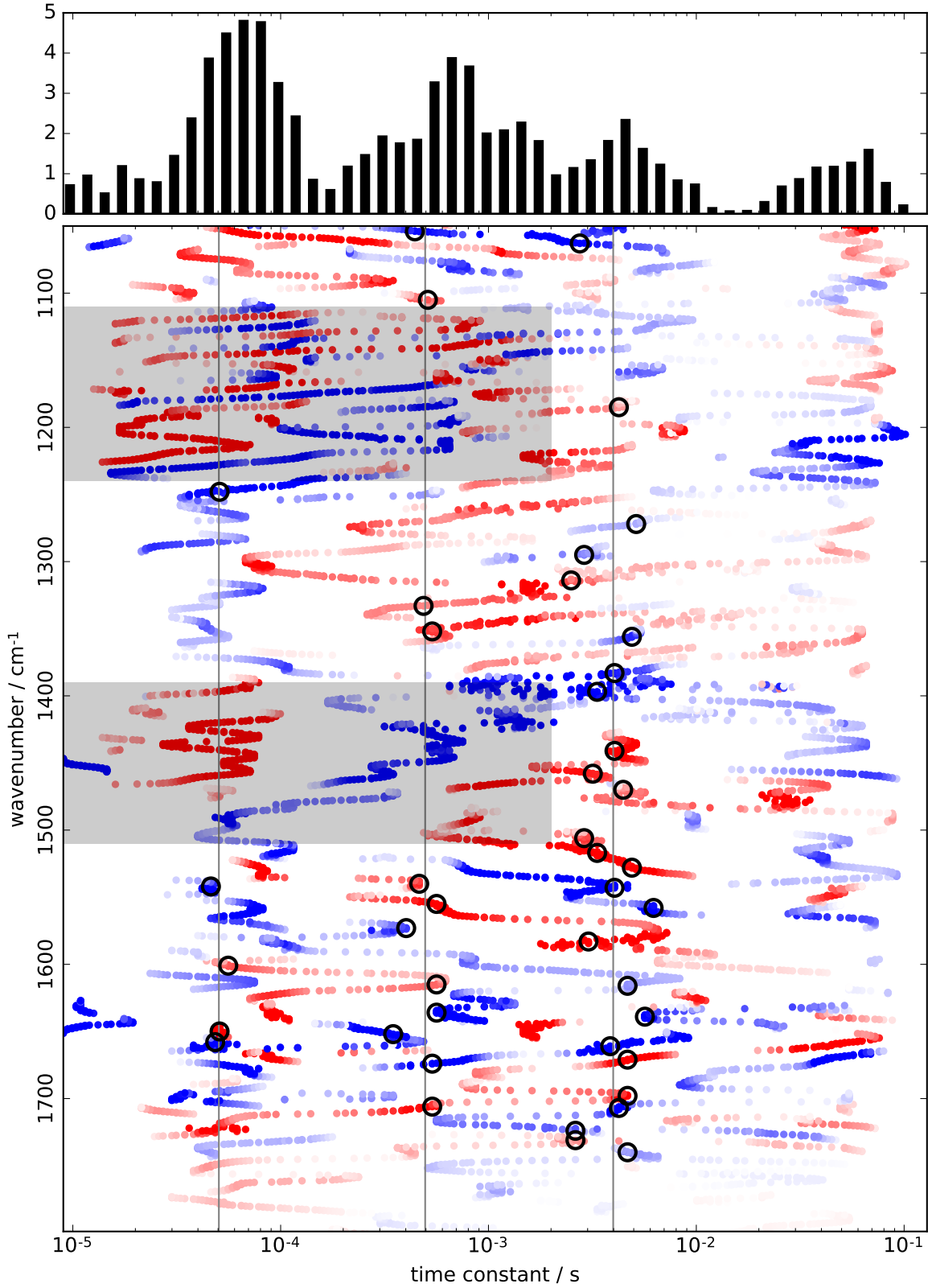

Figure 5.59.: D_2O time constants and their respective amplitudes as obtained through elastic net fitting for the $S_3 \longrightarrow S_0$ transition. Positive amplitudes are colored red, negative ones blue. Regions which are affected by the heat signal are grayed out.

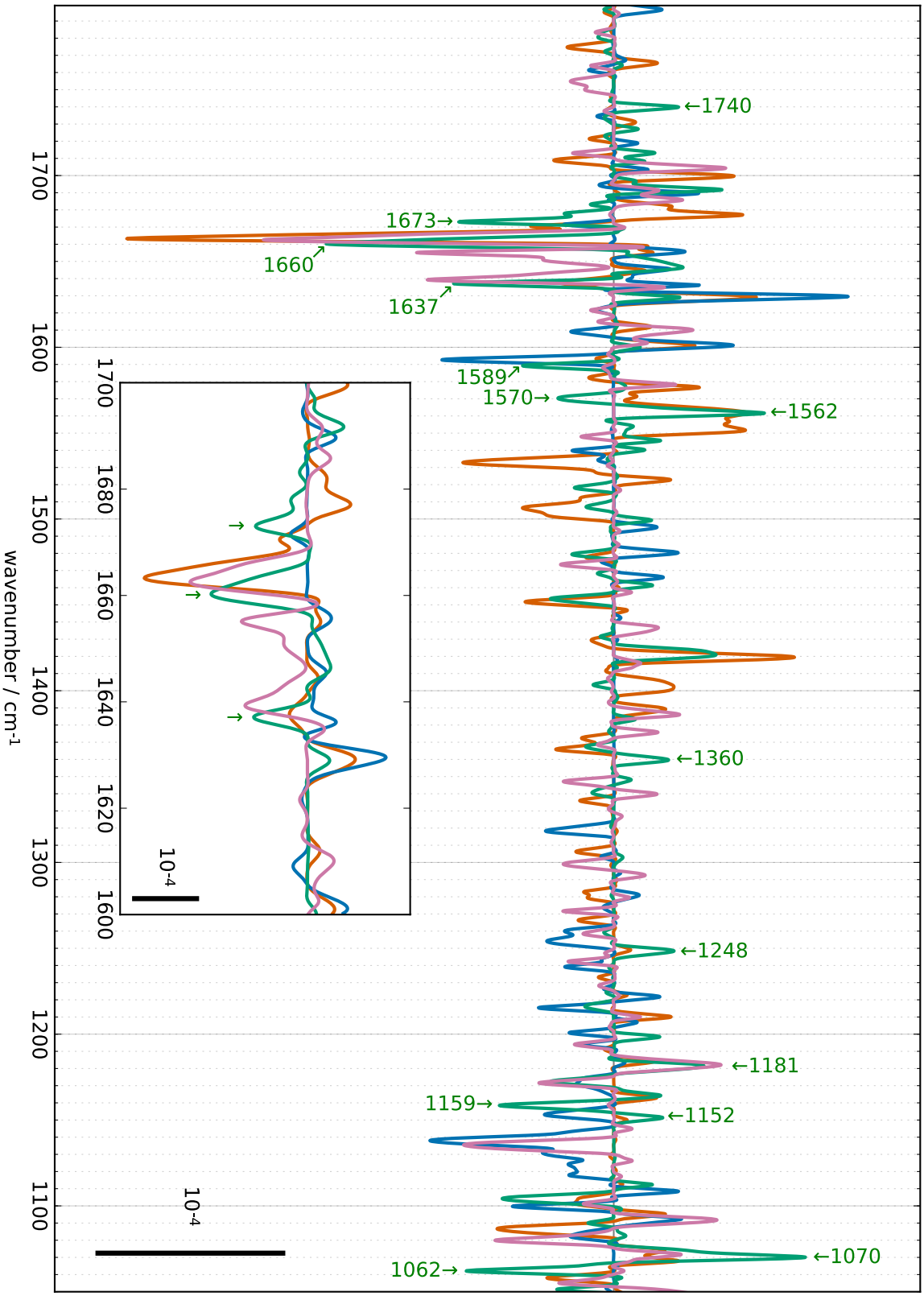

Figure 5.60.: Decay associated spectra (H_2O) obtained by multiplying the time constants obtained through a elastic net fit with a Gaussian function (5.4) where τ = 150 µs and σ = 30 µs. Orange: $S_1 \longrightarrow S_2$, aquamarine: $S_2 \longrightarrow S_3$, turquoise: $S_3 \longrightarrow S_0$, pink: $S_0 \longrightarrow S_1$.

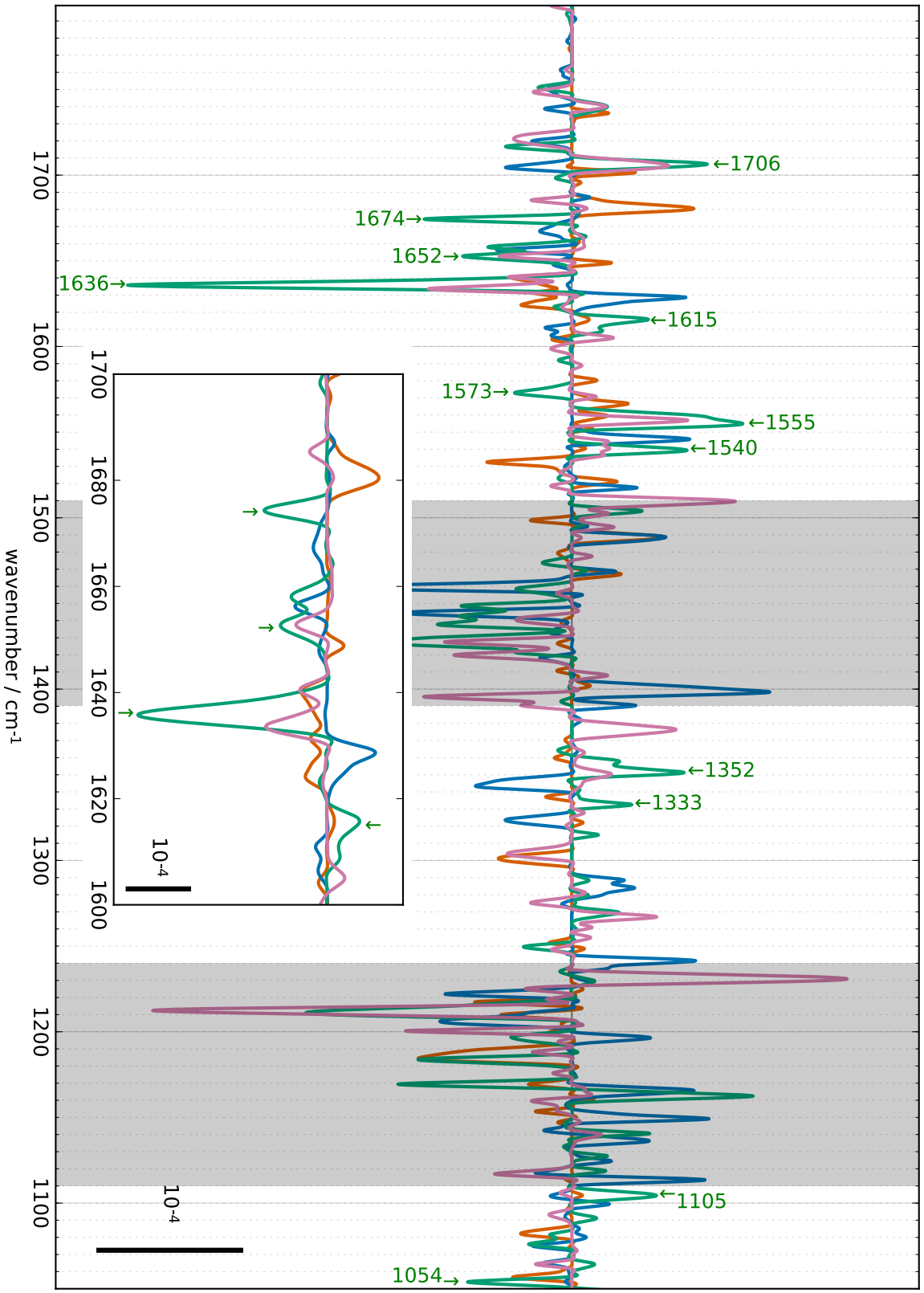

Figure 5.61.: Decay associated spectra (D_2O) obtained by multiplying the time constants obtained through a elastic net fit with a Gaussian function (5.4) where τ = 500 µs and σ = 100 µs. Orange: $S_1 \longrightarrow S_2$, aquamarine: $S_2 \longrightarrow S_3$, turquoise: $S_3 \longrightarrow S_0$, pink: $S_0 \longrightarrow S_1$. Regions which are affected by the heat signal are grayed out.

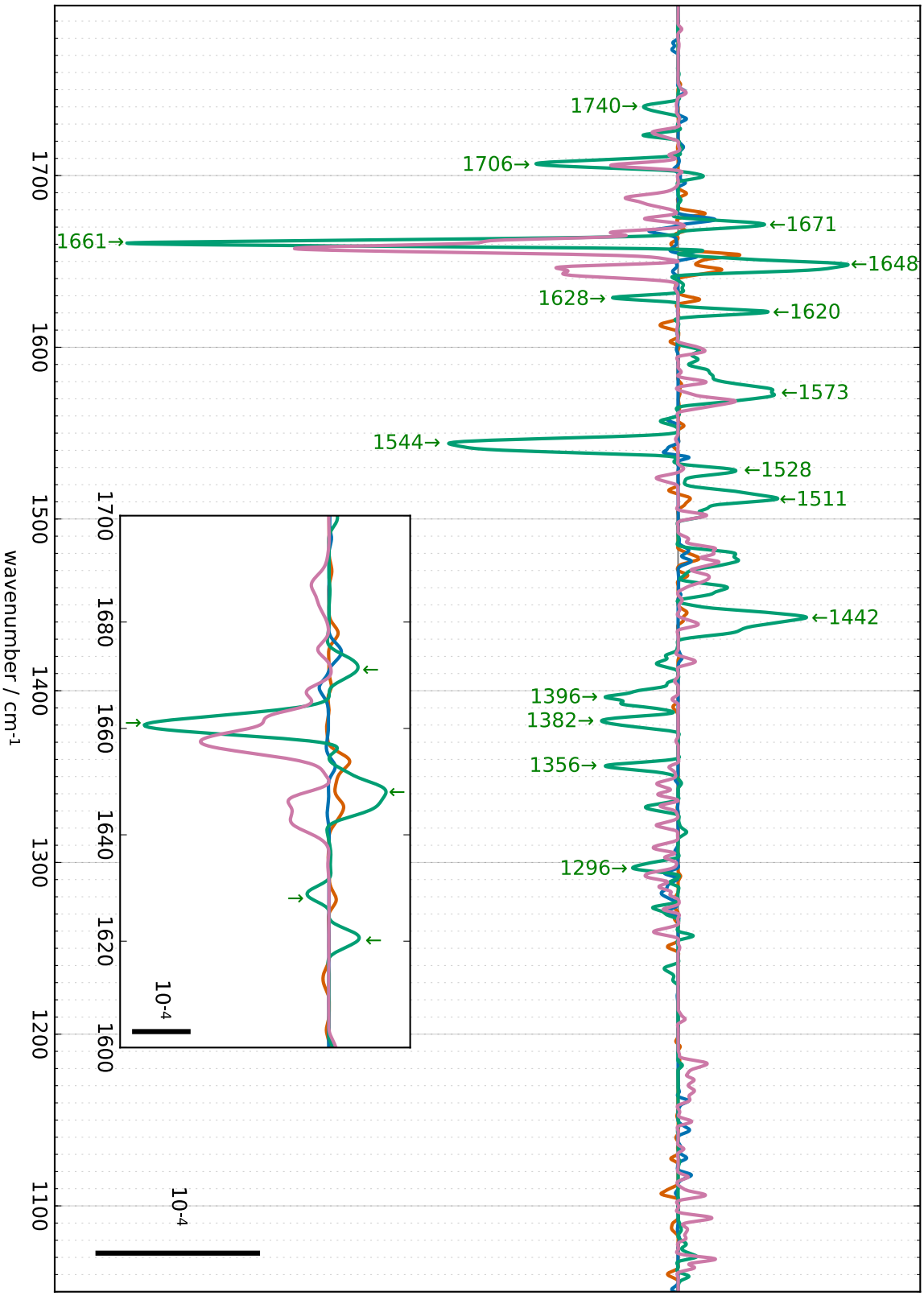

Figure 5.62.: Decay associated spectra (H_2O) obtained by multiplying the time constants obtained through a elastic net fit with a Gaussian function (5.4) where $\tau = 3\,\text{ms}$ and $\sigma = 600\,\mu\text{s}$. Orange: $S_1 \longrightarrow S_2$, aquamarine: $S_2 \longrightarrow S_3$, turquoise: $S_3 \longrightarrow S_0$, pink: $S_0 \longrightarrow S_1$. For a comparison with the D_2O data, see figure 5.65 on page 161.

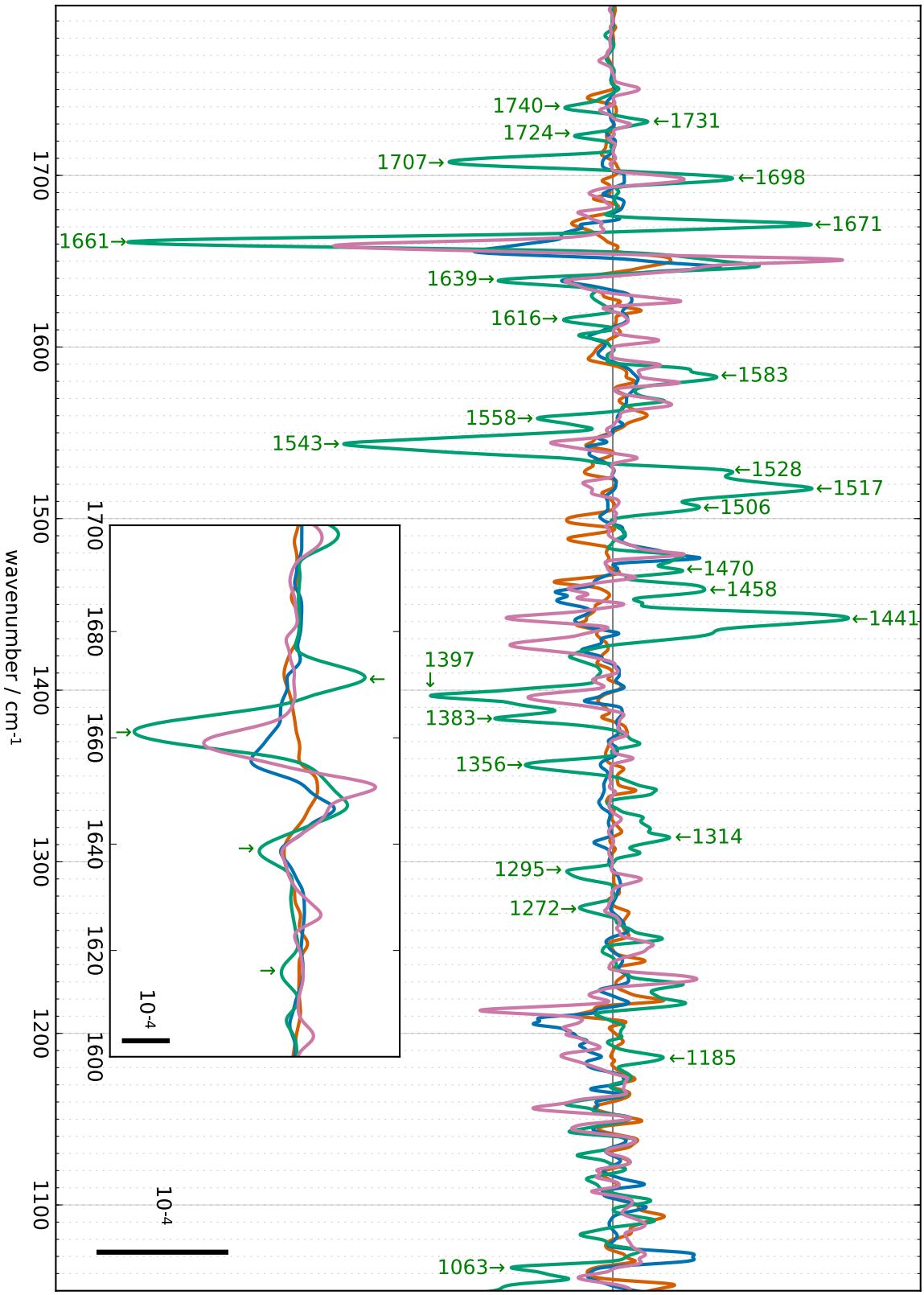

Figure 5.63.: Decay associated spectra (D_2O) obtained by multiplying the time constants obtained through a elastic net fit with a Gaussian function (5.4) where τ = 4 ms and σ = 1.5 ms. Orange: $S_1 \longrightarrow S_2$, aquamarine: $S_2 \longrightarrow S_3$, turquoise: $S_3 \longrightarrow S_0$, pink: $S_0 \longrightarrow S_1$. Regions which are affected by the heat signal are grayed out. For a comparison with the H_2O data, see figure 5.65 on page 161.

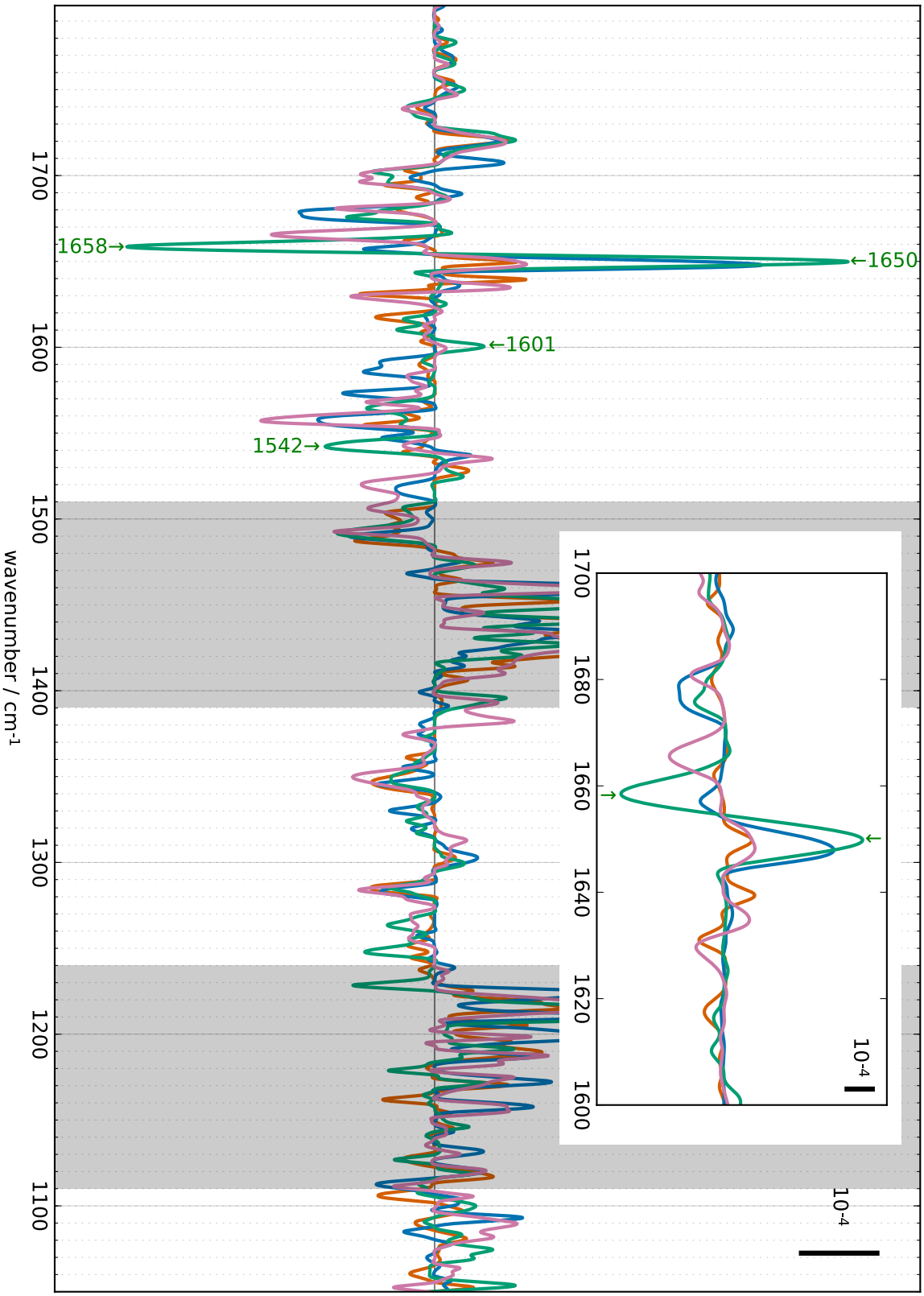

Figure 5.64.: Decay associated spectra (D_2O) obtained by multiplying the time constants obtained through a elastic net fit with a Gaussian function (5.4) where $\tau = 50\,\mu s$ and $\sigma = 15\,\mu s$. Orange: $S_1 \longrightarrow S_2$, aquamarine: $S_2 \longrightarrow S_3$, turquoise: $S_3 \longrightarrow S_0$, pink: $S_0 \longrightarrow S_1$. Regions which are affected by the heat signal are grayed out.

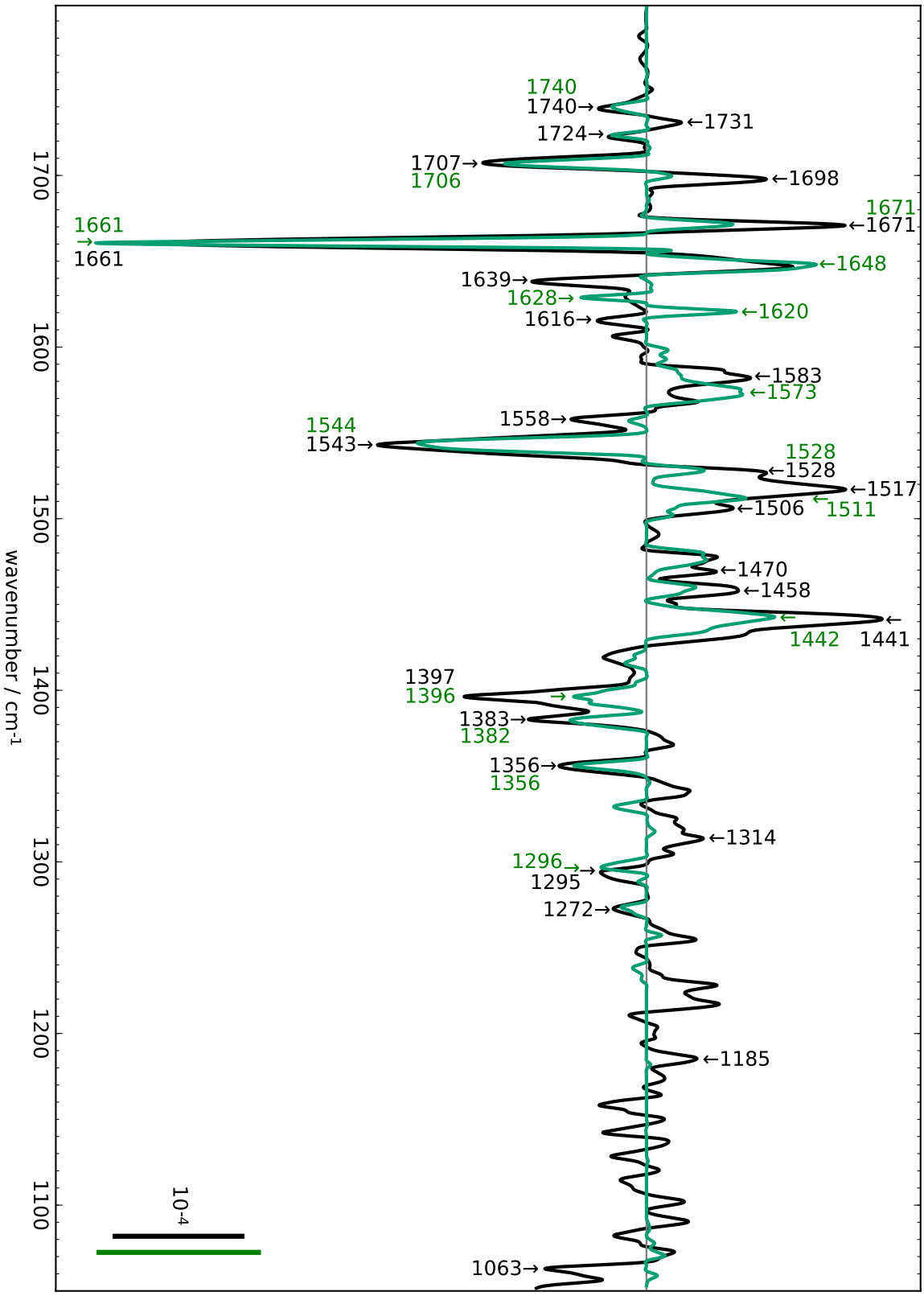

Figure 5.65.: Comparison of 2.9 ms phase in H_2O (turquoise) and 4 ms phase in D_2O (black) in the $S_3 \longrightarrow S_0$ transition. The marked wavenumbers are the same as in figure 5.62 (turquoise) and 5.63 (black). See also table 5.10.

140 µs H_2O phase (fig. 5.60)	2.9 ms H_2O phase (fig. 5.62)
1740 cm^{-1}(+) (fig. A.12)	1740 cm^{-1}(−)
1673 cm^{-1}(−) (fig. A.12)	1671 cm^{-1}(+)
1589 cm^{-1}(−)	1589 cm^{-1}(+), small
1570 cm^{-1}(−) (fig. A.12)	1573 cm^{-1}(+)
1360 cm^{-1}(+) (fig. A.12)	1356 cm^{-1}(−)

Table 5.7.: Comparison of $S_3 \longrightarrow S_0$ transition (H_2O) features in the 140 µs and 2.9 ms decay associated spectra (figures 5.60 and 5.62). The referenced figures show the timecourses at the respective wavenumbers.

500 µs D_2O phase (fig. 5.61)	4 ms D_2O phase (fig. 5.63)
1706 cm^{-1}(+) (fig. A.13)	1707 cm^{-1}(−)
1674 cm^{-1}(−)	1671 cm^{-1}(+) (fig. A.15)
1652 cm^{-1}(−)	~1648 cm^{-1}(+) (hidden behind $S_0 \longrightarrow S_1$ feature)
1615 cm^{-1}(+)	1616 cm^{-1}(−)
1573 cm^{-1}(−) (fig. A.13)	1568 cm^{-1}(+) (hidden behind $S_0 \longrightarrow S_1$ feature)
1555 cm^{-1}(+) (fig. A.13)	1558 cm^{-1}(−)
1540 cm^{-1}(+) (fig. A.13)	1543 cm^{-1}(−) (fig. A.15)
1352 cm^{-1}(+) (fig. A.13)	1356 cm^{-1}(−)

Table 5.8.: Comparison of $S_3 \longrightarrow S_0$ transition (D_2O) features in the 500 µs and 4 ms decay associated spectra (figures 5.61 and 5.63). The referenced figures show the timecourses at the respective wavenumbers.

140 µs H_2O phase	500 µs D_2O phase
1673 cm^{-1}(−)	1674 cm^{-1}(−)
1660 cm^{-1}(−)	1659 cm^{-1}(−) (small, not marked)
1637 cm^{-1}(−)	1636 cm^{-1}(−)
1570 cm^{-1}(−)	1573 cm^{-1}(−)
1562 cm^{-1}(+)	~1560 cm^{-1}(+) (as a shoulder of 1555 cm^{-1}(+))
1360 cm^{-1}(+)	1360 cm^{-1}(+) (as a small peak on a shoulder of 1352 cm^{-1}(+))

Table 5.9.: Features which are present in both 140 µs H_2O and 500 µs D_2O decay associated spectra in the $S_3 \longrightarrow S_0$ transition.

in figure A.15), 1731 cm^{-1}(−), 1707 cm^{-1}(−), 1698 cm^{-1}(+), 1671 cm^{-1}(+) (timecourse in figure A.15), 1671 cm^{-1}(+), 1661 cm^{-1}(−), 1639 cm^{-1}(−), 1616 cm^{-1}(−), 1583 cm^{-1}(+), 1558 cm^{-1}(−), 1543 cm^{-1}(−) (timecourse in figure A.15), 1528 cm^{-1}(+) (timecourse in figure A.15), 1517 cm^{-1}(+) (timecourse in figure A.15), 1506 cm^{-1}(+), 1470 cm^{-1}(+), 1458 cm^{-1}(+), 1441 cm^{-1}(+), 1397 cm^{-1}(−), 1383 cm^{-1}(−), 1356 cm^{-1}(−), 1314 cm^{-1}(+), 1295 cm^{-1}(−) (timecourse in figure A.15), 1272 cm^{-1}(−), 1185 cm^{-1}(+), and 1063 cm^{-1}(−).

Most of the features in the 500 µs (D_2O) spectrum (fig. 5.61) are reversed in the 4 ms spectrum (fig. 5.63); these reversals are shown in table 5.8. Features which are not reversed are a very large feature at 1636 cm^{-1}(−) (see also figure A.13 for the timecourse) and very small features at 1333 cm^{-1}, 1105 cm^{-1}, and 1054 cm^{-1}.

There are some features present in both the 140 µs phase in H_2O and the 500 µs phase in D_2O. These features are summarized in table 5.9. Another feature may be at 1740 cm^{-1} (+) which is clearly visible in the H_2O dataset, but somewhat obscure in the D_2O dataset. In the D_2O dataset, the same feature is visible in the $S_0 \longrightarrow S_1$ transition. It may be the case that the miss factor correction did not work at this wavenumber and time region; if the amplitude from the $S_0 \longrightarrow S_1$ transition were to be added to the $S_3 \longrightarrow S_0$ transition, the peak would closely resemble the one of the H_2O dataset. Moreover, this would fit to the fact that there is a negative feature 1740 cm^{-1}(−) in both H_2O and D_2O datasets in the later millisecond phase.

There are many features conserved in the H_2O and D_2O millisecond decay associated spectra. Table 5.10 and figure 5.65 summarize these features. There are basically no matching lines between 1550 cm^{-1} and 1645 cm^{-1}; this is the region which is also affected upon exchange of H_2O for D_2O (see the rapid-scan results in figure 5.9 on page 88). The differences could be explained by an upshift of the 1628 cm^{-1}(−) feature in H_2O to 1639 cm^{-1}(−) in D_2O, and the upshift of the 1573 cm^{-1}(+) feature in H_2O to 1583 cm^{-1}(+) in D_2O. These suggested upshifts both have a magnitude of 10 cm^{-1} (compare also with the results of the $S_2 \longrightarrow S_3$ transition which imply an upshift of 9 cm^{-1} in D_2O). Then the 1620 cm^{-1}(+) feature in H_2O and the 1616 cm^{-1}(−) feature in D_2O would be the only mismatched features, besides small features below 1300 cm^{-1} in D_2O which have no counterpart in H_2O.

2.9 ms phase in H_2O	4 ms phase in D_2O
1740 cm^{-1}(–)	1740 cm^{-1}(–)
1724 cm^{-1}(–) (not marked; hidden behind $S_0 \longrightarrow S_1$ feature)	1724 cm^{-1}(–)
1706 cm^{-1}(–)	1707 cm^{-1}(–)
1700 cm^{-1}(+) (very small)	1698 cm^{-1}(+)
1671 cm^{-1}(+)	1671 cm^{-1}(+)
1661 cm^{-1}(–)	1661 cm^{-1}(–)
1648 cm^{-1}(+)	1648 cm^{-1}(+) (not marked; hidden behind $S_0 \longrightarrow S_1$ feature)
1628 cm^{-1}(–)	1639 cm^{-1}(–)
1573 cm^{-1}(+)	1583 cm^{-1}(+)
1544 cm^{-1}(–)	1543 cm^{-1}(–)
1528 cm^{-1}(+)	1528 cm^{-1}(+)
1511 cm^{-1}(+)	1517 cm^{-1}(+)
1472 cm^{-1}(+) (not marked)	1470 cm^{-1}(+)
1459 cm^{-1}(+) (not marked)	1458 cm^{-1}(+)
1442 cm^{-1}(+)	1441 cm^{-1}(+)
1396 cm^{-1}(–)	1397 cm^{-1}(–)
1382 cm^{-1}(–)	1383 cm^{-1}(–)
1356 cm^{-1}(–)	1356 cm^{-1}(–)
1296 cm^{-1}(–)	1295 cm^{-1}(–)

Table 5.10.: Features which are present in both 2.9 ms H_2O and 4 ms D_2O decay associated spectra in the $S_3 \longrightarrow S_0$ transition.

The $S_0 \rightarrow S_1$ transition in H_2O and in D_2O

The $S_0 \longrightarrow S_1$ transition in H_2O features two phases (figure 5.66) with average time constants of 22 µs and 200 µs respectively (tables A.4 and A.5).

The signals of the 22 µs phase (figure 5.68) are relatively small and, as discussed for the 20 µs phase in the $S_2 \longrightarrow S_3$ transition, partially overlap with signals from the $S_2 \longrightarrow S_3$ transition. This indicates period-of-two oscillations. Signals in the $S_0 \longrightarrow S_1$ transitions can be found at 1734 cm^{-1}(+), 1721 cm^{-1}(+) (timecourse in figure A.16 on page 274), 1691 cm^{-1}(–), 1662 cm^{-1}(+) (timecourse in figure A.16 on page 274), 1651 cm^{-1}(+), 1637 cm^{-1}(–), 1610 cm^{-1}(–), 1562 cm^{-1}(–) (timecourse in figure A.16 on page 274), 1488 cm^{-1}(+) (timecourse in figure A.16 on page 274), 1381 cm^{-1}(+), 1252 cm^{-1}(+), 1239 cm^{-1}(+), 1173 cm^{-1}(+) (timecourse in figure A.16 on page 274), 1127 cm^{-1}(+), 1079 cm^{-1}(+) (timecourse in figure A.16 on page 274), 1071 cm^{-1}(–), and 1059 cm^{-1}(–).

The slower 200 µs phase in the H_2O $S_0 \longrightarrow S_1$ transition (figure 5.69) shows more distinct features: 1712 cm^{-1}(–), 1677 cm^{-1}(–), 1661 cm^{-1}(–), 1642 cm^{-1}(–), 1620 cm^{-1}(–) (timecourse in figure A.17 on page 275), 1577 cm^{-1}(+), 1547 cm^{-1}(–), 1439 cm^{-1}(+), 1388 cm^{-1}(+) (timecourse in figure A.17 on page 275), 1377 cm^{-1}(+) (timecourse in figure A.17 on page 275), 1325 cm^{-1}(+), 1228 cm^{-1}(–) (timecourse in figure A.17 on page 275), 1192 cm^{-1}(–), 1170 cm^{-1}(–) (timecourse in figure A.17 on page 275), 1138 cm^{-1}(–) (timecourse in figure A.17 on page 275), 1127 cm^{-1}(+), and 1078 cm^{-1}(–).

There are only two features which are reversed in the two phases: at 1662 cm^{-1}(+) / 1661 cm^{-1}(–) and at 1079 cm^{-1}(+) / 1078 cm^{-1}(–).

Figure 5.70 shows decay associated spectra with a time constant of 1 ms and will be discussed in section 6.7 on page 207.

The D_2O $S_0 \longrightarrow S_1$ transition can be decomposed into three phases (figure 5.67): a fast 30 µs phase (figure 5.71), a 190 µs phase which almost exclusively shows amide changes (figure 5.72), and a 330 µs phase (figure 5.73).

The 30 µs phase shows distinct features at 1750 cm^{-1}(+), 1721 cm^{-1}(+), 1679 cm^{-1}(–) (timecourse in figure A.18 on page 276), 1664 cm^{-1}(–), 1649 cm^{-1}(+), 1628 cm^{-1}(–), 1571 cm^{-1}(–), 1513 cm^{-1}(–) (timecourse in figure A.18 on page 276), 1388 cm^{-1}(+) (timecourse in figure A.18 on page 276), 1372 cm^{-1}(–), 1343 cm^{-1}(–) (timecourse in figure A.18 on page 276), 1330 cm^{-1}(–), 1310 cm^{-1}(+) (timecourse in figure A.18 on page 276), 1300 cm^{-1}(+), 1280 cm^{-1}(–) (timecourse in figure A.18 on page 276), 1086 cm^{-1}(+), and 1060 cm^{-1}(+).

The 190 µs phase shows comparably few signals in mostly amide I and II regions: 1665 cm^{-1}(+), 1646 cm^{-1}(–), 1628 cm^{-1}(–), 1620 cm^{-1}(–), 1550 cm^{-1}(–), and 1089 cm^{-1}(–). The timecourses at these wavenumbers are shown in figure A.19 on page 277.

On the other hand, the slowest phase (330 µs) shows almost no amide I signals. Fea-

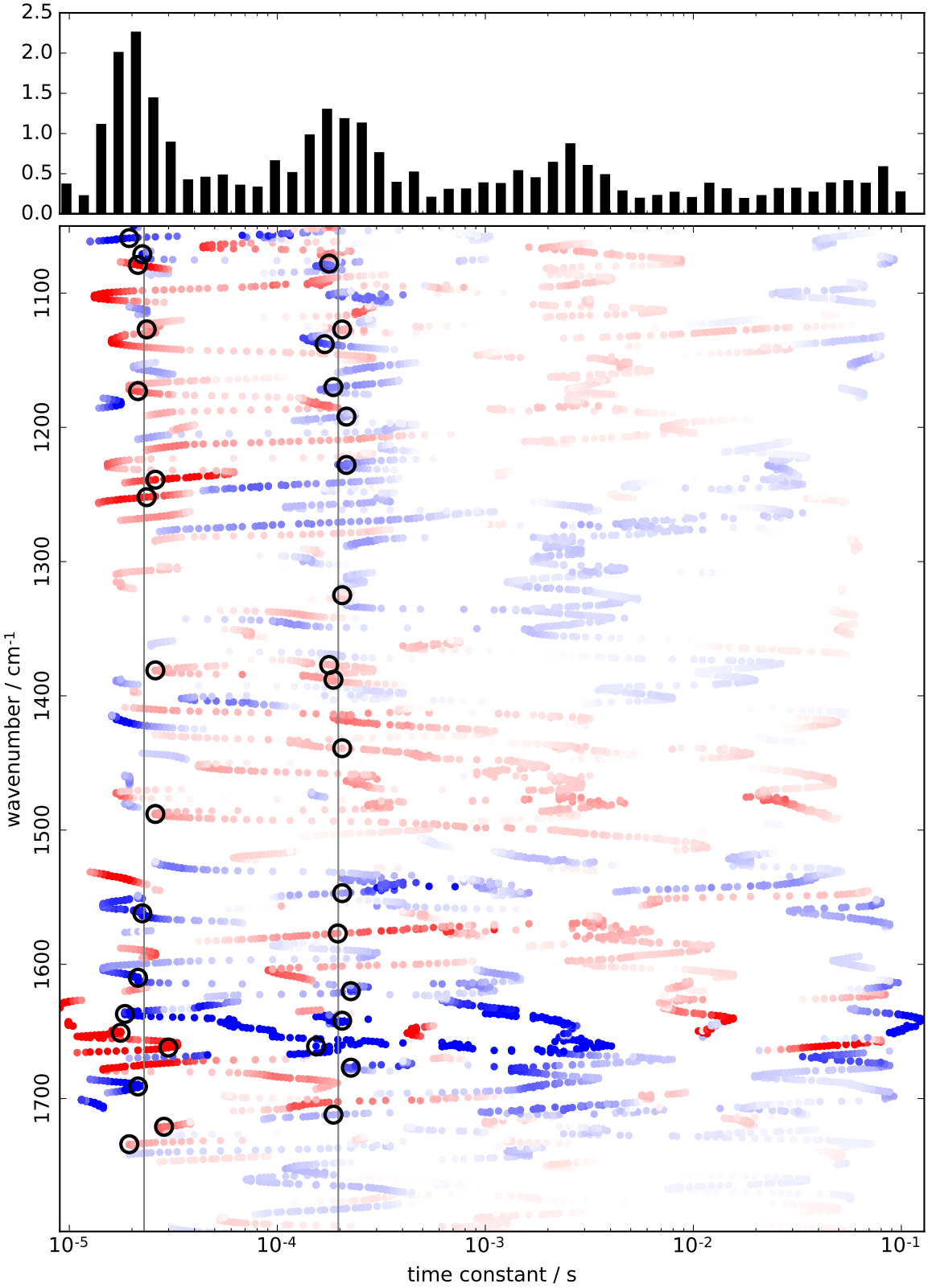

Figure 5.66.: H_2O time constants and their respective amplitudes as obtained through elastic net fitting for the $S_0 \rightarrow S_1$ transition. Positive amplitudes are colored red, negative ones blue.

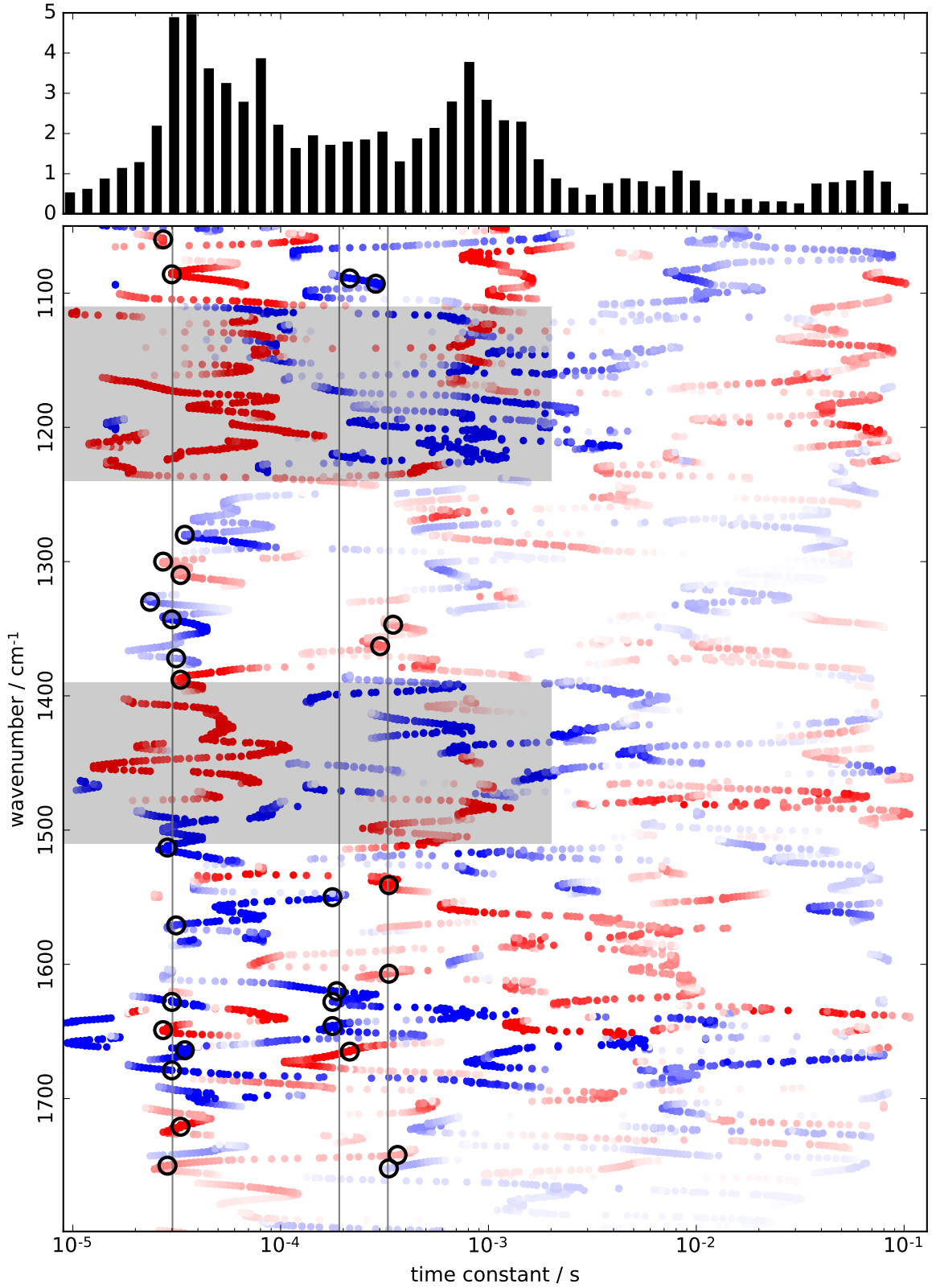

Figure 5.67.: D_2O time constants and their respective amplitudes as obtained through elastic net fitting for the $S_0 \longrightarrow S_1$ transition. Positive amplitudes are colored red, negative ones blue. Regions which are affected by the heat signal are grayed out.

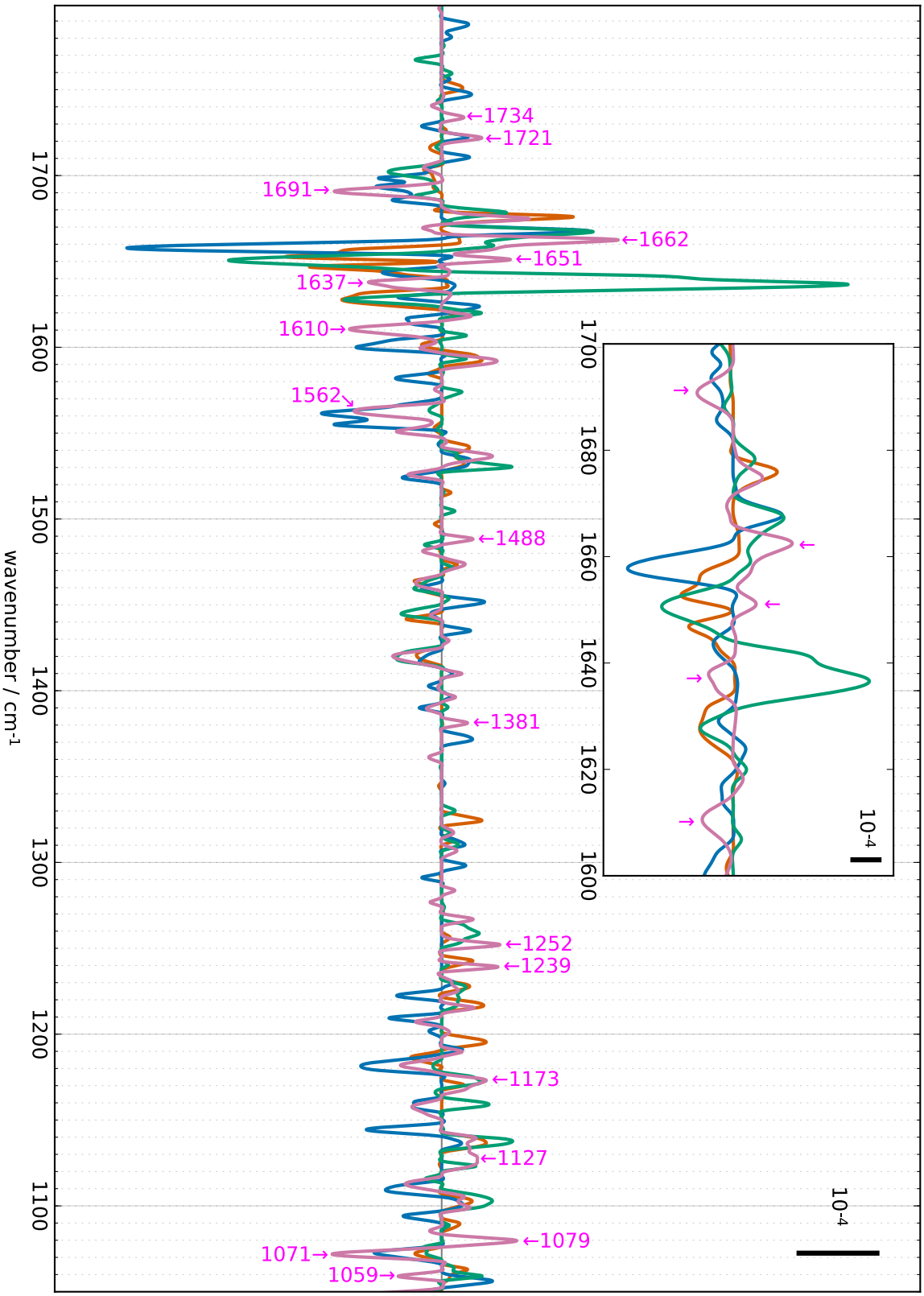

Figure 5.68.: Decay associated spectra (H_2O) obtained by multiplying the time constants obtained through a elastic net fit with a Gaussian function (5.4) where $\tau = 25\,\mu s$ and $\sigma = 6\,\mu s$. Orange: $S_1 \longrightarrow S_2$, aquamarine: $S_2 \longrightarrow S_3$, turquoise: $S_3 \longrightarrow S_0$, pink: $S_0 \longrightarrow S_1$.

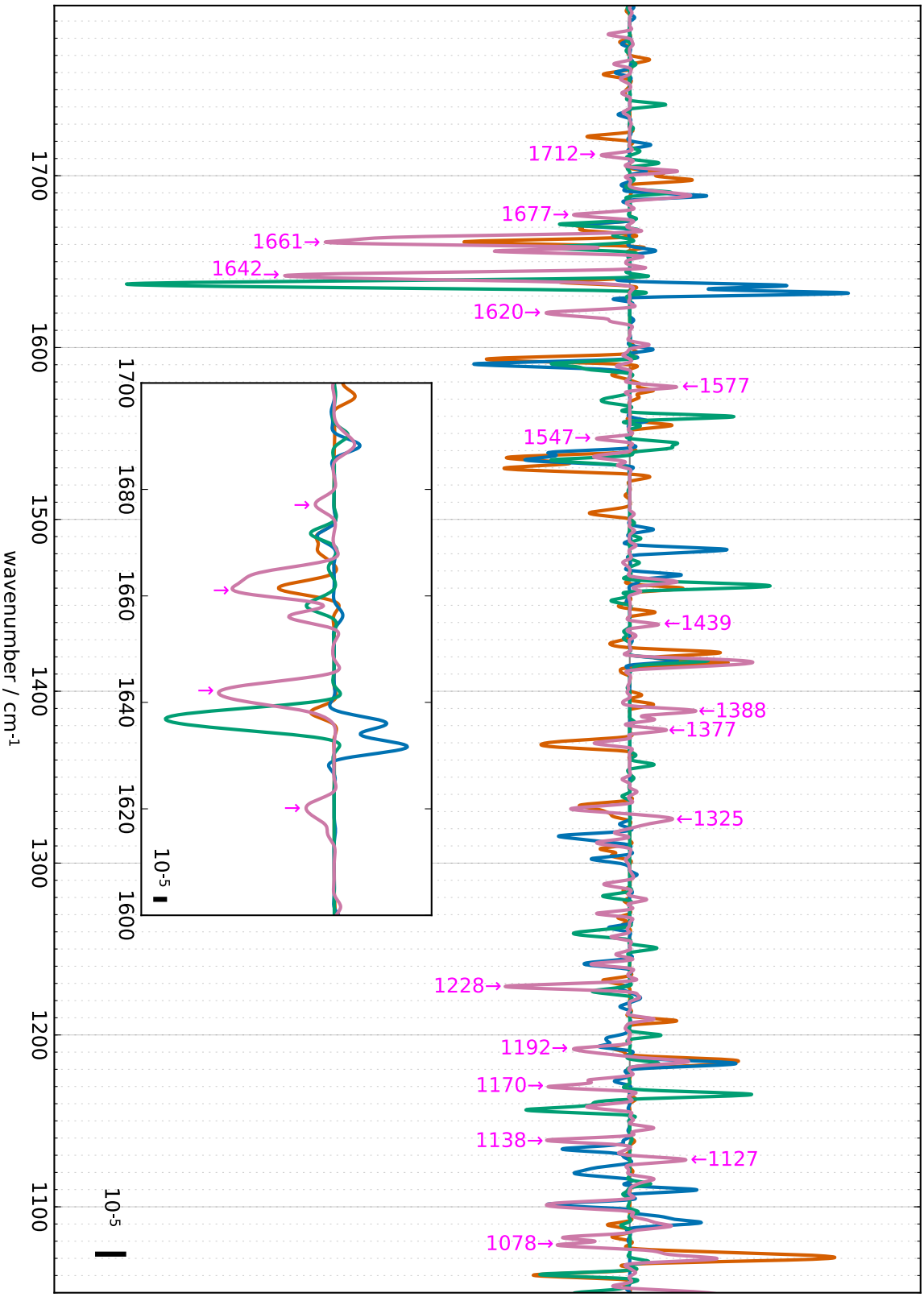

Figure 5.69.: Decay associated spectra (H_2O) obtained by multiplying the time constants obtained through a elastic net fit with a Gaussian function (5.4) where τ = 200 µs and σ = 20 µs. Orange: $S_1 \longrightarrow S_2$, aquamarine: $S_2 \longrightarrow S_3$, turquoise: $S_3 \longrightarrow S_0$, pink: $S_0 \longrightarrow S_1$.

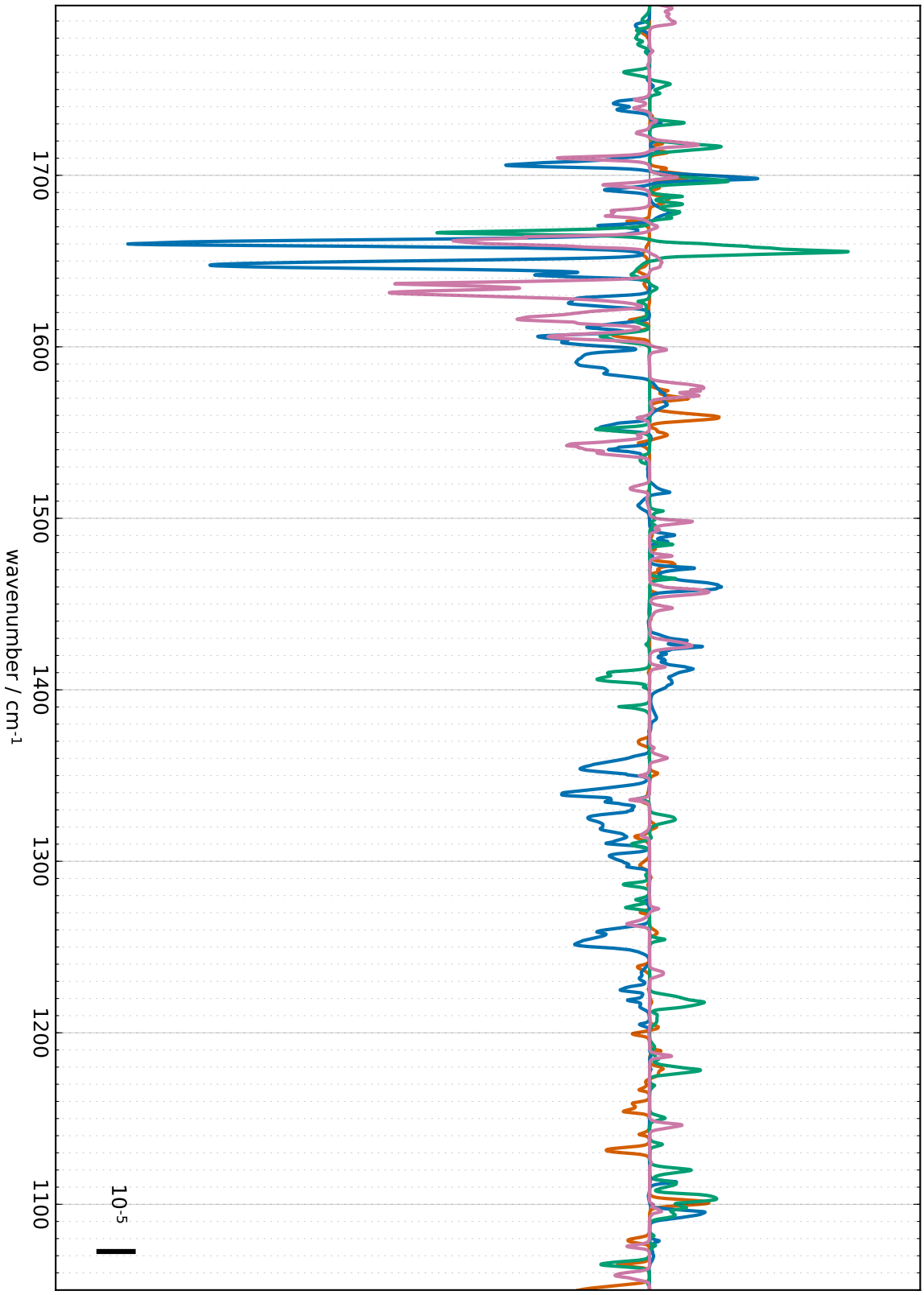

Figure 5.70.: Decay associated spectra (H_2O) obtained by multiplying the time constants obtained through a elastic net fit with a Gaussian function (5.4) where τ = 1 ms and σ = 200 µs. Orange: $S_1 \longrightarrow S_2$, aquamarine: $S_2 \longrightarrow S_3$, turquoise: $S_3 \longrightarrow S_0$, pink: $S_0 \longrightarrow S_1$.

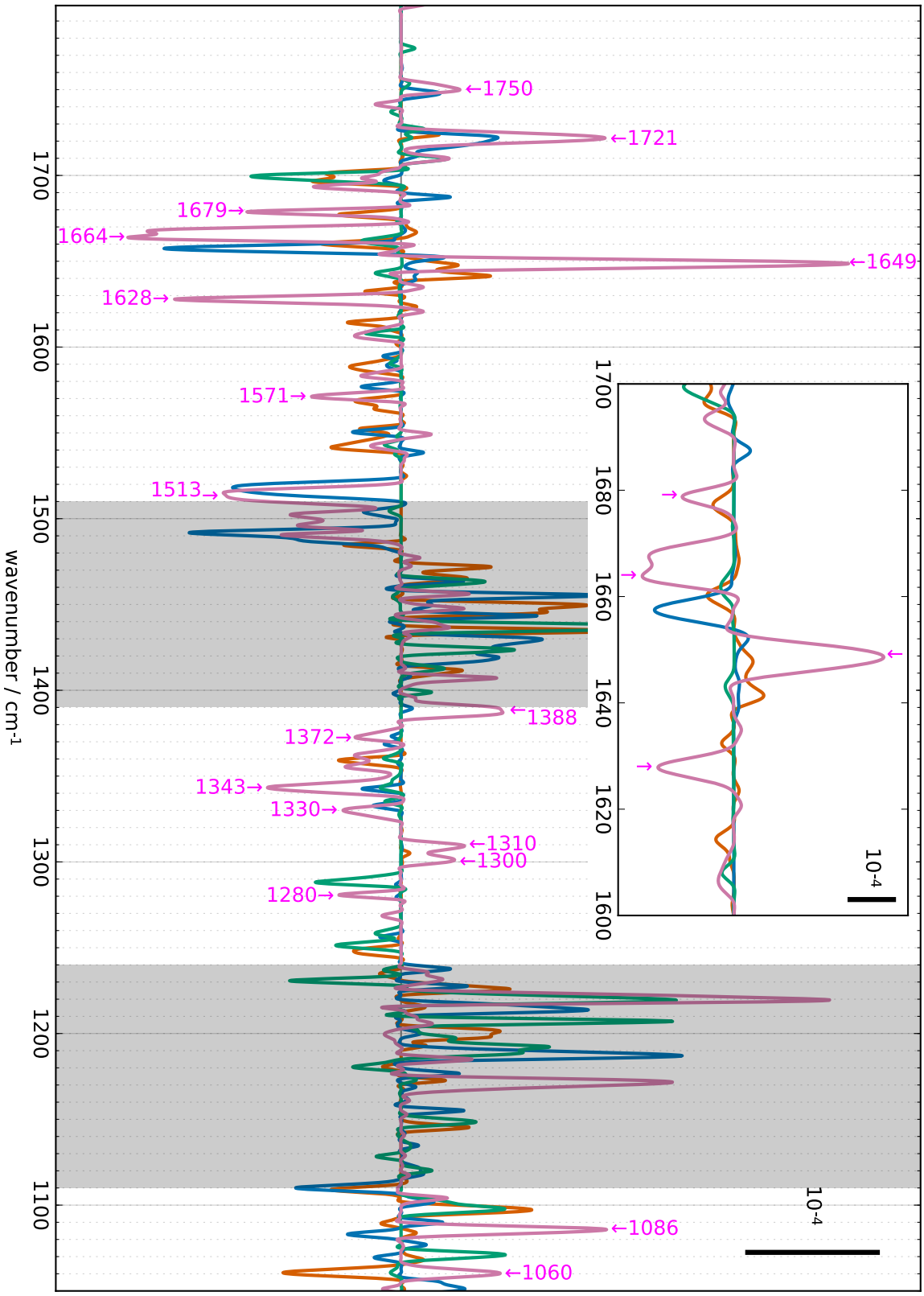

Figure 5.71.: Decay associated spectra (D_2O) obtained by multiplying the time constants obtained through a elastic net fit with a Gaussian function (5.4) where $\tau = 30\,\mu s$ and $\sigma = 6\,\mu s$. Orange: $S_1 \longrightarrow S_2$, aquamarine: $S_2 \longrightarrow S_3$, turquoise: $S_3 \longrightarrow S_0$, pink: $S_0 \longrightarrow S_1$. Regions which are affected by the heat signal are grayed out.

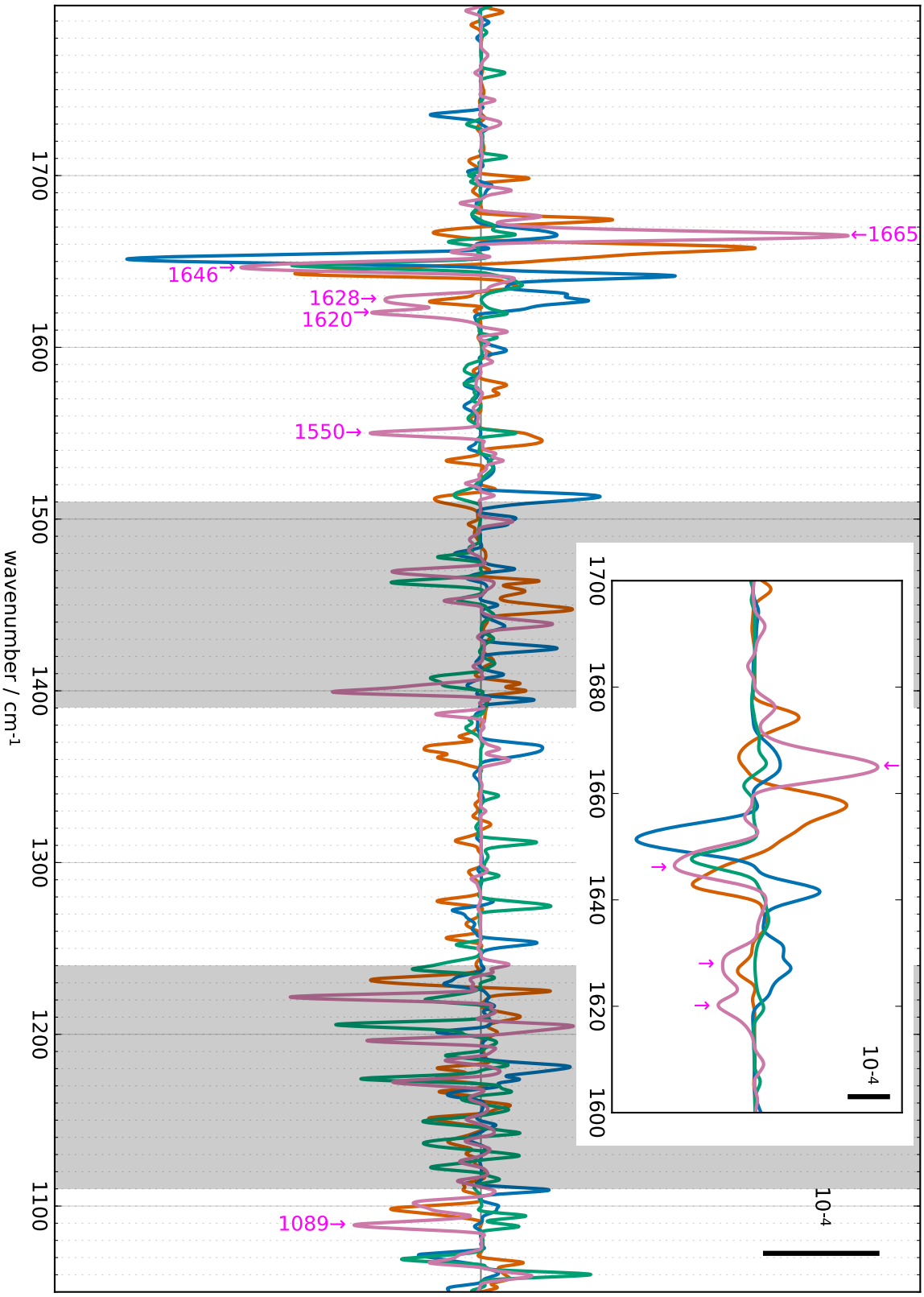

Figure 5.72.: Decay associated spectra (D_2O) obtained by multiplying the time constants obtained through a elastic net fit with a Gaussian function (5.4) where τ = 200 µs and σ = 50 µs. Orange: $S_1 \longrightarrow S_2$, aquamarine: $S_2 \longrightarrow S_3$, turquoise: $S_3 \longrightarrow S_0$, pink: $S_0 \longrightarrow S_1$. Regions which are affected by the heat signal are grayed out.

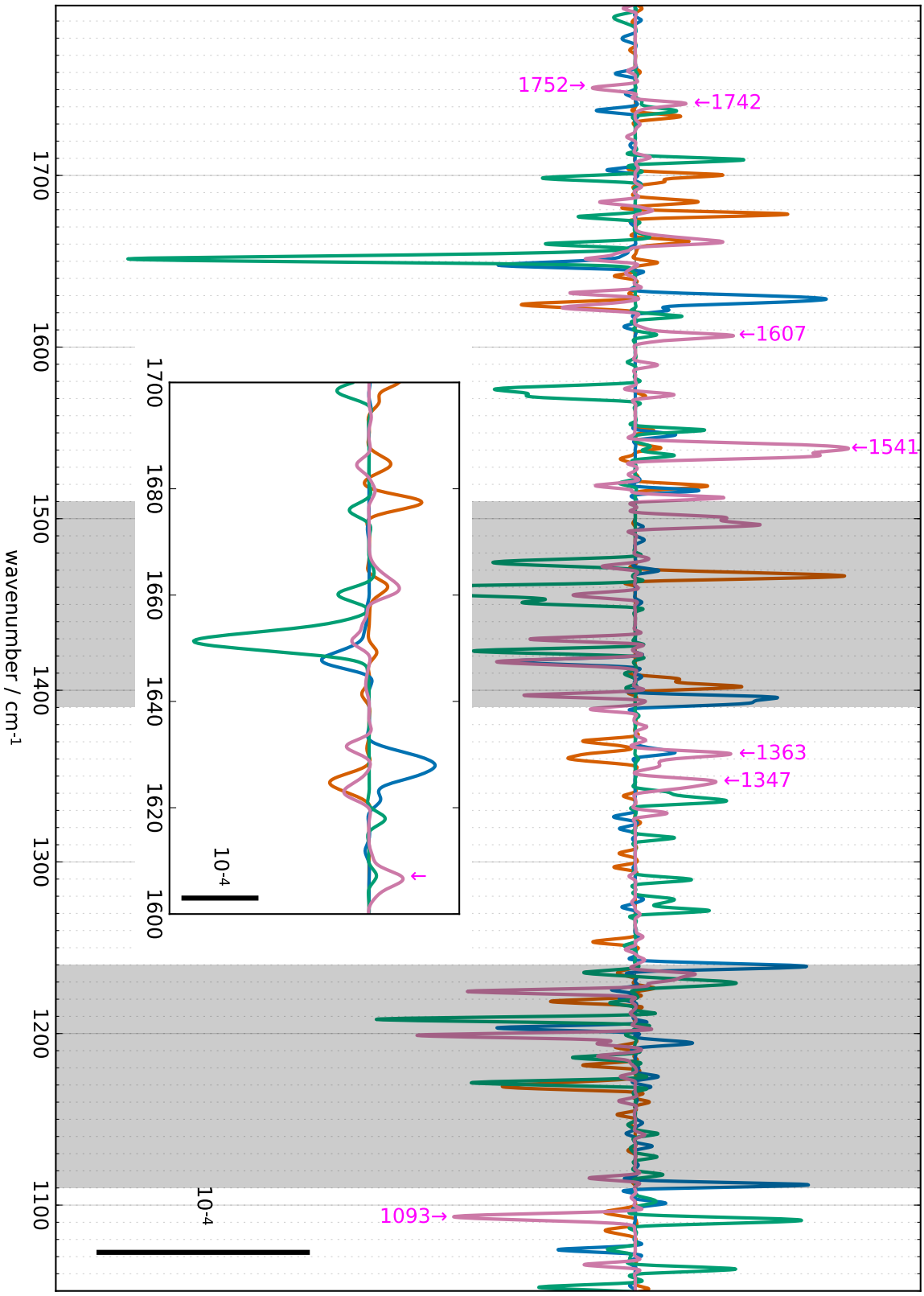

Figure 5.73.: Decay associated spectra (D_2O) obtained by multiplying the time constants obtained through a elastic net fit with a Gaussian function (5.4) where τ = 340 µs and σ = 50 µs. Orange: $S_1 \longrightarrow S_2$, aquamarine: $S_2 \longrightarrow S_3$, turquoise: $S_3 \longrightarrow S_0$, pink: $S_0 \longrightarrow S_1$. Regions which are affected by the heat signal are grayed out.

tures can be seen at 1752 cm^{-1}(−), 1742 cm^{-1}(+), 1607 cm^{-1}(+), 1541 cm^{-1}(+), 1363 cm^{-1}(+), 1347 cm^{-1}(+), and 1093 cm^{-1}(−). The timecourses at these wavenumbers (except for 1093 cm^{-1}) are shown in figure A.20 on page 278.

The reversal of features has been summarized in table 5.11. In particular, all the marked features of the 330 µs phase except for the 1541 cm^{-1}(+) one can be assigned to features with opposite sign in the 30 µs phase. The amide I changes at 1664 cm^{-1}(−) and 1649 cm^{-1}(+) in the 30 µs phase are reversed in the 190 µs phase (1665 cm^{-1}(+) and 1646 cm^{-1}(−)).

30 µs phase	190 µs phase	330 µs phase
1750 cm^{-1}(+)		1752 cm^{-1}(−)
1742 cm^{-1}(−) (not marked)		1742 cm^{-1}(+)
1664 cm^{-1}(−)	1665 cm^{-1}(+)	
1649 cm^{-1}(+)	1646 cm^{-1}(−)	
1607 cm^{-1}(−) (very small, not marked)		1607 cm^{-1}(+)
1571 cm^{-1}(−)		1571 cm^{-1}(+) (very small, not marked)
1513 cm^{-1}(−)		1513 cm^{-1}(+) (not marked)
1388 cm^{-1}(+)	1386 cm^{-1}(−)	1389 cm^{-1}(−)
1363 cm^{-1}(−) (not marked)		1363 cm^{-1}(+)
1343 cm^{-1}(−)		1347 cm^{-1}(+)
1330 cm^{-1}(−)		1328 cm^{-1}(+) (small, not marked)
1086 cm^{-1}(+)	1089 cm^{-1}(−)	1093 cm^{-1}(−)
1060 cm^{-1}(+)		1064 cm^{-1}(−) (small, not marked)

Table 5.11.: Reversal of features in the D_2O $S_0 \longrightarrow S_1$ transition. Corresponding timecourses are shown in figures A.18-A.20 on pages 276-278 respectively.

5.8.7. Decay associated spectra

This section shows decay associated spectra (DAS) obtained from sums of exponential functions with fixed time constants. The decay associated spectra have been obtained for each transition by calculating the amplitudes of a sum of exponential functions (see section 4.15.1 on page 51) with time constants of 20 µs, 106 µs, 390 µs, 1 ms, 2.9 ms, and 30 ms. The obtained amplitudes are shown in figures 5.74-5.80.

In figure 5.74 DAS for all four transitions with a time constant of 20 µs are shown. The four spectra show very similar behaviour in the region of symmetric and asymmetric carboxylic modes. This figure relates to section 6.5 on page 202.

In figures 5.75, 5.76, and 5.78, the time constants relate to characteristic time constants

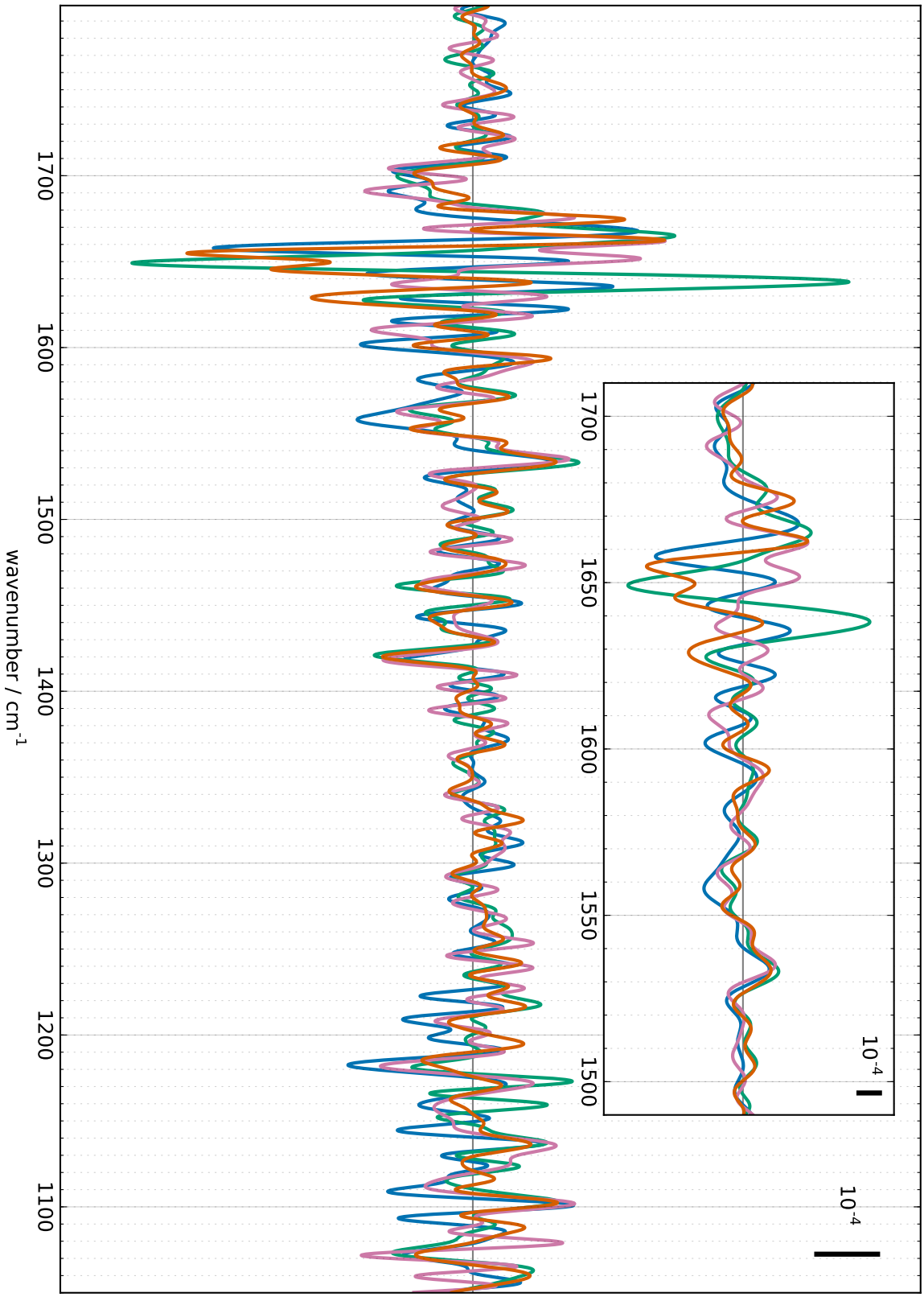

Figure 5.74.: 20 µs phase of all four S-state transitions obtained through calculating the amplitudes of a sum of exponential functions with fixed time constants. Orange: $S_1 \longrightarrow S_2$, aquamarine: $S_2 \longrightarrow S_3$, turquoise: $S_3 \longrightarrow S_0$, pink: $S_0 \longrightarrow S_1$.

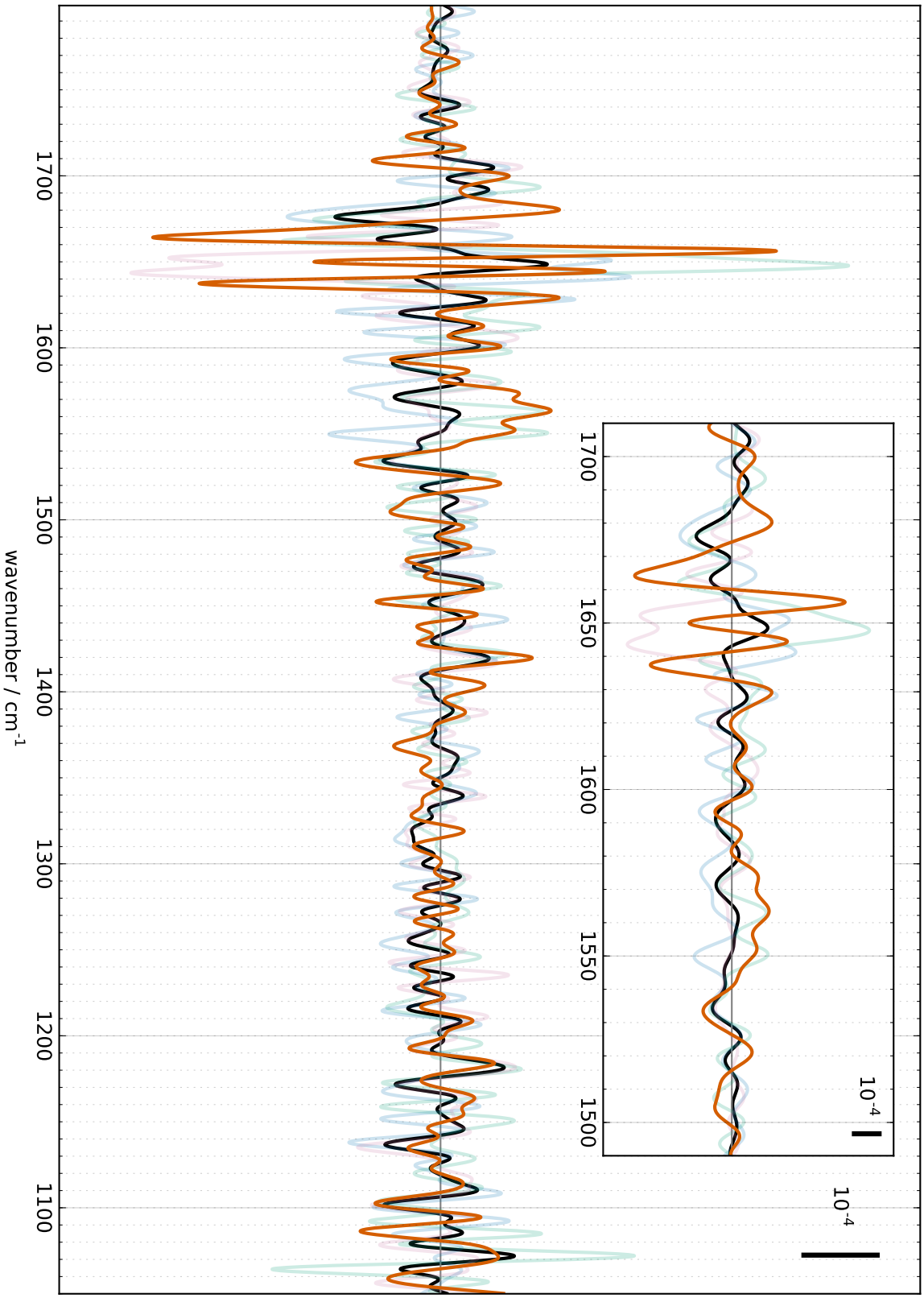

Figure 5.75.: 100 µs phase of all four S-state transitions obtained through calculating the amplitudes of a sum of exponential functions with fixed time constants. Orange: $S_1 \longrightarrow S_2$, aquamarine: $S_2 \longrightarrow S_3$, turquoise: $S_3 \longrightarrow S_0$, pink: $S_0 \longrightarrow S_1$. The black line represents the average of the S-state transitions excluding the $S_1 \longrightarrow S_2$ transition.

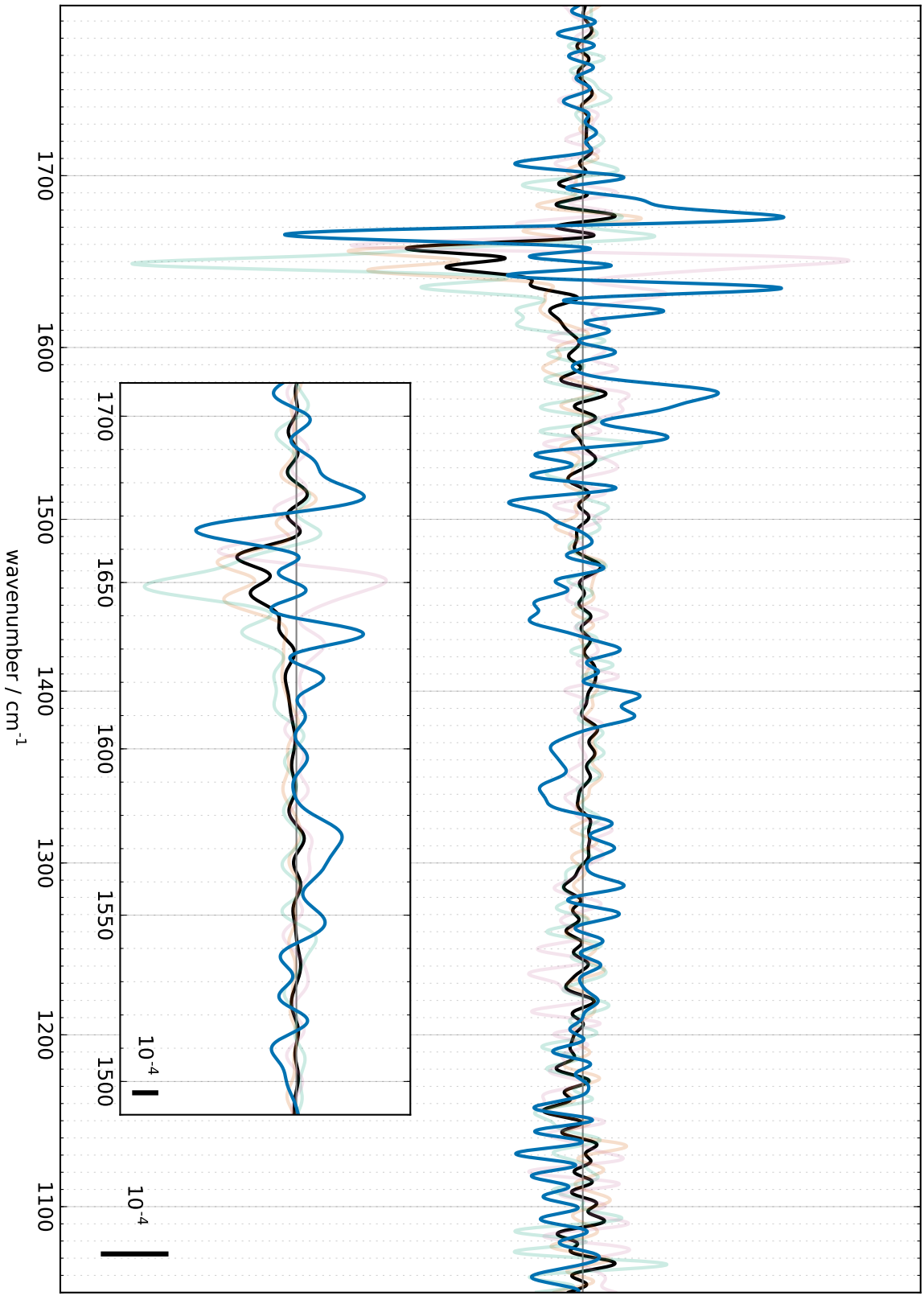

Figure 5.76.: 390 µs phase of all four S-state transitions obtained through calculating the amplitudes of a sum of exponential functions with fixed time constants. Orange: $S_1 \longrightarrow S_2$, aquamarine: $S_2 \longrightarrow S_3$, turquoise: $S_3 \longrightarrow S_0$, pink: $S_0 \longrightarrow S_1$. The black line represents the average of the S-state transitions excluding the $S_2 \longrightarrow S_3$ transition.

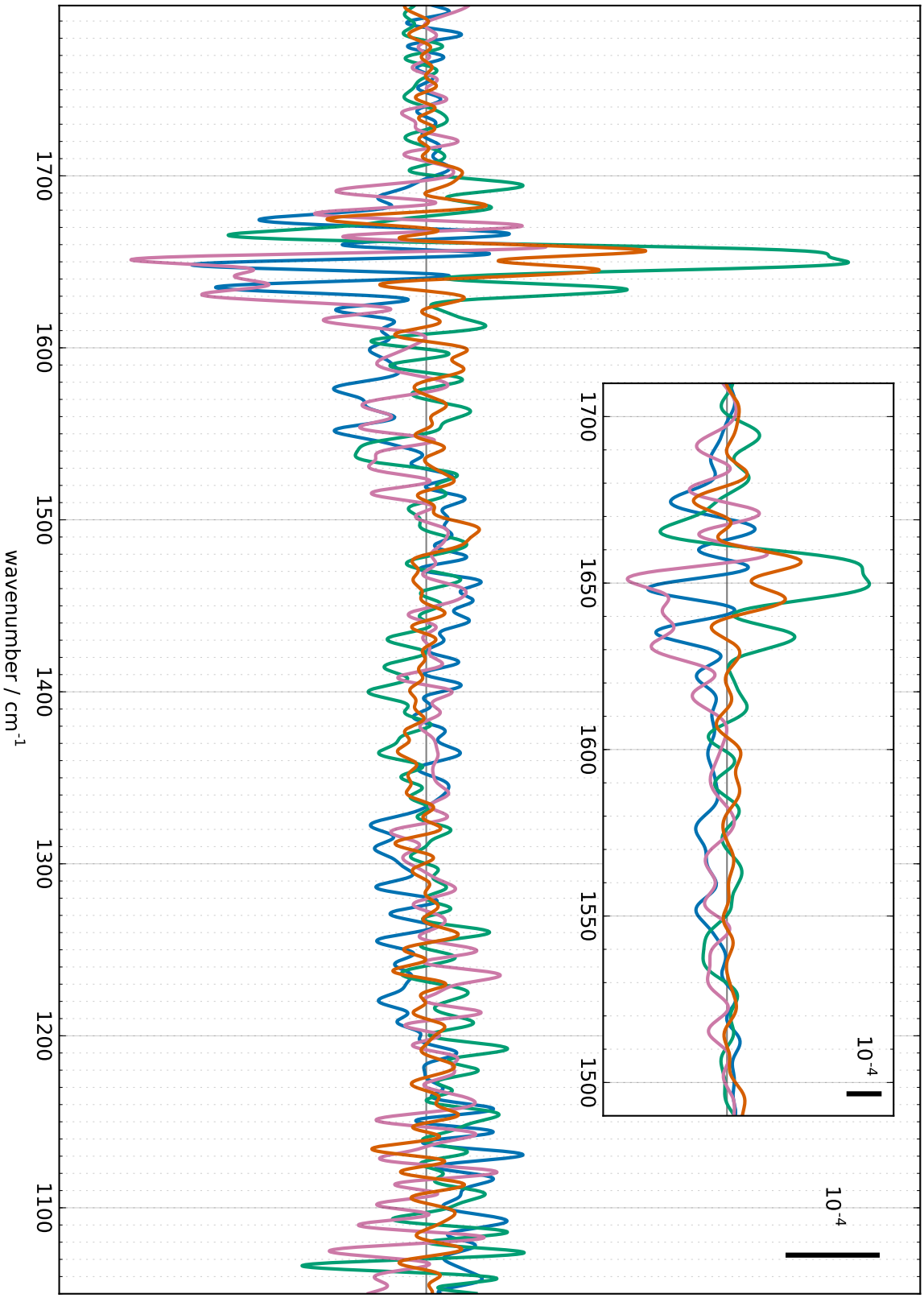

Figure 5.77.: 1 ms phase of all four S-state transitions obtained through calculating the amplitudes of a sum of exponential functions with fixed time constants. Orange: $S_1 \rightarrow S_2$, aquamarine: $S_2 \rightarrow S_3$, turquoise: $S_3 \rightarrow S_0$, pink: $S_0 \rightarrow S_1$.

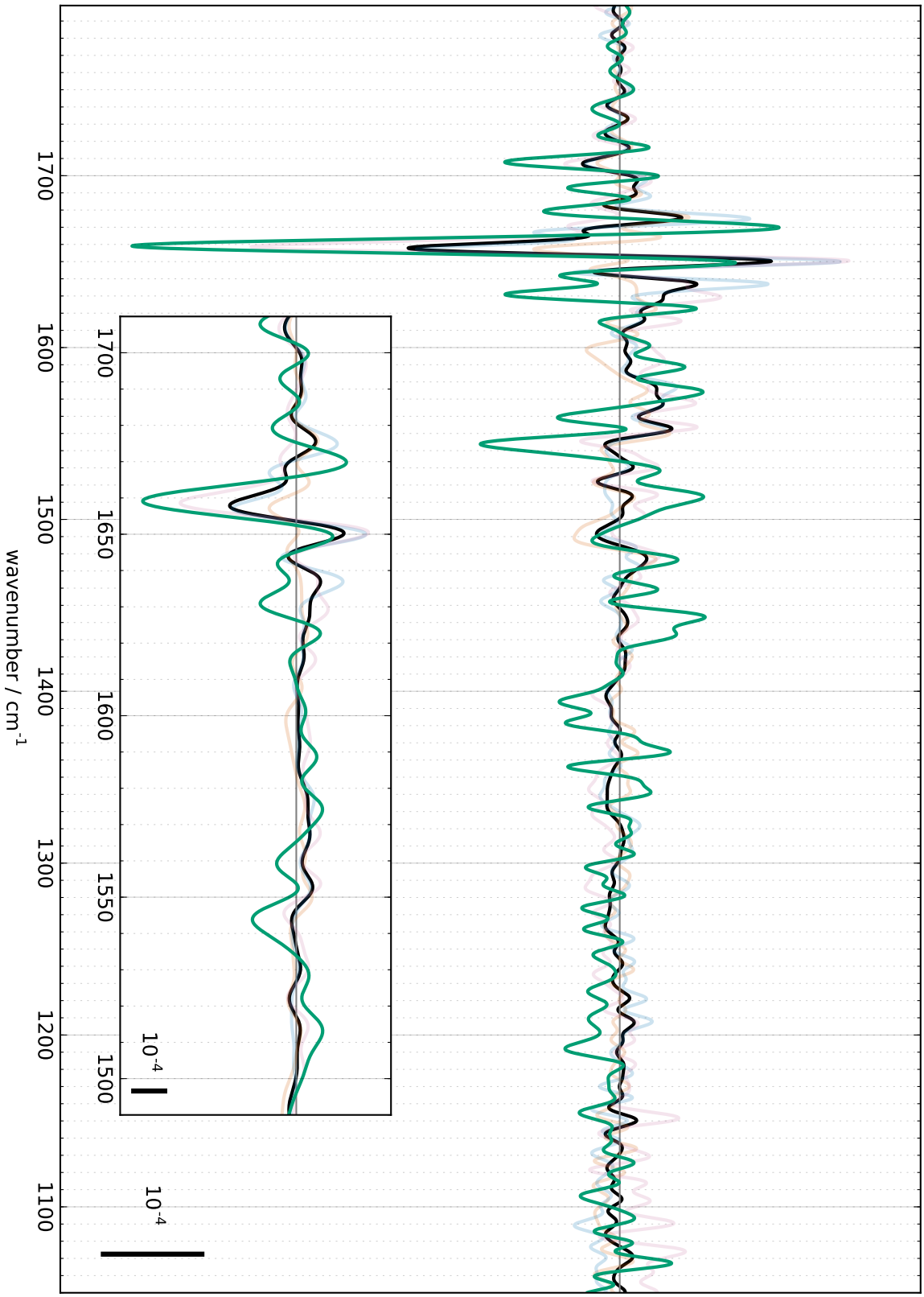

Figure 5.78.: 2.9 ms phase of all four S-state transitions obtained through calculating the amplitudes of a sum of exponential functions with fixed time constants. Orange: $S_1 \rightarrow S_2$, aquamarine: $S_2 \rightarrow S_3$, turquoise: $S_3 \rightarrow S_0$, pink: $S_0 \rightarrow S_1$. The black line represents the average of the S-state transitions excluding the $S_3 \rightarrow S_0$ transition.

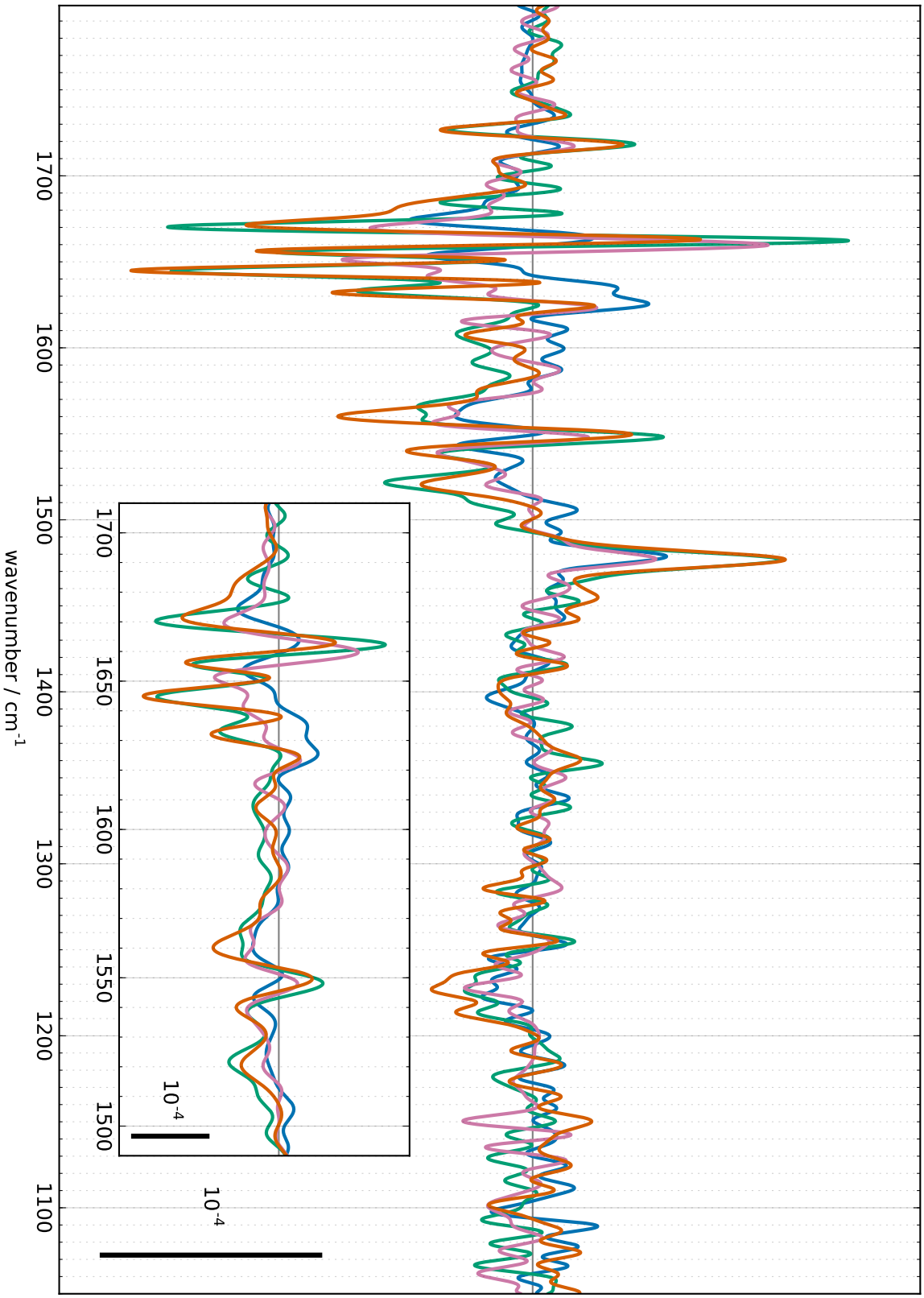

Figure 5.79.: 30 ms phase of all four S-state transitions obtained through calculating the amplitudes of a sum of exponential functions with fixed time constants. Orange: $S_1 \rightarrow S_2$, aquamarine: $S_2 \rightarrow S_3$, turquoise: $S_3 \rightarrow S_0$, pink: $S_0 \rightarrow S_1$.

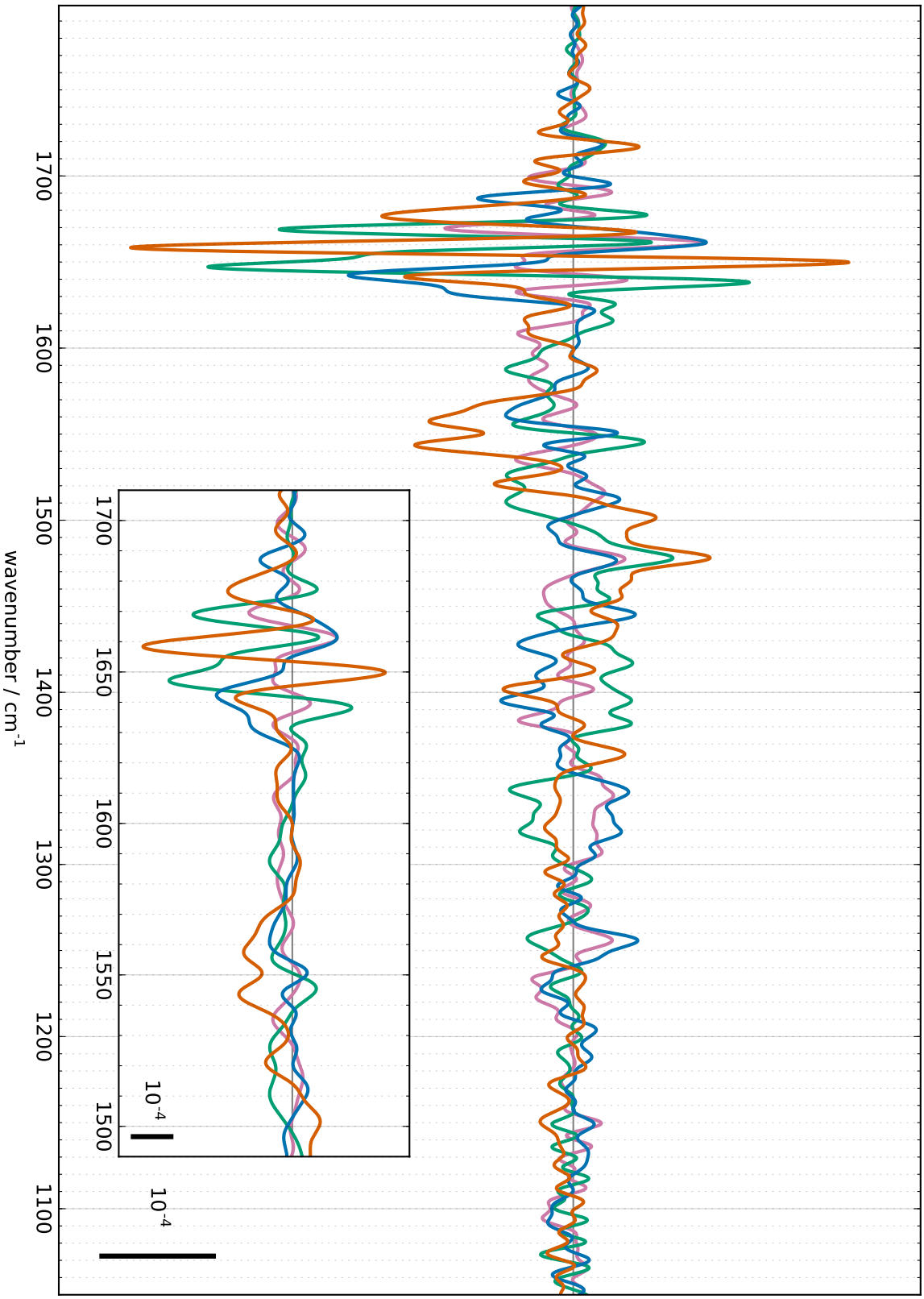

Figure 5.80.: Offsets of all four S-state transitions obtained through calculating the amplitudes of a sum of exponential functions with fixed time constants. Orange: $S_1 \longrightarrow S_2$, aquamarine: $S_2 \longrightarrow S_3$, turquoise: $S_3 \longrightarrow S_0$, pink: $S_0 \longrightarrow S_1$.

of the $S_1 \rightarrow S_2$, $S_2 \rightarrow S_3$, and $S_3 \rightarrow S_0$ transitions respectively. To facilitate discussion of the DAS of the respective transition, the spectra of the other transitions (which are shown in very light colors) have been averaged and are shown as black line.

Figure 5.77 shows DAS with a time constant of 1 ms. None of the four transitions shows clearly outstanding peaks. As a general motive the orange and turquoise line (first and third transition) overlap and are different from the overlapping aquamarine and pink lines (second and fourth transition). This is equivalent to binary oscillations. These binary oscillations can be found throughout the spectral region.

In figure 5.79 DAS for all four transitions with a time constant of 30 ms are shown. In this figure weak binary oscillations can be found: there are many features where the orange and turquoise lines overlap and differ from the overlapping aquamarine and pink lines. This figure is discussed in section 6.8.

Finally, figure 5.80 shows the offset obtained from the amplitude calculations. The offset reflects the final value of the timecourses.

6. Discussion

6.1. Time-resolved rapid-scan

Time-resolved rapid-scan measurements of the sample (in H_2O and in D_2O) have been completed to investigate several aspects of the sample. The spectral resolution of the data is about 10 cm^{-1} and the temporal resolution is about 34 ms.

The most important point of these measurements was to verify the integrity of the sample over the whole measurement time. In figure 5.2 on page 79 the results from a rapid-scan measurement are shown. In this measurement each sample was measured once every 12 hours. Even after almost 60 hours of measurement time the S-state difference spectra still show the same features with the same amplitude. This was crucial for the completion of the step-scan measurements which were only completed after running the setup continuously for several months.

In figure 5.2 on page 79, which shows the integrity of the sample over several days of measurement, the larger amplitude of the first flash difference spectrum compared to the other spectra is apparent. In figure 5.6 on page 85 the difference spectra of a train of ten flashes are shown to facilitate this comparison. Comparing the first flash difference spectrum to the difference spectra of the later flashes, it can be found that the features with exceptionally large amplitude are features of the $S_1 \longrightarrow S_2$ transition. In particular the electron transfer is not blocked, since the Q_A^- feature at 1478 cm^{-1} has disappeared and the Fe^{2+}/Fe^{3+} feature at 1100 cm^{-1} has a large amplitude. This means that there are some centers which are able to complete the $S_1 \longrightarrow S_2$ transition but unable to complete further transitions.

Binary oscillations are visible in the time-resolved rapid-scan spectra 17 ms after laser flash excitation: below 1300 cm^{-1} only very small features are visible after the first and third flash, but large features are visible after the second and fourth flash (figure 5.9 on page 88 and figure 5.25 on 113). The binary oscillations of the steady-state spectra which show features with opposite sign in every flash are visible in figure 5.6 on page 85 (steady-state difference spectra in one plot) and figure 5.4 on page 81 (effect of ammonia on PSII).

The time-resolved rapid-scan data has been used to identify two phases of acceptor side events (table 5.1 on page 90): a fast phase with a time constant of ~57 ms and a slow phase

with a time constant of about ~500 ms. The two time constants were obtained for every flash independently through global fitting. Although binary oscillations in the obtained time constants can be conceived, at least the obtained time constants of the fast phase lie within the error of the fit in the same range.

The decay associated spectra associated with the fast and slow phases are shown in figure 5.10 on page 89. While the fast phase has a maximum at 1477 cm^{-1}, the slow phase shows a maximum at 1479 cm^{-1}. This implies that the fast phase represents electron transfer from the primary electron acceptor Q_A to the secondary electron acceptor (Q_B and/or PPBQ), while the slow phase represents electron transfer from Q_B to PPBQ or the release of reduced Q_B or PPBQ.

6.2. Step-scan S-state transitions in H_2O and D_2O

In section 5.8.6 time constants for all S-state transitions have been obtained. The measured data was corrected for heat signal contributions by fitting the interferogram timecourse to the measured timecourses at each wavenumber as described in section 5.6.6 on page 106. Time constants for individual timecourses were obtained using an elastic net fit as described in section 4.15.4 on page 55. In section 5.8.6 on page 134 and the thereafter following sections, the obtained time constants were examined. Lifetime maps were used to identify clusters of time constants which correspond to individual phases of a S-state transition. Decay associated spectra were used to distinguish between S-state dependent and S-state independent processes in each phase. The time constants were obtained from averaging the corresponding time constants of selected features as listed in the tables in the results section. The individual S-state transitions are further discussed in the following sections.

Table 6.1 summarizes the determined time constants and assigns the phases to the individual S-state transition steps. The kinetic isotope effects are given accordingly.

6.2.1. $S_1 \rightarrow S_2$ transition

The $S_1 \longrightarrow S_2$ transition decay associated spectrum shows time constants of 106 µs and 103 µs in H_2O and in D_2O respectively, which corresponds to a kinetic isotope effect of 1.0. There are no additional phases visible in H_2O and in D_2O. Features which change in time with a time constant corresponding to this transition can be found around 1708 cm^{-1}, 1666 cm^{-1}, 1654 cm^{-1}, 1576 cm^{-1}, 1511 cm^{-1}, 1401 cm^{-1}, 1281 cm^{-1}, and 1102 cm^{-1} in both H_2O and D_2O.

		H_2O	D_2O	KIE
$S_1 \longrightarrow S_2$	${S_1}^n \longrightarrow {S_2}^+$	106 µs	103 µs	1.0
$S_2 \longrightarrow S_3$	${S_2}^+ \longrightarrow {S_2}^n$	19 µs 48 µs	76 µs	1.6-4.0
	${S_2}^n \longrightarrow {S_3}^+$	393 µs	860 µs	2.2
$S_3 \longrightarrow S_0$	${S_3}^+ \longrightarrow {S_3}^n$	18 µs	50 µs	2.8
		142 µs	500 µs	3.5
	${S_3}^n \longrightarrow {S_0}^n$	2.9 ms	4.0 ms	1.4
$S_0 \longrightarrow S_1$	${S_0}^n \longrightarrow {S_0}^+$	22 µs	30 µs	1.4
	${S_0}^+ \longrightarrow {S_1}^n$	200 µs	191 µs 327 µs	1.0-1.6

Table 6.1.: Time constants obtained from the elastic net fits (see section 5.8.6 on page 134).

6.2.2. $S_2 \rightarrow S_3$ transition

Three phases have been identified in the $S_2 \longrightarrow S_3$ transition in H_2O and two phases in D_2O. In H_2O, the time constants of these transitions are 20 µs, 50 µs, and 390 µs.

The 20 µs decay associated phase (figure 5.53 on page 145) shows features in the amide I region which are not larger than the features of the other transitions, one minor feature at 1451 cm^{-1}, and several features below 1230 cm^{-1}. Most features of this decay associated spectrum are overlaid with features of the $S_0 \longrightarrow S_1$: this is equivalent to period-of-two oscillations which are readily explained with acceptor side contributions. Moreover, there are virtually no features in the $\nu_s(COO^-)$ region to be seen. These findings all speak against an assignment of the features to $S_2 \longrightarrow S_3$-specific processes. Nevertheless, some of the features are reversed in the later phases, which is a strong argument for a specific $S_2 \longrightarrow S_3$ process. I will discuss the reversal of features after characterizing the later two phases.

The 50 µs phase in H_2O in the $S_2 \longrightarrow S_3$ transition (figure 5.54 on page 146) shows distinct features in the amide I and II regions (1679 cm^{-1}(−), 1664 cm^{-1}(+), 1651 cm^{-1}(+), 1576 cm^{-1} (−), 1550 cm^{-1}(−)). Minor additional features can be seen at 1519 cm^{-1}(−), 1387 cm^{-1}(−), 1212 cm^{-1}(−) and 1198 cm^{-1}(−). The $S_0 \longrightarrow S_1$ transition shows almost no features in this decay associated spectrum and none of them overlap with $S_2 \longrightarrow S_3$ features, which is equivalent to the absence of period-of-two oscillations. In other words, no acceptor side signals are seen in this decay associated spectrum.

The 390 µs phase in H_2O in the $S_2 \longrightarrow S_3$ transition (figure 5.55 on page 147) shows many distinct features in the amide I and II regions as well as in the $\nu_s(COO^-)$ region. Again only very few acceptor side signals are visible.

Table 5.4 on page 150 summarizes the reversal of features in the three different phases. The two early phases, 20 µs and 50 µs, do not show any reversal of features; on the other

hand, both early phases share reversed features with the later 390 µs phase. During the 390 µs phase, features at 1692 cm^{-1}(–), 1559 cm^{-1}(–), and 1451 cm^{-1}(+) of the 20 µs phase are reversed, and features at 1679 cm^{-1}(–), 1575 cm^{-1}(–), 1550 cm^{-1}(–), and 1387 cm^{-1}(–) of the 50 µs phase are reversed. The 20 µs and 50 µs phases share a positive feature around 1667 cm^{-1} which is reversed in the 390 µs phase. Selected timecourses are shown in figures A.7-A.9 on pages 256-258.

A straightforward explanation for the reversal of features is the reversal of structural changes caused by the sequential removal of opposite charges from the OEC. In the $S_2 \longrightarrow S_3$ transition first a proton and then an electron is removed from the OEC. Because the first two fast phases do not show a mutual reversal of features, the same (positive) charge is involved in a multiphasic process. The features created by these two processes are reversed when a negative charge is removed from the OEC.

The transition from an open-cubane structure to a closed-cubane structure during the $S_2 \longrightarrow S_3$ transition (e.g. Pérez-Navarro et al. 2016) will cause further structural changes. This transition might be represented by fast non-reversed changes in both buffers, that is a 50 µs change at 1645 cm^{-1} in H_2O and a 80 µs change at 1651 cm^{-1} in D_2O.

In the case of the D_2O dataset only two phases in the $S_2 \longrightarrow S_3$ transition can be identified (figure 5.52 on page 144). Their time constants of 76 µs and 860 µs (tables A.7 and A.8 on pages 254 and 255 respectively) differ by one order of magnitude. Features which are reversed in the two phases were identified around 1699 cm^{-1}, 1691 cm^{-1}, 1677 cm^{-1}, 1582 cm^{-1}, 1379 cm^{-1}, and 1338 cm^{-1}.

The 390 µs phase in H_2O and the 860 µs phase in D_2O compare quite well. Almost 20 features can be assigned to each other (table 5.6 on page 152), assuming that features at 1575 cm^{-1}(+), 1561 cm^{-1}(+), 1546 cm^{-1}(+), and 1333 cm^{-1}(–) in H_2O are upshifted by about 10 cm^{-1} to 1583 cm^{-1}(+), 1570 cm^{-1}(+), 1558 cm^{-1}(+), and 1338 cm^{-1}(–) in D_2O. This is a very strong indication that the two phases represent the same process, namely the PCET in the $S_2 \longrightarrow S_3$ transition. In this case the kinetic isotope effect for the electron removal in the ${S_2}^{n} \longrightarrow {S_3}^{+}$ transition equals 2.2.

The earlier phases (20 µs and 50 µs in H_2O and 80 µs in D_2O) do not compare very well. The features which were identified to be reversed in the later phases are listed in table 6.2.

It is only possible to align the features of the early phases as in table 6.2 if one assumes a wavenumber upshift of about 10 cm^{-1} in D_2O. The wavenumber position of the features then correspond reasonably well, but the sign of the changes does not match. For example, in table 6.2 the 50 µs decay at 1679 cm^{-1} in H_2O is aligned to the 80 µs rise at 1691 cm^{-1} in D_2O. While a wavenumber upshift might be arguable there is no obvious reason why the sign of the transition should change; therefore, in this study the early phases of the $S_2 \longrightarrow S_3$ transition in H_2O and D_2O cannot be directly compared.

20 µs, H_2O	50 µs, H_2O	80 µs, D_2O
1692 cm^{-1}(−)		1700 cm^{-1}(−)
	1679 cm^{-1}(−)	1691 cm^{-1}(+)
1669 cm^{-1}(+)	1664 cm^{-1}(+)	1677 cm^{-1}(−)
	1576 cm^{-1}(−)	1582 cm^{-1}(−)

Table 6.2.: Comparison of the early phases in the $S_2 \longrightarrow S_3$ transition in H_2O and in D_2O. Listed are only features which are reversed in their respective later phases.

6.2.3. $S_3 \rightarrow S_0$ transition

The $S_3 \longrightarrow S_0$ transition starts with a fast phase (18 µs in H_2O and 50 µs in D_2O) with a KIE of ~2.5. This phase shows almost only amide I changes at 1666 cm^{-1}(+), 1650 cm^{-1}(−), and 1639 cm^{-1}(+) in H_2O, and at 1658 cm^{-1}(−) and 1650 cm^{-1}(+) in D_2O. The correspondence of the 1650 cm^{-1}(−) feature in H_2O to the 1658 cm^{-1}(−) feature in dto and the 1639 cm^{-1}(+) feature in H_2O to the 1650 cm^{-1}(+) feature in D_2O seems plausible assuming a wavenumber upshift of about 10 cm^{-1} in D_2O. The kinetic isotope is then 2.8.

This early amide I phase could correspond to structural rearrangements at the OEC which influence the protein backbone, but without influencing carboxylate groups.

The 1639 cm^{-1}(+) H_2O feature is reversed in the following 150 µs phase; the 1650 cm^{-1} (−) H_2O feature might be reversed in the 150 µs or 2.9 ms phase. In D_2O, the 1650 cm^{-1}(+) feature might be reversed in the following 500 µs phase.

The 150 µs H_2O phase shows only minor features; the most remarkable feature is a 1740 cm^{-1}(+) feature which is reversed in the following 2.9 ms phase, revealing a protonation event with a time constant of about 150 µs which is reversed in the millisecond phase.

In contrast to the 150 µs phase the H_2O millisecond phase (2.9 ms) shows very distinct features. Comparing the two phases, reversal of features can be seen around 1740 cm^{-1}, 1672 cm^{-1}, 1589 cm^{-1}, 1571 cm^{-1}, and ~1358 cm^{-1}.

In D_2O the fast 50 µs amide I phase is followed by a 500 µs phase. The 500 µs phase in D_2O shares features with the 150 µs phase in H_2O around 1673 cm^{-1}(−), 1660 cm^{-1}(−), 1637 cm^{-1} (−), 1571 cm^{-1}(−), 1560 cm^{-1}(+), and 1360 cm^{-1}(+). The 150 µs phase in H_2O and the 500 µs phase in D_2O thus represent the same process and the KIE equals 3.3.

In D_2O there is also a positive feature at 1740 cm^{-1} which is hidden behind an identical $S_0 \longrightarrow S_1$ transition peak; possibly the miss factor deconvolution did not work here. If the intensity from the $S_0 \longrightarrow S_1$ transition were to be added to the peak, it would be as large as the one in H_2O. It would then reverse the negative peak at 1740 cm^{-1} in the D_2O millisecond phase. Further reversal of features during the 500 µs and 4 ms phases in D_2O can be

found around 1707 cm^{-1}, 1672 cm^{-1}, 1650 cm^{-1}, 1616 cm^{-1}, 1571 cm^{-1}, 1556 cm^{-1}, 1541 cm^{-1}, and 1354 cm^{-1}.

The high KIE of this intermediate phase as well as the changes at 1740 cm^{-1} suggest that this process corresponds to the first proton removal ($S_3^+ \rightarrow S_3^n$) in the $S_3 \rightarrow S_0$ transition.

The millisecond phase in D_2O corresponds very well to the one in H_2O, almost 20 features can be aligned. Two features in H_2O (1573 cm^{-1}(+) and 1628 cm^{-1}(−)) are upshifted by 10 cm^{-1} in D_2O.

The millisecond phase in D_2O shows a timeconstant of 4 ms. Therefore, the kinetic isotope effect for the electron removal equals 1.4. The KIE is rather low, and therefore a proton transfer step seems unlikely; yet, there is a deprotonation event clearly visible at 1740 cm^{-1}. The low KIE could be explained by the (proton independent) electron transfer being the rate limiting step.

6.2.4. $S_0 \rightarrow S_1$ transition

The $S_0 \rightarrow S_1$ transition shows two phases in H_2O (time constants 22 µs and 200 µs) and three phases in D_2O (time constants 30 µs, 190 µs, 330 µs). In H_2O, the signals are very small and, as discussed in the $S_2 \rightarrow S_3$ section, overlap with $S_2 \rightarrow S_3$ transition signals. This is indicative of acceptor-side processes since these overlaps are equivalent to period-of-two oscillations.

In H_2O there are only two features reversed in the two phases: at 1662 cm^{-1} and 1079 cm^{-1}.

The D_2O phases consist of a fast 30 µs phase, a 190 µs phase which shows exclusive amide changes, and a 330 µs phase which shows very little amide changes. The 190 µs and 330 µs phases show distinct, mostly mutually exclusive features which all show time constants which are very close to their respective average phase time constant. These are good indications that there are indeed two distinct phases.

In D_2O the 30 µs and 330 µs phases show reversal of features around 1751 cm^{-1}, 1742 cm^{-1}, 1607 cm^{-1}, 1571 cm^{-1}, 1513 cm^{-1}, 1388 cm^{-1}, 1363 cm^{-1}, 1345 cm^{-1}, 1329 cm^{-1}, 1089 cm^{-1}, and 1062 cm^{-1}. The 30 µs and 190 µs phases show reversal of features around 1665 cm^{-1}, 1647 cm^{-1}, 1387 cm^{-1} and 1087 cm^{-1}. NB: The 190 µs and 330 µs phases share negative features at 1386 cm^{-1} and around 1090 cm^{-1}.

The 22 µs phase in H_2O and the 30 µs in D_2O correspond to the electron removal in the $S_0^n \rightarrow S_0^+$ transition; the KIE equals 1.4.

The 200 µs reversal of features in H_2O at 1662 cm^{-1} and 1079 cm^{-1} corresponds to the 190 µs reversal of features in D_2O at 1665 cm^{-1} and 1090 cm^{-1} (11 cm^{-1} upshift in D_2O in the latter case). Although the slower time constant should correspond to the proton removal step in the $S_0^+ \rightarrow S_1^n$ transition, this would imply a KIE of 1. On the other hand, there

are considerably more features reversed when comparing the 30 µs and the 330 µs phases in D_2O. Still, if the 200 µs phase in H_2O is compared to the 330 µs phase in D_2O, the KIE is 1.7.

Noguchi, Suzuki, et al. (2012) reported an unexpected 800 µs phase at 1400 cm^{-1}. In the step-scan data such a phase can neither be found in the lifetime map (figure 5.66 on page 166) nor in the timecourse at 1400 cm^{-1} (figure 5.37 on page 126).

6.2.5. Comparison of the individual transitions in H_2O and discussion of Y_Z signals

The features found in the decay associated spectra in H_2O are summarized in the table below. Each wavenumber corresponds to a feature which is marked as a text label in the decay associated spectra and as a black ring in the lifetime maps. Additionally, small features which have been inferred from reversal of features are given in brackets. Some transitions, for example the proton transfer in the $S_2 \longrightarrow S_3$ transition, show two phases (in this example, 20 µs and 50 µs). Features from either phase are marked with roman numerals (I and II).

$S_1{}^n \longrightarrow S_2{}^+$ 106 µs e^-	$S_2{}^+ \longrightarrow S_2{}^n$ I: 19 µs II: 48 µs p^+	$S_2{}^n \longrightarrow S_3{}^+$ 393 µs e^-	$S_3{}^+ \longrightarrow S_3{}^n$ I: 18 µs II: 142 µs p^+	$S_3{}^n \longrightarrow S_0{}^n$ 2.9 ms e^- (p^+)	$S_0{}^n \longrightarrow S_1{}^+$ 22 µs e^-	$S_1{}^+ \longrightarrow S_1{}^n$ 200 µs p^+
			1740 (+)^{II}	1740 (−)		
				[1724 (−)]	1724 (+)	
					1721 (+)	
1708 (−)		1711 (−)		1706 (−)		1712 (−)
	1700 (−)^{I}	[1702 (−)]		[1700 (+)]		
	1692 (−)^{I}				1691 (−)	
		1685 (+)				
1680 (+)	1679 (−)^{II}	1676 (+)	1673 (−)^{II}			1677 (−)
	1669 (+)^{I}			1671 (+)		
1665 (−)	1664 (+)^{II}	1667 (−)	1666 (+)^{I}			
	1658 (−)^{I}		1660 (−)^{II}	1661 (−)	1662 (+)	1661 (−)
1655 (+)						
	1651 (+)^{II}		1650 (−)^{I}	1648 (+)	1651 (+)	

$S_1^n \rightarrow S_2^+$ 106 µs e^-	$S_2^+ \rightarrow S_2^n$ I: 19 µs II: 48 µs p^+	$S_2^n \rightarrow S_3^+$ 393 µs e^-	$S_3^+ \rightarrow S_3^n$ I: 18 µs II: 142 µs p^+	$S_3^n \rightarrow S_0^n$ 2.9 ms e^- (p^+)	$S_0^n \rightarrow S_1^+$ 22 µs e^-	$S_1^+ \rightarrow S_1^n$ 200 µs p^+
1638 (–)			1639 (+)^{I} 1637 (–)^{II}		1637 (–)	1642 (–)
				1628 (–)		
	1622 (+)^{I}			1620 (+)		1620 (–)
	1616 (–)^{I}					
					1610 (–)	
	1602 (–)^{I}					
			1589 (–)^{II}	[1589 (+)]		
1576 (+)	1576 (–)^{II}	1575 (+)		1573 (+)		1577 (+)
			1570 (–)^{II}			
1564 (+)	1559 (–)^{I}	1561 (+)	1562 (+)^{II}		1562 (–)	
	1550 (–)^{II}					
		1546 (+)		1544 (–)		1547 (–)
		1526 (–)		1528 (+)		
1521 (+)	1519 (–)^{II}					
1511 (–)		1511 (–)		1511 (+)		
		1503 (–)				
					1488 (+)	
1454 (–)	1451 (+)^{I}	1448 (–)				
		1437 (–)				1439 (+)
		1423 (+)				
1403 (+)		1397 (+)		1396 (–)		
	1387 (–)^{II}	1390 (+)				1388 (+)
		1380 (+)		1382 (–)	1381 (+)	1377 (+)
		1371 (–)				
			1360 (+)^{II}	1356 (–)		
		1349 (–)				
		1333 (–)				
						1325 (+)

$S_1^n \rightarrow S_2^+$ 106 µs e^-	$S_2^+ \rightarrow S_2^n$ I: 19 µs II: 48 µs p^+	$S_2^n \rightarrow S_3^+$ 393 µs e^-	$S_3^+ \rightarrow S_3^n$ I: 18 µs II: 142 µs p^+	$S_3^n \rightarrow S_0^n$ 2.9 ms e^- (p^+)	$S_0^n \rightarrow S_1^+$ 22 µs e^-	$S_1^+ \rightarrow S_1^n$ 200 µs p^+
				1296 (−)		
			1248 $(+)^{II}$			
1281 (−)						
					1252 (+)	
					1239 (+)	
	1223 $(-)^{I}$					1228 (−)
	1209 $(-)^{I}$ 1212 $(-)^{II}$					
	1198 $(-)^{II}$					
						1192 (−)
	1182 $(-)^{I}$		1181 $(+)^{II}$			
					1173 (+)	1170 (−)
			1159 $(-)^{II}$			
			1152 $(+)^{II}$			
	1144 $(-)^{I}$					
						1138 (−)
					1127 (+)	1127 (+)
	1110 $(-)^{I}$					
1102 (−)		1105 (−)				
1094 (+)	1094 $(-)^{I}$					
					1079 (+)	1078 (−)
		1074 (+)	1070 $(+)^{II}$		1071 (−)	
		[1060 (−)]	1062 $(-)^{II}$		1059 (−)	

Table 6.3.: Comparison of visible features in the decay associated spectra for each individual transition in H_2O. Roman numerals give the phase the feature belongs to: for example, two phases with 20 µs and 50 µs have been assigned to the $S_2^+ \rightarrow S_2^n$ transition. Brackets mark features which have not been labelled in the decay associated spectra, but have been inferred by comparison with other phases (see the tables regarding the reversal of features, the tables regarding the comparison with D_2O data and the decay associated spectra).

The table allows to find wavenumbers of special interest, i.e. wavenumbers at which many S-state transitions are visible. The sign of the features—(-) for rises, (+) for decays—can be compared with the sign of the charge which is removed from the OEC during any specific S-state transition. If there is a wavenumber where signals show the same behaviour for the same sign of the removed charge, this wavenumber is a good candidate to serve as probe for processes happening in the vicinity of Y_Z. The signals caused by Y_Z should be characterized by an amplitude which is created instantly after each flash which decays to zero with the specific electron removal time constant of the S-state transition.

Around 1710 cm^{-1}, negative features are visible in the $S_1^n \rightarrow S_2^+$ (1708 cm^{-1}(−)), $S_2^n \rightarrow S_3^+$ 1711 cm^{-1}(−)), and $S_3^n \rightarrow S_0^+$ (1706 cm^{-1}(−)) electron removal steps. Additionally there is a negative feature at 1712 cm^{-1} in the $S_0 \rightarrow S_1$ proton removal step. The time-courses at 1709 cm^{-1} and 1700 cm^{-1} (the corresponding negative peak of the differential feature 1709/1700 cm^{-1}) are shown in figure 5.39 on page 128.

Around 1678 cm^{-1}, electron removal steps are visible by decays, while proton removal steps cause rises: $S_1^n \rightarrow S_2^+$: 1680 cm^{-1}(+), $S_2^+ \rightarrow S_2^n$: 1679 cm^{-1}(−), $S_2^n \rightarrow S_3^+$: 1676 cm^{-1} (+), $S_3^+ \rightarrow S_3^n$: 1673 cm^{-1}, and $S_1^+ \rightarrow S_1^n$: 1677 cm^{-1}(−). The $S_3^n \rightarrow S_0^n$ and $S_0^n \rightarrow S_1^+$ transitions do not give rise to features in the decay associated spectra.

A similar behaviour can be seen around 1665 cm^{-1} with inversed signs: $S_1^n \rightarrow S_2^+$: 1665 cm^{-1}(−), $S_2^+ \rightarrow S_2^n$: 1664 cm^{-1}(+), $S_2^n \rightarrow S_3^+$: 1667 cm^{-1}(−), and $S_3^+ \rightarrow S_3^n$: 1666 cm^{-1} (+). The timecourses at 1665 cm^{-1} are shown in figure 5.39 on page 128.

Rises caused by proton removal can be seen around 1660 cm^{-1}: $S_2^+ \rightarrow S_2^n$: 1658 cm^{-1}(−), $S_3^+ \rightarrow S_3^n$: 1660 cm^{-1}(−), $S_3^n \rightarrow S_0^n$: 1661 cm^{-1}(−), $S_0^n \rightarrow S_0^+$: 1662 cm^{-1}(+), $S_1^+ \rightarrow S_1^n$: 1661 cm^{-1}(−). The timecourse is shown in figure 5.41 on page 130.

Around 1650 cm^{-1} there are features in four different charge removal steps, but the signs of the changes do not match the signs of the removed charges: $S_2^+ \rightarrow S_2^n$: 1651 cm^{-1}(+), $S_3^+ \rightarrow S_3^n$: 1650 cm^{-1}(−), $S_3^n \rightarrow S_0^n$: 1648 cm^{-1}(+), and $S_0^n \rightarrow S_1^+$: 1651 cm^{-1}(+). This means that the changes visible at this wavenumber are not directly caused by changes at Y_Z, but other structural changes.

There are almost only negative signals (rises) to be found around 1638 cm^{-1}: $S_1^n \rightarrow S_2^+$: 1638 cm^{-1}(−), $S_3^+ \rightarrow S_3^n$: 1639 cm^{-1}(+) (18 µs) / 1637 cm^{-1}(−) (142 µs), $S_0^n \rightarrow S_1^+$: 1637 cm^{-1} (−), $S_1^+ \rightarrow S_1^n$: 1642 cm^{-1}(−). The two signals in the $S_0 \rightarrow S_1$ transition differ by 5 cm^{-1} and they show the same sign; therefore, these may be features caused by unrelated chemical groups. In other words, maybe the 1642 cm^{-1} signal deserves its own row.

Many transitions are represented around 1575 cm^{-1}: $S_1^n \rightarrow S_2^+$: 1576 cm^{-1}(+), $S_2^+ \rightarrow S_2^n$: 1576 cm^{-1}(−), $S_2^n \rightarrow S_3^+$: 1575 cm^{-1}(+), $S_3^n \rightarrow S_0^n$: 1573 cm^{-1}(+), $S_1^+ \rightarrow S_1^n$: 1577 cm^{-1} (+). The signs of the changes match the signs of the charges removed except for the $S_1^+ \rightarrow S_1^n$ signal at 1577 cm^{-1}(+). The timecourses at 1575 cm^{-1} are shown in figure 5.39 on page

128.

There are many transitions represented around 1560 cm^{-1}, but the signs of the changes do not match the signs of the charges removed. Additionally there are acceptor side contributions visible at this wavenumber. The changes visible are $S_1{}^n \longrightarrow S_2{}^+$: 1564 cm^{-1}(+), $S_2{}^+ \longrightarrow S_2{}^n$: 1559 cm^{-1}(−), $S_2{}^n \longrightarrow S_3{}^+$: 1561 cm^{-1}(+), $S_3{}^+ \longrightarrow S_3{}^n$: 1562 cm^{-1}(+), and $S_0{}^n \longrightarrow S_1{}^+$: 1562 cm^{-1}(−).

There are two wavenumbers of interest which show the electron removal in the $S_1 \longrightarrow S_2$, $S_2 \longrightarrow S_3$, and $S_3 \longrightarrow S_0$ transitions with reversed signs: 1511 cm^{-1} and 1400 cm^{-1}. The features in the respective transitions are found at 1511 cm^{-1}(−), 1511 cm^{-1}(−), 1511 cm^{-1}(+); 1403 cm^{-1}(+), 1397 cm^{-1}(+), and 1396 cm^{-1}(−). The timecourses at these wavenumbers are shown on page 126 respectively; they show very similar, mirrored behaviour for each S-state transition. Therefore it is very likely that the features visible at 1511 cm^{-1} and 1400 cm^{-1} belong to the very same processes which take place during the transitions.

Surprisingly, besides the aforementioned signals in the amide I and II regions (1709, 1700, 1665, 1575, 1560 cm^{-1}) no clear indications for further Y_Z-like signals can be found. This is an important result obtained from table 6.3.

6.3. Final evaluation via DAS calculated from a fixed set of time constants

The elastic net approach is merely a heuristic tool which lacks an actual theoretic model, in the sense of modelling processes in the protein, underlying the math. A reasonable model for processes in the protein consists of a discrete set of linear equations, which then implies that the time constants are independent of the wavenumber; only the amplitudes should change. The lifetime maps (figures 5.47, 5.51, 5.58, 5.66, on pages 138, 143, 154, 166) show a different behaviour: the time constants seem to be highly dependent on the wavenumber, which contradicts the model described above. Nevertheless, there is one advantage in the elastic net approach: the constraint to obtain amplitudes with small magnitude, which is implemented in the routine.

This shall be illustrated with an example. In the $S_3 \longrightarrow S_0$ transition, the decay associated spectra shown in figure A.37 on page 298 show very large peaks at 1650 cm^{-1}. The peaks stem from alternating, large amplitudes. From the timecourse, shown in figure A.29 on page 289, one would expect amplitudes smaller than $2 \cdot 10^{-4}$. The fit calculated from a fixed set of time constants does not implement a constraint on the magnitude of the amplitudes though, and thus increases the amplitudes to obtain the best possible fit. The elastic net fit uses smaller amplitudes. Thus, the static fit calculated from a fixed set of time constants is

best used when the different phases are well separated in time. Because the DAS calculated from a fixed set of time constants still provide the better physical model, they are used in the following final evaluation.

The histograms of the lifetime maps obtained through the elastic net fits (figures 5.47, 5.51, 5.58, 5.66, on pages 138, 143, 154, 166) provide valuable information about prominent time constants in the individual S-state transitions. Combined with previous results (see table 3.1 on page 10) time constants can be chosen for each S-state transition to calculate corresponding fits. The time constants are given in table 6.4 on page 194. The resulting fits are shown in figures 6.1, 6.2, 6.3, and 6.5 and compared to the steady-state spectrum of the respective transition.

transition	time constants					
$S_1 \longrightarrow S_2$	20 µs	100 µs	2 ms	30 ms		
$S_2 \longrightarrow S_3$	20 µs	50 µs	390 µs	10 ms	30 ms	
$S_3 \longrightarrow S_0$	20 µs	80 µs	170 µs	1 ms	3 ms	30 ms
$S_0 \longrightarrow S_1$	20 µs	50 µs	200 µs	1 ms	3 ms	30 ms

Table 6.4.: Time constants chosen for amplitude calculation to obtain decay associated spectra.

Figure 6.1 on page 195 compares the $S_1 \longrightarrow S_2$ 100 µs DAS ($\times -1$) transition to the corresponding steady-state rapid-scan difference spectrum. Deviations of the DAS from the steady-state spectrum can be explained by four different categories. 1. Large differences can be observed especially in the amide I region (timecourses in figures 5.39 and 5.43 on pages 128 and 132). These differences reflect timecourses which start at a very large, negative amplitude and relax with the characteristic time constant of 110 µs to the final value of the steady-state spectrum. Contrary to features in the steady-state spectrum being created with a time constant of 10 µs, instantaneously created features disappear with a time constant of 110 µs and thus give rise to large features in the DAS which are invisible in the steady-state spectrum. A good example is also the derivative feature at 1774/1766 cm^{-1} (timecourses on page 133). 2. Relaxation from the 20 µs phase. In section 6.5 on page 202 the S-state independent built-up of features with 20 µs is discussed. Some of these features are visible in the DAS because they decay with 100 µs (timecourses on page 131). These decays are typically S-state independent. 3. Acceptor side contributions. These cause differences between the DAS and the steady-state spectrum through changes in the millisecond regime. 4. Y_Z-like behaviour. These features are discussed in section 6.2.5 on page 189. In the DAS, the Y_Z-like features are found at 1708/1699 cm^{-1}, 1665 cm^{-1}, 1574 cm^{-1}, and 1562 cm^{-1} (timecourses on pages 128 and 130).

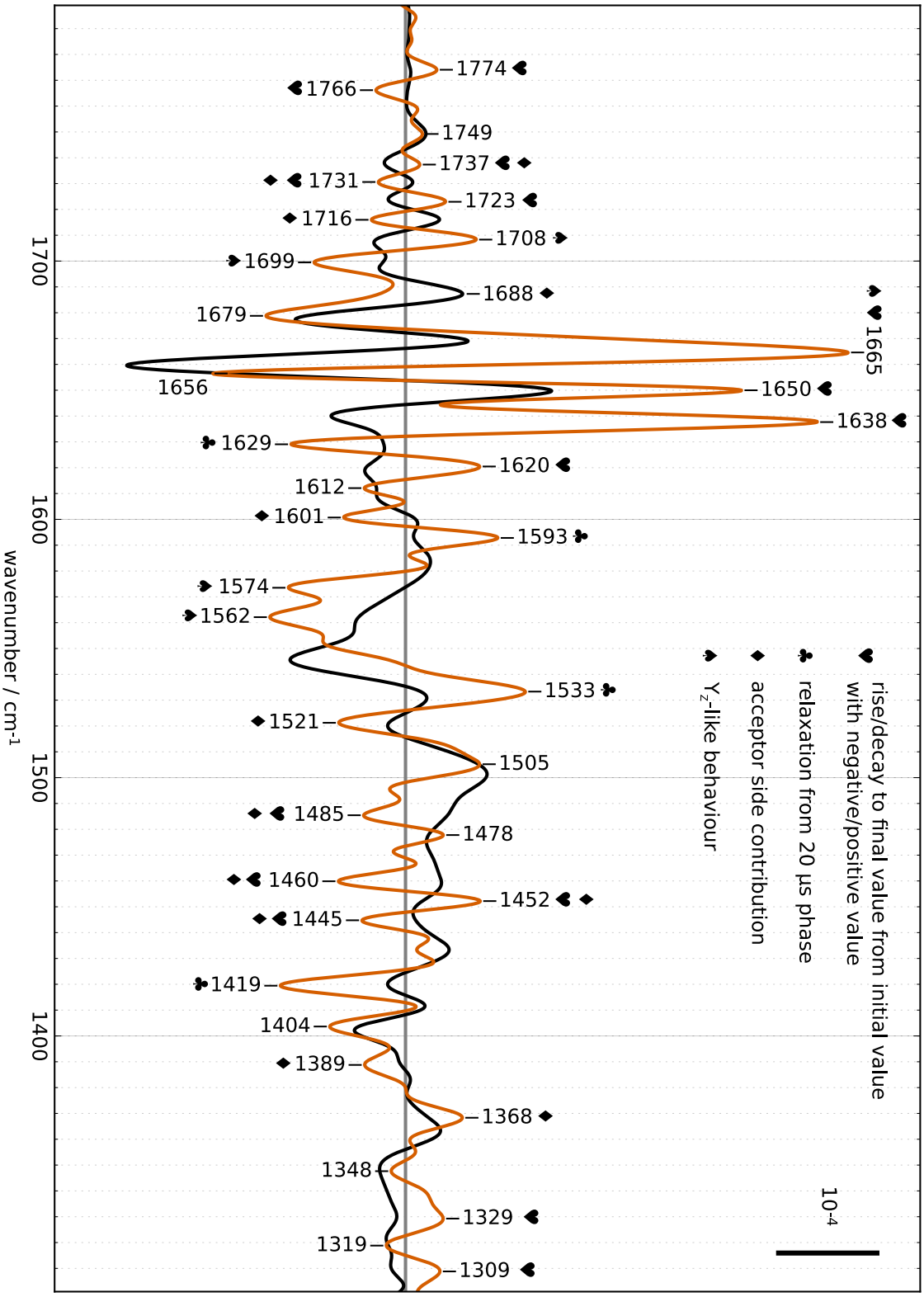

Figure 6.1.: Orange: 100 µs phase of the $S_1 \longrightarrow S_2$ transition obtained through calculating the amplitudes of a sum of exponential functions with fixed time constants (multiplied by -1). Black: rapid-scan $S_1 \longrightarrow S_2$ steady-state spectrum.

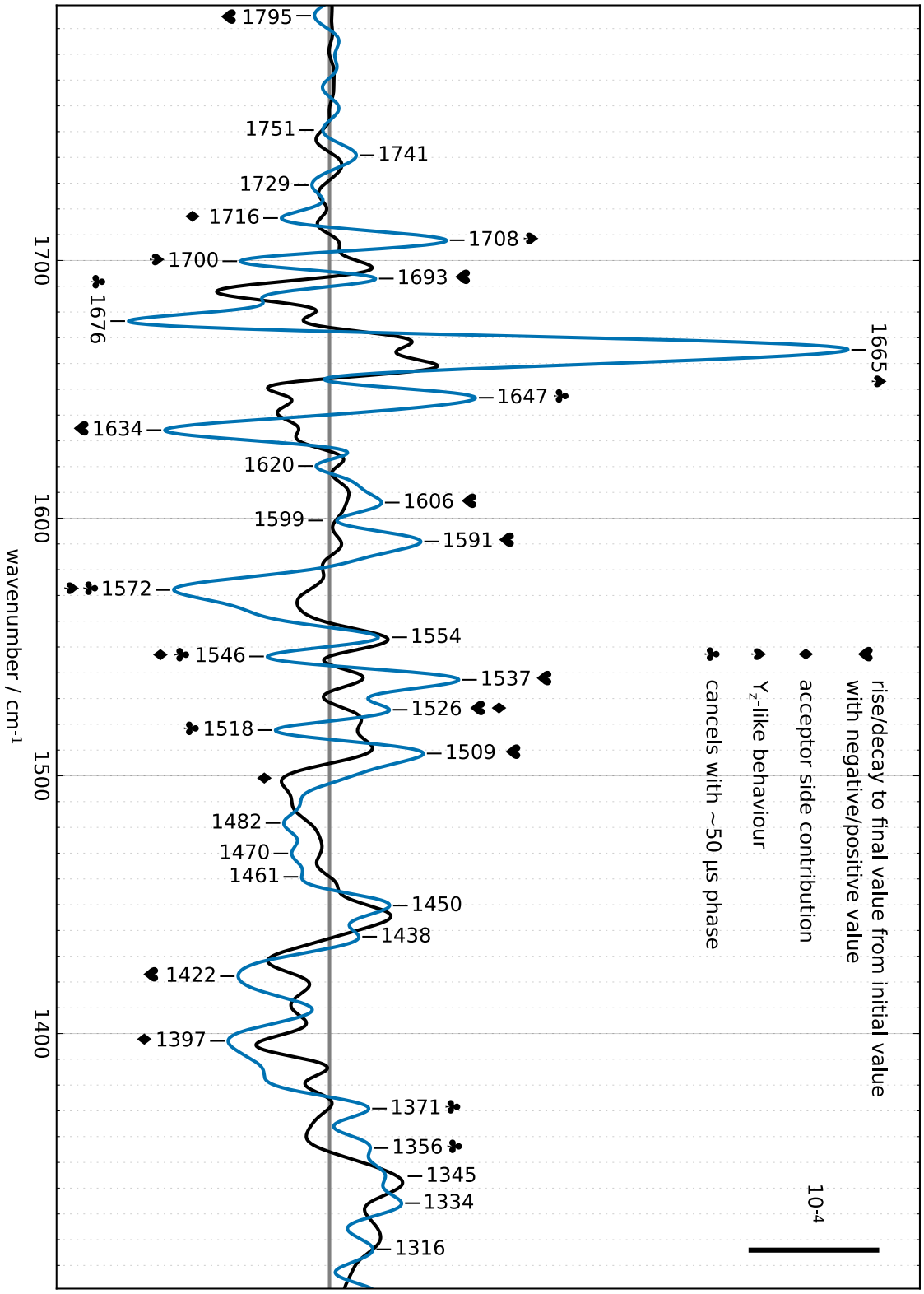

Figure 6.2.: Aquamarine: 390 µs phase of the $S_2 \longrightarrow S_3$ transition obtained through calculating the amplitudes of a sum of exponential functions with fixed time constants (multiplied by -1). Black: rapid-scan $S_2 \longrightarrow S_3$ steady-state spectrum.

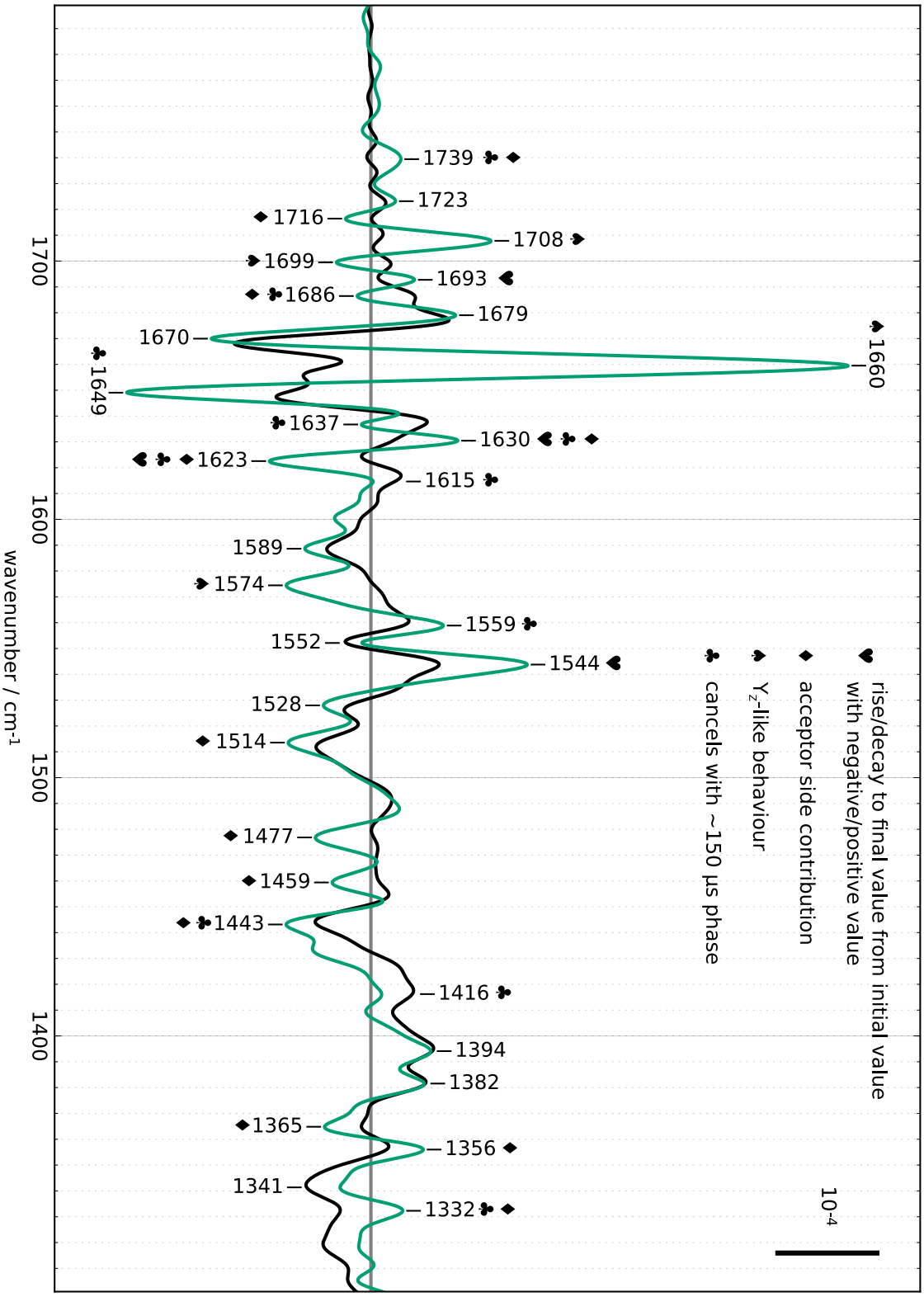

Figure 6.3.: Turquoise: 3 ms phase of the $S_3 \longrightarrow S_0$ transition obtained through calculating the amplitudes of a sum of exponential functions with fixed time constants (multiplied by -1). Black: rapid-scan $S_3 \longrightarrow S_0$ steady-state spectrum.

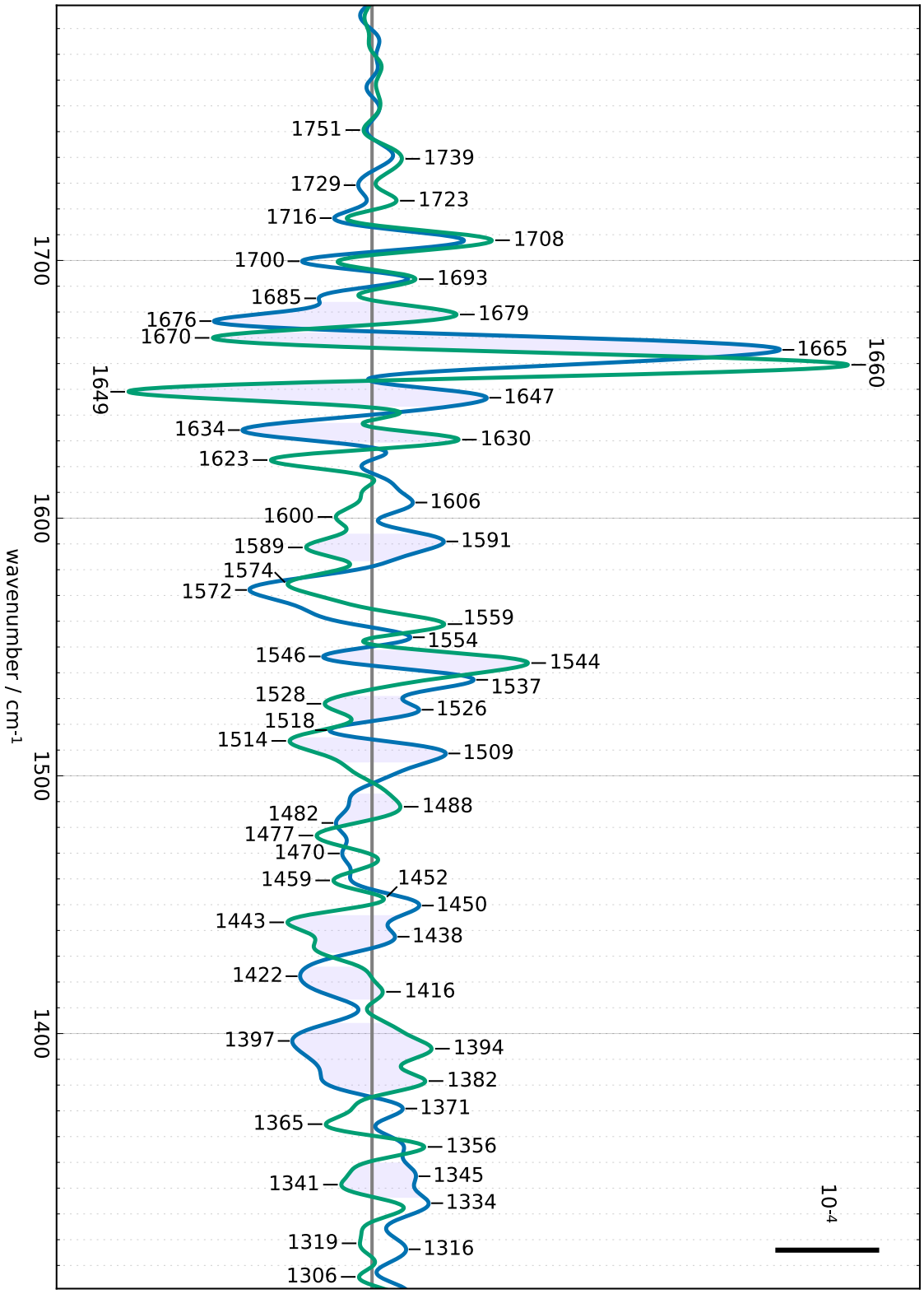

Figure 6.4.: Decay associated spectra for the electron transfers in the $S_2 \longrightarrow S_3$ transition (τ = 390 µs, aquamarine) and in the $S_3 \longrightarrow S_0$ transition (τ = 3 ms, turquoise). The shaded areas mark regions where both spectra show features with opposite sign.

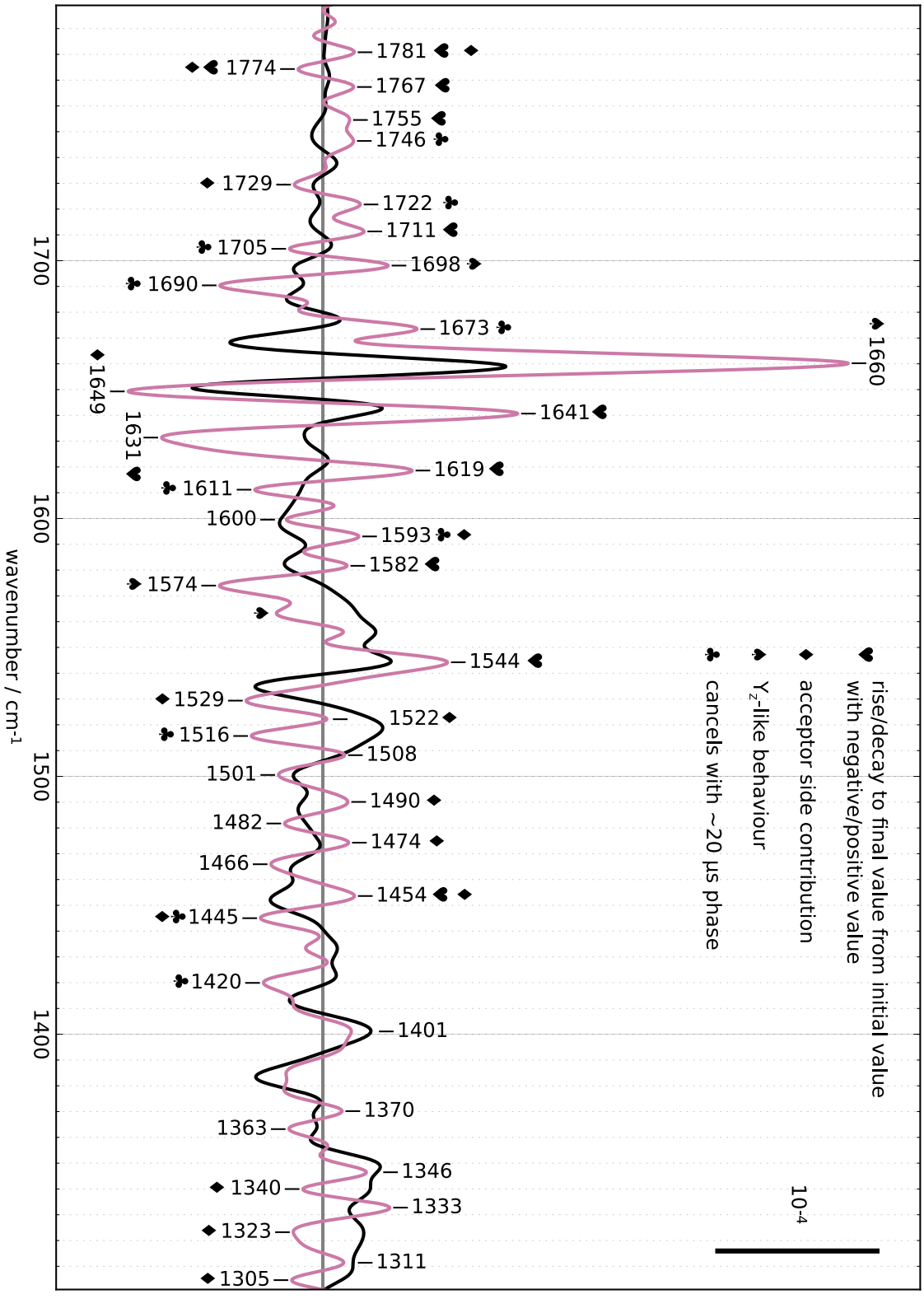

Figure 6.5.: Pink: 200 µs phase of the $S_0 \longrightarrow S_1$ transition obtained through calculating the amplitudes of a sum of exponential functions with fixed time constants (multiplied by -1). Black: rapid-scan $S_0 \longrightarrow S_1$ steady-state spectrum.

The DAS obtained from the elastic net fit shown in figure 5.49 on page 140 corresponds very well to the calculated DAS shown in figure 6.1 on page 195. Every peak assigned in the elastic net fit can be found in the calculated DAS. In this way it can be confirmed that the changes are indeed S-state dependent and unique to the $S_1 \longrightarrow S_2$ transition.

Figure 6.2 on page 196 compares the $S_2 \longrightarrow S_3$ 390 µs DAS (× − 1) transition to the corresponding steady-state rapid-scan difference spectrum. Again four categories cover deviations of the DAS from the steady-state spectrum: 1. The rise (decay) to the final value of the steady-state spectrum from a starting value with large negative (positive) amplitude; 2. acceptor side contributions; 3. Y_Z-like behaviour; and 4. the cancellation of features with a 50 µs phase. The fourth category was not observed in the $S_1 \longrightarrow S_2$ transition, in line with the rationale that there is only one electron abstracted from the OEC in that transition. In the $S_2 \longrightarrow S_3$ transition however, proton release precedes electron release. This leads to timecourses which show the cancellation of these processes. Since in the DAS in figure 6.2 on page 196 only the electron removal is reflected, features can be found which correspond to changes in the timecourse which cancel with 50 µs changes and are thus invisible in the steady-state spectrum. Prominent examples in the DAS can be found at 1676 cm^{-1} (page 133) and 1647 cm^{-1} (page 132). These reflect protein dynamics resulting from proton and electron removal from the OEC which are not visible in the steady-state spectrum.

Again the DAS obtained from the elastic net fit (figure 5.55 on page 147 correspond very well to the calculated DAS shown in figure 6.2 on page 196. Every peak assigned in the elastic net fit can be found in the calculated DAS, although there are some neighbouring features in the elastic net DAS which are not resolved in the calculated DAS (figure 6.2 on page 196). The elastic net DAS therefore seems to have a higher spectral resolution. Through the comparison with the elastic net DAS, the S-state dependent behaviour of the features shown in figure 6.2 on page 196 can be confirmed.

Figure 6.3 on page 197 compares the $S_3 \longrightarrow S_0$ 3 ms DAS (× − 1) transition to the corresponding steady-state rapid-scan difference spectrum. Differences can be classified as in the previous transition, only that this time some features correspond to cancellation with features with a time constant of 150 µs, which corresponds to the proton removal. Examples are 1739 cm^{-1} (page 133), 1649 cm^{-1} (page 132), and 1623 cm^{-1} (page 132). The DAS also includes some millisecond acceptor side contributions, for example visible at 1477 cm^{-1} (page 130). Although it might be possible to separate these contributions through including another 1 ms time constant in the fit calculation, I decided to omit the 1 ms time constant because this also severly degrades the quality of the 3 ms DAS.

As in the previous transitions, every labelled feature in the elastic net DAS (figure 5.62 on page 158) can be found in the calculated DAS (figure 6.3).

Figure 6.4 on page 198 compares the decay associated spectra of the electron removal

steps in the $S_2 \longrightarrow S_3$ and $S_3 \longrightarrow S_0$ transitions. Below 1690 cm^{-1} many features show opposite sign (shaded areas), and above 1690 cm^{-1} the features are mostly identical. The figure shows how structural changes especially in the carboxylic region which are established through the electron removal in the $S_2 \longrightarrow S_3$ transition are reversed during the $S_3 \longrightarrow S_0$ transition. Additionally, the overlapping 1708/1700 cm^{-1} derivative feature can be interpreted as the reduction of Y_Z^{ox}, which leads to the same changes in both transitions. In both transitions a 1739 cm^{-1} feature can be seen which hints at a protonation step.

Finally, figure 6.5 on page 199 compares the $S_0 \longrightarrow S_1$ 200 µs DAS (× − 1) transition to the corresponding steady-state rapid-scan difference spectrum. The two spectra show similar shapes especially in the lower wavenumber region, but also in the amide I region similarities can be found. In contrast to the previously discussed DAS, this DAS represents proton instead of electron transfer. The comparison of the two spectra in figure 6.5 on page 199 shows that features in the steady-state spectra can be assigned to the proton removal step, e.g. at 1401 cm^{-1} (figure 5.37 on page 126) and 1649 cm^{-1} (figure 5.43 on page 132).

Although the SNR is concerningly low for the DAS in the $S_0 \longrightarrow S_1$ transition, all features in the elastic net DAS (figure 5.69 on page 169) can be found in the calculated DAS (figure 6.5), except for one very small feature at 1439 cm^{-1} (which has an amplitude smaller than $1 \cdot 10^{-5}$).

In conclusion, the time-resolved step-scan data explains how the features in the steady-state spectra come about; donor-side processes can be separated from acceptor-side processes. Additionally, processes which are not visible in the steady-state spectra can be observed, most notably the reduction of Y_Z^{ox} which is visible in the amide I and II regions, but not in the $\nu_s(COO^-)$ and $\nu_{as}(COO^-)$ regions. The decay associated spectra which have been obtained through two independent approaches–the elastic net fit and the calculation of amplitudes corresponding to fixed time constants–show very good agreement and justify both approaches. In particular, the good agreement between the DAS concerning the slow time constants imply that also the elastic net DAS for the faster time constants provide significant information, information that cannot be easily obtained using DAS calculated from a fixed set of time constants.

A future approach could be to run the elastic net routine with a fixed number of time constants. In section 4.15.3 on page 54, a global fit approach was outlined, where the value of several time constants is calculated using the whole time-resolved spectrum. This approach also lacks the ability to find a set of time constants with overall very small magnitude of the amplitudes. The result is that in order to find a good fit, two time constants will converge to the same value, and the amplitudes corresponding to these time constants will be very large in magnitude but show opposite sign. Now in order to prevent this from happening, instead of simply calculating the amplitudes through matrix inversion the amplitudes could

be calculated using the elastic net routine in the residual function. The elastic net would only have to provide the property of using a solution with overall small magnitude. The restraint of providing a sparse solution would not be needed, because the time constants are already limited to a small number. The global fit, which varies the time constants, would then be combined with a residual function which minimizes the magnitude of the amplitudes. The convergence of two time constants combined with the amplitudes developing very large magnitudes with opposite signs could be prevented in this way.

6.4. Mirrored behaviour of carboxylic groups

A carboxylic residue is expected to show both $\nu_s(COO^-)$ and $\nu_{as}(COO^-)$ vibrational modes. If the symmetric mode changes, the asymmetric mode should change as well and vice versa. The timecourses should reflect this behaviour at any point in time. Figure 6.6 shows two pairs of timecourses which show mirrored behaviour.

The figure shows good agreement for two pairs of timecourses: 1400 cm^{-1}/1511 cm^{-1} and 1433 cm^{-1}/1544 cm^{-1}. These timecourses also show interesting behaviour in the ammonia investigation (figure 5.4 on page 81): the peaks at these wavenumbers are reduced in amplitude and show a mirrored behaviour during the $S_2 \longrightarrow S_3$ and $S_3 \longrightarrow S_0$ transitions. In the timecourses, the $S_3 \longrightarrow S_0$ transition shows changes with very large amplitude changes and crossings of the zero line.

The timecourses can be interpreted in the following way. In the $S_3 \longrightarrow S_0$ transition, vibrational modes at 1443 cm^{-1} and 1511 cm^{-1} (difference of ~70 cm^{-1}) disappear and vibrational modes at 1400 cm^{-1} and 1544 cm^{-1} (difference of ~144 cm^{-1}) appear. This drastic change in separation of $\nu_s(COO^-)$ and $\nu_{as}(COO^-)$ modes from 70 cm^{-1} to 144 cm^{-1} can only be explained by a coordination change of this carboxylic residue. In conclusion, the data presented in this study reveal a carboxylic residue with vibrational modes at 1443 cm^{-1} and 1511 cm^{-1} in the S_3 state which change to 1400 cm^{-1} and 1545 cm^{-1} in the S_0 state.

6.5. 20 μs decay associated spectra and P_{680}

On page 175 in figure 5.74, decay associated spectra obtained through global fitting with a time constant of 20 µs are shown. Especially in the region of the carboxylic modes it is conceivable that the individual spectra of the four transitions match very well. To investigate the changes in this time region, all four spectra were averaged and are shown in figure 6.7. The spectrum matches very well with the 20 µs decay associated spectrum obtained by Köhne (2017) by measuring a step-scan spectrum of PSII with equally populated

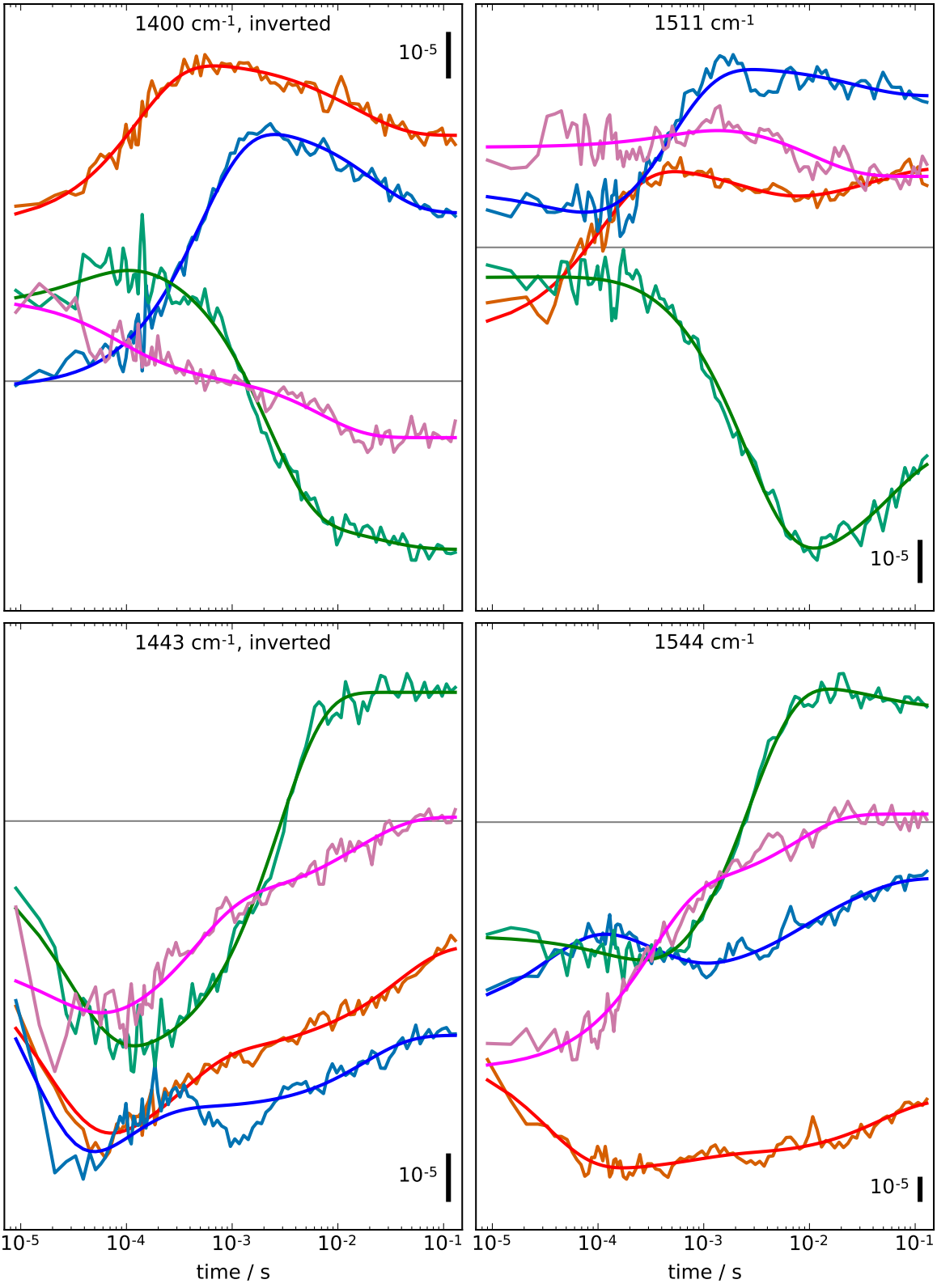

Figure 6.6.: Deconvoluted timecourses in H_2O at selected wavenumbers. Top left: 1400 cm^{-1} (amplitudes × −1), top right: 1511 cm^{-1}, bottom left: 1443 cm^{-1} (amplitudes × −1), bottom right: 1544 cm^{-1}. Orange: $S_1 \longrightarrow S_2$, aquamarine: $S_2 \longrightarrow S_3$, turquoise: $S_3 \longrightarrow S_0$, pink: $S_0 \longrightarrow S_1$. Elastic net fits are colored red, blue, green, magenta respectively.

reaction-cycle intermediates.

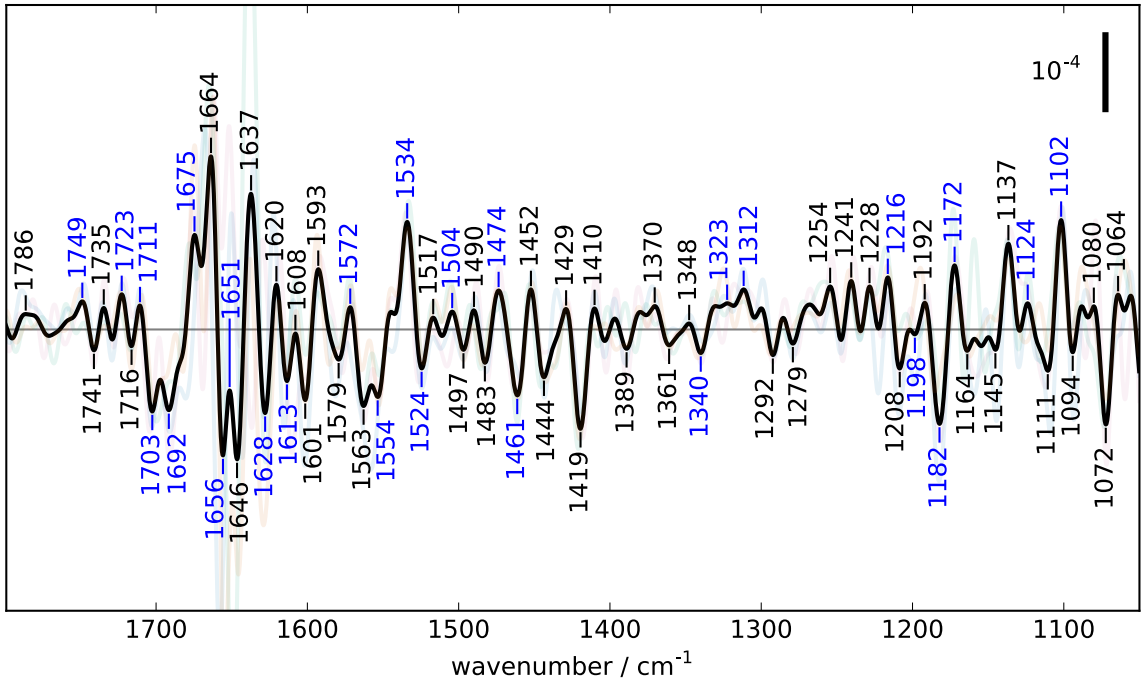

Figure 6.7.: The four S-state dependent 20 µs global fit decay associated spectra shown in figure 5.74 on page 175 were averaged to give the black spectrum. The blue labels mark features which correspond to features assigned to Chl vibrations (see text and section 3.3.2 on page 19).

The spectrum features prominent peaks at 1703, 1534, 1419, and 1182 cm^{-1}. The timecourses of these wavenumbers are shown in figure 5.42 on page 131. A common motive of the timecourses is the build-up, not the decay, of a local extremum at around 50 µs which only later decays in the hundreds of µs range.

In the following I will compare the spectrum in figure 6.7 on page 204 with the reported spectra introduced in section 3.3.2 on page 19 ("The special chlorophyll pair P_{680} and accessory chlorophyll Chl_Z"). Table 6.5 on page 205 compares the features visible in figure 6.7 on page 204 with the spectra reported in the literature.

The spectrum in figure 6.7 on page 204 compares remarkably well with the $P_{680}Chl^+/P_{680}$-Chl spectrum reported by Berthomieu, Hienerwadel, et al. (1998). Every labelled peak in the $P_{680}Chl^+/P_{680}Chl$ spectrum reported by Berthomieu, Hienerwadel, et al. (1998) can be found in figure 6.7 on page 204, with one exception: there is a negative peak in the spectra reported by Allakhverdiev et al. (1994), Noguchi and Inoue (1995b), Berthomieu, Hienerwadel, et al. (1998), and Okubo et al. (2007) around ~1682 cm^{-1} which can be envisioned as a negative shoulder in figure 6.7 on page 204.

The Chl_Z^+/Chl_Z features reported by Noguchi and Inoue (1995b) can be found in the spec-

fig. 6.7	$^3P_{680}/P_{680}$ N. 1993	P_{680}^+/P_{680} A. 1994	Chl_Z^+/Chl_Z N. 1995	$P_{680}Chl^+/P_{680}Chl$ B. 1998	P_{680}^+/P_{680} O. 2007
1749 (+)			1747 (+)	1752 (+)	
1741 (−)				1741 (+)	1743 (+)
1735 (+)		1735 (−)	1736 (−)		1735 (−)
1723 (+)	1723 (−)			1725 (+)	1723 (+)
1716 (−)	1716 (+)	1714 (+)	1714 (+)		
1711 (+)				1710 (+)	1711 (+)
1703 (−)				1700 (−)	1701 (−)
1692 (−)		1694 (−)			
1675 (+)		1676 (+)			
1664 (+)	1669 (−)				
1656 (−)	1659 (+)	1656 (−)	1660 (−)	1658 (−)	1658 (−)
1651 (+)		1652 (−)			1650 (+)
1628 (−)	1627 (+)	1626 (−)		1629 (−)	1630 (−)
1613 (−)			1614 (−)		1615 (−)
1572 (+)				1571 (+)	
1554 (−)	1556 (−)		1551 (−)	1550 (−)	1557 (−)
1534 (+)			1537 (−)		1531 (+)
1524 (−)					1521 (−)
1504 (+)				1504 (+)	
1490 (+)			1491 (−)		
1474 (+)		1477 (+)			1477 (+)
1461 (−)		1460 (−)			
1340 (−)			1346 (−)	1343 (−)	1345 (−)
1323 (+)	1322 (+)		1317 (+)		
1312 (+)				1310 (+)	1310 (+)
1285 (+)	1284 (−)		1286 (−)	1285 (−)	1286 (−)
1216 (+)					1218 (+)
1198 (−)					1202 (−)
1182 (−)	1178 (−)		1182 (−)	1180 (−)	1181 (−)
1172 (+)				1168 (+)	1170 (+)
1124 (+)	1124 (−)				
1102 (+)	1101 (+)				

Table 6.5.: Comparison of the features visible in figure 6.7 (first column) with literature spectra. Second column: triplet state of P_{680} reported by Noguchi, Inoue, and Satoh (1993). Third column: P_{680}^+ spectrum reported by Allakhverdiev et al. (1994). Fourth column: Chl_Z^+/Chl_Z^+ spectrum reported by Noguchi and Inoue (1995b). Fifth column: $P_{680}Chl^+/P_{680}Chl$ spectrum reported by Berthomieu, Hienerwadel, et al. (1998). Sixth column: P_{680}^+/P_{680} spectrum reported by Okubo et al. (2007).

trum too, but the positions of the peaks in figure 6.7 on page 204 deviate up to 6 cm^{-1} compared to the positions of the reported Chl_Z^+/Chl_Z spectrum.

There are only weak indications for a formation of tripled P_{680} in figure 6.7 on page 204. Although there are some peak positions which can be found in the triplet spectrum reported by Noguchi, Inoue, and Satoh (1993), they often have opposite signs. Furthermore, the following peaks reported by Noguchi, Inoue, and Satoh (1993) can not be found in the step-scan spectrum: 1707 cm^{-1}, 1539 cm^{-1}(−), 1510 cm^{-1}(+), 1345 cm^{-1}(−), and 1134 cm^{-1} (possibly found at 1137 cm^{-1} in figure 6.7 on page 204).

Allakhverdiev et al. (1994) and Okubo et al. (2007) reported $P_{680}{}^+/P_{680}$ difference spectra. Many peaks can be found in figure 6.7 on page 204, but there are also some deviations, notably around 1547 cm^{-1} and 1511 cm^{-1}. The spectrum reported by Allakhverdiev et al. (1994) shows additional features at 1607 cm^{-1}, 1577 cm^{-1}, 1566 cm^{-1}, 1539 cm^{-1}, 1436 cm^{-1}, 1427 cm^{-1}, 1404 cm^{-1}, and 1393 cm^{-1} which cannot be found in figure 6.7 on page 204. The spectrum reported by Okubo et al. (2007) shows an additional features at 1492 cm^{-1} which cannot be found in figure 6.7 on page 204.

In conclusion, the remarkable agreement with the reported $P_{680}Chl^+/P_{680}Chl$ spectrum implies that P_{680} and Chl_Z are still involved in S-state independent processes in the time regime of tens of microseconds.

It stands to reason to compare the 20 µs DAS in figure 6.7 on page 204 with reported spectra of $Y_Z^{ox}Y_Z$ (see section 3.3.1 on page 18). In the lower wavenumber region strong features of Y_Z^{ox}/Y_Z were reported at 1552 cm^{-1}(+)/1543 cm^{-1}(−), 1513 cm^{-1}(+), 1256 cm^{-1}(−) and 1105 cm^{-1}(−). These are not clearly visible in figure 6.7 on page 204; if at all, only with small amplitudes with opposite sign. In the amide I region, the reported 1638 cm^{-1}(+) and 1627 cm^{-1}(−) features can be found as 1637 cm^{-1}(+) and 1628 cm^{-1}(−) in figure 6.7 on page 204. The strong negative 1665 cm^{-1}(−) feature is a strong positive 1664 cm^{-1}(+) feature in figure 6.7 on page 204; see also the timecourse at 1665 cm^{-1} in figure 5.39 on page 128 which shows Y_Z-like behaviour at later times. Finally, a reported negative peak around 1706 cm^{-1} in the Y_Z^{ox}/Y_Z spectrum can not be found in figure 6.7 on page 204: in the 20 µs DAS, 1706 cm^{-1} is right on the shoulder of a 1711 cm^{-1}(+)/1703 cm^{-1} feature. In conclusion, there are no clear indications for Y_Z^{ox}/Y_Z features in figure 6.7 on page 204 and the 20 µs DAS most likely does not reflect Y_Z oxidation.

6.6. No clear S-state dependent signals caused by D1-Ala344

Chu, Hillier, and Debus (2004) assigned vibrational modes of D1-Ala344 to ~1356 cm^{-1} in the S_1 state and a peak at either ~1339 cm^{-1} or ~1320 cm^{-1} in the S_2 state (see section 3.3 on page 15). The authors argued that the changes visible in the FTIR spectrum correspond to the oxidation of the Mn ion which is ligated by D1-Ala344 in the $S_1 \longrightarrow S_2$ transition. Consequently, a reversal of these features should be visible in the $S_3 \longrightarrow S_0$ transition, when the stored oxidation equivalents are used up to oxidize water. From crystallographic results (Suga et al. 2015) it is known that D1-Ala344 ligates the Ca and the Mn-2 ion, which is the only Mn ion which is not supposed to change its oxidation state throughout the S-state cycle (Krewald, Retegan, Cox, et al. 2015). Therefore, other causes for the change in FTIR features need to be considered.

In the $S_1 \longrightarrow S_2$ transitions the local extrema of the difference spectra 1 ms after laser flash application can be found at 1322 cm^{-1}(–), 1339 cm^{-1}(+) (near zero), and 1364 cm^{-1}(+). The shoulder of the positive peak at 1364 cm^{-1} diminishes to less than 10% of the maximum amplitude at about 1355 cm^{-1}.

The timecourses at 1364, 1356, 1339, and 1320 cm^{-1} are shown in figure 5.38 on page 127. The discussion of the timecourses at 1339 cm^{-1} are hindered by the Fe^{2+}/Fe^{3+} features (see also figure 6.8 on page 209) which lead to an instantaneously created binary oscillation (negative, positive, negative, positive). The timecourses at 1356 cm^{-1} clearly show the electron transfer rates of the $S_1 \longrightarrow S_2$, $S_2 \longrightarrow S_3$, and $S_3 \longrightarrow S_0$ transitions. The electron transfer rate of the $S_0 \longrightarrow S_1$ transition is weakly present.

In the $S_1 \longrightarrow S_2$ there is a vibrational mode appearing at 1356 cm^{-1} (instead of disappearing), and another vibrational mode disappearing at 1320 cm^{-1} (instead of appearing). The timecourse at 1339 cm^{-1} shows the instantaneous disappearance of a vibrational mode being reversed to the zero level within 200 µs, i.e. no net S-state change for this vibrational mode in the $S_1 \longrightarrow S_2$ transition.

In conclusion, the timecourses do not support the interpretation of Chu, Hillier, and Debus (2004).

6.7. No clear millisecond-phase in the $S_0 \rightarrow S_1$ transition

Noguchi, Suzuki, et al. (2012) reported a slow rearrangement of carboxylate groups in the $S_0 \longrightarrow S_1$ transition based on a 1 ms rise in the corresponding IR timecourse at 1400 cm^{-1}.

Although such a behaviour is not present in the reported data (see figure 5.37 on page 126), I will shortly discuss a possible 1 ms phase in the $S_0 \longrightarrow S_1$ transition.

Figure 5.77 on page 178 shows DAS (τ =1 ms) for all four transitions. To some extent the spectra resembles the overall noise level. Still, binary oscillations can be found: at many wavenumbers the orange and turquoise spectra ($S_1 \longrightarrow S_2$ and $S_3 \longrightarrow S_0$) overlap and differ from the overlapping aquamarine and pink spectra ($S_2 \longrightarrow S_3$ and $S_0 \longrightarrow S_1$). These features are therefore most likely caused by acceptor side contributions.

Figure 5.70 on page 170 shows elastic net decay associated spectra (τ = 1 ms, σ = 200 µs). The noise level is much lower, but also the overall amplitude of the signals is extremely small. Distinct $S_0 \longrightarrow S_1$ transition signals can be found in the amide I and II regions, although $S_2 \longrightarrow S_3$ transition signals are even stronger in these regions. Notable peaks are located at 1543 cm^{-1}(–) (compare with the timecourse at 1544 cm^{-1} on page 126), 1573 cm^{-1} (+) (timecourse at 1575 cm^{-1} on page 128), 1618 cm^{-1}(–) (timecourse not shown; low amplitude, but 50 Hz influence), 1631/1638 cm^{-1}(–), and 1710 cm^{-1}(–) (timecourse at 1709 cm^{-1} on page 128).

The fact that notable 1 ms $S_0 \longrightarrow S_1$ transition features only appear in the amide I and II regions implies that these features are caused by an overall influence on the protein backbone, and disfavors a slow rearrangement of carboxylate groups. Furthermore, the prominent features of the $S_2 \longrightarrow S_3$ transition–although not at the same wavenumbers–implies a binary oscillation, which hints at the acceptor side. A binary process at the acceptor side could meet with a S-state dependent protein conformation, which leads to these binary oscillations at different wavenumbers in the amide region. In summary, this study provides only very weak evidence for a 1 ms phase specific to the $S_0 \longrightarrow S_1$ transition.

6.8. Acceptor side spectra

The time domains of the rapid-scan and step-scan measurements both cover the tens-of-milliseconds range; the rapid-scan measurement also covers the hundreds-of-milliseconds range. Consequently, decay associated spectra have been obtained to investigate the processes at the acceptor side.

In figure 5.79 on page 180, 30 ms decay associated spectra for all four deconvoluted transitions are shown. There are some binary oscillations visible, i.e. where the red and turquoise spectra differ from the aquamarine and pink spectra. Nevertheless, the general shape of the spectra is similar. The spectra have been averaged and are shown as black line in figure 6.8.

The rapid-scan measurements revealed decays with time constants of 60 ms and ~500 ms (see figure 5.10 on page 89). Binary oscillations were notprominent. For each of the two

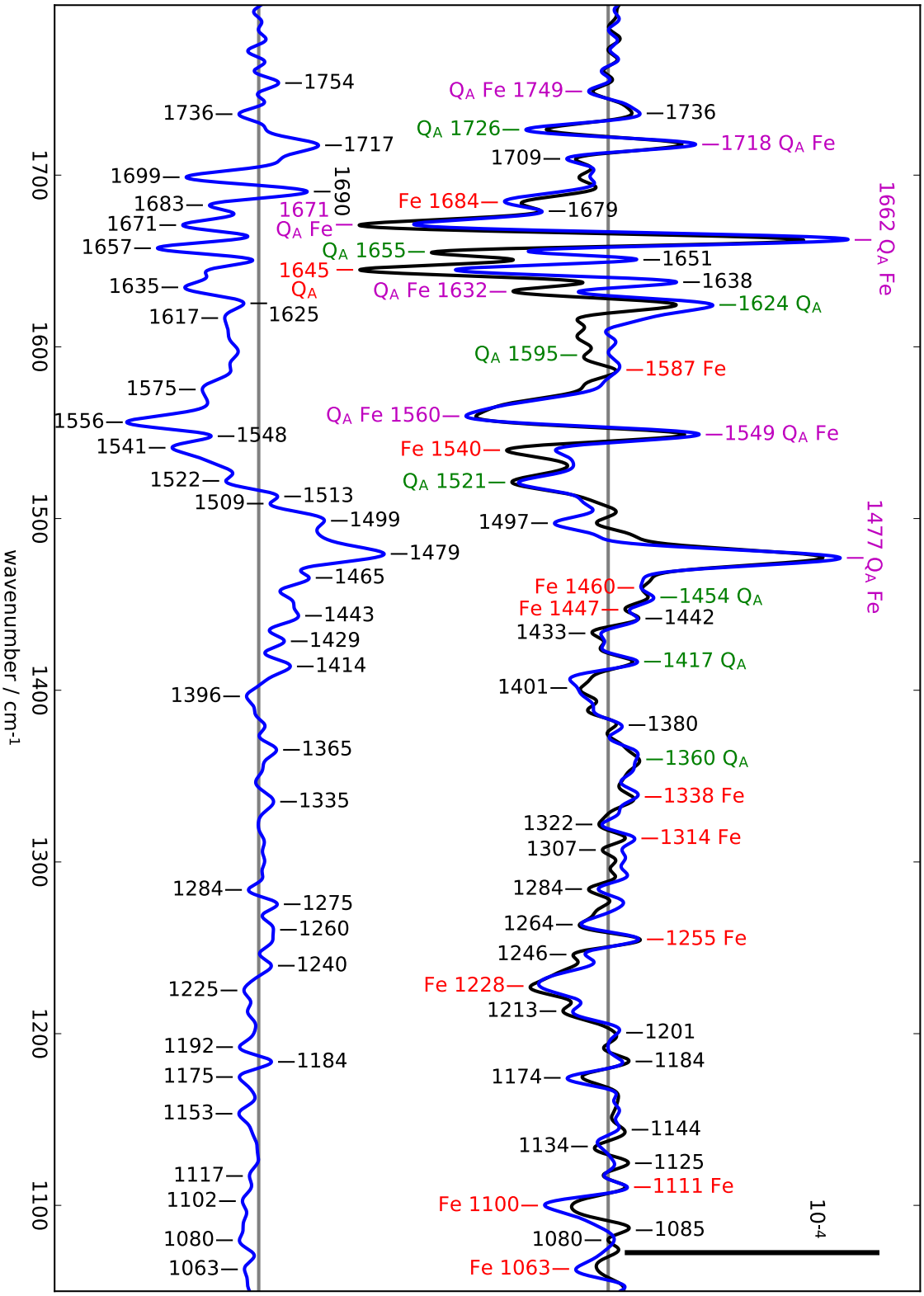

Figure 6.8.: Decay associated spectra in the ms-domain obtained through step-scan (black) and rapid-scan (blue) measurements. The black spectrum was obtained by averaging all four 30 ms associated step-scan spectra as shown in figure 5.79 on page 180. The blue spectra are the averages of the 58 ms and 473 ms associated rapid-scan spectra shown in figure 5.10 on page 89. The labels of the fast phase refer to wavenumber positions of the average of the two spectra.

fig. 6.8	Q_A^-/Q_A B. 1992	Fe^{2+}/Fe^{3+} N. 1995	Fe^{2+}/Fe^{3+} H. 1995
1749 (–)	1744 (–)		1753 (–)
1736 (+)		1734 (–)	1732 (–)
1726 (–)	1724 (–)		
1718 (+)	1719 (+)	1720 (+)	1720 (+)
1684 (–)			1687 (–)
1671 (–)	1672 (–)	1674 (–)	1673 (–)
1662 (+)	1662 (+)	1659 (+)	1660 (+)
1655 (–)	1657 (–)		
1645 (–)	1644 (–)		1643 (+)
1632 (–)	1632 (–)	1635 (–)	1636 (–)
1624 (+)	1625 (+)		
1595 (–)	1594 (–)		
1587 (+)		1589 (+)	1585 (+)
1560 (–)	1559 (–)	1566 (–)	1563 (–)
1549 (+)	1550 (+)	1552 (+)	1552 (+)
1540 (–)		1539 (–)	1539 (–)
1521 (–)	1520 (–)	1520 (+)	1517 (+)
1477 (+)	1478 (+)		1476 (+)
1460 (–)			1465 (–)
1454 (+)	1456 (+)		
1447 (–)			1449 (–)
1417 (+)	1417 (+)		
1360 (+)	1366 (+)		
1338 (+)		1335 (+)	1338 (+)
1314 (+)			1316 (+)
1255 (+)		1257 (+)	1257 (+)
1228 (–)		1227 (–)	1228 (–)
1111 (+)		1111 (+)	
1100 (–)		1103 (–)	
1063 (–)			1064 (–)

Table 6.6.: Comparison of the features visible in the 30 ms spectrum in figure 6.8 (first column) with literature spectra. Second column: Q_A^-/Q_A spectrum reported by Berthomieu, Nabedryk, et al. (1992). Third column: Fe^{2+}/Fe^{3+} spectrum reported by Noguchi and Inoue (1995a). Fourth column: Fe^{2+}/Fe^{3+} spectrum reported by Hienerwadel and Berthomieu (1995).

time constants, all ten decay associated spectra have been averaged. The resulting spectra are plotted as blue lines in figure 6.8.

The 30 ms phase of the step-scan and the 60 ms phase of the rapid-scan agree remarkably well; note that the spectra have not been rescaled. The time resolution of the rapid-scan measurement was 34 ms; the observed time constant of 30 ms in the step-scan measurement is smaller than the time resolution of the rapid-scan measurement. Therefore, the 60 ms spectrum of the rapid-scan measurement will from now on, together with the step-scan spectrum, be referenced as 30 ms spectrum. This spectrum is composed of Q_A^-/Q_A and Fe^{2+}/Fe^{3+} signals; the peak positions of the average of the two spectra are compared to earlier reported spectra in table 6.6. Every labelled peak in the Q_A^-/Q_A spectrum reported by Berthomieu, Nabedryk, et al. (1992) can be assigned unambiguously in the 30 ms spectrum. Likewise, every labelled peak in the Fe^{2+}/Fe^{3+} spectrum reported by Noguchi and Inoue (1995a) and Hienerwadel and Berthomieu (1995) can be found in the decay associated spectra, except for a positive peak at 1743 cm^{-1} (which is probably present as a positive shoulder in the decay associated spectra) and extremely small labelled features visible in the spectrum reported by Hienerwadel and Berthomieu (1995) at 1615 cm^{-1}, 1409 cm^{-1}, 1400 cm^{-1}, and 1163/1150 cm^{-1}.

In figure 6.8, the 500 ms spectrum shows no Fe^{2+}/Fe^{3+} contributions and can be interpreted as the recombination of non-Q_B centers. Additionally, the shift of the peak at 1477 cm^{-1} in the 30 ms spectrum to 1479 cm^{-1} in the 500 ms spectrum can be interpreted as the movement of an electron from Q_A to Q_B.

In figures 5.40 and 5.41 on pages 129 and 130 timecourses of selected acceptor-side wavenumbers are shown. Figure 5.40 shows primarily Fe^{2+}/Fe^{3+} timecourses while figure 5.41 shows primarily Q_A^-/Q_A timecourses. The timecourses share two general motifs: the first one is the presence of binary oscillations, which manifests itself in the orange and turquoise lines and the pink and aquamarine lines overlapping. The second motif is the (within the time resolution) instantaneously created positive or negative amplitude which then slowly (within tens of milliseconds) decays to the zero level.

7. Summary

This work presents results from FTIR measurements on photosystem II. In a previous project of our group, a custom made sample chamber was combined with a Vertex 70 spectrometer (Bruker, USA) to facilitate fully automated measurements (Süss 2011). In the current project, after several rectifications of the setup, time-resolved step-scan measurements of photosystem II in H_2O and D_2O have been completed successfully.

Rapid-scan measurements showed that the sample fully retains its activity through three to four days of measurements. The influence of ammonium on photosystem II FTIR (rapid-scan) difference spectra was reported for the first time for all S-state transitions. Different methods to eliminate a signal in the microsecond to millisecond domain caused by heating of the sample upon the application of an actinic laser flash were introduced and discussed. Finally, the time-resolved step-scan H_2O and D_2O datasets were carefully analyzed and discussed. The miss factor of the rapid-scan and step-scan measurements was as low as 9%.

In this work seven electron and proton removal steps of the S-state cycle have been identified using decay associated spectra obtained from different fitting approaches. Their time constants and kinetic isotope effects have been obtained. For the first time, the oxygen evolution spectrum in the ${S_3}^n \longrightarrow {S_0}^n$ transition has been obtained: the vibrational modes which are involved in the oxygen evolution step can be identified unambiguously.

Conclusions about the FTIR signature of Y_Z in intact photosystem II have been reported. The expected kinetic behaviour can be observed in certain protein backbone modes.

The time-resolved step-scan and rapid-scan measurements show excellent agreement regarding the comparably slow acceptor side processes.

The decay-associated spectrum of a very fast phase ($\tau \approx 20\,\mu s$) surprisingly shows agreement with P_{680} and Chl_Z spectra.

Two pairs of symmetric and asymmetric carboxylate modes match very well regarding the evolution in time in each S-state transition. These features are remarkably influenced by ammonia treatment and indicate substrate water movement during the catalytic cycle.

It has been an important goal to assign individual amino acid residues around the OEC to specific vibrational modes, for example through the use of site-directed mutagenesis. Once more modes can be assigned to specific amino acid residues, the reported datasets can be revistited to obtain valuable information about the evolution in time of these modes.

8. Zusammenfassung

Diese Arbeit präsentiert zeitaufgelöste FTIR-Spektren des Photosystem II. In einem vorausgegangenem Projekt wurde ein kommerzielles Spektrometer (Vertex 70, Bruker, USA) durch einen vollautomatisierten Probenwechsler ergänzt (Süss 2011). In diesem Projekt wurden nach kritischen Modifizierungen des Aufbaus erfolgreich zeitaufgelöste step-scan Messungen des PSII in H_2O und D_2O durchgeführt.

In dieser Arbeit belegen rapid-scan Messungen, dass das Protein selbst während drei- bis viertägigen Messungen seine Aktivität behält. Der Einfluss von Ammonium auf PSII FTIR Differenzspektren wurde zum ersten Mal für sämtliche S-Zustandsübergänge präsentiert. Verschiedene Methoden zur Kompensierung eines wärmeinduzierten Signals im Mikrosekunden- bis Millisekunden-Zeitbereich wurden vorgestellt und diskutiert. Schließlich wurden die zeitaufgelösten step-scan Messungen in H_2O und D_2O ausführlich analysiert und diskutiert. Der Missfaktor der Messungen betrug nur 9%.

Sieben Elektronen- und Protonenabstraktionsschritte des S-Zustandszyklus können mit Hilfe von Zerfallsspektren, die auf unterschiedliche Weise berechnet wurden, in den step-scan Daten identifiziert werden. Die Zeitkonstanten und der kinetische Isotopeneffekt dieser Schritte wurden berechnet. Zum ersten Mal wurde das Sauerstoffentwicklungsspektrum im ${S_3}^n \longrightarrow {S_0}^n$-Übergang präsentiert. Dadurch können nun eindeutige diejenigen Vibrationsmoden identifiziert werden, die in diesem Übergang modifiziert werden.

Diese Arbeit geht auch auf die Signale von Y_Z-moden in intaktem PSII ein: das erwartete dynamische Verhalten kann in Proteinstruktursignalen beobachtet werden.

Das mit einer sehr schnellen Phase ($\tau \approx 20\,\mu s$) assoziierte Spektrum zeigt überraschenderweise Übereinstimmungen mit P_{680} und Chl_Z-Spektren.

Zwei Paare von symmetrischen und asymmetrischen Carboxylatmoden spiegeln sehr gut ihr Verhalten im Zeitbereich während der S-Zustandsübergänge. Diese Moden werden auch durch Ammonium modifiziert und zeigen die Änderungen im Wasserstoffbrückenbindungsnetzwerk rund um den OEC während des katalytischen Zyklusses.

Ein wichtiges Ziel der derzeitigen PSII-Forschung ist es, spezifische FTIR-Signale spezifischen Amminosäureresten zuzuordnen, beispielsweise durch Punktmutationen. Die gewonnenen Datensätze werden auch in Zukunft weitere wichtige Informationen liefern können, sobald diese Zuordnungen getroffen werden können.

9. Acknowledgements

I would like to express my sincere gratitude to my supervisor Prof. Dr. Holger Dau for his support of my research, for his patience, for very helpful discussions and for giving me important advice whenever I needed it.

Likewise, I would like to thank Prof. Dr. Joachim Heberle for serving as my second supervisor, as well as the members of the Promotionskomission.

Furthermore, I would like to thank Dr. Petko Chernev for his support in my work, most importantly the incredible fast realization of software requests I had for the experimental setup. I am also grateful for showing me how to run the experiment and for programming software for data processing.

Philipp Simon and I always had very stimulating discussions about our newest findings, expensive instrumentation and intricate technological details of our setups. These discussions are gratefully acknowledged.

It was never boring in the office. For the good time in the office and their support I thank Dr. Yvonne Zilliges, Philipp Simon, Janis Hantke, and all current and former users of our office.

When I had a first final version of my thesis ready, Paul Greife read my thesis from beginning to end in a very short time and provided very helpful corrections and suggestions, which I am very grateful for.

All current and former members of the AG Dau are gratefully acknowledged for the good cooperation in the labs. I thank especially Oliver Karge for his introduction into several lab routines, Dr. Ivelina Zaharieva for showing me how to obtain photosystem II from spinach, and Philipp Simon, Jan Köhne, Zhiyong Liang, Ricardo Assunção, André Kussicke, and others for the successful time spent in the fridge in the dark processing spinach leaves. I would like to thank Dr. Yvonne Zilliges for her commitment to the organization of the S1 labs.

Administration is a necessary but often overlooked task. I feel grateful to Sylvia Luther for her support regarding formal requests, and to Kerstin Wagner and Christian Frischkorn for organizing the events of the collaborative research center. Likewise I would like to thank Sieglinde Endrias and the staff members of the administrative divisions of the institute.

I would like to thank Till Stensitzki for crucial advice regarding different techniques for

fitting functions to data points, and for his contribution to open source fitting libraries.

The collaborative research center (SFB) regularly provided opportunities to get in touch with fellow PhD students. Therefore I would like to thank the organizers of the SFB, and my fellow PhD students for the interesting discussions. In this regard I thank the Deutsche Forschungsgemeinschaft for funding through the Sonderforschungsbereich 1078.

For the help regarding technical modifications of the setup I thank the members of the university workshop, especially Melanie Klockenberg. I gratefully acknowledge the help of the electronics workshop, especially Martin Rust, regarding various tasks. I would like to thank the members of the Tieftemperaturlabor for their support in delivering liquid nitrogen to the setup. I especially thank Michael Prüfer of the Tieftemperaturlabor for providing a student workshop with courses and access to spinning, milling, and drilling machines.

A very important part in completing this thesis was fulfilled by my wife Dr. Yanping Peng, who I thank for her unconditional support and for a kick up the backside at the right time.

Finally I would like to thank my parents and my siblings for their support and for believing in me.

Bibliography

Ahlbrink, R et al. (1998). "Function of tyrosine Z in water oxidation by photosystem II: electrostatical promotor instead of hydrogen abstractor". In: *Biochemistry* 37, pp. 1131–1142. DOI: 10.1021/bi9719152.

Allakhverdiev, SI et al. (1994). "Light-induced Fourier transform infrared spectrum of the cation radical P680+". In: *FEBS Letters* 339, pp. 151–154. ISSN: 0014-5793. DOI: 10.1016/0014-5793(94)80404-4.

Alonso-Mori, R et al. (2016). "Towards characterization of photo-excited electron transfer and catalysis in natural and artificial systems using XFELs". In: *Faraday Discussions* 194, pp. 621–638. DOI: 10.1039/C6FD00084C.

Barth, A (2000). "The infrared absorption of amino acid side chains". In: *Progress in Biophysics and Molecular Biology* 74, pp. 141–173. ISSN: 0079-6107. DOI: 10.1016/S0079-6107(00)00021-3.

Berthold, DA, GT Babcock, and CF Yocum (1981). "A highly resolved, oxygen-evolving photosystem II preparation from spinach thylakoid membranes". In: *FEBS Letters* 134, pp. 231–234. ISSN: 1873-3468. DOI: 10.1016/0014-5793(81)80608-4.

Berthomieu, C, A Boussac, et al. (1992). "Molecular changes following oxidoreduction of cytochrome b559 characterized by Fourier transform infrared difference spectroscopy and electron paramagnetic resonance: Photooxidation in photosystem II and electrochemistry of isolated cytochrome b559 and iron protoporphyrin IX-bisimidazole model compounds". In: *Biochemistry* 31, pp. 11460–11471. DOI: 10.1021/bi00161a026.

Berthomieu, C, R Hienerwadel, et al. (1998). "Hydrogen bonding of redox-active tyrosine Z of photosystem II probed by FTIR difference spectroscopy". In: *Biochemistry* 37, pp. 10547–10554. DOI: 10.1021/bi980788m.

Berthomieu, C, E Nabedryk, et al. (1992). "Further characterization of QA photoreduction using 15 N-labeled PSII membranes". In: *Research in photosynthesis: Proceedings of the IXth international congress on photosynthesis, Nagoya, Japan, August 30-September 4, 1992*. Ed. by N Murata. Vol. 3. Springer Netherlands, pp. 53–56. ISBN: 978-0-7923-2073-9.

Buchta, J, M Grabolle, and H Dau (2007). "Photosynthetic dioxygen formation studied by time-resolved delayed fluorescence measurements—method, rationale, and results on

the activation energy of dioxygen formation". In: *Biochimica et Biophysica Acta (BBA) - Bioenergetics* 1767, pp. 565–574.

Chernev, P et al. (2010). In: *Photosynthesis research for food, fuel and future: 15th international conference on photosynthesis*. Ed. by TY Kuang, CM Lu, and LX Zhang. Springer Berlin Heidelberg, pp. 95–101. ISBN: 9783642320347.

— (2011). "Carboxylate shifts steer interquinone electron transfer in photosynthesis". In: *Journal of Biological Chemistry* 286, pp. 5368–5374. DOI: 10.1074/jbc.M110.202879.

Chu, HA, YW Feng, et al. (2004). "Ammonia-induced structural changes of the oxygen-evolving complex in photosystem II as revealed by light-induced FTIR difference spectroscopy". In: *Biochemistry* 43, pp. 10877–10885.

Chu, HA, W Hillier, and RJ Debus (2004). "Evidence that the C-terminus of the D1 polypeptide of photosystem II is ligated to the manganese ion that undergoes oxidation during the S1 to S2 transition: an isotope-edited FTIR study". In: *Biochemistry* 43, pp. 3152–3166. DOI: 10.1021/bi035915f.

Cole, J et al. (1987). "Assignment of the g=4.1 ERP signal to manganese in the S2 state of the photosynthetic oxygen-evolving complex: An X-ray absorption edge spectroscopy study [sic]". In: *Biochimica et Biophysica Acta (BBA) - Bioenergetics* 890, pp. 395–398. DOI: 10.1016/0005-2728(87)90169-1.

Connes, J (1963). "Spectroscopic studies using Fourier transformations". In: *US Naval Ordnance Test Station China Lake, CA*.

Dau, H, JC Andrews, et al. (1995). "Structural consequences of ammonia binding to the manganese center of the photosynthetic oxygen-evolving complex: An X-ray absorption spectroscopy study of isotropic and oriented photosystem II particles". In: *Biochemistry* 34, pp. 5274–5287. DOI: 10.1021/bi00015a043.

Dau, H and I Zaharieva (2009). "Principles, efficiency, and blueprint character of solar-energy conversion in photosynthetic water oxidation". In: *Accounts of Chemical Research* 42, pp. 1861–1870. DOI: 10.1021/ar900225y.

de Wijn, R and HJ van Gorkom (2001). "Kinetics of electron transfer from QA to QB in photosystem II". In: *Biochemistry* 40, pp. 11912–11922. DOI: 10.1021/bi010852r.

Debus, RJ (2014). "Evidence from FTIR Difference Spectroscopy That D1-Asp61 Influences the Water Reactions of the Oxygen-Evolving Mn4CaO5 Cluster of Photosystem II". In: *Biochemistry* 53, pp. 2941–2955. DOI: 10.1021/bi500309f.

— (2015). "FTIR studies of metal ligands, networks of hydrogen bonds, and water molecules near the active site Mn4CaO5 cluster in Photosystem II". In: *Biochimica et Biophysica Acta (BBA) - Bioenergetics* 1847, pp. 19–34. ISSN: 0005-2728. DOI: 10.1016/j.bbabio.2014.07.007.

— (2016). "Identifying carboxylate ligand vibrational modes in photosystem II with QM/MM methods". In: *Proceedings of the National Academy of Sciences* 113, pp. 12613–12615.

Douglas Jr., J (1955). "On the numerical integration of $\frac{\partial^2 u}{\partial x^2} + \frac{\partial^2 u}{\partial y^2} = \frac{\partial u}{\partial t}$ by implicit methods". In: *Journal of the Society for Industrial and Applied Mathematics* 3, pp. 42–65. DOI: 10.1137/0103004.

Forman, ML, WH Steel, and GA Vanasse (1966). "Correction of asymmetric interferograms obtained in Fourier spectroscopy". In: *Journal of the Optical Society of America* 56, pp. 59–63. DOI: 10.1364/JOSA.56.000059.

Fowler, CF (1977). "Proton evolution from photosystem II stoichiometry and mechanistic considerations". In: *Biochimica et Biophysica Acta (BBA) - Bioenergetics* 462, pp. 414–421. ISSN: 0005-2728. DOI: 10.1016/0005-2728(77)90139-6.

Gerencsér, L and H Dau (2010). "Water oxidation by photosystem II: H2O–D2O exchange and the influence of pH support formation of an intermediate by removal of a proton before dioxygen creation". In: *Biochemistry* 49, pp. 10098–10106.

— (2013). "Role of protons in photosynthetic water oxidation: pH influence on the rate constants of the S-state transitions and hypotheses on the S2⟶S3 transition". In: *Photosynthesis research for food, fuel and the future: 15th international conference on photosynthesis*. Berlin, Heidelberg: Springer Berlin Heidelberg, pp. 244–249. ISBN: 978-3-642-32034-7. DOI: 10.1007/978-3-642-32034-7_51.

Gorkom, HJ van and P Gast (1996). "Measurement of Photosynthetic Oxygen Evolution". In: *Biophysical Techniques in Photosynthesis*. Ed. by J Amesz and AJ Hoff. Dordrecht: Springer Netherlands, pp. 391–405. ISBN: 978-0-306-47960-1. DOI: 10.1007/0-306-47960-5_24.

Görlin, M (2012). "Light-induced and time-resolved FTIR difference spectroscopy of photosystem II". MA thesis. Sweden: Uppsala University.

Grabolle, M and H Dau (2007). "Efficiency and role of loss processes in light-driven water oxidation by PSII". In: *Physiologia Plantarum* 131, pp. 50–63. ISSN: 1399-3054. DOI: 10.1111/j.1399-3054.2007.00941.x.

Griffiths, PR and JA de Haseth (1986). *Fourier transform infrared spectrometry*. Wiley. ISBN: 9780471099024.

Han, GY, F Mamedov, and S Styring (2012). "Misses during water oxidation in photosystem II are S state-dependent". In: *Journal of Biological Chemistry* 287, pp. 13422–13429. DOI: 10.1074/jbc.M112.342543.

Haumann, M, O Bögershausen, et al. (1997). "Photosynthetic oxygen evolution: H/D isotope effects and the coupling between electron and proton transfer during the redox reactions at the oxidizing side of photosystem II". In: *Photosynthesis Research* 51, pp. 193–208. ISSN: 1573-5079. DOI: 10.1023/A:1005861917596.

Haumann, M, A Grundmeier, et al. (2008). "Photosynthetic water oxidation at elevated dioxygen partial pressure monitored by time-resolved X-ray absorption measurements". In: *Proceedings of the National Academy of Sciences* 105, pp. 17384–17389. DOI: 10.1073/pnas.0802596105.

Haumann, M, P Liebisch, et al. (2005). "Photosynthetic O2 formation tracked by time-resolved X-ray experiments". In: *Science* 310, pp. 1019–1021. ISSN: 0036-8075. DOI: 10.1126/science.1117551.

Hienerwadel, R and C Berthomieu (1995). "Bicarbonate binding to the non-heme iron of photosystem II, investigated by Fourier transform infrared difference spectroscopy and 13C-labeled bicarbonate". In: *Biochemistry* 34, pp. 16288–16297. DOI: 10.1021/bi00050a008.

Hienerwadel, R, A Boussac, et al. (1997). "Fourier transform infrared difference spectroscopy of photosystem II tyrosine D using site-directed mutagenesis and specific isotope labeling". In: *Biochemistry* 36, pp. 14712–14723. DOI: 10.1021/bi971521a.

Huang, HH, TH Wang, and HA Chu (2008). "Ammonia-induced structural changes of the oxygen-evolving complex in photosystem II diminished at 277 K as revealed by light-induced FTIR difference spectroscopy". In: *Photosynthesis. Energy from the sun: 14th international congress on photosynthesis*. Ed. by JF Allen et al. Dordrecht: Springer Netherlands, pp. 389–391. ISBN: 978-1-4020-6709-9. DOI: 10.1007/978-1-4020-6709-9_87.

Iuzzolino, L et al. (1998). "X-ray absorption spectroscopy on layered photosystem II membrane particles suggests manganese-centered oxidation of the oxygen-evolving complex for the S0-S1, S1-S2, and S2-S3 transitions of the water oxidation cycle". In: *Biochemistry* 37, pp. 17112–17119. DOI: 10.1021/bi9817360.

Jackson, M and HH Mantsch (1995). "The use and misuse of FTIR spectroscopy in the determination of protein structure". In: *Critical Reviews in Biochemistry and Molecular Biology* 30, pp. 95–120. DOI: 10.3109/10409239509085140.

Jones, E, T Oliphant, P Peterson, et al. (2017). *SciPy: Open source scientific tools for Python*. [Online; accessed 2017-03-03]. URL: http://www.scipy.org/.

Karge, O, AN Bondar, and H Dau (2014). "Cationic screening of charged surface groups (carboxylates) affects electron transfer steps in photosystem-II water oxidation and quinone reduction". In: *Biochimica et Biophysica Acta (BBA) - Bioenergetics* 1837, pp. 1625–1634. DOI: 10.1016/j.bbabio.2014.07.012.

Kim, JS (2009). "Zeitaufgelöste polarographische Messungen der photosynthetischen Sauerstoffentwicklung des Photosystem II aus Spinacia oleracea". MA thesis. Germany: Humboldt-Universität zu Berlin.

Kim, SY and BA Barry (1998). "The protein environment surrounding tyrosyl radicals D and Z in photosystem II: A difference Fourier-transform infrared spectroscopic study".

In: *Biophysical Journal* 74, pp. 2588–2600. ISSN: 0006-3495. DOI: 10.1016/S0006-3495(98)77965-2.

Kimura, Y and T Ono (2001). "Chelator-induced disappearance of carboxylate stretching vibrational modes in S2/S1 FTIR spectrum in oxygen-evolving complex of photosystem II". In: *Biochemistry* 40, pp. 14061–14068.

Klauss, A, M Haumann, and H Dau (2012). "Alternating electron and proton transfer steps in photosynthetic water oxidation". In: *Proceedings of the National Academy of Sciences* 109, pp. 16035–16040.

— (2015). "Seven steps of alternating electron and proton transfer in photosystem II water oxidation traced by time-resolved photothermal beam deflection at improved sensitivity". In: *The Journal of Physical Chemistry B* 119, pp. 2677–2689. DOI: 10.1021/jp509069p.

Köhne, J (2017). "Time-resolved step-scan FTIR spectroscopy on photosystem II with equally populated reaction-cycle intermediates". MA thesis. Germany: Freie Universität Berlin.

Kok, B, B Forbush, and M McGloin (1970). "Cooperation of charges in photosynthetic O2 evolution–I. A linear four step mechanism". In: *Photochemistry and Photobiology* 11, pp. 457–475. ISSN: 1751-1097. DOI: 10.1111/j.1751-1097.1970.tb06017.x.

Krewald, V, M Retegan, N Cox, et al. (2015). "Metal oxidation states in biological water splitting". In: *Chemical Science* 6 (3), pp. 1676–1695. DOI: 10.1039/C4SC03720K.

Krewald, V, M Retegan, and DA Pantazis (2016). "Principles of natural photosynthesis". In: *Solar energy for fuels*. Ed. by H Tüysüz and CK Chan. Springer International Publishing, pp. 23–48. ISBN: 978-3-319-23099-3. DOI: 10.1007/128_2015_645.

Lichtenthaler, HK (1987). "Chlorophylls and carotenoids: pigments of photosynthetic biomembranes". In: *Plant Cell Membranes*. Ed. by T Aartsma and J Matysik. Vol. 148. Academic Press, pp. 350–382. DOI: 10.1016/0076-6879(87)48036-1.

Mäntele, W (1996). "Infrared and Fourier-Transform Infrared Spectroscopy". In: *Biophysical Techniques in Photosynthesis*. Ed. by J Amesz and AJ Hoff. Dordrecht: Springer Netherlands, pp. 137–160. ISBN: 978-0-306-47960-1. DOI: 10.1007/0-306-47960-5_9.

McEvoy, JP and GW Brudvig (2006). "Water-splitting chemistry of photosystem II". In: *Chemical Reviews* 106, pp. 4455–4483. DOI: 10.1021/cr0204294.

Menzel, J (2009). "Fourier-Transformation-Infrarot-Spektroskopie am Photosystem II zur Untersuchung des Reaktionszyklus". MA thesis. Germany: Freie Universität Berlin.

Mezzetti, A and W Leibl (2016). "Time-resolved infrared spectroscopy in the study of photosynthetic systems". In: *Photosynthesis Research*, pp. 1–24.

Murata, N, ed. (1992). *Research in photosynthesis: Proceedings of the IXth international congress on photosynthesis, Nagoya, Japan, August 30-September 4, 1992*. Vol. 3. Springer Netherlands.

Nakamoto, K (1986). *Infrared and raman spectra of inorganic and coordination compounds*. Wiley. ISBN: 9780471010661.

Nakamura, S et al. (2014). "Fourier transform infrared detection of a polarizable proton trapped between photooxidized tyrosine YZ and a coupled histidine in photosystem II: Relevance to the proton transfer mechanism of water oxidation". In: *Biochemistry* 53, pp. 3131–3144. DOI: 10.1021/bi500237y.

Noguchi, T (2013). "Monitoring the reactions of photosynthetic water oxidation using infrared spectroscopy". In: *Biomedical Spectroscopy and Imaging* 2, pp. 115–128.

Noguchi, T and Y Inoue (1995a). "Identification of Fourier transform infrared signals from the non-heme iron in photosystem II". In: *The Journal of Biochemistry* 118, pp. 9–12.

— (1995b). "Molecular interactions of the redox-active accessory chlorophyll on the electron-donor side of photosystem II as studied by Fourier transform infrared spectroscopy". In: *FEBS Letters* 370, pp. 241–244. ISSN: 1873-3468. DOI: 10.1016/0014-5793(95)00833-U.

Noguchi, T, Y Inoue, and K Satoh (1993). "FT-IR studies on the triplet state of P680 in the photosystem II reaction center: triplet equilibrium within a chlorophyll dimer". In: *Biochemistry* 32, pp. 7186–7195.

Noguchi, T, T Ono, and Y Inoue (1992). "Detection of structural changes upon S1-to-S2 transition in the oxygen-evolving manganese cluster in photosystem II by light-induced Fourier transform infrared difference spectroscopy". In: *Biochemistry* 31, pp. 5953–5956.

— (1995). "Direct detection of a carboxylate bridge between Mn and Ca^{2+} in the photosynthetic oxygen-evolving center by means of Fourier transform infrared spectroscopy". In: *Biochimica et Biophysica Acta (BBA) - Bioenergetics* 1228, pp. 189–200.

Noguchi, T and M Sugiura (2003). "Analysis of flash-induced FTIR difference spectra of the S-state cycle in the photosynthetic water-oxidizing complex by uniform 15N and 13C isotope labeling". In: *Biochemistry* 42, pp. 6035–6042. DOI: 10.1021/bi0341612.

Noguchi, T, H Suzuki, et al. (2012). "Time-resolved infrared detection of the proton and protein dynamics during photosynthetic oxygen evolution". In: *Biochemistry* 51, pp. 3205–3214. DOI: 10.1021/bi300294n.

Okubo, T et al. (2007). "Perturbation of the structure of P680 and the charge distribution on its radical cation in isolated reaction center complexes of photosystem II as revealed by fourier transform infrared spectroscopy". In: *Biochemistry* 46, pp. 4390–4397. DOI: 10.1021/bi700157n.

Pedregosa, F et al. (2011). "Scikit-learn: Machine Learning in Python". In: *Journal of Machine Learning Research* 12, pp. 2825–2830.

Pérez-Navarro, M et al. (2016). "Recent developments in biological water oxidation". In: *Current Opinion in Chemical Biology* 31, pp. 113–119. ISSN: 1367-5931. DOI: 10.1016/j.cbpa.2016.02.007.

Pokhrel, R, RJ Debus, and GW Brudvig (2015). "Probing the Effect of Mutations of Asparagine 181 in the D1 Subunit of Photosystem II". In: *Biochemistry* 54, pp. 1663–1672. DOI: 10.1021/bi501468h.

Press, W et al. (1997). *Numerical Recipes in C*. 2nd ed. Cambridge University Press. ISBN: 0-521-43108-5.

Rahmelow, K, W Hübner, and T Ackermann (1998). "Infrared absorbances of protein side chains". In: *Analytical Biochemistry* 257, pp. 1–11. ISSN: 0003-2697. DOI: 10.1006/abio.1997.2502.

Saphon, S and AR Crofts (1977). "Protolytic reactions in photosystem II: A new model for the release of protons accompanying the photooxidation of water". In: *Zeitschrift für Naturforschung C* 32, pp. 617–626. DOI: 10.1515/znc-1977-7-822.

Schiller, H and H Dau (2000). "Preparation protocols for high-activity photosystem II membrane particles of green algae and higher plants, pH dependence of oxygen evolution and comparison of the S2-state multiline signal by X-band EPR spectroscopy". In: *Journal of Photochemistry and Photobiology B: Biology* 55, pp. 138–144. ISSN: 1011-1344. DOI: 10.1016/S1011-1344(00)00036-1.

Schiller, H, J Dittmer, et al. (1998). "Structure and orientation of the oxygen-evolving manganese complex of green algae and higher plants investigated by X-ray absorption linear dichroism spectroscopy on oriented photosystem II membrane particles". In: *Biochemistry* 37, pp. 7340–7350. DOI: 10.1021/bi972329b.

Schönborn, M (2012). "Numerische Simulation und experimentelle Unteruchung eines Nd:YVO_4-Hochleistungs-Verstärkers". MA thesis. Germany: Technische Universität Berlin.

Service, RJ, W Hillier, and RJ Debus (2014). "Network of hydrogen bonds near the oxygen-evolving Mn4CaO5 cluster of photosystem II probed with FTIR difference spectroscopy". In: *Biochemistry* 53, pp. 1001–1017. DOI: 10.1021/bi401450y.

Service, RJ, J Yano, et al. (2011). "Participation of Glutamate-354 of the CP43 polypeptide in the ligation of manganese and the binding of substrate water in photosystem II". In: *Biochemistry* 50, pp. 63–81. DOI: 10.1021/bi1015937.

Shimada, Y et al. (2009). "Effect of a single-amino acid substitution of the 43 kDa chlorophyll protein on the oxygen-evolving reaction of the cyanobacterium Synechocystis sp. PCC 6803: Analysis of the Glu354Gln mutation". In: *Biochemistry* 48, pp. 6095–6103. DOI: 10.1021/bi900317a.

Strickler, MA et al. (2008). "Glutamate-354 of the CP43 polypeptide interacts with the oxygen-evolving Mn4Ca cluster of photosystem II: a preliminary characterization of the Glu354Gln

mutant". In: *Philosophical Transactions of the Royal Society of London B: Biological Sciences* 363, pp. 1179–1188. ISSN: 0962-8436. DOI: 10.1098/rstb.2007.2213.

Suga, M et al. (2015). "Native structure of photosystem II at 1.95 A resolution viewed by femtosecond X-ray pulses". In: *Nature* 517, pp. 99–103.

Süss, B (2011). "Entwicklung eines Step-scan FTIR-Experiments zur Untersuchung der lichtinduzierten Wasserspaltung der oxygenen Photosynthese". PhD thesis. Germany: Freie Universität Berlin.

Süss, B, F Ringleb, and J Heberle (2016). "New ultrarapid-scanning interferometer for FT-IR spectroscopy with microsecond time-resolution". In: *Review of Scientific Instruments* 87, p. 063113. DOI: 10.1063/1.4953658.

Tsuno, M et al. (2011). "Interaction and inhibitory effect of ammonium cation in the oxygen evolving center of photosytem II". In: *Biochemistry* 50, pp. 2506–2514. DOI: 10.1021/bi101952g.

Umena, Y et al. (2011). "Crystal structure of oxygen-evolving photosystem II at a resolution of 1.9 Å". In: *Nature* 473, pp. 55–60.

Venyaminov, SY and NN Kalnin (1990). "Quantitative IR spectrophotometry of peptide compounds in water (H2O) solutions. I. Spectral parameters of amino acid residue absorption bands". In: *Biopolymers* 30, pp. 1243–1257. ISSN: 1097-0282. DOI: 10.1002/bip.360301309.

Wellburn, AR (1994). "The spectral determination of chlorophylls a and b, as well as total carotenoids, using various solvents with spectrophotometers of different resolution". In: *Journal of Plant Physiology* 144, pp. 307–313. ISSN: 0176-1617. DOI: 10.1016/S0176-1617(11)81192-2.

Wydrzynski, T, JA Freeman, and K Satoh (2006). *Photosystem II: the light-driven water:plastoquinone oxidoreductase*. Springer Netherlands. ISBN: 9781402042546.

Zaharieva, I, H Dau, and M Haumann (2016). "Sequential and coupled proton and electron transfer events in the S2 ⟶ S3 transition of photosynthetic water oxidation revealed by time-resolved X-ray absorption spectroscopy". In: *Biochemistry* 55, pp. 6996–7004. DOI: 10.1021/acs.biochem.6b01078.

Zaharieva, I, M Grabolle, et al. (2013). "Water oxidation in photosystem II: Energetics and kinetics of intermediates formation in the S2⟶S3 and S3⟶S0 transitions monitored by delayed chlorophyll fluorescence". In: *Photosynthesis research for food, fuel and the future: 15th international conference on photosynthesis*. Berlin, Heidelberg: Springer Berlin Heidelberg, pp. 234–238. ISBN: 978-3-642-32034-7. DOI: 10.1007/978-3-642-32034-7_49.

Zhang, HM et al. (1997). "A time-resolved FTIR difference study of the plastoquinone QA and redox-active tyrosine YZ interactions in photosystem II". In: *Biochemistry* 36, pp. 11762–11768. DOI: 10.1021/bi970815t.

Zimmermann, JL and AW Rutherford (1986). "Photoreductant-induced oxidation of Fe2+ in the electron-acceptor complex of Photosystem II". In: *Biochimica et Biophysica Acta (BBA) - Bioenergetics* 851, pp. 416–423. DOI: 10.1016/0005-2728(86)90078-2.

Zou, H and T Hastie (2005). "Regularization and variable selection via the elastic net". In: *Journal of the Royal Statistical Society: Series B (Statistical Methodology)* 67, pp. 301–320. ISSN: 1467-9868. DOI: 10.1111/j.1467-9868.2005.00503.x.

A. Appendix

A.1. Data processing: utility functions

It is convenient to save the function definitions in this section in a single python file, which then can be imported in any data processing script using `from utility_functions.py import *`.

```
#!/usr/bin/python
# coding=UTF8

import numpy as np
import re # is needed for sorted_nicely
```

A.1.1. Generally useful functions

```
def inspect(iobject):
    if type(iobject) == type([]) or type(iobject) == type(np.array([])):
        print type(iobject), ":", len(iobject)
        inspect(iobject[0])
    else:
        print type(iobject)

def sorted_nicely(l):
    import re
    """ Sort the given iterable in the way that humans expect."""
    convert = lambda text: int(text) if text.isdigit() else text
    alphanum_key = lambda key: \
                   [ convert(c) for c in re.split('([0-9]+)', key) ]
    return sorted(l, key = alphanum_key)
```

The function `inspect()` can be used on any variable to show its structure. It is similar to numpy's `shape`. `sorted_nicely` can be used to sort a list of strings numerically as humans

would expect, e.g. sorting 100 after 1.

A.1.2. Functions to calculate the Fourier transform

The following function is needed to shift step-scan interferograms to their corresponding rapid-scan levels:

```
def shift_ifg(rapid_scan, step_scan):
    shifted_timecourses = []
    for position in range(len(rapid_scan)):
        timecourse = step_scan[position]
        target_level = rapid_scan[position]
        original_level = np.mean(timecourse[50:950])
        shift = target_level - original_level
        shifted_timecourses.append(np.array(timecourse) + shift)

    return np.array(shifted_timecourses)
```

The next function implements the Forman correction and returns the interferogram with its centerburst at the first position:

```
def forman_correct(interferogram, phase_center_index):
    interferogram = interferogram - np.mean(interferogram[10:130])
    center = int(np.mean([np.argmax(interferogram[10:-10]),\
                          np.argmin(interferogram[10:-10])])) + 10
    shortie = interferogram[center-phase_center_index:\
                            center+phase_center_index+1]
    shortie = np.roll(shortie, len(shortie)/2)
    shortie_fft = np.fft.fft(shortie)
    theta = np.arctan2(np.imag(shortie_fft), np.real(shortie_fft))
    phase_ifg = np.fft.irfft(np.exp(-1j * theta[:len(theta)/2]))
    phase_ifg = np.roll(phase_ifg, len(phase_ifg)/2)
    corrifg = np.convolve(interferogram, phase_ifg, mode='same')
    # this is needed for splitting up the data correctly:
    new_center = np.argmax(abs(corrifg))
    corrifg = list(corrifg[new_center:]) + list(corrifg[:new_center])
    return corrifg
```

The following two functions are used to calculate the difference cosine FFT and the absolute FFT:

```
def roll_ifg(interferogram):
    new_center = np.argmax(abs(np.array(interferogram)))
    interferogram = np.roll(interferogram, new_center)
    return interferogram

def cos_window(input_data, reverse=False):
    if reverse == True:
        x_array = np.array(range(len(input_data)))[::-1]
    else:
        x_array = np.array(range(len(input_data)))
    return np.cos(x_array*np.pi/(len(input_data)*2))**2 \
           * np.array(input_data)

def cosfft_diff(interferogram, elements, window):
    center = len(interferogram)/2
    zeros = list(np.zeros(elements-len(interferogram)))
    interferogram = list(interferogram[:center]) \
                    + zeros + list(interferogram[center:])

    # windowing the interferogram: left half
    interferogram[0:window] = \
        cos_window(interferogram[0:window], True)
    interferogram[168-window:168] = \
        cos_window(interferogram[168-window:168], False)

    # windowing the interferogram: right half
    next_part = interferogram[elements-167:elements-167+window]
    interferogram[elements-167:elements-167+window] = \
        cos_window(next_part, True)
    interferogram[elements-window:] = \
        cos_window(interferogram[elements-window:], False)

    fft = np.real(np.fft.fft(interferogram))
    fft = fft[0:len(fft)/2]
```

```
    fft = fft[10:-10]
    return fft

def cosfft_absolute(interferogram, elements):
    interferogram = roll_ifg(interferogram)
    center = len(interferogram)/2
    zeros = list(np.zeros(elements-len(interferogram)))
    interferogram = list(interferogram[:center]) \
                    + zeros + list(interferogram[center:])
    fft = np.real(np.fft.fft(interferogram))
    fft = fft[0:len(fft)/2]
    fft = fft[10:-10]
    return fft
```

A.1.3. Reading Opus files

The files returned by the spectrometer have a binary format and are supposed to be read with a proprietary software from Bruker, which would be able to convert the data to a freely accessible format. Due to the large size of the dataset though it is of tremendous advantage—both in terms of disk usage and data processing speed—to be able to read the binary files directly. Although there was no official documentation obtainable on how to read the files, Dr. Petko Chernev found a routine to access the data in the binary files. An implementation of the routine in python is given below.

```
with open("binary_interferogram_data.0", 'rb') as f:
    f.seek(12) # skip 12 bytes
    while True:
        T = np.fromstring(f.read(2), dtype=np.int16)[0]
        f.read(2) # skip 2 bytes
        S = np.fromstring(f.read(4), dtype=np.uint32)[0]
        A = np.fromstring(f.read(4), dtype=np.uint32)[0]
        if T == 2055: # "interferogram data"
            break

    f.seek(A + 4) # go to byte A + 4
    C = np.fromstring(f.read(4), dtype=np.uint32)[0]
    N = ((S-8)/C)-38
    # C = number of curves, N = number of floats per curve
```

```
    f.seek(A + 32) # go to byte A + 32; the data starts here
    data = []
    for index in range(C):
        this_data = np.fromstring(f.read(N*4), dtype=np.float32)
        f.read(152) # skip 152 bytes
        data.append(this_data)
```

The data is then stored in the variable `data`. The individual floating point values are saved with single precision (4 bytes). It is advisable to save this routine in an utility function file which can be imported into each individual evaluation script (see section A.1 on page 229).

Sometimes it is desirable to just load portions of the data, for example to calculate the dark-spectra of the step-scan measurements (see section 4.14.1 on page 46). In this case one can modify the above function to access parts of the data while reading the file as a `mmap` object first. This will decrease the access time by about 50 %.

If it is foreseeable that parts of the data will be accessed many times, it may be feasible to read the whole file first and then save the interferogram data as a `numpy` object. In this case `numpy`'s own `mmap` functionality can be used which will vastly decrease the access time. However, the process of saving the file as `numpy` array will take a long time itself and use additional disc space.

A.1.4. Logarithmic averaging

```
def log_average(timecourse):
    averaged_timecourse = []
    times = []

    # before the flash: 19 times 50 points
    for i in range(1,20):
        averaged_timecourse.append(np.mean(timecourse[i*50:(i+1)*50]))
        start = i*50
        stop = (i+1)*50
        middle = start + 25 - 1
        time = (middle-zero_time_index) * time_resolution
        times.append(time)

    # around the flash
    for i in range(zero_time_index-10, zero_time_index+20):
        averaged_timecourse.append(timecourse[i])
```

```
        time = (i-zero_time_index)*time_resolution
        times.append(time)

    # after the flash
    increment = 1.0
    index = zero_time_index+20

    while index + increment < len(timecourse):
        intinc = int(increment)
        averaged_timecourse.append(np.mean(timecourse[index:index+intinc]))
        delta_t = (intinc-1) * time_resolution / 2.0
        time = (index - zero_time_index) * time_resolution + delta_t
        times.append(time)
        index += intinc
        increment = increment * factor

    return averaged_timecourse, times
```

A.1.5. Calculating time-resolved difference spectra

```
diff_spectra = []
diff_ifgs = []
for ifg in ifgs:
    diff_ifg = ifg - dark_ifg
    for position in replace_list:
        diff_ifg[position] = 0

    diff_ifgs.append(diff_ifg)
    diff_spectrum = - (1/np.log(10)) \
                    * cosfft_diff(diff_ifg, elements, window) \
                    / cosfft_absolute(dark_ifg, elements)

    diff_spectra.append(diff_spectrum)
```

The functions `cosfft_diff` and `cosfft_absolute` take as arguments the interferograms and an integer `elements` which tells the function the length of the array it should return, in other words implements the zero filling factor. `cosfft_diff` additionally takes an argument `window` which is an integer and applies a $\cos^2$ window of length `window` to

the very ends and the centerburst of the difference interferogram. For the definition of the functions, see section A.1 on page 229.

A.1.6. Linear least squares in python

```
def calculate_amplitudes(times, timecourse, taus, B=[]):
    # calculate the amplitudes for a given set of taus by solving Ax = b;
    # B = np.linalg.pinv(A.T.dot(A)).dot(A.T) can be provided to avoid
    # repeated matrix inversion; the offset is in the last column of A

    taus = np.abs(np.array(taus)) # needed when fitting taus

    if B == []:
        A = [ [ np.exp(-time/tau) for tau in taus ] + [ 1 ] \
              for time in times ]
        solution = np.linalg.lstsq(A, timecourse)[0]
    else:
        solution = B.dot(timecourse)

    amplitudes = solution[:-1]
    offset = solution[-1]

    # calculate the fit as a timecourse
    fit = np.zeros(len(times))
    fit += offset
    for index, tau in enumerate(taus):
        fit += amplitudes[index] * np.exp(-times/tau)

    return amplitudes, offset, fit
```

A.1.7. Fitting time constants

```
def fit_taus(times, timecourse, taus, limits=[]):
    from scipy.optimize import least_squares

    def residual(r_taus):
        amplitudes, offset, fit = \
```

```
            calculate_amplitudes(times, timecourse, r_taus)
        return timecourse - fit

    if limits != []:
        solution = least_squares(residual, taus, \
                                 bounds=np.transpose(limits))
    else:
        solution = least_squares(residual, taus)

    amplitudes, offset, fit = \
        calculate_amplitudes(times, timecourse, list(solution.x))

    return sorted(np.abs(solution.x)), amplitudes, offset, fit
```

A.2. Buffer ingredients

Table A.1 on page 237 shows the ingredients for the buffers used in this work.

A.3. Handling air displacement pipettes

In our study we frequently used air displacement pipettes. While it may seem to the untrained scientist that using these pipettes solely comprises pushing a button, there are many things to be considered. The most important is to never lay the pipette flat on the table with a used pipette tip still fixed to the pipette. Residual liquid will move into the pipette even if the used tip seems to be completely empty. If a tip is to be reused (which it should not) the pipette should be hang on a holder with the tip pointing down. It is good practice to discard a tip immediately after use.

Many factors influence the precision of the pipette:

- The volume might change due to the heat from the operator's hand. Likewise, most pipettes are calibrated to operate at room temperature; if precise pipetting is required in a cooling chamber, a room-temperature pipette should be picked up outside of the cooling chamber and the pipetting should be done immediately.

- It is important to dip the pipette tip with the right angle and deep enough, but not too deep into the liquid.

		ingredient weight in g			
		0.25 l	0.5 l	1.0 l	2.0 l
buffer A (pH 7.5)					
saccharose	0.4 M		68.46	136.92	273.84
HEPES	25 mM		2.99	5.96	11.92
EDTA	1 mM		0.15	0.29	0.58
NaCl	15 mM		0.44	0.88	1.75
$MgCl_2$	5 mM		0.51	1.02	2.03
$CaCl_2$	5 mM		0.28	0.55	1.11
Added shortly before use:					
BSA	2 g/l	0.5	1.0	2.0	4.0
sodium ascorbate	1 g/l	0.25	0.5	1.0	2.0
buffer B (pH 6.2)					
MES	25 mM		2.44	4.88	9.76
NaCl	150 mM		4.38	8.77	17.53
$MgCl_2 \cdot 6H_2O$	5 mM		0.51	1.02	2.03
buffer C (pH 6.2)					
Betaine	1 M	29.29	58.58	117.5	235
MES	25 mM	1.22	2.44	4.88	9.76
NaCl	15 mM	0.22	0.44	0.88	1.76
$MgCl_2 \cdot 6H_2O$	10 mM	0.51	1.02	2.03	4.06
$CaCl_2$	5 mM	0.14	0.28	0.55	1.10
buffer D (pH 6.2)					
Betaine	1 M	29.29	58.58	117.5	235
MES	25 mM	1.22	2.44	4.88	9.76
NaCl	15 mM	0.22	0.44	0.88	1.76
$MgCl_2 \cdot 6H_2O$	5 mM	0.25	0.51	1.02	2.04
$CaCl_2$	5 mM	0.14	0.28	0.55	1.10

Table A.1.: Ingredients used for the different buffers used. For step-scan measurements the measurement buffer is buffer D without betaine. BSA and sodium ascorbate should be added to buffer A shortly before use and stored at 4 ℃ otherwise.

- There are two kinds of pipettes: made to "deliver" and made to "contain". While the former kind is to deliver the selected volume, the latter is made to suck up the selected volume from the original sample.
- Pipetting volumes smaller than 100 µl is very difficult. Oftentimes when taking up the volume from the original liquid tiny drops will stick to the outside of the tip without the operator noticing. For quantitative measurements the solution should be diluted so that a larger volume can be pipetted.
- The humidity in the lab also plays a role and should be considered for precise pipetting.
- The calibration of any pipette should be checked from time to time using a very precise scale. Over time, the pipette may become contaminated with remains of unsuspecting physicists' samples. In this case many pipettes can be disassembled and cleaned.

This incomplete list is just an illustration to show that for quantitative pipetting many aspects must be considered, otherwise the results will not be reliable.

A.4. Manufacturing oxygen polarography electrodes

In our workgroup centrifugable oxygen polarography electrodes have been developed and used, inter alia, to measure the oxygen evolution in PSII (J. Kim 2009; Karge, Bondar, and Dau 2014). The data obtainable from oxygen polarography complements FTIR data in several ways, so I planned to measure using the electrodes. Especially the FTIR ammonia investigations motivated complimentary data measured using the polarography electrodes. However, before I could start to measure one of our two electrodes broke and the other one was damaged, so I took the task to create new ones. Since this process is not very trivial and takes a number of different steps, I try to give a full account of the manufacturing process and additionally suggest alternative construction approaches in the next section. Note that due to the complexity of the project no data is presented in this thesis, but instead in the theses of my colleagues.

As a side node, it is very advantageous to take part in the institute's workshop courses. Mr. Prüfer offers courses to learn how to use drilling, milling and turning machines. With this knowledge it is not only possible to quickly manufacture small parts needed, but it also tremendously helps when designing pieces which should be done by the institute's professional workshop.

A.4.1. General description of the finished electrode

The general concept is that a polarized silver-platinum-electrode can be used to detect oxygen by oxygen reduction. To achieve the necessary time resolution, the sample needs to be centrifuged onto the electrode; therefore, the electrode body needs to be small enough and light enough to fit into a swinging bucket of a centrifuge which is able to spin the rotor fast enough.

The design consists of an electrode body (made from PVC) which incorporates the metal surfaces and a push-on shell which can be removed easily to allow for cleaning of the electrode. There is an additional body shell which is fixed to the electrode body after the metal parts have been soldered to the cinch connector. Light can be applied to the sample from the top.

A.4.2. Needed parts and equipment

The three plastic body parts (electrode body, push-on shell, body shell) as described in (J. Kim 2009) were manufactured as described in the original thesis by the institute workshop. Minor modifications were done: there is no need to screw the push-on shell onto the electrode body, so the threading (item 6 in the figure on p. 17 in J. Kim 2009) and the associated hole in the push-on shell ("große Bohrung", ib. next page) can be ommited. There is one channel each for the silver wires of the metal electrodes themselves; an additional channel like the one for the silver electrode was drilled on the opposite side to allow air to escape during the gluing step (see below). The channels for the wires were widened to a diameter of 3 mm. The tilting angle of the silver channel had to be adjusted slightly to accomodate for the larger radius. Additional, a round cap for each electrode was manufactured to accomodate the bottom of the electrode to the rounded centrifuge bucket.

The metal electrodes consist of 999 platinum and 999 silver respectively. The first generation of electrodes I manufactured were made with less pure platinum and did not work, which could be linked to the copper content in the platinum. In any event, I noticed corrodation of the copper content in the silver a few months after the manufacture of this first generation of electrodes. In any event, only the purest metal available should be used. It was quite difficult to obtain the raw metal electrodes, because there was only one jeweller who was willing to put in the time and effort to manufacture them (Leihhaus Katz, Berlin). The wires, which are attached to the metal rings, are both 999 silver wires. The dimensions can be found in (J. Kim 2009). The distance between the outer part of the silver ring to the inner part of the electrode body is 1 mm. I suppose that this is on purpose to accomodate for the adhesive. However, if I were to manufacture electrodes again, I would eliminate this space and provide 0.2 mm space between the silver ring and the electrode body. This helps

during the glueing process to keep the metal ring in the right position.

The two-component adhesive was the same as used in (J. Kim 2009): EPL285 and EPH285 by bacuplast, Germany. However, it was very difficult to use a syringe to apply it. The two components of the epoxy are warmed in a water bath to 50 ℃, then mixed quickly (but thoroughly enough) and applied to the electrode using a syringe. I had only success to do so using a syringe with 1.5 mm diameter.

The connector used is a high-end cinch connector (WBT-0110 AG) which needs to be cut to the right length to fit in the electrode body. Using a high-end connector but then cutting it down begs the question if there is not be a more appropriate, i.e. compact connector available. Since the cinch connection itself is quite standardized, high quality but more compact alternatives should be readily available.

During the glueing step the cinch connector will not lie on the rotational symmetry axis of the electrode body if it is not fixed in this position. An additional plug which can be attached to the bottom of the electrode body to hold the cinch connector in place during the glueing step is necessary.

Two o-rings per electrode are needed to prevent leaking of the sample between the push-on shell and the electrode body. I tried EPDM 18×1.3 mm and NBR 17.8×1.5 mm, and the latter ones seem to work better.

During the assembly the metal parts are fixed to the electrode body using a different two-component epoxy in an intermediate step (see below).

A.4.3. Assembly

Before the general assembly the cinch plug needs to be shortened in a turning machine. Then the wires of the metal electrodes can be cut to the right length by inserting the metal parts into the body and checking how they fit with the cinch plug.

In a preparatory step the metal parts are fixed to the eletrode body using instant adhesive or equivalent glue. I decided to use two-component glue which does not dry that fast but provides additional stability. In this step it would be nice to have some sort of adapter which can be put on top of the electrode to make sure that the metal rings are exactly in place. After this step I waited for the next day to give the glue time to dry.

Once the electrodes are fixed in place the electrode body is put upside down and the channels for the glue below the metal rings is filled with the two-component adhesive. The two components need to be warmed to 50 ℃, otherwise the glue cannot be injected through the channels using a syringe. The high temperature, however, leads to a very fast hardening of the glue; thus, only a few minutes remain to complete the glueing step.

It is important to visualize how the glue fills the channel: if any air bubbles form, these

will be impossible to get rid off since the viscosity of the glue is so high. This is why I decided to have another channel drilled for the silver ring: The syringe can be inserted through this channel while making sure that the air escapes through the channel with the silver wire.

In this step also the channels are filled with glue. The cinch plug is set in place and the wires are positioned to be soldered the next day. To make sure that the cinch plug is absolutely centered an additional adapter made of a polyamide is attached to the bottom of the electrode. The electrode rests upside down until the glue is dry.

The next day the wires can be soldered to the plug. This is a good time to double-check with a voltmeter to see if the connections are right. Afterwards, the bottom shell is fixed to the electrode body. It is important that all surfaces that are in contact with the electrode body are covered with glue so as to create a very rigid connection. It is beneficial if a little bit of glue squeezes out of the part where the two parts touch; it can be later removed in the turning machine to give a perfectly flat connection. Otherwise, a small gap will remain after the assembly. The inner volume of the electrode is filled with glue. During this step, the outer shell of the cinch connector is slipped over the soldered plug. The electrode then rests upside down until the glue is dry.

After one more day the space between the metal rings and the electrode body can be filled up with glue. Since the viscosity is so high, air bubbles might form in the small space. These can be removed using a thin syringe tip by sucking up the air or by pushing the bubbles upwards. It is important not to have any bubbles since these would lead to holes later on. After the glue has dried, the electrode is put into the oven for 24 hours at 50 ℃ to harden the glue. Afterwards, the upper side of the electrode is revealed using a turning machine. Multiple electrodes can be balanced by applying additional glue to their bottoms next to the cinch plug.

A.5. Spectral decay of step-scan data in H_2O

Figures A.1-A.4 on pages 242-245 show the changes of the step-scan data with time for each of the four deconvoluted flash-induced S-state transitions. Each figure corresponds to one flash and shows the step-scan data at seven different time points after laser-flash excitation: 9 µs, 27 µs, 100 µs, 300 µs, 1 ms, 3 ms, and 10 ms. The spectra which correspond to earlier times are shown using darker colors, while spectra corresponding to later times are shown using lighter colors.

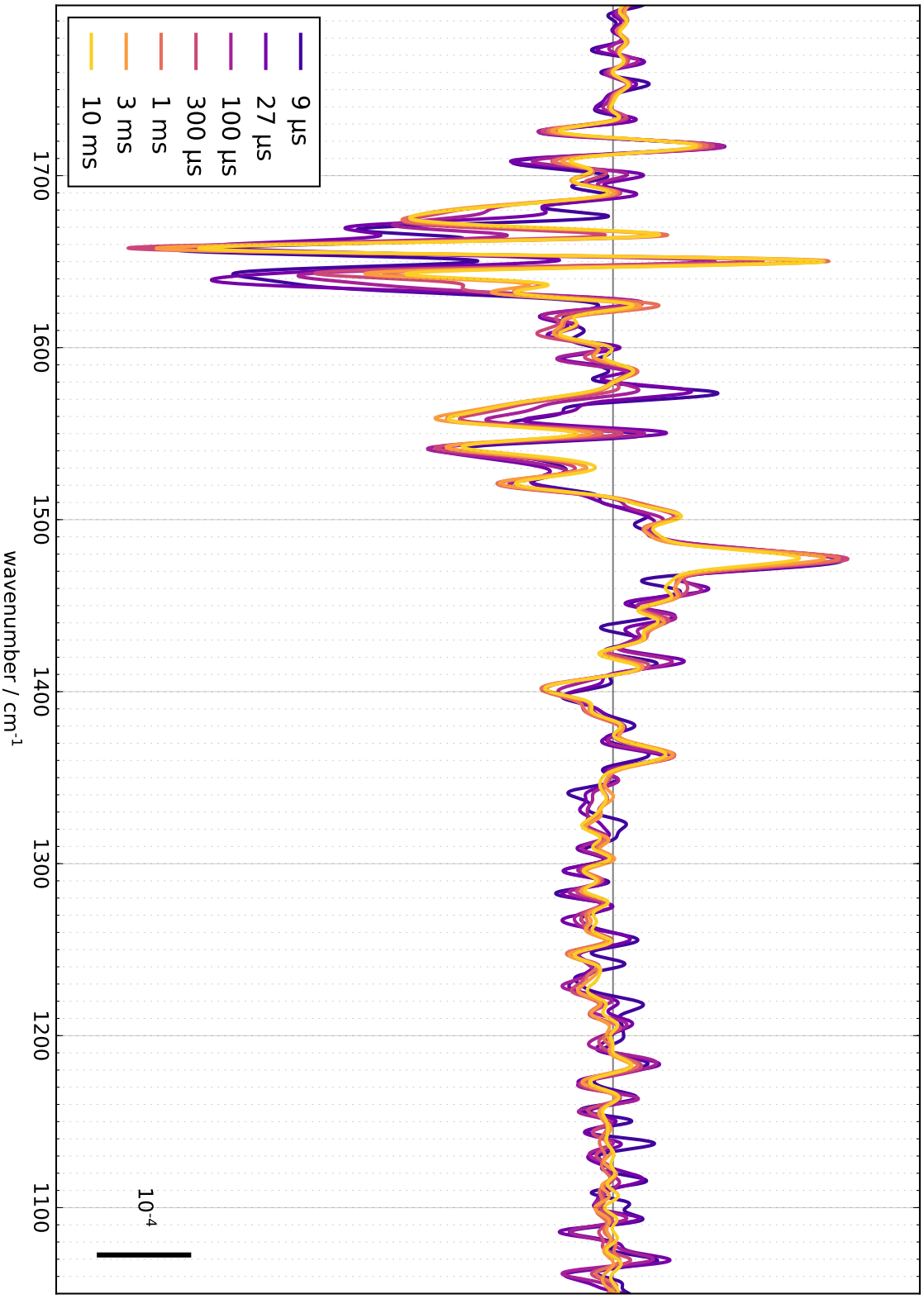

Figure A.1.: Step-scan difference spectra of the $S_1 \rightarrow S_2$ transition at different points in time. From dark to light colors: spectra at 9 µs, 27 µs, 100 µs, 300 µs, 1 ms, 3 ms, and 10 ms after laser flash excitation.

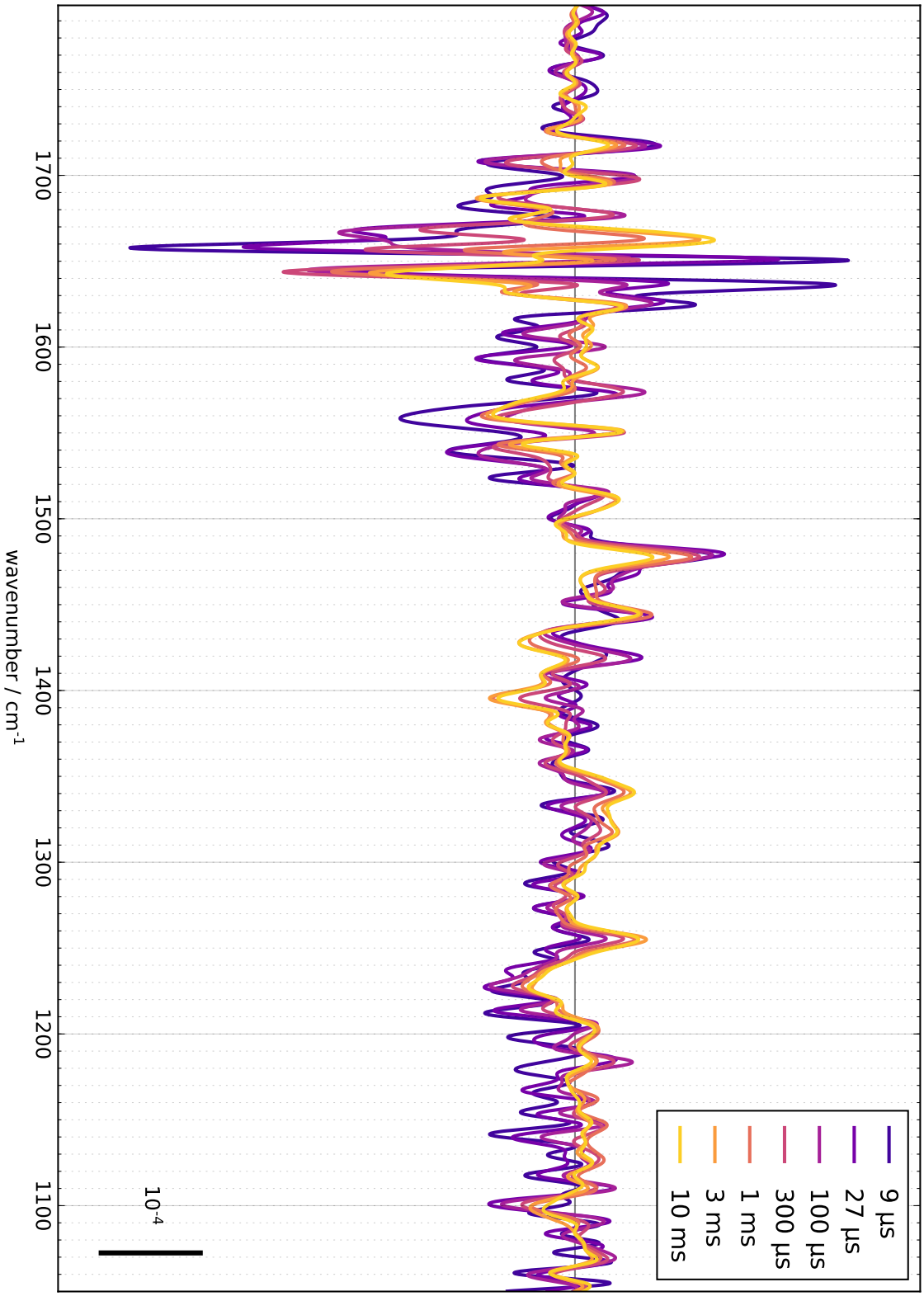

Figure A.2.: Step-scan difference spectra of the $S_2 \longrightarrow S_3$ transition at different points in time. From dark to light colors: spectra at 9 µs, 27 µs, 100 µs, 300 µs, 1 ms, 3 ms, and 10 ms after laser flash excitation.

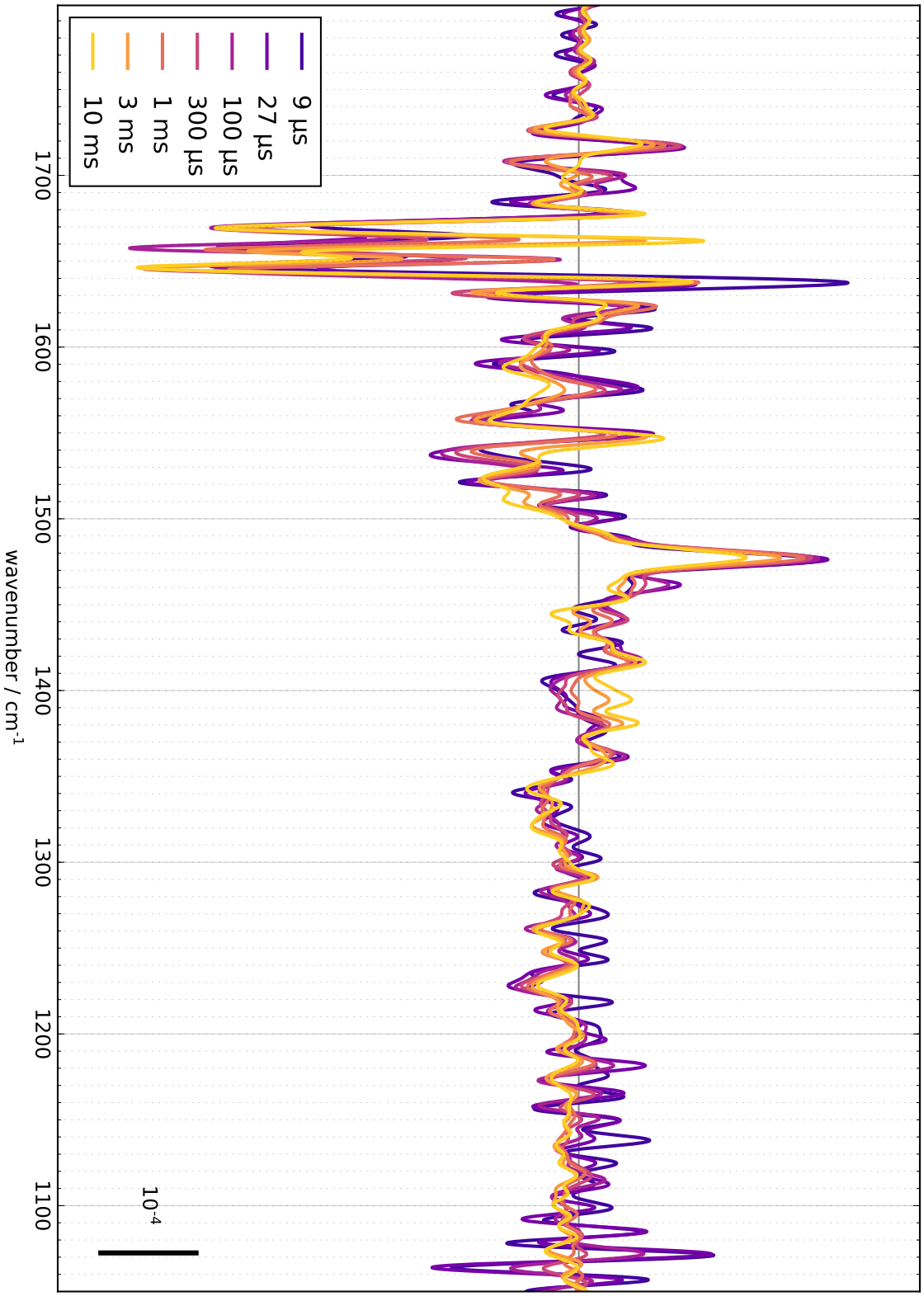

Figure A.3.: Step-scan difference spectra of the $S_3 \rightarrow S_0$ transition at different points in time. From dark to light colors: spectra at 9 µs, 27 µs, 100 µs, 300 µs, 1 ms, 3 ms, and 10 ms after laser flash excitation.

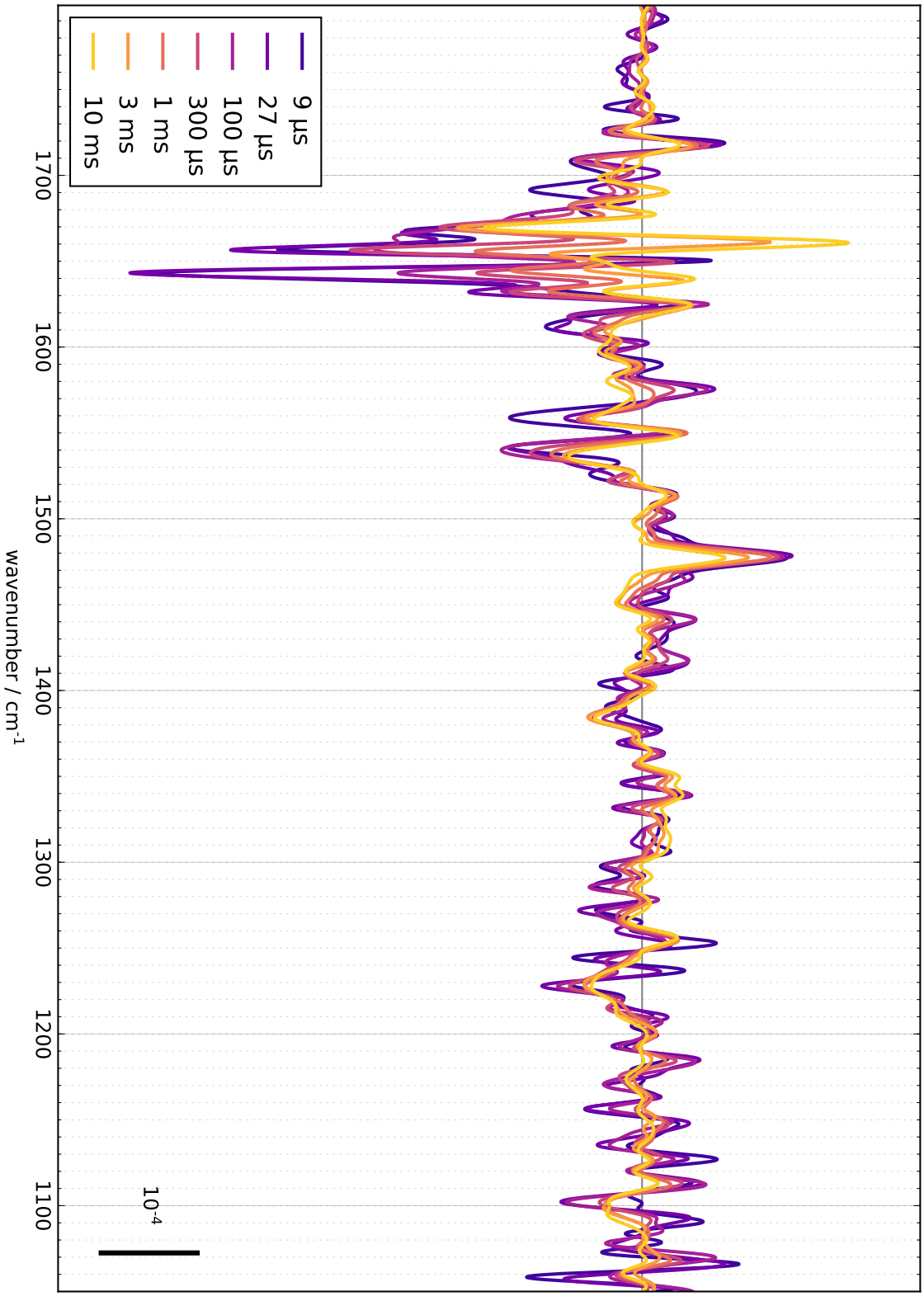

Figure A.4.: Step-scan difference spectra of the $S_0 \rightarrow S_1$ transition at different points in time. From dark to light colors: spectra at 9 µs, 27 µs, 100 µs, 300 µs, 1 ms, 3 ms, and 10 ms after laser flash excitation.

A.6. Elastic net evaluation: supporting information

The following tables and figures support the chosen time constants in the elastic net evaluation. Significant peaks in the decay associated spectra have been investigated for the time constants observed in a fit for the timecourse at this wavenumber. The time constants obtained have been averaged to obtain an average time constant for each phase. The timecourses shown serve as examples for these phases.

1094 cm^{-1}	a		$45 \cdot 10^{-6}$	$-11 \cdot 10^{-6}$		
	τ		100 µs	7.9 ms		
1102 cm^{-1}	a	$130 \cdot 10^{-6}$	$-50 \cdot 10^{-6}$	$19 \cdot 10^{-6}$	$-29 \cdot 10^{-6}$	
	τ	15 µs	110 µs	910 µs	19 ms	
1281 cm^{-1}	a		$-37 \cdot 10^{-6}$	$-1 \cdot 10^{-6}$	$-7 \cdot 10^{-6}$	
	τ		100 µs	620 µs	6.5 ms	
1403 cm^{-1}	a		$73 \cdot 10^{-6}$	$-2 \cdot 10^{-6}$	$-15 \cdot 10^{-6}$	
	τ		110 µs	6.9 ms	24 ms	
1454 cm^{-1}	a		$-43 \cdot 10^{-6}$	$3 \cdot 10^{-6}$	$28 \cdot 10^{-6}$	
	τ		110 µs	6.9 ms	37 ms	
1511 cm^{-1}	a		$-45 \cdot 10^{-6}$	$11 \cdot 10^{-6}$	$-9 \cdot 10^{-6}$	
	τ		110 µs	2.5 ms	43 ms	
1521 cm^{-1}	a		$56 \cdot 10^{-6}$	$-60 \cdot 10^{-6}$		
	τ		100 µs	16 ms		
1564 cm^{-1}	a		$110 \cdot 10^{-6}$	$17 \cdot 10^{-6}$	$-71 \cdot 10^{-6}$	
	τ		120 µs	1.5 ms	57 ms	
1576 cm^{-1}	a		$88 \cdot 10^{-6}$	$16 \cdot 10^{-6}$	$-30 \cdot 10^{-6}$	
	τ		130 µs	2.4 ms	84 ms	
1638 cm^{-1}	a	$240 \cdot 10^{-6}$	$-290 \cdot 10^{-6}$	$-140 \cdot 10^{-6}$	$3 \cdot 10^{-6}$	
	τ	9 µs	91 µs	380 µs	13 ms	
1655 cm^{-1}	a	$-509 \cdot 10^{-6}$	$280 \cdot 10^{-6}$	$-130 \cdot 10^{-6}$	$44 \cdot 10^{-6}$	$-130 \cdot 10^{-6}$
	τ	15 µs	82 µs	400 µs	2.3 ms	28 ms
1665 cm^{-1}	a	$220 \cdot 10^{-6}$	$-350 \cdot 10^{-6}$	$-51 \cdot 10^{-6}$	$4 \cdot 10^{-6}$	$52 \cdot 10^{-6}$
	τ	11 µs	110 µs	350 µs	4.2 ms	15 ms
1680 cm^{-1}	a		$140 \cdot 10^{-6}$	$19 \cdot 10^{-6}$	$-60 \cdot 10^{-6}$	
	τ		95 µs	1.7 ms	34 ms	
1708 cm^{-1}	a		$-63 \cdot 10^{-6}$	$-27 \cdot 10^{-6}$		
	τ		120 µs	12 ms		

Table A.2.: Elastic fit time constants for selected wavenumbers, $S_1 \longrightarrow S_2$ transition in H_2O. Note the time constants in the second column which correspond to the electron removal step in the ${S_1}^n \longrightarrow {S_2}^+$ transition. The average time constant is τ = 106 µs.

1263 cm^{-1}	a		$-120 \cdot 10^{-6}$	$94 \cdot 10^{-6}$	$-6 \cdot 10^{-6}$	
	τ		91 µs	950 µs	18 ms	
1280 cm^{-1}	a		$-70 \cdot 10^{-6}$	$1 \cdot 10^{-6}$	$3 \cdot 10^{-6}$	
	τ		95 µs	3.5 ms	12 ms	
1311 cm^{-1}	a		$-43 \cdot 10^{-6}$	$13 \cdot 10^{-6}$		
	τ		120 µs	39 ms		
1330 cm^{-1}	a		$-45 \cdot 10^{-6}$	$7 \cdot 10^{-6}$	$17 \cdot 10^{-6}$	
	τ		86 µs	1.6 ms	20 ms	
1364 cm^{-1}	a		$-90 \cdot 10^{-6}$	$-57 \cdot 10^{-6}$	$53 \cdot 10^{-6}$	
	τ		86 µs	270 µs	45 ms	
1576 cm^{-1}	a		$95 \cdot 10^{-6}$	$14 \cdot 10^{-6}$		
	τ		100 µs	16 ms		
1628 cm^{-1}	a		$-150 \cdot 10^{-6}$	$-15 \cdot 10^{-6}$	$-21 \cdot 10^{-6}$	
	τ		110 µs	400 µs	45 ms	
1645 cm^{-1}	a	$110 \cdot 10^{-6}$	$-300 \cdot 10^{-6}$	$190 \cdot 10^{-6}$	$-91 \cdot 10^{-6}$	
	τ	20 µs	130 µs	910 µs	17 ms	
1653 cm^{-1}	a	$53 \cdot 10^{-6}$	$380 \cdot 10^{-6}$	$-120 \cdot 10^{-6}$	$52 \cdot 10^{-6}$	$11 \cdot 10^{-6}$
	τ	42 µs	120 µs	1.1 ms	5.1 ms	60 ms
1667 cm^{-1}	a	$88 \cdot 10^{-6}$	$-150 \cdot 10^{-6}$	$-58 \cdot 10^{-6}$	$-62 \cdot 10^{-6}$	
	τ	19 µs	120 µs	1.4 ms	20 ms	
1692 cm^{-1}	a		$-120 \cdot 10^{-6}$	$8 \cdot 10^{-6}$	$-10 \cdot 10^{-6}$	
	τ		78 µs	750 µs	21 ms	

Table A.3.: Elastic fit time constants for selected wavenumbers, $S_1 \longrightarrow S_2$ transition in D_2O. Note the time constants in the second column which correspond to the electron removal step in the ${S_1}^n \longrightarrow {S_2}^+$ transition. The average time constant is τ = 103 µs.

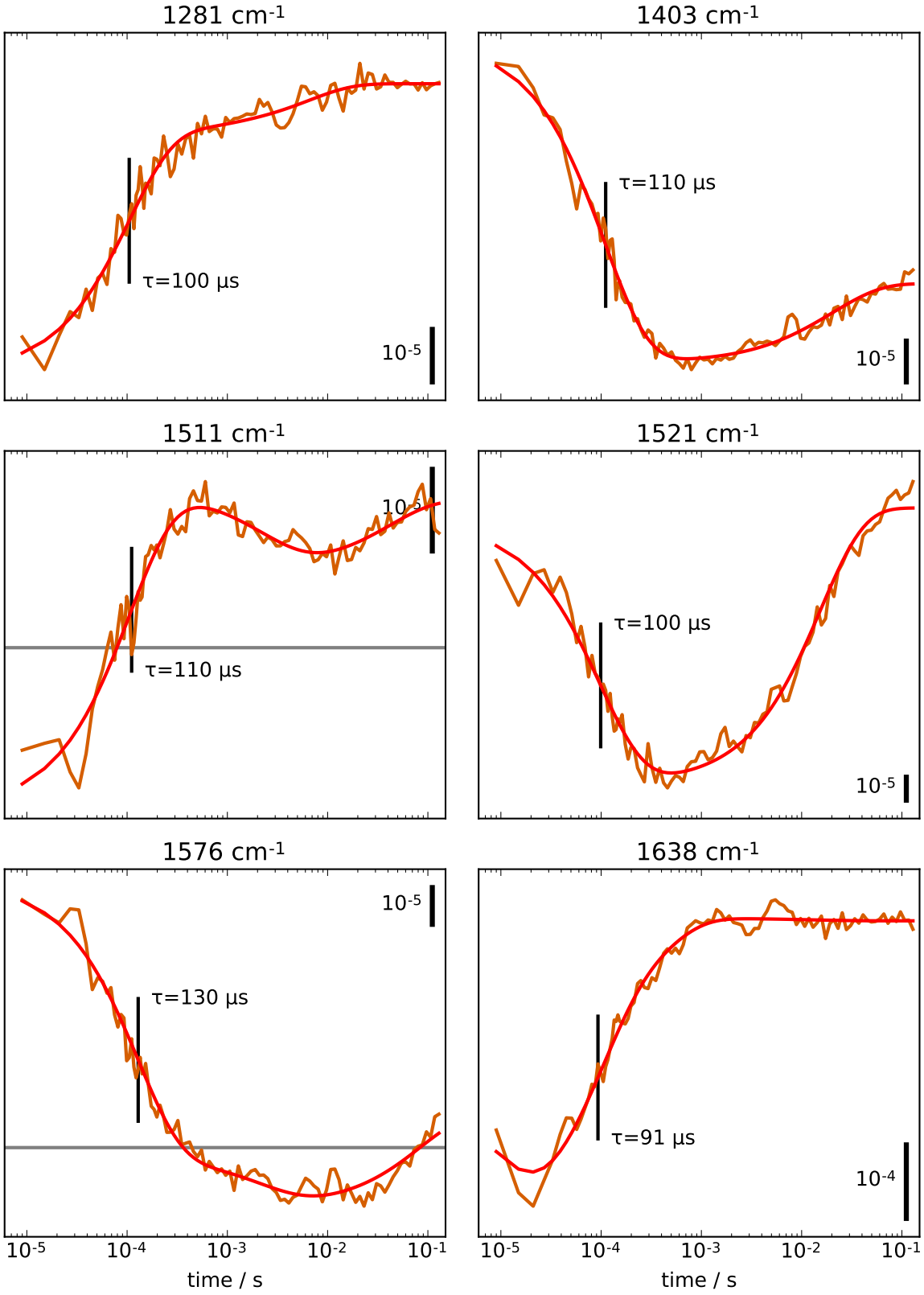

Figure A.5.: Selected H_2O timecourses (orange) and elastic net fits (red), $S_1 \longrightarrow S_2$ transition.

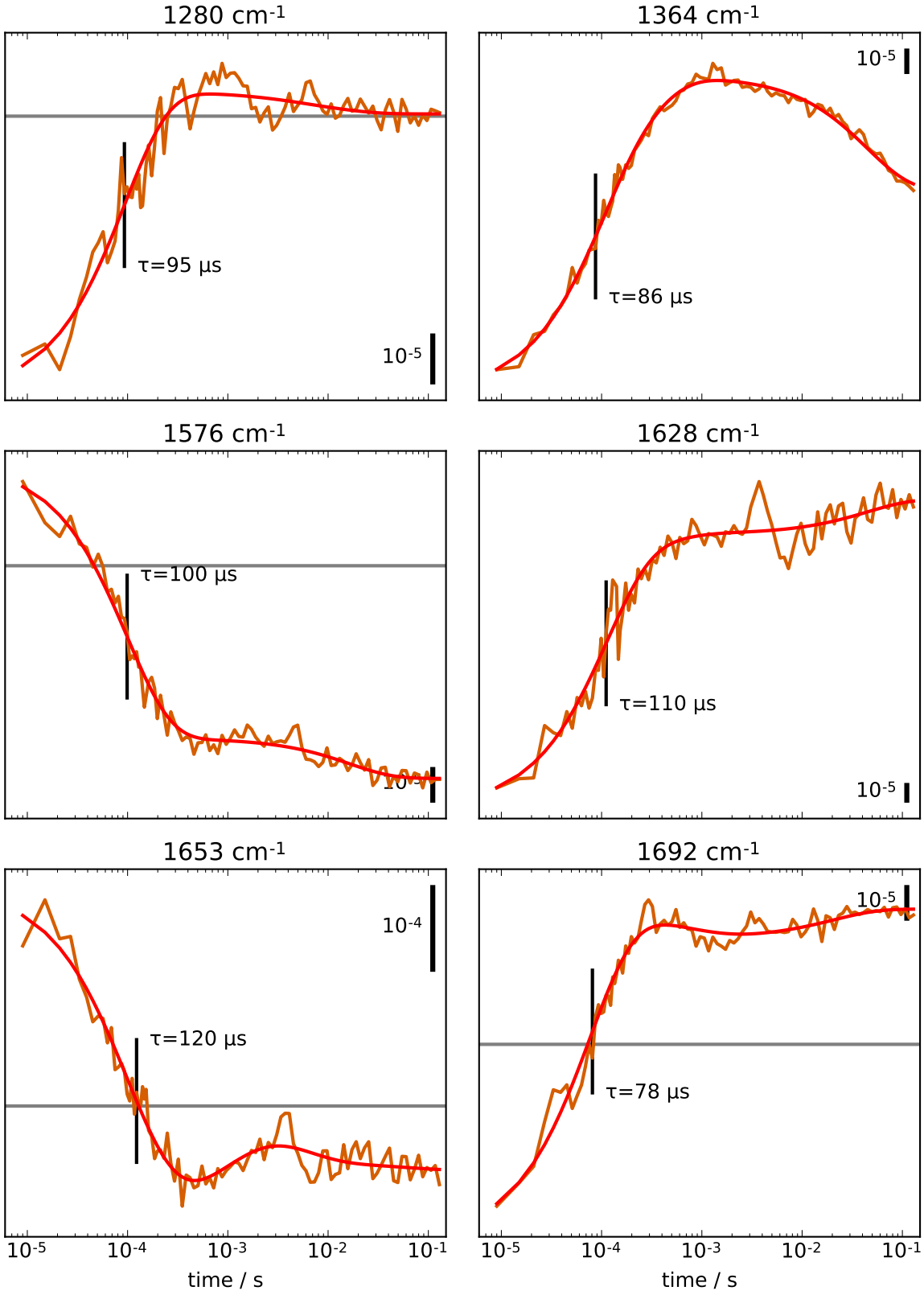

Figure A.6.: Selected D_2O timecourses (orange) and elastic net fits (red), $S_1 \longrightarrow S_2$ transition..

1094 cm^{-1}	a	$-79 \cdot 10^{-6}$	$31 \cdot 10^{-6}$	$17 \cdot 10^{-6}$	$-5 \cdot 10^{-6}$
	τ	19 µs	180 µs	950 µs	43 ms
1110 cm^{-1}	a	$-94 \cdot 10^{-6}$	$47 \cdot 10^{-6}$	$0 \cdot 10^{-6}$	$17 \cdot 10^{-6}$
	τ	20 µs	190 µs	1.7 ms	49 ms
1144 cm^{-1}	a	$-94 \cdot 10^{-6}$	$-19 \cdot 10^{-6}$	$12 \cdot 10^{-6}$	$5 \cdot 10^{-6}$
	τ	25 µs	150 µs	2.4 ms	15 ms
1182 cm^{-1}	a	$-170 \cdot 10^{-6}$	$46 \cdot 10^{-6}$	$14 \cdot 10^{-6}$	
	τ	19 µs	220 µs	16 ms	
1209 cm^{-1}	a	$-82 \cdot 10^{-6}$	$6 \cdot 10^{-6}$	$-11 \cdot 10^{-6}$	
	τ	20 µs	5.1 ms	69 ms	
1223 cm^{-1}	a	$-68 \cdot 10^{-6}$	$21 \cdot 10^{-6}$	$-15 \cdot 10^{-6}$	$-15 \cdot 10^{-6}$
	τ	21 µs	160 µs	1.5 ms	32 ms
1451 cm^{-1}	a	$62 \cdot 10^{-6}$	$-62 \cdot 10^{-6}$	$9 \cdot 10^{-6}$	
	τ	21 µs	260 µs	39 ms	
1559 cm^{-1}	a	$-170 \cdot 10^{-6}$	$33 \cdot 10^{-6}$	$-35 \cdot 10^{-6}$	
	τ	19 µs	300 µs	32 ms	
1602 cm^{-1}	a	$-160 \cdot 10^{-6}$	$70 \cdot 10^{-6}$	$-42 \cdot 10^{-6}$	$19 \cdot 10^{-6}$
	τ	19 µs	130 µs	1.2 ms	20 ms
1616 cm^{-1}	a	$-120 \cdot 10^{-6}$	$6 \cdot 10^{-6}$	$3 \cdot 10^{-6}$	
	τ	15 µs	200 µs	12 ms	
1622 cm^{-1}	a	$130 \cdot 10^{-6}$	$-45 \cdot 10^{-6}$	$-5 \cdot 10^{-6}$	$39 \cdot 10^{-6}$
	τ	15 µs	100 µs	1.5 ms	47 ms
1658 cm^{-1}	a	$-400 \cdot 10^{-6}$	$-150 \cdot 10^{-6}$	$-170 \cdot 10^{-6}$	$140 \cdot 10^{-6}$
	τ	25 µs	1.3 ms	12 ms	110 ms
1669 cm^{-1}	a	$270 \cdot 10^{-6}$	$-270 \cdot 10^{-6}$	$-49 \cdot 10^{-6}$	$-6 \cdot 10^{-6}$
	τ	18 µs	380 µs	3.9 ms	11 ms
1692 cm^{-1}	a	$-93 \cdot 10^{-6}$	$-18 \cdot 10^{-6}$		
	τ	19 µs	910 µs		
1700 cm^{-1}	a	$-120 \cdot 10^{-6}$	$69 \cdot 10^{-6}$	$4 \cdot 10^{-6}$	
	τ	17 µs	650 µs	2.5 ms	

Table A.4.: Elastic fit time constants for selected wavenumbers, $S_2 \longrightarrow S_3$ transition in H_2O. The average time constant of the first column is $\tau = 19\,\mu s$.

1198 cm^{-1}	a	$-83 \cdot 10^{-6}$	$-18 \cdot 10^{-6}$	$7 \cdot 10^{-6}$	
	τ	42 µs	229 µs	30 ms	
1212 cm^{-1}	a	$-77 \cdot 10^{-6}$	$-20 \cdot 10^{-6}$		
	τ	48 µs	380 µs		
1387 cm^{-1}	a	$-48 \cdot 10^{-6}$	$48 \cdot 10^{-6}$	$-13 \cdot 10^{-6}$	
	τ	44 µs	459 µs	9.2 ms	
1519 cm^{-1}	a	$-37 \cdot 10^{-6}$	$30 \cdot 10^{-6}$	$-21 \cdot 10^{-6}$	
	τ	44 µs	509 µs	12 ms	
1550 cm^{-1}	a	$-140 \cdot 10^{-6}$	$9 \cdot 10^{-6}$		
	τ	56 µs	14 ms		
1576 cm^{-1}	a	$-100 \cdot 10^{-6}$	$77 \cdot 10^{-6}$	$16 \cdot 10^{-6}$	
	τ	48 µs	459 µs	6.5 ms	
1651 cm^{-1}	a	$300 \cdot 10^{-6}$	$-61 \cdot 10^{-6}$	$140 \cdot 10^{-6}$	$-89 \cdot 10^{-6}$
	τ	53 µs	750 µs	5.4 ms	120 ms
1664 cm^{-1}	a	$190 \cdot 10^{-6}$	$-320 \cdot 10^{-6}$	$-110 \cdot 10^{-6}$	$25 \cdot 10^{-6}$
	τ	44 µs	290 µs	1.3 ms	21 ms
1679 cm^{-1}	a	$-180 \cdot 10^{-6}$	$110 \cdot 10^{-6}$	$-37 \cdot 10^{-6}$	
	τ	51 µs	540 µs	80 ms	

Table A.5.: Elastic fit time constants for selected wavenumbers, $S_2 \longrightarrow S_3$ transition in H_2O. The average time constant of the first column is τ = 48 µs.

1074 cm^{-1}	a	$-75 \cdot 10^{-6}$	$30 \cdot 10^{-6}$	$4 \cdot 10^{-6}$		
	τ	24 µs	440 µs	57 ms		
1105 cm^{-1}	a		$-23 \cdot 10^{-6}$	$3 \cdot 10^{-6}$		
	τ		459 µs	45 ms		
1333 cm^{-1}	a		$-45 \cdot 10^{-6}$	$-17 \cdot 10^{-6}$		
	τ		300 µs	1.3 ms		
1349 cm^{-1}	a		$-35 \cdot 10^{-6}$	$-4 \cdot 10^{-6}$		
	τ		380 µs	2.0 ms		
1371 cm^{-1}	a	$41 \cdot 10^{-6}$	$-34 \cdot 10^{-6}$	$-1 \cdot 10^{-6}$		
	τ	26 µs	400 µs	12 ms		
1380 cm^{-1}	a	$7 \cdot 10^{-6}$	$40 \cdot 10^{-6}$			
	τ	68 µs	370 µs			
1390 cm^{-1}	a	$-39 \cdot 10^{-6}$	$62 \cdot 10^{-6}$	$-14 \cdot 10^{-6}$		
	τ	27 µs	380 µs	16 ms		
1397 cm^{-1}	a	$17 \cdot 10^{-6}$	$73 \cdot 10^{-6}$	$-25 \cdot 10^{-6}$		
	τ	24 µs	380 µs	21 ms		
1423 cm^{-1}	a		$62 \cdot 10^{-6}$	$19 \cdot 10^{-6}$		
	τ		350 µs	950 µs		
1437 cm^{-1}	a	$53 \cdot 10^{-6}$	$-22 \cdot 10^{-6}$	$7 \cdot 10^{-6}$		
	τ	36 µs	380 µs	7.9 ms		
1448 cm^{-1}	a		$-48 \cdot 10^{-6}$	$11 \cdot 10^{-6}$		
	τ		300 µs	30 ms		
1503 cm^{-1}	a		$-38 \cdot 10^{-6}$	$16 \cdot 10^{-6}$		
	τ		370 µs	39 ms		
1511 cm^{-1}	a	$18 \cdot 10^{-6}$	$-51 \cdot 10^{-6}$	$7 \cdot 10^{-6}$		
	τ	62 µs	490 µs	28 ms		
1526 cm^{-1}	a	$-32 \cdot 10^{-6}$	$-37 \cdot 10^{-6}$	$-15 \cdot 10^{-6}$		
	τ	24 µs	420 µs	29 ms		
1546 cm^{-1}	a	$-82 \cdot 10^{-6}$	$48 \cdot 10^{-6}$	$-18 \cdot 10^{-6}$	$-17 \cdot 10^{-6}$	
	τ	46 µs	380 µs	5.9 ms	29 ms	
1561 cm^{-1}	a	$-170 \cdot 10^{-6}$	$47 \cdot 10^{-6}$	$-35 \cdot 10^{-6}$		
	τ	22 µs	400 µs	34 ms		
1667 cm^{-1}	a	$270 \cdot 10^{-6}$	$-360 \cdot 10^{-6}$	$-67 \cdot 10^{-6}$		
	τ	31 µs	350 µs	2.0 ms		
1676 cm^{-1}	a	$-160 \cdot 10^{-6}$	$150 \cdot 10^{-6}$	$42 \cdot 10^{-6}$	$-56 \cdot 10^{-6}$	
	τ	59 µs	420 µs	3.9 ms	80 ms	
1685 cm^{-1}	a	$-82 \cdot 10^{-6}$	$56 \cdot 10^{-6}$	$-21 \cdot 10^{-6}$		
	τ	29 µs	350 µs	26 ms		
1711 cm^{-1}	a	$35 \cdot 10^{-6}$	$-56 \cdot 10^{-6}$	$20 \cdot 10^{-6}$	$-17 \cdot 10^{-6}$	$-8 \cdot 10^{-6}$
	τ	26 µs	459 µs	1.5 ms	4.2 ms	16 ms

Table A.6.: Elastic fit time constants for selected wavenumbers, $S_2 \longrightarrow S_3$ transition in H_2O. The average time constant of the second column is $\tau = 393$ µs. For the values at 1576 cm^{-1}, see 1575 cm^{-1} in table A.5.

1096 cm^{-1}	a		$130 \cdot 10^{-6}$	$17 \cdot 10^{-6}$	$7 \cdot 10^{-6}$
	τ		82 µs	2.1 ms	47 ms
1338 cm^{-1}	a		$39 \cdot 10^{-6}$	$-86 \cdot 10^{-6}$	$15 \cdot 10^{-6}$
	τ		75 µs	869 µs	43 ms
1350 cm^{-1}	a		$-77 \cdot 10^{-6}$	$-21 \cdot 10^{-6}$	$7 \cdot 10^{-6}$
	τ		86 µs	620 µs	39 ms
1380 cm^{-1}	a		$-72 \cdot 10^{-6}$	$63 \cdot 10^{-6}$	
	τ		75 µs	750 µs	
1545 cm^{-1}	a		$-120 \cdot 10^{-6}$	$77 \cdot 10^{-6}$	$-35 \cdot 10^{-6}$
	τ		75 µs	509 µs	6.9 ms
1582 cm^{-1}	a		$-130 \cdot 10^{-6}$	$170 \cdot 10^{-6}$	$-6 \cdot 10^{-6}$
	τ		82 µs	1.3 ms	28 ms
1645 cm^{-1}	a	$35 \cdot 10^{-6}$	$340 \cdot 10^{-6}$	$100 \cdot 10^{-6}$	$-30 \cdot 10^{-6}$
	τ	17 µs	65 µs	2.9 ms	49 ms
1677 cm^{-1}	a		$-300 \cdot 10^{-6}$	$180 \cdot 10^{-6}$	$-41 \cdot 10^{-6}$
	τ		68 µs	750 µs	6.5 ms
1691 cm^{-1}	a		$110 \cdot 10^{-6}$	$-52 \cdot 10^{-6}$	$9 \cdot 10^{-6}$
	τ		82 µs	950 µs	24 ms
1700 cm^{-1}	a		$-120 \cdot 10^{-6}$	$82 \cdot 10^{-6}$	
	τ		78 µs	1.1 ms	

Table A.7.: Elastic fit time constants for selected wavenumbers, $S_2 \longrightarrow S_3$ transition in D_2O. The average time constant of the second column is $\tau = 76\,\mu s$.

1060 cm^{-1}	a		$83 \cdot 10^{-6}$	$-200 \cdot 10^{-6}$	$-26 \cdot 10^{-6}$	$30 \cdot 10^{-6}$
	τ		100 µs	830 µs	8.3 ms	92 ms
1091 cm^{-1}	a		$86 \cdot 10^{-6}$	$-49 \cdot 10^{-6}$	$5 \cdot 10^{-6}$	
	τ		42 µs	650 µs	25 ms	
1286 cm^{-1}	a		$-36 \cdot 10^{-6}$	$84 \cdot 10^{-6}$	$-11 \cdot 10^{-6}$	
	τ		44 µs	650 µs	23 ms	
1302 cm^{-1}	a		$68 \cdot 10^{-6}$	$-36 \cdot 10^{-6}$	$-5 \cdot 10^{-6}$	
	τ		59 µs	910 µs	45 ms	
1338 cm^{-1}	a		$39 \cdot 10^{-6}$	$-86 \cdot 10^{-6}$	$15 \cdot 10^{-6}$	
	τ		75 µs	869 µs	43 ms	
1377 cm^{-1}	a		$-58 \cdot 10^{-6}$	$62 \cdot 10^{-6}$	$12 \cdot 10^{-6}$	
	τ		75 µs	910 µs	32 ms	
1386 cm^{-1}	a		$-29 \cdot 10^{-6}$	$79 \cdot 10^{-6}$	$-16 \cdot 10^{-6}$	
	τ		110 µs	830 µs	11 ms	
1520 cm^{-1}	a		$-110 \cdot 10^{-6}$	$63 \cdot 10^{-6}$	$-23 \cdot 10^{-6}$	
	τ		29 µs	750 µs	22 ms	
1538 cm^{-1}	a		$53 \cdot 10^{-6}$	$-170 \cdot 10^{-6}$	$25 \cdot 10^{-6}$	
	τ		44 µs	1.1 ms	35 ms	
1570 cm^{-1}	a		$-140 \cdot 10^{-6}$	$130 \cdot 10^{-6}$	$0 \cdot 10^{-6}$	
	τ		68 µs	1.0 ms	13 ms	
1583 cm^{-1}	a		$-130 \cdot 10^{-6}$	$160 \cdot 10^{-6}$	$5 \cdot 10^{-6}$	
	τ		71 µs	1.1 ms	30 ms	
1618 cm^{-1}	a		$-75 \cdot 10^{-6}$	$100 \cdot 10^{-6}$	$0 \cdot 10^{-6}$	
	τ		82 µs	950 µs	15 ms	
1666 cm^{-1}	a		$220 \cdot 10^{-6}$	$-440 \cdot 10^{-6}$	$9 \cdot 10^{-6}$	
	τ		120 µs	790 µs	37 ms	
1677 cm^{-1}	a		$-300 \cdot 10^{-6}$	$180 \cdot 10^{-6}$	$-41 \cdot 10^{-6}$	
	τ		68 µs	750 µs	6.5 ms	
1698 cm^{-1}	a	$-32 \cdot 10^{-6}$	$-90 \cdot 10^{-6}$	$99 \cdot 10^{-6}$		
	τ	21 µs	75 µs	1.0 ms		
1708 cm^{-1}	a		$91 \cdot 10^{-6}$	$-120 \cdot 10^{-6}$	$7 \cdot 10^{-6}$	
	τ		51 µs	720 µs	41 ms	
1741 cm^{-1}	a		$-9 \cdot 10^{-6}$	$-40 \cdot 10^{-6}$		
	τ		44 µs	869 µs		

Table A.8.: Elastic fit time constants for selected wavenumbers, $S_2 \longrightarrow S_3$ transition in D_2O. The average time constant of the third column is τ = 860 µs.

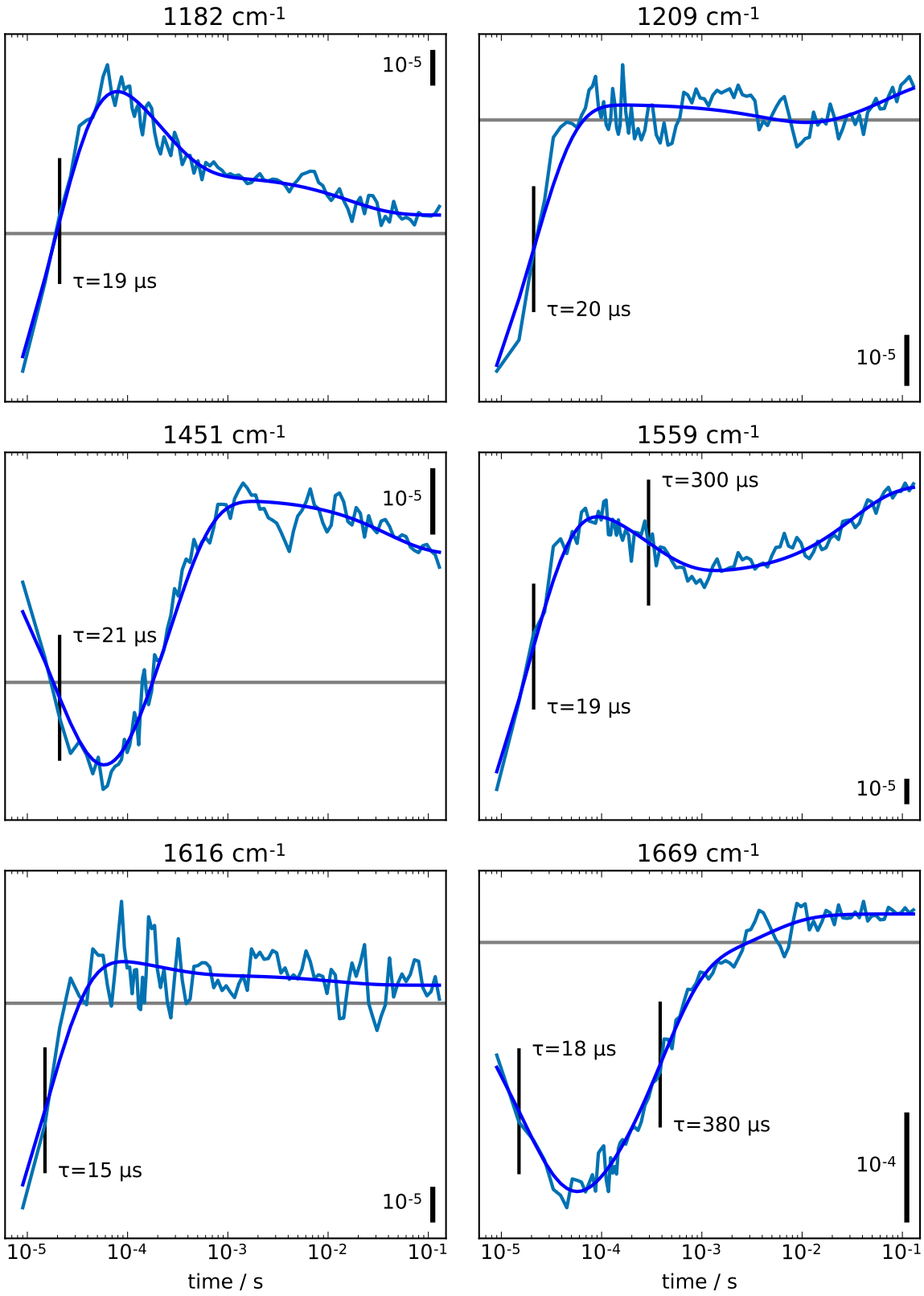

Figure A.7.: Selected H_2O timecourses (aquamarine) and elastic net fits (blue), $S_2 \longrightarrow S_3$ transition.

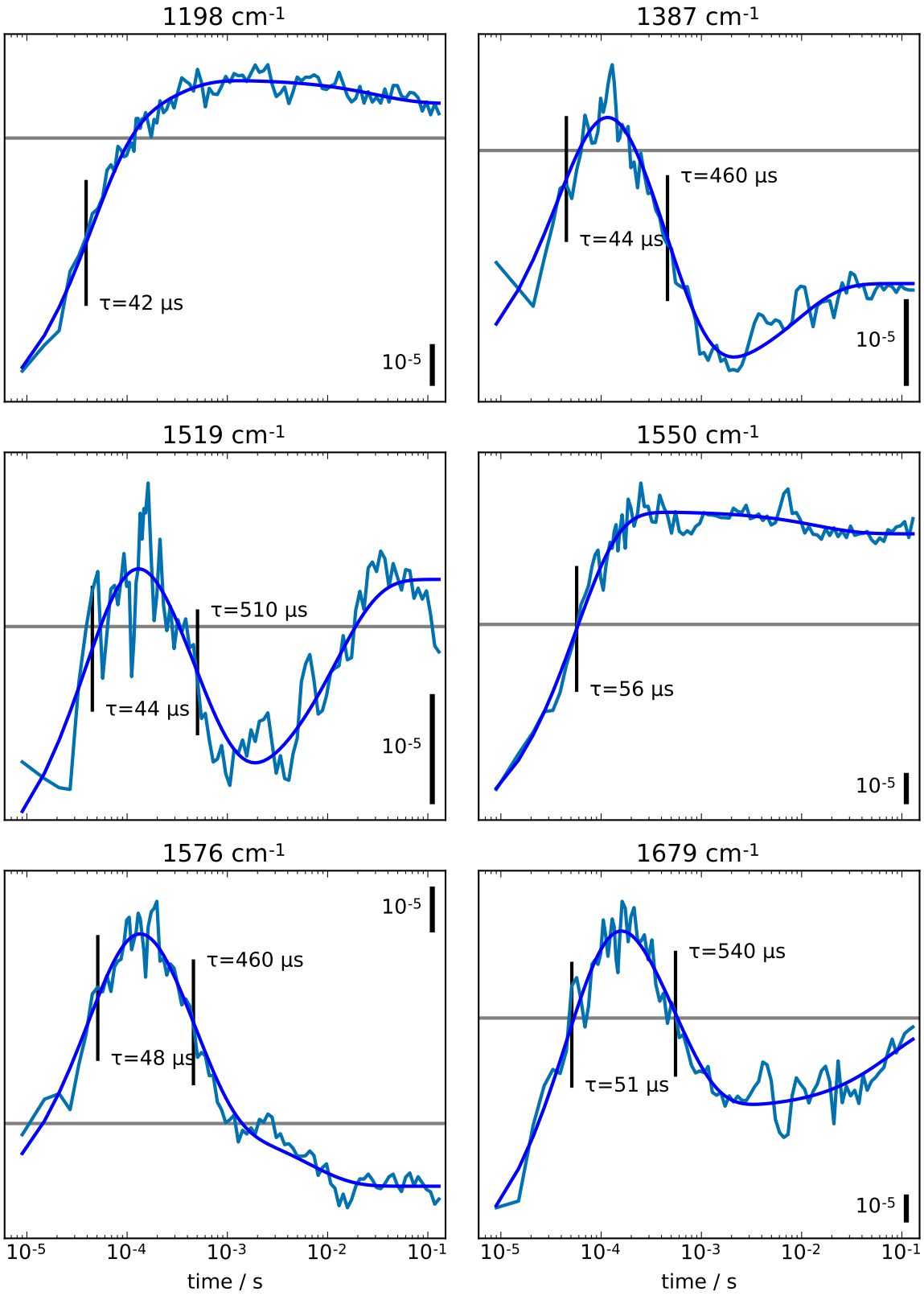

Figure A.8.: Selected H_2O timecourses (aquamarine) and elastic net fits (blue), $S_2 \longrightarrow S_3$ transition.

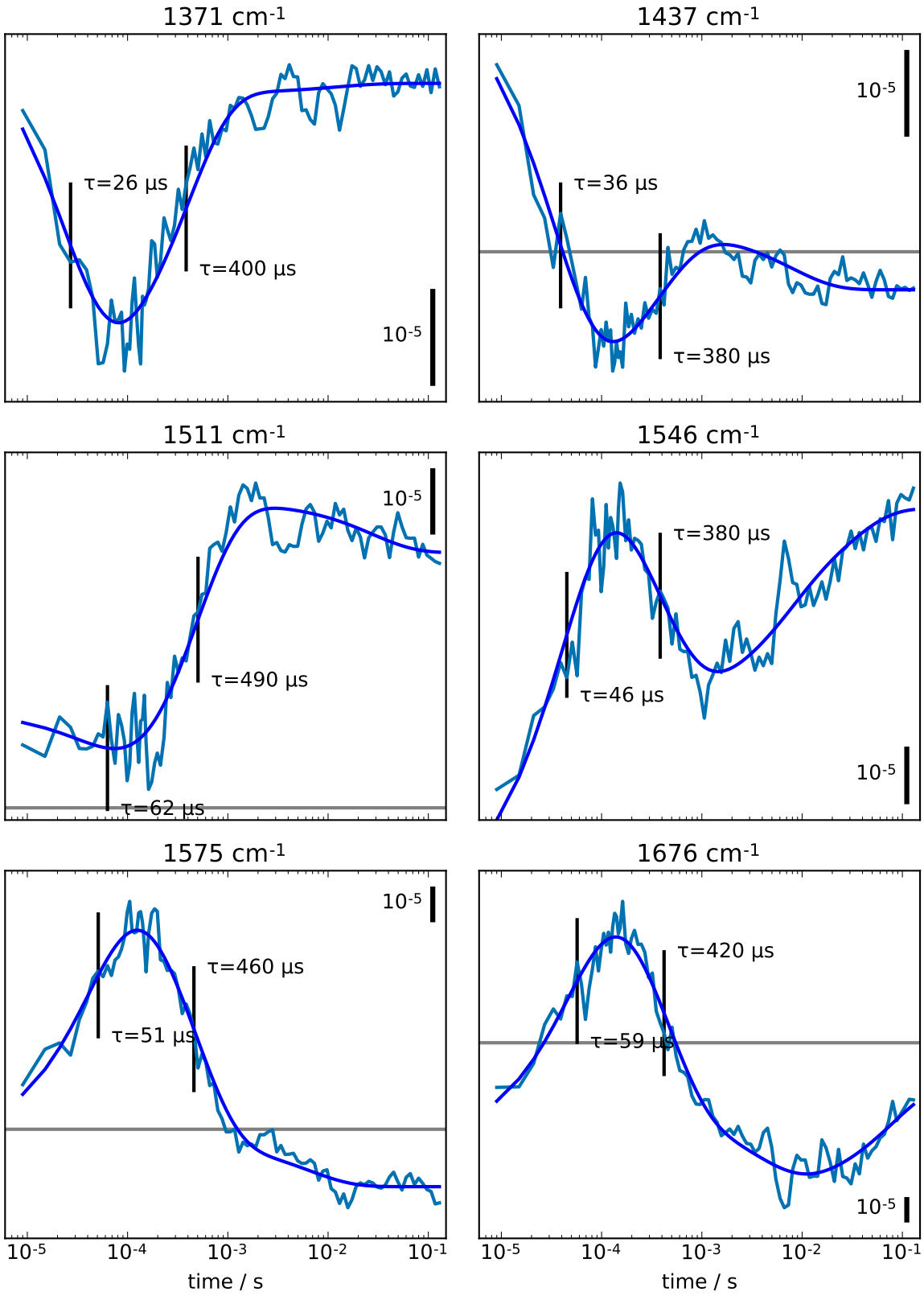

Figure A.9.: Selected H_2O timecourses (aquamarine) and elastic net fits (blue), $S_2 \longrightarrow S_3$ transition.

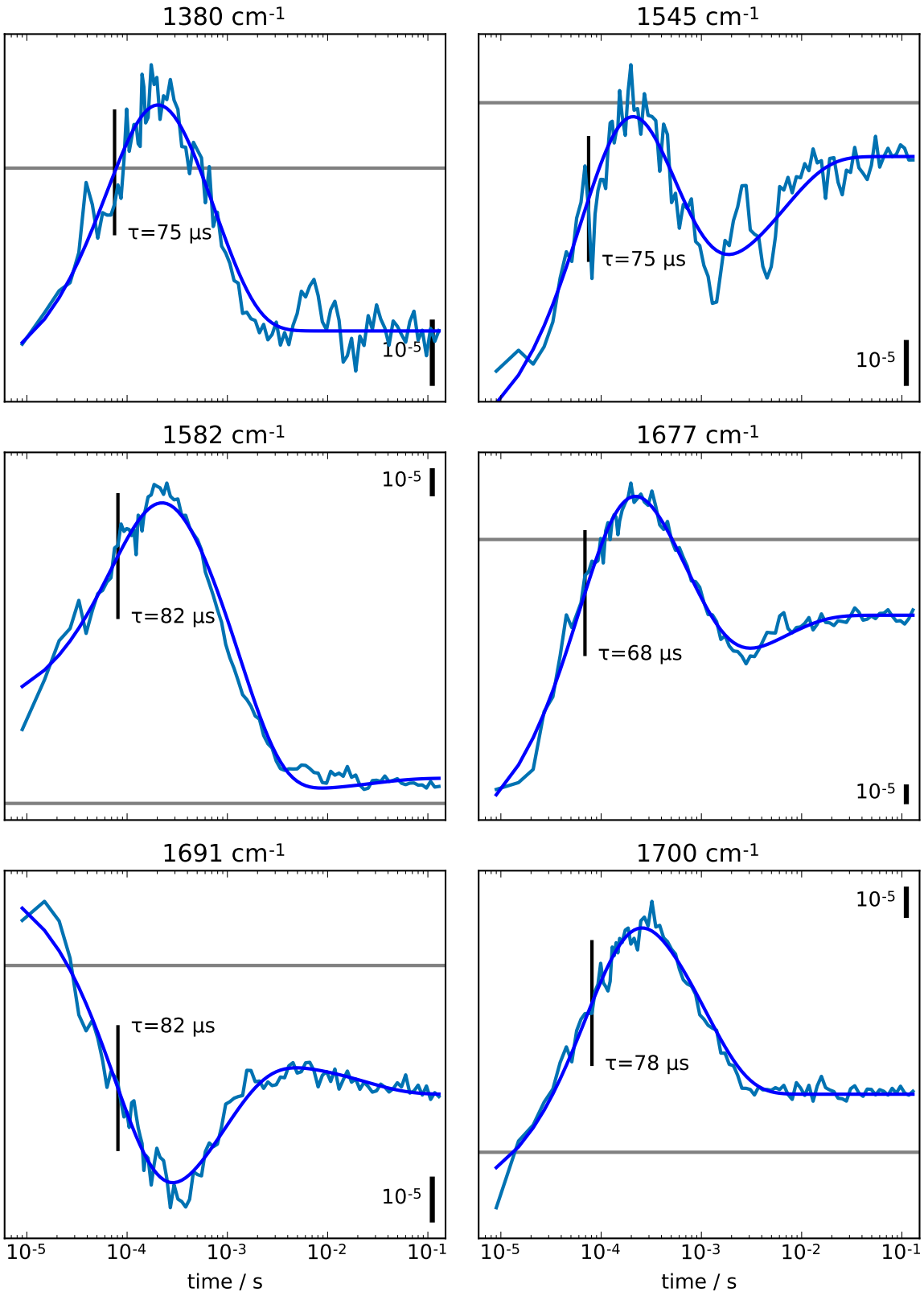

Figure A.10.: Selected D_2O timecourses (aquamarine) and elastic net fits (blue), $S_2 \longrightarrow S_3$ transition.

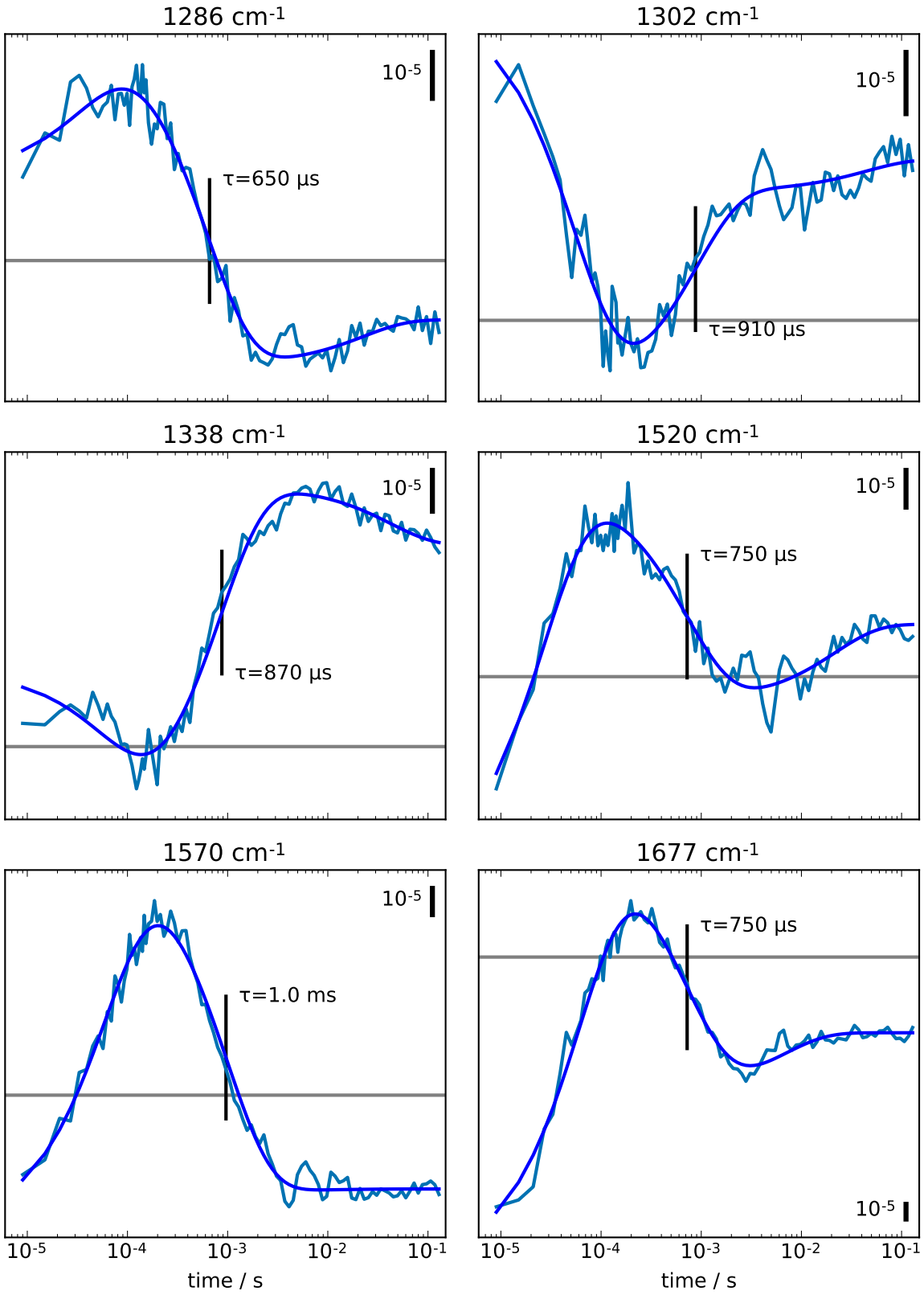

Figure A.11.: Selected D_2O timecourses (aquamarine) and elastic net fits (blue), $S_2 \longrightarrow S_3$ transition.

1639 cm^{-1}	a	$550 \cdot 10^{-6}$	$-200 \cdot 10^{-6}$	$-13 \cdot 10^{-6}$	$-57 \cdot 10^{-6}$	
	τ	19 µs	229 µs	1.8 ms	21 ms	
1650 cm^{-1}	a	$-620 \cdot 10^{-6}$	$450 \cdot 10^{-6}$	$-420 \cdot 10^{-6}$	$370 \cdot 10^{-6}$	$-22 \cdot 10^{-6}$
	τ	18 µs	78 µs	330 µs	1.7 ms	45 ms
1666 cm^{-1}	a	$280 \cdot 10^{-6}$	$-150 \cdot 10^{-6}$	$0 \cdot 10^{-6}$		
	τ	19 µs	1.3 ms	20 ms		

Table A.9.: Elastic fit time constants for selected wavenumbers, $S_3 \longrightarrow S_0$ transition in H_2O. The average time constant of the first column is $\tau = 18\,\mu s$.

1062 cm^{-1}	a	$110 \cdot 10^{-6}$	$-150 \cdot 10^{-6}$	$-11 \cdot 10^{-6}$	$0 \cdot 10^{-6}$	
	τ	14 µs	120 µs	5.1 ms	24 ms	
1070 cm^{-1}	a		$150 \cdot 10^{-6}$	$18 \cdot 10^{-6}$	$-10 \cdot 10^{-6}$	
	τ		120 µs	2.8 ms	39 ms	
1152 cm^{-1}	a		$41 \cdot 10^{-6}$	$2 \cdot 10^{-6}$	$2 \cdot 10^{-6}$	
	τ		130 µs	790 µs	21 ms	
1159 cm^{-1}	a	$79 \cdot 10^{-6}$	$-68 \cdot 10^{-6}$	$-5 \cdot 10^{-6}$		
	τ	20 µs	170 µs	11 ms		
1181 cm^{-1}	a	$-93 \cdot 10^{-6}$	$61 \cdot 10^{-6}$	$21 \cdot 10^{-6}$	$-2 \cdot 10^{-6}$	
	τ	13 µs	120 µs	1.3 ms	60 ms	
1248 cm^{-1}	a		$40 \cdot 10^{-6}$	$-22 \cdot 10^{-6}$		
	τ		130 µs	17 ms		
1360 cm^{-1}	a		$31 \cdot 10^{-6}$	$-18 \cdot 10^{-6}$	$30 \cdot 10^{-6}$	
	τ		150 µs	1.9 ms	41 ms	
1562 cm^{-1}	a	$-52 \cdot 10^{-6}$	$90 \cdot 10^{-6}$	$-71 \cdot 10^{-6}$		
	τ	15 µs	130 µs	28 ms		
1570 cm^{-1}	a		$-33 \cdot 10^{-6}$	$50 \cdot 10^{-6}$	$-39 \cdot 10^{-6}$	
	τ		170 µs	2.8 ms	47 ms	
1589 cm^{-1}	a		$-59 \cdot 10^{-6}$	$36 \cdot 10^{-6}$	$-27 \cdot 10^{-6}$	
	τ		160 µs	4.0 ms	66 ms	
1637 cm^{-1}	a	$550 \cdot 10^{-6}$	$-229 \cdot 10^{-6}$	$26 \cdot 10^{-6}$	$-53 \cdot 10^{-6}$	
	τ	24 µs	190 µs	1.8 ms	39 ms	
1660 cm^{-1}	a	$140 \cdot 10^{-6}$	$-180 \cdot 10^{-6}$	$56 \cdot 10^{-6}$	$-430 \cdot 10^{-6}$	$75 \cdot 10^{-6}$
	τ	16 µs	150 µs	720 µs	3.2 ms	41 ms
1673 cm^{-1}	a	$55 \cdot 10^{-6}$	$-130 \cdot 10^{-6}$	$57 \cdot 10^{-6}$	$-110 \cdot 10^{-6}$	
	τ	12 µs	130 µs	3.5 ms	37 ms	
1740 cm^{-1}	a		$44 \cdot 10^{-6}$	$-22 \cdot 10^{-6}$	$8 \cdot 10^{-6}$	
	τ		140 µs	2.9 ms	47 ms	

Table A.10.: Elastic fit time constants for selected wavenumbers, $S_3 \longrightarrow S_0$ transition in H_2O. The average time constant of the second column is $\tau = 142\,\mu s$.

1296 cm^{-1}	a			$13 \cdot 10^{-6}$	$-31 \cdot 10^{-6}$	
	τ			56 µs	2.8 ms	
1356 cm^{-1}	a			$6 \cdot 10^{-6}$	$-49 \cdot 10^{-6}$	$26 \cdot 10^{-6}$
	τ			240 µs	2.9 ms	49 ms
1382 cm^{-1}	a			$8 \cdot 10^{-6}$	$-50 \cdot 10^{-6}$	$13 \cdot 10^{-6}$
	τ			180 µs	2.9 ms	49 ms
1396 cm^{-1}	a			$21 \cdot 10^{-6}$	$-83 \cdot 10^{-6}$	
	τ			86 µs	2.4 ms	
1442 cm^{-1}	a			$-43 \cdot 10^{-6}$	$86 \cdot 10^{-6}$	$-3 \cdot 10^{-6}$
	τ			35 µs	3.3 ms	24 ms
1511 cm^{-1}	a			$-3 \cdot 10^{-6}$	$81 \cdot 10^{-6}$	$-32 \cdot 10^{-6}$
	τ			91 µs	2.6 ms	60 ms
1528 cm^{-1}	a			$60 \cdot 10^{-6}$	$33 \cdot 10^{-6}$	$-27 \cdot 10^{-6}$
	τ			40 µs	3.2 ms	43 ms
1544 cm^{-1}	a			$39 \cdot 10^{-6}$	$-170 \cdot 10^{-6}$	$13 \cdot 10^{-6}$
	τ			229 µs	2.8 ms	45 ms
1573 cm^{-1}	a			$36 \cdot 10^{-6}$	$69 \cdot 10^{-6}$	$-24 \cdot 10^{-6}$
	τ			16 µs	2.6 ms	63 ms
1620 cm^{-1}	a		$66 \cdot 10^{-6}$	$-66 \cdot 10^{-6}$	$53 \cdot 10^{-6}$	$-12 \cdot 10^{-6}$
	τ		29 µs	420 µs	3.0 ms	57 ms
1628 cm^{-1}	a		$-140 \cdot 10^{-6}$	$40 \cdot 10^{-6}$	$-48 \cdot 10^{-6}$	$-19 \cdot 10^{-6}$
	τ		24 µs	120 µs	2.5 ms	20 ms
1648 cm^{-1}	a	$-570 \cdot 10^{-6}$	$409 \cdot 10^{-6}$	$-350 \cdot 10^{-6}$	$310 \cdot 10^{-6}$	$-100 \cdot 10^{-6}$
	τ	15 µs	82 µs	370 µs	2.2 ms	35 ms
1661 cm^{-1}	a		$150 \cdot 10^{-6}$	$-150 \cdot 10^{-6}$	$-400 \cdot 10^{-6}$	$90 \cdot 10^{-6}$
	τ		16 µs	130 µs	2.6 ms	37 ms
1671 cm^{-1}	a		$110 \cdot 10^{-6}$	$-86 \cdot 10^{-6}$	$94 \cdot 10^{-6}$	$-160 \cdot 10^{-6}$
	τ		13 µs	270 µs	3.7 ms	37 ms
1706 cm^{-1}	a		$-28 \cdot 10^{-6}$	$39 \cdot 10^{-6}$	$-95 \cdot 10^{-6}$	$14 \cdot 10^{-6}$
	τ		20 µs	270 µs	3.5 ms	47 ms
1740 cm^{-1}	a			$44 \cdot 10^{-6}$	$-22 \cdot 10^{-6}$	$8 \cdot 10^{-6}$
	τ			140 µs	2.9 ms	47 ms

Table A.11.: Elastic fit time constants for selected wavenumbers, $S_3 \longrightarrow S_0$ transition in H_2O. The average time constant of the fourth column is $\tau = 2.9$ ms.

1248 cm^{-1}	a		$-93 \cdot 10^{-6}$	$-23 \cdot 10^{-6}$	$-18 \cdot 10^{-6}$	
	τ		51 µs	590 µs	6.9 ms	
1542 cm^{-1}	a		$-150 \cdot 10^{-6}$	$51 \cdot 10^{-6}$	$-200 \cdot 10^{-6}$	$22 \cdot 10^{-6}$
	τ		46 µs	440 µs	4.0 ms	63 ms
1601 cm^{-1}	a		$68 \cdot 10^{-6}$	$-47 \cdot 10^{-6}$	$17 \cdot 10^{-6}$	
	τ		56 µs	869 µs	9.6 ms	
1650 cm^{-1}	a	$-310 \cdot 10^{-6}$	$550 \cdot 10^{-6}$	$-280 \cdot 10^{-6}$	$360 \cdot 10^{-6}$	
	τ	9 µs	51 µs	290 µs	1.5 ms	
1658 cm^{-1}	a		$-409 \cdot 10^{-6}$	$-73 \cdot 10^{-6}$	$-260 \cdot 10^{-6}$	$190 \cdot 10^{-6}$
	τ		48 µs	440 µs	5.1 ms	54 ms

Table A.12.: Elastic fit time constants for selected wavenumbers, $S_3 \longrightarrow S_0$ transition in D_2O. The average time constant of the second column is $\tau = 50$ µs.

1054 cm^{-1}	a		$130 \cdot 10^{-6}$	$-90 \cdot 10^{-6}$	$-81 \cdot 10^{-6}$	$73 \cdot 10^{-6}$	
	τ		59 µs	440 µs	3.2 ms	63 ms	
1105 cm^{-1}	a			$66 \cdot 10^{-6}$	$9 \cdot 10^{-6}$	$-31 \cdot 10^{-6}$	
	τ			509 µs	3.3 ms	52 ms	
1333 cm^{-1}	a		$-22 \cdot 10^{-6}$	$47 \cdot 10^{-6}$	$-11 \cdot 10^{-6}$		
	τ		46 µs	490 µs	5.7 ms		
1352 cm^{-1}	a		$-45 \cdot 10^{-6}$	$78 \cdot 10^{-6}$	$-51 \cdot 10^{-6}$	$41 \cdot 10^{-6}$	
	τ		48 µs	540 µs	5.4 ms	63 ms	
1540 cm^{-1}	a		$-120 \cdot 10^{-6}$	$81 \cdot 10^{-6}$	$-170 \cdot 10^{-6}$	$-14 \cdot 10^{-6}$	
	τ		46 µs	459 µs	3.7 ms	16 ms	
1555 cm^{-1}	a		$-120 \cdot 10^{-6}$	$130 \cdot 10^{-6}$	$-56 \cdot 10^{-6}$		
	τ		71 µs	560 µs	5.1 ms		
1573 cm^{-1}	a		$-45 \cdot 10^{-6}$	$-75 \cdot 10^{-6}$	$67 \cdot 10^{-6}$		
	τ		95 µs	400 µs	6.2 ms		
1615 cm^{-1}	a		$-63 \cdot 10^{-6}$	$60 \cdot 10^{-6}$	$-44 \cdot 10^{-6}$		
	τ		68 µs	560 µs	4.7 ms		
1636 cm^{-1}	a	$-120 \cdot 10^{-6}$	$420 \cdot 10^{-6}$	$-459 \cdot 10^{-6}$	$-90 \cdot 10^{-6}$	$20 \cdot 10^{-6}$	
	τ	12 µs	91 µs	560 µs	6.2 ms	45 ms	
1652 cm^{-1}	a		$370 \cdot 10^{-6}$	$-220 \cdot 10^{-6}$	$270 \cdot 10^{-6}$	$-98 \cdot 10^{-6}$	$42 \cdot 10^{-6}$
	τ		51 µs	350 µs	1.5 ms	7.6 ms	63 ms
1674 cm^{-1}	a		$-64 \cdot 10^{-6}$	$-140 \cdot 10^{-6}$	$85 \cdot 10^{-6}$	$-81 \cdot 10^{-6}$	
	τ		46 µs	540 µs	3.9 ms	37 ms	
1706 cm^{-1}	a			$94 \cdot 10^{-6}$	$-120 \cdot 10^{-6}$	$25 \cdot 10^{-6}$	
	τ			540 µs	4.4 ms	49 ms	

Table A.13.: Elastic fit time constants for selected wavenumbers, $S_3 \longrightarrow S_0$ transition in D_2O. The average time constant of the third column is $\tau = 500$ µs.

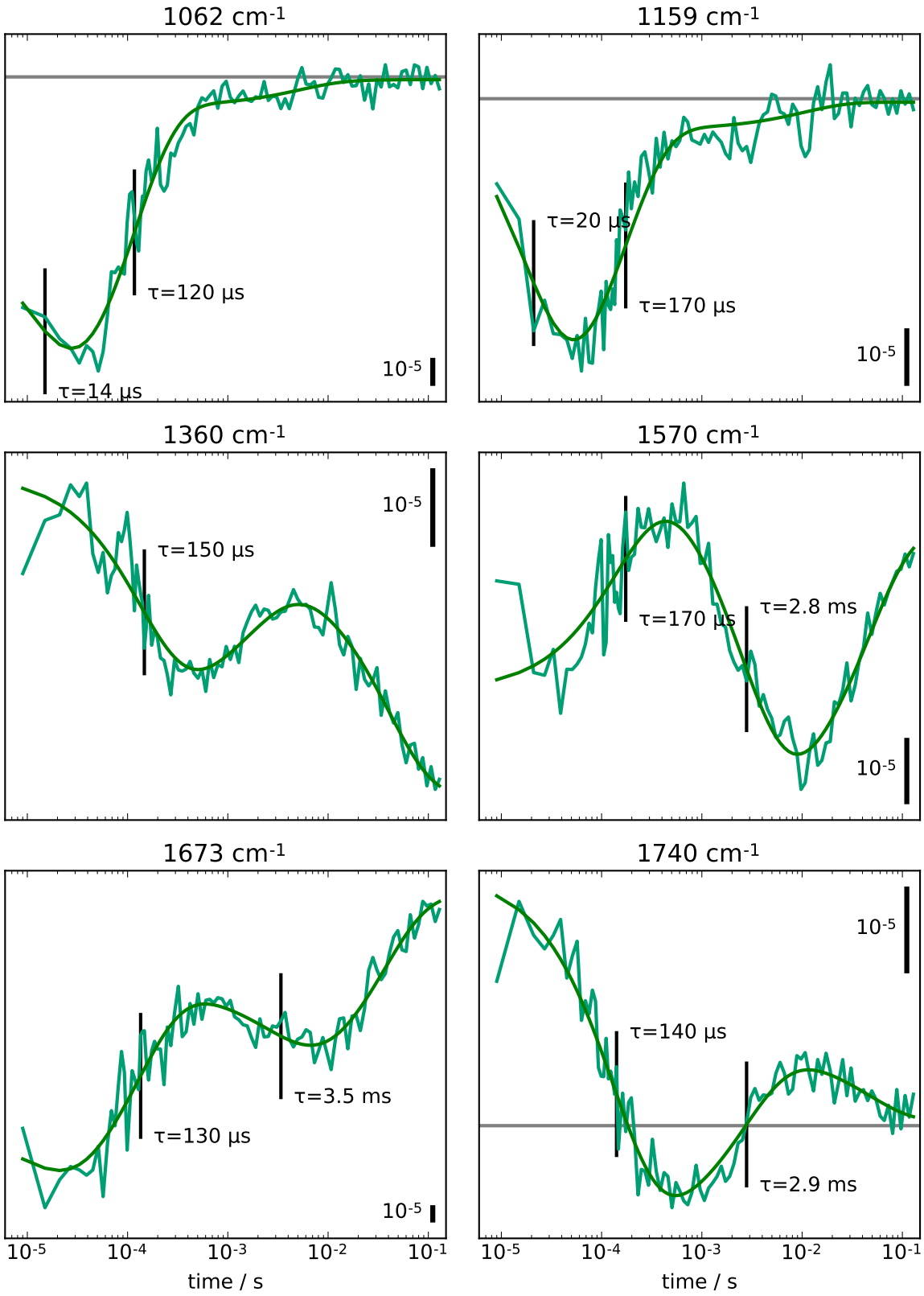

Figure A.12.: Selected H_2O timecourses (turquoise) and elastic net fits (green), $S_3 \longrightarrow S_0$ transition.

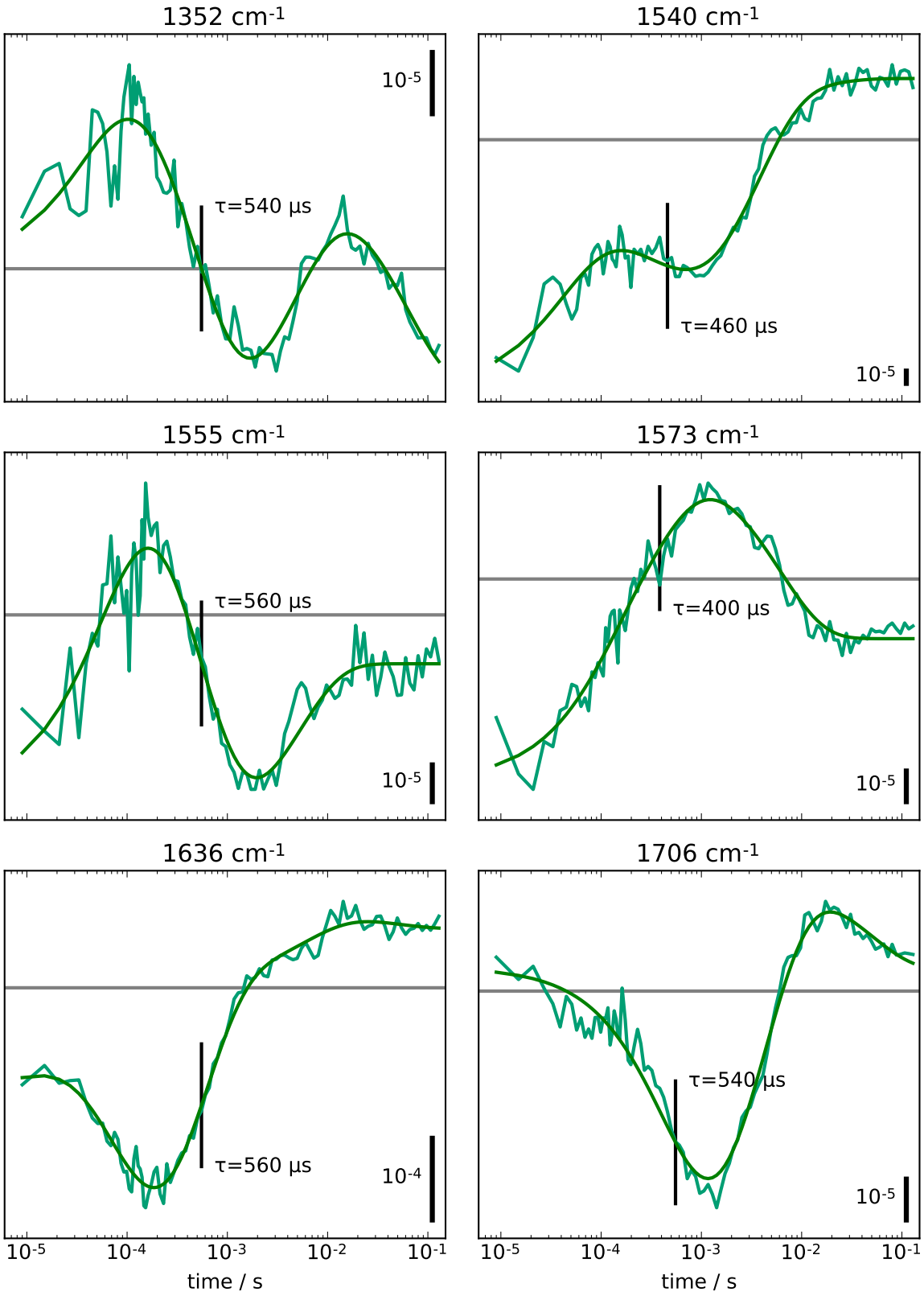

Figure A.13.: Selected D_2O timecourses (turquoise) and elastic net fits (green), $S_3 \longrightarrow S_0$ transition.

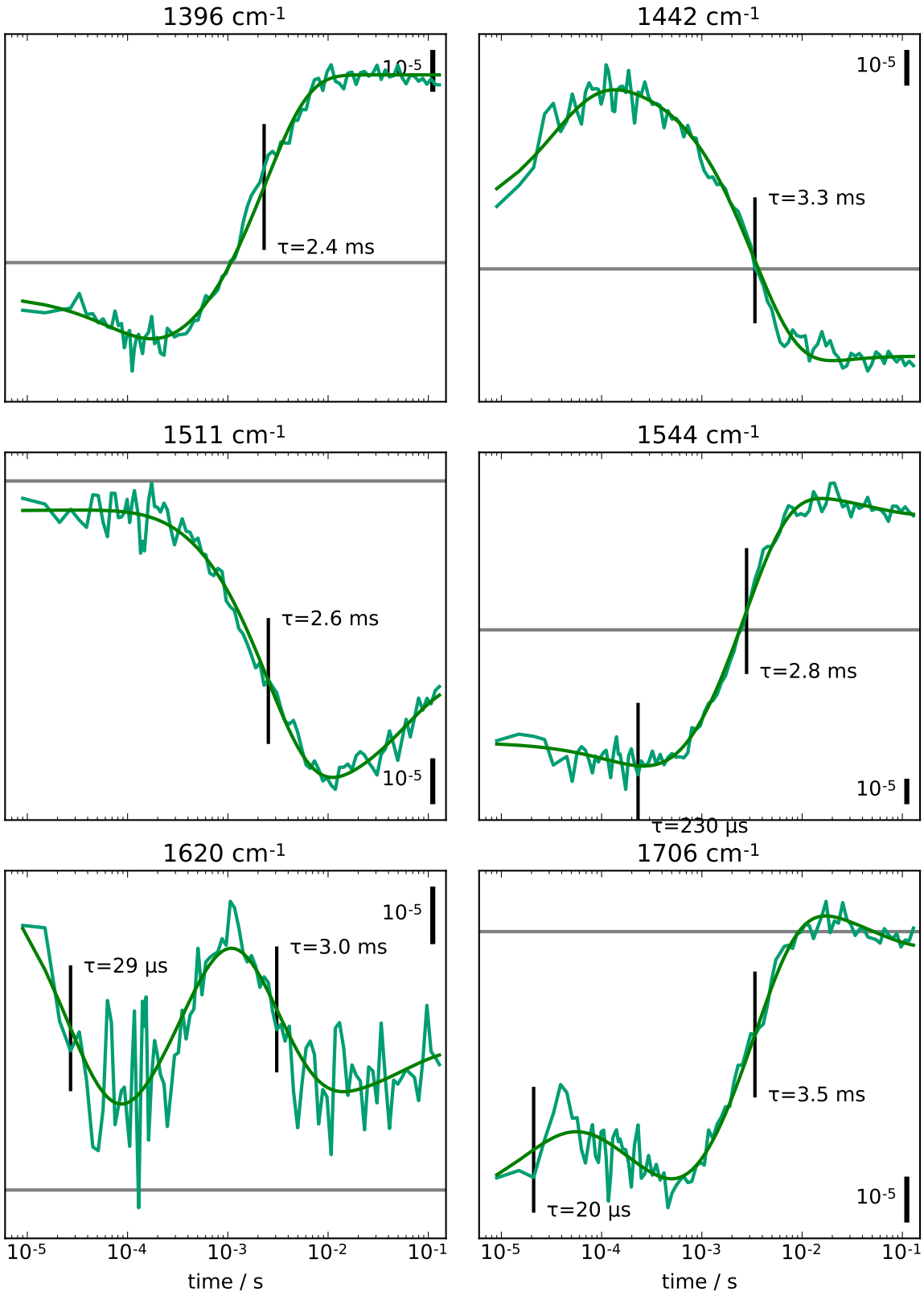

Figure A.14.: Selected H_2O timecourses (turquoise) and elastic net fits (green), $S_3 \longrightarrow S_0$ transition.

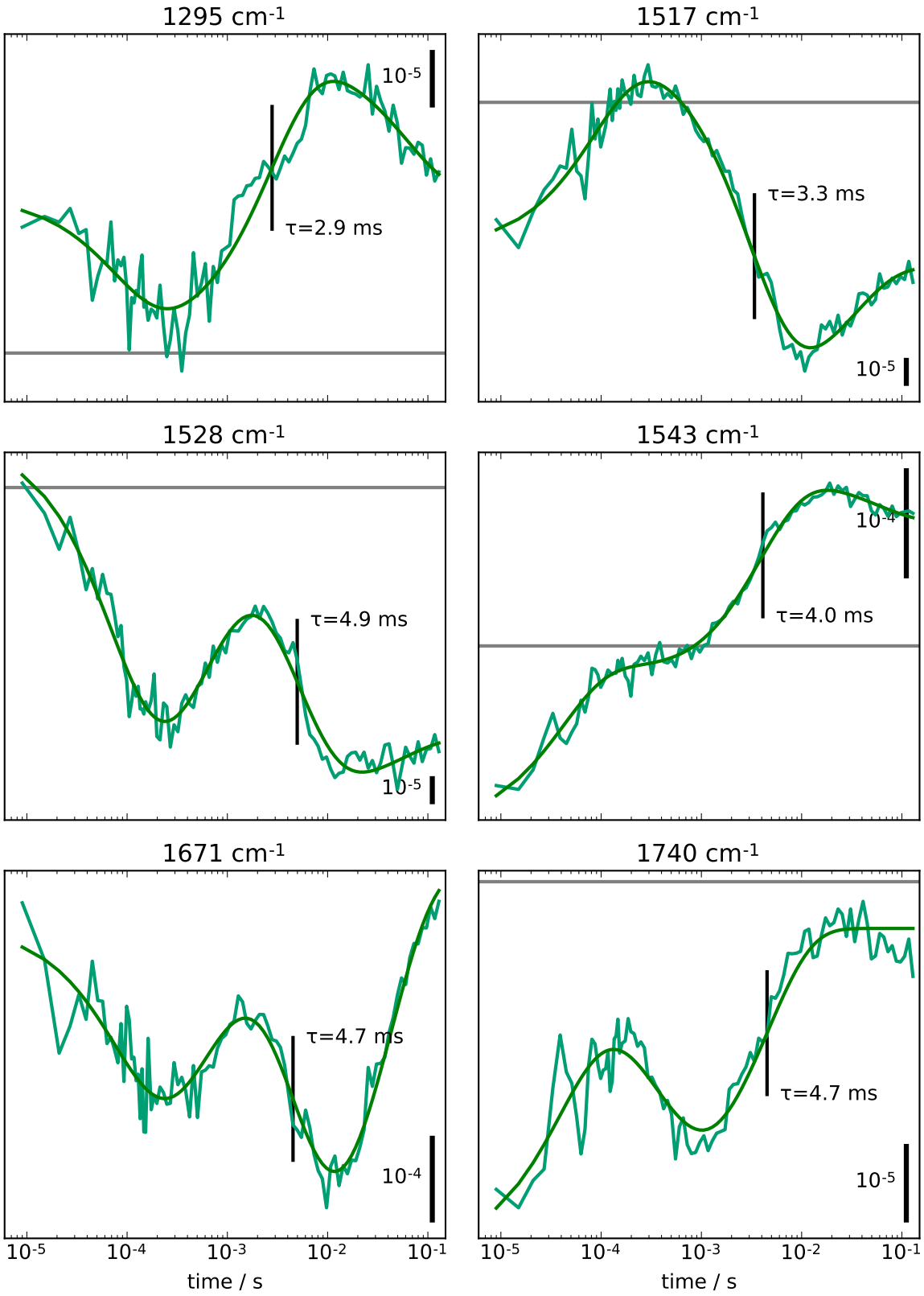

Figure A.15.: Selected D_2O timecourses (turquoise) and elastic net fits (green), $S_3 \longrightarrow S_0$ transition.

1063 cm^{-1}	a		$-85 \cdot 10^{-6}$	$79 \cdot 10^{-6}$	$-110 \cdot 10^{-6}$	$25 \cdot 10^{-6}$
	τ		15 µs	320 µs	2.8 ms	72 ms
1185 cm^{-1}	a		$42 \cdot 10^{-6}$	$-100 \cdot 10^{-6}$	$41 \cdot 10^{-6}$	$-23 \cdot 10^{-6}$
	τ		68 µs	459 µs	4.2 ms	66 ms
1272 cm^{-1}	a			$65 \cdot 10^{-6}$	$-35 \cdot 10^{-6}$	$33 \cdot 10^{-6}$
	τ			300 µs	5.1 ms	66 ms
1295 cm^{-1}	a			$25 \cdot 10^{-6}$	$-50 \cdot 10^{-6}$	$24 \cdot 10^{-6}$
	τ			86 µs	2.9 ms	63 ms
1314 cm^{-1}	a			$45 \cdot 10^{-6}$	$63 \cdot 10^{-6}$	
	τ			290 µs	2.5 ms	
1356 cm^{-1}	a		$-27 \cdot 10^{-6}$	$64 \cdot 10^{-6}$	$-85 \cdot 10^{-6}$	$53 \cdot 10^{-6}$
	τ		56 µs	620 µs	4.9 ms	60 ms
1383 cm^{-1}	a			$-27 \cdot 10^{-6}$	$-93 \cdot 10^{-6}$	$17 \cdot 10^{-6}$
	τ			130 µs	4.0 ms	57 ms
1397 cm^{-1}	a			$50 \cdot 10^{-6}$	$-229 \cdot 10^{-6}$	
	τ			48 µs	3.3 ms	
1441 cm^{-1}	a	$30 \cdot 10^{-6}$	$270 \cdot 10^{-6}$	$-95 \cdot 10^{-6}$	$190 \cdot 10^{-6}$	$-22 \cdot 10^{-6}$
	τ	15 µs	56 µs	620 µs	4.0 ms	41 ms
1458 cm^{-1}	a		$110 \cdot 10^{-6}$	$-140 \cdot 10^{-6}$	$88 \cdot 10^{-6}$	$-71 \cdot 10^{-6}$
	τ		62 µs	350 µs	3.2 ms	54 ms
1470 cm^{-1}	a		$22 \cdot 10^{-6}$	$26 \cdot 10^{-6}$	$57 \cdot 10^{-6}$	$47 \cdot 10^{-6}$
	τ		56 µs	650 µs	4.4 ms	32 ms
1506 cm^{-1}	a		$-45 \cdot 10^{-6}$	$83 \cdot 10^{-6}$	$78 \cdot 10^{-6}$	$-35 \cdot 10^{-6}$
	τ		42 µs	680 µs	2.9 ms	47 ms
1517 cm^{-1}	a			$-100 \cdot 10^{-6}$	$180 \cdot 10^{-6}$	$-66 \cdot 10^{-6}$
	τ			95 µs	3.3 ms	34 ms
1528 cm^{-1}	a		$150 \cdot 10^{-6}$	$-130 \cdot 10^{-6}$	$120 \cdot 10^{-6}$	$-23 \cdot 10^{-6}$
	τ		82 µs	750 µs	4.9 ms	57 ms
1543 cm^{-1}	a		$-160 \cdot 10^{-6}$	$20 \cdot 10^{-6}$	$-210 \cdot 10^{-6}$	$47 \cdot 10^{-6}$
	τ		42 µs	400 µs	4.0 ms	57 ms
1558 cm^{-1}	a		$-210 \cdot 10^{-6}$	$170 \cdot 10^{-6}$	$-130 \cdot 10^{-6}$	$-15 \cdot 10^{-6}$
	τ		82 µs	620 µs	6.2 ms	39 ms

1583 cm^{-1}	a			$-69 \cdot 10^{-6}$	$100 \cdot 10^{-6}$	
	τ			91 µs	3.0 ms	
1616 cm^{-1}	a		$-51 \cdot 10^{-6}$	$59 \cdot 10^{-6}$	$-45 \cdot 10^{-6}$	
	τ		59 µs	509 µs	4.7 ms	
1639 cm^{-1}	a		$270 \cdot 10^{-6}$	$-440 \cdot 10^{-6}$	$-110 \cdot 10^{-6}$	$56 \cdot 10^{-6}$
	τ		95 µs	720 µs	5.7 ms	45 ms
1661 cm^{-1}	a		$-330 \cdot 10^{-6}$	$-75 \cdot 10^{-6}$	$-360 \cdot 10^{-6}$	$200 \cdot 10^{-6}$
	τ		44 µs	320 µs	3.9 ms	41 ms
1671 cm^{-1}	a		$110 \cdot 10^{-6}$	$-130 \cdot 10^{-6}$	$190 \cdot 10^{-6}$	$-190 \cdot 10^{-6}$
	τ		95 µs	790 µs	4.7 ms	43 ms
1698 cm^{-1}	a		$-110 \cdot 10^{-6}$	$-45 \cdot 10^{-6}$	$100 \cdot 10^{-6}$	$-21 \cdot 10^{-6}$
	τ		35 µs	350 µs	4.7 ms	54 ms
1707 cm^{-1}	a		$19 \cdot 10^{-6}$	$100 \cdot 10^{-6}$	$-130 \cdot 10^{-6}$	$25 \cdot 10^{-6}$
	τ		21 µs	459 µs	4.2 ms	49 ms
1724 cm^{-1}	a			$100 \cdot 10^{-6}$	$-31 \cdot 10^{-6}$	$-38 \cdot 10^{-6}$
	τ			42 µs	2.6 ms	14 ms
1731 cm^{-1}	a			$-30 \cdot 10^{-6}$	$43 \cdot 10^{-6}$	
	τ			120 µs	2.6 ms	
1740 cm^{-1}	a		$-38 \cdot 10^{-6}$	$31 \cdot 10^{-6}$	$-39 \cdot 10^{-6}$	
	τ		46 µs	420 µs	4.7 ms	

Table A.14.: Elastic fit time constants for selected wavenumbers, $S_3 \longrightarrow S_0$ transition in D_2O. The average time constant of the fourth column is $\tau = 4.0$ ms.

1059 cm^{-1}	a	$-97 \cdot 10^{-6}$	$-31 \cdot 10^{-6}$	$-11 \cdot 10^{-6}$	$-12 \cdot 10^{-6}$	
	τ	19 µs	91 µs	1.0 ms	45 ms	
1071 cm^{-1}	a	$-140 \cdot 10^{-6}$	$49 \cdot 10^{-6}$	$20 \cdot 10^{-6}$		
	τ	22 µs	180 µs	3.9 ms		
1079 cm^{-1}	a	$110 \cdot 10^{-6}$	$-65 \cdot 10^{-6}$	$5 \cdot 10^{-6}$		
	τ	21 µs	160 µs	6.5 ms		
1127 cm^{-1}	a	$46 \cdot 10^{-6}$	$33 \cdot 10^{-6}$	$20 \cdot 10^{-6}$		
	τ	24 µs	200 µs	20 ms		
1173 cm^{-1}	a	$67 \cdot 10^{-6}$	$-36 \cdot 10^{-6}$	$12 \cdot 10^{-6}$	$-12 \cdot 10^{-6}$	
	τ	21 µs	180 µs	2.6 ms	60 ms	
1239 cm^{-1}	a	$84 \cdot 10^{-6}$	$-16 \cdot 10^{-6}$	$-15 \cdot 10^{-6}$		
	τ	26 µs	350 µs	23 ms		
1252 cm^{-1}	a	$86 \cdot 10^{-6}$	$-24 \cdot 10^{-6}$	$7 \cdot 10^{-6}$	$2 \cdot 10^{-6}$	
	τ	24 µs	320 µs	4.4 ms	39 ms	
1381 cm^{-1}	a	$36 \cdot 10^{-6}$	$16 \cdot 10^{-6}$	$-4 \cdot 10^{-6}$		
	τ	26 µs	290 µs	12 ms		
1488 cm^{-1}	a	$43 \cdot 10^{-6}$	$10 \cdot 10^{-6}$	$14 \cdot 10^{-6}$		
	τ	26 µs	2.6 ms	43 ms		
1562 cm^{-1}	a	$-120 \cdot 10^{-6}$	$21 \cdot 10^{-6}$	$-30 \cdot 10^{-6}$		
	τ	22 µs	440 µs	35 ms		
1610 cm^{-1}	a	$-140 \cdot 10^{-6}$	$56 \cdot 10^{-6}$	$-29 \cdot 10^{-6}$	$9 \cdot 10^{-6}$	
	τ	21 µs	130 µs	1.4 ms	13 ms	
1637 cm^{-1}	a	$-140 \cdot 10^{-6}$	$-6 \cdot 10^{-6}$	$-120 \cdot 10^{-6}$	$61 \cdot 10^{-6}$	$-89 \cdot 10^{-6}$
	τ	19 µs	200 µs	1.1 ms	11 ms	97 ms
1651 cm^{-1}	a	$210 \cdot 10^{-6}$	$-210 \cdot 10^{-6}$	$140 \cdot 10^{-6}$	$110 \cdot 10^{-6}$	$-190 \cdot 10^{-6}$
	τ	18 µs	95 µs	440 µs	11 ms	88 ms
1662 cm^{-1}	a	$290 \cdot 10^{-6}$	$-240 \cdot 10^{-6}$	$-130 \cdot 10^{-6}$	$-190 \cdot 10^{-6}$	$80 \cdot 10^{-6}$
	τ	30 µs	180 µs	750 µs	3.3 ms	34 ms
1691 cm^{-1}	a	$-160 \cdot 10^{-6}$	$29 \cdot 10^{-6}$	$-62 \cdot 10^{-6}$	$-11 \cdot 10^{-6}$	
	τ	21 µs	170 µs	1.7 ms	63 ms	
1721 cm^{-1}	a	$56 \cdot 10^{-6}$	$-4 \cdot 10^{-6}$			
	τ	29 µs	2.3 ms			
1734 cm^{-1}	a	$41 \cdot 10^{-6}$	$-5 \cdot 10^{-6}$	$-2 \cdot 10^{-6}$		
	τ	19 µs	229 µs	69 ms		

Table A.15.: Elastic fit time constants for selected wavenumbers, $S_0 \longrightarrow S_1$ transition in H_2O. The average time constant of the third column is $\tau = 22\,\mu s$.

1078 cm^{-1}	a	$99 \cdot 10^{-6}$	$-58 \cdot 10^{-6}$	$13 \cdot 10^{-6}$	$-18 \cdot 10^{-6}$	
	τ	19 µs	180 µs	7.9 ms	84 ms	
1127 cm^{-1}	a	$46 \cdot 10^{-6}$	$33 \cdot 10^{-6}$	$20 \cdot 10^{-6}$		
	τ	24 µs	200 µs	20 ms		
1138 cm^{-1}	a	$83 \cdot 10^{-6}$	$-62 \cdot 10^{-6}$	$-6 \cdot 10^{-6}$		
	τ	18 µs	170 µs	34 ms		
1170 cm^{-1}	a	$61 \cdot 10^{-6}$	$-50 \cdot 10^{-6}$	$5 \cdot 10^{-6}$		
	τ	19 µs	190 µs	2.8 ms		
1192 cm^{-1}	a		$-32 \cdot 10^{-6}$			
	τ		220 µs			
1228 cm^{-1}	a	$58 \cdot 10^{-6}$	$-57 \cdot 10^{-6}$	$-30 \cdot 10^{-6}$		
	τ	15 µs	220 µs	25 ms		
1325 cm^{-1}	a		$19 \cdot 10^{-6}$	$-8 \cdot 10^{-6}$		
	τ		200 µs	4.0 ms		
1377 cm^{-1}	a		$31 \cdot 10^{-6}$	$-11 \cdot 10^{-6}$		
	τ		180 µs	24 ms		
1388 cm^{-1}	a	$-34 \cdot 10^{-6}$	$39 \cdot 10^{-6}$	$-15 \cdot 10^{-6}$		
	τ	18 µs	190 µs	19 ms		
1439 cm^{-1}	a		$26 \cdot 10^{-6}$	$14 \cdot 10^{-6}$	$7 \cdot 10^{-6}$	
	τ		200 µs	2.9 ms	11 ms	
1547 cm^{-1}	a		$-37 \cdot 10^{-6}$	$-30 \cdot 10^{-6}$	$20 \cdot 10^{-6}$	
	τ		200 µs	1.5 ms	63 ms	
1577 cm^{-1}	a		$47 \cdot 10^{-6}$	$30 \cdot 10^{-6}$	$26 \cdot 10^{-6}$	
	τ		200 µs	869 µs	5.1 ms	
1620 cm^{-1}	a	$32 \cdot 10^{-6}$	$-67 \cdot 10^{-6}$	$-21 \cdot 10^{-6}$	$4 \cdot 10^{-6}$	$7 \cdot 10^{-6}$
	τ	19 µs	229 µs	1.1 ms	11 ms	63 ms
1642 cm^{-1}	a	$-280 \cdot 10^{-6}$	$-150 \cdot 10^{-6}$	$-180 \cdot 10^{-6}$	$110 \cdot 10^{-6}$	$-220 \cdot 10^{-6}$
	τ	59 µs	200 µs	2.1 ms	14 ms	120 ms
1661 cm^{-1}	a	$320 \cdot 10^{-6}$	$-210 \cdot 10^{-6}$	$-210 \cdot 10^{-6}$	$-220 \cdot 10^{-6}$	$110 \cdot 10^{-6}$
	τ	33 µs	150 µs	650 µs	4.0 ms	43 ms
1677 cm^{-1}	a	$120 \cdot 10^{-6}$	$-66 \cdot 10^{-6}$	$-80 \cdot 10^{-6}$	$-28 \cdot 10^{-6}$	
	τ	17 µs	229 µs	1.5 ms	76 ms	
1712 cm^{-1}	a		$-31 \cdot 10^{-6}$	$-24 \cdot 10^{-6}$	$-5 \cdot 10^{-6}$	
	τ		190 µs	2.3 ms	35 ms	

Table A.16.: Elastic fit time constants for selected wavenumbers, $S_0 \longrightarrow S_1$ transition in H_2O. The average time constant of the third column is $\tau = 200$ µs.

1060 cm^{-1}	a	$86 \cdot 10^{-6}$	$100 \cdot 10^{-6}$	$-72 \cdot 10^{-6}$	$-40 \cdot 10^{-6}$	
	τ	27 µs	140 µs	1.5 ms	12 ms	
1086 cm^{-1}	a	$160 \cdot 10^{-6}$	$-50 \cdot 10^{-6}$	$87 \cdot 10^{-6}$	$-81 \cdot 10^{-6}$	$51 \cdot 10^{-6}$
	τ	30 µs	180 µs	1.5 ms	7.9 ms	69 ms
1280 cm^{-1}	a	$-67 \cdot 10^{-6}$	$11 \cdot 10^{-6}$	$-5 \cdot 10^{-6}$		
	τ	35 µs	540 µs	41 ms		
1300 cm^{-1}	a	$41 \cdot 10^{-6}$	$-14 \cdot 10^{-6}$	$-3 \cdot 10^{-6}$		
	τ	27 µs	680 µs	49 ms		
1310 cm^{-1}	a	$52 \cdot 10^{-6}$	$-19 \cdot 10^{-6}$	$-3 \cdot 10^{-6}$		
	τ	33 µs	720 µs	22 ms		
1330 cm^{-1}	a	$-72 \cdot 10^{-6}$	$13 \cdot 10^{-6}$	$-24 \cdot 10^{-6}$		
	τ	24 µs	240 µs	15 ms		
1343 cm^{-1}	a	$-100 \cdot 10^{-6}$	$24 \cdot 10^{-6}$	$-1 \cdot 10^{-6}$	$21 \cdot 10^{-6}$	
	τ	30 µs	330 µs	4.2 ms	37 ms	
1372 cm^{-1}	a	$-41 \cdot 10^{-6}$	$27 \cdot 10^{-6}$	$17 \cdot 10^{-6}$		
	τ	31 µs	459 µs	8.7 ms		
1388 cm^{-1}	a	$81 \cdot 10^{-6}$	$-39 \cdot 10^{-6}$	$2 \cdot 10^{-6}$	$-6 \cdot 10^{-6}$	
	τ	33 µs	260 µs	3.7 ms	54 ms	
1513 cm^{-1}	a	$-140 \cdot 10^{-6}$	$54 \cdot 10^{-6}$	$-7 \cdot 10^{-6}$	$-29 \cdot 10^{-6}$	
	τ	29 µs	290 µs	4.2 ms	20 ms	
1571 cm^{-1}	a	$-71 \cdot 10^{-6}$	$27 \cdot 10^{-6}$	$36 \cdot 10^{-6}$		
	τ	31 µs	420 µs	5.4 ms		
1628 cm^{-1}	a	$-180 \cdot 10^{-6}$	$-87 \cdot 10^{-6}$	$81 \cdot 10^{-6}$	$-16 \cdot 10^{-6}$	
	τ	30 µs	180 µs	2.4 ms	76 ms	
1649 cm^{-1}	a	$370 \cdot 10^{-6}$	$-210 \cdot 10^{-6}$	$310 \cdot 10^{-6}$	$83 \cdot 10^{-6}$	
	τ	27 µs	190 µs	1.7 ms	60 ms	
1664 cm^{-1}	a	$-290 \cdot 10^{-6}$	$330 \cdot 10^{-6}$	$-180 \cdot 10^{-6}$	$-16 \cdot 10^{-6}$	$7 \cdot 10^{-6}$
	τ	35 µs	229 µs	1.3 ms	5.9 ms	69 ms
1679 cm^{-1}	a	$-150 \cdot 10^{-6}$	$17 \cdot 10^{-6}$	$-62 \cdot 10^{-6}$		
	τ	30 µs	270 µs	5.9 ms		
1721 cm^{-1}	a	$170 \cdot 10^{-6}$	$-46 \cdot 10^{-6}$	$-11 \cdot 10^{-6}$		
	τ	33 µs	490 µs	5.1 ms		
1750 cm^{-1}	a	$47 \cdot 10^{-6}$	$-31 \cdot 10^{-6}$	$22 \cdot 10^{-6}$	$-13 \cdot 10^{-6}$	
	τ	29 µs	400 µs	4.7 ms	60 ms	

Table A.17.: Elastic fit time constants for selected wavenumbers, $S_3 \longrightarrow S_0$ transition in D_2O. The average time constant of the first column is $\tau = 30$ µs.

1089 cm^{-1}	a	$130 \cdot 10^{-6}$	$-130 \cdot 10^{-6}$	$97 \cdot 10^{-6}$	$-83 \cdot 10^{-6}$	$88 \cdot 10^{-6}$
	τ	42 µs	220 µs	1.6 ms	9.2 ms	76 ms
1550 cm^{-1}	a	$33 \cdot 10^{-6}$	$-110 \cdot 10^{-6}$	$62 \cdot 10^{-6}$		
	τ	26 µs	180 µs	15 ms		
1620 cm^{-1}	a	$29 \cdot 10^{-6}$	$-110 \cdot 10^{-6}$	$33 \cdot 10^{-6}$	$31 \cdot 10^{-6}$	
	τ	30 µs	190 µs	1.6 ms	9.2 ms	
1628 cm^{-1}	a	$-180 \cdot 10^{-6}$	$-87 \cdot 10^{-6}$	$81 \cdot 10^{-6}$	$-16 \cdot 10^{-6}$	
	τ	30 µs	180 µs	2.4 ms	76 ms	
1646 cm^{-1}	a	$190 \cdot 10^{-6}$	$-240 \cdot 10^{-6}$	$370 \cdot 10^{-6}$	$2 \cdot 10^{-6}$	
	τ	31 µs	180 µs	1.3 ms	76 ms	
1665 cm^{-1}	a	$-320 \cdot 10^{-6}$	$340 \cdot 10^{-6}$	$-140 \cdot 10^{-6}$	$-10 \cdot 10^{-6}$	
	τ	36 µs	220 µs	1.2 ms	29 ms	

Table A.18.: Elastic fit time constants for selected wavenumbers, $S_3 \longrightarrow S_0$ transition in D_2O. The average time constant of the second column is $\tau = 191$ µs.

1093 cm^{-1}	a	$89 \cdot 10^{-6}$	$-130 \cdot 10^{-6}$	$64 \cdot 10^{-6}$	$-54 \cdot 10^{-6}$	$60 \cdot 10^{-6}$
	τ	65 µs	290 µs	1.5 ms	12 ms	100 ms
1347 cm^{-1}	a	$-120 \cdot 10^{-6}$	$40 \cdot 10^{-6}$	$11 \cdot 10^{-6}$		
	τ	40 µs	350 µs	66 ms		
1363 cm^{-1}	a	$-39 \cdot 10^{-6}$	$59 \cdot 10^{-6}$	$38 \cdot 10^{-6}$		
	τ	27 µs	300 µs	11 ms		
1541 cm^{-1}	a	$-45 \cdot 10^{-6}$	$100 \cdot 10^{-6}$	$-62 \cdot 10^{-6}$	$-19 \cdot 10^{-6}$	
	τ	38 µs	330 µs	2.3 ms	52 ms	
1607 cm^{-1}	a	$-36 \cdot 10^{-6}$	$57 \cdot 10^{-6}$	$41 \cdot 10^{-6}$		
	τ	29 µs	330 µs	7.2 ms		
1742 cm^{-1}	a	$-25 \cdot 10^{-6}$	$34 \cdot 10^{-6}$	$-15 \cdot 10^{-6}$		
	τ	27 µs	370 µs	10 ms		
1752 cm^{-1}	a	$45 \cdot 10^{-6}$	$-18 \cdot 10^{-6}$	$17 \cdot 10^{-6}$	$-12 \cdot 10^{-6}$	
	τ	26 µs	330 µs	3.9 ms	57 ms	

Table A.19.: Elastic fit time constants for selected wavenumbers, $S_3 \longrightarrow S_0$ transition in D_2O. The average time constant of the second column is $\tau = 327$ µs.

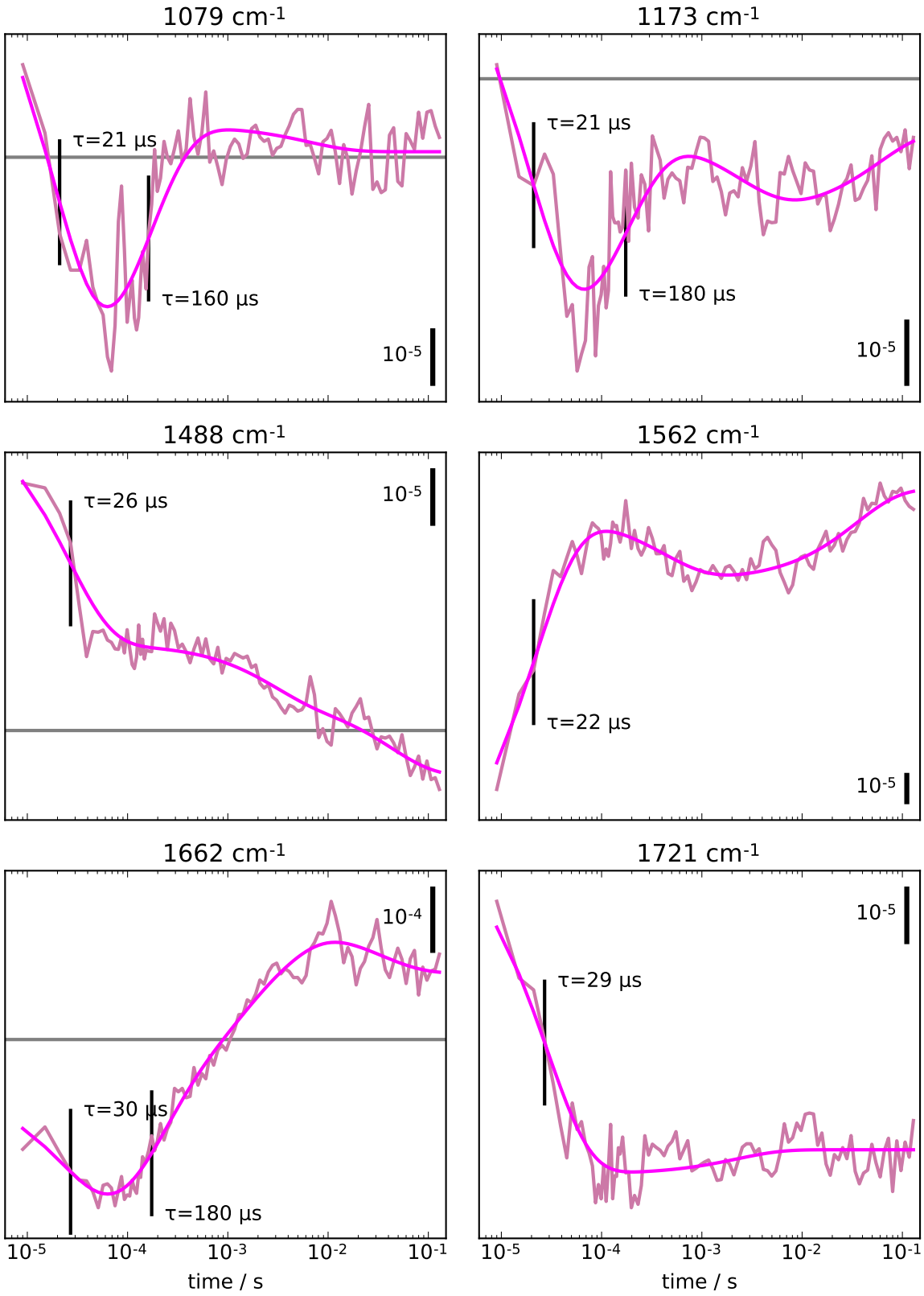

Figure A.16.: Selected H_2O timecourses (pink) and elastic net fits (magenta), $S_0 \longrightarrow S_1$ transition.

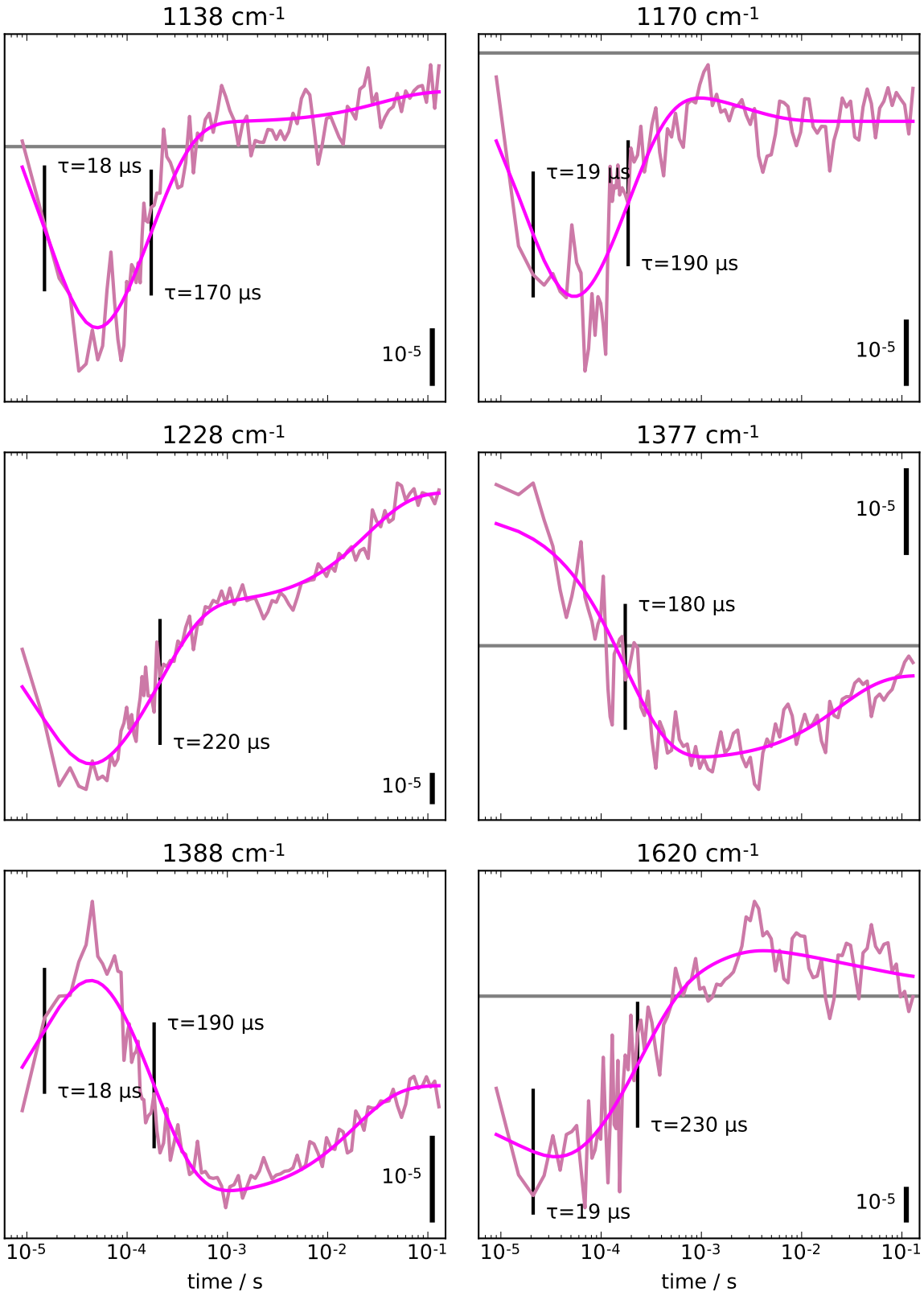

Figure A.17.: Selected H_2O timecourses (pink) and elastic net fits (magenta), $S_0 \longrightarrow S_1$ transition.

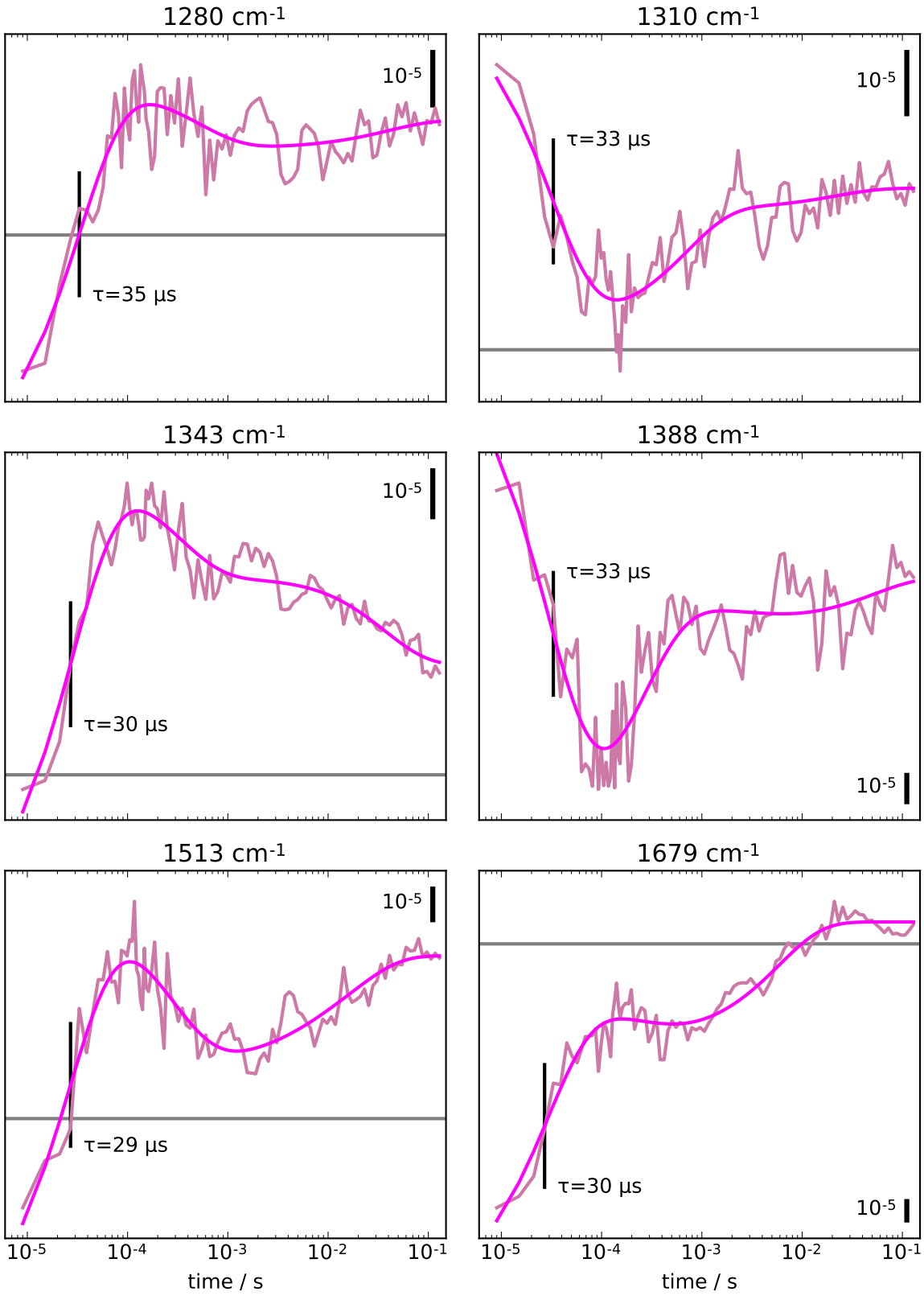

Figure A.18.: Selected D_2O timecourses (pink) and elastic net fits (magenta), $S_0 \longrightarrow S_1$ transition.

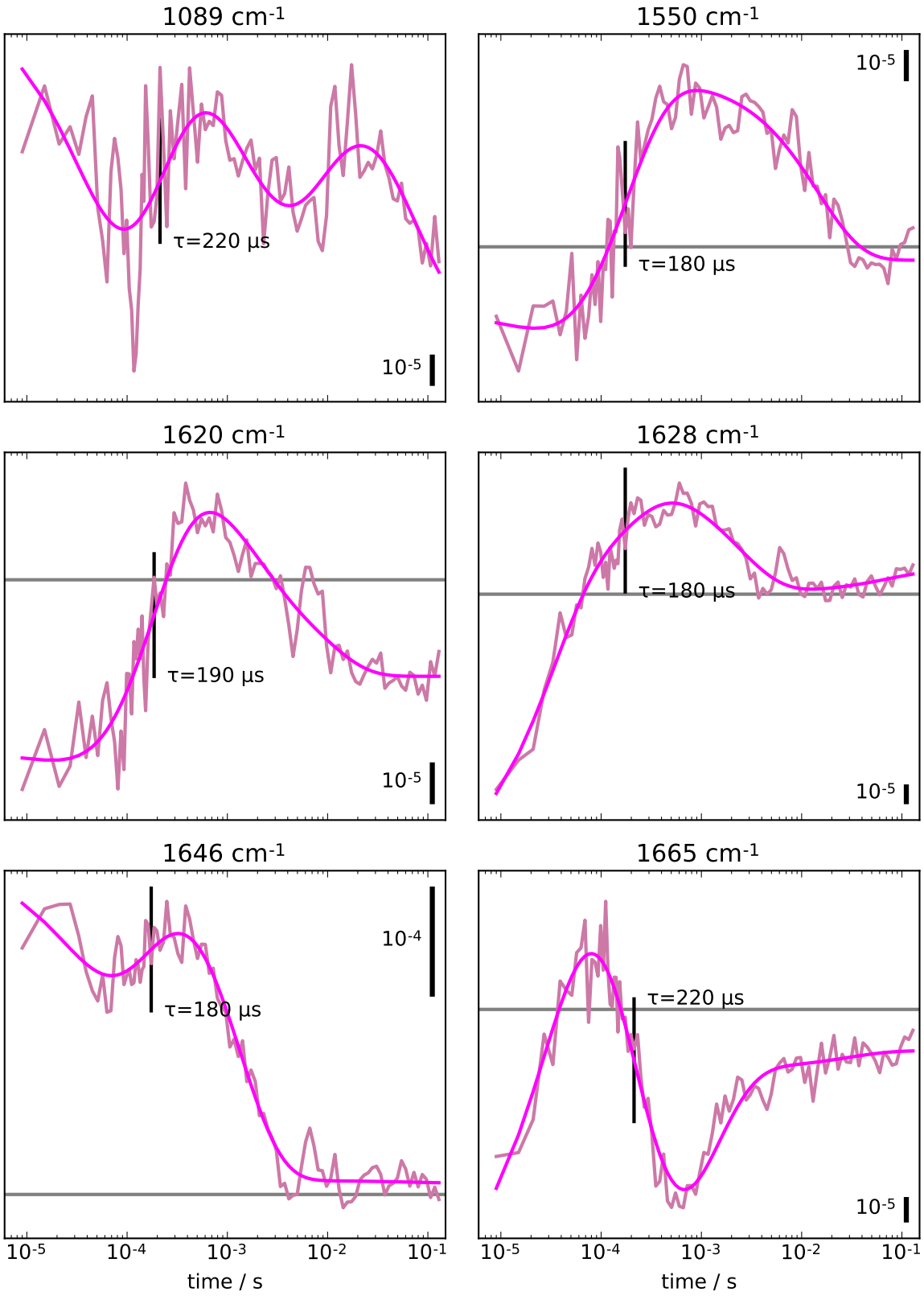

Figure A.19.: Selected D_2O timecourses (pink) and elastic net fits (magenta), $S_0 \longrightarrow S_1$ transition.

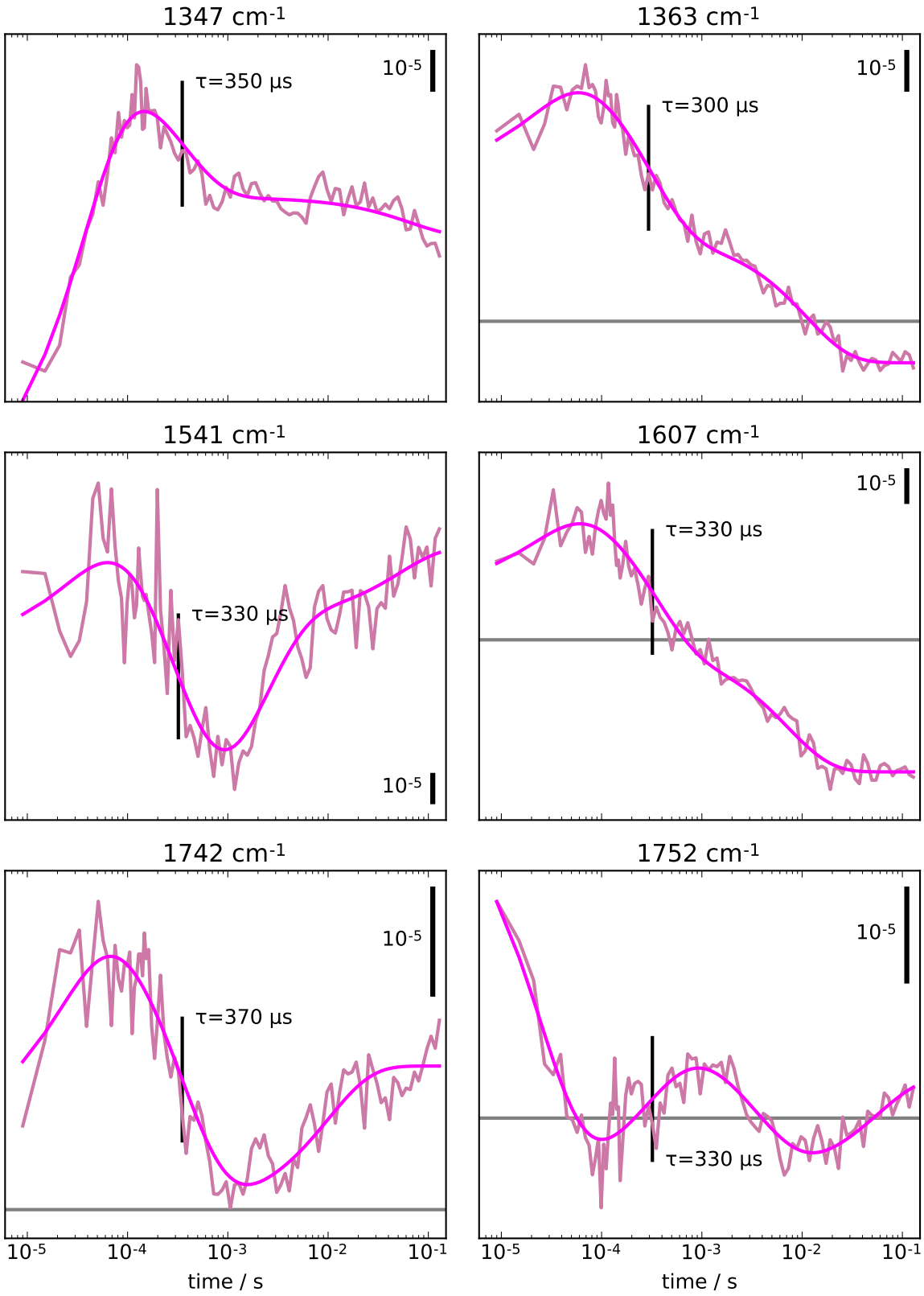

Figure A.20.: Selected D_2O timecourses (pink) and elastic net fits (magenta), $S_0 \longrightarrow S_1$ transition.

A.7. Comparison of static fits with step-scan data: selected spectra

Figures A.21-A.28 on pages 280-287 compare the fit calculated using a fixed set of time constants to the time-resolved step-scan difference spectra. The time constants used in the calculation are given in table 6.4 on page 194. For each flash induced S-state transition, both data and fit are shown 9 µs, 27 µs, 100 µs, 300 µs, 1 ms, 3 ms, 10 ms, and 100 ms after laser flash excitation.

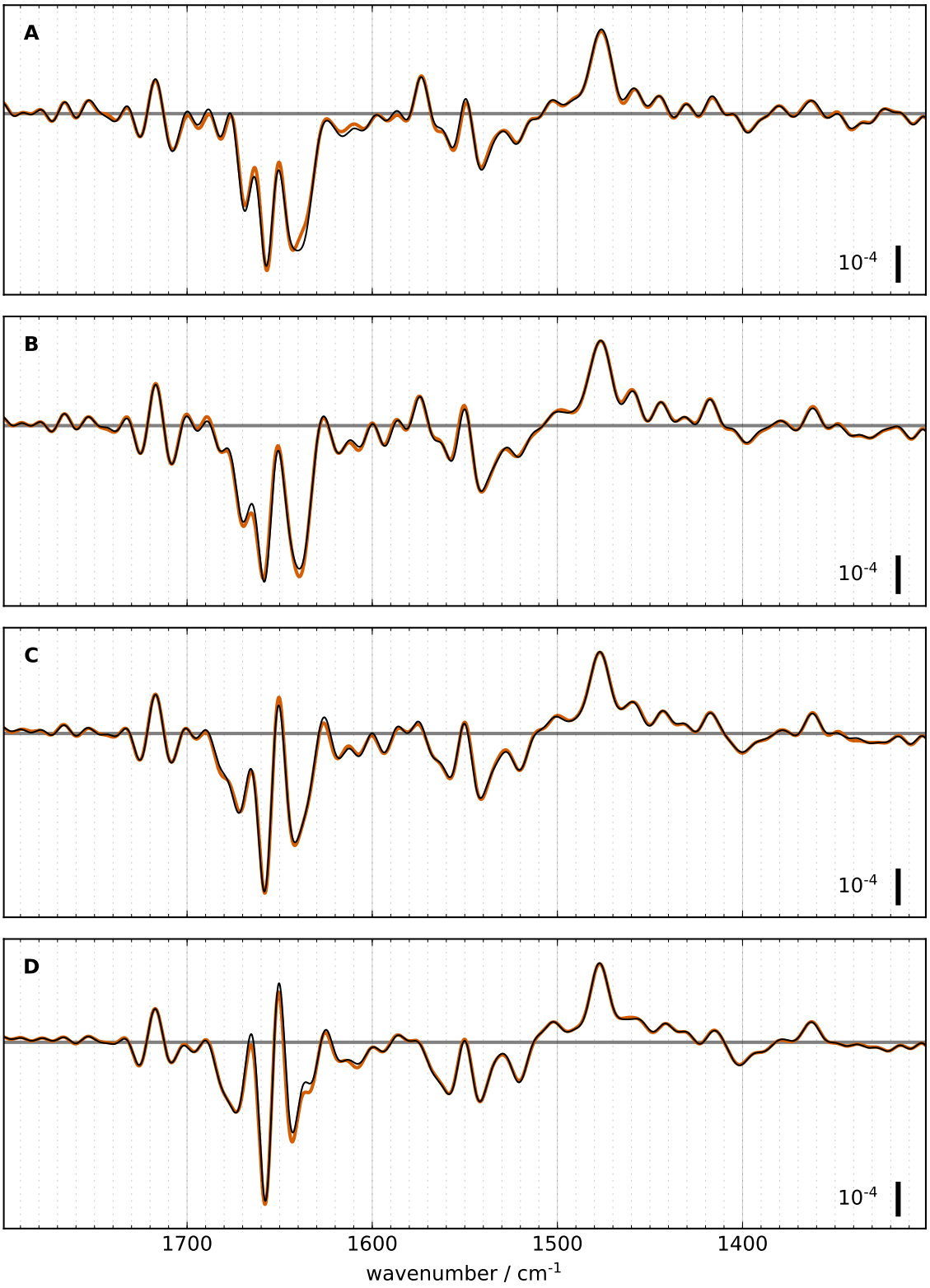

Figure A.21.: Comparison of step-scan difference spectra (thick colored line) with a fit (thin black line) calculated using a fixed set of time constants of the $S_1 \longrightarrow S_2$ transition. A: 9 µs, B: 27 µs, C: 100 µs, D: 300 µs, E: 1 ms, F: 3 ms, G: 10 ms, H: 100 ms after laser flash excitation.

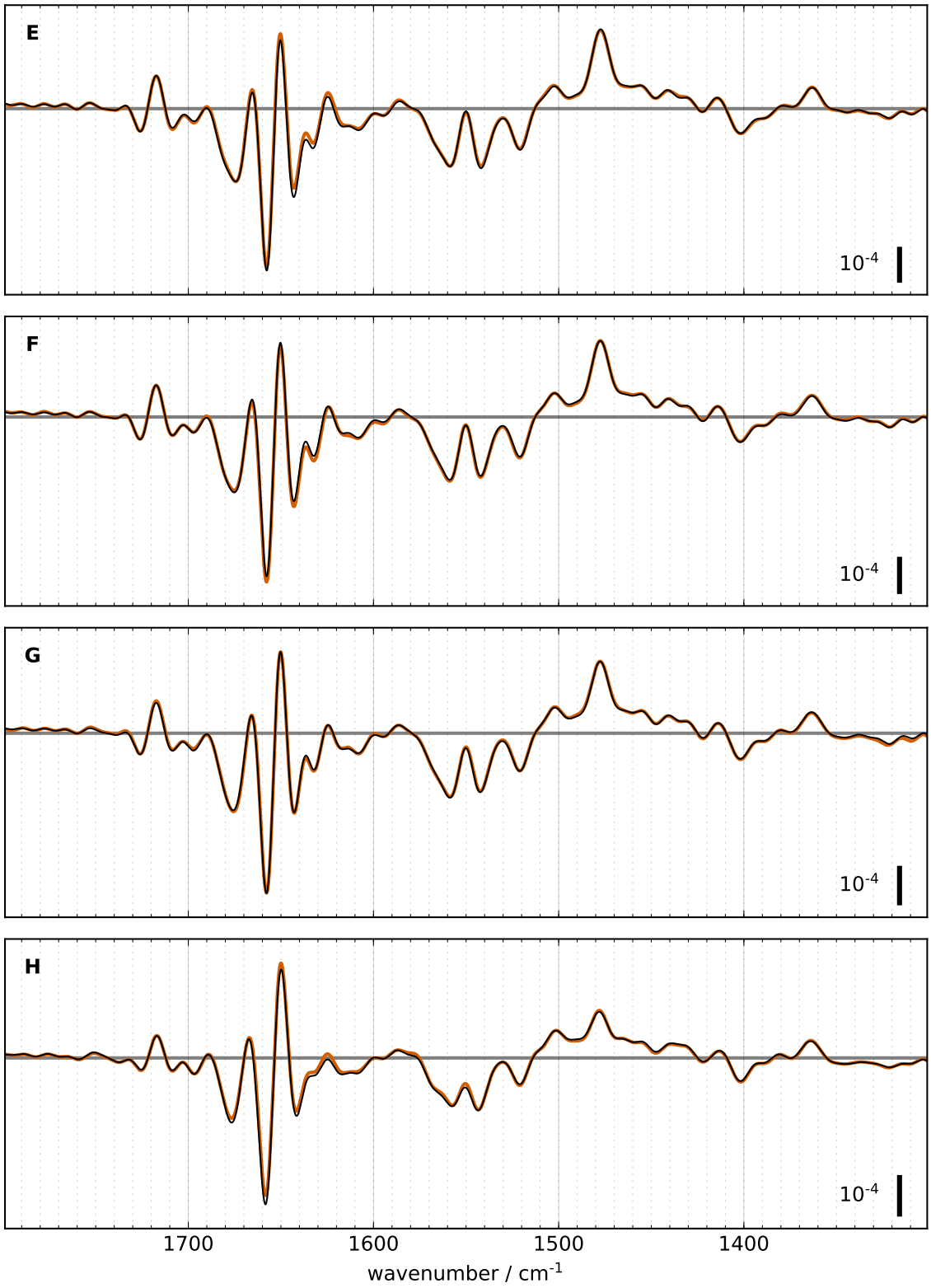

Figure A.22.: Comparison of step-scan difference spectra (thick colored line) with a fit (thin black line) calculated using a fixed set of time constants of the $S_1 \longrightarrow S_2$ transition. A: 9 µs, B: 27 µs, C: 100 µs, D: 300 µs, E: 1 ms, F: 3 ms, G: 10 ms, H: 100 ms after laser flash excitation.

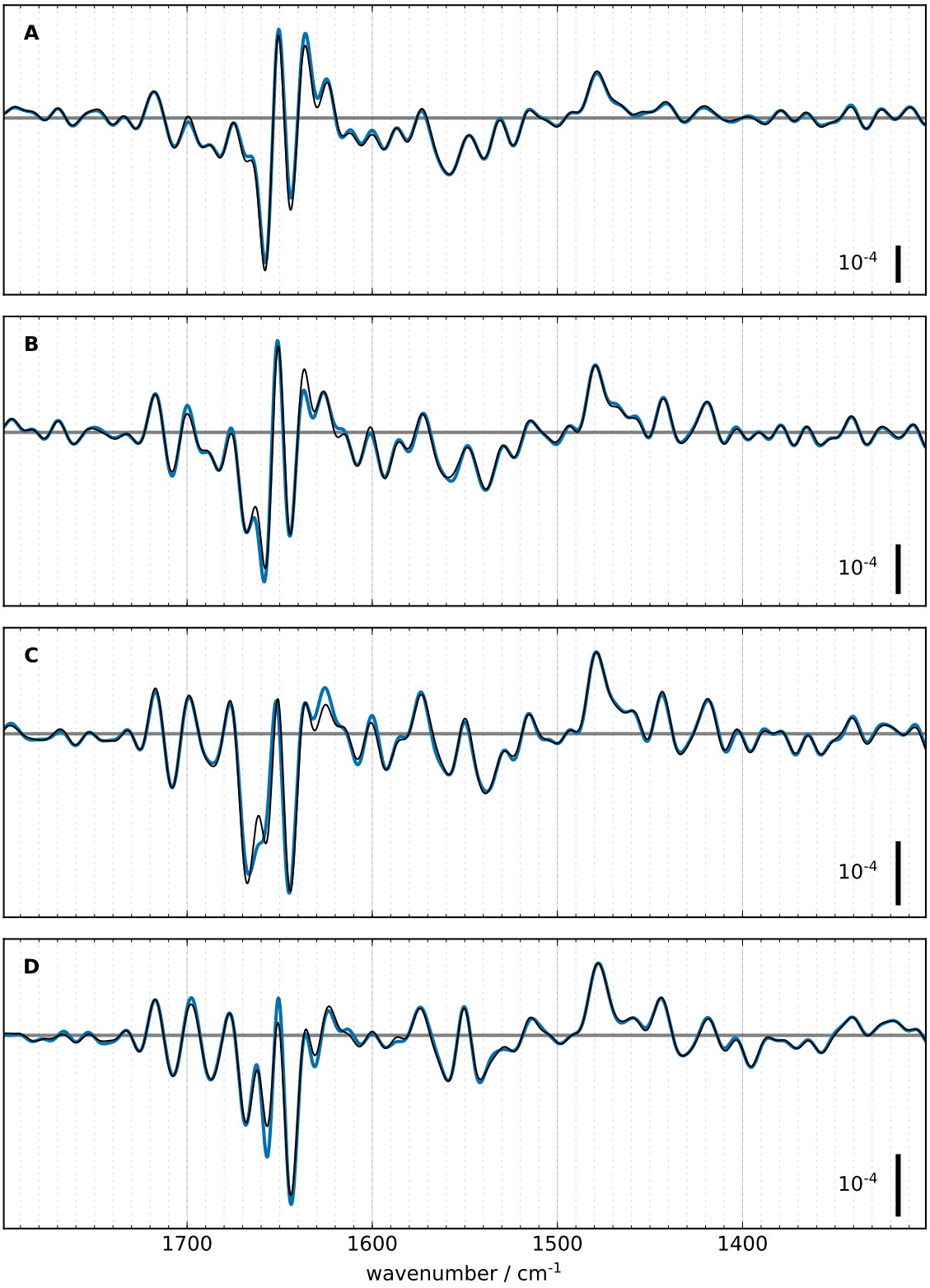

Figure A.23.: Comparison of step-scan difference spectra (thick colored line) with a fit (thin black line) calculated using a fixed set of time constants of the $S_2 \longrightarrow S_3$ transition. A: 9 µs, B: 27 µs, C: 100 µs, D: 300 µs, E: 1 ms, F: 3 ms, G: 10 ms, H: 100 ms after laser flash excitation.

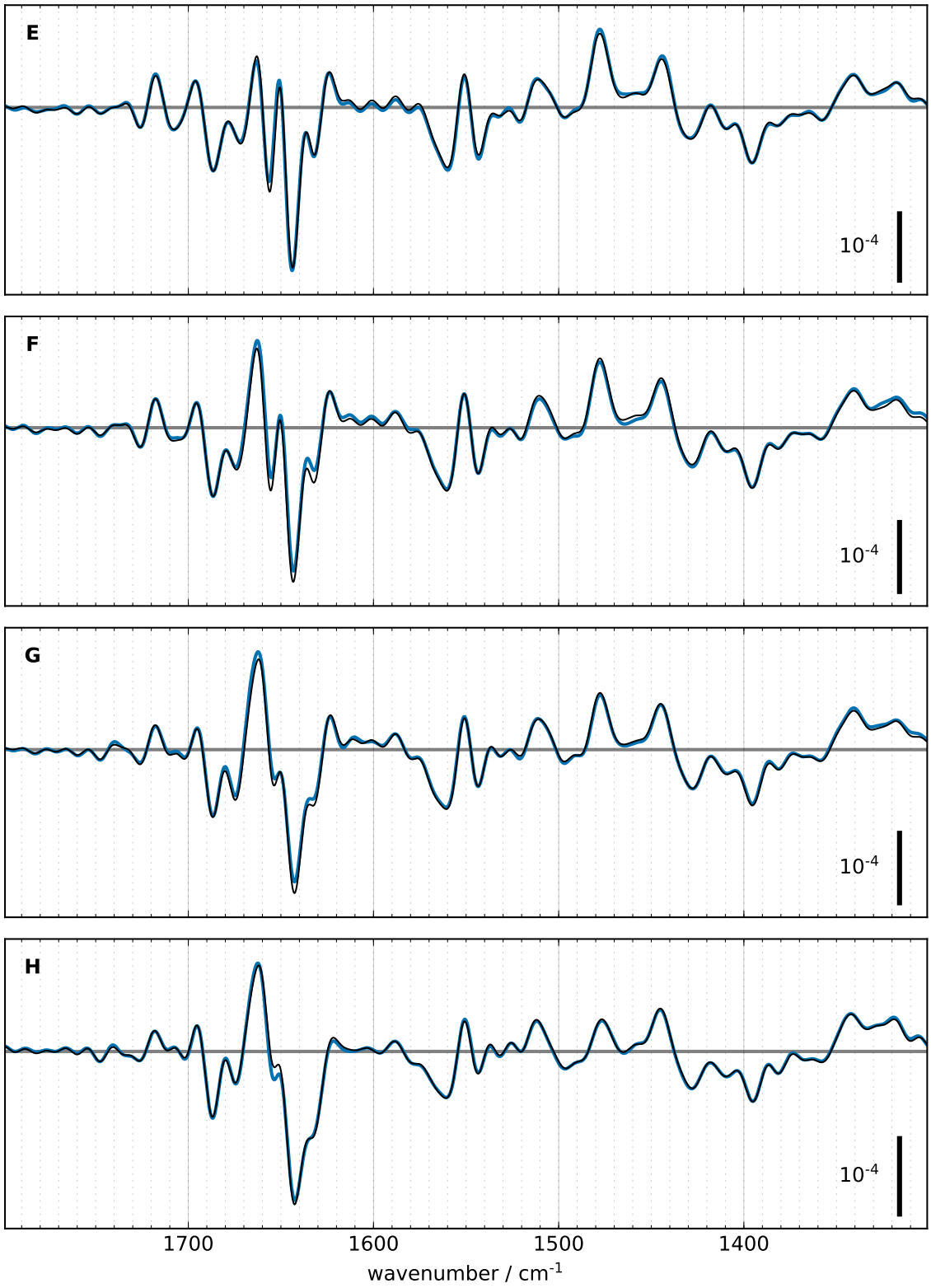

Figure A.24.: Comparison of step-scan difference spectra (thick colored line) with a fit (thin black line) calculated using a fixed set of time constants of the $S_2 \longrightarrow S_3$ transition. A: 9 µs, B: 27 µs, C: 100 µs, D: 300 µs, E: 1 ms, F: 3 ms, G: 10 ms, H: 100 ms after laser flash excitation.

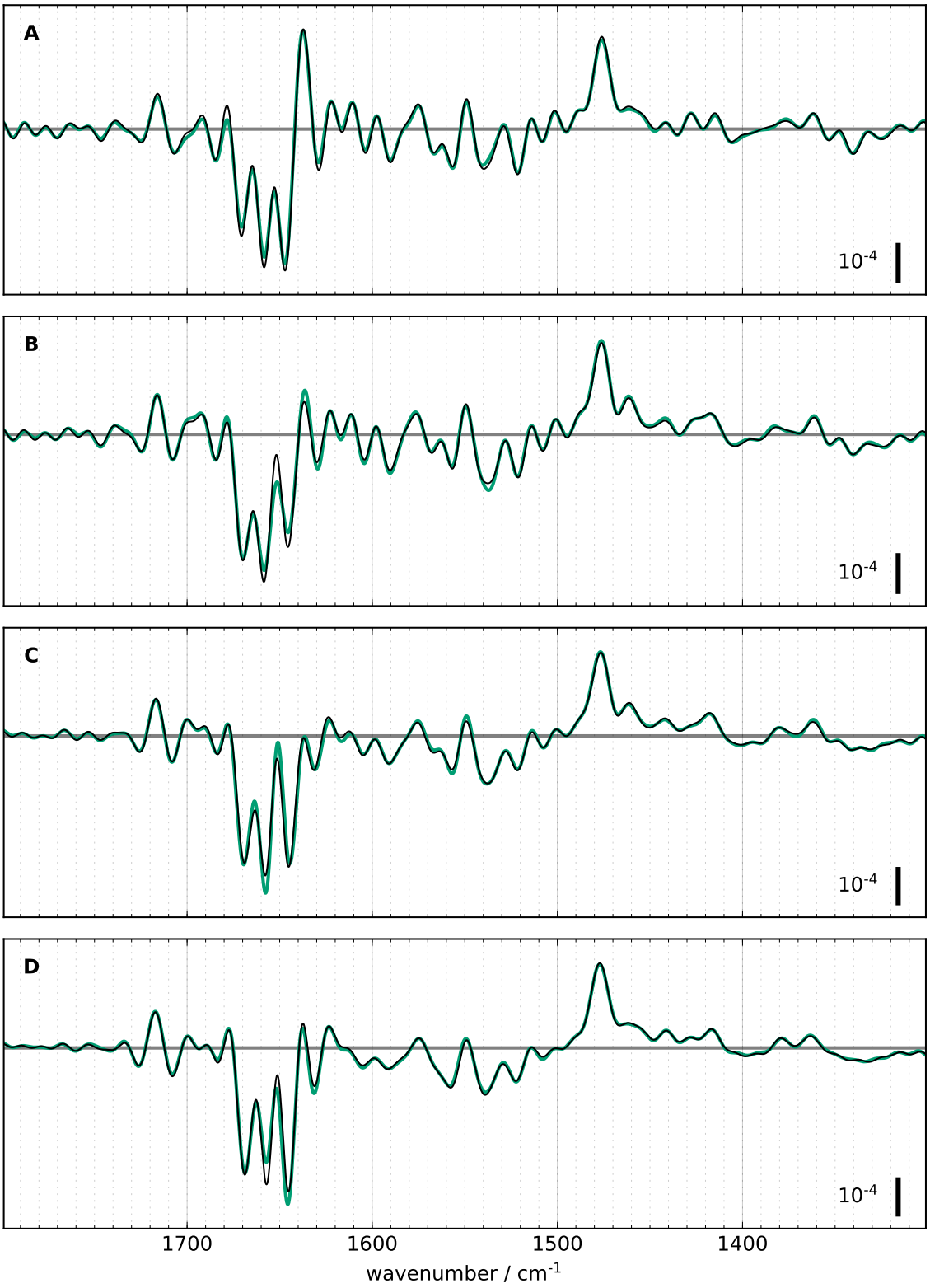

Figure A.25.: Comparison of step-scan difference spectra (thick colored line) with a fit (thin black line) calculated using a fixed set of time constants of the $S_3 \longrightarrow S_0$ transition. A: 9 µs, B: 27 µs, C: 100 µs, D: 300 µs, E: 1 ms, F: 3 ms, G: 10 ms, H: 100 ms after laser flash excitation.

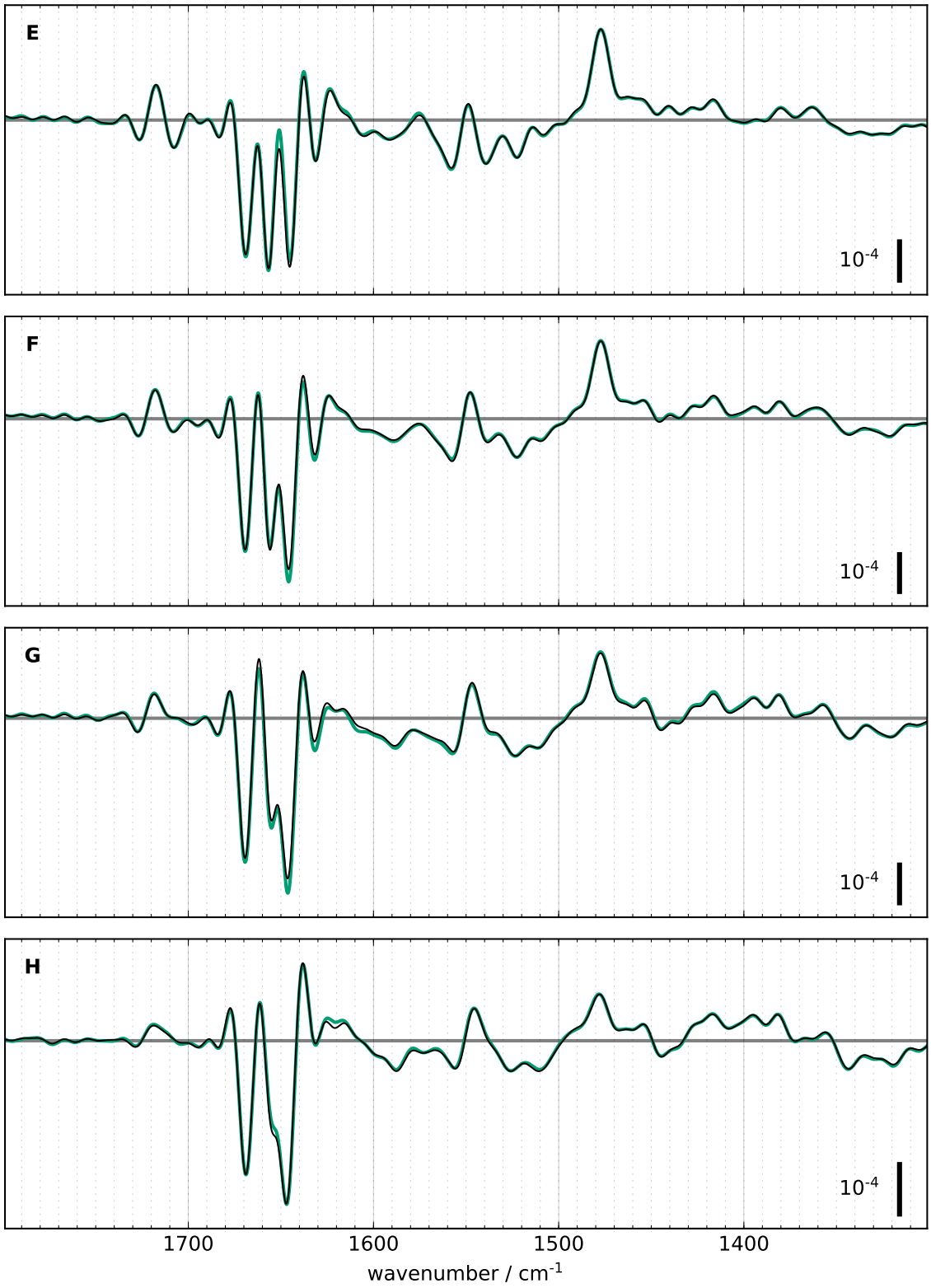

Figure A.26.: Comparison of step-scan difference spectra (thick colored line) with a fit (thin black line) calculated using a fixed set of time constants of the $S_3 \longrightarrow S_0$ transition. A: 9 µs, B: 27 µs, C: 100 µs, D: 300 µs, E: 1 ms, F: 3 ms, G: 10 ms, H: 100 ms after laser flash excitation.

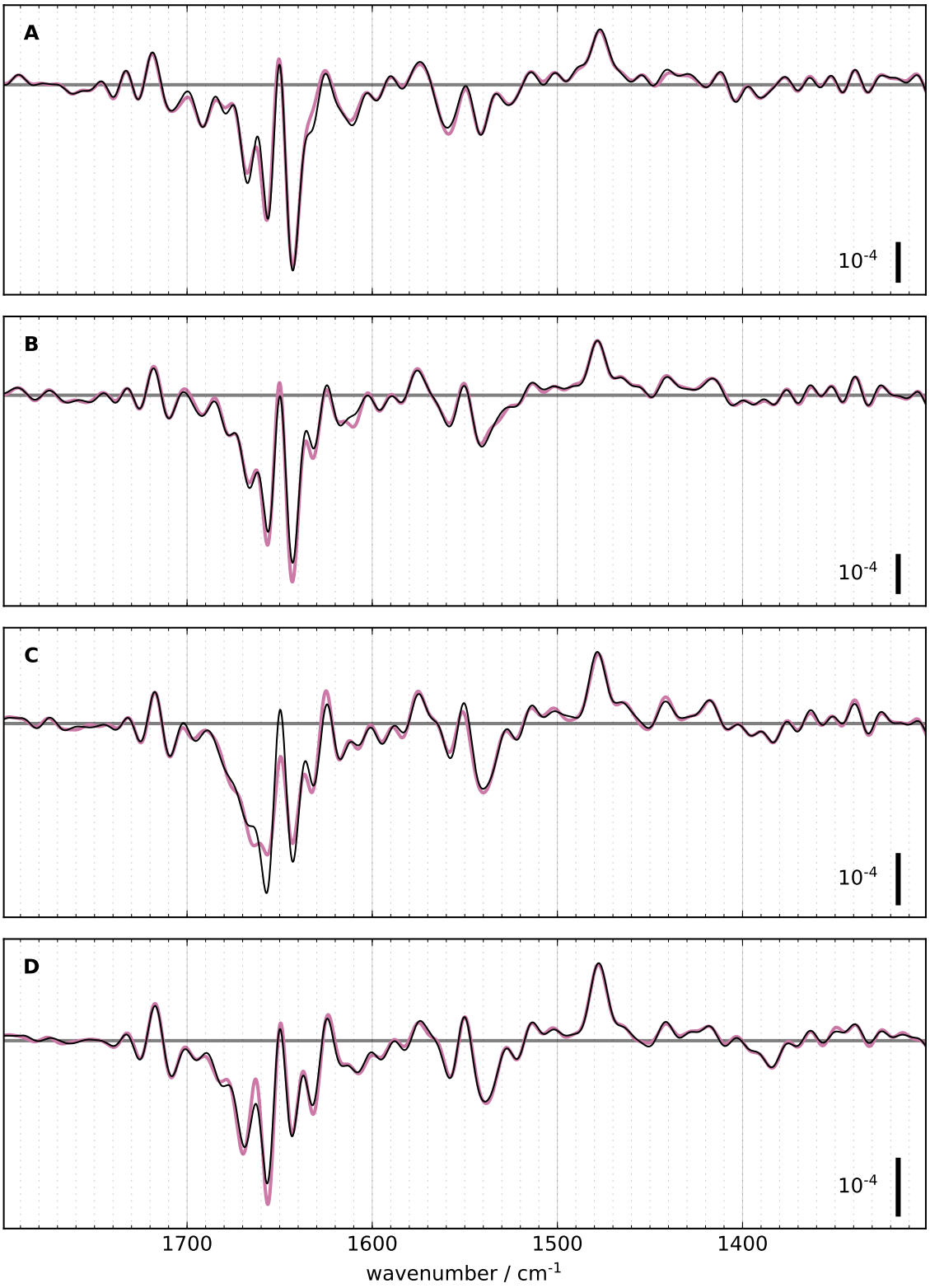

Figure A.27.: Comparison of step-scan difference spectra (thick colored line) with a fit (thin black line) calculated using a fixed set of time constants of the $S_0 \longrightarrow S_1$ transition. A: 9 µs, B: 27 µs, C: 100 µs, D: 300 µs, E: 1 ms, F: 3 ms, G: 10 ms, H: 100 ms after laser flash excitation.

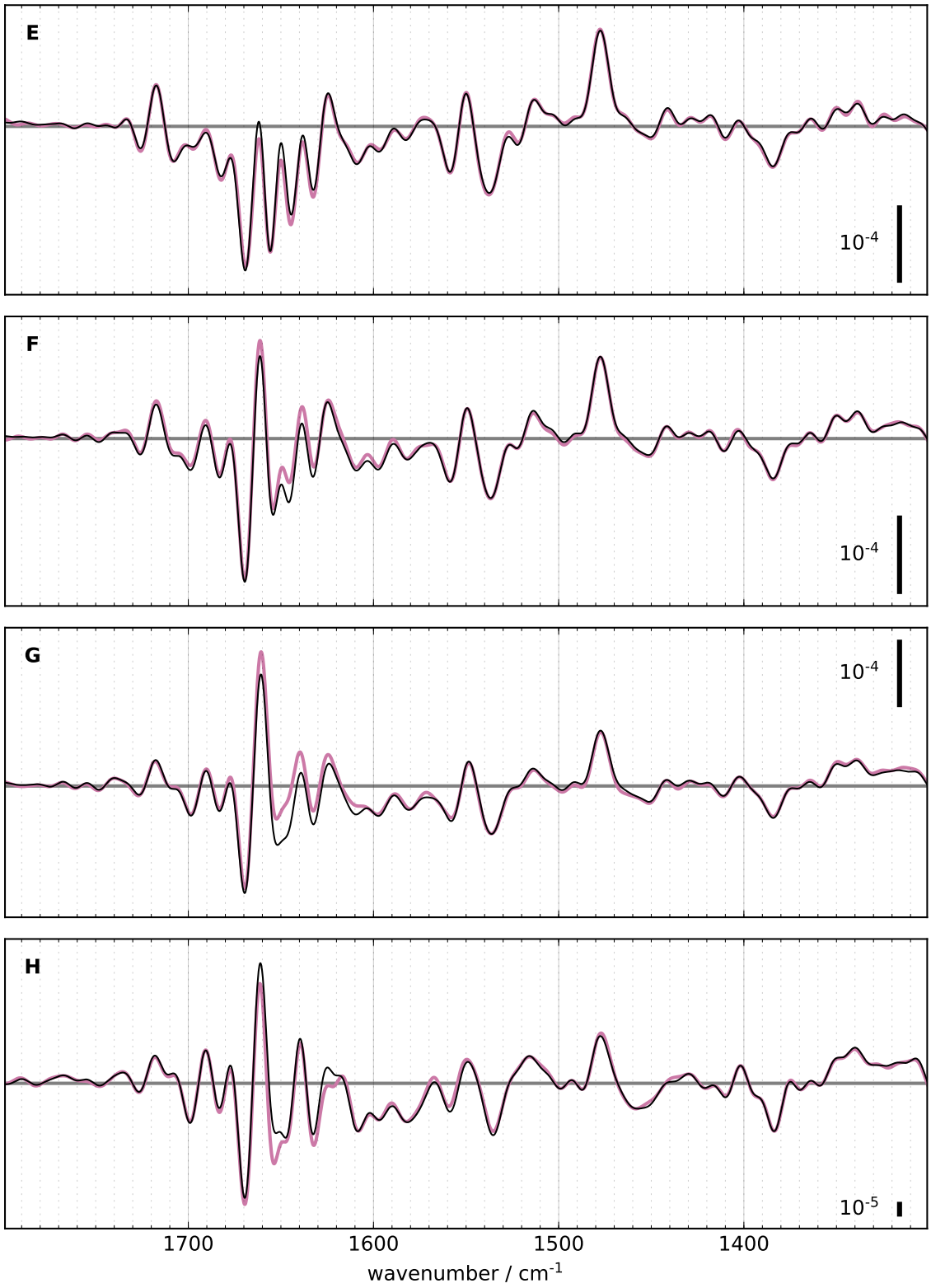

Figure A.28.: Comparison of step-scan difference spectra (thick colored line) with a fit (thin black line) calculated using a fixed set of time constants of the $S_0 \longrightarrow S_1$ transition. A: 9 µs, B: 27 µs, C: 100 µs, D: 300 µs, E: 1 ms, F: 3 ms, G: 10 ms, H: 100 ms after laser flash excitation.

A.8. Comparison of static fits with step-scan data: selected timecourses

Figures A.29-A.31 on pages 289-291 show deconvoluted timecourses at selected wavenumbers and their corresponding fits calculated using a fixed set of time constants. The time constants are given in table 6.4 on page 194. The triangles in the figures resemble the time constants and their amplitudes.

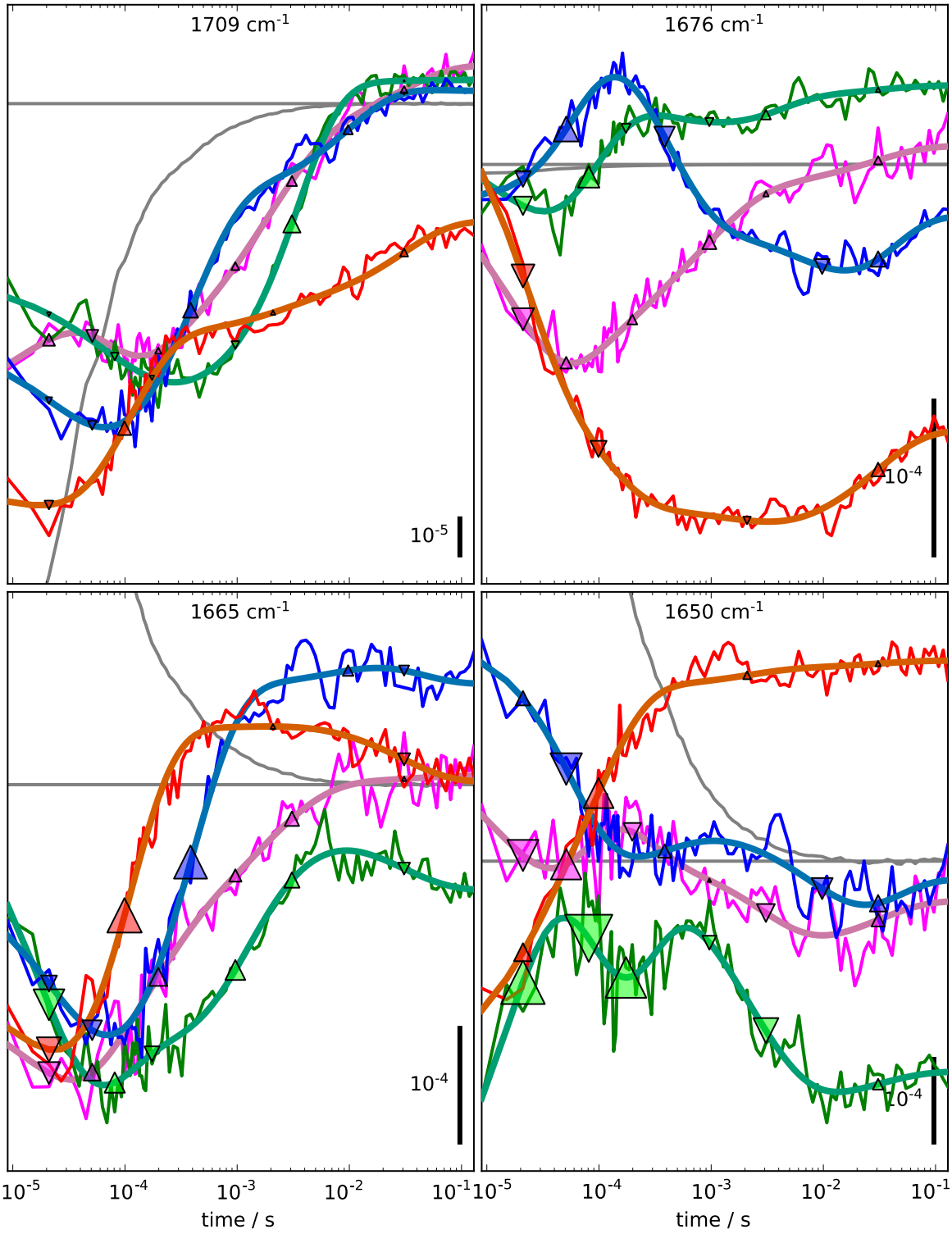

Figure A.29.: Deconvoluted timecourses in H_2O at selected wavenumbers. Red: $S_1 \longrightarrow S_2$, blue: $S_2 \longrightarrow S_3$, green: $S_3 \longrightarrow S_0$, magenta: $S_0 \longrightarrow S_1$. The calculated fits are colored orange, aquamarine, turquoise, and pink respectively. The triangles resemble the time constants used in the fit and their calculated amplitudes. The gray curve resembles the subtracted heat signal.

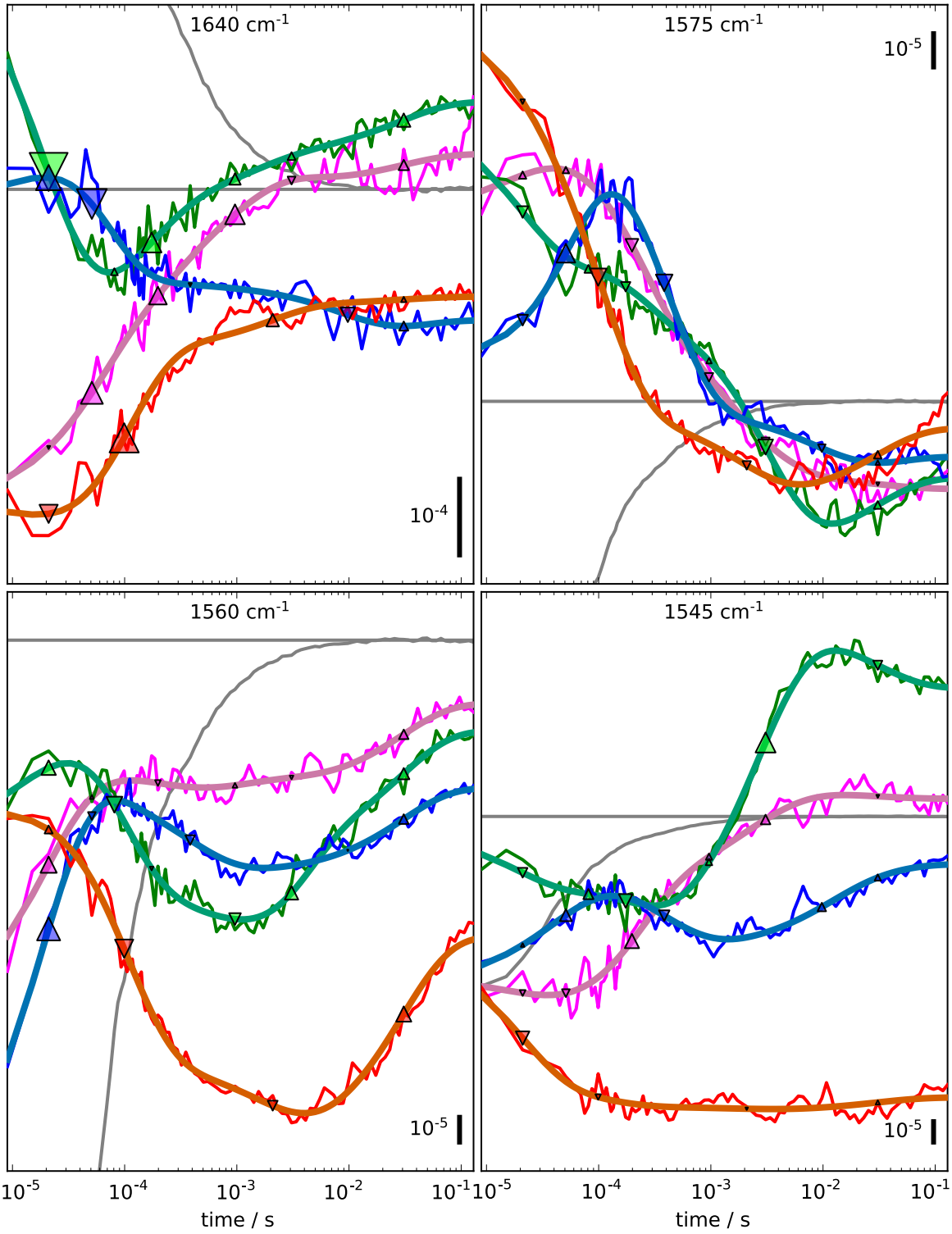

Figure A.30.: Deconvoluted timecourses in H_2O at selected wavenumbers. Red: $S_1 \longrightarrow S_2$, blue: $S_2 \longrightarrow S_3$, green: $S_3 \longrightarrow S_0$, magenta: $S_0 \longrightarrow S_1$. The calculated fits are colored orange, aquamarine, turquoise, and pink respectively. The triangles resemble the time constants used in the fit and their calculated amplitudes. The gray curve resembles the subtracted heat signal.

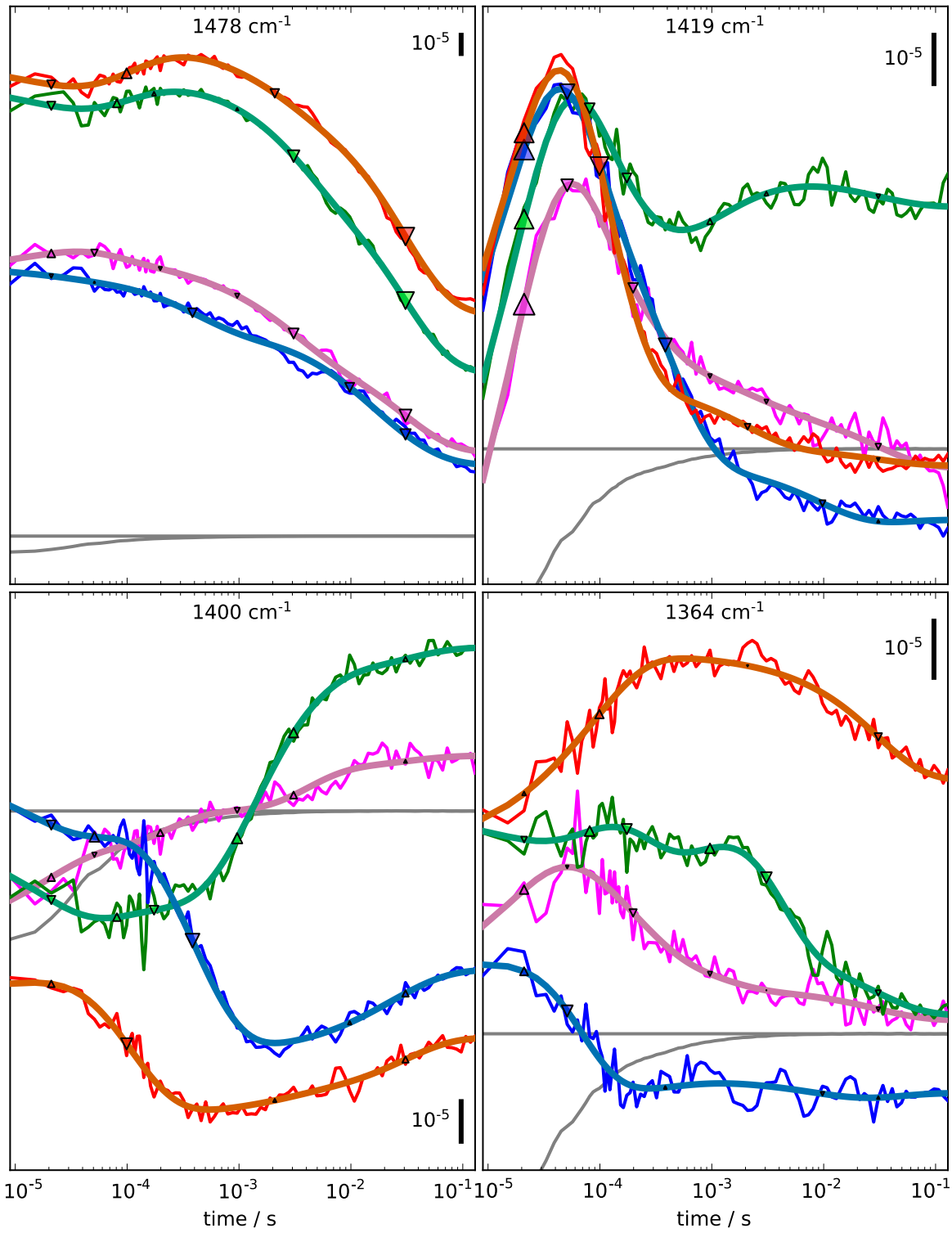

Figure A.31.: Deconvoluted timecourses in H_2O at selected wavenumbers. Red: $S_1 \longrightarrow S_2$, blue: $S_2 \longrightarrow S_3$, green: $S_3 \longrightarrow S_0$, magenta: $S_0 \longrightarrow S_1$. The calculated fits are colored orange, aquamarine, turquoise, and pink respectively. The triangles resemble the time constants used in the fit and their calculated amplitudes. The gray curve resembles the subtracted heat signal.

A.9. Decay associated spectra calculated using a set of fixed time constants

Figures A.32-A.39 on pages 293-300 show decay associated spectra obtained by calculating fits using a fixed set of time constants. The time constants are given in table 6.4 on page 194 and are given in the figure captions. Each panel A, B, C, D, E, or F shows one decay associated spectrum associated with one time constant. Panel O shows the offset resulting from the calculation (colored thick line) and the step-scan difference spectra at the last time point (130 ms after laser flash excitation; black thin line). Panel S shows the sum of all amplitudes and the offset, i.e. $\mathrm{OD}(\nu) = o(\nu) + \sum_i a_i(\nu)$, $i = 1 \ldots 6$ (colored thick line) and the step-scan difference spectra at the first time point (9 µs; black thin line).

The offset of the $S_0 \longrightarrow S_1$ transition fit calculation does not fit the value recorded 130 ms after laser flash excitation in the amide I region (panel O in figure A.39 on page 300). This is caused by a very late phase with a time constant slower than 50 ms and a very small amplitude, which can be seen in the corresponding timecourses at 1640 cm^{-1} and 1650 cm^{-1} shown in figures A.29 and A.30 on pages 289 and 290 respectively. The amplitude of this very late phase is very small, and this phase is restricted to the amide I region only.

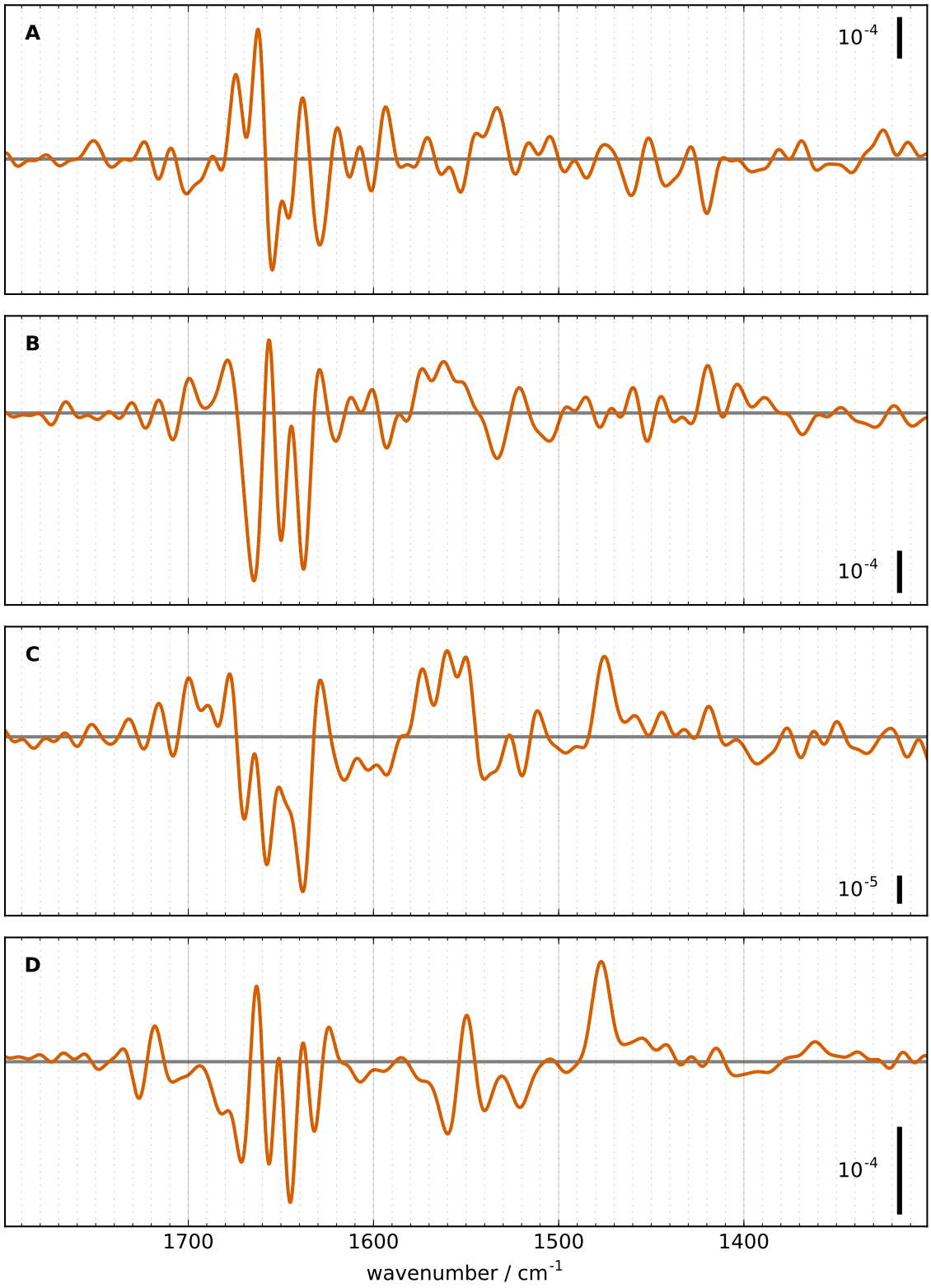

Figure A.32.: A-D: Decay associated spectra obtained by calculating fits using a fixed set of time constants for the $S_1 \longrightarrow S_2$ transition. A: 20 µs, B: 100 µs, C: 2 ms, D: 30 ms. O: offset (thick colored line) and difference spectrum 130 ms after laser flash excitation (thin black line). S: sum of all wavenumber-dependent amplitudes and the offset (thick colored line) and difference spectrum 9 µs after laser flash excitation (thin black line).

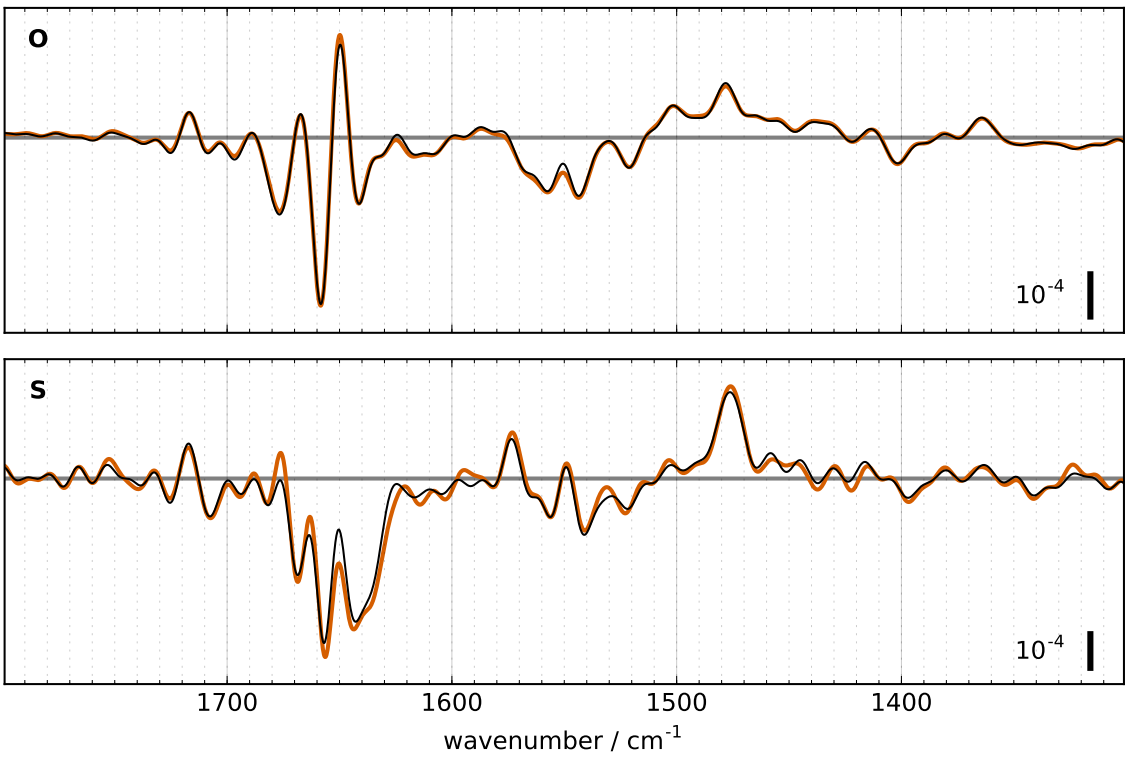

Figure A.33.: A-D: Decay associated spectra obtained by calculating fits using a fixed set of time constants for the $S_1 \longrightarrow S_2$ transition. A: 20 µs, B: 100 µs, C: 2 ms, D: 30 ms. O: offset (thick colored line) and difference spectrum 130 ms after laser flash excitation (thin black line). S: sum of all wavenumber-dependent amplitudes and the offset (thick colored line) and difference spectrum 9 µs after laser flash excitation (thin black line).

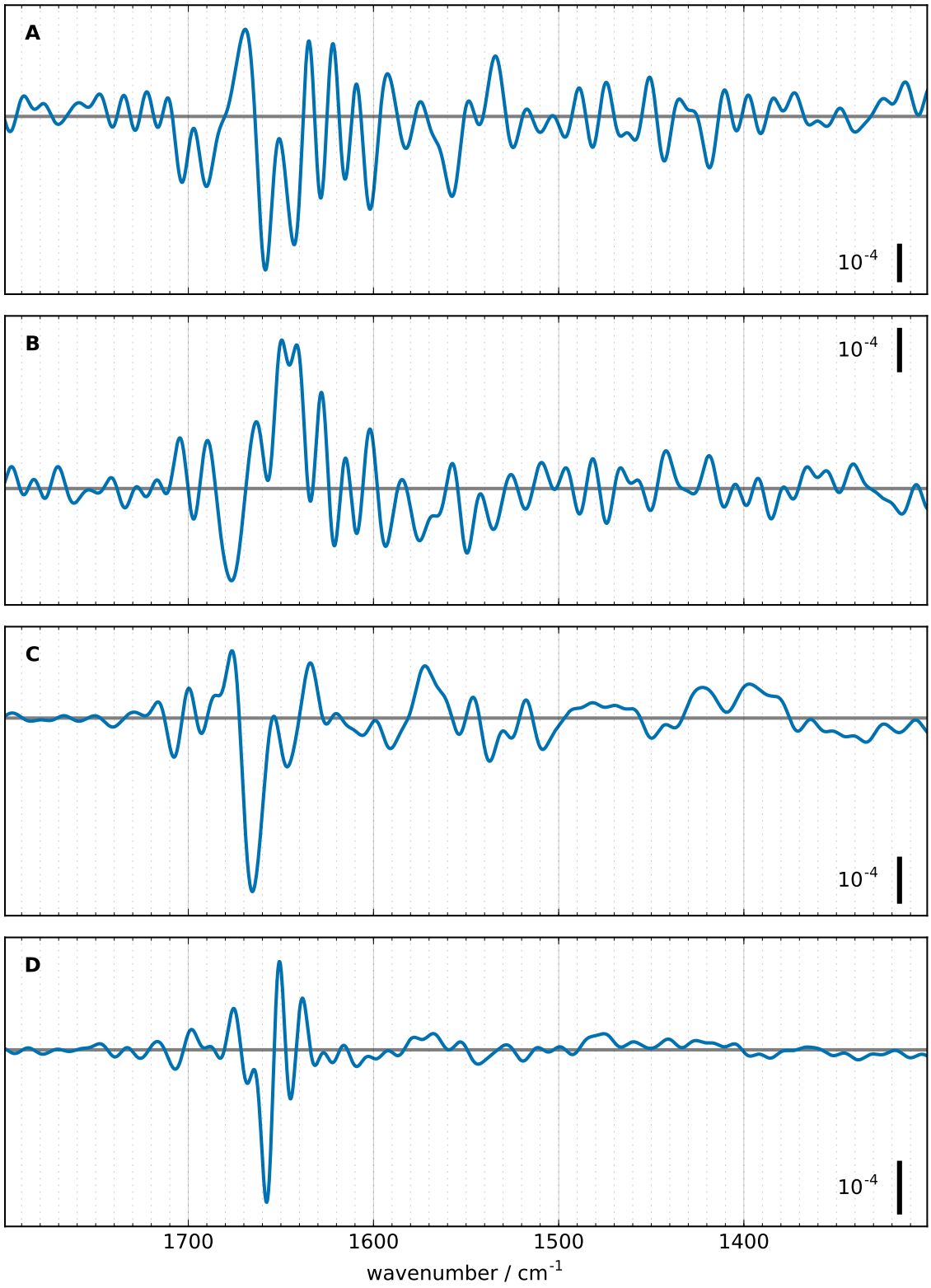

Figure A.34.: A-E: Decay associated spectra obtained by calculating fits using a fixed set of time constants for the $S_2 \longrightarrow S_3$ transition. A: 20 µs, B: 50 µs, C: 390 µs, D: 10 ms, E: 30 ms. O: offset (thick colored line) and difference spectrum 130 ms after laser flash excitation (thin black line). S: sum of all wavenumber-dependent amplitudes and the offset (thick colored line) and difference spectrum 9 µs after laser flash excitation (thin black line).

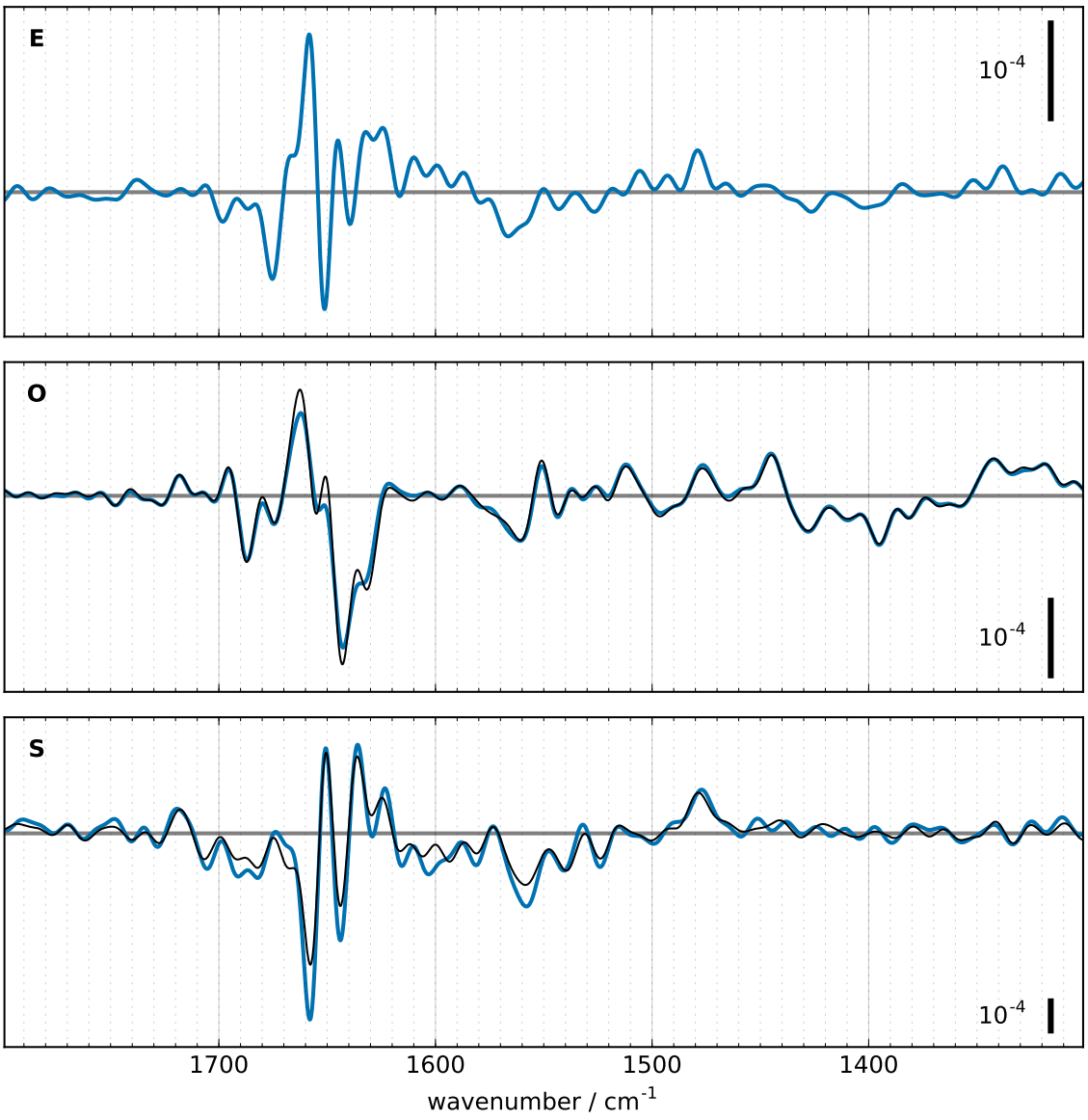

Figure A.35.: A-E: Decay associated spectra obtained by calculating fits using a fixed set of time constants for the $S_2 \longrightarrow S_3$ transition. A: 20 µs, B: 50 µs, C: 390 µs, D: 10 ms, E: 30 ms. O: offset (thick colored line) and difference spectrum 130 ms after laser flash excitation (thin black line). S: sum of all wavenumber-dependent amplitudes and the offset (thick colored line) and difference spectrum 9 µs after laser flash excitation (thin black line).

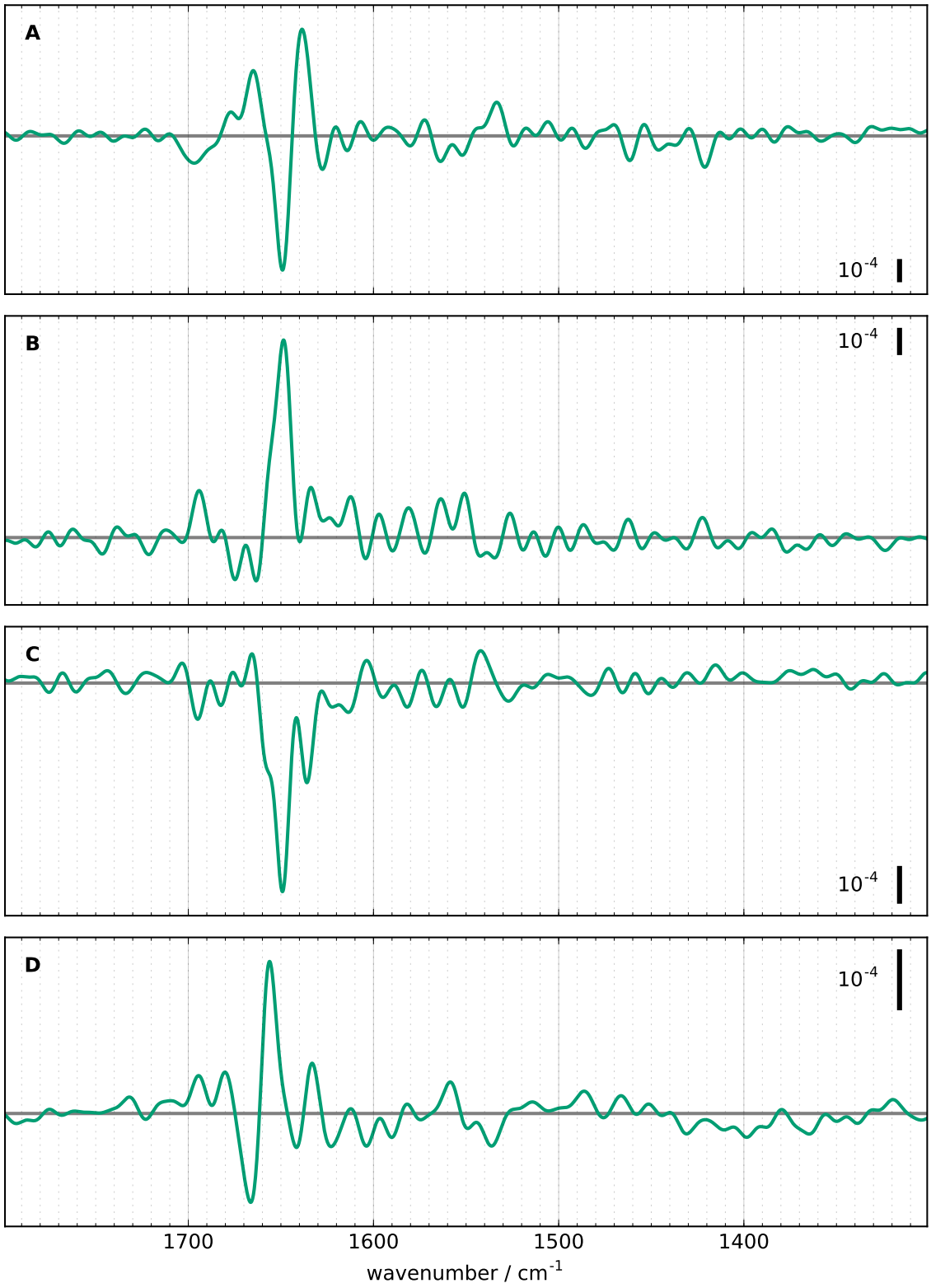

Figure A.36.: A-F: Decay associated spectra obtained by calculating fits using a fixed set of time constants for the $S_3 \longrightarrow S_0$ transition. A: 20 µs, B: 80 µs, C: 170 µs, D: 1 ms, E: 3 ms, F: 30 ms. O: offset (thick colored line) and difference spectrum 130 ms after laser flash excitation (thin black line). S: sum of all wavenumber-dependent amplitudes and the offset (thick colored line) and difference spectrum 9 µs after laser flash excitation (thin black line).

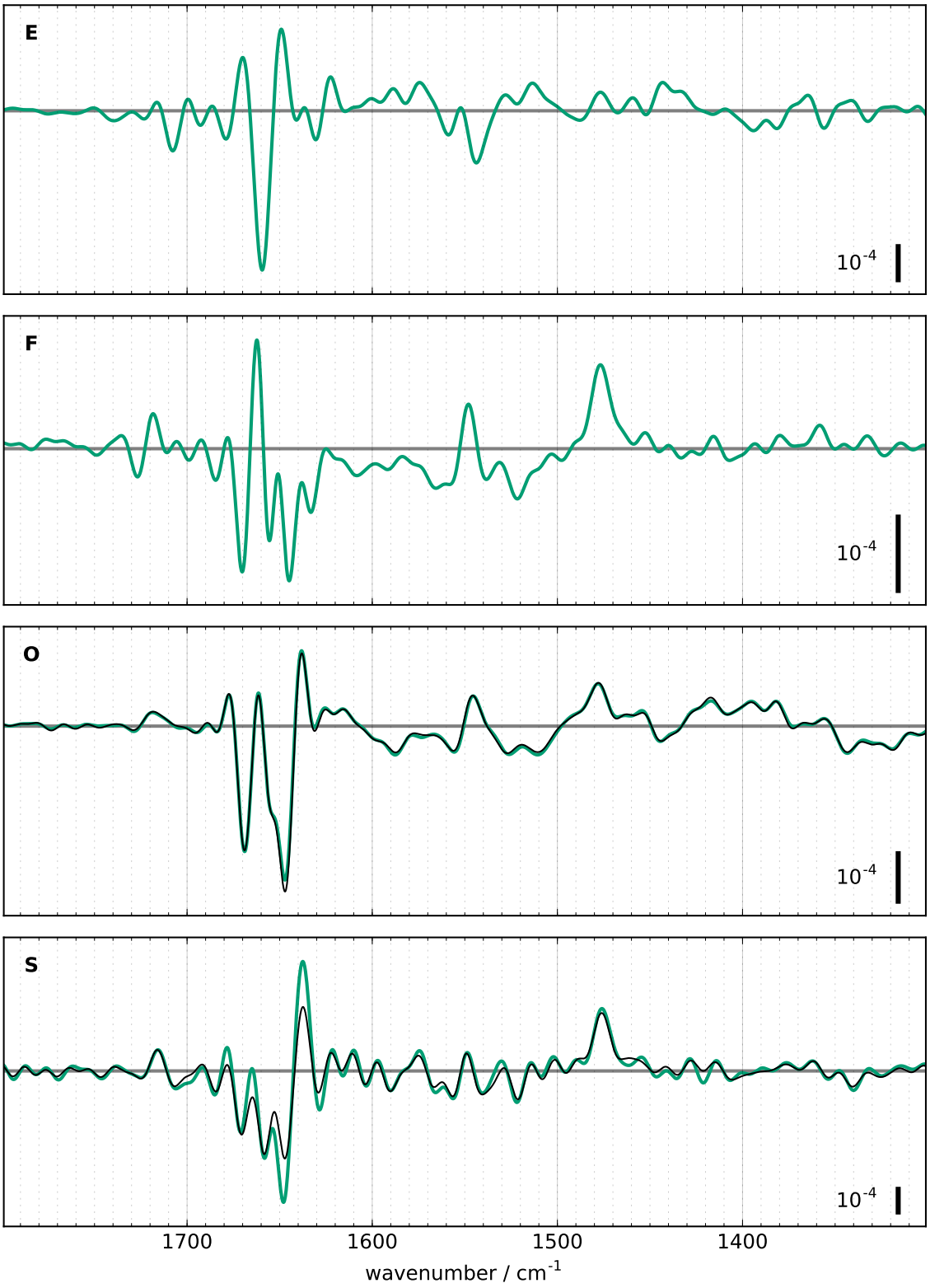

Figure A.37.: A-F: Decay associated spectra obtained by calculating fits using a fixed set of time constants for the $S_3 \longrightarrow S_0$ transition. A: 20 µs, B: 80 µs, C: 170 µs, D: 1 ms, E: 3 ms, F: 30 ms. O: offset (thick colored line) and difference spectrum 130 ms after laser flash excitation (thin black line). S: sum of all wavenumber-dependent amplitudes and the offset (thick colored line) and difference spectrum 9 µs after laser flash excitation (thin black line).

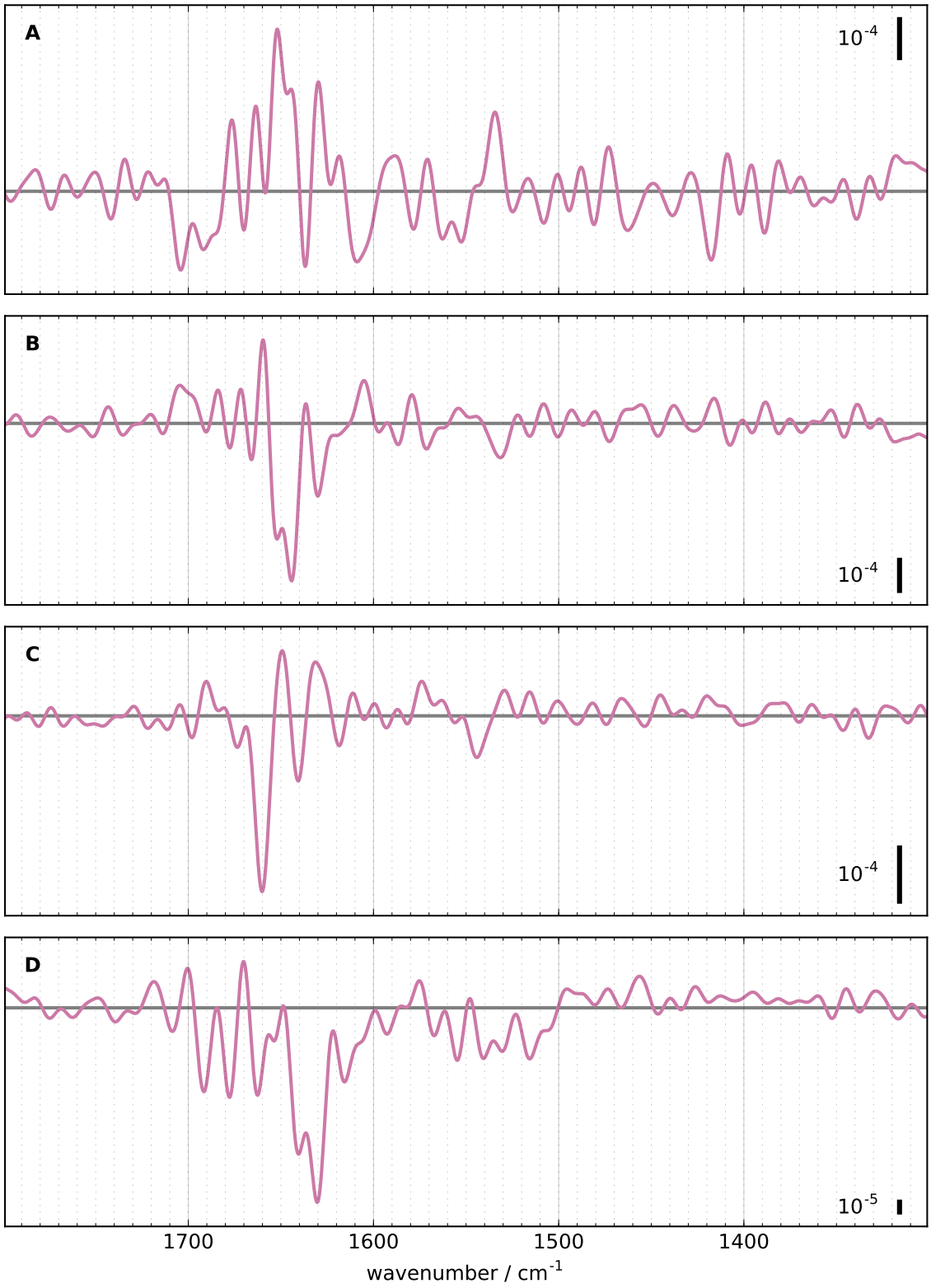

Figure A.38.: A-F: Decay associated spectra obtained by calculating fits using a fixed set of time constants for the $S_0 \longrightarrow S_1$ transition. A: 20 µs, B: 50 µs, C: 200 µs, D: 1 ms, E: 3 ms, F: 30 ms. O: offset (thick colored line) and difference spectrum 130 ms after laser flash excitation (thin black line). S: sum of all wavenumber-dependent amplitudes and the offset (thick colored line) and difference spectrum 9 µs after laser flash excitation (thin black line).

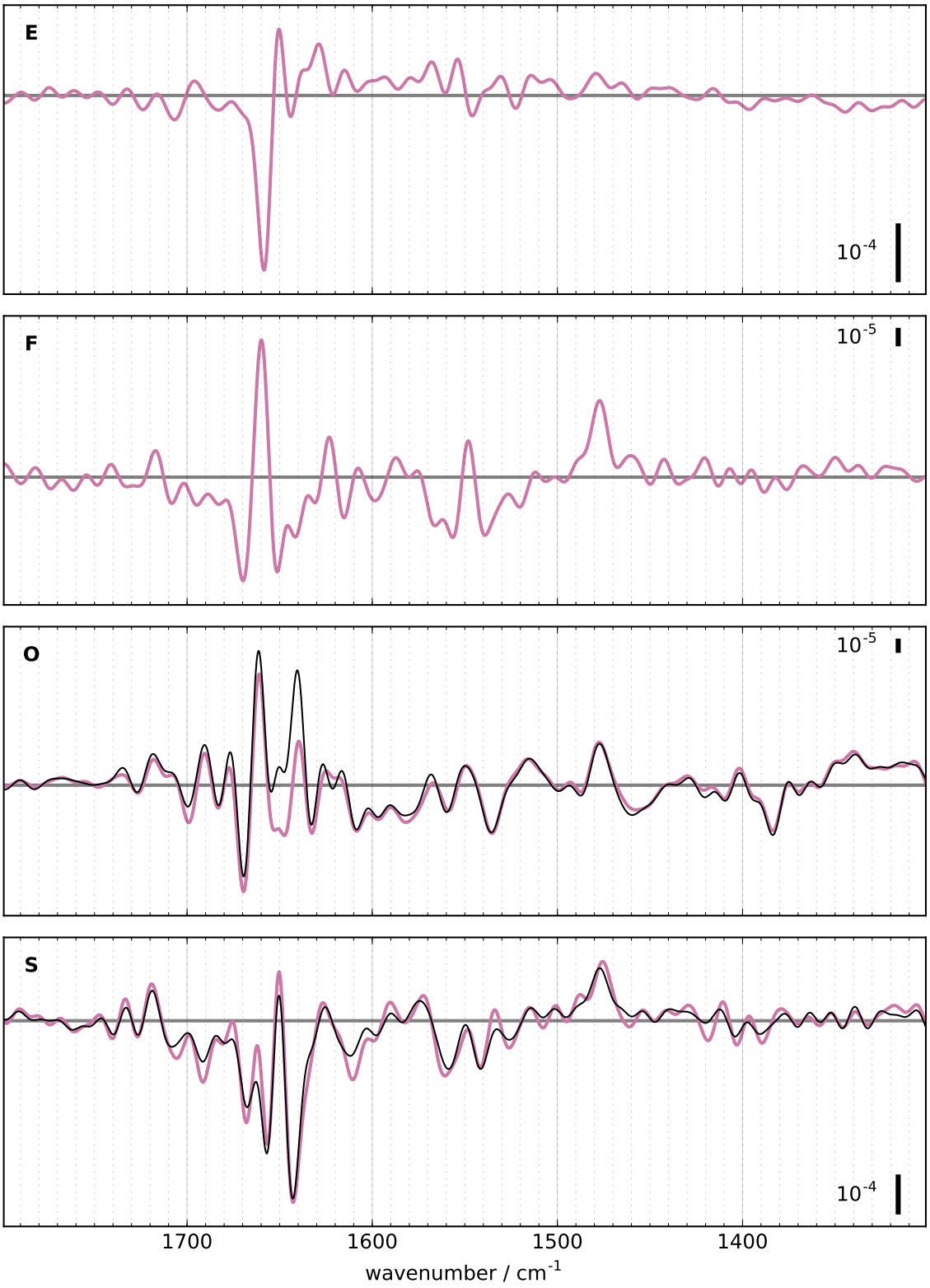

Figure A.39.: A-F: Decay associated spectra obtained by calculating fits using a fixed set of time constants for the $S_0 \longrightarrow S_1$ transition. A: 20 µs, B: 50 µs, C: 200 µs, D: 1 ms, E: 3 ms, F: 30 ms. O: offset (thick colored line) and difference spectrum 130 ms after laser flash excitation (thin black line). S: sum of all wavenumber-dependent amplitudes and the offset (thick colored line) and difference spectrum 9 µs after laser flash excitation (thin black line).

A.10. Timecourses before and after deconvolution of step-scan data

Figures A.40-A.42 on pages 302-304 demonstrate the effect of deconvolution by showing timecourses at selected wavenumbers. On the left hand side, the original, convoluted data is shown. On the right hand side, the deconvoluted data is shown. For a certain wavenumber, the scales at the left and right hand sides are the same. In the original data the fifth flash is shown as thin orange line. The first to forth flash are shown in orange, aquamarine, turquoise, and pink respectively.

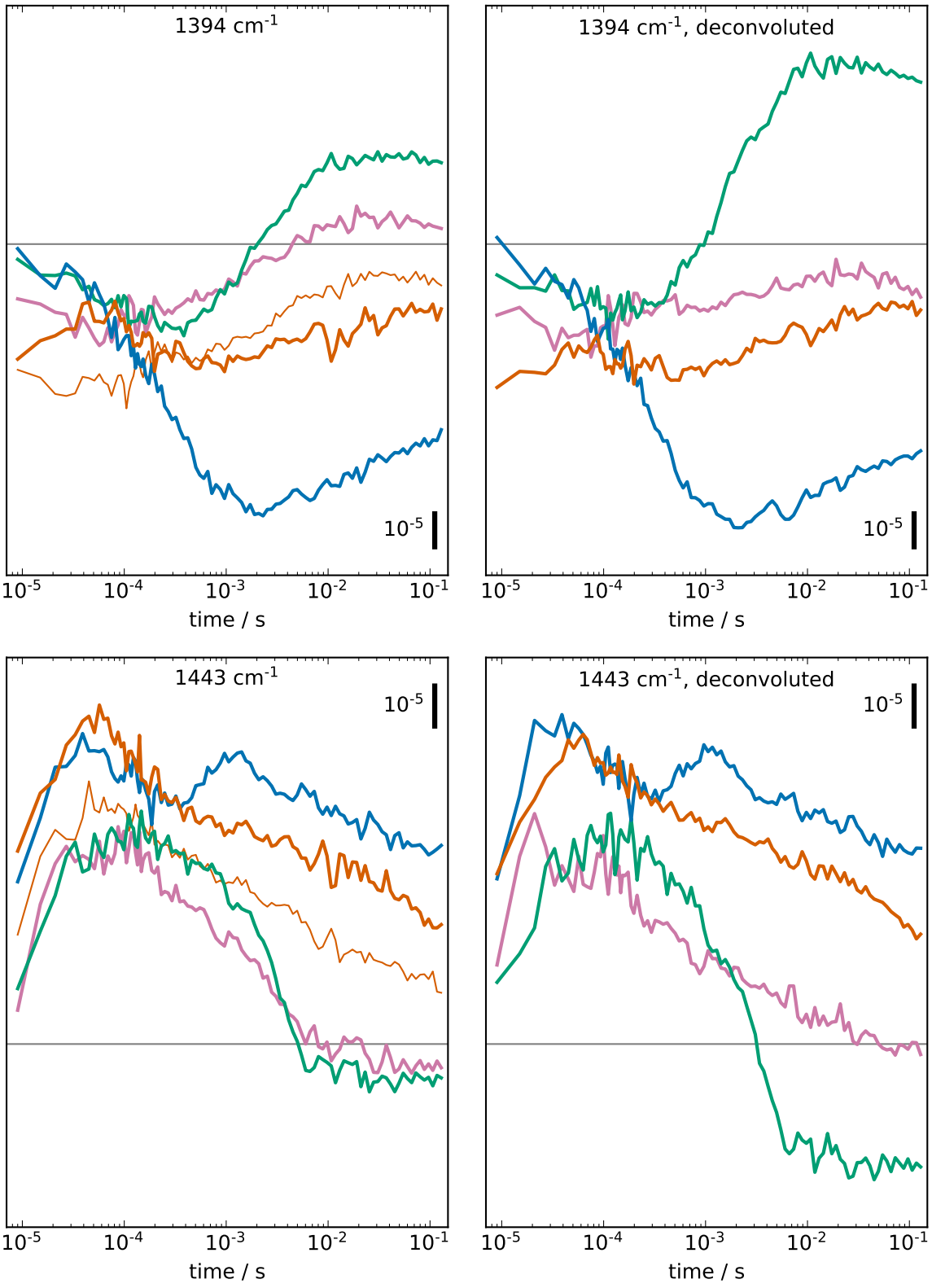

Figure A.40.: Original (left) and deconvoluted (right) timecourses in H_2O at selected wavenumbers. Left: orange: first (thick line) and fifth (thin line) flash, aquamarine: second flash, turquoise: third flash, pink: fourth flash. Right: orange: $S_1 \longrightarrow S_2$, aquamarine: $S_2 \longrightarrow S_3$, turquoise: $S_3 \longrightarrow S_0$, pink: $S_0 \longrightarrow S_1$.

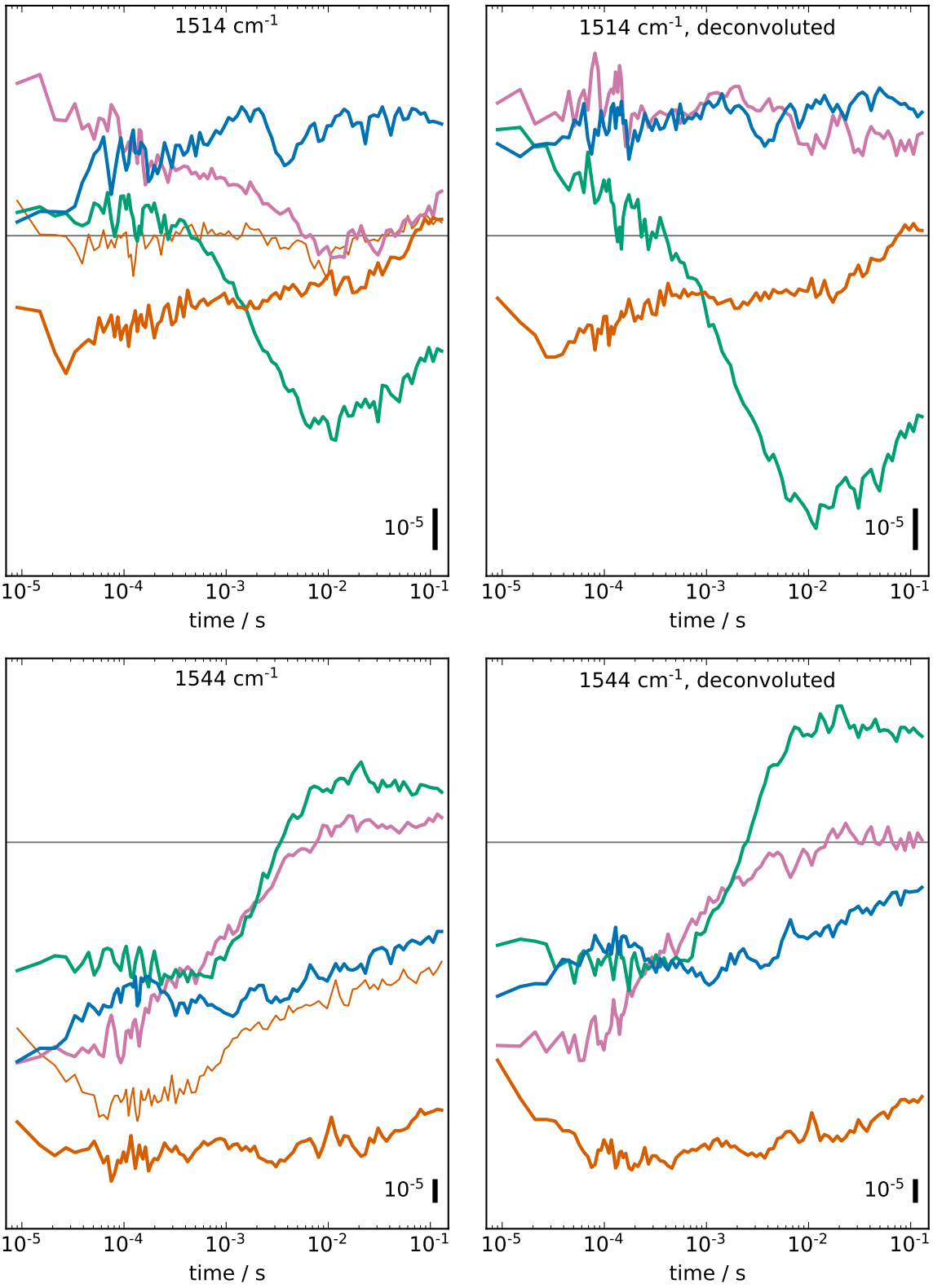

Figure A.41.: Original (left) and deconvoluted (right) timecourses in H_2O at selected wavenumbers. Left: orange: first (thick line) and fifth (thin line) flash, aquamarine: second flash, turquoise: third flash, pink: fourth flash. Right: orange: $S_1 \longrightarrow S_2$, aquamarine: $S_2 \longrightarrow S_3$, turquoise: $S_3 \longrightarrow S_0$, pink: $S_0 \longrightarrow S_1$.

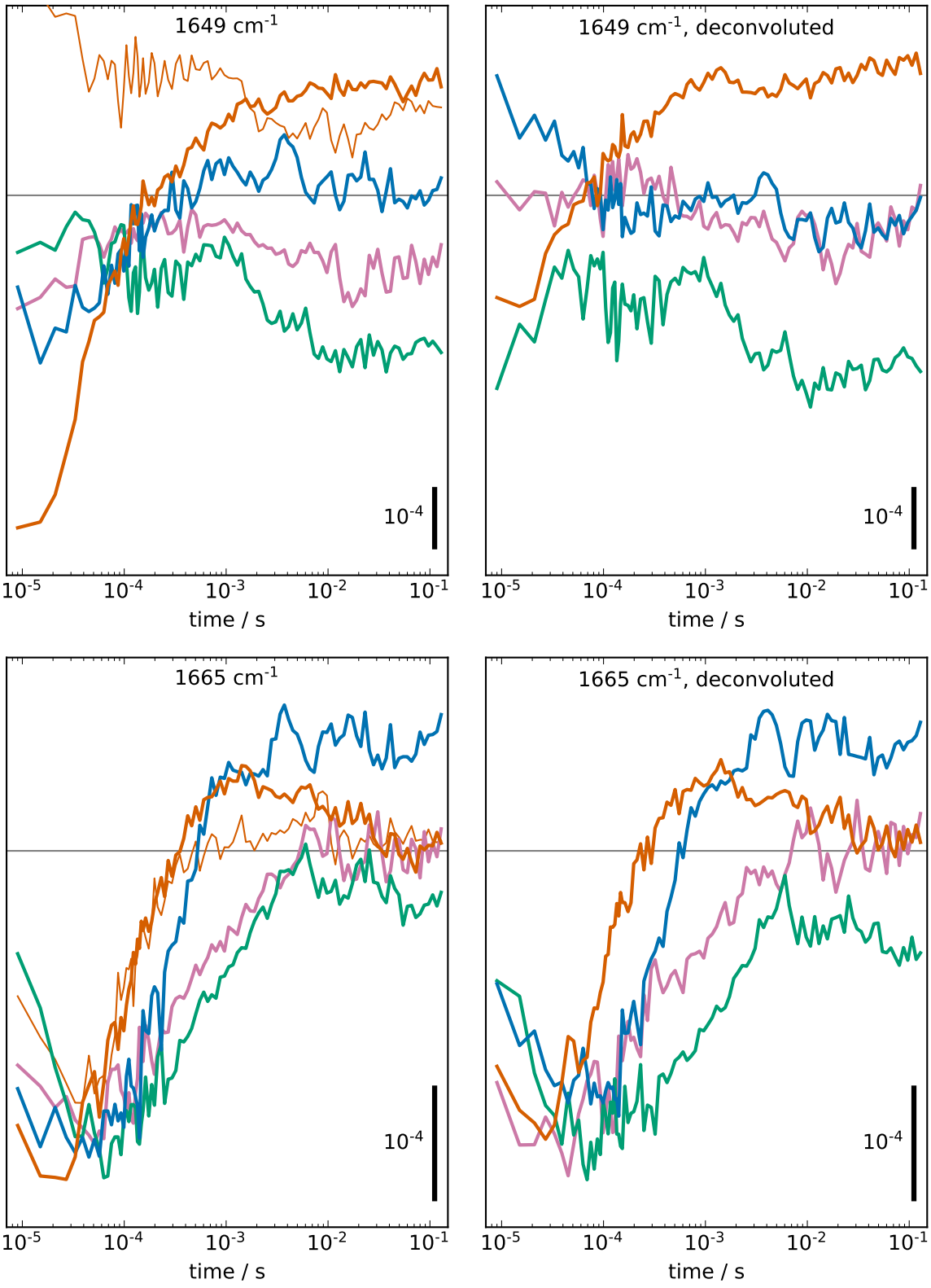

Figure A.42.: Original (left) and deconvoluted (right) timecourses in H_2O at selected wavenumbers. Left: orange: first (thick line) and fifth (thin line) flash, aquamarine: second flash, turquoise: third flash, pink: fourth flash. Right: orange: $S_1 \longrightarrow S_2$, aquamarine: $S_2 \longrightarrow S_3$, turquoise: $S_3 \longrightarrow S_0$, pink: $S_0 \longrightarrow S_1$.

Selbstständigkeitserklärung

Ich erkläre gegenüber der Freien Universität Berlin, dass ich die vorliegende Doktorarbeit selbstständig und ohne Benutzung anderer als der angegebenen Quellen und Hilfsmittel angefertigt habe. Die vorliegende Arbeit ist frei von Plagiaten. Alle Ausführungen, die wörtlich oder inhaltlich aus anderen Schriften entnommen sind, habe ich als solche kenntlich gemacht. Diese Arbeit wurde in gleicher oder ähnlicher Form noch bei keiner anderen Universität als Prüfungsleistung eingereicht und ist auch noch nicht veröffentlicht.